

283

AIO-601364

RADC-TDR-64-25, Vol I



RADAR REFLECTIVITY MEASUREMENTS SYMPOSIUM

TECHNICAL DOCUMENTARY REPORT NO. RADC-TDR-64-25

April 1964

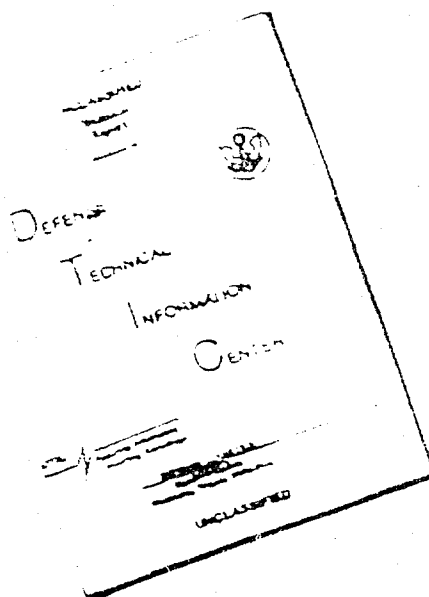
Space Surveillance and Instrumentation Branch
Rome Air Development Center
Research and Technology Division
Air Force Systems Command
Griffiss Air Force Base, New York

Project No. 6503

REPRODUCED BY
NATIONAL TECHNICAL
INFORMATION SERVICE
U.S. DEPARTMENT OF COMMERCE
SPRINGFIELD, VA 22161

3540

DISCLAIMER NOTICE



THIS DOCUMENT IS BEST
QUALITY AVAILABLE. THE COPY
FURNISHED TO DTIC CONTAINED
A SIGNIFICANT NUMBER OF
PAGES WHICH DO NOT
REPRODUCE LEGIBLY.

REPRODUCED FROM
BEST AVAILABLE COPY

AVAILABILITY NOTICE

Qualified requesters may obtain copies from the Defense Documentation Center, (TISIR), Cameron Station, Alexandria, Va., 22314.

Defense Documentation Center release to Office of Technical Services is authorized.

Responsibility for the contents of papers presented at the Symposium and published herein rests solely upon the authors and not upon RADC or MIT, Lincoln Laboratory.

FOREWORD

The subject to be discussed at this Symposium is perhaps typical of many new specialties, most of them non-existent in their present form only a decade or two ago. Created by the recent incredibly rapid expansion of science and technology, these can be likened to sparks flying in all directions from an exploding firecracker. The lifetime of sparks is usually short, but while they last, it may be worthwhile looking in detail at this or that one in hopes of learning not only about it, but also others like it.

Radar reflectivity measurements typically have strong ties to the more general technology of electromagnetism and optics, and to such established specialties as antenna measurements and optical scattering. Like many other technologies with which it has teamed to create new and spectacular devices and systems, it has received concentrated, almost feverish attention simultaneously by many groups of workers. Unfortunately, this single minded concentration, which has been responsible for many individual successes, has also, in many cases, prevented the persons involved from engaging in dialogue or other forms of communication with colleagues engaged in parallel endeavors. Considerations of official or commercial secrecy also seem to have played a negative role occasionally in inhibiting beneficial discussion and exchanges of opinions and results.

In surveying recent history, one might argue that the experimental technology of radar reflectivity measurements has, in the United States, experienced at least two peaks of activity. Broadly speaking, the first peak coincided with our rearmament following the beginning of the Korean War, when weapons systems centered on aircraft posed many new technical problems. The second peak was triggered about ten years later by the introduction of complex missile systems, especially of the ballistic variety. The subsequent appearance of satellites, spacecraft, and a growing interest in the exploration of celestial objects (only recently within the exclusive domain of the astronomer) may serve to extend this second epoch of radar reflectivity technology; it may even introduce a third era.

Whether to conclude a chapter, then, or perhaps even a book in the history of a highly specialized technology, or to aid in erecting a springboard for a new departure, this seems to some of us a propitious time to "stop, look, and listen." That is why a very capable and distinguished group drawn from the numerous industrious workers in the field consented some time ago to join in organizing the attempt at technical mass-communications represented by this Symposium. In this, all of us have also benefited by the generous cooperation of a number of U. S. Government and non-profit organizations; both the individuals and organizations referred to are listed below.

The attention of those about to peruse the subsequent collection of dozens of excellent papers is directed to the following important distinction: this collection does not constitute the Symposium; at best, it can be but an incomplete anthology. What is hoped is that this collection will contribute a valuable cornerstone to the Symposium as

a whole. The structure, the very essence, of the Symposium remains to be fashioned by those of you who will attend and participate in its discussions. The more actively and intelligently you take part, the more you will benefit yourself, your colleagues, your special field of endeavor, and your profession, through this, your Symposium on Radar Reflectivity Measurements.

STEERING COMMITTEE

Symposium Chairman - P.C. Fritsch

Panel Chairman

I - A. C. Diana

II - R. E. Hiatt

III - R. E. Kell

IV - E. M. Kennaugh

V - S. L. Johnston

IV - C. G. Bachman

SPECIAL ACKNOWLEDGMENT

Special thanks are due the M.I.T. Lincoln Laboratory for hosting the symposium under the guidance of Mr. P.C. Fritsch, and to Rome Air Development Center of the U. S. Air Force for publishing this document, under the guidance of Mr. A. C. Diana.

COOPERATING ORGANIZATIONS

Advanced Research Projects Agency

Aerospace Corporation

Air Force Cambridge Research Laboratories

Air Force Electronic Systems Division

Army Materiel Command

Cornell Aeronautical Laboratory

M.I.T. Lincoln Laboratory

Ohio State University

Rome Air Development Center

University of Michigan

Key words: Radar reflectivity; measurements; radar cross section.

ABSTRACT

This report is a collection of technical papers which will be reviewed and discussed at the Symposium on Radar Reflectivity Measurement on June 2-4, 1964 at M.I.T. Lincoln Laboratory.

The prime goal of the symposium is the exchange of ideas and information relative to research efforts, past, present and future in the field of radar reflectivity measurements. The technical papers dwell on the following reflectivity range subjects: geometry and techniques, special equipment, models, model supports, special materials, calibration, range intercalibration, measurement proceedings, data standards, correlations and applications.

PUBLICATION REVIEW

This report has been reviewed and is approved.

Approved:



JOSEPH FALLIK
Chief, Space Surveillance and
Instrumentation Branch
Surveillance and Control Division

Approved:



THOMAS S. BOND, JR.
Colonel, USAF
Chief, Surveillance and
Control Division

FOR THE COMMANDER



IRVING J. GABELMAN
Chief, Advanced Studies Group

NOT
Preceding Page BLANK - FILMED

TABLE OF CONTENTS (Vol I)

<i>Contents</i>	<i>Page</i>
SECTION I - REFLECTIVITY MEASUREMENTS - PAST, PRESENT, FUTURE	
Some Notes on the History of Radar Reflectivity Measurements Using Models 1 George Sinclair	1
Methods of Measuring Scattered Fields 2 Keigo Iizuka	2
Future Trends in Radar Cross Section Measurement 23 Keeve M. Siegel	23
SECTION II - REFLECTIVITY RANGES, THEIR GEOMETRY AND TECHNIQUES FOR THEIR USE	
Comments on Static Radar Reflectivity Measurements Techniques 25 W. F. Bahret	25
Radar Cross Section Model Measurements 37 W. E. Blore R. I. Primich R. A. Hayami P. E. Robillard H. M. Musal	37
State-of-the-Art Anechoic Backscatter Ranges 50 W. H. Emerson F. P. Brownell	50
Transmission Line Scattering Range 66 Michael J. Gans	66
An Effect of Wall Illumination Upon Microwave Anechoic Chamber Performance 77 R. J. Garbacz J. L. George	77
Complete Radar Cross-Section Measurements 93 J. Richard Huynen	93
A Comparison Between Longitudinal Baffling and Transverse Fence for Reducing Range Ground Scattering 110 Alan F. Kay	110
An Analysis of Reflection Measuring Systems 127 Robert G. Kouyoumjian	127
Measuring the Phase and the Amplitude of Backscattered Radar Energy on A Static Range 146 Norman R. Landry	146

Preceding page blank

Surface Currents in Thin Conducting Sheets	164
R. Magoulas P. A. Matthews	
CW Measurements of An Echo II Balloon in the Near Zone.....	192
R. K. Ritt A. W. Wren, Jr.	
Application of Surface Field Measurements to Radar Cross Section Studies	205
T. B. A. Senior	
The Terrain Scattering Problem.....	216
Robert C. Taylor	
Studies in Radar Cross Section Measurements	226
P. H. Ware	
Precision Measurement of the Radar Scattering Matrix	233
J. A. Webb W. P. Allen	
Very Small Radar Cross-Section Measurements at UHF	246
Phillip J. Willcox	
Indoor Range Design.....	257
R. J. Wohlers	
An Analysis of the Polarization Capabilities of a Ground Plane Cross Section Range.....	287
A. W. Wren, Jr. J. A. Green C. M. McDowell	

SECTION III - SPECIAL EQUIPMENT FOR REFLECTIVITY RANGES

Pulsed Backscatter Range Instrumentation.....	301
A. J. Cann	
The Hughes Back Scatter Measurement Radar and Recording Equipment.....	312
James D. Carlson	
A Method of Phase Measurement for Pulsed Radar Systems	323
Bernd Falk	
RF Phase Stability Requirements for Balanced CW Reflectometers	330
William D. Fortner	
Nanosecond Pulse Scattering Systems	344
Robert R. Hively	
The Automatic Recording of Effective Radar Cross Section.....	349
Charles W. Matthis, Jr.	
A Method of Static Radar Cross Section Measurement for Pulsed Radar Systems	356
J. M. Murchison	

Polarization Aspects of Radar Reflectivity Measurements	365
R. D. Tompkins	
SECTION IV - MODELS, MODEL SUPPORTS, SPECIAL MATERIALS	
Reflecting Properties of Aircraft Materials at 0.6943 and 1.06 Microns Using Pulsed Lasers	375
Stephen E. Barber	
Microwave Back-Scattering from Supersonic Laboratory Plasma Streams	382
A. I. Carswell M. P. Bachynski	
The Spin-Drop Method of Measuring Model Radar Cross Section	400
Peter C. Fritsch	
A Method of Measuring Small Radar Cross Sections by Digital Vector- Field Subtraction	410
F. E. Heart P. C. Fritsch	
Radar Cross-Section Model Fabrication at Cornell Aeronautical Laboratory	415
John E. Hopkins	
Metal-sprayed Fiberglass Radar Target Models	419
Forest M. Hudson	
Antenna Scattering Measurements	426
D. L. Moffatt	
The Effect of Finite Conductivity on Radar Cross Sections	440
Leon Peters, Jr.	
Dielectric Properties; Data and Measurement Techniques	456
Paul E. Rowe Eino J. Luoma Elery F. Buckley	
Nanosecond Pulse Scattering from Extended Laboratory Targets	475
H. S. Rothman H. Guthart T. Morita	
Surface Roughness and Tolerances in Model Scattering Experiments	503
T. B. A. Senior	
Estimates of the 'Volume' Return from Styrofoam	521
T. B. A. Senior E. F. Knott	
The Near Field of A Styrofoam Cylinder	527
T. B. A. Senior E. F. Knott	
Modeling of RAM-Covered Complex Bodies	542
A. S. Thomas	

SECTION I
REFLECTIVITY MEASUREMENTS-PAST, PRESENT, FUTURE

Panel Chairman: A.C. Diana

SOME NOTES ON THE HISTORY OF RADAR REFLECTIVITY MEASUREMENTS USING MODELS

George Sinclair
University of Toronto
Toronto, Canada

When radar equipment came into common use during World War II, there immediately arose a need for detailed information on the radar echo areas of various targets. While some of the information was obtainable from measurements made with operating radar systems, it was quite apparent that it was essential to develop methods for making measurements in the laboratory under controlled conditions. Model techniques which had already proven so successful in the study of airborne antennas, seemed to offer a logical answer to the problem.

One of the earliest investigations was based on the use of optical models to simulate radar targets. While useful information could be obtained, such models suffered from the lack of coherent sources of monochromatic radiation, and from the extreme amount of scaling involved which made it difficult to produce an accurate simulation of practical targets.

The development of model techniques at radio frequencies originated as a result of a study on methods of measuring antenna patterns by a technique involving reradiation of the received antenna power. The field reradiated by the antenna was distinguished from the radar echo field by modulating the antenna power before radiating it.

In the early days of radar, it was not practical to use pulse techniques for laboratory measurements on models because of the difficulty in obtaining pulses which were sufficiently short as to permit operating at reasonably small distances to the model target. It was necessary to employ CW methods, using directional couplers of extremely high directivities to separate the echo signal from the transmitted signal. There were severe equipment requirements arising from the use of these couplers.

The successful development of model techniques made it possible to consider measuring the complete scattering matrix. Methods were developed for treating radar systems of arbitrary polarization characteristics, operating against targets with arbitrary scattering matrices.

METHODS OF MEASURING SCATTERED FIELDS
(A Historical Survey of the Development at Harvard University)
by
Keigo Iizuka

(A) INTRODUCTION

Toward the end of world war II both theoretical and experimental studies of scattering and diffraction were accelerated in various institutions due to the invention of RADAR. Harvard University was not an exception. The first paper on this subject at this institution is dated as early as 1948 (1). Theoretical studies at Harvard were focused on scattering and diffraction from obstacles of very simple shapes and structures most of whose mathematical solutions could be expressed in closed forms. This approach was based on the philosophy that only through profound and thorough understanding of the simpler cases could light be thrown on the complexity of actual physical situations. The shapes and structures for which theoretical studies have been attempted include the following:

- (1) A general description of the diffracted field of circular cylinder of infinite length with either magnetic or electric field parallel to the axis. This was also extended to the dielectric coated cylinder.
- (2) Theories of diffraction and scattering for both bare and dielectric coated spheres.
- (3) A general study of the diffracted field of the elliptic cylinder; this has been extended to other general cases.
- (4) Theory (19, 20, 21, 22) of scattering and diffractions by parallel circular cylinders, thin wires and strips.
- (5) Theory (23 - 38) of transmission scattering and diffraction by

miscellaneous obstacles such as loaded dipoles, slotted cylinders, unidirectionally conducting screens, various apertures etc.

For the verification of the theories developed and the study of more complicated problems which do not permit a simple mathematical analysis, various experimental techniques for measuring back-scattering cross sections and the diffracted field were developed. These include:

- (1) Standing-wave-ratio method.
- (2) Cancellation method.
- (3) Partial reflection method.
- (4) Doppler-shift method.
- (5) Pulse-technique method.
- (6) Application of scattering technique to field measurements.

In the following, an outline of each technique developed or to which substantial contributions were made at Harvard for measuring back scattering cross sections and diffracted fields will be given. Most of the methods employed an image-plane technique so that all auxiliary apparatus could be arranged under a ground plane. Only the obstacle under study, the source and a receiving antenna or probe were above the ground plane. This technique, however, restricts the shapes of the obstacle to those characterized by a plane of symmetry and the polarization of the \bar{E} field to the one perpendicular to the ground plane. In most cases, the same method can be utilized with or without the image plane but extreme care must be taken with regard to the disturbances in the field caused by the auxiliary equipments; especially by lead wires to the probes which usually cannot be made small enough to be of insignificant effect even though the effect of the probe itself could be made negligible.

(B) STANDING-WAVE RATIO METHOD (D.D. King (39), A. L. Aden (12)

Just as a standing wave ratio inside a waveguide determines the reflection coefficient of the load, the standing wave ratio consisting of the incident traveling wave and reflected traveling wave in the space between the source and the obstacle under test, determines a reflection coefficient of the obstacle from which it is possible to calculate the back scattering cross section. The only difference is that the amplitudes of the two waves decay in the simple spherical $1/r$ form in the Fraunhofer region. The formula (12, 39) for the reflection coefficient P is

$$|\Gamma| = \frac{W_2}{l - W_2} \left[\frac{S_{\pm} - 1 / (1 \mp \Delta / (1 - W_2))}{S_{\pm} + 1 / (1 \mp \Delta / W_2)} \right] \quad (1)$$

$$\sigma_B = \lim_{l \rightarrow \infty} 4 \pi l^2 |\Gamma|^2 \quad (2)$$

where

S is the ratio of a maximum amplitude to the next adjacent minimum amplitude.

W_1 is the distance from the location of the maximum to the obstacle.

W_2 is the distance from the location of the minimum to the obstacle.

$$\Delta = |W_1 - W_2|$$

When $W_1 > W_2$ the standing wave ratio is denoted by $S = S +$. When

$W_1 < W_2$ $S = S -$.

Fig. 1 shows a block diagram of this method (40); the measured back-scattering cross section of a metal sphere is shown in Fig. 2 (40). The experimental results show quite a satisfactory agreement with theory.

Since this method depends critically on a movable probe between the source and the obstacle, the image-plane technique is indispensable. Even though this method has the advantage of utilizing a low power source, efforts should be made to reduce the residual SWR on the ground plane either by using a very large ground plane or by properly arranging absorbers along its edges. The further improvement of this method is due to Sletten (40) in Air Force Cambridge Research Center.

(C) CANCELLATION METHOD (J. Sevick) (41, 42)

The scattered field can be obtained by taking the difference between the fields with and without the obstacle. In Fig. 3 (42) a magic T is used to carry out this differencing operation. First, with switch S_1 in position B, balance the input signals to the magic T to obtain the null output of the receiver. in the absence of the obstacle. Then, install the obstacle, the signal output from the receiver is proportional to the scattered signal. The incident field is measured with S_1 in position A. The back-scattering cross section in this case is obtained from (42)

$$\sigma_B^- = 4 \pi \left[\frac{(d_1 + d_2) d_2}{d_1} \left(\frac{E^s}{E^i} - 1 \right) \right]^2 \quad (3)$$

where the assumption was made that the amplitude of the field decays as $1/r$.

E^s is the scattered field intensity

E^i is the incident field intensity.

d_1 is the distance from the source to the probe

d_2 is the distance from the obstacle to the probe

Especially with a small obstacle the ratio of E^s/E^i becomes quite small and this method encounters difficulty. A modification was attempted by R. V. Row (43) who used a directional antenna as a probe in order to increase the gain of the probe in the direction of arrival of the scattered signal.

Another modification was tried by S. H. Dike and D. D. King (21) who measured the scattering field of a very thin obstacle whose scattering field can be considered to be rotationally symmetric. On account of this rotational symmetry, the receiving horn can be located at an arbitrary angle with respect to the direction of the propagation of the incident wave. The scattered field could be measured with a receiving horn which was located at the angle where it was insensitive to the incident wave.

The measured results of the back-scattering cross section of a single antenna of radius $a/\lambda = 3.5 \times 10^{-3}$ as a function of its length is shown in Fig. 4 (41).

On the one hand this method has the advantage of having a fixed probe and no moving parts; on the other hand the accuracy is restricted by the electronic stability of the r-f power supply, mechanical stability of the structure, limited degree of isolation of the magic T, and multiple reflection between the source horn and the obstacle.

(D) PARTIAL REFLECTION METHOD (H. J. Schmitt and B-O Ås)^o(26,44)

In order to achieve a more complete isolation of the receiving horn from the incident field, a semi-transparent microwave mirror was placed between the transmitting and receiving horns. Consider the arrangement shown in Fig. 5 (44). A part of the incident wave is transmitted to

the obstacle and the rest is reflected toward the absorbers by the mirror placed in a 45 degree angle between the source and the obstacle. The back scattered signal from the obstacle is reflected again by the mirror toward the receiving horn. Thus, the incident wave reaching the receiving horn directly is minimized. The back-scattering cross section σ_B per unit length of an infinitely long strip of width δ at normal incidence measured by this method is shown in Fig. 6 (25). While this method applies to any shape (the use of the ground plane is not essential), it has the disadvantage of requiring standardization by means of an obstacle with a known back-scattering cross section. This is necessary since the incident field intensity at the obstacle is not a known quantity.

(E) DOPPLER EFFECT (H. Scharfman and D. D. King (45),
C. C. H. Tang (9))

The effect of a Doppler frequency shift of the reflected signal from the moving obstacle was used to measure the back-scattered signal. Consider the block diagram in Fig. 7 (45). The obstacle under test and the standard metal sphere are installed on a turntable such that they move into the field and toward the source in turn. The reflected signal is received by the same horn as that used for transmission and is fed into a mixer circuit in which the back-scattered signal is allowed to beat with the original signal to obtain the audio signal at the Doppler shift frequency. The separation of the back-scattered Doppler signals from the obstacle under test on the one hand and from the standard on the other hand is accomplished by means of a commutator. The ratio between the two amplitudes determines

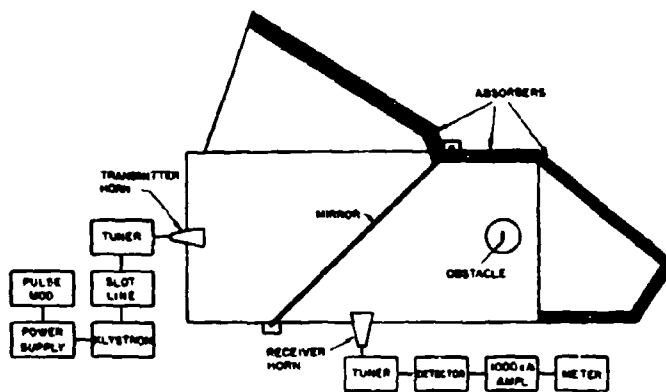


FIG. 5 Schematic diagram of the experimental setup for the partial-reflection method.

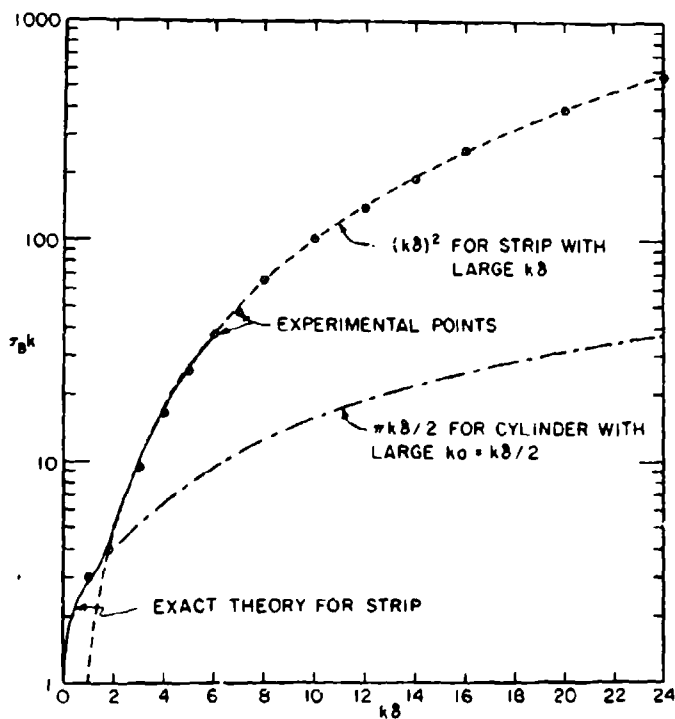


FIG. 6 Back-scattering cross section σ_B per unit length of a strip of width δ at normal incidence; $k = 2\pi/\lambda$ (Macraakis).

the back-scattering cross section. A good separation of the scattered field from that reflected from the surroundings can be obtained by this method. The measured results obtained by the Doppler shift method for the back-scattering cross section of an infinitely long cylinder are shown in Fig. 8 (9, 25).

A modified method uses a belt moving around adjacent wheels in order to move the obstacle in a straight line. It is made useful in the measurement of the back-scattering cross section of nonrotationally symmetric obstacles.

(F) PULSE TECHNIQUE METHOD (C. C-H. Tang (46))

In this method use is made of the reflection of a pulse from an obstacle. The pulse duration is chosen in such a way that each pulse is long enough to ensure a steady-state response and yet short enough and spaced far enough apart in time to avoid overlapping with the outgoing pulses.

Fig. 9 (46) shows the arrangement that C. C-H. Tang used to obtain the proper pulse. When a d.c. pulse was applied to the crystal which was used for balancing the arms of magic T, the balance of the magic T was destroyed and a pulse-shaped r-f signal appears as the output of the magic T. After amplification by a traveling wave tube the r-f pulse was fed into another magic T which served to separate the outgoing pulse from the reflected one when some overlapping in time between them was unavoidable. The back-scattering cross section is determined by a comparison of the detected pulse height of the reflected signal from the obstacle in question with that of the standard. In Fig. 10 (46) the back-scattering cross section

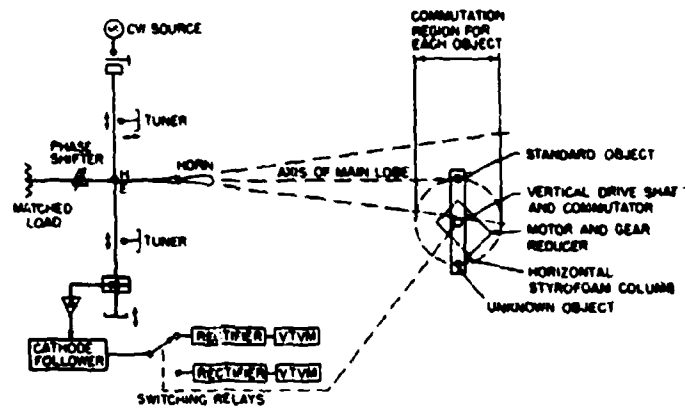
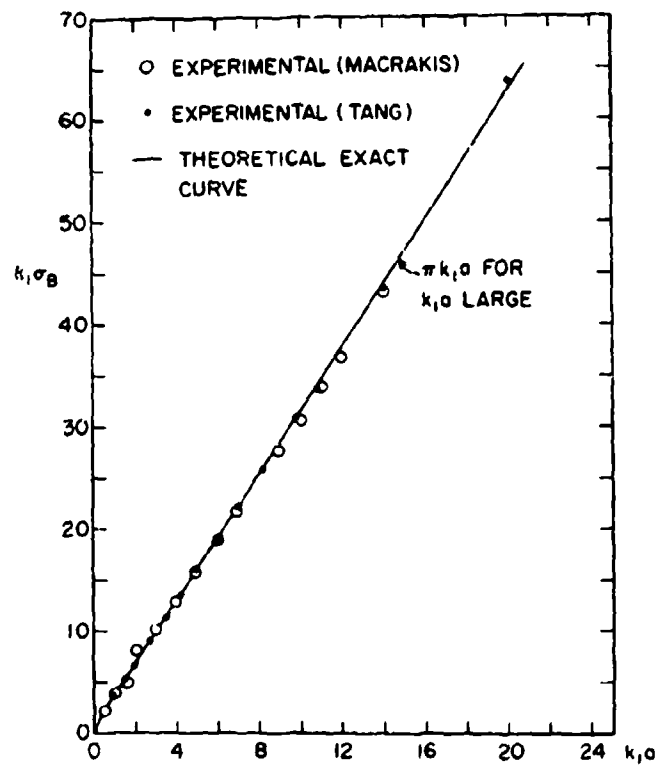


FIG. 7 Block diagram of the Doppler system (Scharfman and King).



Back-scattering cross section of a conducting cylinder.
FIG. 8

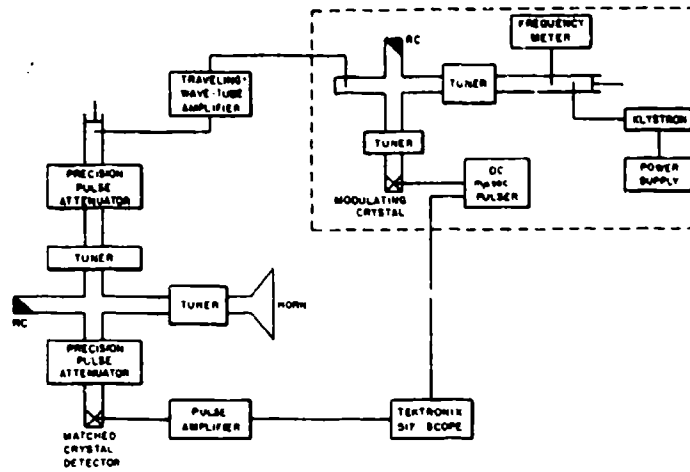


FIG. 9 Schematic diagram of the apparatus for back-scattering measurements using a pulse technique.

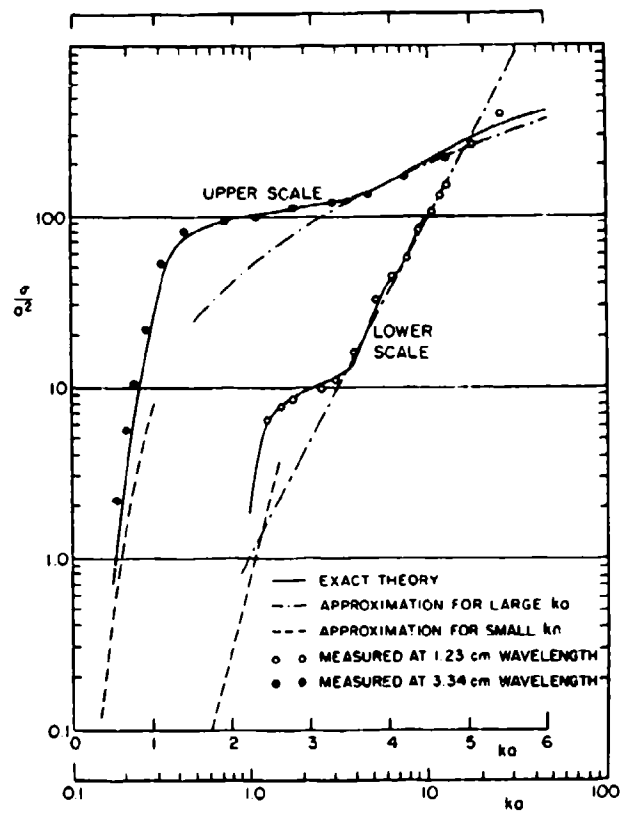


FIG. 10 Back-scattering cross section of plane conducting circular disks of radius a (Schmitt).

of circular disks measured by this method is shown.

Aside from the complexity of the setup, this method has the advantages of good (or even complete) separation of the signal from possible reflections from the background, and no restrictions on the shape of the obstacle.

(G) APPLICATION OF A SCATTERING TECHNIQUE TO FIELD MEASUREMENTS I
(Photoconductive probe - K. Iizuka (47, 48))

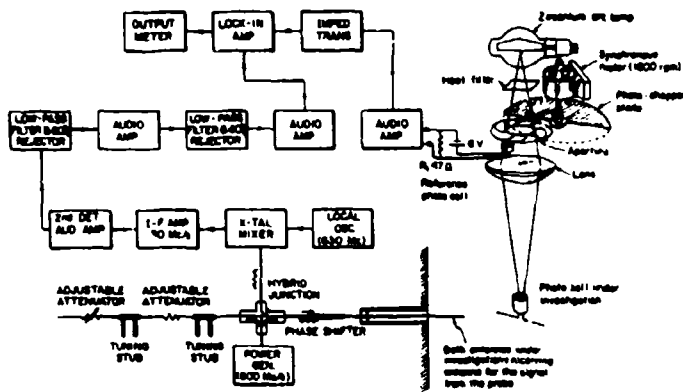
Probes in which the usual connecting leads to the detector have been eliminated, have been constructed for measuring the intensity of an electromagnetic field. They are based on the principle of scattering and consist of modulated reradiating or scattering antennas in the form of either a small dipole (for measuring the electric field) or a small shielded loop (for measuring the magnetic field) center-loaded with a photocell that is illuminated by a chopped beam of light. Fig. 11 (47) shows a block diagram of the equipment for measuring an electromagnetic field by means of a photo-probe. First, the hybrid junction is balanced in the presence of the photo-probe, but without illumination by the beam of light. When the beam of light is turned on, the signal that is scattered from the probe changes and the hybrid junction is unbalanced. The difference in the back-scattered signals with the beam of light on and off is fed into an amplifier. It is proportional to the square of the field intensity at the probe. The switching of the beam of light at 30 c/s is accomplished mechanically by a photo-chopper disk driven by a synchronous motor. The back-scattered signal is detected and amplified by an amplifier which is locked with a signal from a reference photocell illuminated by the same beam of light that

illuminates the photo-probe. The same principle has been applied to the measurement of the distribution of current along an antenna of arbitrary shape. This was accomplished by sliding a small shielded-loop probe center-loaded with a photocell along the antenna. A very small and constant gap was maintained between the probe and the antenna. In Fig. 12 (47) the near-field pattern of a half-wave dipole measured by this method is shown.

Since the scattered signal from the probe is amplitude modulated, there is no error in the measurement due to possible leakage through an imperfectly balanced hybrid junction or from the reflected waves originating somewhere else than at the probe. These unwanted signals are not amplitude-modulated.

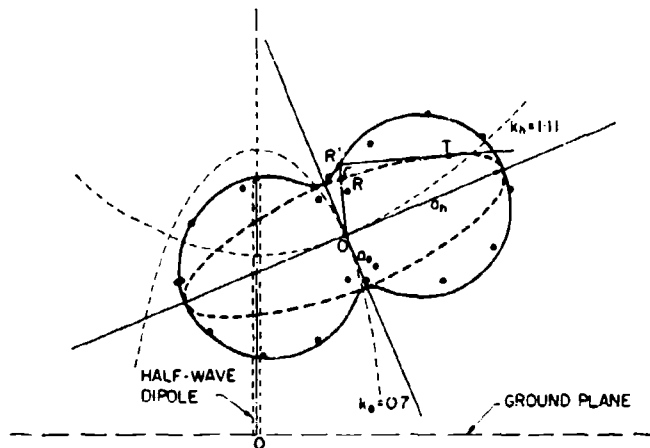
(H) APPLICATION OF A SCATTERING TECHNIQUE TO FIELD MEASUREMENTS II
(Coil spring probe - K. Iizuka (49))

A thin coil spring whose length can be varied periodically by mechanical means has been used as a probe to measure the electric field intensity. The vibrating probe acts as a re-radiating antenna with periodically varying length (It was also analytically demonstrated that the effective length of a thin helical antenna equals the axial length of the helix.) that modulates and scatters the component of the \vec{E} field which is parallel to the axis of the spring. The scattered signal is picked up by a receiving antenna and amplified with an amplifier that is locked-in with the frequency of the mechanical vibration of the coil. The arrangement of the electronic apparatus is similar to the photo-probe mentioned in the previous section. Only the parts which are different from the previous one are shown in Fig. 13 (44). Measurements of the field of a



Block diagram of experimental equipment for measuring electromagnetic field by a photo-probe

FIG. 11



Polarization pattern at the position of $K_e = 1.11$, $K_h = 0.7$ of the confocal co-ordinate of the $\lambda/2$ dipole

- Elliptic pattern (theory)
- Polarization pattern
- ⊙ ⊙ ⊙ Experimental polarization pattern

FIG. 12

half-wave dipole antenna are shown in Fig. 14 (49).

While this method has the advantage of good separation of the signal from the background, it requires special precautions for limiting the mechanical vibration exclusively to the coil spring, because the scattered wave from any vibrating object gives rise to an error signal.

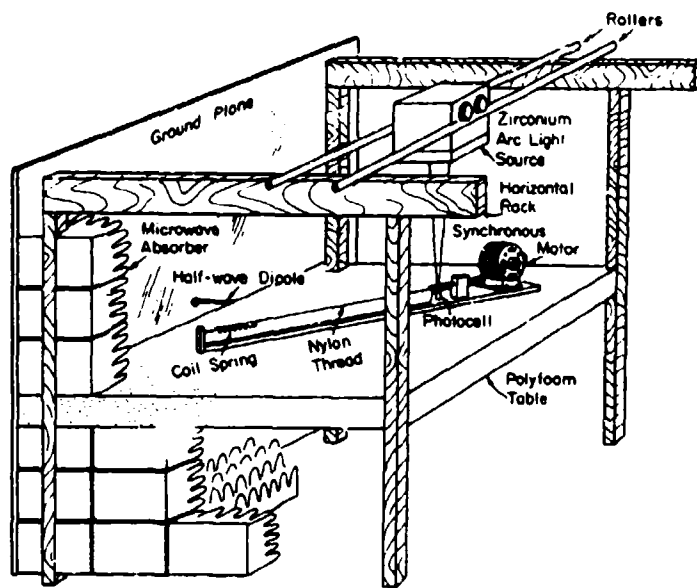


FIG. 13 CONSTRUCTION OF THE SUPPORT OF THE PROBE AND THE SOURCE OF BEAM OF LIGHT.

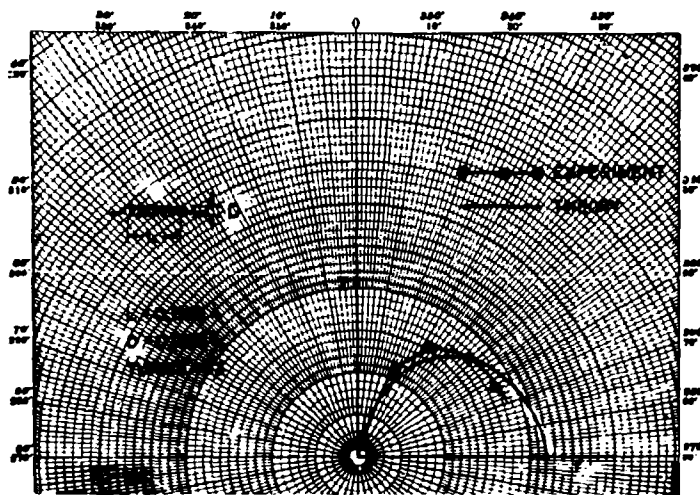


FIG. 14 POLAR GRAPH OF E_e ALONG THE CIRCUMFERENCE $k_e=2.0$ ON ELLIPTIC COORDINATES MEASURED BY A COIL SPRING

REFERENCES

- (1) C. T. Tai, "Reflection and Refraction of a Plane Electromagnetic Wave at a Periodical Surface" Technical Report No. 28, Cruft Laboratory, Harvard University, 1948.
- (2) R. D. Kodis, "Diffraction Measurements at 1.25 Centimeters" J. Appl. Phys. 23, 249-255, 1952.
- (3) C. H. Papas, "Diffraction by a Cylindrical Obstacle" J. Appl. Phys. 21, 318-325, 1950.
- (4) R. W. P. King and T. T. Wu, "The Reflection of Electromagnetic Waves from Surfaces of Complex Shape" Scientific Report No. 13, Cruft Laboratory, Harvard University, 1957.
- (5) L. Wetzel and D. B. Brick "An Experimental Investigation of High-Frequency Current Distributions on Conducting Cylinders" Scientific Report No. 4 Cruft Laboratory, Harvard University, 1955.
- (6) L. Wetzel, "High-Frequency Current Distributions on Conducting Obstacles" Scientific Report No. 10, Cruft Laboratory, Harvard University, 1957.
- (7) R. D. Kodis, "Variational Principles in High-Frequency Scattering" Scientific Report No. 5, Cruft Laboratory, Harvard University, 1956.
- (8) T. T. Wu and S. I. Rubinow, "First Correction to the Geometric-Optics Scattering Cross Section from Cylinders and Spheres" J. Appl. Phys. 27, 1032-1039, 1956.
- (9) C. C. -H. Tang, "Back Scattering from Dielectric-Coated Infinite Cylindrical Obstacles" J. Appl. Phys. 28, 628-633, 1957.
- (10) H. J. Schmitt, "Back-Scattering Cross Sections of Circular Metallic Cylinders Surrounded by a Resistance Foil" Scientific Report No. 11, Cruft Laboratory, Harvard University, 1957.
- (11) T. T. Wu, "The Electromagnetic Theory of Light, I," Scientific Report No. 9, Cruft Laboratory, Harvard University, 1957.
- (12) A. L. Aden, "Electromagnetic Scattering from Spheres with Sizes Comparable to the Wavelength" J. Appl. Phys. 22, 601-605, 1951.
- (13) C. Huang and R. D. Kodis, "Diffraction by Spheres and Edges at 1.25 cm," Technical Report No. 138, Cruft Laboratory, Harvard University, 1951.

- (14) C. L. Tang, "High-Frequency Diffraction by a Sphere" Technical Report No. 303, Cruft Laboratory, Harvard University, 1957.
- (15) T. T. Wu, "High Frequency Scattering" Phys. Rev. 104, 1201-1212, 1956.
- (16) S. I. Rubinow, "On the Forward Scattering from a Dielectric Sphere at High Frequencies" Scientific Report No. 7, Cruft Laboratory, Harvard University, 1956.
- (17) T. T. Wu and S. R. Seshadri, "The Electromagnetic Theory of Light, II," Scientific Report No. 22, Cruft Laboratory, Harvard University, 1958.
- (18) L. Wetzel, "Investigation of High-Frequency Current Distributions on Conducting Obstacles" Quarterly Scientific Report No. 12, Cruft Laboratory, Harvard University.
- (19) R. V. Row, "Theoretical and Experimental study of Electromagnetic Scattering by Two Identical Conducting Cylinders" J. Appl. Phys. 26, 666-675, 1955.
- (20) J. H. Van Vleck, F. Bloch and M. Hamermesh, "Theory of Radar Reflection From Wires or Thin Metallic Strips" J. Appl. Phys. 18, 274-294, 1947.
- (21) S. H. Dike and D. D. King, "Absorption Gain and Back-Scattering Cross Section of the Cylindrical Antenna," Proc. IRE 40, 852-860, 1952 and 41, 926-934, 1958.
- (22) J. Sevick and J. E. Storer, "A General Theory of Plane-Wave Scattering from Finite Conducting Obstacles with Application to the Two Antenna Problem" J. Appl. Phys. 25, 369, 1954.
- (23) H. Levine and Schwinger, "On the Theory of Electromagnetic Wave Diffraction by an Aperture in an Infinite Plane Conducting Screen" Commun. Pure Appl. Math. 3, 355, 1950.
- (24) J. E. Storer, "Wave Propagation in a Two-Dimensional Periodic Medium" Technical Report No. 152, Cruft Laboratory, Harvard University, 1952.
- (25) M. S. Macrakis, "Back-Scattering Cross Section of Slotted Cylinders" Ph. D. Thesis, Harvard University, 1958.
- (26) B-O Å s and H. J. Schmitt, "Back-Scattering Cross Section of Reactively Loaded Cylindrical Antennas" Scientific Report No. 13, Cruft Laboratory, Harvard University, 1958.

- (27) S. R. Seshadri, "High-Frequency Diffraction of Plane Waves by an Infinite Slit" Scientific Report No. 20, Cruft Laboratory Harvard University, 1958.
- (28) S. R. Seshadri and T. T. Wu, "High-Frequency Diffraction of Plane Waves by an Infinite Slit for Near Grazing Incidence" Scientific Report No. 23, Cruft Laboratory, Harvard University, 1958.
- (29) S. R. Seshadri, "High-Frequency Transmission Coefficient of an Infinite Slit in a Plane Screen" Scientific Report No. 17, Cruft Laboratory, Harvard University, 1958.
- (30) H. Levine and T. T. Wu, "Diffraction by an Aperture at High Frequencies" Technical Report No. 71, Cruft Laboratory, Harvard University, 1957.
- (31) S. R. Seshadri and T. T. Wu, "High-Frequency Diffraction of Plane Electromagnetic Waves by a Circular Aperture in an Infinite Plane Conducting Screen", Scientific Report No. 16, Cruft Laboratory, Harvard University, 1958.
- (32) C. Huang, "Variational Approximation to the Diffraction by Circular and Elliptical Apertures," Technical Report No. 164, Cruft Laboratory, Harvard University, 1953.
- (33) C. Huang, R. T. Kodis, and H. Levine, "Diffraction by Apertures," J. Appl. Phys., 26, 151-165, 1955.
- (34) H. H. C. Chang, "On the Diffraction of Electromagnetic Waves by a Circular Aperture," Scientific Report No. 2, Cruft Laboratory, Harvard University, 1955.
- (35) C. C.-H. Tang, "Magnetic Back-Scattering from Thin Circular Disks by the Wave Pulse Method," Scientific Report No. 15, Cruft Laboratory, Harvard University, 1958.
- (36) C. L. Tang, "On the Radiation Pattern of a Base-Driven Antenna Over a Circular Conducting Screen," Technical Report No. 301, Cruft Laboratory, Harvard University, 1959.
- (37) C. Huang, "On the Diffraction of Electromagnetic Waves by Circular, Elliptical and Rectangular Apertures" Technical Report No. 163, Cruft Laboratory, Harvard University, 1953.
- (38) C. L. Tang, "High-Frequency Diffraction of Cylindrical Waves by an Infinite Slit in a Plane Screen," Technical Report No. 297, Cruft Laboratory, Harvard University, 1959.

- (39) D. D. King, "Measurement and Interpretation of Antenna Scattering,"
Proc. IRE 37, 770-777, 1949.
- (40) C. J. Sletten, "Electromagnetic Scattering from Wedges and Cones,"
Air Force Cambridge Research Center, Report No. E5090,
1952.
- (41) J. Seivick, "Experimental and Theoretical Results on the Back-Scattering
Cross Section of Coupled Antennas," Technical Report No.
150, Cruft Laboratory, Harvard University, 1952.
- (42) J. Seivick, "An Experimental Method of Measuring Back-Scattering
Cross Sections of Coupled Antennas," Technical Report
No. 151, Cruft Laboratory, Harvard University, 1952.
- (43) R. V. Row, "Back-Scattering Measurements," Quarterly Scientific
Report No. 12, Cruft Laboratory, Harvard University, 1956.
- (44) H. J. Schmitt, "Back-Scattering Measurements with a Space-Separation
Method," Scientific Report No. 14, Cruft Laboratory, Harvard
University, 1957.
- (45) H. Scharfman and D. D. King, "Antenna Scattering Measurements by Modula-
tion of the Scatterer," Proc. IRE 42, 854-858, 1954.
- (46) C. C.-H. Tang, "Back-Scattering Measurements with a Pulse Method,"
Scientific Report No. 15, Cruft Laboratory, Harvard University,
1958.
- (47) K. Iizuka, "Photoconductive Probe for Measuring Electromagnetic
Fields," Proc. IRE, 110, 1747-1754, 1963.
- (48) K. Iizuka, "Photosensitive Probe," Electronics, 36, 39-43, Jan. 25, 1963
- (49) K. Iizuka, "A New Technique for Measuring the Electromagnetic Field
by a Coil Spring," IRE Trans. PTGMITT, November, 1963.

FUTURE TRENDS IN RADAR CROSS SECTION MEASUREMENT

Keeve M. Siegel
Conductron Corporation

The background cancellation problem for cw ranges at high frequencies for low radar cross section shapes for usual type support systems for large models seems to be reasonably close to reaching diminishing returns. The short-pulse systems cannot operate at long wavelengths and even at medium wavelengths the dispersion of the energy within the absorbing material can significantly affect the measured value for the radar return when it is compared with or is to predict the cross section as observed at the longer pulses. As objects get larger and larger and as cross sections become smaller and smaller, the far field requirement will have to be lifted for all ranges which are ground based. Thus it is felt that before significant breakthroughs are obtained in radar cross section measurements, theoretical analyses will have to predict methods of making near-field measurements and predicting far-field results. Also theoretical methods will have to be obtained for allowing the prediction, when knowing the material characteristics, of utilizing short pulse answers to predict long pulse answers. For bodies which are not bodies of revolution, difficulties will continue to exist on how to obtain correct polarization answers when the background is a function of both the aspect of the model and the polarization being measured. It is felt that the key radar cross section problems for the future lie in measuring objects at low values of signal-to-noise ratio. Here again new radar cross section measurement techniques will have to be utilized if the laboratory method is going to become both the quality control tool as well as the design tool, in addition to being a research tool for tomorrow's ideas, concepts and applications.

SECTION II
REFLECTIVITY RANGES, THEIR GEOMETRY AND TECHNIQUES FOR THEIR USE

Panel Chairman: R.E. Hiatt

COMMENTS ON STATIC RADAR REFLECTIVITY MEASUREMENTS TECHNIQUES

W. F. Bahret, Electronics Physicist
Air Force Avionics Laboratory
Research and Technology Division
Wright-Patterson Air Force Base, Ohio

ABSTRACT

This paper presents the accumulated findings of the Avionics Laboratory on static radar reflectivity measurements systems and techniques which have been built up through ten years of experience in the field. The paper concentrates on indoor measurements. It discusses types of instrumentation and model supports, with specific emphasis on anechoic chamber requirements, which have been substantiated by short pulse radar measurements, and the use of unique and helpful apparatus such as tunnel antennas. The paper also discusses model fabrication techniques, tolerances and the use of non-metallic coatings on models.

THE CONCEPT OF STATIC RADAR REFLECTIVITY MEASUREMENTS

Let us start this discussion with several assumptions:

1. That the terms radar echo area and radar cross section of a vehicle are understood.
2. That it is recognized that these characteristics are functions of the shape and materials of the vehicle, viewing angle, illuminating radar frequency and polarization.
3. That there is no need to justify the desire for radar cross section data.
4. That true "free-space" cross-section information is required.
5. That scaling laws for model measurements are understood.

Strictly speaking, the only way to satisfy all the restraints for obtaining absolute cross section data is to perform flight testing. Yet this approach is extremely expensive and, by its nature, contributes errors and uncertainties particularly with regard to vehicle aspect. Furthermore in the vehicle design stages, such testing is impossible. As a result, one commonly resorts to static testing in which the vehicle is somehow suspended in a "pseudo free-space" environment and echo patterns are recorded while the body undergoes controlled changes in viewing angle.

It is important to recognize that static measurements necessitate compromises between electrical and mechanical/physical requirements. The size, weight, shape and radar cross section of the vehicle often impose incompatible demands, such as extremely low background echo level from a target support system capable of holding hundreds of pounds. It is our intention to emphasize herein the necessity of adapting the measurements instrumentation and techniques to the target being measured and to present solutions to particular problems where possible.

INSTRUMENTATION FOR STATIC MEASUREMENT

For indoor work, CW instrumentation has been used almost exclusively in the past simply because conventional pulse systems require too much range to the target. For example, a radar with a 0.25 microsecond pulse requires that a target be in excess of 250 feet from the antenna for proper measurement. Typical CW systems are shown in block form in Figures 1 and 2. The electronics equipment is all standard and for the most part commercially available. There is no need to dwell on specific units here since different frequencies of operation would require different units. However, the equipment should have the following characteristics:

1. the transmitter must be a frequency-stable source of reasonable power output.
2. the receiver must be stable in frequency and gain and have at least a 40 decibels (DB) dynamic range.
3. the tunable load, attenuators and phase shifters must be capable of precise adjustment.

The one antenna system requires that a tunable load be adjusted in the absence of a target, so that the power into the receiver arm of the hybrid tee junction is very small compared to that from the target itself. Ideally the tunable load serves only to eliminate signals arriving at the receiver arm from mismatches in waveguide and antenna components. In practice in an indoor chamber, however, one actually tunes out all sources of reflection such as the walls of the chamber and the target support. If the echo from these sources remains the same after the introduction of the target, or is changed by a trivial amount, there is no problem. However, if the target significantly alters the illumination of the chamber walls, as is often the case, the background is no longer cancelled and is measured along with the target. Such a situation is a serious source of error in the measurement of low cross section targets.

The two horn system usually contains a phase shifter and attenuator to control a portion of the transmitted signal which is used to "null" the received signal in the absence of a target. Ideally this would only be necessary to eliminate leakage or cross-talk between the antennas. In practice one again cancels all chamber echoes and the above comments on the change in background with target still apply.

Generally, the less "nulling" that is necessary, the longer a null can be maintained. In our use of the two horn system, we have developed a novel "modus operandi" which provides for extended periods (measured in hours) of very low received signal level in the absence of target. First we incorporated a pair of "tunnel antennas" which have low leakage and low sidelobe levels. These are conventional horns (10° beamwidth in E&H planes) which radiate through an extension of their sides. The extension is lined with radar absorber material. The extension in our case is approximately 20 wavelengths long and is lined with Emerson and Cuming type AN-75 absorber. The front face of the absorber is flush with the inner surface of the sides of the basic horn. The beamwidth is determined by the aperture of the horn without extension as can be seen in Figure 3.

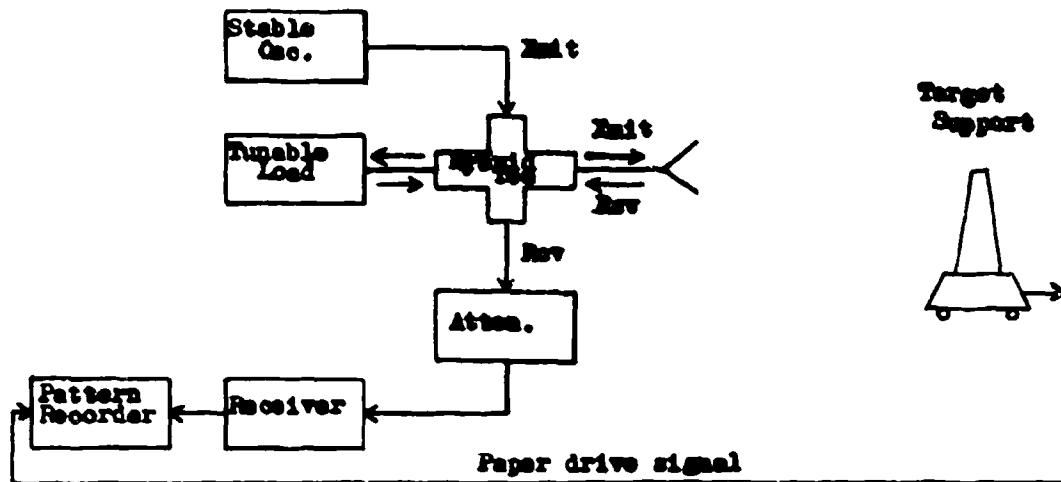


Figure 1. One Antenna CW System

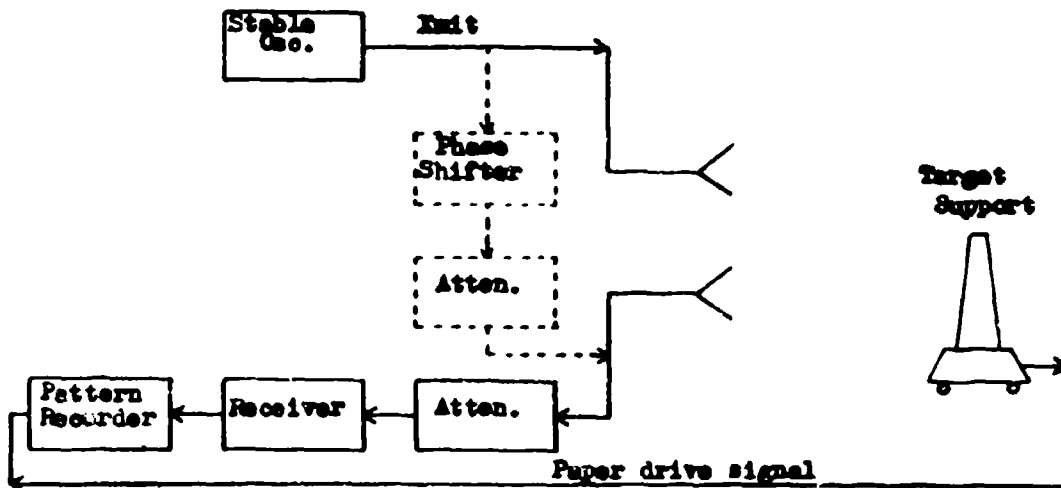


Figure 2. Two Antenna CW System

This figure compares the patterns of the basic horn, the horn with an extension lined with B. F. Goodrich Hairflex type absorber and the horn with the AN-75 lined extension. The reduction in the E plane sidelobe levels is quite apparent. The H plane sidelobes are not significantly reduced by this treatment, but normally these are low and present no major problem. The attainment of low sidelobes means that the illumination of the sidewalls and floor of the chamber is greatly reduced, which in turn reduces the amount of background signal which must be nulled. The cross-talk between the two antennas, when the ends of the extension are within 1/2 inch of one another, is more than 100 DB below the transmitted power. With a short pulse (10 nanoseconds) radar operating at 9325 mc, a reading of 118 DB cross-talk level is repeatedly obtained.

With the virtual elimination of cross-talk, any nulling would only cancel echoes from the target range itself. Rather than apply cancellation techniques to mitigate the effects of chamber echo we prefer to reduce the primary echo itself to a tolerable level. We have found that by physically canting the chamber backwall (that directly behind the target) at an angle we can direct a null in its echo pattern toward the receiver horn and thus minimize the received background signal. That this wall is the major contributor to chamber echoes, which ordinarily must be nulled out, has been confirmed by short pulse radar diagnosis. In practice, the received signal in the absence of the target is thus reduced to levels below the noise level of the receiver. This received signal is approximately 15 DB below that from a 4×10^{-5} square meter (M^2) sphere at a range of 25 feet from the antennas. It is important to note here, as before, that the introduction of the target can disturb the background illumination and thereby eliminate the fine null obtained in the absence of target.

The short pulse system which has been mentioned several times thus far was obtained from Harry Diamond Fuze Laboratories, where it was designed and built. It operates at a fixed frequency of 9325 mc with an output pulse width of 10 nanoseconds and a PRF of 25 kc. The block diagram shown in figure 4 is conventional, but the circuitry is of course special for handling the short pulses. The IF amplifier has a center frequency of 450 mc and a bandwidth of 100 mc. The twin tunnel antennas previously described are used for transmission and reception, hence no T/R device is necessary. The output pulses are displayed on a sampling oscilloscope. As of this writing we have no automatic method of recording echo amplitude with this system, but one is in the planning stage. The present readout technique is a manual one, in which the receiving line attenuator is adjusted to reduce all echoes to a fixed reference value. Readings taken at discrete intervals (normally 1 degree) of target rotation produce an acceptable pattern. However, sharp nulls or peaks which occur between reading points are missed. The only discrepancy between pulse and CW data taken on the same target is in the depths of sharp nulls.

This pulse radar has been an invaluable tool for diagnosing the sources of echo in the measurements chamber since it can resolve, in range, two targets separated by as little as 5 feet. It has also been our only accurate system for measurement of very low cross-section (10^{-5} to $10^{-6} M^2$) targets, because changes in backwall echo do not influence the measured target echo.

THE MEASUREMENTS CHAMBER

We have been using a home-made anechoic chamber for many years and have measured a large variety of targets ranging from those which are physically small and have large echo area to the other extreme - physically large with low echo area. This has forced us to investigate the influence of chamber design upon the measured echoes from this range of targets perhaps to a greater extent than even the commercial organizations which supply complete chambers. The investigation has of necessity been trial and error but the unique capability to observe effects by both short pulse radar and CW systems has revealed many interesting facts. Thus we can make several general but positive statements with regard to the chambers:

1. The antenna(s) used for target illumination should have the least possible beam-width consistent with uniform target illumination and the length of the chamber. Low side-lobe levels are also necessary. These antenna characteristics prevent direct illumination of everything in the chamber except the volume in the immediate vicinity of the target and the sector of the chamber wall directly behind the target.

2. The target support must be as lightweight and low in volume as allowed by target size and weight. Obviously the target support echo, which occurs at the same range as the target echo, cannot be removed from the total signal recorded even with a pulse system. (Fritsch of Lincoln Laboratory has recently demonstrated an interesting technique for removal of the support echo "post facto" by recording phase and amplitude of echo signals for targets-in-place and target-absent conditions.) In any case the signal recorded with target in place is the vector sum of target and support echoes. Styrofoam columns which have been extensively used as target supports, may be tapered to reduce their inherent echo but there is a limit to how far one can go. Thin nylon or dacron string (8 lb test) arranged in a manner suitable for support and rotation of a target provides an echo one to two orders of magnitude below the best styrofoam column. For instance four strands, joined at a point far above the target position and connected to the target turn table rim at four points in quadrature, have an echo area which is immeasurable with a horizontally polarized pulse radar whose minimum discernible target cross section is $8 \times 10^{-7} \text{ M}^2$ for the range involved. Vertical polarization naturally provides a larger echo, but this is just barely measurable as 10^{-6} M^2 . Tolerable support echo is of course relative, but should always be more than 20 DB below the target echo. One problem with supports which we have observed, but have not explored, is their tendency to alter the fields incident or excited on the target. Such alterations could drastically change a recorded echo pattern particularly for low cross section shapes. One last note on the target support - the turn table should be far enough below the target so as not to be directly illuminated by the transmitted signal. If this is not possible, then it must be shrouded by radar absorber material (RAM) for minimum echo. We have also found that the top of the turn table must be covered with RAM to reduce multiple bounce type of echoes which travel from transmitter to target to turn table to target to receiver.

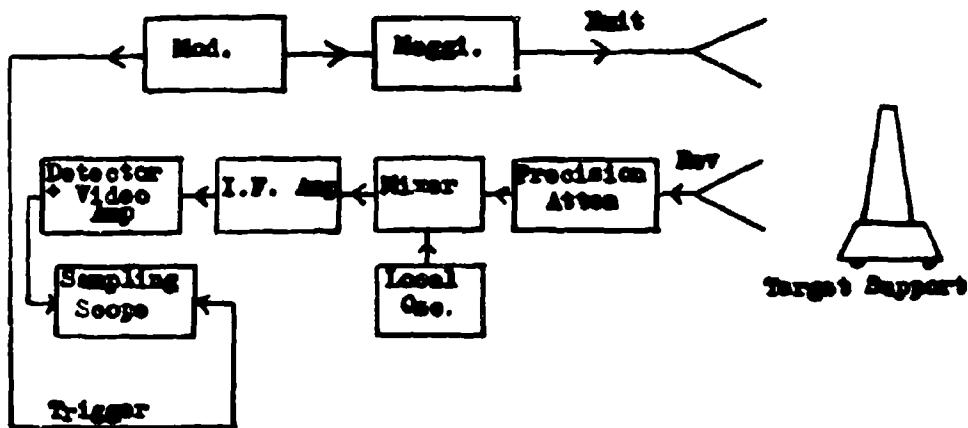
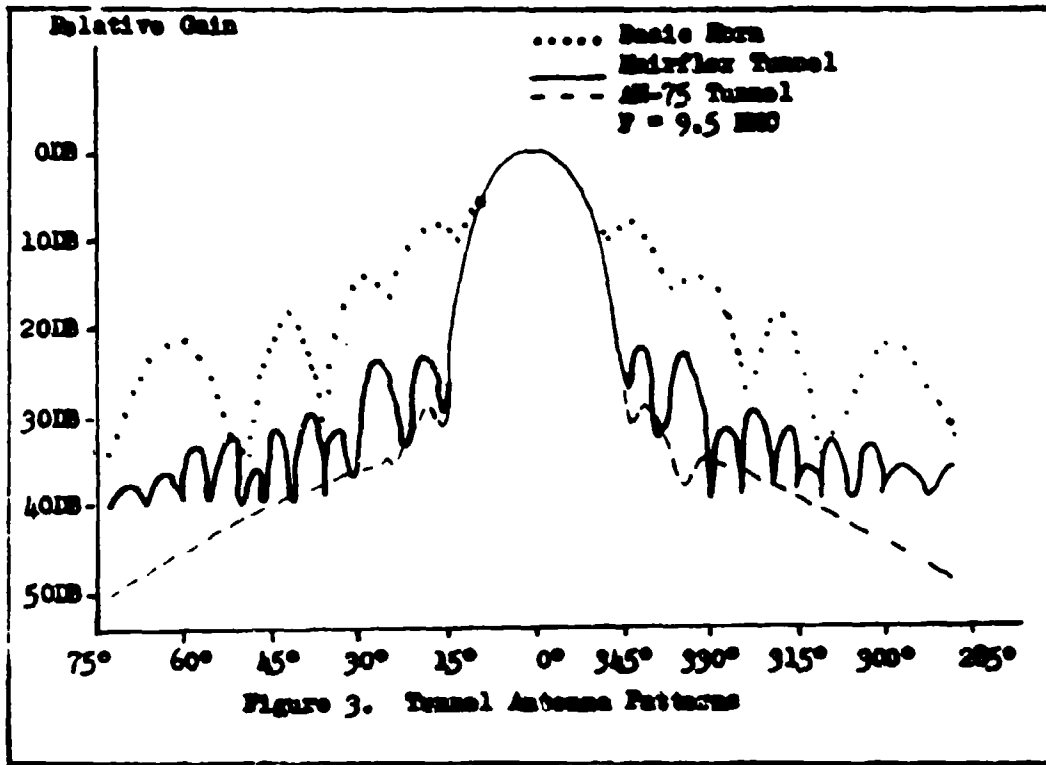


Figure 4. Short Pulse I-Band Radar

3. The radar absorber material used in the chamber must be the very highest quality available particularly for the backwall. Some commercial materials provide as much as 50 DB or more reduction in specular echo from flat surfaces. It is particularly important that the materials maintain this low level of echo for viewing angles within say 30 degrees of normal incidence. Assuming that the proper antennas are used and direct illumination of the chamber sidewalls is avoided, it is of lesser importance that the absorbers have low reflectance at angles far off normal ($> 50^\circ$). We have not seen direct sidewall reflection in our chamber but have observed multiple bounce echoes from target to wall to target. These latter are most pronounced when near normal incidence on the wall is obtained. For this reason, all of our sidewalls are tilted slightly off vertical and our backwall is tilted off vertical and is movable in azimuth. One must remember that a wall covered with absorber still has an echo pattern with peaks and nulls. Obviously orienting the wall so that a null is coincident with the direction of incidence would provide an echo significantly (10 - 20 DB) below that of the specular echo. Bear in mind though that a null in the pattern is obtained for a given illumination condition. Change the distribution of energy across the wall and the null may disappear and become a peak.

4. The target must be located as close to the measuring antennas and as far from the backwall as possible. The free space loss ($1/R^4$) dominates the thinking here. Moving the measuring apparatus far from the backwall reduces that echo power at the receiver while keeping the target close to the apparatus insures maximum target signal-to-background ratio. At the same time maximum distance between target and backwall reduces coupling and mutual interference problems.

5. A movable backwall for the chamber is highly influential in reducing inherent chamber echoes and also, in some cases, in reducing the effect of target introduction upon chamber echo. A standard technique for evaluating the chamber echo when CW systems are used is to record the echo from a small sphere which is rotated off center. From the variations in the pattern, one calculates the magnitude of the interfering echo. We have demonstrated to our own satisfaction that this magnitude is a function of the angular position of the backwall. B. F. Goodrich Co. has repeatedly substantiated these results in evaluation of their chambers. Thus one could optimize the chamber for minimum background for the sphere. Unfortunately this does not mean that the background is then optimum for all targets. Yet regardless of who built a chamber or who evaluates it, we all too often see the background figure derived from sphere tests quoted as the performance capability of the chamber with no qualification for target.

6. The influence of the target upon background signal in an indoor measurements chamber cannot be ignored. When a target is introduced into the chamber it always disturbs the background illumination, thereby altering the magnitude of the chamber echo previously nulled out by one means or another. For targets with large echoes, a moderate increase in background level is insignificant since a ratio of 20 DB is tolerable. But for cross section targets, the increased background level may be greater than that from the

target itself. A CW system would measure the combined echo as if it were only the echo from the target. Figure 5 is an example of CW data (X-band) on a low cross section shape. Figure 6 (solid line) is a plot of short pulse data on the same body. For the CW data, the background echo in the absence of target was less than 10^{-6} square meters. The pulse data was taken with a pulse length (10 nsec or 5 feet) which provided the total echo from the target (20 inches long) but easily separated it from the background signal which was more than 40 feet behind the target. The only difference between the two sets of data is that the CW system could not ignore the increased background level. Despite numerous attempts, we have not been able to devise any chamber arrangement which prevents, or even reduces to an acceptable level, the effect of these types of targets upon the background signal. The only way accurate CW data can be obtained indoors for such bodies appears to be either to rock the target in range and calculate the correct echo at each angle or use the technique of Fritsch. Figure 7 shows the background effect measured by pulse radar. Since photographs were to be avoided in this paper, we had to resort to drawing the sampling scope presentation. Here the solid line shows the amplitude of echo signal versus range in the absence of target. The back wall was adjusted in angle so that its echo, shown at 60 feet, corresponds to approximately $1.5 \times 10^{-6} \text{ M}^2$ at the target range. Note the complete lack of measurable cross talk between the antennas and of target support echo at 15 feet. The dotted lines represent signal level versus range with a low cross section target in place at an arbitrary aspect angle. We think the situation is clear and need not be discussed further.

MODEL REQUIREMENTS

Scale models for radar cross section measurements are a necessity if static techniques are used because full sized bodies would generally require prohibitive ranges or be too heavy for low echo supports. Model fabrication is as sensitive to the magnitude of radar cross section of the body as the measurement procedure.

For bodies with large ($> 10^{-1} \text{ M}^2$ full scale) echo area, the main problem is to insure that all important contributors to cross section are included in the model. For aircraft, the cockpit cover and larger items in the cockpit, the radome and equipment including antennas behind the radome, and jet engine inlet and exhaust ducts must all be constructed in reasonable detail. However, surface irregularities do not noticeably influence the total vehicle and may therefore be ignored.

On the other hand, for low cross section shapes where presumably there is little specular reflection, surface irregularities make a large difference. This can be seen in Figure 6 by comparing the solid curve with the points marked (x). These latter represent maximum values for the respective ten degree azimuth intervals and were taken from a reflection pattern of the same body as was used to obtain the solid curve. The difference in the two sets of data was in the surface of the model. In the case of the larger values, the wood from which the body was made had warped slightly causing a step discontinuity of perhaps 0.010 inches average at the shadow boundary. When the step was removed,

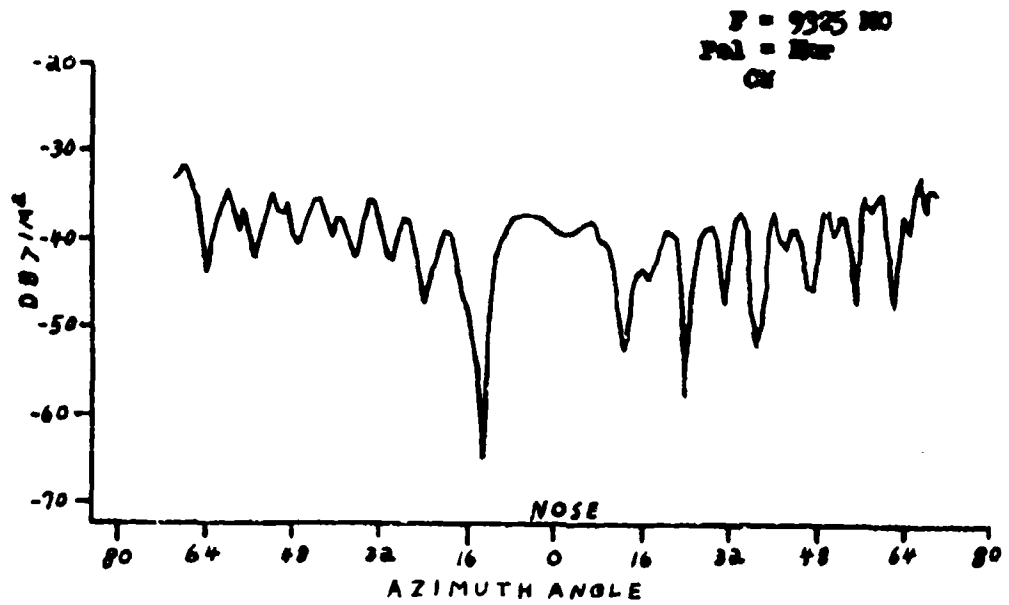


Figure 5. CR Pattern on Low Cross Section Shape

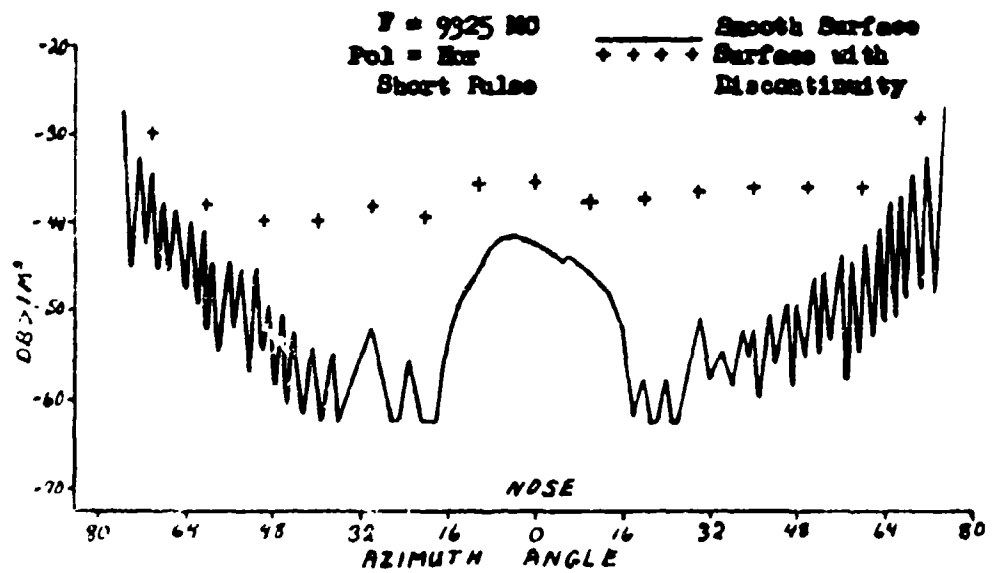


Figure 6. Pulse Pattern on Low Cross Section Shape

the solid curve was obtained. Note that these are unscaled data taken at 9325 mc by pulse radar.

We usually require dimensional accuracy in any model to be within 0.030 inches. Surface irregularity is ordinarily less than 0.001 inches. The dimensional tolerance is based upon a consideration of normal incidence echo from a circular flat metal plate. Here the echo area is proportional to the radius raised to the fourth power. For any other geometry, the echo area is a slower function of linear dimension. For the worst case then, it can be shown that a 2% error in radius only causes 0.3 DB error in echo area. Of course this is a percentage problem and for very small models, or standard spheres for instance, the tolerance is tightened accordingly. But usually for models in the order of a foot or more in dimension, 0.030 inches is satisfactory.

Other than dimensional accuracy and necessary detail, our main concern in modelling is weight. For this reason, wood or plastic painted with metallic silver paint is preferred. Very satisfactory models have been made by laying up glass cloth laminates in a female mold, thus obtaining a very smooth outer surface for the body, and assembling the cured sections over lightweight ribs much the same as an aircraft is built. In this manner bomber models over 14 feet in wing span have been made with total weights of slightly over 100 lbs. For much smaller models of say re-entry vehicles, solid wood turned on a lathe provides necessary surface smoothness and is acceptable from the weight standpoint. Several coats of good conductive paint (such as Dupont 4817) provides an excellent metallic surface so long as the resistance of the coating is less than 1 ohm per square. Only slightly higher values produce measurable changes in echo.

Perhaps the most controversial issue in model measurements is the matter of imperfectly conductive materials such as radar absorbers. Rigorous scaling laws clearly require that thickness be scaled, that magnetic and dielectric properties be the same at the measurement frequency as at the full scale frequency, and that conductivity be scaled. Yet for the optics region, where body dimensions are large in terms of wavelengths and specular reflections dominate the echo from most targets, it is really the reflection coefficient of the material which is influential.

Consider the simple case of a flat metal plate at normal incidence. If we measure the return as a metallic surface then cover it with an absorber whose power reflection coefficient is say .01 we will reduce the metal body return by 20 DB. Now if we assume the body had been scaled, we would compute the full scale echo by multiplying the scaled echo by the scale factor squared. If we measured the full size plate at the full scale frequency, then covered it with an absorber of power reflection coefficient .01, we would again reduce the metal return by 20 DB. But this last echo area is precisely what we would have obtained by calculation from the scaled data. Yet in the two cases, we could have used absorbers whose identical reflection coefficients were obtained by totally different combinations of magnetic and dielectric properties and whose thicknesses were not in the ratio of the scale factor.

Since a very significant portion of the reflection measurements made today involve the use of absorbers on models, it is only reasonable that we take advantage of anything which will make the job easier and cheaper. Even though the statements in the preceding paragraph may apply only to absorptive materials, they have wide application at that. In our efforts to reduce the cross section of a vehicle we use any absorber whose reflection coefficient at the scaled frequency is the same as that of the actual absorber at the full scale frequency. That this obtains valid data has been substantiated in several instances where both full scale and model data have been available. Unfortunately, these data are classified and cannot be presented herein.

We must of course recognize that in the Rayleigh region, these simplifications may not apply. It has been shown by Siegel and others that the formulation of absorbers for bodies small in terms of wavelengths must be adjusted for body shape and dimensions to obtain a given reduction in echo. Since to date we have done very little work which bears on this special problem, we will leave its discussion to others.

COMPARISON BETWEEN CW AND PULSE DATA

As a last point of interest, we would like to present results of measurement of a satellite model which were obtained by both CW and pulse systems at the same frequency. The results, shown in Figure 8, are plotted as actual echo area of the model, uncorrected for scale factor, versus azimuth angle measured from nose. The echo from this model was large enough that the background did not influence the CW result. At nose-on there is a 7 DB difference between the two sets of data which is much too large to be acceptable. However, we found after these particular patterns were taken, that the nose-on echo could be varied by adjustment of the junction between mating sections of the model. Therefore, we cannot blame the nose-on discrepancy on instrumentation error. Other than that difference and the fact that there seems to be an alignment error of perhaps 1 degree, the agreement between the CW and pulse data is excellent. The loss of sharp peaks and nulls by the technique we used to obtain the pulse data, i.e. one degree readings, is evident and teaches that finer readings are necessary when the target aperture, perpendicular to the path of propagation, becomes large. The planned automatic recording system should solve this problem completely.

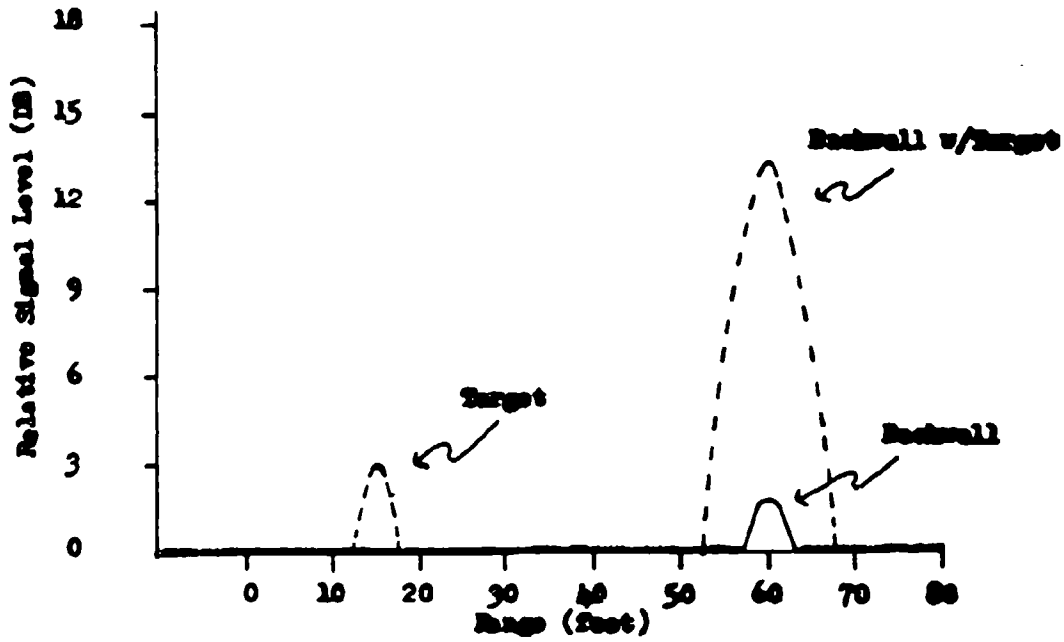


Figure 7. Background Levels Measured by Short Pulse Radar

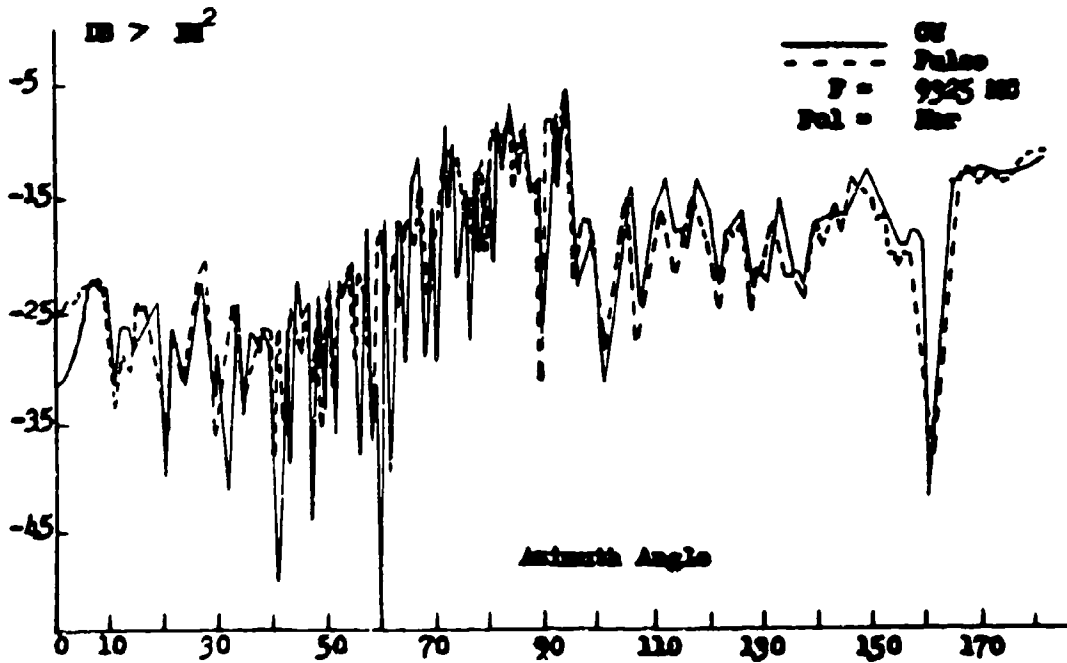


Figure 8. Pulse and CW Data on Satellite Model

RADAR CROSS SECTION MODEL MEASUREMENTS

W. E. Blore
R. I. Primich
R. A. Hayami
P. E. Robillard
H. M. Musal

Microwave Section
Aerospace Operations Department
General Motors Defense Research Laboratories

SUMMARY

It is the purpose of this paper to summarize the experience gained by the authors during the past ten years in the operation of four model measurement radars in an indoor anechoic chamber, three CW Balanced-Bridges operating at frequencies of 10 Gc, 35 Gc, and 70 Gc, and a short-pulse radar operating at 35 Gc. The latest versions of these radars have the following capabilities:

TABLE I

Frequency	10 Gc	35 Gc	70 Gc	35 Gc Pulse
Minimum Measurable (Non-rotating)	-40 db λ^2	-35 db λ^2	-25 db λ^2	-20 db λ^2
Maximum Target Size	12"	3.5"	3.5"	12"
Minimum Tower Cross Section	-40 db λ^2	-35 db λ^2	-25 db λ^2	-20 db λ^2

The above performance figures were measured at λ^0/λ with a plane-wave lens. With smaller targets and focused lenses, significant increases in sensitivity can be achieved. For example, at 10 Gc, a target of 2" diameter and cross section -60 db λ^2 can be measured; and at 35 Gc, a target of 0.8" diameter and cross section -54 db λ^2 can be measured.

The significant features of the CW balanced-bridge radars are as follows. Both transmitter and local oscillator klystrons have been phase-locked through a phase-locked multiplier chain to a 1 Mc frequency standard. The phase stability of the system is such that an isolation of

better than 100 db at 70 Gc and 120 db at 35 Gc between the transmitted and received signals has been maintained across the hybrid for continuous periods of more than ten minutes. Also, phase can be measured directly by comparison of the received signal against a reference signal. A simple cancellation circuit has been included which has enabled the bridge to be balanced in a smooth, controllable manner. The amplitude and phase of the backscattered wave from the model can be measured with accuracy of better than ± 1 db and $\pm 2^\circ$ respectively. Models are supported on styrofoam towers which have been tuned to a maximum cross section of $-35 \text{ db} \lambda^2$ at 35 Gc.

The 35 Gc pulse radar has a pulse width of 15 nS , a dynamic range of 50 db, a transmitter-receiver isolation of 130 db, and may be used to make bistatic as well as backscattering measurements with both plane and circularly polarized radiation.

In the development of these radars, the authors have made extensive investigations of several sources of error in model measurements. In particular, these include the effects of non-plane illumination, various model support methods, cancellation techniques, model dimensions and finishes, transmitter frequency stability, and data recording techniques.

Further, in another development, the authors have used CW doppler radars to measure the nose-on cross section of models in a hypersonic ballistics range. These radars, operating at frequencies of 35 and 70 Gc are essentially CW balanced-bridge radars in which the doppler shift of the moving target has been used to separate the model signal from the stationary background signal. Significant changes in the model cross section due to the plasma sheath have been noted. A high resolution focused 35 Gc oblique doppler radar has also been used to measure parameters of the wake behind the hypersonic velocity projectile.

MM WAVE - RADAR CROSS SECTION MODEL MEASUREMENTS IN ANECHOIC CHAMBERS

Introduction

About ten years ago the authors began to develop a facility which was to be used to make basic studies of the radar cross section of model targets. In the interests of convenience and year-round operation, measurements were to be made in an indoor anechoic chamber, and because of the convenient sized models and ranges which resulted, the operating wavelengths were to be in the millimeter region. Two major problems were immediately apparent. First, it was necessary to simulate free-space conditions around the model. This simulation

entailed three major elements: the elimination of the effects of the anechoic chamber on the measured model cross section, the provision of a model support system which did not significantly affect the model cross section, and the evaluation of the effects of non-plane illumination on the cross section measurements. Second, provided free-space conditions had been successfully simulated, it was necessary to make accurate measurements of large numbers of low cross section models over a wide range of model sizes, wavelengths, aspects, polarizations, and bistatic angles. In the sections which follow, we will deal successively with the problems of non-plane illuminations, model support, background cancellation techniques, and the development of sensitive, accurate, multi-capability radars.

Plane-Wave Illumination

Radar cross section is invariably derived under conditions of plane wave target illumination, and, indeed, in the full-scale case, the target is so far from the radar that the spherical wave is locally plane. In a model range, the target is close to the radar so the illumination is spherical rather than plane, and it is usually assumed that the illumination is a satisfactory approximation to plane wave conditions if the amplitude does not vary by more than 1 db or the phase by $\lambda/16$ over the extent of the model. Many experiments have shown that this is indeed a reasonable criterion, since the effect of slightly non-plane illumination is to decrease the gain and fill in the sharp nulls without significantly changing the major features of the measured cross section pattern. For many of the targets investigated with the radars developed by the authors, the target was smaller than the radar antenna. In this case it is possible to measure target cross section inside the Fresnel zone of the antenna, provided the plane wave illumination conditions are fulfilled. Theoretical predictions of the Fresnel fields of square and circular apertures have been computed^{1, 2} and the authors have experimentally confirmed the predictions³. We have found that the amplitude variation is the limiting restriction on model size at distances closer to the antenna than D^2/λ while phase variation is the limiting restriction from D^2/λ to $2D^2/\lambda$. In a logical extension to this work, the fields in the focal region of a lens have been analyzed¹⁸ and it has been shown that sufficiently uniform fields exist in this region to measure models up to 2λ in diameter, for typical lenses of 10λ aperture and focal lengths ranging from 2 to 5 lens diameters.³

Model Support

The model support must be sufficiently strong and rigid to fix the model securely, yet it must not contribute significantly to the radar cross section of the model. The present authors have used polyfoam

towers as model supports since these towers are easy to construct, are readily tailored to individual models, are rigid enough for small models, are suitable for rapid measurements of a series of models, and most important, they may be easily tuned to have very low radar cross sections. Reference (4) gives the details of adjusting the tower diameter to obtain minimum echo area, and indicates that towers of about 1" diameter have been constructed which have a cross section of $-50 \text{ db } \lambda^2$ (-80 dbm^2) at X-band, $-35 \text{ db } \lambda^2$ (-76 dbm^2) at 35 Gc, and $-25 \text{ db } \lambda^2$ (-62 dbm^2) at 70 Gc. These figures are about 15 db better than results reported with nylon strings¹⁵ and are about 10 db better than previously reported results for polyfoam towers¹⁶.

BACKGROUND ELIMINATION

The Anechoic Chamber

A rectangular anechoic chamber of dimensions 40 x 12 x 60 feet covered on all surfaces with microwave absorber was used to house the scattering range. Although we are aware of the many methods and philosophies regarding the tuning of anechoic chambers to achieve a minimum background cross section, no special effort was made to tune this chamber. Instead, we have attempted to eliminate the interfering range background with two separate techniques. First, the use of the CW balanced-bridge radar, in which the total background signal in the absence of the model is cancelled by a phase-amplitude nulling circuit. Second, the use of a short-pulse radar,⁵ whereby all background except that in the immediate vicinity of the model is eliminated by means of a range gate. Consider first the short-pulse radar.

The Short-Pulse Radar

Since the details of the short-pulse radar are fully presented in reference(5), we mention here only some highlights of the performance and problems of the radar. The radar frequency was 35 Gc, and the minimum pulse length was 12 ns. The transmitted power was 30 kw, the receiver tangential sensitivity was -52 dbm and the IF frequency was 3000 mc.

The received back scattered pulse amplitude was maintained constant with a RF servo-crystalled attenuator driven by a masked-CRT photo-multiplier detection system, so that cross section measurements accurate to one db were possible over a dynamic range of 50 db. Separate antennas were used for the transmitter and receiver so that bistatic and polarization diversity scattering studies with both rectangular and circularly polarized radiation were possible. Tunnel antennas were used to suppress the antenna sidelobes and to provide an isolation of better

than 130 db between the transmitter and receiver so that transmitter receiver leakage was completely eliminated. For a typical target approximately 12 inches in diameter at a range of 23 feet, the minimum measurable cross section was $-20 \text{ db } \lambda^2$ (-61 dbm^2). The major limitation to the radar sensitivity has been the support system. Due both to the relatively large towers required because of the large models, and the wide frequency content of the short pulse, it was not possible to obtain styro-foam towers with cross sections less than $-20 \text{ db } \lambda^2$ (-61 dbm^2). However this sensitivity was adequate for the models to be measured at the time (1958), and the pulse length proved short enough so that adequate time separation was obtained between the pulse scattered from the model and that scattered from the back wall of the anechoic chamber. Even at the present time, five years after the original design, this radar has a unique combination of high frequency, high power, and narrow pulse width.

The CW Balanced-Bridge Radar

With a CW balanced-bridge radar, the output of the receiver in the absence of a model is the vector sum of the backscattered radiation from the anechoic chamber (including the model support system) and the leakage signal due to the imperfect isolation properties of the waveguide magic tee. This output signal may be eliminated if it is combined with a signal of equal amplitude and opposite phase, and, provided the presence of the model does not significantly change the room illumination, or the background does not change position, and both the cancellation signal and the the background signal do not change amplitude or phase, then the background effects are completely eliminated, and the model appears to be in free space. The major limitation to bridge sensitivity is the difficulty in obtaining a complete cancellation of the background signal and of maintaining this cancellation for significant periods of time. The maximum performance is obtained only if the following conditions are met. All waveguide components must be rigidly mounted, the radar must be rigidly fixed in place, the anechoic chamber must be closely temperature controlled, the transmitter frequency must be extremely stable--preferably phase locked to a low frequency standard oscillator, and the cancellation circuits must be capable of fine, repeatable control of both the amplitude and phase of the cancellation signal. Three radars, operating at frequencies of 9 Gc, 35 Gc, and 70 Gc, have been constructed following these principles. Details of the 35 and 70 Gc radars have been published elsewhere⁶ so we only summarize here the performance figures attained.

TABLE II
9, 35 and 70 Gc Radar Performance

Frequency	9 Gc	35 Gc	70 Gc
Target Size	12"	3.5"	3.5"
Minimum Detectable Cross Section at $2 D^2/\lambda$	-76 dbm^2	-76 dbm^2	-62 dbm^2
	$-45 \text{ db } \lambda^2$	$-35 \text{ db } \lambda^2$	$-25 \text{ db } \lambda^2$

The above performance figures were measured at $2D^2/\lambda$ with a plane-wave lens. With smaller targets and focused lenses, significant increases in sensitivity can be achieved. For example, at 10 Gc a target of 2" diameter and cross section -90 dbm^2 ($-60 \text{ db } \lambda^2$) can be measured and at 35 Gc a target of 0.8" diameter and cross section -95 dbm^2 ($-54 \text{ db } \lambda^2$) can be measured. The essential features of these radars are as follows. Both transmitter and local oscillator klystrons have been phase-locked through a phase-locked multiplier chain to a 1 Mc frequency standard. The phase stability of the system is such that an isolation of better than 100 db at 70 Gc and 120 db at 35 Gc between the transmitted and received signals has been maintained across the hybrid for continuous periods of more than ten minutes. Also, phase can be measured directly by comparison of the received signal against a reference signal. A simple cancellation circuit has been included which has enabled the bridge to be balanced in a smooth, controllable manner. The amplitude and phase of the backscattered wave from the model can be measured with an accuracy of better than $\pm 1 \text{ db}$ and $\pm 2^\circ$ respectively. Models are supported on styrofoam towers which have been tuned to a maximum cross section of -76 dbm^2 ($-35 \text{ db } \lambda^2$) at 35 Gc and -62 dbm^2 ($-35 \text{ db } \lambda^2$) at 70 Gc.

Recent measurements which have been made with these radars may be found in References 7, 8, 9.

The Phase Comparison Radar

The CW balanced-bridge radar places stringent requirements on the frequency stability of the microwave transmitter klystron. The best systems have therefore stabilized the klystron frequency with some fairly elaborate techniques--for example, Pound stabilizers, crystal multiplier chains, and phase-locked loops. A technique, called the phase-comparison radar, has been developed in which the microwave frequency stability requirements can be relaxed, and in which, effectively, a CW balanced bridge operates at an audio modulating frequency. Details of this system are presented in Reference (10), so only the essential features of the system are presented here.

The radar consisted of a double-sideband suppressed carrier Klystron transmitter (modulation frequency ω_m) driving the usual CW bridge. The unmodulated Klystron output after being phase modulated at a rate ω_f serves as the local oscillator. The output signal is fed through the π mixer, a bandpass amplifier, a phase detector operating at the modulating frequency ω_m , a tuned amplifier operating at ω_f , and an amplitude detector. It can be shown that the final output of this system is of the form $E_o = K \cos \phi_m$. Thus it is possible to balance the bridge by adjusting the background signal from the far wall of the

range and the leakage through the magic tee to be in phase, and then adjusting both signals to be 90° out of phase with the reference signal in the phase detector, so that the bridge output in the absence of a target is zero. An operating version of this radar has been constructed at 10 Gc, and operated as expected. Background cancellation was effective at both rf and modulating frequencies, and the requirement for extreme frequency stability on the rf source was relaxed. One disadvantage of the bridge was that no tower cancellation was possible.

GENERAL COMMENTS ON MODEL MEASUREMENTS WITH ANECHOIC CHAMBERS

In this section we present some general, possibly controversial conclusions about mm-wave model measurements in anechoic chambers. We have found ± 0.5 db to be about the best possible accuracy with which cross section measurements can be quoted, considering the errors in illumination, background illumination, RF attenuators, servo driven pen recorders, and other error sources, and we feel that ± 1 db is probably closer to the actual error in most cases.

All our models are constructed to tolerances of $0.001''$ in dimension, 0.10° in angle, and 5μ in surface finish, but, for most models, these tolerances could be relaxed by a factor of ten without changing the results significantly.

For small models, we find that commercial rotating gear is inadequate because the excessive vibration of these units changes the model aspect during rotation.

The basic test of the quality of our measurements has always been the ability to reproduce accurately the Mie sphere curves, and the ability to produce symmetrical patterns with deep nulls. The ability to measure the same nose-on cross section in orthogonal polarizations is also important. These criteria are necessary, but not sufficient guarantees of good cross section measurements. We have generally evaluated the quality of the anechoic chamber by rotating a sphere off-center on a tower.

It should be noted that one of the virtues of the CW balanced-bridge technique is that provided only the nose-on cross section of the model is required, and the model does not have to be rotated, the cross section of the support system and the range background are unimportant, and very low cross sections can be measured. The limitations, other than that of changing bridge balance, are only those second order effects caused by the change of background illumination due to the model, and any model-support interactions.

In Figure 1, we present a general curve, which summarizes the experience we have had with the CW balanced bridge. In this figure, we plot minimum measurable model cross section in square wavelengths against the model diameter in wavelengths, and the two shaded areas delineate first the absolute limits of model geometry which can be measured with the balanced-bridge, and second, the combination of model size and cross section which are most easily measured with a balanced bridge. Points typical of our three radars are also included in the figure.

In Figure 2, we present a universal design chart for the CW balanced bridge radar. This figure plots minimum measurable cross section against range to target and target size with both antenna size and hybrid isolation as parameters. The figure has been generated from the radar equation: $\frac{P_r}{P_t} = \frac{\sigma}{(4\pi)^3 R^4} \frac{A^2}{\lambda^4}$ and from the roughly linear relation between model size and distance from the antenna. The three radars we have built all perform essentially in accordance with this nomograph

OTHER APPLICATIONS OF MODELING TECHNIQUES

In the preceding sections, we have discussed the application of millimeter wave radars to the measurement of the radar cross section of model targets in an anechoic chamber. The study of reentry phenomena is another area in which millimeter wave radars and modeling techniques have been successfully applied. Many of the relevant phenomena of reentry can be duplicated under laboratory conditions with a hypersonic ballistics range--a device in which small models are accelerated to high velocities and fired through long tunnels containing controlled atmospheres. In particular it is easy to make detailed studies of the flow field and plasma effects over a wide range of pre-selected velocities and pressures, and, as part of these studies, we have instrumented a CW doppler radar with the beam located along the flight direction to make direct measurements of the nose-on echo area of a projectile in flight. As was the case for model measurements in anechoic chambers, ballistic range measurements require the simulation of free space conditions. The doppler shift produced by the moving projectile has been used to isolate the desired projectile signal from the clutter arising out of the stationary background. Details of this technique are given in References 11, 12, 13 and 14. At present, we operate two CW doppler radars at 35 and 70 Gc simultaneously, diplexing the radar beams by means of a wire grid reflector. Both radars are capable of measuring projectile radar cross section to within +1 db over a range from -10 db λ^2 to +30 db λ^2 (from -51 dbm² to -11 dbm² at 35 Gc and from -57 dbm² to -17 dbm² at 70 Gc) while the projectile range varies from 6 to 30 feet. Radar antennas, reflectors and microwave windows have been designed so that the maximum operating range with a

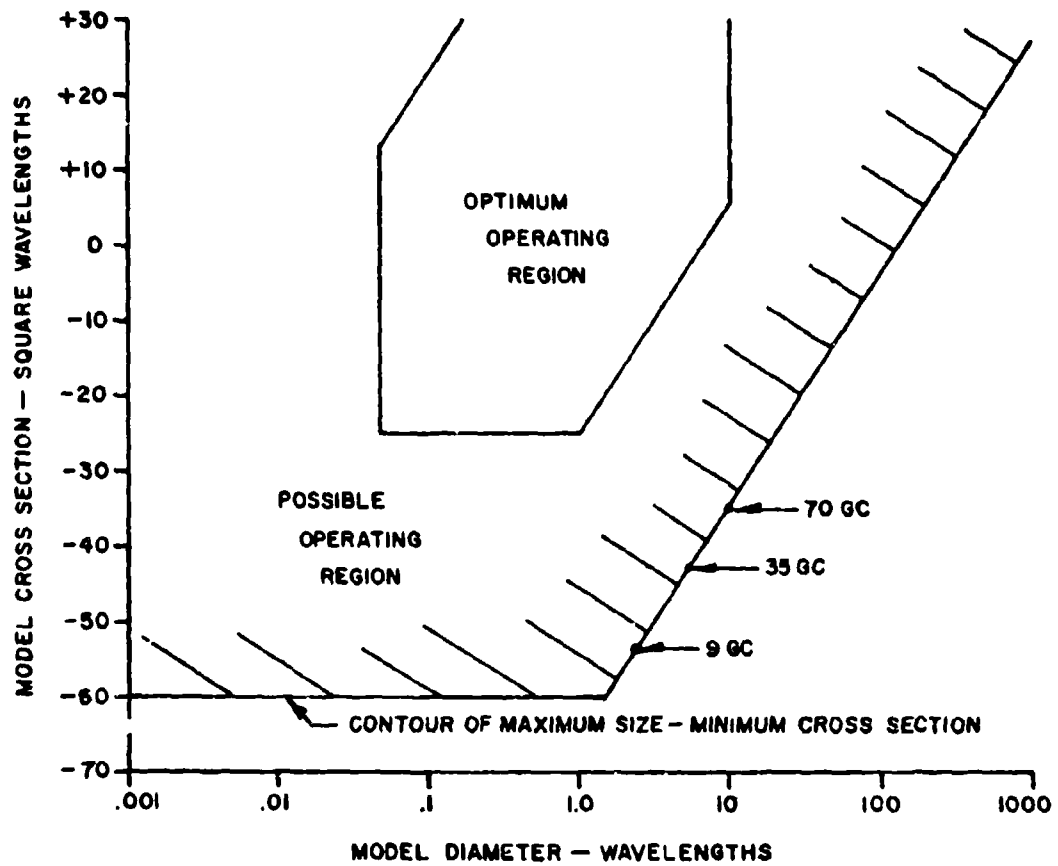


Figure 1. Design Curve for CW Balanced Bridge Radars--
Model Cross Section Versus Model Diameter

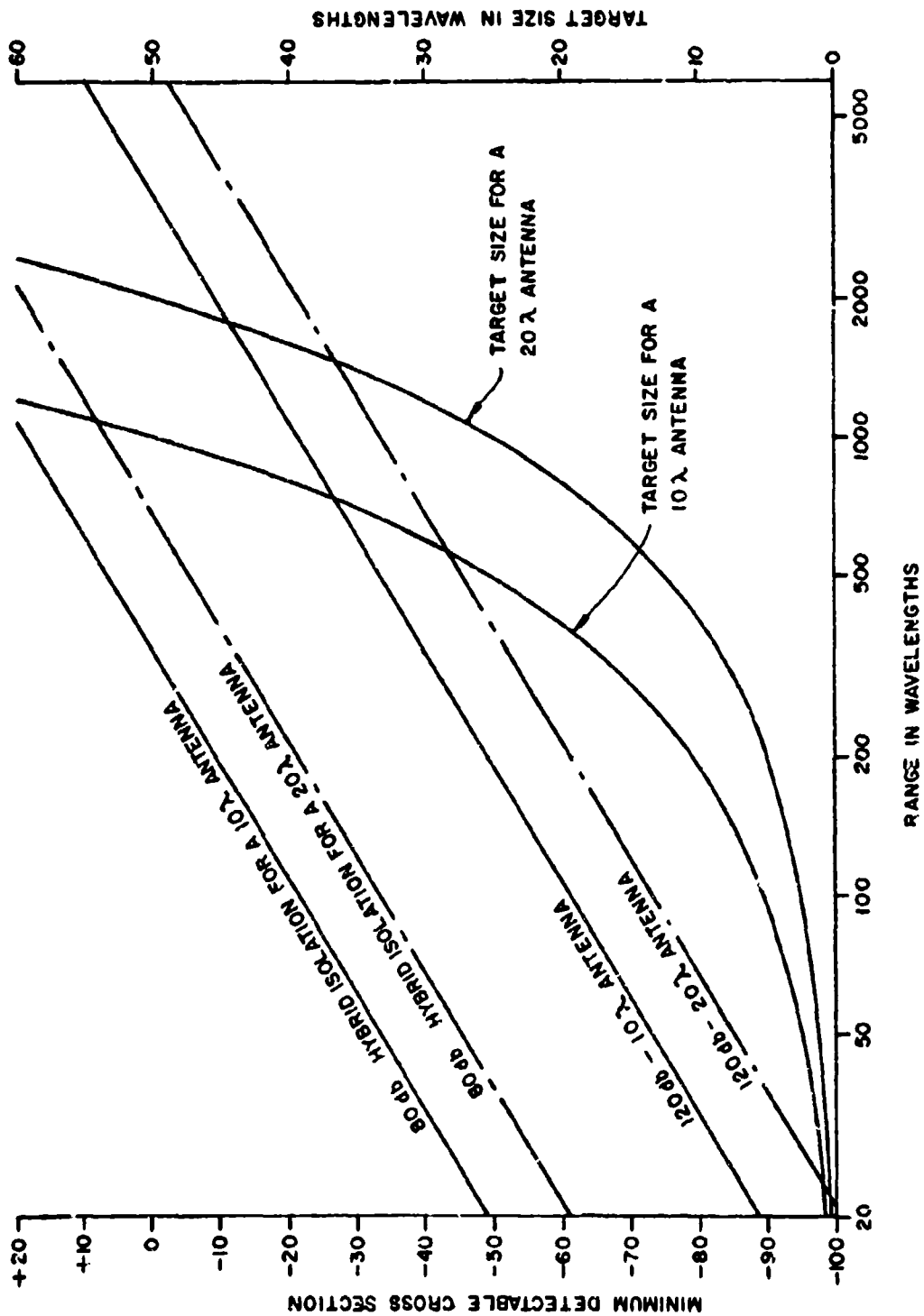


Figure 2. Design Chart for CW Balanced Bridge Radars

minimum of interference from the sides of the ballistic range is achieved, with a minimum use of microwave absorber to line the tank. Excellent agreement between the radar cross section measured in flight and that obtained in the anechoic chamber has been noted. Further, significant changes in the projectile radar cross section due to the plasma sheath have also been noted, and these changes are being correlated with the plasma properties.

Another version of the CW doppler radar has been installed with the beam located at 45° to the flight axis. This oblique radar is used to measure the properties of the wake behind the projectile. In particular, transition from laminar to turbulent flow in the wake can be observed, and measurements of the wake velocity can be made.

The radar operates at 35 Gc and is essentially similar to the two radars described above. A 24" diameter F1 lens focused on the range axis provides a spatial resolution of about two wavelengths along the flight axis. Coarse cancellation of the background is accomplished at microwave frequencies, and the doppler shift is used to isolate the projectile signal from the stationary background. Minimum detectable signal is about $-20 \text{ db } \lambda^2$.

ACKNOWLEDGMENTS

The initial development of the CW balanced-bridge radars was performed by some of the authors at the Defense Research Telecommunications Establishment, Ottawa (DRTE). However significant improvements to these radars have been made at the GM Defense Research Laboratories, Santa Barbara. The phase-comparison radar and the pulse radar are both entirely DRTE work, while the majority of the ballistics range work has been done at GM DRL. In general, the work described in this paper has been a continuing program, carried on both at DRTE and GM DRL and the authors are indebted to both organizations for support.

REFERENCES

1. R. I. Primich, "The Fresnel Field of a Square Aperture Uniformly Illuminated with Microwave Radiation," RPL Project Report 22-23 July 1956, Defence Research Telecommunications Establishment, Ottawa, Canada.
2. M. K. Hu, "Fresnel Region Fields of Circular Aperture Antennas" Journal of Research National Bureau of Standards, Radio Propagation, Vol. 65D #2, March 1961.
3. W. B. Foss, "Experimental Investigation of the Fresnel Field of a Circular Aperture Antenna", 1961, Unpublished Report.
4. W. E. Blore, "The Radar Cross Section of Polyfoam Towers" GM Defense Research Laboratories Rpt #TR63-240, November 1963. Also, IEEE PTG-AP, March 1964.
5. T. H. Legg, R. A. Hayami and R. I. Primich, "An 8-6 mm Short-Pulse Radar for Indoor Model Measurements", Defence Research Telecommunications Establishment Rpt #1085, 1962, Ottawa, Canada. See also RPL Report 47-0-2, 1958 and RPL Rpt 22-2-5 1956.
6. W. E. Blore, P. E. Robillard, and R. I. Primich, "35 and 70 Gc Phase-Locked CW Balanced-Bridge Model Measurement Radars". To be published in the Microwave Journal.
7. W. E. Blore, "Experimental Verification of Scattering Coefficients for Metal Spheres", Proc IEEE, Vol. 51 #9, September 1963, pp 1270.
8. W. E. Blore, "Experimental Measurements of the Radar Cross Section of a Cone Sphere." Proc IEEE, Vol. 51 #9, September 1963, pp 1263.
9. W. E. Blore and G. M. Royer, "The Radar Cross Section of Bodies of Revolution", Defence Research Telecommunications Establishment Rpt #1105, March 1963, also to be published in IEEE PTGAP.
10. R. I. Primich, "Some Proposals for the Measurement of the Radar Cross Section of Models", Defence Research Telecommunications Establishment Rpt #22-2-2 July 1956, Ottawa, Canada.

11. R. I. Primich, "Microwave Techniques for Hypersonic Ballistic Ranges," *Electromagnetic Effects of Re-entry*, pp 186-195 Pergamon Press, London, 1961.
12. R. I. Primich, W. E. Blore, W. A. Pope, and E. T. Atkins, "Hypersonic Ballistic Range Studies With a Microwave CW Doppler Radar", Defence Research Telecommunications Establishment Report #1086, June 1962, Ottawa, Canada.
13. R. I. Primich, W. A. Pope, E. Atkins, W. Blore, and A. L. Broadfoot, "A CW Doppler Radar for the Observation of Projectiles in Hypersonic Ballistic Ranges", Defence Research Telecommunications Establishment Report #1032, January 1960, Ottawa, Canada.
14. "Instrumentation, Calibration, and Data Reduction Methods", Report #TR62-213, December 1962, GM Defense Research Laboratories, Santa Barbara, California.
15. W. P. Melling "An Analysis of Radar Cross Section Measurement Techniques" Cornell Aeronautical Laboratories Rpt UR-1088 pp 104, Buffalo, New York, September 1959.
16. J. E. Keys and R. I. Primich "The Experimental Determination of the Far Field Scattering of Simple Shapes" (paper presented at Symposium on Electromagnetic Theory, 25 June 1959, Toronto). Reprinted by Defence Research Telecommunications Establishment, Ottawa, Canada.
17. P. E. Robillard, H. M. Musal, Jr., and R. I. Primich "Millimeter Radar Techniques for Studying Plasma Effects Associated with Hypersonic Velocity Projectiles", Millimeter and Submillimeter Conference, Orlando, Florida, January 1963. Also N63-21552.
18. R. I. Primich and F. H. Northover "Use of Focused Antenna for Ionized Trail Measurements" Defence Research Telecommunications Establishment Report #1076, October 1961, Ottawa, Canada.

STATE-OF-THE-ART ANECHOIC BACKSCATTER RANGES

W. H. Emerson, Mgr. Absorbent Materials and Systems, B. F. Goodrich
F. P. Brownell, Senior Microwave Engineer, B. F. Goodrich
Shelton, Connecticut

INTRODUCTION

It has now been some ten years since the first "darkroom" was described in the technical literature.¹ This particular room, like the majority of those which have followed, was brought into being primarily as a facility for indoor measurement of antenna parameters. While a number of such rooms have been put to good use in the measurement of radar cross sections, it has only been relatively recently that concerted attention has been given to acquiring an understanding of the particular requirements imposed by backscatter work. Once development effort was directed toward this end, performance of chambers with respect to radar reflectivity characteristics began to show steady improvement; a trend which is continuing through the present and may be expected to continue in the future. We, as chamber designers and suppliers, see solid evidence to indicate that the backscatter chambers of today have inherent radar cross sections which are a number of orders of magnitude better than those of a year or two ago. Much of the interesting recent progress has not yet been reported in the open literature. The primary purpose of this paper therefore becomes the description of the state-of-the-art in backscatter chambers as seen from this vantage point. During the course of this description, emphasis will be placed on aspects such as: 1.) the definition of customary means of describing backscatter chamber performance, 2.) the inherent chamber cross section levels which can be currently achieved, 3.) the design techniques through which such performance can be accomplished and 4.) the measurement techniques through which such levels can be quantitatively measured. Comparison of these performance characteristics with those of other types of ranges is suggested.

DESCRIPTION OF THREE MODERN INDOOR REFLECTIVITY CHAMBERS

There would appear to be no better way to describe the state-of-the-art in anechoic backscatter ranges than to describe existing new chambers which have been specifically designed to provide highest performance for reflectivity measurements. Consequently, we present in Table I a wide variety of comparative data and information on three chambers of this type which have recently been designed and installed by this company. We believe that these facilities qualify for use of the term "state-of-the-art" as a result of their high levels of performance and the fact that this performance is directly attributable to new materials and techniques.

TABLE I

Comparative information on three recent state-of-the-art reflectivity chambers designed and installed by the B. F. Goodrich Company. *

Reflectivity Characteristics at X-Band

Equivalent radar cross section at 25 feet for stated path length

	<u>Martin</u>	<u>Sperry</u>	<u>AIL</u>
σ_t (favorable tilt angle)	60 db $\langle M^2$ 30 db $\langle \lambda^2$	66 db $\langle M^2$ 36 db $\langle \lambda^2$	80 db $\langle M^2$ 50 db $\langle \lambda^2$
σ_v (back wall vertical)	49 db $\langle M^2$	30 db $\langle M^2$	45 db $\langle M^2$
<u>Apparent reflection coefficient</u>			
Γ_t (determined from σ_t)	77 db	85 db	99 db
Γ_v (determined from σ_v)	66 db	49 db	64 db
Γ_v ("Free Space VSWR" technique)	62 db	not meas.	67 db
<u>Measurement Conditions</u>			
Path length to back wall	50 ft.	39 ft.	39 ft.
Frequency	10.0 KMC	10.0 KMC	10.0 KMC
Crosstalk before cancellation	10 db $\langle M^2$	35 db $\langle M^2$	35 db $\langle M^2$
Crosstalk after cancellation	65 db $\langle M^2$	85 db $\langle M^2$	88 db $\langle M^2$
Antennas	Parabolas, D = 1 ft.	Parabolas, D = 1 ft.	Parabolas, D = 1 ft.
Receiver sensitivity	-85 dbm	-85 dbm	-100 dbm
Generator output level	+23 dbm	+23 dbm	+ 20 dbm
Noise level in terms of σ	53 db $\langle M^2$	63 db $\langle M^2$	60 db $\langle M^2$
Reference target sizes	2.10 in., 28 db $\langle M^2$.624 in., 43 db $\langle M^2$	Same	Same
<u>Design Characteristics</u>			
Back wall	VHP-26, Tilt Wall	VHP-45, Tilt Wall	VHP-45 Tilt Wall
Side walls, floor and ceiling	VHP-18	VHP-26, 18	VHP-26, 18
Front wall	VHP-18	HV-8	HV-8
Baffles	None	None	None
Floor work areas	None	Each End	Each End
Shielding requirement	None	Moderate	None
Construction	Outdoor, Gunder block	Indoor, mod. Plywood	Indoor, modular Plywood
Ventilation	Forced air	Air condition.	Forced air
Lighting	Incandescent	Incandescent	Incandescent
Cross section dimensions, Q. D.	20x20 ft.	16x16 ft.	20x20 ft.
Length dimension, O. D.	50 ft.	46 ft.	46 ft.

*It is suggested that those who are interested in detailed design and measurement information on these chambers query the B. F. Goodrich Co. for copies of the evaluation reports which are available on each.

Reflectivity Characteristics

Prior to considering the observed performance levels of these chambers, it would seem appropriate to provide discussion of the means which are commonly employed (and are here used) to quantitatively describe chambers with respect to their backscatter properties. Two systems may be encountered: 1.) one defines chambers in terms of their inherent radar cross section, 2.) the other in terms of their apparent reflection coefficient. While one may readily convert from one system to the other, the two are sufficiently different in viewpoint to suggest continued existence of both for the present. They are separately considered below:

Inherent Radar Cross Section. This terminology describes a chamber in the manner which is customary for other types of radar targets, i. e. in terms of the cross section of the equivalent sphere that would produce the same return signal at the receiver as does the empty chamber. In the case of other targets, the distance to the reference sphere and the target is taken as the same so that the target may be described by a cross section value which is exclusively a function of target reflection properties and independent of distance. In the case of a chamber, however, it is not as obvious as to what distance should be chosen for the reference sphere since a chamber does not appear at a discrete point in space. While the distance to the chamber back wall might have been established as a reference point, it has instead become customary to define the inherent cross section of a chamber with the sphere located at a fixed distance and hence unrelated to chamber dimensions. Values are commonly quoted with the reference distance chosen as 25 feet (as in Table I), 50 feet, or the distance of the target pedestal in a particular chamber.

This means of describing chamber performance provides both advantage and disadvantage. The advantage is that it expresses quality in terms of radar cross section; a concept which is familiar, useful and appropriate for chambers of this type. On the other hand, the cross section numerical value is not exclusively a function of chamber reflection properties but is, in addition, a function of both reference target distance and back wall distance. As a result, a direct comparison between values quoted for one chamber cannot be readily made with values quoted for another unless the values are converted to the same basis with respect to both distance factors. Such conversion can be made with knowledge that: 1.) the radar cross section value for a chamber varies directly as the fourth power of distance to the reference sphere (ref. radar range equation), and 2.) the equivalent radar cross section at a fixed distance varies inversely as the square of the distance to the back wall.⁵ The equation for the conversion follows:

$$\sigma_2 = \sigma_1 + 10 \text{ Log} \left(\frac{R_{t1}}{R_{t2}} \right)^4 \left(\frac{R_{w2}}{R_{w1}} \right)^2 \text{ (db } \langle M^2 \rangle) \quad (1)$$

where σ_1 and σ_2 = chamber equivalent radar cross sections (db $\langle M^2 \rangle$) at reference target distances R_{t1} and R_{t2} in chambers 1 and 2

R_{w1} and R_{w2} = Radar to back wall distances in chambers 1 and 2.

The following is an example of such conversion: Assume it is necessary to convert the equivalent cross section of a chamber known to be 60 db $\langle M^2 \rangle$ at 25 feet with 50 foot distance to the back wall to the equivalent cross section at 100 feet with 120 foot wall distance for purposes of comparison with another chamber. With the aid of the above equation, it may be shown that the numerical value for the first chamber becomes 43.5 db $\langle M^2 \rangle$ at 100 feet with the back wall at 120 foot distance. It might not be apparent to the uninitiated that two numerical values which superficially appear so dissimilar describe the same quantitative phenomena. The disadvantage is evident of this description method in not providing a unique number to describe chamber performance.

Turning now to the X-Band reflectivity values quoted in Table I, we find that these three chambers show equivalent radar cross sections of 10^{-6} to 10^{-8} square meters at 25 feet over close to full path length with the back wall set at a favorable tilt angle. (The effects of back wall tilt are discussed in a later section.)

A comparison of these cross section values with the encountered systems noise levels listed in Table I for these chambers shows that with each the level of chamber reflected energy was so low as to be below receiver noise. (The technique developed to measure cross section when below noise is described in a later section.) It is our understanding that these chambers represent the first time that this condition has been achieved. We speculate that it would be desirable during use of a chamber to know that any observed signal was not coming from the chamber. As a result of the low inherent cross sections, these chambers provide opportunity for work with smaller targets or for higher accuracy on larger targets. An idea of the accuracy available may be determined from the recording of Figure 1 which shows a small target with a cross section of 42 db $\langle M^2 \rangle$ at 25 feet moving in and out of phase with chamber reflected energy. It may be noted that finite reflections from the chamber are here causing an uncertainty of only about plus or minus 0.1 db in the value of cross section for a target of as small a size as this.

Also listed in Table I are values for the inherent cross section of these chambers for the condition where the back wall is vertical. This data has been included to facilitate comparison with chambers having the conventional fixed back wall. It will be noted that one of the chambers showed an

appreciably higher value of cross section for the condition of wall vertical despite the similarity of design to the other two. Study of the recordings of cross section vs. tilt angle for each of these chambers reveals that cross section values averaged over a range of angles are similar on all three chambers but that values at any given tilt angle (including 0°) may vary appreciably. It appears that the quality of the absorbent material determines the general level but that superimposed on this level are maximums and minimums which we attribute to diffraction phenomena (i. e. the particular vector sum of all the unit wall vectors at that particular angle and frequency). These recordings clearly show that a higher value was encountered for this chamber because a peak in the diffraction pattern here happened to fall with the wall vertical. The tilt wall may be thought of a means of insuring that such peaks can always be avoided and that good nulls can always be introduced to achieve lower levels of inherent cross section.

Reflection Coefficient. This terminology describes a chamber on a basis of the ratio of incident to reflected energy just as is done with absorbent materials. In the case of materials, the reflection coefficient describes (and is determined from) the level of reflected energy from the absorber with respect to the level of incident energy from a flat conducting surface. In the case of a chamber, the reflection coefficient similarly describes (and may be determined from) the level of chamber reflected energy with respect to the level of incident energy calculated to come from an infinite flat conducting surface located at the distance of and in the plane of the chamber back wall. Since radar cross section is proportional to power, the reflection coefficient also describes (and may be determined from) the ratio of inherent chamber cross section to the cross section calculated for an infinite conducting surface located at the back wall.

The reflection coefficient of a chamber is thus, by definition, the reflection coefficient of the absorbent material on the back wall as measured in the chamber. To express chamber quality in terms of reflection coefficient is to state that the observed level of chamber reflected energy or the observed level of inherent chamber cross section is that expected for an infinite conducting surface located in the plane of the chamber back wall when covered with an absorber having the stated value of reflection coefficient.

The concept of thinking of chamber reflected energy as emanating from the material of the back wall is well related to practice since back-scatter chambers are typically used and defined with sufficient antenna directivity to limit illumination to the back wall and thus avoid degradation of chamber cross section by reflection from side wall, floor and ceiling regions. It is for reason of such illumination that the reference value for the conducting surface is calculated from the case of an infinite wall rather than a finite wall with dimensions of the chamber cross section. Use of the latter case is not considered here appropriate since, with typical chamber illumination, the edges of the back wall are indefinite as the result of low illumination.

The expression of interest for the infinite wall case is $\sigma = \pi R^2$ where R is the distance to the chamber back wall in meters and σ is the equivalent cross section at the distance of the back wall expressed in square meters. In view of the importance here of this expression and the fact that it is not familiar to all, we include a derivation in Appendix A.

Defining chamber performance in terms of reflection coefficient also presents disadvantages. The chief disadvantage appears to be that definition is less familiar to users of backscatter chambers, and, in addition, cannot be directly applied to backscatter problems without conversion back to cross section units. On the other hand, advantage is offered since the reflection coefficient definition describes both chambers and materials in the same manner and hence both have essentially the same numerical value. The only difference is that the chamber reflection coefficient describes (and is determined from) an aggregate of absorber pieces mounted on the back wall in a chamber whereas the reflection coefficient of the material describes (and is determined from) individual pieces or small groups of pieces. The reflection coefficient concept thus provides distinct advantage in choosing a back wall material to meet a particular requirement or in predicting chamber performance. Perhaps the most important advantage to use of reflection coefficient is that it provides a unique numerical value to describe a chamber. This value is exclusively a function of chamber reflection properties and is thus independent of the distances to a reference sphere or a back wall. Values for various chambers can, with this definition, be directly compared without need for conversion to common distances as is required for the radar cross section definition.

Table I contains reflection coefficient values for each of the three chambers under conditions where, in one case, the back wall is set at a favorable angle and in the other where the back wall is fixed at vertical. Note that in the best chamber a reflection coefficient value of approximately 100 db was encountered at a favorable back wall tilt angle. This value actually means that the amount of chamber reflected energy measured back at the receiving antenna was the amount that would be expected from a conducting wall at the other end of the chamber when this wall was covered with an absorbing material having normal incidence reflection coefficient of approximately 100 db. Since materials are not known which reduce reflection by this amount, measurement of this low a value for the chamber gives evidence of the effectiveness of the tilt wall in further reducing the level of reflected energy beyond that provided by the material with fixed vertical mounting.

It will be noted that the table lists reflection coefficient values for the condition of back wall vertical as determined in two different ways. In one case the values were obtained from the ratio of the inherent cross section measured in the chamber to the cross section calculated for the conducting wall. In the other case, values for two of the three chambers were

acquired by measurements of reflection coefficient by the "free space VSWR" technique which is commonly employed to measure the reflection properties of chambers designed for antenna measurements. A comparison of the reflection coefficient values from the two methods is of interest. It will be noted from the data of Table I that the values for both chambers by both methods differed by not more than 4 db. Such agreement is interpreted as lending support for the concepts here presented.

The magnitude of values for the condition of back wall vertical is also of interest since opportunity is here provided for comparing the reflection coefficient measured in a chamber with the reflection coefficient of the materials covering the back wall. The fact that the values for the chamber are here found to be the range of 60 to 70 db would indicate that the back wall materials were characterized by similar reflection coefficient values. Such a comparison is limited in the case of these chambers however, since the reflection properties of the materials here used are not quantitatively well known. This is the case because techniques are not available at this time for making measurements on individual pieces or small groups of pieces which have such low reflection coefficients. A variety of both practical and conceptual problems involving factors such as edge reflections, size effects, etc.², limit measurements with reasonable accuracy to the 50 db range at the present state-of-the-art. On the other hand, we propose that in view of the manner in which these measurements were made, they may be considered as providing: 1.) the first quantitative measurement of the normal incidence reflection coefficient of any materials into the 60-70 db range and 2.) the first confirmation that materials can be provided which have a reflection coefficient as low as 60 to 70 db down.

Prior to completing this section it might be well to point out certain limitations to both of the above means of describing the reflection properties of backscatter chambers.

a. Both describe chamber performance for the case where the chamber is empty or contains a physically small target. Some classes of targets cause significant enhancement of apparent chamber cross section which in turn causes measurement error above that predicted on the basis of known values of chamber cross section or reflection coefficient.

b. Both describe chamber performance for the condition of low side wall illumination. During such times as it is necessary to measure with smaller antennas, it should be borne in mind that the inherent chamber cross section will be degraded and will be a function of the degree of side wall illumination.

c. Neither describes how much undesired energy may be arriving at the test site via specular or non specular reflection from the side wall, floor and ceiling surfaces to constitute a source of measurement error.

d. Neither describes how good a chamber is in regard to secondary reflections, i. e. reflections from large objects under test to adjacent wall surfaces, and thence back to the object to appear as a form of error.

It may be anticipated that future definitions of chamber reflectivity performance will be expanded to include description in terms of these factors and that this will provide impetus to development of improved solutions to the basic chamber problems represented by these factors.

Design Aspects of These Chambers

While a variety of second order factors have contributed to the observed performance levels, comment will be limited in this section to the two design factors which are primarily responsible for the advancement of these chambers over prior art. These important factors are: a.) the absorbing materials used on the back wall and b.) the arrangement for tilting the back wall. In view of their significance, they are separately considered below.

a. Absorbing Materials. Each of the three chambers used the B. F. Goodrich VHP (Very High Performance) materials to completely cover the back wall regions. This particular type was chosen in view of interest that each of these chambers exhibit performance at the state-of-the-art.

This particular material is in the form of an aggregate of flexible foam dissipative pyramids. The function of the geometrical shaping is to effectively reduce reflection by providing a long, gradual, discontinuity free taper from the propagation characteristics of free space to the propagation characteristics of the dissipative medium. Use of the pyramidal shape provides a transition where the loss increases at an exponential rate. This particular rate of change is known to be desirable for two reasons: 1.) it is economical in terms of thickness for a given performance at the low frequency end, 2.) it provides a general trend of decreasing reflection with increasing taper length which allows achievement of very low reflection coefficients with very long tapers.

Forty-five (45) inch thick versions of VHP material were used on the back wall in two of these chambers. This physical thickness provides at X-Band a taper which is extremely long in terms of wavelengths (approximately 40λ) and a taper which is extremely gradual in terms of change per wavelength. These factors are undoubtedly important in the attainment of the 60 - 70 db normal incidence reflection coefficient attributed to this material at this frequency. While use of such thick materials at such high frequencies may be surprising to some, it is our understanding that performance at this level cannot be attained in any other manner at the present state-of-the-art.

b. Tilt Wall. What is referred to here is an arrangement which has been designed into each of these three chambers to allow the back wall to be tilted through an angle range of approximately 20° from the vertical and set at an angle which directs a good null in wall reflection back down axis. The idea is carried out with a motor drive on a hinged absorber covered wall that is of a size approximating this inside dimension of the chamber. Controls for the motor are returned to the receiving position so that the operator may conveniently find such a null by observing receiver output.

It will be appreciated that motion of a wall in this manner may be expected to provide variations of reflected energy at the receiver as a result of what might be considered as a scanning through a portion of the back wall diffraction pattern. The observed results appear to be in keeping with the complex diffraction pattern that might be expected for a large surface which varies in both phase and amplitude of reflection from point to point on its surface. Figure 2 shows a typical recording of the encountered variation of reflected energy (and hence inherent radar cross section) with tilt angle.

What is of primary importance here, however, is that tilting the back wall exhibits deep nulls which represent a significant improvement in radar cross section. Figure 2, for example shows a number of nulls going down into noise at $53 \text{ db} \langle M^2$. Noise level is here expressed in equivalent cross section at 25 feet. Measurements which are described in the following section have shown that the level of energy in the nulls may be as much as 20 db below noise. These measurements have also revealed that there may be a ratio in excess of 40 db between the level of the worst peak and the best null with tilt over a 20° range of angles.

Reference is again made to Figure 1 in view of its importance in demonstrating the achievement of a very low inherent chamber cross section using the tilt wall to provide a favorable wall angle. At the upper right of this recording is shown the trace of a swinging sphere of a size $28 \text{ db} \langle M^2$. No sign of periodicity is detected which might be attributed to the sphere passing in and out of phase with the chamber. In the center left region of the recording is noted the trace of a swinging $43 \text{ db} \langle M^2$ sphere. With this small target a periodic variation of approximately 0.2 db is noted as the moving sphere alternately passed in and out of phase with the fixed chamber reflection. It may be shown that a periodic variation of this magnitude is attributable to a signal some 38 db below the level of the sphere. We, therefore, determine that the level of the chamber is here 38 db below the $43 \text{ db} \langle M^2$ sphere or at approximately $81 \text{ db} \langle M^2$. Ambiguity as to whether the weaker or stronger level represents the sphere or the chamber is easily resolved in view of the change of average level with change of sphere size. It was established in a manner described in the following section that the crosstalk between transmitter and receiver during this recording was cancelled to a level at least $88 \text{ db} \langle M^2$. Receiver noise was at a level

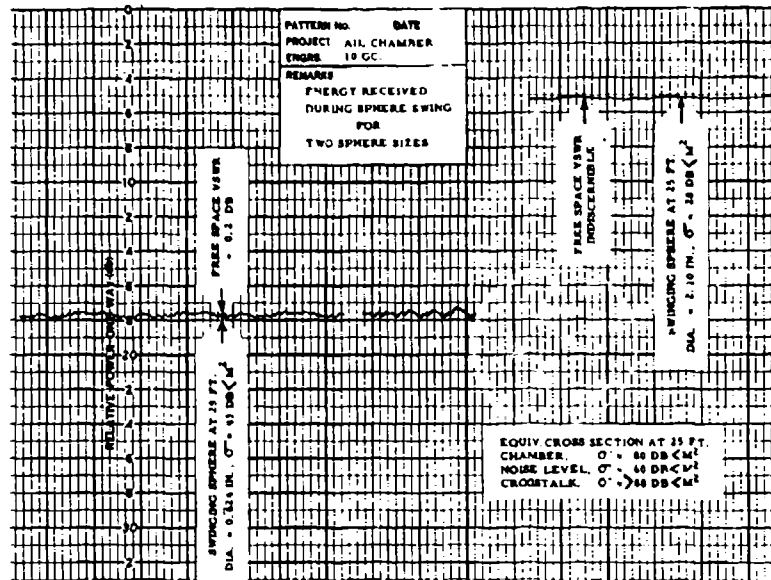


Fig. 1: Recording of received energy with reference sphere swinging. Vector summation of sphere and chamber produces observed VSWR. Magnitude of VSWR at 0.2 db indicates chamber is 38 db below sphere and therefore has equivalent radar cross section at 25 feet of approx. 80 db below a square meter.

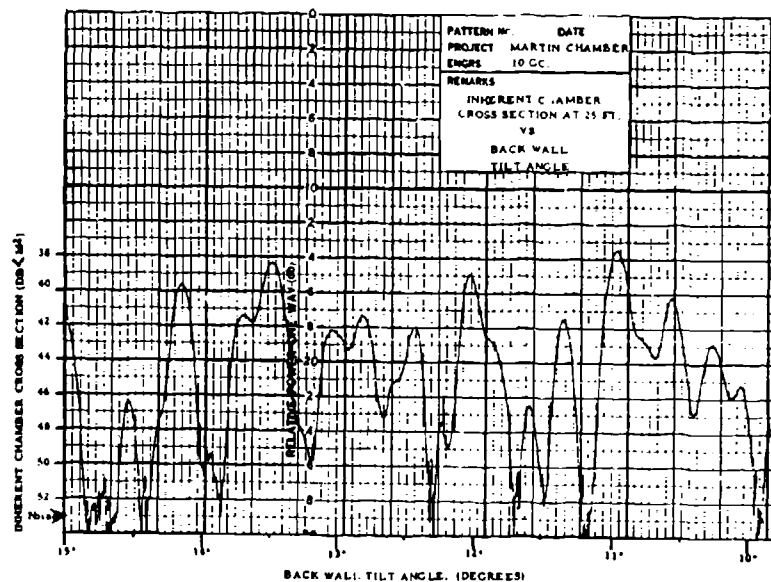


Fig. 2: Recording of inherent radar cross section during back wall tilt. Note: Signal goes into noise (at $\sigma = 53 \text{ db} \langle \text{M}^2 \rangle$) at a number of points.

equivalent to 60 db $\langle M^2$.

We thus see that a combination of state-of-the-art absorbing materials in conjunction with a tilt wall can offer opportunity for accurate cross section measurements to a level close to noise. Patent application has been made on the proprietary tilt wall feature by the B. F. Goodrich Co.

Measurement Techniques

Inherent Radar Cross Section. A number of organizations have used the technique described in these references^{2, 3} to measure the inherent radar cross section of backscatter chambers. This method basically compares the level of reflected energy from the chamber with that of a sphere of known cross section at known distance. This particular technique is characterized by the way in which crosstalk between transmitter and receiver is handled. Here crosstalk is set to be either in phase or out of phase with chamber reflected energy by small physical movement of the antennas to a location which provides the desired phase of relationship between the two components. The vector sum (or difference) of these two voltages is then cancelled down into receiver noise. Further antenna movement is then used to introduce an additional 180° phase shift in the return from the chamber. Under this condition, it may be shown that the remaining voltage is equal to twice the voltage from the chamber and thus provides a measure of the inherent chamber reflection level.

While this method provides accurate measurements of reflection levels which are well above noise, it also provides values which become increasingly inaccurate as the chamber level under measurement approaches the noise level. This is because one of the steps of this procedure requires cancellation. In practice, with this method, one is able to insure cancellation only to the point where the signal goes into noise. An "uncertainty vector" voltage which may be almost as large as the difference between 0 and noise level is therefore left in the problem. This error voltage combines vectorially with the chamber reflected voltage to limit measurement accuracy.

Since modern design techniques are able to provide chambers in which the level of reflected energy is below noise, it is apparent that the above measurement technique is inapplicable since it may possess an inherent error voltage which may be larger than the chamber reflected voltage, rather than some 20 db below it as is desirable for accurate measurement. In view of the above, this company has developed a measurement technique which extends the opportunity to make quantitative radar cross section measurements of a given accuracy downward by a few orders of magnitude. As a result, this new method is well adapted for use with modern chambers. This method which we refer to as the "B. F. Goodrich technique" is described in principle below:

Rather than use this as an opportunity to discuss the method in all detail, consideration will be limited to the two main concepts which primarily determine the improvement in measurement sensitivity. These are:

1.) the means used by this method to measure the magnitude of a signal which may be some orders of magnitude below noise, and 2.) the means used by this method to greatly reduce the size of the previously referenced "uncertainty vector" which provides the main limitation to accuracy.

a. Quantitative Measurement of a Signal Below Noise. Those of us who cut our engineering teeth on routine slotted line measurements may not have realized that many of the values being measured were of levels appreciably below noise. Consider the case where a VSWR of 1.04 is measured on an antenna or load where the level of incident energy on the line is 15 db above detector noise. It may be shown that a VSWR of this magnitude is caused by reflected signal at a level of 35 db below incident as the two go in and out of phase. For the chosen example, the level of reflected energy is actually about 20 db below the detector noise level.

What is being taught above is that quantitative measurements can be made of reflection levels that are well below noise by adding this energy vectorially with changing phase to an incident signal which is above noise. This may be viewed as the modulation of a carrier where the depth of modulation is proportional to the level of the modulating signal.

This concept is used by the B. F. Goodrich technique to measure the level of reflected energy below noise level. It is employed in practice by swinging a sphere of known cross section on a monofilament line and recording the periodic amplitude variations which are caused by the sphere passing in and out of phase with chamber reflected energy as is shown in Figure 1.

A note of caution should be here introduced. A swinging sphere simultaneously measures the level of chamber reflected energy and the level of the "uncertainty vector" with some arbitrary vector relationship between them. One is justified in accepting the value which issues from a swinging sphere as the level of reflected energy only after it has been established that the "uncertainty vector" is at an appreciably lower level.

b. Reduction of the "Uncertainty Vector". Our technique achieves a condition where the error voltage which exists as a result of incomplete cancellation is known to be a number of orders of magnitude below noise rather than near noise as with the previously considered method. Rather than cancel the vector sum (or difference) of cross talk and chamber down to noise, our technique uses the somewhat simpler and more straightforward arrangement of cancelling only crosstalk. It will be appreciated that if crosstalk can be well cancelled, energy from the chamber will predominate above it with minimum error. Cancelling only crosstalk opens up opportunities for using procedures which allow cancelling to much lower levels. The following procedure was developed for this purpose and forms a feature of the B. F. Goodrich technique:

Consider a case where the antennas and the cancellation network (phase shifter and attenuator) are mounted on a rolling platform which allows linear movement over a few wavelengths in a direction parallel to the direction of propagation. When a fixed target is located at the test site, movement of the antennas will produce a periodic amplitude variation in the level of detected energy as a result of target energy of variable phase passing in and out of phase with crosstalk of fixed phase. If the phase shifter and attenuator are tuned to minimize this periodic variation (analogous to matching an antenna with stubs to achieve a "flat line"), a condition is achieved where the crosstalk is well cancelled and the remaining signal is that from the target. In practice this periodic variation is read on the expanded scale of a bolometer amplifier at the output of the receiver. Tuning of the cancellation network generally is able to provide a condition where periodicity is no longer discernible and is known to be less than 0.05 db. This would represent a condition where the level of crosstalk would be known to be at least 50 db below the target level. If the target were 10 db above noise, it would thus be known that the crosstalk was cancelled to a level at least 40 db below noise. This would represent an improvement of perhaps 40 db in the level of the "uncertainty vector" over the other measurement method.

The combination of this cancellation procedure and this means of determining chamber level below noise allow measurement of the inherent cross section of a chamber to be made to something like a 40 db lower level with the B. F. Goodrich technique in contrast to the previously referenced technique.

Reflection Coefficient During the course of evaluation of these chambers, measurements were made of the chamber reflection coefficient by two different methods. In one case this quantity was obtained by taking the ratio of the measured inherent cross section of a chamber to the cross section calculated for a flat conductive surface located in the plane of the back wall. The reflection coefficient values shown in Table I which were determined in this manner are identified as "determined from σ ".

In the other case, reflection coefficient values were obtained by the so-called "free space VSWR" technique which was developed by the B. F. Goodrich Co. and has seen wide use in the measurement of reflection properties of chambers designed for pattern work. These values are identified as such in the table. The manner in which the reflection coefficient of chambers is measured by this technique is discussed below:

It will be recalled that to describe a backscatter chamber in terms of reflection coefficient is really to describe it in terms of the reflection coefficient of the back wall covering material. Thus the reflection coefficient value for a chamber is obtained by measurement of the reflection coefficient of the back wall material in place. The technique here employed is, in principle, the same as that used in the well known "arch method" developed by the Naval Research Laboratory for measurement of the reflecting properties of

individual absorber pieces.⁴ This method obtains the ratio of reflected to incident energy by comparing the energy level over a path involving reflection from the absorbing material to the energy level over a path of the same length without the material. The ratio of the two levels is the reflection coefficient.

This basic technique is easily applied to a chamber by comparing the energy level over a path involving reflection from the back wall of the chamber to the energy level over a path of the same length without the material. In practice this is accomplished in the following manner: The chamber is illuminated at the appropriate end with a directional antenna. Another directional antenna is used as a receiver in the vicinity of the test site near the other end of the chamber. The level of incident or direct energy is obtained by orienting the receiving antenna toward the source. The level of energy reflected from the wall is obtained after rotating the receiving antenna toward the back wall of the chamber. When oriented in this direction, the antenna will receive energy not only over the desired wall reflected path but also, at the same time, over the direct path via a back lobe of the antenna. It becomes necessary to separate these two signals, measure the level of each, and identify which is the one representing reflection from the wall. The "free space VSWR" technique has been developed for handling this type of problem in the evaluation of pattern chambers. It accomplishes these ends by measuring the "free space VSWR" encountered in a chamber as a probe antenna is physically moved to make the two signals pass in and out of phase. From the magnitude of this VSWR the difference in level between the two signals is determined. This technique will be recognized as being the free space analogy to the measurement of the reflection coefficient of a dummy load in a waveguide system. This technique is applied to the problem at hand by moving the directional antenna parallel to the direction of propagation (perpendicular to the wall surface) to allow the wall reflected component to pass in and out of phase with the direct energy coming in off the back of the antenna. Ambiguity as to whether the wall reflected energy is represented by the value of the stronger or weaker signal can be resolved in a number of ways, the most common of which is by comparing these levels with the known back lobe level of the antenna. Since the path involving the wall is slightly longer than the direct path, a small correction for the difference in distance is applied prior to quoting the ratio of the wall reflected energy level to the direct energy level as the chamber (i. e. wall) reflection coefficient.

IMPROVING CHAMBER ACCURACY

In using backscatter chambers such as these, one has at his disposal two important factors upon which measurement accuracy is dependent. These are: 1.) chamber illumination and 2.) distance to the target. Familiarity with these factors will allow them to be used to advantage rather than contributing to unnecessary error.

Illumination Directivity

Good backscatter chambers at the present state-of-the-art may exhibit much higher levels of reflected energy from side walls, floor and ceiling than from the back wall. This point was graphically brought out in the additional measurement of one of these three chambers with antennas of very low directivity. The inherent cross section under this condition was actually 52 db poorer than when measured with antennas which restricted illumination to the back wall. This very large difference is attributable to: 1.) the loss of effectiveness of the back wall tilt feature since here only a small percentage of the total energy was on the back wall and 2.) the fact that the majority of radiated energy here fell on absorbing material at wide angles of incidence where the effectiveness of conventional materials is well reduced. Measurements of inherent cross section vs. azimuth which were made with high directivity antennas in two of these chambers provided additional confirmation that side wall regions reflect much more energy than the back wall region.

It is thus apparent that measurements of highest accuracy are to be achieved when sufficient antenna directivity is employed to limit illumination to the back wall and discriminate against the poorer regions. This factor should be given attention in the establishment of height and width dimensions for anticipated facilities.

Target Distance

It is our belief that all backscatter chambers should have a convenient arrangement for locating the target under test at the minimum distance allowed by far field. This is to take advantage of the opportunity offered by the sharp inverse fourth power function of received power with distance to improve the ratio of target level to chamber level. Appreciate that this advantage is available only when distance is reduced by moving the target toward the source and not if the source is moved toward the target as a result of back wall distance.

FUTURE STATE-OF-THE-ART

Those involved in radar cross section measurements can expect that current development in the absorber field will provide materials, designs, and facilities which are conducive to more demanding future work. For example, the following two ideas seem sufficiently close to commercial realization and sufficiently significant to backscatter efforts as to justify mentioning at this time:

1. A Wide Angle Material. The first successful development of a material designed specifically to provide high performance at wide angles of incidence has been completed. It is now apparent that this material will offer a radar cross section at wide angles of incidence which is some two

orders of magnitude below that from conventional materials designed for normal incidence application. The material will be in the form of a VHP type which will have the pyramids inclined to be approximately parallel to the direction of propagation. Future chambers will offer lower cross sections (especially where wider illumination has to be used) as a result of this development.

2. A Weatherproof Low Backscatter Material. Development has also been completed on a means of providing a weatherproof coating for very high performance material. As a result, absorbers offering in excess of 30 and 40 db reflection coefficient will, for the first time, become available for outdoor work. Both the regular and new wide angle versions of VHP material will be offered in this flexible weatherproof form. These materials will make a significant contribution to the improvement of existing outdoor ranges and will help to insure that future outdoor facilities will represent an improvement over those of the present state-of-the-art.

BIBLIOGRAPHY

1. Simmons, A. J. and W. H. Emerson, "An Anechoic Chamber Making Use of a New Broadband Absorbing Material." Presented at 1953 National Convention of the IRE. Published in Convention Record of the IRE, Part 2 - Antennas and Communications, 1953.
2. Hiatt, R. E., E. F. Knott, and T. A. B. Senior, "A Study of VHF Absorbers and Anechoic Rooms." University of Michigan Report No. 5391-1-F, (Feb. 1963).
3. Emerson and Cuming, Inc., "Outline of Electrical Evaluation Procedures for Microwave Anechoic Chambers," Un-numbered report, (October 1962).
4. Emerson, W. H., A. G. Sands and M. V. McDowell, "Development of Broadband Absorbing Materials for Frequencies as Low as 500 MCS." Naval Research Laboratory Report No. MR. 3 00, (May 1954).
5. Kerr, D. E., "Propagation of Short Radio Waves," Radiation Laboratory Series, Vol. 13, pp. 466-467, McGraw-Hill Book Company, Inc., (1951).

TRANSMISSION LINE SCATTERING RANGE

Michael J. Gans
Electrical Engineer
MB Associates

ABSTRACT

A new type of scattering range is described in which the radar reflection properties of objects are measured by inserting the object into a transmission line. The theoretical justification for this technique is presented from the basis of the reciprocity theorem. A theoretical comparison is then made between a specific two wire transmission line range and an image plane range to illustrate the increased signal and decreased spurious return provided by the transmission line range. Its utility in the following areas is discussed: simplification of model support, positioning and orientation equipment; polarization and phase measurements; forward and bistatic cross-section measurements; frequency sweep measurements; and controlled environment measurements. The experimental program presently in progress to determine the limitations of the transmission line range is also described.

INTRODUCTION

When one attempts to measure the scattering cross-section of very small objects on a conventional scattering range, the return is so small that extremely sensitive instruments and stable systems are required. A great deal of attenuation on scattering ranges is due to the spreading of the waves: $1/4 \pi r^2$ for the incident wave times $1/4 \pi r^2$ for the reflected wave. Thus the attenuation in power is proportional to $1/r^4$ where r is the distance to the scatterer. The following is a method of eliminating the $1/r^4$ attenuation and yet keeping the received voltage proportional to the square root of the free space scattering cross-section. The method consists of placing the scatterer into a uniform transmission line. An example of such a range is shown in Figure 1. In this example, the signal in the receiver arm of the directional coupler is nulled in the absence of the scatterer by means of the tuner. The scatterer is then inserted into the transmission line, and it introduces a new reflection which is measured by the receiver. As shown in the next section, this signal, V , is proportional to the square root of the free space back-scattering cross-section of the scatterer.

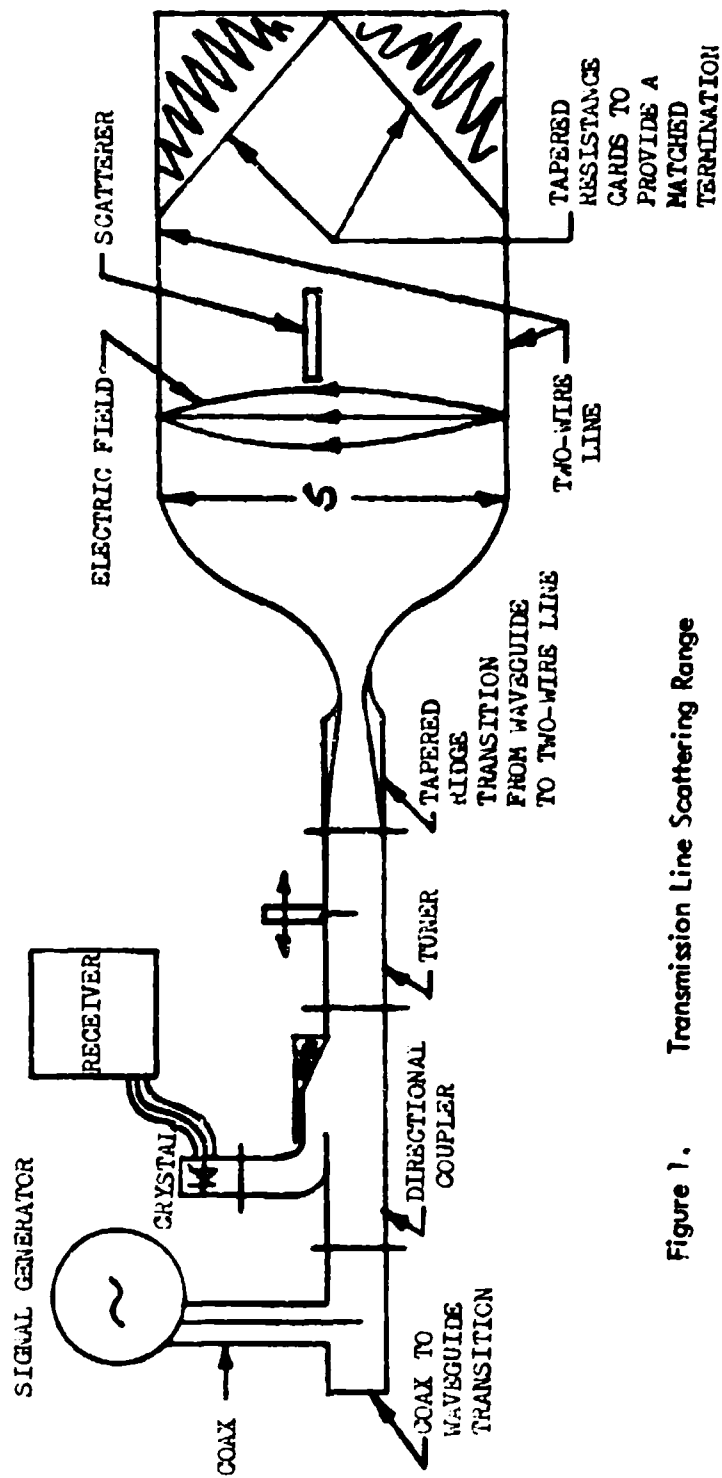


Figure 1. Transmission Line Scattering Range

PRINCIPLE OF THE METHOD

The justification for this technique is based upon the reciprocity theorem^{1,2}, which states that the above-mentioned signal, V , is determined by an equation of the form

$$V = C \iiint_{\text{scatterer}} \underline{E} \cdot \underline{J} \, dS \quad (1)$$

where C is a constant, \underline{E} is the field when the scatterer is absent, \underline{J} is the current distribution on the scatterer. From equation (1) it is seen that, if one can produce the same field in the absence of the scatterer as a free space plane wave, and if one can cause the current distribution on the scatterer to be the same as if it were immersed in a free space plane wave, then the received voltage would be the same as that for a free space scattering range. These conditions can be satisfied with a uniform transmission line. On a uniform transmission line the wave travels at the velocity of light and the wave impedance is that of free space³. Furthermore, if the scatterer is small compared to the dimensions of the transmission line, the transmission line field will be essentially uniform over the volume into which the scatterer is to be inserted. Thus if the transmission line is terminated in a matched load it will provide the same field in the absence of the scatterer as a free space plane wave. Some currents will be induced on the scatterer due to the field reflected by the transmission line or surrounding objects. If these currents are negligible compared to the currents induced by the incident field, the current distribution on the scatterer will be the same as if it were immersed in a free space plane wave. The interaction of the scatterer with the transmission line and other surrounding objects is not too difficult to minimize. For instance Justice and Rumsey² point out that the currents on a scatterer, one half wavelength long, are changed by only one percent when a ground plane is brought to within a quarter wavelength. Also, they measured the cosine distribution of the TE_{01} field in a rectangular waveguide by means of a scatterer, obtaining nearly perfect agreement to within $1/20$ of a wavelength from the wall, confirming their prediction that "conducting surfaces in the vicinity of the scatterer do not appreciably alter the square law dependence of echo voltage on incident electric field." Also they point out that, if the surface of the reflector with which the scatterer interacts is convex, the inter-action will be significantly less.

TYPICAL SENSITIVITY

As an example of the sensitivity of the transmission line range the following comparison is made between a two wire line scattering range shown in Figure 1, and an image plane scattering range. If one desires to measure the radar cross section of an object small compared to wavelength, then the distance, s , between

the two wires need only be a half wavelength to make the mutual interaction between the wires and the scatterer negligible and to make the field uniform over the volume of the scatterer. With a half wavelength spacing between the wires, one must be careful to provide a balanced and well tapered input to the line in order to prevent radiation and excitation of undesired modes (a typical surface wave excitation problem). A cross-sectional view of the two wire transmission line is shown in Figure 2. Assume that the signal generator output is one watt and there are no mismatches in the circuit of Figure 1. Then the voltage on the transmission line is

$$V = \sqrt{Z_0 \times \text{Power}} = \sqrt{Z_0} \quad (2)$$

where Z_0 , the characteristic impedance of the transmission line, is given by⁴

$$Z_0 = 120 \cosh^{-1} \left(\frac{s}{b} \right) \quad (3)$$

For this example, the wires were chosen to be #10 AWG copper. Thus

$$S = \lambda/2 = 1.5 \text{ cm} = 0.59 \text{ inch}; 2b = 0.1 \text{ inch} \quad (4)$$

It is possible to express the electric field on a two wire transmission line in the form⁵

$$E = \frac{\cosh \xi + \cos \theta}{2a \xi_0} V \quad (5)$$

where ξ and θ are the bipolar coordinates, E is the electric field which is in the θ direction, a is the proper interfocal distance and ξ_0 is determined from the following two relations

$$S = 2a \coth \xi_0 \quad \text{and} \quad b = \frac{a}{2} \operatorname{csch} \xi_0 \quad (6)$$

By the use of equations (2) - (6) it is seen that the incident electric field at the center between the two wires is 15.6 volts/cm; so that the power incident on the scatterer is given by

$$P_{\text{inc}} = \frac{E^2}{120\pi} = 6.48 \times 10^3 \text{ watts/m}^2 \quad (7)$$

For comparison, the University of California image plane scattering range is examined. At 9300 mc ($\lambda = 3.23 \text{ cm}$) the minimum far field distance, r_{min} , is given as 25 inches (63.5 cm)⁶. Thus, the size of the illuminating horns aperture, d , is

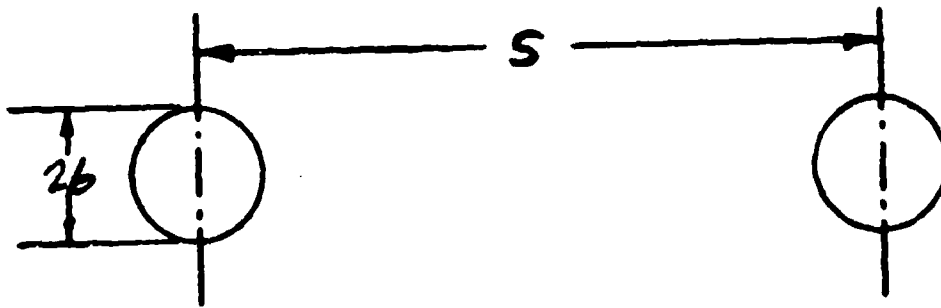


Figure 2

Cross Sectional View of Two Wire Transmission Line

$$d = \sqrt{\frac{\lambda 635}{2}} = 10.15 \text{ cm.} \quad (8)$$

Whereas the gain, g , of the horn is⁷ (at $\lambda = 3 \text{ cm}$)

$$g = 4\pi \left(\frac{d}{\lambda}\right)^2 = 143. \quad (9)$$

However, the attenuation due to spreading of the waves at r_{\min} is $1/(4\pi r_{\min}^2)$.
At $\lambda = 3 \text{ cm}$, r_{\min} is

$$r_{\min} = \frac{2d^2}{\lambda} = 68.7 \text{ cm.} \quad (10)$$

Hence the incident power level for a generator on the University of California scattering range is⁷

$$P_{\text{inc}} = \frac{g}{4\pi r_{\min}^2} = \frac{143}{4\pi (.687)^2} = 24.2 \text{ watts/m}^2. \quad (11)$$

Therefore, the voltage ratio of the scattered signal received by the two-wire line scattering range to the signal received by the free space range is determined by means of (1), (7), and (11) as

$$\frac{V_{2W}}{V_{FS}} = \frac{6.48 \times 10^3}{24.2} = 267 \quad (12)$$

$$\text{db}_{\text{signal power}} = 20 \log_{10} \frac{V_{2W}}{V_{FS}} = 20 (2.426) = 48.5 \text{ db.} \quad (13)$$

Equation (13) shows the considerable advantage of the two-wire scattering over the free space scattering range for small objects. Other configurations for the two-wire line can be applied if larger objects are to be measured, e.g., Bus Bars, etc..... These configurations can give a more uniform field over a larger volume and less expansion of the power outside the scattering region if care is used not to excite higher order modes or to radiate.

EXPERIMENTAL RESULTS

In order to test the accuracy of the transmission line scattering range a system was constructed as shown in Figure 1 with $S = 1.7 \text{ cm} = \lambda/2$ at 8.75 gigacycles. Since metal spheres much smaller than one wavelength in radius have a theoretical cross section which is well known, it was decided to test the accuracy of the range by using 3 balls, 1/8", 3/16", and 1/4" in diameter, respectively. Also, since the transmission line scattering range should give the same result for radar cross section independent of how far along the line the scatterer is placed, each ball was measured at three positions along the line. As seen in Figure 3, there was close agreement between the cross sections measured at the three positions.

The measurements were normalized by equating the average cross section of the 1/8" diameter ball, as measured at the three positions, to the theoretical cross section for a 1/8" diameter metal sphere. It is shown in Figure 3 that the rest of the measurements agree with the theoretical values. The theoretical back-scattering cross section of a metal sphere of radius, a , small compared to wavelength, λ , is⁸

$$\sigma_B = 13,950 \left(\frac{a}{\lambda}\right)^4 (\pi a^2). \quad (14)$$

For example the back-scattering cross section for a 1/4" diameter metal sphere at 8.75 gigacycles is 0.317 square centimeters.

POTENTIAL ADVANTAGES AND APPLICATIONS

An experimental program has been initiated in order to determine the possibilities and limitations of the transmission line scattering range in the following areas.

Signal to Noise Ratio

Since the signal power is not reduced by $1/r^4$ as in a free space scattering range, the signal power is potentially higher in a transmission line scattering range. In conventional ranges power is spread out and reflected from many obstacles besides the target. These spurious reflections are tuned out before the target is inserted; however, slight movements of the spurious reflectors introduce noise which is difficult to eliminate, especially since the spurious reflections are usually much larger than the target reflections. In the transmission line scattering range, however, the field is concentrated on the target, and what gets by the target is absorbed by a standard transmission line matched load. Thus, the transmission line scattering range potentially gives a higher signal and a lower noise than conventional scattering ranges.

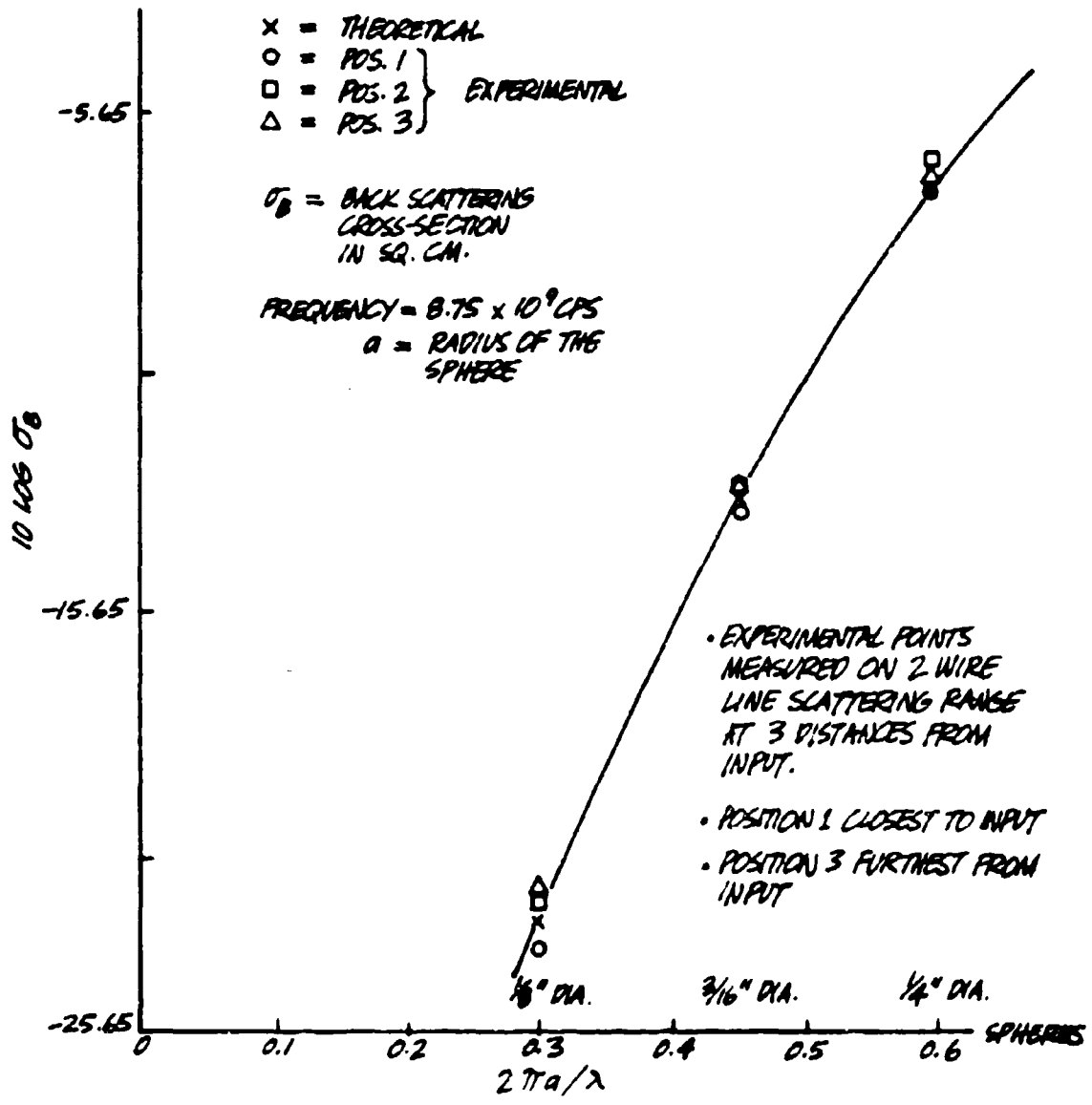


Figure 3
Plot of Back Scattering Cross Section of Small Metal Spheres

Construction

Due to its inherent high sensitivity and minimum spurious reflections, the transmission line scattering range should have less stringent demands of stability and close construction tolerances and so make it easier to build than conventional ranges. Also, conventional ranges must operate in the far field of both the illuminating antenna and the target (unless the target is short enough to remain in one fresnel zone of the near field). This means that the target must be $2d^2/\lambda$ from the illuminating antenna⁷; where d equals the largest dimension of the antenna aperture and λ is the free space wavelength. There is no such distance requirement for the transmission line scattering range, which may allow it to be constructed smaller than conventional ranges.

Support of Models

Since the field is concentrated on the target, supporting devices (rotating motors, etc.) may be brought in closer to the target without disturbing the field. This may reduce the problem of positioning and rotating the target without introducing inaccuracies into the measurements.

Frequency Scanning

Since the spurious reflections are minimized, it may be possible to change the frequency of the illumination over a complete band without retuning the system. Thus, it may be possible to measure the reflection properties of a target when subjected to frequency scanning.

Phase Measurements

Since there is no far field distance requirement in the transmission line scattering range, the distance from the target to a phase measuring bridge can be only a few wavelengths. This may enable one to measure the phase of the target reflections easily without requiring an extremely stable frequency signal generator.

Polarization Measurements

By placing two transmission lines with the same axis but rotated 90° with respect to each other, it is possible to impress any polarization on the target by controlling the relative phase and amplitudes of the incident waves on the two transmission lines. Also the reflected signals received on each of the lines allows the complete scattering matrix for the target to be determined.

Forward and Bistatic Cross Section Measurements

It is possible to measure the forward cross section of a target on a transmission line scattering range by constructing the output of the transmission line the same as its input and balancing this output with a constant signal so that a null in the output receiver is obtained when the scatterer is absent. When a scatterer is inserted, this receiver voltage will indicate the forward cross section.

In conventional ranges it is difficult to make bistatic measurements because the coupling from the transmitter to the receiver varies with bistatic angle even with the target absent. This variation is difficult to separate from the variation of target cross section with bistatic angle. Since the field is concentrated on the target in the transmission line scattering range, by making the receiving transmission line wide spaced compared to the illuminating transmission line, it may be possible to have negligible coupling between the two lines with the target absent. If this coupling is negligible, then, when the target is inserted, the receiving transmission line will pick up a signal due only to the differential cross section of the target in the direction of the axis of the receiving transmission line. The receiving transmission line may then be rotated around the target and its variation in signal will be due and proportional to the variation in target cross section with bistatic angle.

Environmental Control

Since the field is concentrated on the target, the transmission line range is small and relatively insensitive to its surroundings. This may allow it to be placed into a vacuum chamber, for instance, where controlled cross-section measurements could be made on wake phenomena, etc.

CONCLUSIONS

The transmission line scattering range displays a high degree of accuracy and sensitivity. This accuracy is mainly due to the fact that the transmission line scattering range does not allow the $1/r^4$ power spreading inherent in free space scattering ranges. It is felt that the transmission line scattering range will work effectively for any size object for the same reason. Also its potential versatility calls for a thorough investigation of its capabilities.

REFERENCES

1. Schelkunoff, S. A., "Electromagnetic Waves", D. Van Nostrand Company, New York, 1943, p. 477.
2. Justice, R. and V. H. Rumsey, "Measurement of Electric Field Distributions," IRE Transactions on Antennas and Propagation, Volume AP-3, No. 4, p. 177, October 1955.
3. Collin, R. E., "Field Theory of Guided Waves", New York, McGraw Hill Book Company, Inc., 1960, p. 68.
4. Ramo, S. and J. R. Whinnery, "Fields and Waves in Modern Radio", New York, J. Wiley and Sons, Inc., 1953, p. 364.
5. Morse, P. M., and H. Feshbach, "Methods of Theoretical Physics, Part II", New York, McGraw Hill Book Company, Inc., 1952; p. 1210.
6. Olte, A., and S. Silver, "New Results in Backscattering from Cones and Spheroids", IRE Transactions on Antennas and Propagation, Volume AP-7, December 1959, p. 561-567.
7. Kraus, J. D., "Antennas," New York, McGraw Hill Book Company, Inc., 1950, p. 549-556.
8. Van De Hulst, H. D., "Light Scattering by Small Particles", New York, J. Wiley and Sons, Inc., 1957; p. 159.

**AN EFFECT OF WALL ILLUMINATION UPON
MICROWAVE ANECHOIC CHAMBER PERFORMANCE***

**R. J. Garbacz and J. L. George
Antenna Laboratory
Department of Electrical Engineering
The Ohio State University
Columbus, Ohio 43210**

ABSTRACT

The use of scaled model targets and improved absorber wall coverings have made CW measuring systems housed in anechoic chambers a practical and attractive radar cross-section tool. However, as targets having lower and lower cross-sections become of interest, demands are placed on the anechoic chamber which rarely required consideration before. One of these is target-wall interaction, by which we mean the perturbation in the background level (due to wall illumination) upon introduction and rotation of the target in the field. Such a non-stationary background clearly is deleterious to the nulling of CW systems and may even dictate minimum measurable cross-section criteria. An analysis of target-wall interaction is proposed which distinguishes between two types of interaction, that of the target upon the wall, and that of the wall upon the target. From the resulting expressions, recommendations can be made concerning the scattering characteristics of the target and its location. Some experimental verification of these results is given.

* The research reported in this paper is supported in part by Air Force Avionics Laboratory, Research Technology Division, Wright-Patterson Air Force Base, Ohio under Contract AF 33(616)-8039 with The Ohio State University Research Foundation.

AN EFFECT OF WALL ILLUMINATION UPON MICROWAVE ANECHOIC CHAMBER PERFORMANCE*

R. J. Garbacz and J. L. George
Antenna Laboratory
Department of Electrical Engineering
The Ohio State University
Columbus, Ohio 43210

INTRODUCTION

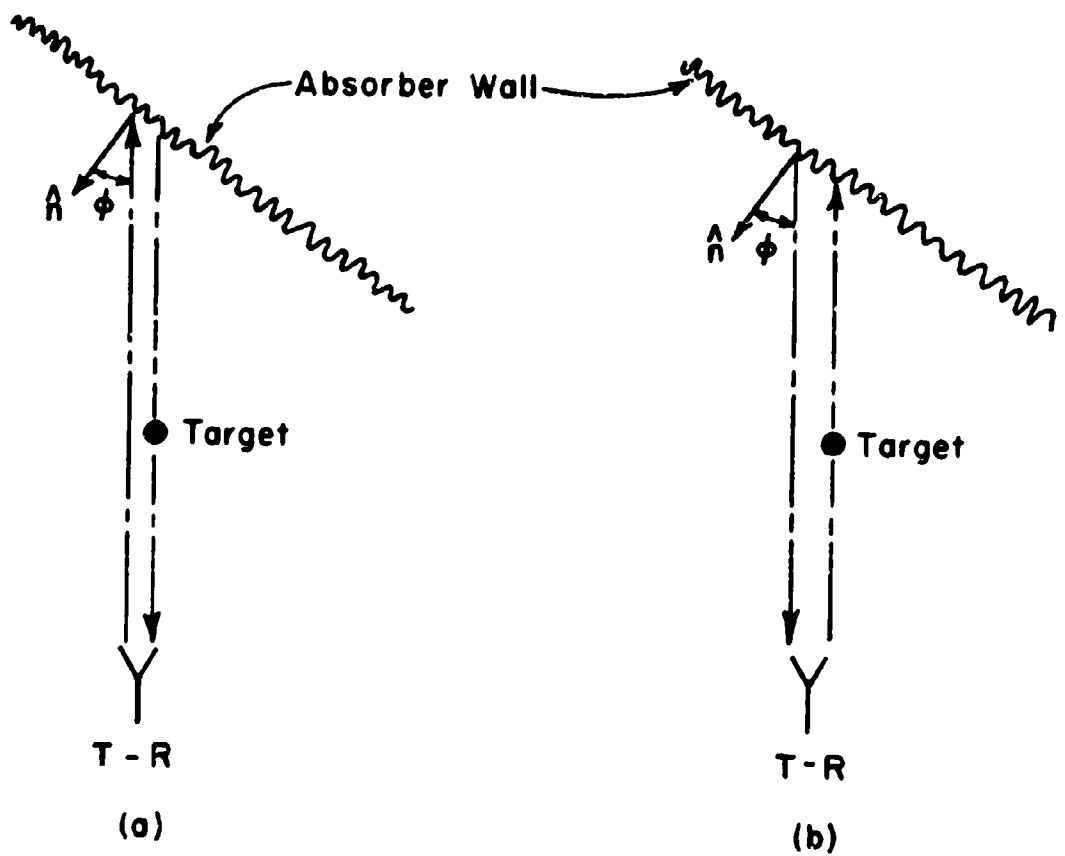
The most common indoor cross-section ranges are of the CW type in which introduction of a target into an electromagnetic field disturbs the balance of a microwave bridge circuit. If this unbalance is due solely to the presence of the target the resultant voltage can easily be related to its scattering cross-section. If, however, introduction of the target into the field simultaneously disturbs the background signal (i. e., scatter from chamber walls, supports, etc.) which had previously been balanced out, there is no assurance that the unbalanced voltage is due to the target alone. This background disturbance, sometimes called "wall shadowing" or "target-wall interaction," is analyzed below under simplifying assumptions and resultant conclusions are verified experimentally.

THEORETICAL ANALYSIS

Two effects which are discernible in the target-wall interaction phenomenon are sketched in Fig. 1. The one effect (Fig. 1a) is that of the energy scattered from the wall to the target, which in turn scatters into the receiver antenna. The other effect (Fig. 1b) is that of the energy scattered in the forward direction by the target illuminating the back wall, which re-radiates into the receiver.

Initially, let us assume a monostatic configuration ($\beta = 0^\circ$) as shown in Fig. 2. The power received through the wall-to-target interaction of Fig. 1a and the power transmitted are related by

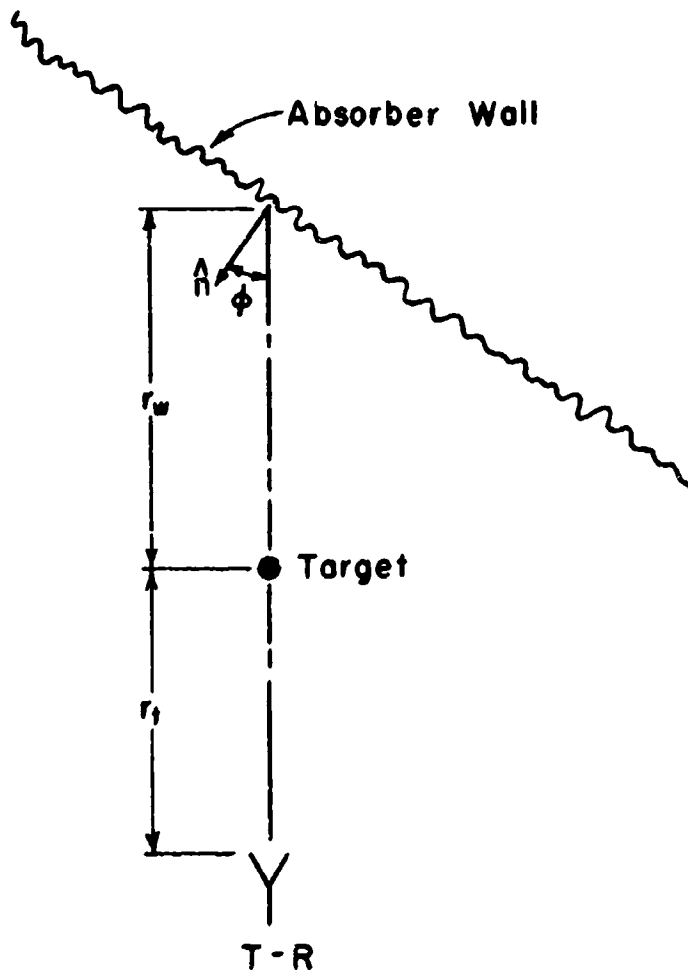
* The research reported in this paper is supported in part by Air Force Avionics Laboratory, Research Technology Division, Wright-Patterson Air Force Base, Ohio under Contract AF 33(616)-8039 with The Ohio State University Research Foundation.



Monostatic Wall - to - Target
Interaction

Monostatic Target-to-Wall
Interaction

Figure 1



Notation for Analysis of Monostatic Wall-to-Target Interaction

Figure 2

$$(1) \quad P_1(0) = [P_T R^2(\phi)] \cdot \left[\frac{\sigma_T(\pi)}{4\pi r_w^2} \right] \cdot \left[\frac{A_R}{4\pi r_t^2} \right],$$

where P_1 is the power received, P_T is the total power transmitted, $R^2(\phi)$ is the power reflection coefficient of the absorber wall in a direction ϕ from normal, $\sigma_T(\pi)$ is the forward scattering cross-section of the target (viewing the target from the absorber wall*), and A_R is the aperture of the receiving antenna. The three bracketed quantities in Eq. (1) can be identified as the total power reflected by the wall, the fraction of this power that is collected and reradiated forward by the scatterer, and the fraction of this that is collected in the receiving aperture. On the other hand, the power which is backscattered directly from the target is

$$(2) \quad P_t(0) = P_T \frac{G_T}{4\pi r_t^2} \sigma_T(0) \frac{A_R}{4\pi r_t^2},$$

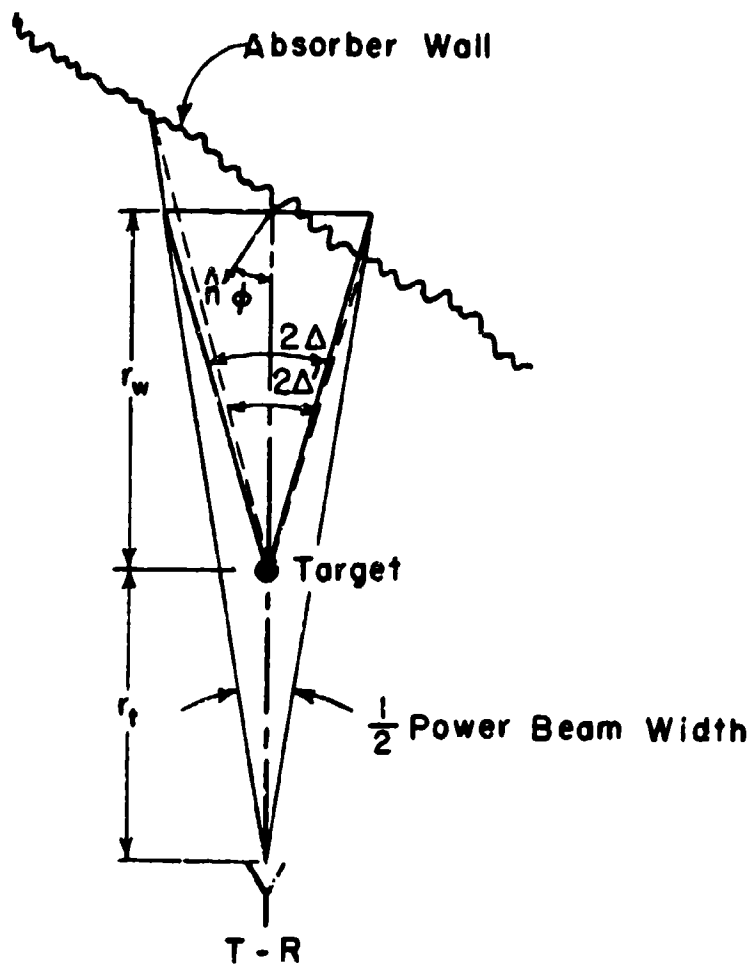
where G_T is the power gain of the transmitting antenna and $\sigma_T(0)$ is the backscattering cross-section of the target viewed from the transmitter. Dividing Eq. (2) by Eq. (1),

$$(3) \quad \frac{P_t(0)}{P_1(0)} = \frac{G_T}{R^2(\phi)} \frac{\sigma_T(0)}{\sigma_T(\pi)} \left(\frac{r_w}{r_t} \right)^2,$$

which is the desired relationship.

In order to study the target-to-wall interaction of Fig. 1b, consider Fig. 3. The receiving antenna is assumed to collect energy only over the angle subtended by its half-power points; hence, only that energy reradiated by the target into the cone subtending the angle $2\Delta \sim 2\Delta^2$ is seen by the receiver. Further, the illuminated region on the wall is approximated by its projection normal to the beam axis forming a disk of radius d coated with an absorber with power reflection coefficient $R^2(\phi)$ rather than $R^2(0)$. This disk subtends a solid angle at the target of approximately

* By reciprocity this is the same value as that obtained looking at the target from the transmitter.



Notation for Analysis of Monostatic Target-to-Wall Interaction

Figure 3

$\pi d^2 / 4\pi r_w^2$. Under these assumptions, the power received through target-to-wall interaction is given by

$$(4) \quad p_2(0) = \left[\frac{P_T G_T}{4\pi r_t^2} \bar{\sigma}_T(\pi \pm \Delta) \right] \cdot \left[\frac{\pi d^2}{4\pi r_w^2} \right] \cdot \left[\frac{R^2(\phi) A_R}{4\pi(r_t + r_w)^2} \right],$$

where $\bar{\sigma}_T(\pi \pm \Delta)$ is a value of the target scattering cross-section averaged over the aforementioned solid angle centered in the forward direction (looking from the transmitter). The three bracketed quantities in Eq. (4) can be identified as the effective source induced by the transmitter at the target position (a radiation intensity), the solid angle about the forward direction subtended by the disk of radius d , and that part of the energy within this solid angle that is reflected by the wall into the receiving aperture. The power gain of the receiving antenna is approximately $G_R \approx 4\pi(r_t + r_w)^2 / \pi d^2$, and if $G_R = G_T$ Eq. (4) reduces to

$$(5) \quad p_2(0) = \frac{P_T}{4\pi r_t^2} \bar{\sigma}_T(\pi \pm \Delta) R^2(\phi) A_R,$$

which, divided into Eq. (2) yields,

$$(6) \quad \frac{p_t(0)}{p_2(0)} = \frac{G_T}{R^2(\phi)} \frac{\sigma_T(0)}{\bar{\sigma}_T(\pi \pm \Delta)} \left(\frac{r_w}{r_t} \right)^2.$$

If the transmitter-receiver gain is high, its beamwidth is small, and if the target is relatively small, its scattering cross-section is approximately constant within the solid angle over which it is averaged, whence $\bar{\sigma}_T(\pi \pm \Delta) \approx \sigma_T(\pi)$. Hence

$$(7) \quad \frac{p_t(0)}{p_2(0)} = \frac{G_T}{R^2(\phi)} \frac{\sigma_T(0)}{\sigma_T(\pi)} \left(\frac{r_w}{r_t} \right)^2,$$

which is identical to Eq. (3). The fact that wall-to-target interaction equals target-to-wall interaction is a result of reciprocity.

The target-wall interaction analysis may be extended to the bistatic configuration sketched in Fig. 4. Figure 5a represents the wall-to-target interaction and Fig. 5b represents target-to-wall interaction. It is clear from the first of these sketches that the wall-to-target interaction analysis in the bistatic case exactly parallels that for the monostatic case, that is

$$(8) \quad P_t(\beta) = [P_T R^2(\phi)] \cdot \left[\frac{\sigma_T(\pi-\beta)}{4\pi r_{wt}^2} \right] \cdot \left[\frac{A_r}{4\pi r_r^2} \right],$$

where all symbols mean the same as in Eq. (1), and $\sigma(\pi-\beta)$ is the bistatic scattering cross-section of the target viewed from the wall and receiving at bistatic angle $\pi-\beta$ measured counterclockwise from the wall. The power received directly from the target is

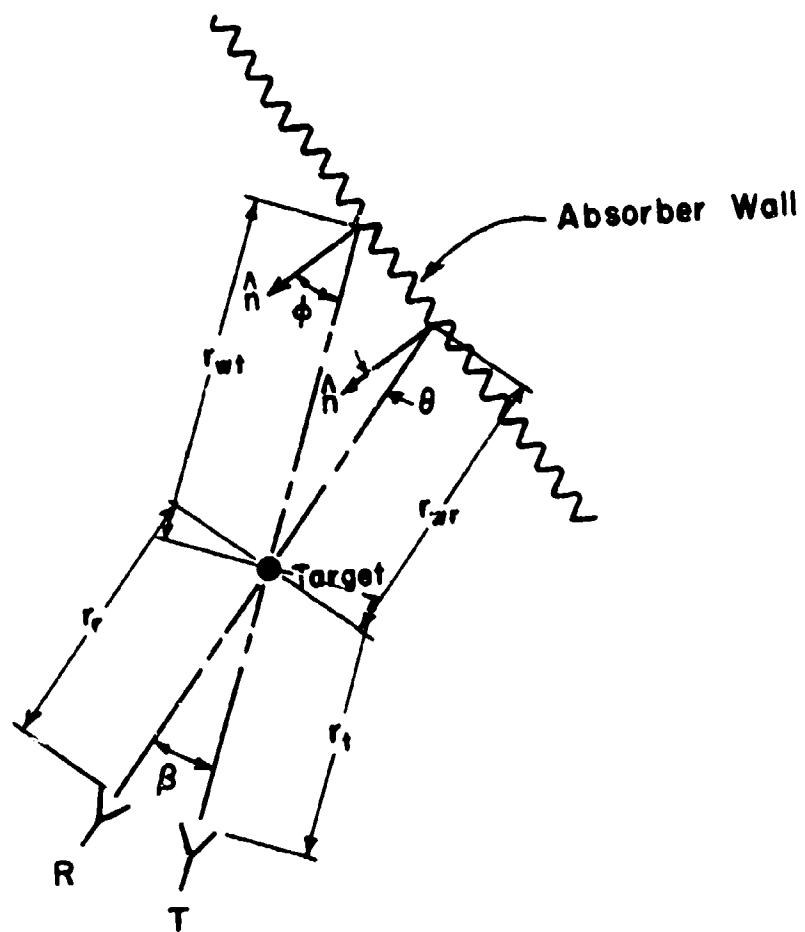
$$(9) \quad P_t(\beta) = \frac{P_T G_T}{4\pi r_t^2} \sigma_T(\beta) \frac{A_R}{4\pi r_r^2},$$

where $\sigma_T(\beta)$ is the bistatic scattering cross-section of the target viewed from the transmitter and receiving at a bistatic angle β measured clockwise from the transmitter. Hence

$$(10) \quad \frac{P_t(\beta)}{P_t(\beta)} = \frac{G_T}{R^2(\phi)} \frac{\sigma_T(\beta)}{\sigma_T(\pi-\beta)} \left(\frac{r_{wt}}{r_t} \right)^2.$$

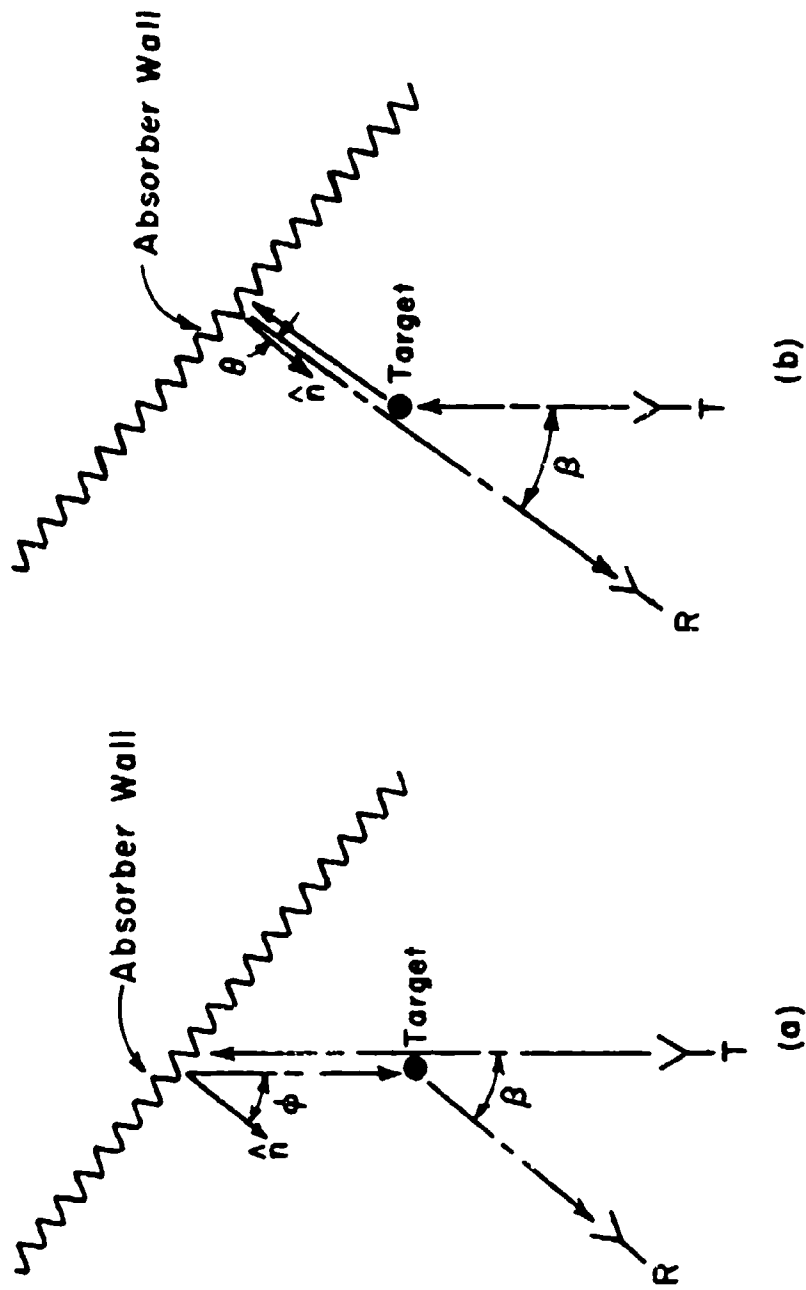
Note that $\sigma_T(\beta)$ and $\sigma_T(\pi-\beta)$ are the only quantities in Eq. (10) which vary with bistatic angle β .

To study the bistatic target-to-wall interaction, consider Fig. 6. Again, assume that the receiving antenna collects energy only over the angle formed by its half-power points; hence only that energy reradiated by the target into the cone subtending the angle $\sim 2\Delta$ is seen by the receiver. Furthermore, the illuminated region on the inclined wall is approximated by its projection normal to the receiver beam axis forming a disk of radius d coated with an absorber with power reflection coefficient $R^2(\phi)$. The disk subtends a solid angle at the target of approximately



Bistatic Configuration

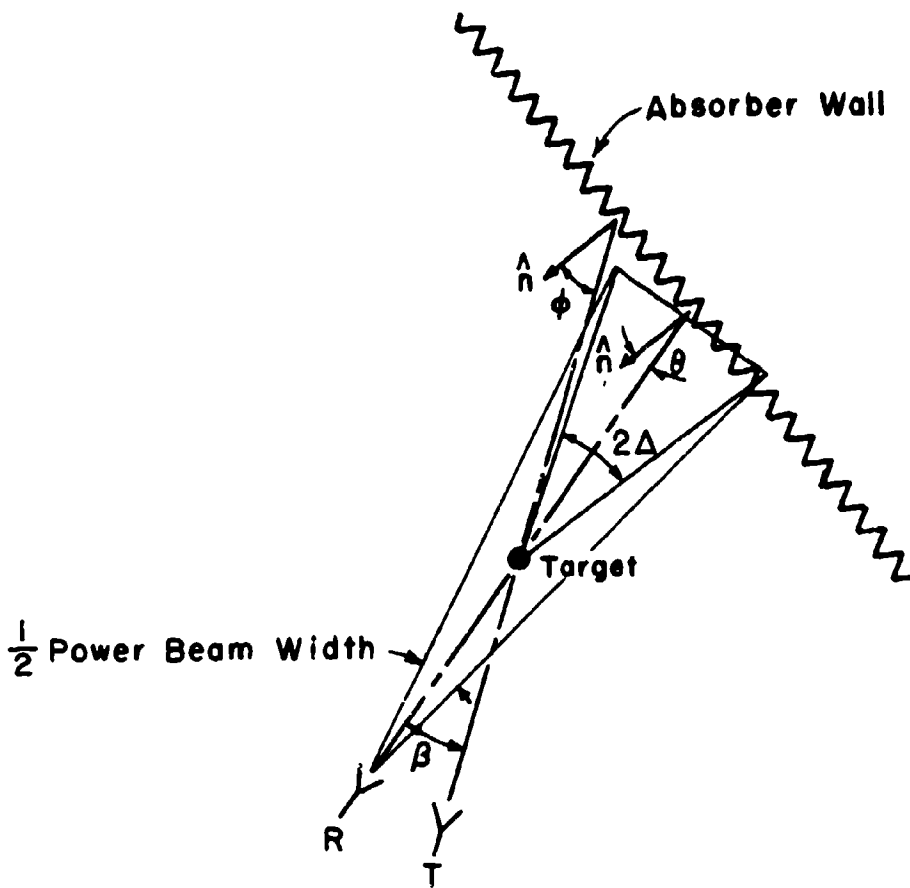
Figure 4



Bistatic Far et-to-Wall Interaction

Bistatic Wall-to-Far et Interaction

Figure 5



Notation for Analysis of Bistatic Target-to-Wall Interaction

Figure 6

$\pi d^2 / 4\pi r_{WR}^2$. Similarly to Eq. (4)

$$(11) \quad P_2(\beta) = \left[\frac{P_T G_T}{4\pi r_t^2} \bar{\sigma}'_T(\pi-\beta \pm \Delta) \right] \cdot \left[\frac{\pi d^2}{4\pi r_{WR}^2} \right] \cdot \left[\frac{R^2(\theta) A_R}{4\pi(r_I + r_{WR})^2} \right],$$

where $\bar{\sigma}'_T(\pi-\beta \pm \Delta)$ is a value of the target scattering cross-section averaged over the aforementioned solid angle centered about the bistatic angle $(\pi-\beta)$ measured counterclockwise from the transmitter. Since $G_R \approx 4\pi(r_I + r_{WR})^2 / \pi d^2$, this becomes

$$(12) \quad P_2(\beta) = \frac{P_T G_T}{G_R} \frac{\bar{\sigma}'_T(\pi-\beta \pm \Delta)}{4\pi r_t^2} \frac{R^2(\theta) A_R}{4\pi r_{WR}^2},$$

whence

$$(13) \quad \frac{P_t(\beta)}{P_2(\beta)} = \frac{G_R}{R^2(\theta)} \frac{\sigma_T(\beta)}{\bar{\sigma}'_T(\pi-\beta \pm \Delta)} \left(\frac{r_{WR}}{r_I} \right)^2.$$

If a high gain receiver is used and the target is relatively small, the scattering cross-section over the solid angle 2Δ is approximately constant so $\bar{\sigma}'_T(\pi-\beta \pm \Delta) \approx \sigma'_T(\pi-\beta)$ and Eq. (13) becomes

$$(14) \quad \frac{P_t(\beta)}{P_2(\beta)} = \frac{G_R}{R^2(\theta)} \frac{\sigma_T(\beta)}{\sigma'_T(\pi-\beta)} \left(\frac{r_{WR}}{r_I} \right)^2.$$

Note that not only $\sigma_T(\beta)$ and $\sigma'_T(\pi-\beta)$ but also $R^2(\theta)$ are functions of bistatic angle β in Eq. (14).

Equations (3), (7), (10), and (14) express the desired relationships between power received from the target, and power due to target-wall interaction effects for monostatic and bistatic configurations. To maximize these ratios notice that maximizing the distance between the target and wall and minimizing the distance between the target and receiver (or transmitter) is advisable. Notice also that more difficulty can be expected from target-wall interaction with targets which have a high forward-to-backward

cross-section ratio than from those whose corresponding ratio is low. Evident too is the fact that a 10 db improvement in absorber performance yields a 10 db improvement in interaction effects. And in the case of the target-to-wall interaction for the bistatic case (Eq. (14)) the absorber must be good over a suitable range of angles.

The theory presented here is very approximate; it says nothing about effects of corners and sidelobes and multiple reflections, all of which enter in a very complicated fashion. However, from experience in the Antenna Laboratory darkroom, it does appear that the region illuminated by the transmitter on the back wall is the greatest offender; this explains the fact that at certain bistatic angles, as the illumination region on the back wall common to both transmitter and receiver decreases, so does the background. We have found, in general, that background and interaction effects are less serious for bistatic configurations. One additional point brought out by Eq. (14) is that a good absorbing wall in the line-of-sight of the bistatic receiver is advisable. The possibility also exists of angling the back wall slightly so that it is more nearly normal to both the transmitter and receiver beam axes over the most used bistatic angle range, keeping in mind that popular absorbers degenerate rapidly beyond incidence angles of $\pm 35^\circ$ to the normal.

EXPERIMENTAL RESULTS

Because wall-target interaction effects exist only upon introduction of a target which itself generally contributes an echo, these effects are elusive to evaluation. From one viewpoint, we desire a scatterer-probe which has a backscatter, say 20 db down from typical interaction return, so that its introduction into the field upsets the microwave bridge essentially only by interaction with the room, not by direct backscatter. The resulting unbalance is then almost wholly due to the interaction phenomenon. However, measurement of such extremely low cross sections is complicated by spurious noise, drifting, etc., which obscures the effect under study. An alternative method was employed here using large scatterers (a flat plate coated with 20 db absorber and a thin rod); these were placed into the field of a nulled phase-sensitive system¹ and moved at a constant rate along the line-of-sight, producing outputs recorded in time which were sinusoidal in shape. If no interaction exists, the average levels of these sinusoids should

be coincident; if interaction does exist, the average levels should separate, indicating a constant unbalance of the microwave bridge due to wall shadowing.² Figure 7 presents curves of this sort for two target-to-wall spacings. Since the forward to backward cross section ratio of the absorber coated plate is ~ 20 db while that of the rod is ~ 0 db, we expect a separation of the average levels of these curves in both cases, but more pronounced in the instance of the small target-to-wall spacing. This is verified in these curves.

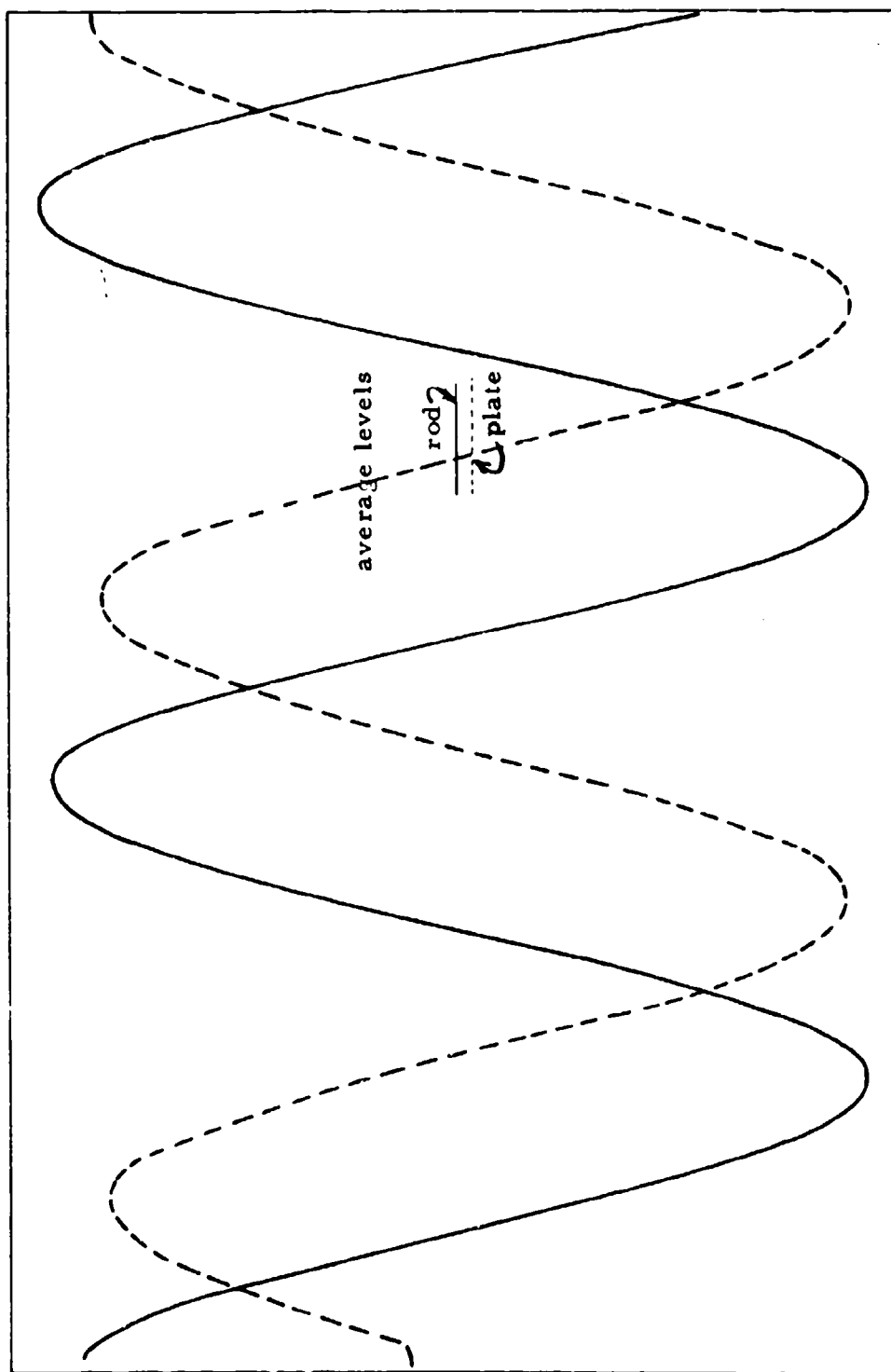
This paper has merely introduced the subject of target-wall interactions; much more experimental investigation is required to obtain a full understanding of the phenomenon and ways to combat it. The brief experiments which were performed for this paper do indicate that target-wall interaction can be a source of error for large targets of low cross-section and that for small targets of low cross-section, other system errors are probably more important and must be accounted for before the interaction phenomenon. The experiments also verified that the motion method of obtaining cross-section is an effective means of avoiding first order interaction errors since the amplitude of the sinusoid, which is proportional to scattered field, is relatively independent of the sinusoid average level. Second order effects of wall reflections, which appear as warpings of the field into which the target is immersed, do affect the shape of the sinusoid and thereby introduce error; these effects were not evident in the present experiments.

ACKNOWLEDGMENT

The authors wish to thank Dr. E. M. Kennaugh who suggested this study, and Mr. R. W. St. Clair who recorded the experimental data.

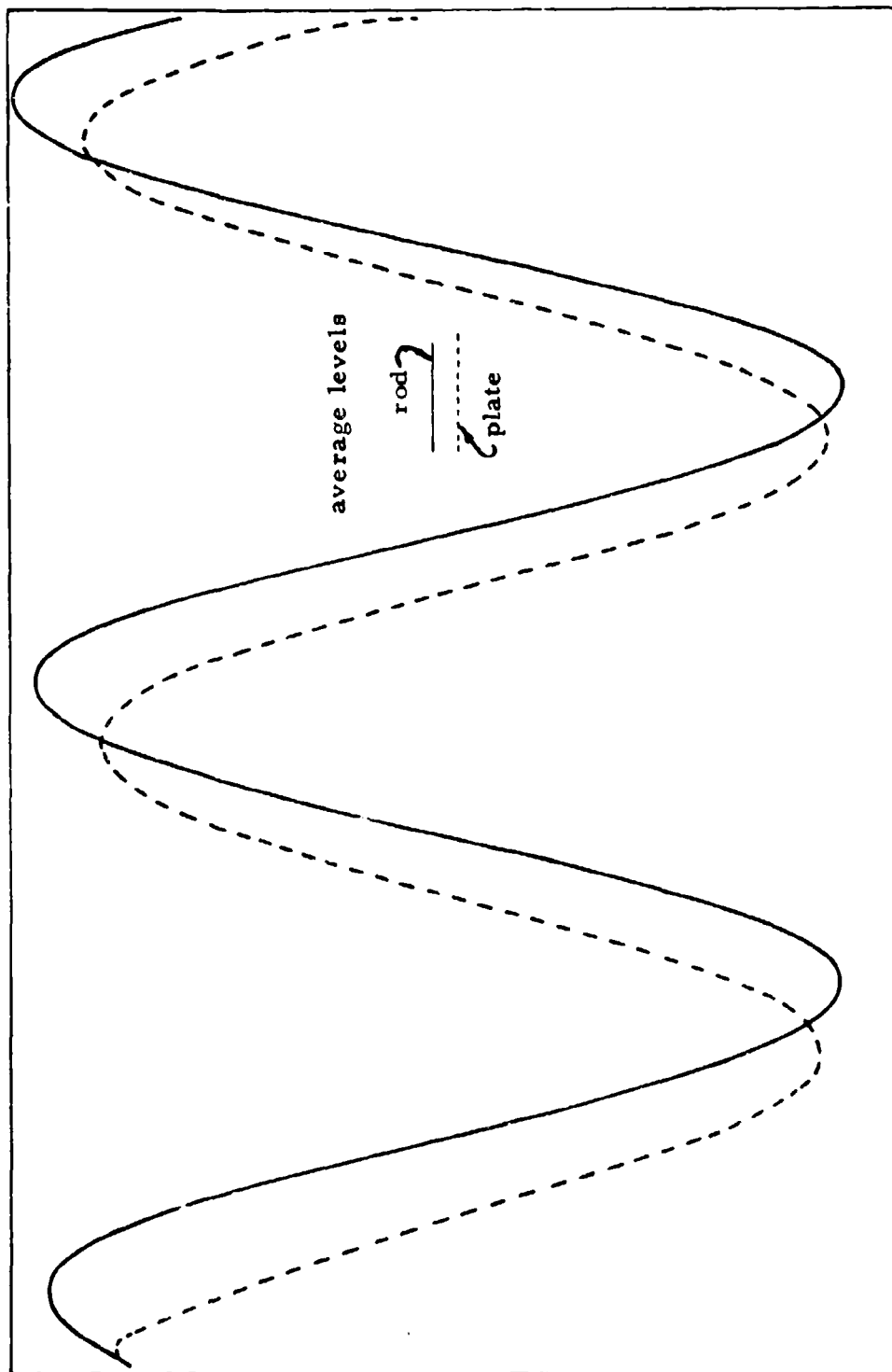
BIBLIOGRAPHY

1. Garbacz, R. J., and Eberle, J. W., "The Measurement of Time-Quadrature Components of a Scattered Field," IRE-WESCON Convention Record, Part 1, August 1960.
2. Garbacz, R. J., "A Memorandum on a Measurement Technique for Low Cross Sections," Report 1223-7, 1 May 1962, Antenna Laboratory, The Ohio State University Research Foundation; prepared under Contract AF 33(616)-8039, Aeronautical Systems Division, Wright-Patterson Air Force Base, Ohio. AD 276 102



Signal variation with target motion for absorber-coated flat plate and thin rod.
Wall to target spacing 12'.

Figure 7a.



Signal variation with target motion for absorber-coated flat plate and thin rod.
Wall-to-target spacing 2'.
Figure 7b.

COMPLETE RADAR CROSS-SECTION MEASUREMENTS

J. Richard Huynen
Lockheed Missiles and Space Company
Electromagnetics
Sunnyvale, California

ABSTRACT

The concept of a complete set of radar target cross-section data is useful to compare and evaluate different systems of radar target measurements. It leads naturally to the question of a minimum set of data and this in turn leads to the requirement of built-in redundancy in a complete system of measurements. This report deals with the techniques for a complete set of data in the form of a minimum set of compatible patterns. Using this technique a complete set can be obtained for rotationally symmetrical targets. For non-symmetrical targets in general no complete system can be devised. For those targets emphasis should be placed on selected characteristic parameters.

INTRODUCTION

The concept of complete radar cross-section data is introduced here as an important systems concept which serves to bring together several ideas concerning radar target signature analysis. A complete set of data obtained from a general radar target is defined to be such data that at every aspect the radar cross-section of the target is known.

To show the use of this concept we consider a target which depolarizes. For such a target, patterns taken at different linear polarizations (for instance horizontal and vertical) will not be the same. Since the target (in space) in general is free to move in any position relative to the radar site, it will be desirable to obtain cross-sections at all linear polarizations. One "brute force" technique consists of taking patterns at equal increments of orientation of the linear polarizations. In order to cover 180° using increments of 10°, a total of 18 patterns would have to be obtained for each "cut" through the target. And this technique still leaves gaps in between the 10° intervals.

Another procedure would be to recognize that the patterns obtained at several linear polarizations are equivalent (except for an ambiguity) to the knowledge of the scattering matrix of the target as a function of aspect. On the other hand, if the scattering matrix of the target is known, the radar cross-section at all linear polarizations can be determined. Thus knowledge of the scattering matrix of a target at all aspect angles, gives rise to a complete set of radar

cross-section data, (i.e. without gaps in aspects).

It is natural to ask about the minimum set of data required for a complete set. A system has been developed, such that for targets with an axis of rotational symmetry, only four patterns (a set of compatible patterns) supply complete data.

There is a peculiar feature in radar patterns which makes the concept of completeness more significant than at first sight expected. It is well known that a pattern, say for horizontal polarization, exhibits aspect angles for which the signal disappears in the noise level but that for the same target at that same aspect the cross-section at a different polarization (say vertical or circular) may be considerably above the noise level. In that case the choice of horizontal polarization to obtain scattering matrix data (which is our choice) was a poor one since the signal disappears and an information gap results in incomplete data. This deficiency points to a requirement of redundancy in the minimum set of input data, i.e. we have to select an extra pattern such that if one pattern of the set disappears in the noise level, the extra pattern exhibits a high cross-section and vice versa. Such a complete set with built-in redundancy is called a compatible minimum set of radar patterns.

This report deals with the detail requirements for obtaining a minimum set of compatible patterns. For rotationally symmetrical targets, it can be shown that the four patterns described above satisfy this requirement.

The concept of redundancy is relatively new in radar cross-section work but is clearly a necessary requirement for the employment of computer techniques which cannot tolerate information gaps.

For non-rotationally symmetric targets, it can easily be shown that in general no complete set of data is possible! This means for those targets there will always be information gaps no matter which method of measurement one chooses. The reason for this is purely a matter of geometry. Rotationally symmetric targets are defined by only one aspect angle, i.e. the pattern angle α , while targets which do not have an axis of rotational symmetry will also depend on the roll angle (or cut angle) β . This means that several sets of patterns, one set for each "Cut" through the target have to be obtained and since cuts are not continuous in β , there always will be information gaps. Naturally, it is possible to take many cuts (small increments in β) but this leads to a tremendous increase in amount of labor required and ideally there still will be small gaps remaining. Depending on the size and structure of the target the diffraction patterns may exhibit rapid changes even within a few degrees. This is a basic reason why it is discouraging to get complete data, i.e. complete scattering matrix information, from non-symmetrical targets. The amount of labor involved to even approach a complete set is many orders of magnitude larger than that required for complete data on symmetrical targets which can be done by a relatively simple effort.

What then can we do to analyze non-symmetrical targets? The answer has to be found in the direction of selection of special parameters which are significant for systems considerations. Based on these parameters we can make important statements about the targets without having to know a complete set of data.

It should be noted that the requirement of completeness of data is necessarily an ideal one.

However, it serves a useful purpose to evaluate systems as to their degree of completeness. Completeness as a function of frequency is clearly an impossible requirement since it would require coverage of the whole spectrum. Within a specified frequency range completeness can be approximated. Finally there are orientations of a target at which the maximum return itself disappears below the noise level. (We refer to the notion of "diffraction null" in the discussion of the targets below). For those rare cases target information is lost and retrieval of it is impossible but solely because of intrinsic target properties and not because of a poor choice of measurement.

POLARIZATION CHART

A useful technique of representing polarization was suggested by Poincaré. The method consists of using the orientation angle ϕ and the ellipticity angle τ , which determine the elliptically polarized wave, as polar angles of a point on a unit sphere. The actual polar angles are given by 2ϕ and 2τ . Points on one hemisphere correspond to right-sensed polarizations, while points which belong to the other hemisphere indicate the left-sensed polarizations. In this manner, a unique representation of all possible polarization is given by points on the unit sphere. This sphere will be referred to as polarization sphere. (4)

A cylindrical projection of the sphere on a plane will be used in this work to obtain a polarization chart. Figure 1 shows the polarization chart. The outside periphery of the chart supplies all linear polarizations with horizontal polarization on the right and vertical polarization on the left of the horizontal axis. The position angle of a point on the chart is twice the major axis orientation of the ellipse. The radius vector is a function of ellipticity only. Two such charts - one belonging to the upper, and the other to the lower hemisphere - determine all transmitter polarizations uniquely. The center of the chart corresponds to the two circular polarizations. In many applications, it will be more convenient to use one polarization chart instead of two, to indicate all points on the polarization sphere, where points belonging to differently sensed polarizations are distinguished by some labeling procedure.

PRINCIPLE OF TARGET SCATTERING

A radar is defined as a sensor of electromagnetic energy, which uses the same antenna for transmitting and receiving. The mechanism of radar reception is illustrated in Figure 2. The signal back-scattered from the target is in general decomposed into two orthogonal components: one is the received signal which has a polarization "parallel" to the transmitted signal; the other is the rejected signal which is "orthogonal" to the received polarization. As the names indicate, the received signal contributes to a voltage at the terminals of the radar receiver.

In mathematical terms, the process is described as follows. Consider the normalized transmitted polarized signal represented by a two-component complex vector \underline{h} , then the return signal is given by the target scattering operator T applied to the transmitted signal \underline{h} (7). The received voltage will then be found as a scalar product of the return signal $T\underline{h}$ with the transmitted signal \underline{h} as shown by the equation $V = T\underline{h} \cdot \underline{h}$. The received voltage squared is the power density

in the returned wave: $P = |T\underline{h} \cdot \underline{h}|^2$. The scattering operator T which describes the radar backscattering properties of the target at fixed aspect angles is a symmetric operator because of reciprocity.

If \underline{h} is determined by two independent components of electric field in a given frame of reference, the scattering operator T is represented by a two-by-two symmetric matrix.

In general the returned signal is considered decomposed into a component "parallel" to the transmitted polarization \underline{h} and a component "orthogonal" to \underline{h} : $T\underline{h} = a\underline{h} + b\underline{h}_\perp$ (in this notation * indicates complex conjugation). Two special cases are of interest: If the transmit polarization \underline{h} is such that the scalar $b = 0$, it is the solution of the eigen-value problem: $T\underline{h} = t\underline{h}$. Two orthogonal eigen vectors \underline{h}_1 , and \underline{h}_2 solve this problem. We can show that one polarization, say \underline{h}_1 is the so-called maximum polarization \underline{h}_{max} , with corresponding eigen-value t_{max} . For this case the power density in the returned wave: $P = |t_{max}|^2$ is maximum. The other case is where the scalar $a = 0$ and we have: $T\underline{h}_\perp = t_{\perp}\underline{h}_\perp$. This case solves for the two so-called null polarizations \underline{h}_{o1} and \underline{h}_{o2} , since then: $V = t_{\perp}\underline{h}_\perp \cdot \underline{h} = 0$. For these transmit polarizations the antenna appears blind to the target.

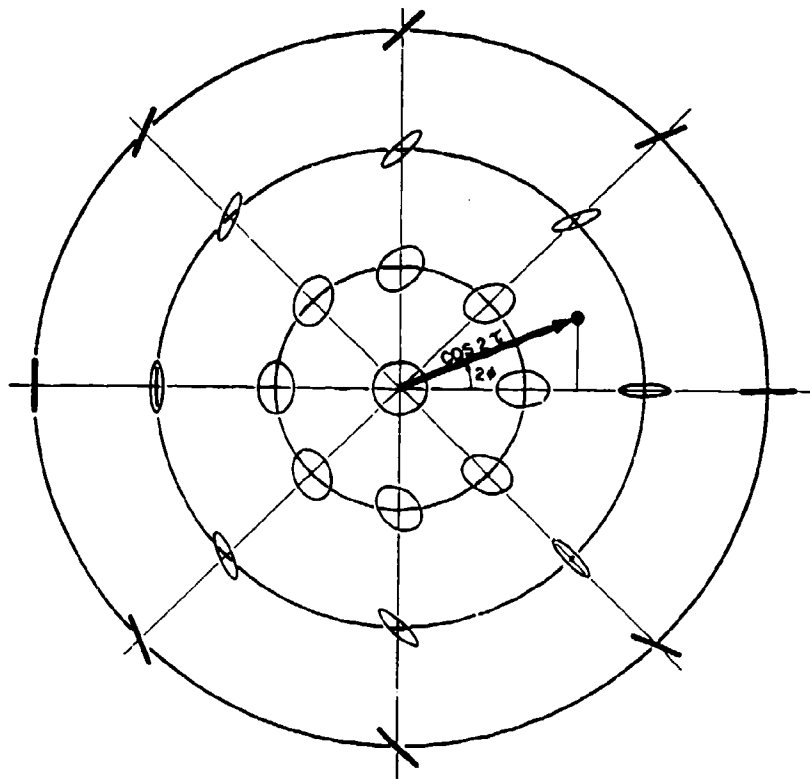


Fig. 1 Polarization chart

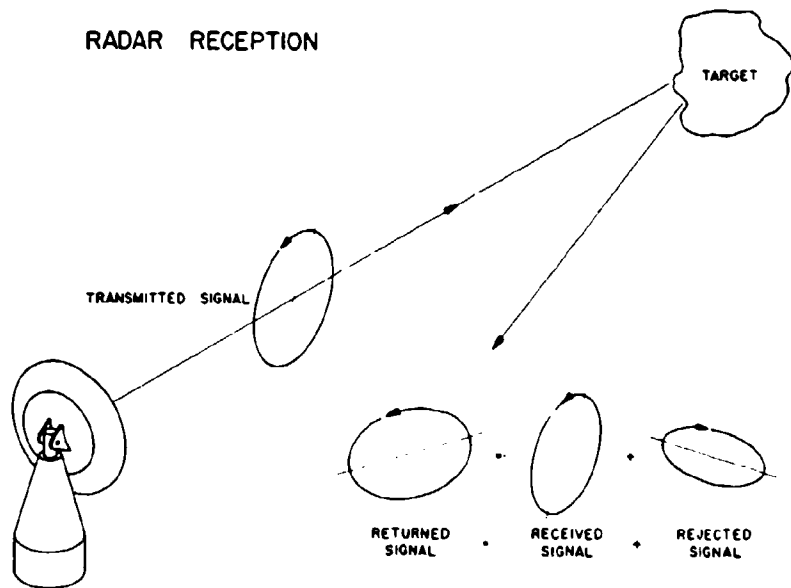


Fig. 2 Principle of radar reception

Each null-polarization being represented as a point on the polarization sphere is given by two real parameters. Consequently, the general target matrix T has five independent parameters by which it is defined (except for a common phase factor which plays no role with radar amplitude measurements). If the positions of the two null-polarizations are known as two points on the polarization sphere, then, for an arbitrary transmitted polarization, one can compute the return from the target. It is clear from this discussion that the two nulls and maxima specify the parameters which determine the scattering operator in an invariant form, i.e. without dependence on a particular reference frame.

The five target parameters which completely determine the scattering matrix for any target at a fixed frequency are:

- ψ_0 is the orientation angle of the maximum polarization and is the internal target orientation parameter.
- σ is the ellipticity angle of the maximum polarization and is a measure of "helicity" of the target.
- γ is obtained from the phase of the maximum polarization and is a measure of depolarization by the target.
- χ is an intrinsic target parameter possibly related to local surface curvature (for specular targets).
- P_m is the maximum receivable cross-section of the target.

The quantities are all a function of aspect (α, β) of the target (15). The remaining part of the paper describes specific techniques for measuring these invariant parameters.

In contrast to the described technique, it has been customary in the past to determine the scattering matrix by measuring its coefficients directly. It is clear that, although this method also would describe the scattering operator (since the reference frame in which the operator is represented is known), the matrix coefficients themselves contain a mixture of information about the target and reference frame, and thus are not pure target parameters. To try to correlate information obtained from two different targets by a comparison of scattering matrix coefficients will be a frustrating task.

INSTRUMENTATION

A special antenna was designed to produce variable polarizations. Figure 3 shows a schematic view of the antenna construction. The reflector consists of an 18-in diameter parabola with an 8-in focal length. The feed consists of a tapered circular waveguide with a specially designed teflon back feed.

A quarter wave vane is positioned within the circular waveguide feed providing a 90° phase lag between the two orthogonal linear polarizations. The orientation of the vane with respect to the linear input polarization determines the ellipticity of the transmitted polarization. If the vane assembly and the linear polarization are simultaneously rotated, a change of major axis orientation of the transmitted ellipse occurs. Figure 4 shows a block diagram of the CW, X-band system which was employed. For monostatic operation, the same antenna was used for transmitting and receiving, as was mentioned before. This requires that the received signal shall be separated from the transmitted signal. With the CW system, this requirement can be met by utilizing a magic T as a balanced bridge. To accurately determine the radar return from small targets, isolation between transmitted and received signals of the order of 100 db must be achieved.

Measurements on targets having radar cross-sections exceeding one square foot were accurate to within .25 db.

THE FOUR POLARIZATION TECHNIQUE FOR SYMMETRICAL TARGETS

A target with horizontal symmetry was placed upon a foam tower and rotated along the vertical axis (Figure 5).

Four patterns of different polarizations were obtained and recorded on transparent paper. The four polarizations used were horizontal, vertical, linear at 45° and right circular. The patterns as a function of rotation angle were superimposed upon each other and db differences from three different patterns relative to the local maximum were obtained.

The polarization null-locator chart Figure 6 is constructed such that knowledge of the db differences establishes the position of the characteristic target nulls on the circular polarization chart.

The db-level lines for each of the four polarizations are indicated on the null-locator chart in Figure 6. The technique for finding or plotting a target polarization-null consists simply of reading from the four superimposed patterns the three db differences relative to a local maximum (either H or V). The intersection of any two curves corresponding to the db difference values for the corresponding pattern gives the position of the right-sensed null on the polarization chart. For symmetrical targets the left-sensed null is then uniquely determined.

Notice that each point (polarization null) on the chart is obtained from intersections of three db-difference curves. This means that the method is overdetermined, since a point can be obtained from the intersection of two db-difference curves alone. The extra pattern gives built-in redundancy for the system of measurements, i.e. if one pattern disappears below the noise level no information is lost, since the system guarantees a high return for the other polarization patterns.

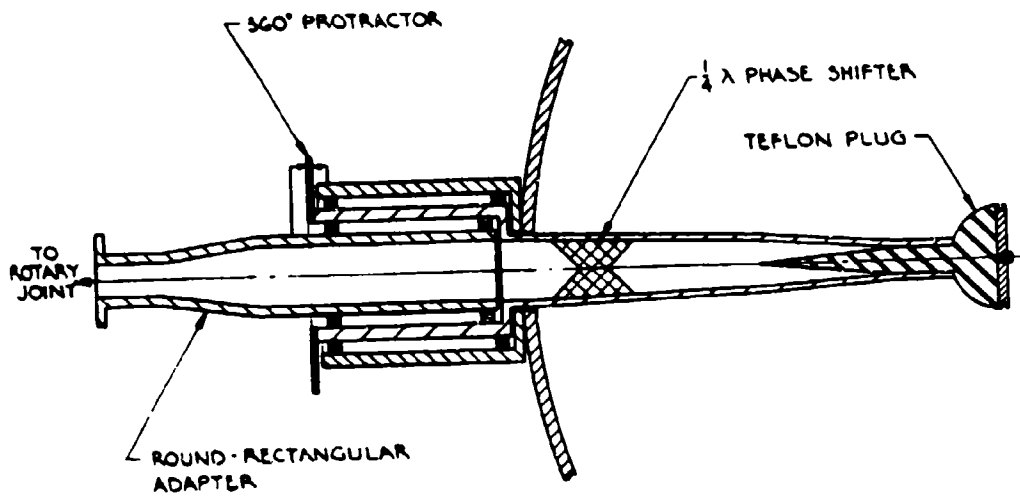


Fig. 2 Variable polarization antenna

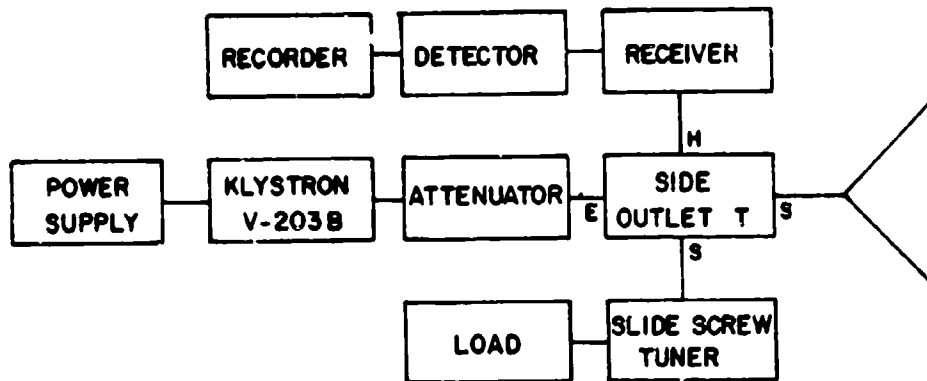


Fig. 1 Schematic diagram of CW X-band system

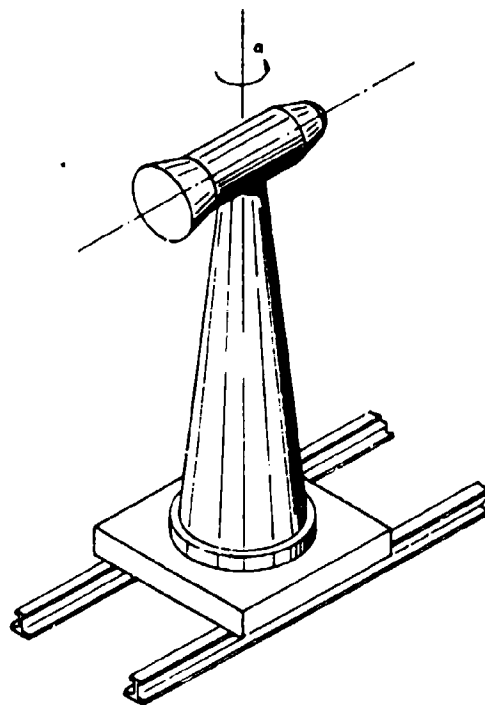


Fig. 5 Target laboratory position

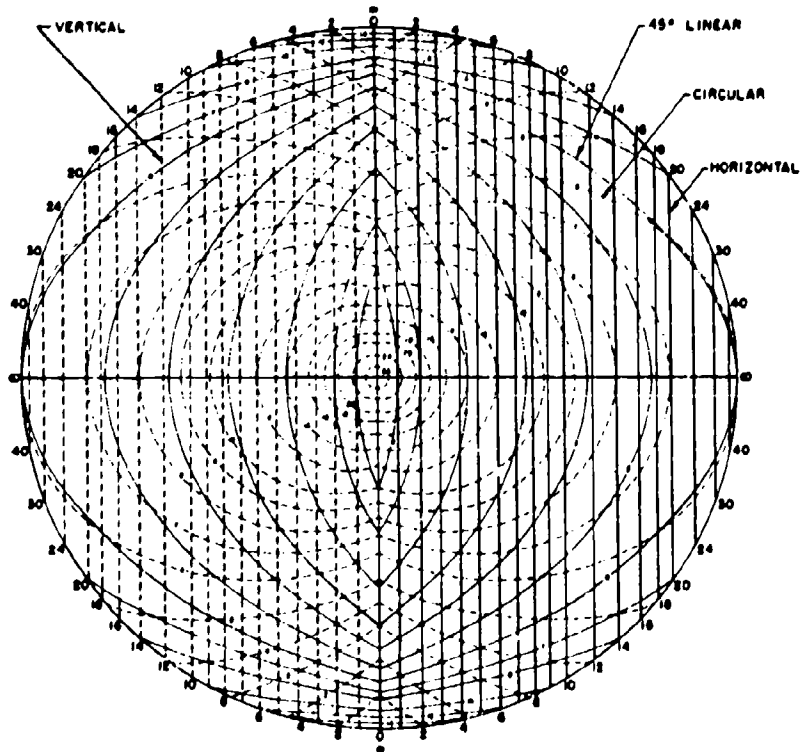


Fig. 6 Polarization null locator chart (45° linear)

The only exception to this rule is when the maximum return, i.e. the return for the maximum-polarization itself disappears below the noise level. This happens rarely however; we refer to the discussion on "diffraction-nulls" below.

The four polarization method works very fast and efficiently for hand plotting target information obtained in the laboratory or on the pattern range. Observe that the null-locator chart is symmetric with respect to the horizontal axis. This makes an ambiguity check necessary.

A new four polarization system has been worked out recently which uses an elliptical polarization instead of the 45° linear and which eliminates the ambiguity. Figure 7 shows the null-locator chart designed for the improved method. Figure 8 actually illustrates the null determination for this case.

The fourth pattern in the new case with elliptical polarization thus serves two purposes: 1) It resolves the ambiguity between two possible null-polarizations. 2) It supplies built-in redundancy for the system. Thus this technique supplies a minimum set of compatible data for complete radar target cross-section determination.

EXPERIMENTAL RESULTS

Experimental results are shown for two types of targets. The first measurements show the results for a pair of plates crossed at 90° with respect to each other. The intersecting axis was kept vertical during the measurement and the dihedral was rotated about the vertical axis with the angle α . Figure 9 shows the four patterns thus obtained separately and super-imposed upon each other. The resulting null-plot for this target is shown in Figure 10. We obtain a highly interesting question mark curve, formed by the null-locus for right-handed polarizations on the polarization chart.

One notices the remarkable regularity which the null-locus for the dihedral exhibits, compared to the fluctuating patterns of Figure 9. Notice that on these patterns the local maximum is attained either at horizontal polarization or at vertical polarization. At no aspect angle does either the circular polarization pattern or the 45° linear polarization pattern exceed the maximum level. This result is characteristic for symmetrical targets.

The second experimental result was obtained from a convex-shaped body. Figures 11 and 12 show the patterns and the corresponding null-locus for the right-sensed polarizations. The convex-shaped object can be expected to exhibit a null-locus characteristic (Figure 12) which is distributed around the center of the chart, at circular polarization, because of specular reflection. It is interesting to note, however, that deviations from the center position occur even for relatively strong signals. This indicates that for convex-

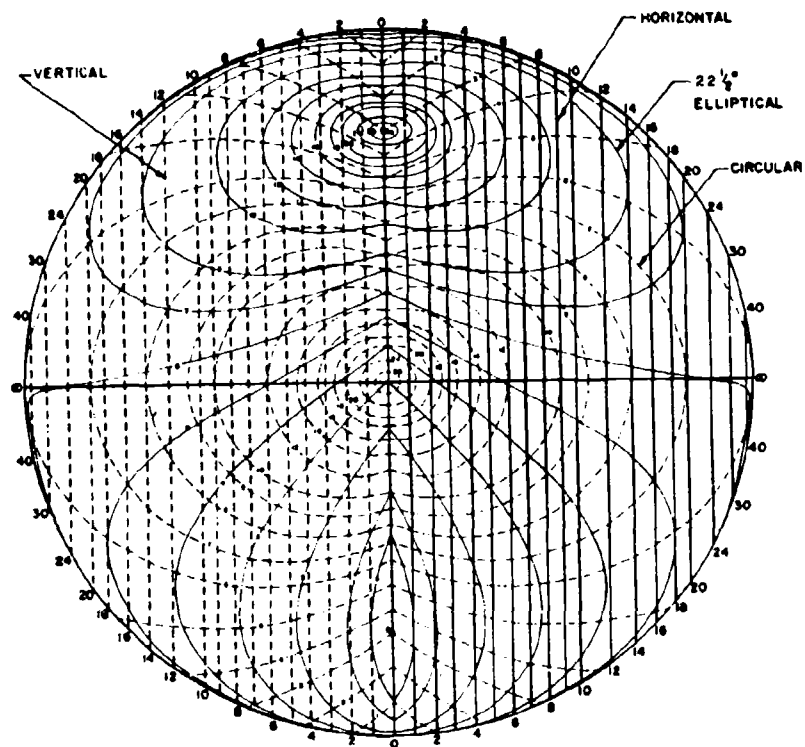


Fig. 7 Polarization null locator chart (elliptical)

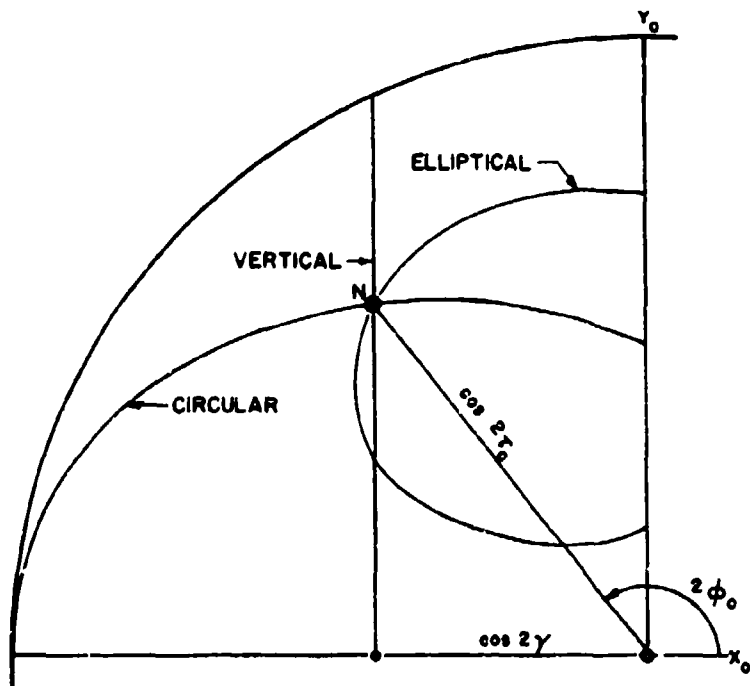


Fig. 8 Procedure for null-location

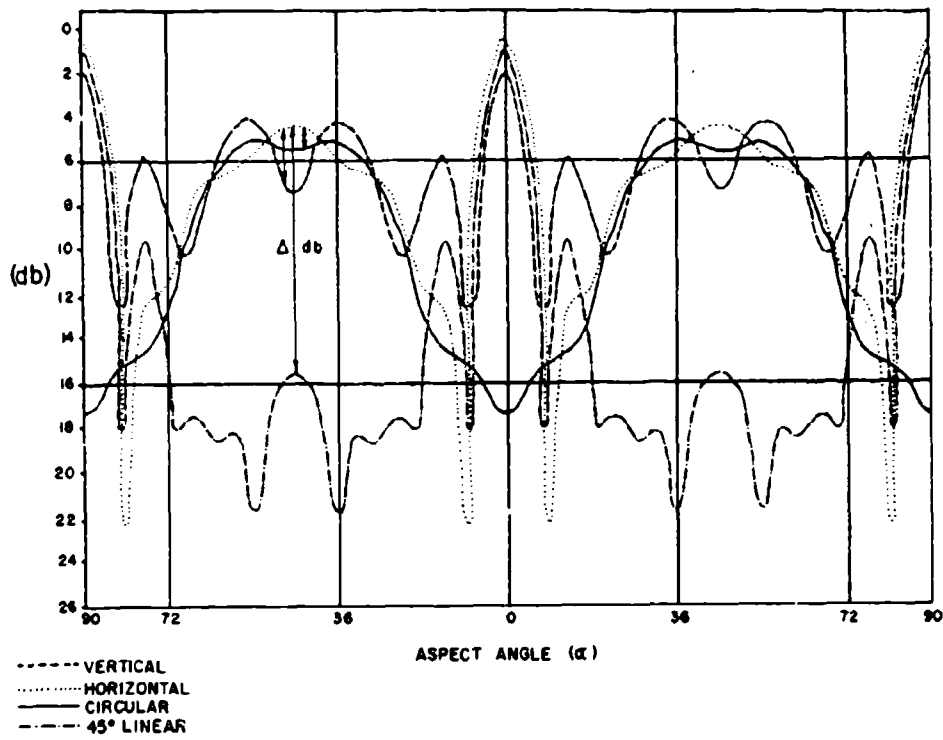


Fig. 9 Four patterns for dihedral plate

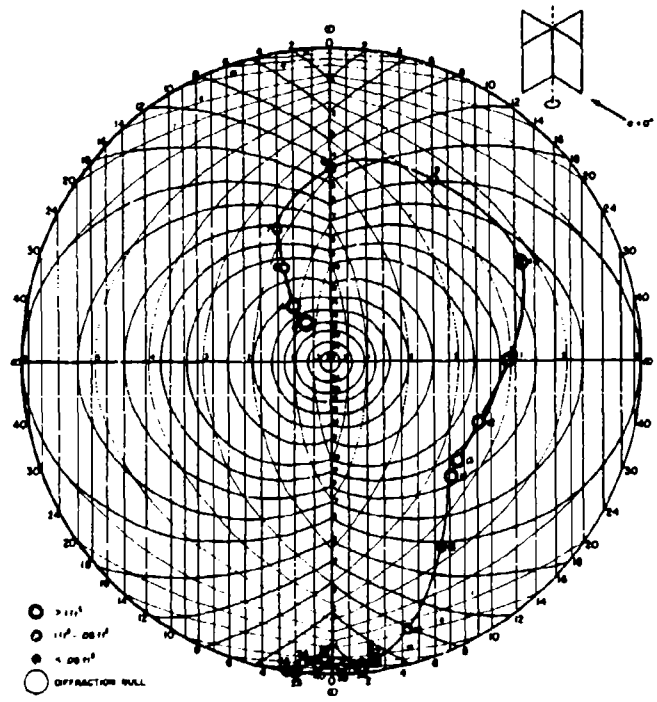


Fig. 10 Characteristic diagram for dihedral

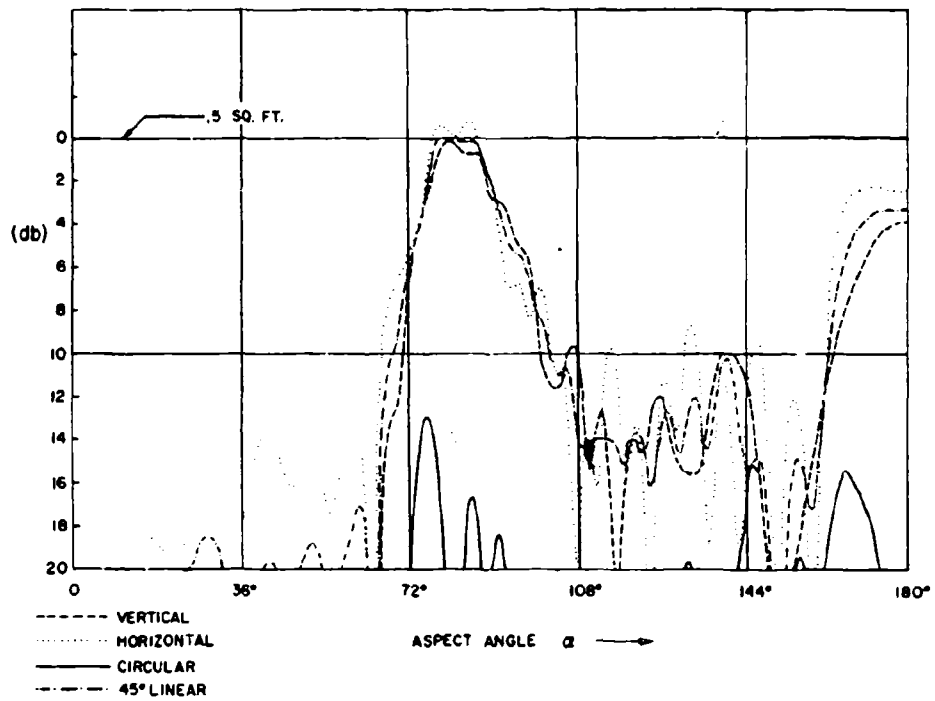
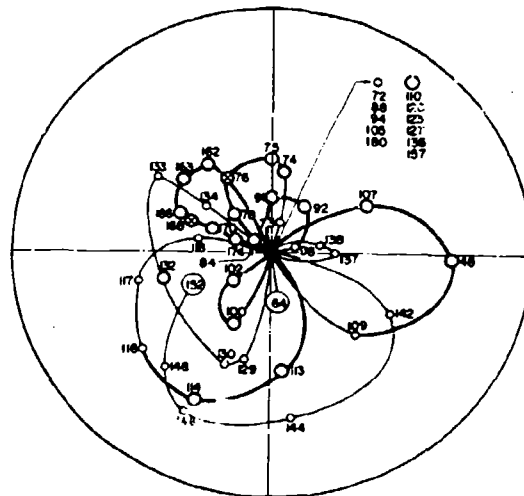
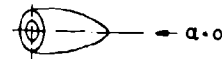


Fig. 11 Four patterns for a convex surface

OGIVE



- 45° - 111°
- 111° - 59°
- < 59°
- DIFFRACTION NULL

Fig. 12 Characteristic diagram for convex surface

shaped objects of a few wavelengths, the specular reflection considered as a local flat plate is no longer a valid assumption at all aspects. Indeed, the null-locus behavior of convex-shaped objects could be used to determine the extent to which stationary phase methods are applicable for predicting diffraction patterns. We notice a peculiar phenomenon happening at $\alpha = 64^\circ$. At this angle the maximum return itself disappears in the noise. At this angle a so-called "diffraction null" exists for the target. At this angle no energy is returned to the radar, i.e. the target is "invisible" to the radar for any type of polarization!

MEASUREMENT OF A GENERAL TARGET

The technique thus far presented is suitable for radar cross-section measurements of targets which have rotational symmetry. Many targets are of this type, or are approximately symmetric. These targets are particularly suitable to measure, since scattering matrix information obtained for one cut through the rotation axis determines this information for all aspect angles. For a non-symmetrical target, several cuts have to be obtained to cover all aspect angles. For this reason, the information obtained cannot be complete.

Basically, there are two approaches to the measurement technique of non-symmetrical targets, for each cut in which data are obtained. The first consists of a "symmetrization" procedure and involves a rotatable antenna. The second method computes the data from inputs to a stationary antenna. The first method consists of a "maximum following" principle in which the maximum polarization is found either by scanning with linear polarization, or by some other technique. Most targets exhibit the property of having no "helicity" i.e. there is no internal preference for right or left circular polarization. For those targets, the maximum polarization is a linear polarization with orientation angle ψ_0 . By "following" this angle ψ_0 by rotation of the polarization antenna, either manually in the laboratory, or by using a servo device for automatic operation, the angle ψ_0 can be eliminated as a variable parameter. Thus a symmetrized target is obtained of which patterns are measured, and from which null-polarizations can be deduced in exactly the same manner as was shown for symmetrical targets, except that several loci are now necessary, one locus for each cut through the target.

If the target has appreciable "helicity", this procedure cannot be followed and only a computing scheme will suffice to analyze the data. The computing scheme consists of a measurement of the scattering matrix by conventional means (using a stationary antenna which receives amplitude and phase of parallel as well as orthogonal components of the backscattered signal). Through the solution of the two eigen-value problems discussed before, the invariant parameters which are characteristic for the target are computed. These values could be presented graphically, or stored in the computer for further computations.

CONCLUSION

For a target having axial symmetry, a complete set of radar cross-section data is obtained by the four polarization method, which supplies a minimum set of compatible patterns. From these patterns the invariant target parameters can be presented graphically as a null-locus on a polarization chart or stored in a computer for data analysis. If the target is non-symmetrical, complete data can be supplied only for each "cut" through the target at which measurements are performed. If the target has no "helicity" (i.e. its maximum polarization is linear) symmetrized null loci for each cut can be obtained for graphical display. In either case complete scattering matrix determination is available in invariant form. This information is essential for signature data analysis and comparison of radar targets.

ACKNOWLEDGEMENT

The author gratefully acknowledges the use of some unclassified material and photographs of experiment apparatus which were first published in reports submitted to the Electronics Research Directorate of the Air Force Cambridge Research Center, Air Research and Development Commander, under Contract AF 19 (604)-5550.

REFERENCES

1. C. Sinclair, "The Transmission and Reception of Elliptically Polarized Waves", Proc. IRE, pp. 148 - 151, February, 1950.
2. H. G. Booker, "Introduction to Techniques for Handling Elliptically Polarized Waves with Special Reference to Antennas", Proc. IRE, pp. 533 - 534, May, 1951.
3. V. H. Rumsey, "Transmission Between Elliptically Polarized Antennas", Proc. IRE, pp. 535 - 540, May, 1951.
4. G. A. Deschamps, "Geometrical Representation of the Polarization of a Plane Electromagnetic Wave", Proc. IRE, pp. 540 - 544, May, 1951.
5. M. L. Kales, "Elliptically Polarized Waves and Antennas", Proc. IRE, pp. 544 - 549, May, 1951.
6. J. F. Bohmert, "Measurements on Elliptically Polarized Antennas", Proc. IRE, pp. 549 - 552, May, 1951.
7. E. M. Kennaugh, Antenna Laboratory, The Ohio State University, Research Foundation, "Effects of Type of Polarization on Echo Characteristics", Contract No. AF 28(099)-90 Progress Reports 389-4, 9, 12, 14, 19 June, 1950 to July, 1953.
8. J. P. Huynen, R. W. Thille, W. H. Thormahlen, Dalmo Victor Company, "Interim Engineering Report on Effect of Polarization on the Radar Return From Ground Targets and Rain", Contract No. AF 33(038)-20926, Report Nos. R-135-598, R-135-620, R-135-639, R-135-669, R-135-683, and R-135-697, June 1951 to May, 1952. Contract AF 33(600)-22711 Class 16A, Report Nos. R-135-848, R-135-867, R-135-889, R-135-916, R-135-943, R-135-968, R-135-1008, and R-135-1015, January, 1953 to May, 1954. (Recently declassified).
9. C. D. Graves, "Radar Polarization Power Scattering Matrix", Proc. IRE, pp. 248 - 252, February, 1956.
10. J. R. Copeland, "Radar Target Classification by Polarization Properties", Proc. IRE, pp. 1290 - 1296, July, 1960.
11. J. W. Crispin, Jr., R. E. Hiatt, F. E. Sleator, and K. M. Siegel, "The Measurement and Use of Scattering Matrices", University of Michigan Radiation Laboratory Report No. 2500-3-T (May 1960) Unclassified.
12. J. P. Huynen, Lockheed Missiles and Space Company, "Study on Ballistic-Missile Sorting Based on Radar Cross-Section Data", Report No. 4, "Radar Target Sorting Based Upon Polarization Signature Analysis", LMSC-288216, (S), May, 1960.

13. J. R. Huynen, Lockheed Missiles and Space Company, "Radar Measurements on Scattering Operators." Presentation delivered to URSI-IRE May, 1961 Spring meeting, Washington, D. C. Also, presented at 1961 Aerospace Symposium on Ballistic Missiles and Space Technology, proceedings published by Academic Press, (vol. II), January, 1962.

14. J. R. Huynen, "A New Approach to Radar Cross-Section Measurements", 1962 IRE International Convention Record Part 5.

15. J. R. Huynen, "Dynamic Radar Cross-Section Predictions," Sept. 1963, 7th Mil-E-Con, Conference Proceedings.

16. A full account on theory and applications of polarization measurements will be found in the forthcoming book Space Age Electromagnetics, Vol. I, Chapter VII, "Polarization Dependence of Radar Targets" by J. R. Huynen, to be published by McGraw-Hill.

A COMPARISON BETWEEN LONGITUDINAL BAFFLING AND TRANSVERSE FENCE FOR REDUCING RANGE GROUND SCATTERING

Alan F. Kay

1) INTRODUCTION

If a baffle or fence is sufficiently large in wavelengths the theory of ref[1] may be used to predict its performance. In this theory, the Green's theorem expression for the field in a half space due to a planar diffracting metal object or hole in an infinite metal screen is expanded asymptotically for small λ . The results are interpreted physically as "diffraction" or edge rays. The expressions for these rays may then be used to predict the effect of edges wherever they occur in scattering by large objects. The advantage of this theory lies principally in the fact that the non-tractable surface integral expressions of Green's formula are reduced to relatively simple algebraic formulas and a simple geometrical picture. These formulas have been obtained in the case of the longitudinal baffle (Figure 1) and the transverse fence both of which are often used to suppress ground reflections in an antenna or backscatter range.

2) LONGITUDINAL BAFFLE THEORY

In this case there are six edge rays, two each for each half of the baffle and one each for each remaining semi-infinite ground plane. The general expression which results from the theory of ref[1] is given in [2] and is quite complicated. However a special case is sufficient for first

* This work was performed for the Jet Propulsion Laboratory, California Institute of Technology, sponsored by the National Aeronautics and Space Administration under Contract NAS 7-100.

order baffle design. If the transmitting antenna is an isotropic point source and both antenna and target are at the same height H above ground and are both in the symmetry plane of the baffle, then the relative one-way power

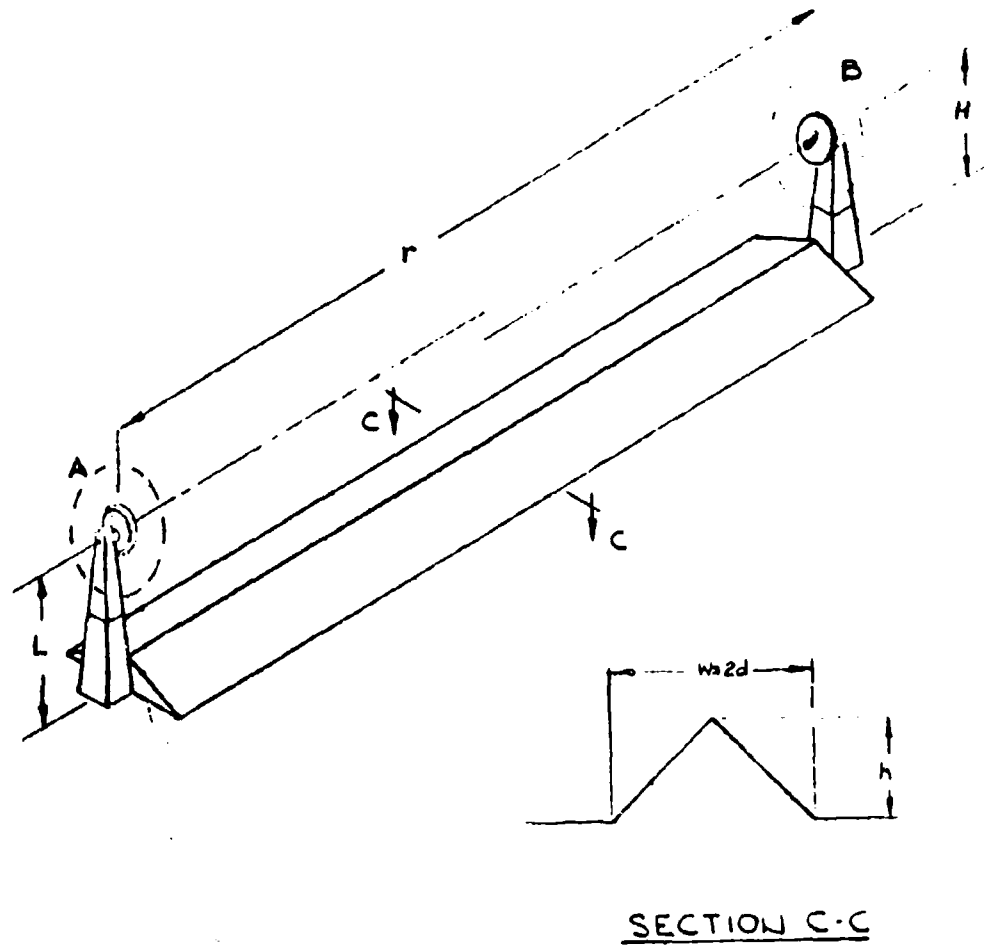


FIG. 1

VIEW OF PROPOSED PATTERN RANGE

of the ground reflected field when the baffle is present to the power radiated directly from the transmitter, is given by

$$(1) \quad \frac{r^2 \lambda}{4\pi^2} \left(\frac{d}{h(H-h)[2(H-h)^2 + r^2]^{1/4}} + \frac{h\sqrt{d^2+H^2} e^{i\phi}}{d(d^2+hH)[2(d^2+H^2) + r^2]^{1/4}} \right)^2$$

where r is the distance from source to target, h is the height and d is the half width of the baffle, and ϕ is a real phase factor which varies rapidly with λ , d , h , and H . Eq. (1) is valid for a perfectly conducting baffle and ground. If an imperfectly reflecting baffle or ground (e. g. absorber) is involved, (1) must be modified by the appropriate reflection coefficients of the six rays. However perfect conductivity is the worst case (most ground reflection) and conditions in practice often approximate to it.

A further condition for the validity of (1) is that the baffle be sufficiently large compared to a wavelength. Detailed analysis in this case shows that sufficiently large can be expressed algebraically by two formulas which reduce to

$$(2) \quad 4h^2(H-h)^2 > \lambda r(d^2+h^2), \quad 4d^2 > \lambda r$$

when $r^2 \gg H^2 + d^2$ and $r^2 \gg d^2(H-h)^2/(d^2+h^2)$ which is the case most of the time. More general formulas than (1) and (2) are available in ref[2].

In a given backscatter range, r , H , and λ would be given. For an optimum baffle design the values of d and h minimizing (1) in the worst case (when $\phi = 0$) would be desired. Computations with (1) show that the

optimum generally occurs when the baffle height and half width are both equal to about half of the height of the line of sight above ground. That is,

$$(3) \quad d \approx h \approx \frac{H}{2} .$$

For example, when $r = 100'$, $\lambda = .5'$, $H = 10'$, $d = h = 5'$, then according to (1) the reflected field is about 9 db below the direct field. If the height of target and source are raised to 20' and the baffle increased to 10' high and 10' in half-width, the undesired ground signal is reduced to about 14.5 db below the direct signal. These are approximately optimum values of d and h in both cases.

Unfortunately it turns out that some practical baffles do not satisfy equations(2). The best design, in fact, is not a baffle satisfying (3) but one somewhat smaller. This fact was discovered by an experimental program. The program also seemed to verify the validity of eq(1) under the conditions of eq(2).

3) EXPERIMENTAL RESULTS

An 8' x 8' aluminum ground plane was set up as shown in Figure 2 for scale model studies. In all cases reported here r was kept equal to 62.2" and $f = 38.8$ gc ($\lambda = .305''$). The transmitter was fixed at a height H above the ground plane and a height gain curve recorded as the receiving antenna was elevated a height L above the ground plane. Figure 3 is a typical result without a baffle with the deep nulls indicating a good ground image. Typical results with a baffle are shown in Figure 4. The SWR of reflected

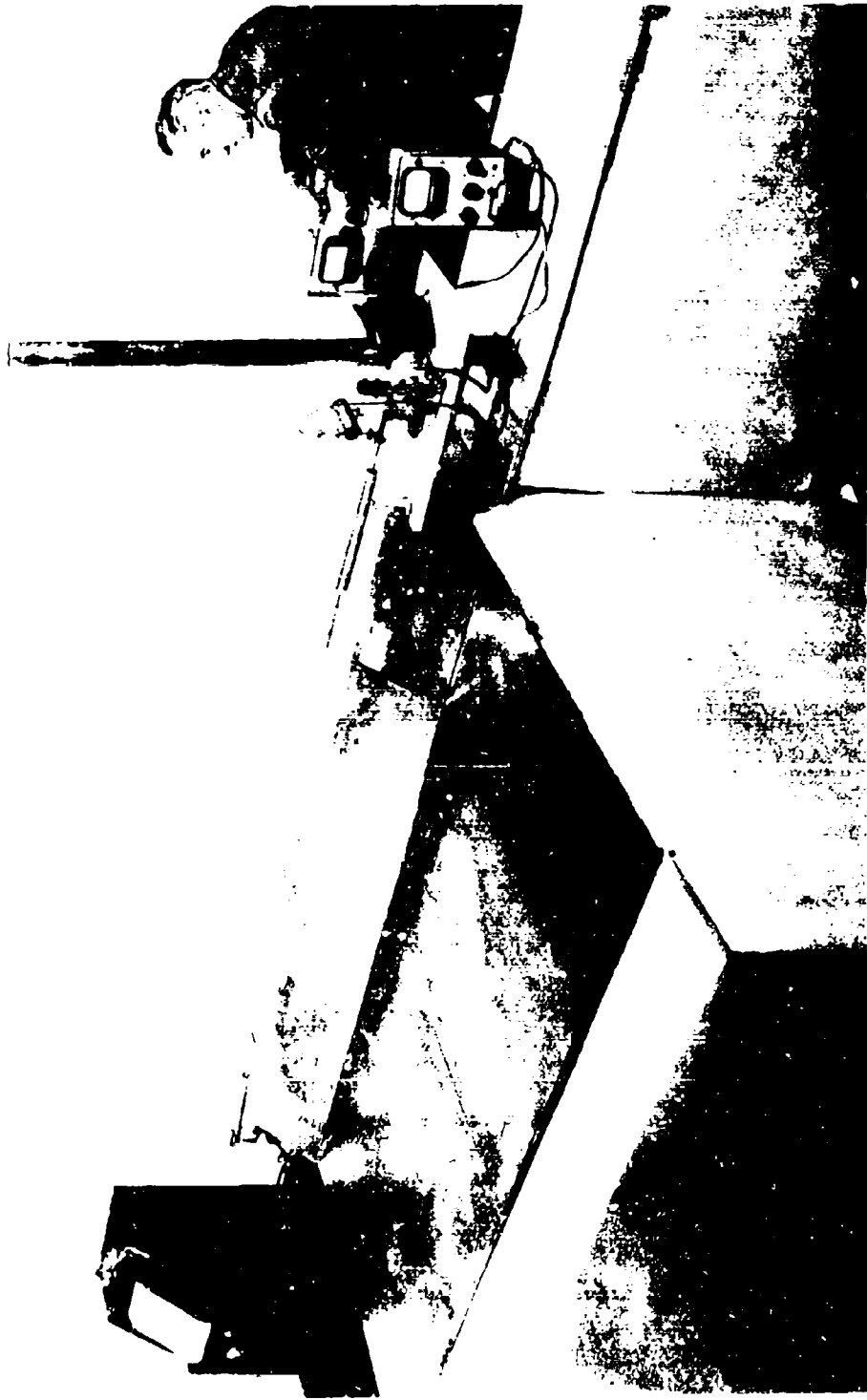
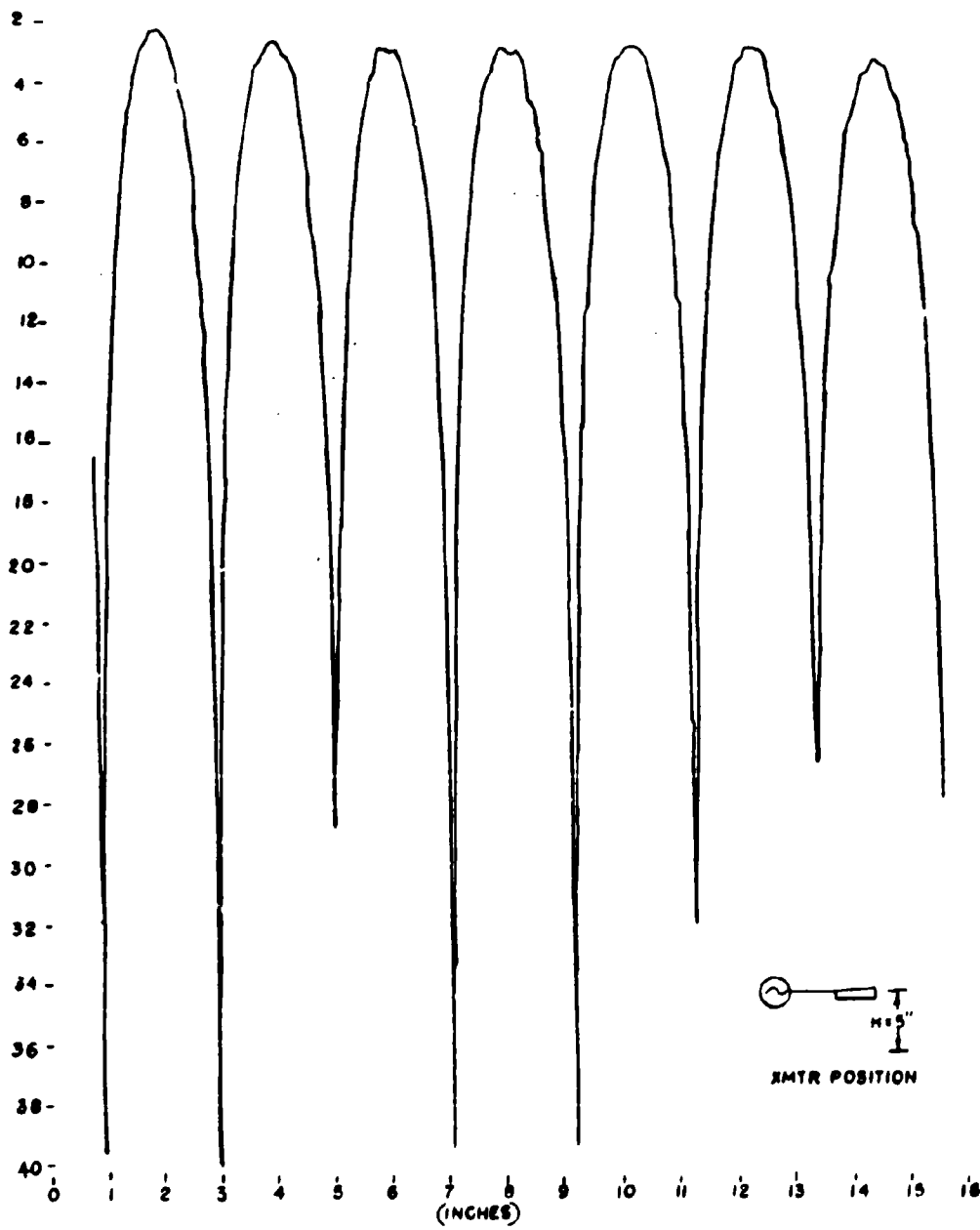
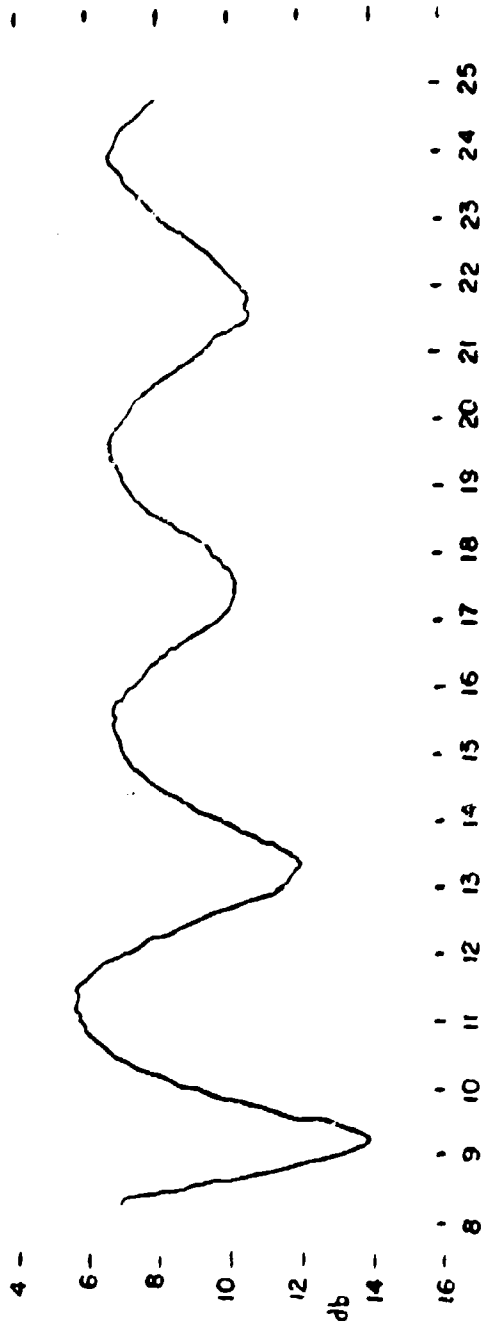


FIGURE 2 SCALE MODEL OF 8' x 8' ALUMINUM GROUND PLANE AND LARGE
BAFFLE WITH H PLANE FLARED HORNS.

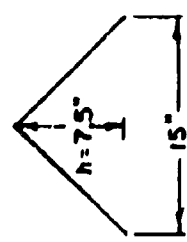
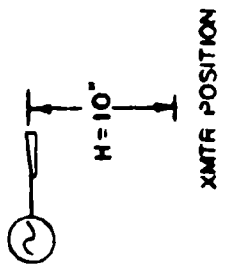


HEIGHT OF RECEIVER ABOVE GROUND PLANE
 38.8 G.C.
 E-PLANE PATTERN-HORNS FLARED IN H-PLANE
 FIG. 3



(INCHES)

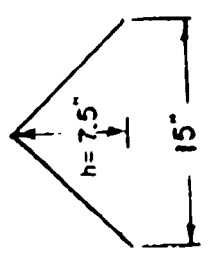
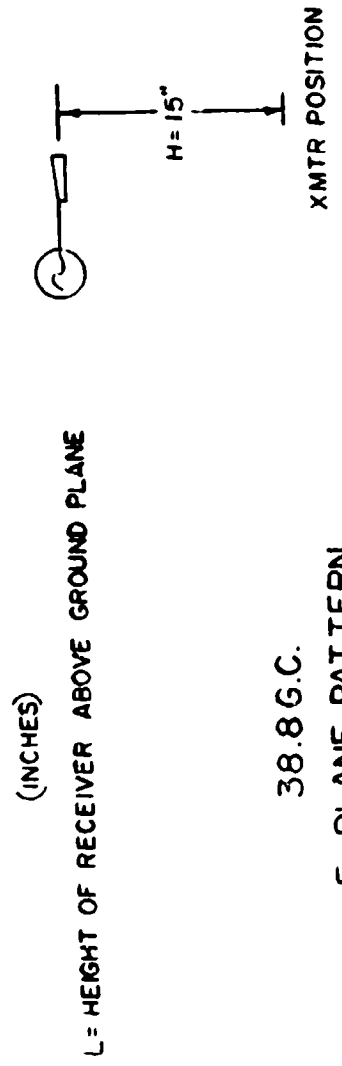
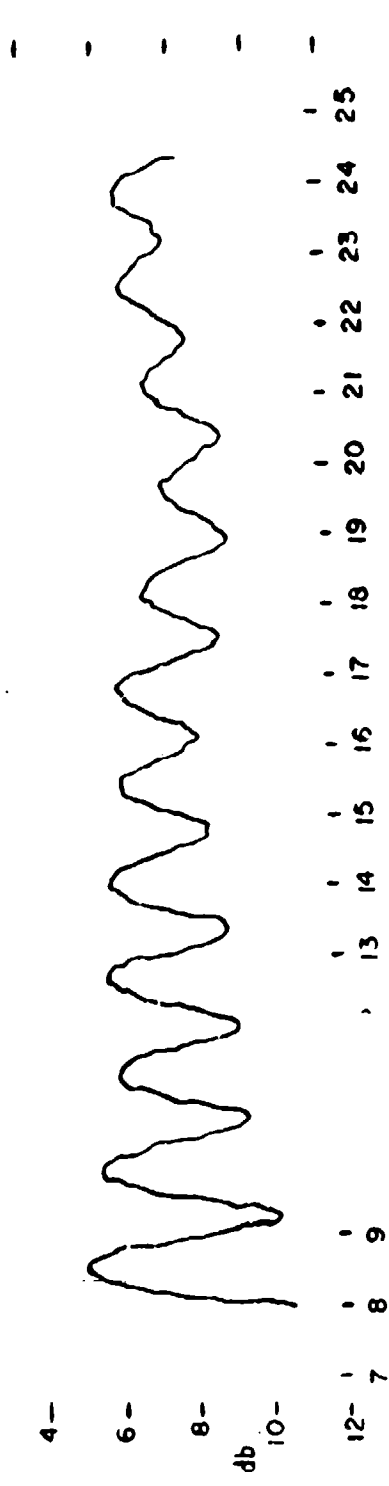
L=HEIGHT OF RECEIVER ABOVE GROUND PLANE



38.8 G.C.

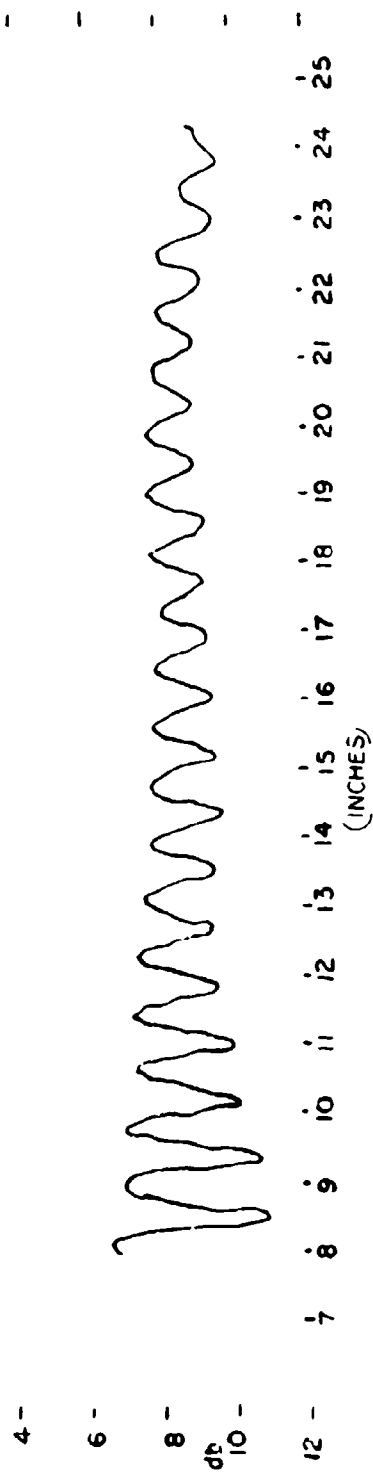
E-PLANE PATTERN
HORNS FLARED IN H-PLANE

FIG. 4a

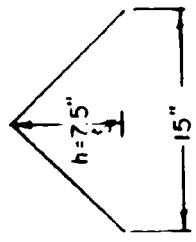


38.8 G.C.
 E- PLANE PATTERN
 HORNS FLARED IN II- PLANE

FIG. 4b



L = HEIGHT OF RECEIVER ABOVE GROUND PLANE
(INCHES)



38.8 G.C.

E-PLANE PATTERN
HORNS FLARED IN H-PLANE

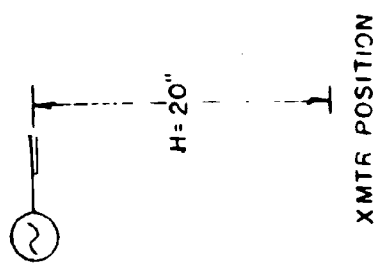
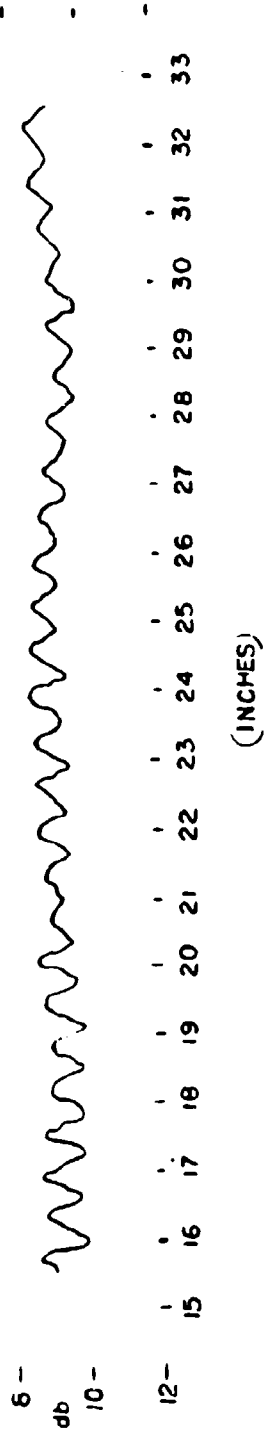
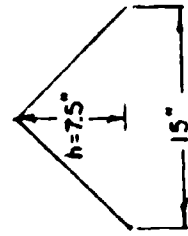
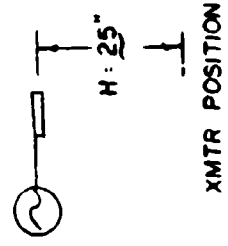


FIG 4c



L = HEIGHT OF RECEIVER ABOVE GROUND PLANE

13



38.8 G. C.
E-PLANE PATTERN
HORNS FLARED IN H-PLANE

FIG 4d

to direct signals at $L = H$ may easily be read from these curves and (when corrected for transmitter and receiver directivities) compared to the SWR implied by (1). The comparison is given in Figure 5 in several cases and indicates reasonable agreement.*

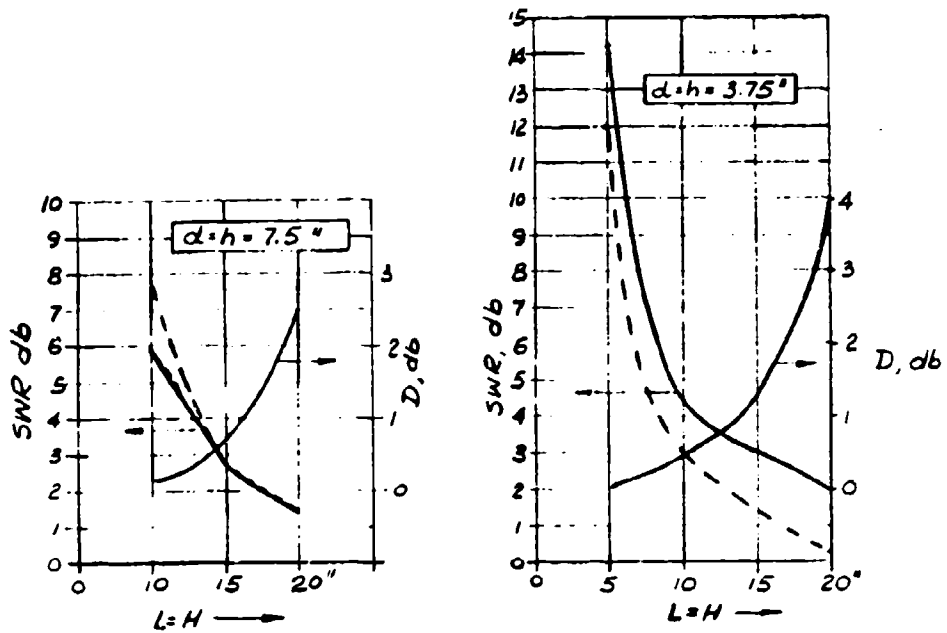
It should be pointed out that a longitudinal baffle also produces cross-polarization and for designs near the optimum the level of the cross-polarized field is about the same as that of the principally-polarized reflected field (see ref[2]).

4) TRANSVERSE FENCE

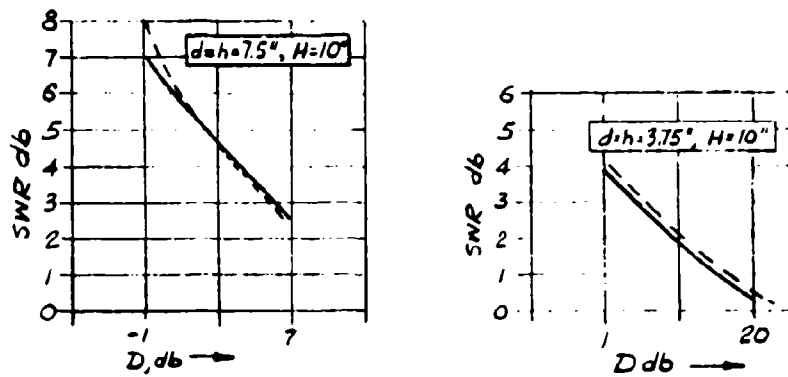
There are four edge rays for a transverse fence as shown in Figure 6. The expression analogous to (1) for the relative strength of ground to direct field power flow with fence when the source and target are at the same height H and when the fence is transverse of height t and half-way between them is

$$(4) \quad \frac{r^4 \lambda}{64\pi^2} \left[\frac{1}{\sqrt{2} \left[\left(\frac{r}{2}\right)^2 + (H-t)^2 \right]^{3/4} (H-t)} + \frac{1}{\sqrt{2} \left[\left(\frac{r}{2}\right)^2 + (H+t)^2 \right]^{3/4} (H+t)} \right. \\ \left. + \frac{2 \left[\frac{1}{\left[\left(\frac{r}{2}\right)^2 + (H+t)^2 \right]^{1/2}} + \frac{1}{\left[\left(\frac{r}{2}\right)^2 + (H-t)^2 \right]^{1/2}} \right]^{1/2}}{(H+t) \sqrt{\left(\frac{r}{2}\right)^2 + (H+t)^2} - (H-t) \sqrt{\left(\frac{r}{2}\right)^2 + (H-t)^2}} \right]^2$$

* In this Figure, D is the sum of the decibel directivities of transmitting and receiving antennas in the direction of the diffraction ray to the top edge of the baffle relative to that for the direct ray.



E-PLANE DATA
H-PLANE FLARED HORNS



H-PLANE DATA
RECEIVER: OPEN WAVEGUIDE
TRANSMITTER: GAIN STANDARD HORN

FIG. 5

$r = 62.2''$, $f = 38.8$ GC,

----- MEASURED
————— THEORETICAL

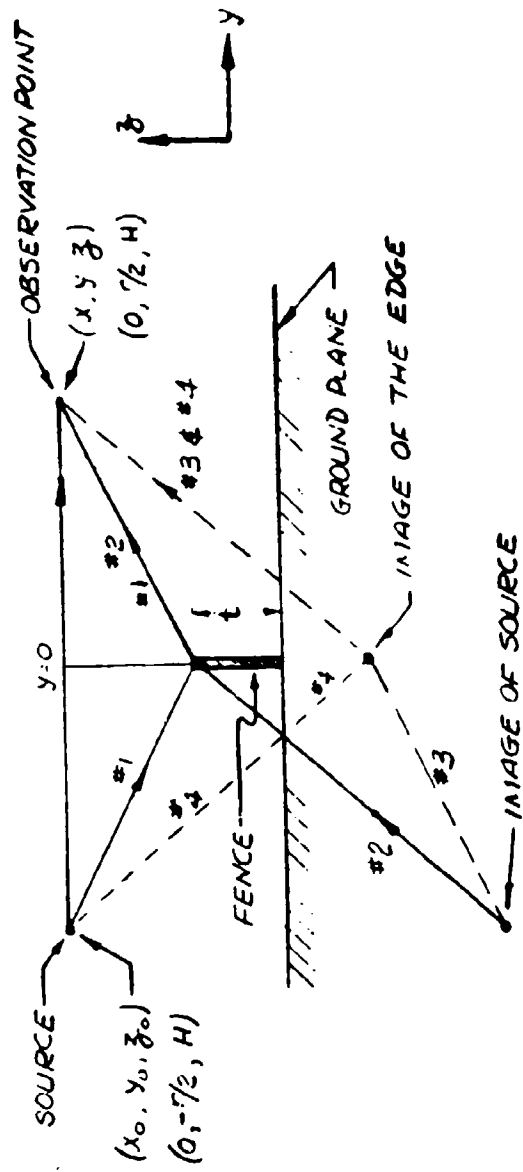


FIGURE 6

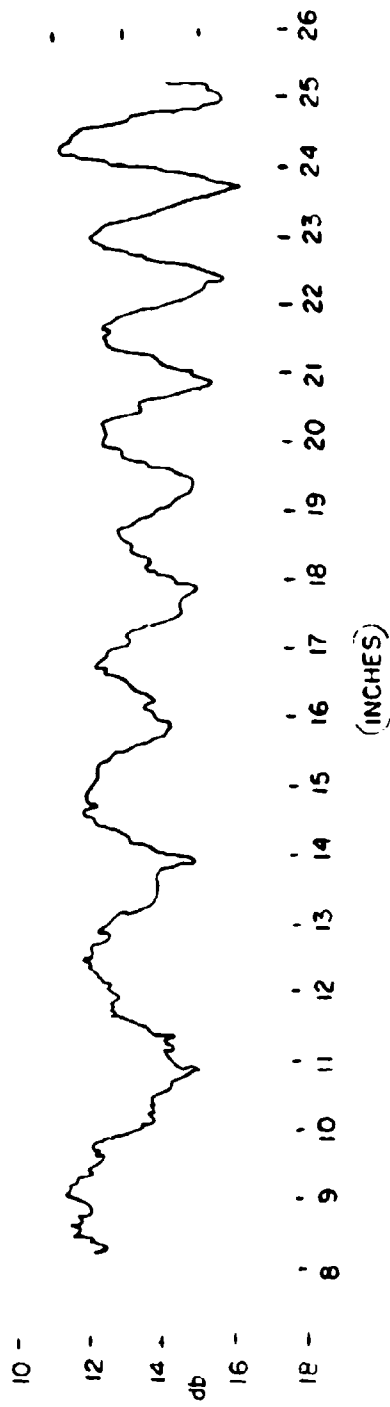
TRANSVERSE FENCE

Eq(4) is only valid if the transmitter pattern is isotropic, if the ground is perfectly conducting, and if conditions analogous to (2) which imply that $H-t$ and t are not too small compared to λ are satisfied. It is interesting to note that when the baffle and the fence are the same height ($t=h$) the value of (4) is fairly close to that of (1) (for values of d minimizing (1)) and in fact usually (4) is a little less than (1).

From this fact, one suspects that the fence might generally be more desirable than the baffle, and this seems to be the case. Figure 7 is an experimental height gain curve for a typical fence. Figure 8 compares the measured SWR of ground to direct energy for various baffles and fences with the line of sight at various heights. For all of this data $r = 62.2''$ and $\lambda = .305''$. From this data it appears that in this case the fence of height $3.75''$ is the best and better than any baffle, and that a line of sight height of $10''$ is about the lowest that one could operate while still suppressing most of the ground reflected signal. Even at a line of sight height of $20''$ little further improvement appears possible by use of a baffle or a fence.

5) CONCLUSIONS AND SUMMARY

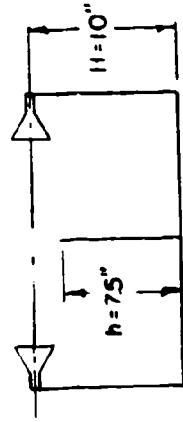
We have derived approximate equations for the suppression of the ground reflected signal by longitudinal baffles and transverse fences which have been verified by an experimental program in some cases. In a particular case these expressions (plus measured values extending data beyond the range of their validity) indicate that the best fence is superior to the best baffle and can make a substantial improvement in decreasing ground reflections. These same techniques could be used for quantitatively analyzing the performance



52

L = HEIGHT OF RECEIVER ABOVE GROUND PLANE

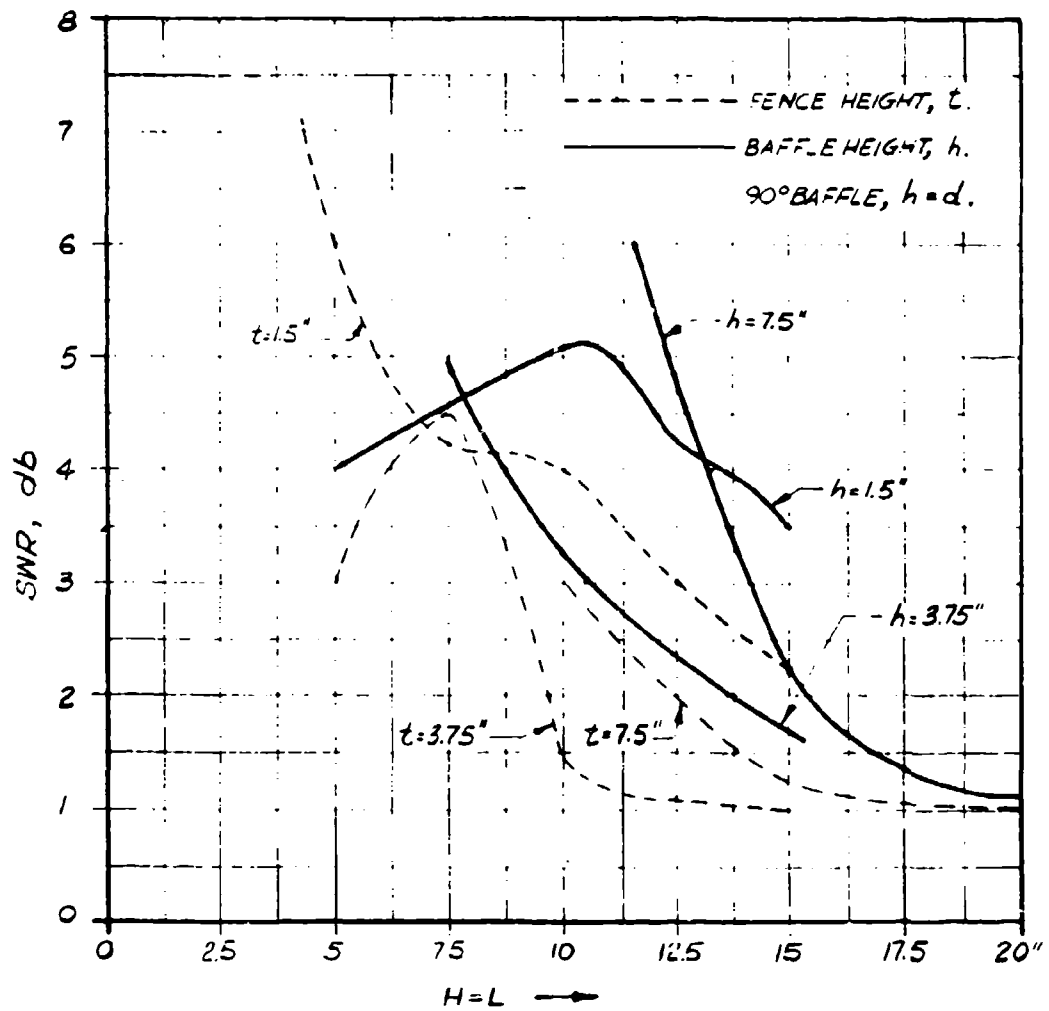
(INCHES)



38.8 G.C.

E-PLANE PATTERN
HORNS FLARED IN H-PLANE

FIG. 7



MEASURED VALUES

E-PLANE DATA

H-PLANE FLARED HORNS

FIG. 8

of baffles and fences in free space.

REFERENCES

- [1] Keller, J. B., Lewis, R. M., and Seckler, B. D., "Diffraction by an Aperture II," *Journal of Applied Physics*, Vol. 28, No. 5, 570-579, May 1957, work sponsored by AFCRC, ARDC under Contract No. AF19(122)-42.
- [2] TRG Final Report 234, "An Analysis of Longitudinal Ground Baffling in an Outdoor Pattern Range," JPL P. O. No. AJ4-225409, January 8, 1964.

AN ANALYSIS OF REFLECTION MEASURING SYSTEMS

Robert G. Kouyoumjian
Associate Supervisor
Antenna Laboratory
Department of Electrical Engineering
The Ohio State University
Columbus, Ohio 43210

ABSTRACT

In measuring the radar reflectivity of an obstacle it is frequently desired to minimize the range of measurement or maximize the back scattered signal while maintaining prescribed limits on the departure of the incident field from a uniform plane wave at the obstacle. Although it is not possible to analyze this optimization of the measurement rigorously for the general case, the optimization will be treated here for an idealized measuring antenna. The results are assumed to be useful in estimating the limitations and requirements of practical reflection measuring systems. The analysis is employed also to find the approximate size of the largest model which can be measured satisfactorily with a CW reflection measuring system. This paper is essentially a condensed version of Reference 1.

1. ECHO AREA

Let a rectangular coordinate system be fixed in a scattering object as shown in Fig. 4. The vector $\underline{\rho}$ determines a point on the surface S of the object and \hat{n} is a unit normal vector to the surface at $\underline{\rho}$ (the symbol " $\hat{\ }$ " will be used to indicate vectors of unit magnitude). The antenna of the reflection measuring system is linearly polarized in the x -direction and is located at a range R from the obstacle. The input terminals to the antenna are designated by 1, 2.

* The work reported in this paper was supported in part by Contract DA 36-039-sc-5506 between Signal Corps Supply Agency, Laboratory Procurement Office, Fort Monmouth, New Jersey and The Ohio State University Research Foundation.

The incident field with electric and magnetic vectors \bar{E}^0, \bar{H}^0 is the field generated by the current I^0 at the terminals 1, 2 with the obstacle removed. The total field \bar{E}, \bar{H} is the field generated by the current I^0 with the object present. The scattered field by definition is $\bar{E}^s = \bar{E} - \bar{E}^0, \bar{H}^s = \bar{H} - \bar{H}^0$.

For an incident plane wave linearly polarized in the x-direction the echo area σ is defined by

$$\sigma = \lim_{R \rightarrow \infty} 4\pi R^2 \frac{|\bar{E}_x^s|^2}{|\bar{E}_x^0|^2} \quad (1)$$

In the far-zone of the scatterer, as $R \rightarrow \infty$, \bar{E}_x^s has the form

$$\bar{E}_x^s = -\frac{jkz_0}{4\pi} \left(\frac{e^{-jkR}}{R} \right) |\bar{E}_x^0| U_x \quad (2)$$

where the far-zone amplitude

$$\begin{aligned} U_x &= \oint_S \left\{ \bar{J}_x e^{jk\bar{\rho} \cdot \hat{z}} + \frac{K_y e^{jk\bar{\rho} \cdot \hat{z}}}{z_0} \right\} dS \\ &= \frac{1}{|\bar{E}_x^0|} \oint_S \{ \bar{J} \cdot \bar{E}^0 - \bar{K} \cdot \bar{H}^0 \} dS \end{aligned} \quad (3)$$

in which $k = 2\pi/\lambda$, z_0 is the impedance of free space, and (\bar{J}, \bar{K}) are the equivalent electric and magnetic surface currents of the scattered field induced by an incident electric field of unit amplitude.^{2,3} From Eqs. (1) and (2)

$$\sigma = \frac{k^2 z_0^2}{4\pi} |U_x|^2 \quad (4)$$

Next, using the Lorentz reciprocal theorem^{4,5} one obtains

$$V^r I^0 = -|\bar{E}_x^0| \oint_S \{ \bar{J} \cdot \bar{E}^0 - \bar{K} \cdot \bar{H}^0 \} dS \quad (5)$$

in which V^r is the open-circuit voltage received at terminals 1, 2. It is important to note that \bar{E}^o , \bar{H}^o used in Eq. (5) describe a general incident field which need not be a uniform plane wave. However, it follows from Eqs. (3), (4), and (5) that \bar{E}^o , \bar{H}^o must have the form of a uniform plane wave, or approximately so, in the vicinity of the obstacle, if V^r is to be used to determine echo area. This does not necessarily mean that the obstacle must be in the far-zone of the antenna; we shall see that in the Fresnel zone there are regions where the field of the antenna is approximately a uniform plane wave. If a proper measurement of σ is to be made, then

$$V^r I^o \approx - |E_x^o|^2 U_x \quad (6)$$

where the integral in Eq. (5) is approximately equal to $|E_x^o| U_x$.

2. RECEIVED POWER

The radiation resistance of the antenna is R_a , and the transmitted power

$$P^o = \frac{1}{2} |I^o|^2 R_a \quad (7)$$

Let P^r be the power received when the antenna and receiver of the reflection system are matched; then since V^r is the open-circuit received voltage,

$$P^r = \frac{|V^r|^2}{8 R_a} \quad (8)$$

From Eqs. (6), (7), (8)

$$P^r P^o = \frac{|V^r I^o|^2}{16} \approx |E_x^o|^4 |U_x|^2 \quad (9)$$

Now if the incident field at the obstacle is nearly a uniform plane wave

$$|E_x^o|^2 \approx 2 z_o S^o \quad (10)$$

in which S^0 is the incident power density. Introducing a generalized gain^{6,7}

$$G(R) = \frac{\text{incident power density at range } R}{\text{power density for } P^0 \text{ radiated isotropically at range } R}$$

$$= 4\pi R^2 S^0(R)/P^0 \quad (11)$$

we obtain the familiar radar range equation from Eqs. (9), (10), and (11), except that the following expression can be used in both the near and far zones of the measuring antenna.

$$P^r \approx \frac{P^0 G^2(R) \sigma \lambda^2}{(4\pi)^3 R^4} \quad (12)$$

In the equations to follow the "approximately equal" symbol will be replaced by the "equal" symbol.

From Eqs. (9) and (12) it is seen that $\sigma \propto |V^r|^2$ when the incident field is a uniform plane wave in the region occupied by the obstacle and when \underline{J} , \underline{K} are not perturbed by the presence of the measuring antenna. The echo area may be determined by comparing the received squared voltage amplitude with that from a scatterer with known echo area, such as a sphere or corner reflector located at the same point. Although echo patterns are usually taken at sufficient range so that obstacle-antenna interaction is not significant, the uniform plane wave condition on the incident field at the obstacle only can be approximated in general. The error in σ resulting from this approximation can not be ascertained for an arbitrary scatterer, but this error has been studied for certain types of scatterers and the results serve to estimate the allowable departure of the incident field from a uniform plane wave in the region occupied by the obstacle.^{8,9,10,11} It is seen from Eq. (5) that the echo area measurement does not depend on the nature of the scattered field at the antenna aperture. This is an important point when one notes that attempts have been made to establish range criteria based on prescribed variations from the plane wave condition at the antenna aperture as well as the obstacle.

3. OPTIMIZATION OF THE MEASUREMENT

Let an obstacle of maximum dimension L be positioned at a range R on the symmetry axis of the measuring antenna. The antenna aperture is taken to be square in shape with a side length l , and the aperture field distribution is taken to be uniform in amplitude and phase. This type of aperture distribution simplifies the solution of the problem, and as was mentioned earlier, it is assumed that the results obtained will bear a reasonable relationship to those of parabola and horn antennas of comparable dimensions used with reflection measuring systems.

The obstacle aperture is the projection of the model on a plane perpendicular to the direction of incidence. In taking a complete set of echo patterns, all aspects of the model are presented to the reflection system. An area which would include all model apertures is the square area whose side length is equal to the largest model dimension. Since the reflection systems of interest here are employed in echo pattern measurement covering all aspects of the scatterer, this square area will be used as an effective aperture in the following development. Generally, the variation in amplitude and phase of the incident field at the effective aperture represents the maximum departure of the incident field from the plane wave field at the target. Thus for a series of echo patterns, the allowed departure of the incident field from the uniform plane wave condition may be specified by the amplitude and phase variation of the incident field over the effective aperture. An obvious exception to the previous discussion is the long thin scatterer where measurements are limited to the end-on aspects; in this case the radial variation of the field must also be considered.

It is seen from Eq. (12) that the smallest measurable echo area in square wavelengths is

$$\sigma_{\lambda m} = \sigma_m / \lambda^2 = (4\pi)^3 \left(\frac{P_m^r}{P^o} \right) \left(\frac{R^4}{\lambda^4 G^2} \right) ; \quad (13)$$

P_m^r is the smallest measurable power. The first factor in the above equation depends upon the equipment employed, i. e., the transmitter receiver, model support, and method of isolation between the transmitted and received power. However, at this point in the discussion our attention is directed to the second factor, which determines the

optimization of the experiment in terms of minimum range or minimum measurable power for an obstacle of given L/λ and prescribed incident field variation at its aperture.

The field of a square aperture with a uniform electric field distribution $\overline{E}^a = \hat{x} E^a$ is given by Schelkunoff¹² as

$$E_x \approx \frac{j E^a}{2} e^{-jkz} \left[E \left(\frac{l + 2x}{\sqrt{2\lambda z}} \right) + E \left(\frac{l - 2x}{\sqrt{2\lambda z}} \right) \right] \\ \times \left[E \left(\frac{l + 2y}{\sqrt{2\lambda z}} \right) + E \left(\frac{l - 2y}{\sqrt{2\lambda z}} \right) \right] \quad (14)$$

in which

$$E(t) = \int_0^t e^{-j\frac{\pi}{2} \tau^2} d\tau ; \quad (15)$$

this expression is valid provided x, y are substantially less than z , and z is large enough so that the field point is not close to the aperture.

On the axis of the antenna $H_y \approx E_x/z_0$, the power density $S^0 \approx 2 |E^a|^2 [E(W)]^4 / z_0$, and $P^0 \approx l^2 |E^a|^2 / 2z_0$, where $W = l/\sqrt{2\lambda z}$. It then follows from Eq. (11) that

$$G(z) = 4\pi \left(\frac{l}{\lambda} \right)^2 \left[\frac{E(W)}{W} \right]^4, \quad (16)$$

where R clearly equals z , $4\pi(l/\lambda)^2$ is recognized as the far-zone gain of the square aperture, and the \approx sign again has been replaced by an = sign.

We shall now give a measure of the variation of the incident field at the obstacle aperture by defining the ratio A of the incident field amplitude at the edge of the obstacle aperture to the amplitude of the center of the aperture and the phase difference ϕ between the center and edge of the aperture:*

* Strictly speaking, Eq (17) describes the field variation only in the E- and H-planes.

$$A e^{j\phi} = \frac{E(u) + E(v)}{2E(W)} \quad (17)$$

where

$$u = (l-L)/\sqrt{2\lambda R}, \quad (18)$$

$$v = (l+L)/\sqrt{2\lambda R}, \quad (19)$$

and

$$W = (u + v)/2. \quad (20)$$

The variables involved are A , ϕ , L/λ , R/λ , l/λ , $\sigma_{\lambda m}$ with R/λ and $\sigma_{\lambda m}$ the dependent variables which may be minimized. For a given wavelength and scatterer L/λ is fixed and $\sigma_{\lambda m}$ or R are minimized subject to the conditions that

$$A_0 \leq A \leq 1, \quad (21a)$$

$$0 \leq \phi \leq \phi_0, \quad (21b)$$

where A_0 is the maximum allowed amplitude variation and ϕ_0 is the maximum allowed phase variation of the incident field at the effective aperture. The solution to this minimization problem is facilitated by expressing R/λ and $\sigma_{\lambda m}$ in terms of u and v . From Eqs. (13), (16), (18), and (19)

$$\frac{R}{\lambda} = \frac{2}{(v-u)^2} \left(\frac{L}{\lambda}\right)^2 \quad (22)$$

$$\sigma_{\lambda m} = 4\pi \left(\frac{P_m^r}{P^o}\right) \left\{ \frac{2}{v^2 - u^2} \frac{1}{\left|\frac{E(W)}{W}\right|^2} \right\}^4 \left(\frac{L}{\lambda}\right)^4 \quad (23)$$

where $v \geq u$; moreover

$$\frac{R}{\lambda} = \frac{(v+u)}{(v-u)} \frac{L}{\lambda} \quad (24)$$

It is clear from Eq. (17) that u, v are functions of A, ϕ only so that from the limits expressed in (21) the range of values of u, v depends upon A_0, ϕ_0 , i.e., our measure of the departure of the incident field from a uniform plane wave. Since u, v are independent of L/λ , it is clear that $R/\lambda \propto (L/\lambda)^2$ and $\sigma_{\lambda m} \propto (L/\lambda)^4$; thus R/λ and $\sigma_{\lambda m}$ increase rapidly as the obstacle size increases in terms of wavelength.

As an example let us choose $\phi_0 = \pi/8$ and $A_0 = 0.9$; these conditions on the variation of the amplitude and phase of the incident field are frequently used in recording echo patterns.* The range of values of u, v shown in Fig. 1 corresponding to these values of ϕ_0 and A_0 appear in the region enclosed by the curves labeled $A = 1, \phi = 0, A = 1, \phi = 22.5^\circ, A = 0.9$ and the edge of the figure. In this figure it follows that curves of constant R/λ for fixed L/λ are described by the equation $v-u = k$ and appear as a family of straight lines of slope 1. The value of k is given by the intersection of these straight lines with the v axis. Contours of constant $\sigma_{\lambda m}$ for fixed L/λ may be presented as the curves described by

$$n = \frac{2}{v^2 - u^2} \left| \frac{E(W)}{W} \right|^{-2} = \text{constant}; \quad (25)$$

these appear as dotted curves and may be referred to as curves of constant sensitivity. From Fig. 1 it is seen that the maximum value of k (minimum R) occurs at $v = 1, u = 0$; also it is seen that the minimum value of n (minimum $\sigma_{\lambda m}$) occurs for $v = 1, u = 0$. It follows from Eqs. (22) to (24) that for this example

* As an illustration of the error which may occur with this type of variation in the incident field, Mentzer¹³ found that for the same ϕ_0 and $A_0 = 0.85$ the error in the broadside echo areas of cylinders is no greater than 0.7 db.

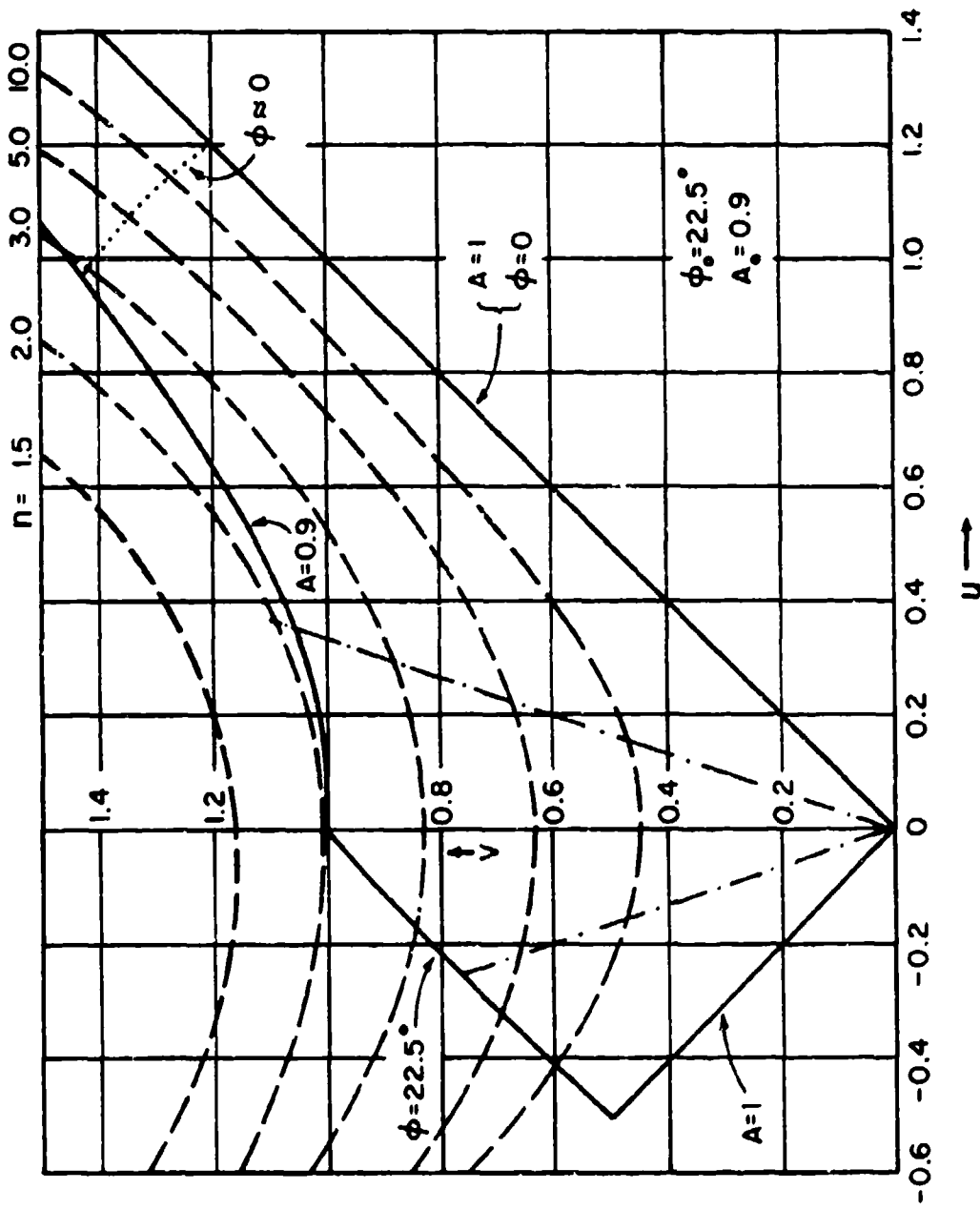


Fig. 1. Diagram for Sensitivity and Range.

$$\frac{R}{\lambda} = 2 \left(\frac{L}{\lambda} \right)^2 \quad (26a)$$

$$\sigma_{\lambda m} = 64\pi \left(\frac{P_m^r}{P^o} \right) \left(\frac{L}{\lambda} \right)^4 \quad (26b)$$

and

$$\frac{\ell}{\lambda} = \frac{L}{\lambda} \quad (26c)$$

This optimization of range and sensitivity was accomplished by varying the aperture of the measuring antenna. It is seen that this optimization is achieved when the antenna aperture is equal to the obstacle aperture, and that the measurement is carried out in the far-zones of both apertures. A study of other examples where only modest variations of the incident field at the target is permitted reveals essentially the same conditions for optimization. In the case where large variations in the incident field at the obstacle are permitted, e. g., $\phi_0 = 6\pi$, $A_0 = 0.7$ which have been employed in the measurement of the median echo areas of large models,¹ one finds it impossible to simultaneously minimize the range of measurement and the smallest measurable echo area. The condition $\ell = L$ for maximum sensitivity also was obtained by Fails and Fubini¹⁴ under more general assumptions involving a restriction on the maximum allowable phase difference between a point on the aperture and a point on the effective aperture.

It is interesting to minimize the range and maximize the sensitivity when the antenna and effective obstacle apertures are not equal. Let us examine two cases $\ell = 2L$ and $\ell = L/2$. It is seen from Eq. (24) that $\ell = 2L$ results in a line of slope 3 passing through the origin of the u, v plane, whereas $\ell = L/2$ results in a line of slope -3 passing through the origin; these are shown as dot-dashed lines in Fig. 1. From Eqs. (22), (23) and Fig. 2 one obtains for

$$\begin{aligned} \ell = 2L: \quad \frac{R}{\lambda} &= 4 \left(\frac{L}{\lambda} \right)^2 = \left(\frac{\ell}{\lambda} \right)^2 \\ \sigma_{\lambda m} &= 84\pi \left(\frac{P_m^r}{P^o} \right) \left(\frac{L}{\lambda} \right)^4 \end{aligned}$$

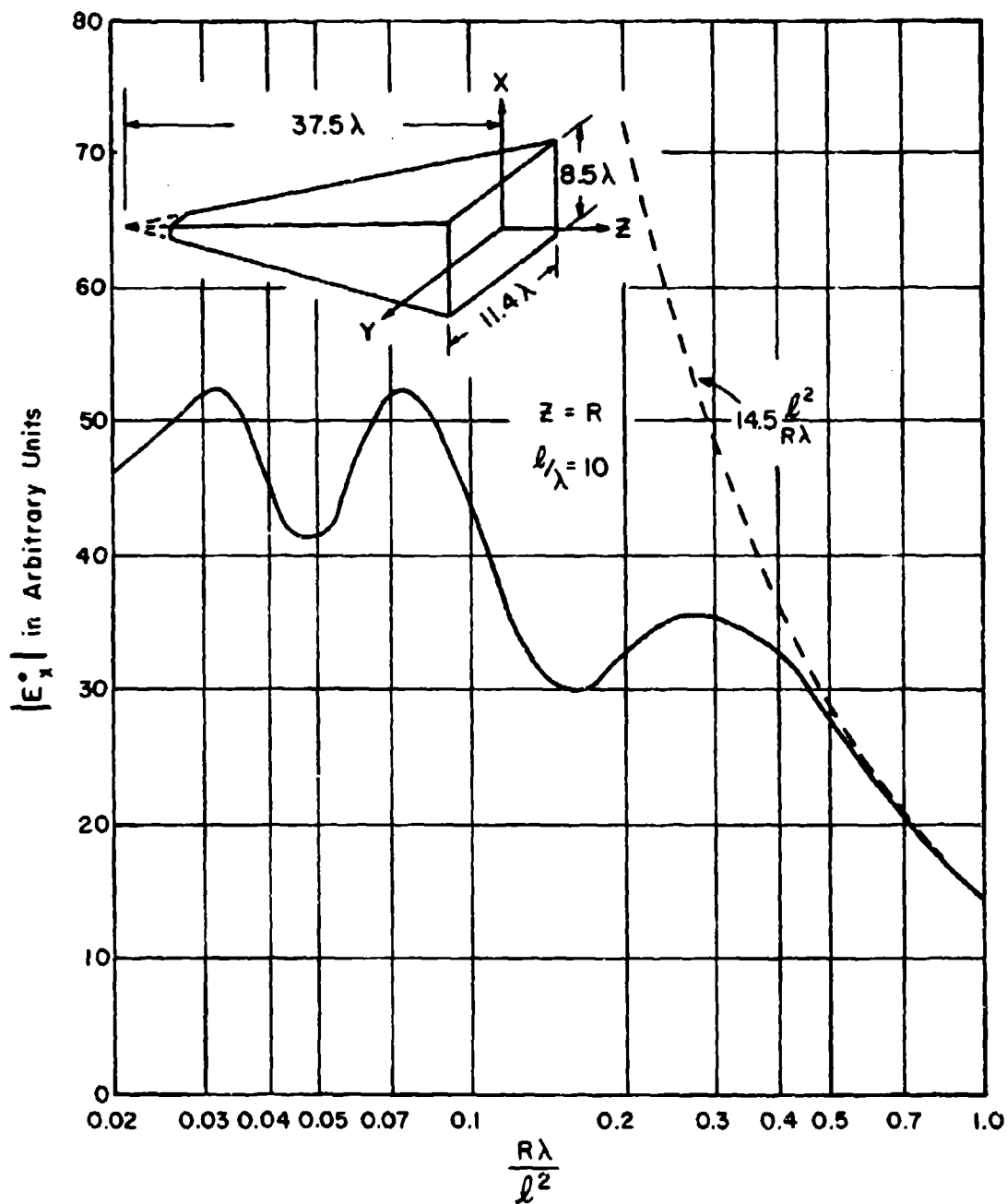


Fig. 2. Measured Axial Electric Field of a Horn.

$$l = L/2: \quad \frac{R}{\lambda} = 2 \left(\frac{L}{\lambda} \right)^2 = 8 \left(\frac{l}{\lambda} \right)^2$$

$$\sigma_{\lambda m} = 1024\pi \left(\frac{P_m^r}{P^o} \right) \left(\frac{L}{\lambda} \right)^4 .$$

Thus for fixed L/λ , choosing an antenna aperture larger than the obstacle aperture results in an increased range and slightly decreased sensitivity compared with our first example; on the other hand, choosing an antenna aperture smaller than the obstacle aperture results in an unchanged range and a greatly reduced sensitivity.

The disadvantages of carrying out an echo measurement in the near field of an antenna aperture much larger than the obstacle aperture also may be seen from Fig. 2. In this case the aperture relationship is described by a line through the origin with slope a little larger than one. We see from Eqs. (22) and (24) that

$$\frac{R}{\lambda} = \frac{2}{(v+u)^2} \left(\frac{l}{\lambda} \right)^2$$

so that the near zone of the measuring antenna corresponds to the upper right hand part of the enclosed region. This is clearly a region of lower sensitivity; furthermore for a fixed L/λ , its use results in larger ranges than would be required if $l = L$.

The conclusions reached in the previous paragraph will now be checked by a different method. As pointed out earlier, it is necessary in measuring σ that the incident field closely approximate a uniform plane wave at the scatterer. It has been shown¹⁵ that the near-zone field of a horn antenna closely approximates a uniform plane wave in the neighborhood of its axis. The accuracy of the approximation improves where the magnitude of the field is stationary with respect to axial (or z) variation. Thus σ may be measured in the near zone of a horn at such stationary points provided that the target is not so large that there is an undesired variation of the field over its effective aperture. The measured field of a horn antenna taken along its axis is shown in Fig. 2; a drawing of the horn is also shown in this figure. Since $\sigma_{\lambda m}$ is proportional to $|E_x^o|^4$, as may be seen from Eqs. (4) and (9), it is desirable to choose $R\lambda/l^2 = .032$ or $.075$ if maximum

sensitivity is to be obtained in the near zone measurement. In carrying out the echo measurement of some plates and spheres, the latter range was selected,¹⁵ because of its broader maximum along the axis. Referring to Fig. 3, which presents the measured field of the horn in the E- and H-planes, it is evident that an obstacle with $L/\lambda = 1$ can be measured with $A_0 = 0.9$. A square plate with a one wavelength side was found to have a 0.9 db error in its broadside echo area at this range; on the other hand, a sphere of one wavelength diameter was found to have an error in its echo area of less than 0.3 db. This near zone* measurement is 22.4 db more sensitive than a measurement in the far-zone with $R\lambda/l^2 = 1$; however, if we optimize the measurement by setting $l = L$ and $R = 2L^2/\lambda$, the sensitivity would be about 10 db greater than that occurring at $R\lambda/l^2 = .075$. The example illustrates that given a small obstacle and large antenna aperture, the sensitivity can be increased appreciably by choosing the proper range in the near field of the antenna; however, the sensitivity is increased to a maximum when $l = L$ and $R/\lambda = 2(L/\lambda)^2$. With $l = 10L$ and $R\lambda/l^2 = .075$, $u = 2.32$ and $v = 2.84$, which is in the upper right hand region of the u, v diagram, outside the range of values shown in Fig. 2.

In the measurement of small obstacles in the near field of large, focused apertures an improvement in the sensitivity is to be expected. It is of interest to determine the extent of this improvement together with the associated range of measurement; this will be considered for the general case and then applied to the example just treated. A theoretical treatment of the focused, rectangular aperture has been given by Sherman.¹⁶ In his paper he presents a theorem that in the focal plane of the aperture near its axis, the electric field has the same properties as the far-zone field. As a corollary, at the focus the electric field varies inversely with the focal distance and may be calculated from its far-zone expression using the far-zone gain. Experiments reported by Goodrich and Hiatt,¹⁷ which give the magnitude of the electric field in the vicinity of a focal point, are in general agreement with the results of Sherman.

When small scatterers are measured in the near field of a large aperture with $A_0 = 0.9$, $\phi_0 = 22.5^\circ$, the permissible nonuniformity in the incident field generally is determined by A_0 (the restriction on the phase variation usually is satisfied easily). From the theorem given in the previous paragraph and the pattern function for a square aperture with a uniform aperture distribution, the angle α between the pattern

* The definition of near zone here is $1, 2\lambda < R < l^2/\lambda$.

points at which the electric field intensity is 0.9 of its maximum value is found to be $\lambda/2\ell$ ($\ell \gg \lambda$). The range of measurement, or focal distance in this case, is obtained from $L = R\alpha$. Next, employing the formula for the far-zone gain and substituting into Eq. (13),

$$\sigma_{\lambda m} = 64\pi \left(\frac{P_m^r}{P^0} \right) \left(\frac{L}{\lambda} \right)^4,$$

with

$$\frac{R}{\lambda} = 2 \left(\frac{\ell}{L} \right) \left(\frac{L}{\lambda} \right)^2.$$

Thus for the large, focused aperture one can achieve the optimum sensitivity reported in Eq. (26b); however, the range of measurement is increased by a factor of (ℓ/L) with respect to the optimized range. In the example of the unfocused near-zone measurement $\ell/\lambda = 10$, $L/\lambda = 1$; if this aperture were focused on the scatterer, $R\lambda/\ell^2 = 0.2$ and the sensitivity would be increased about 10 db with respect to that of the unfocused case. On the other hand, the range is nearly three times that used in the unfocused case.

APPLICATION

It is assumed that the reader is familiar with the essential features of the CW and pulsed reflection measuring systems similar to those which have been used at this laboratory.^{18,19,20} The pulsed systems are inherently more sensitive than the CW systems, but are more costly and complicated than the latter; consequently, we are interested in the approximate size of the largest obstacle which can be measured using a CW system.

First let us establish criteria for a satisfactory echo pattern. Again, A_0 and ϕ_0 are chosen to be 0.9 and 22.5° , respectively. The coherent component of the background power is required to be 20 db below the received power from the median echo area $\bar{\sigma}$, so that the background power can cause an error no greater than 1 db in $\bar{\sigma}$. Assuming that the indirect obstacle-antenna interaction is insignificant, the background power is the power observed with the obstacle absent. Its coherent component may be caused by ungated reflections from the ground or obstacle support in the case of a pulsed system or by unbalanced reflections in the hybrid junction circuit in the case of a CW system. A practical upper limit to the balance of the hybrid

junction circuit appears to be about 100 db, i. e., the background power in the receiver arm of the circuit is 100 db below the power in the transmitter arm.²¹ With the 6 db loss in the hybrid junction circuit, the background power is about 94 db below the transmitted power.

Using the above data it is found from Eq. (26b) that the minimum measurable σ in square wavelengths is

$$\sigma_{\lambda m} = 8 \times 10^{-6} \left(\frac{L}{\lambda} \right)^4 .$$

A curve for this equation is shown in Fig. 5, where $\bar{\sigma}_{\lambda}$ is plotted as a function of L/λ for different artillery shells and aircraft models. The $\bar{\sigma}_{\lambda}$ were found for 0-degree elevation patterns, because σ_{λ} is usually smallest for these patterns. These targets are more or less cylindrical in shape so the fairly regular behavior of σ_{λ} with L/λ is not surprising. The larger dispersion of data below $L/\lambda = 7$ is to be expected from target resonances. From the intersection of the two curves, one notes that CW reflection systems can be used to measure targets of this type with L/λ as large as 40. This answer agrees with the opinion based on experience that a CW reflection system can be used to record satisfactory patterns provided the scatterer is not more than a few dozen wavelengths long.

In conclusion, although certain theoretical results presented here have been confirmed experimentally for reflection systems employing horn and parabolic antennas, the analysis is based in part on the use of a square aperture with a field distribution uniform in amplitude and phase. A more precise statement of the limitations on these results can be given after this analysis has been extended to include other aperture shapes and field distributions.

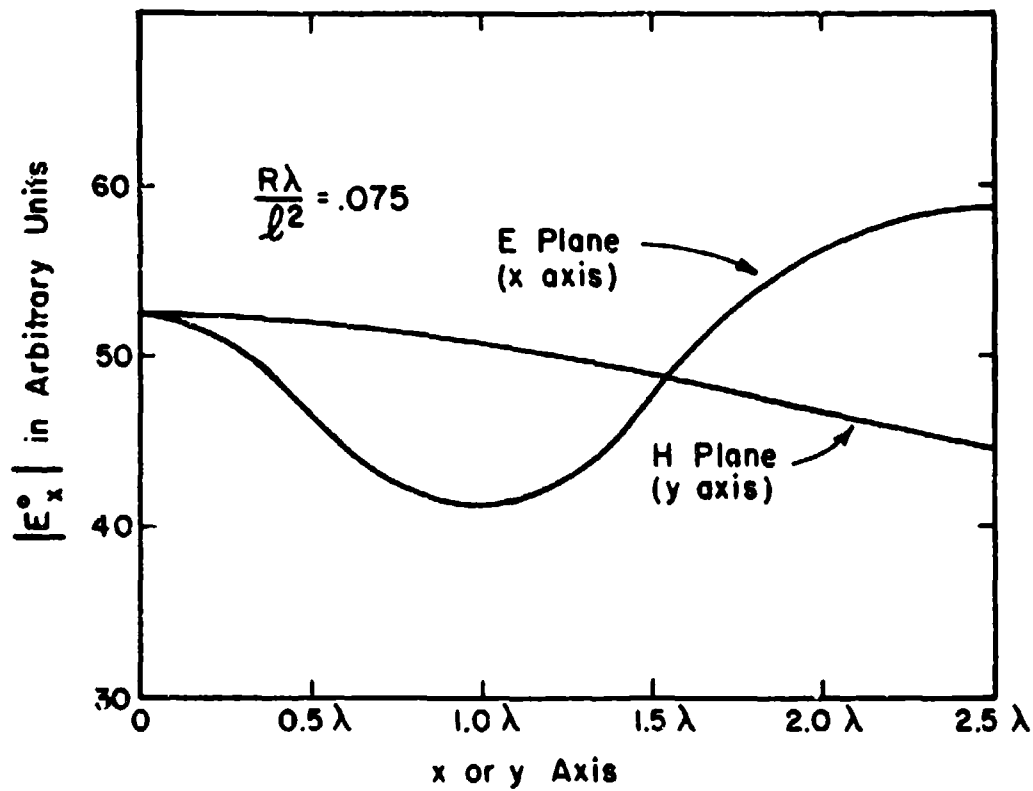


Fig. 3. Measured Transverse Electric Field of a Horn.

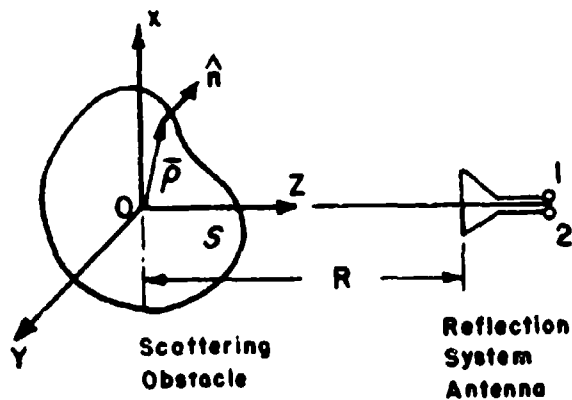


Fig. 4. Coordinate System for the Obstacle and Measuring Antenna.

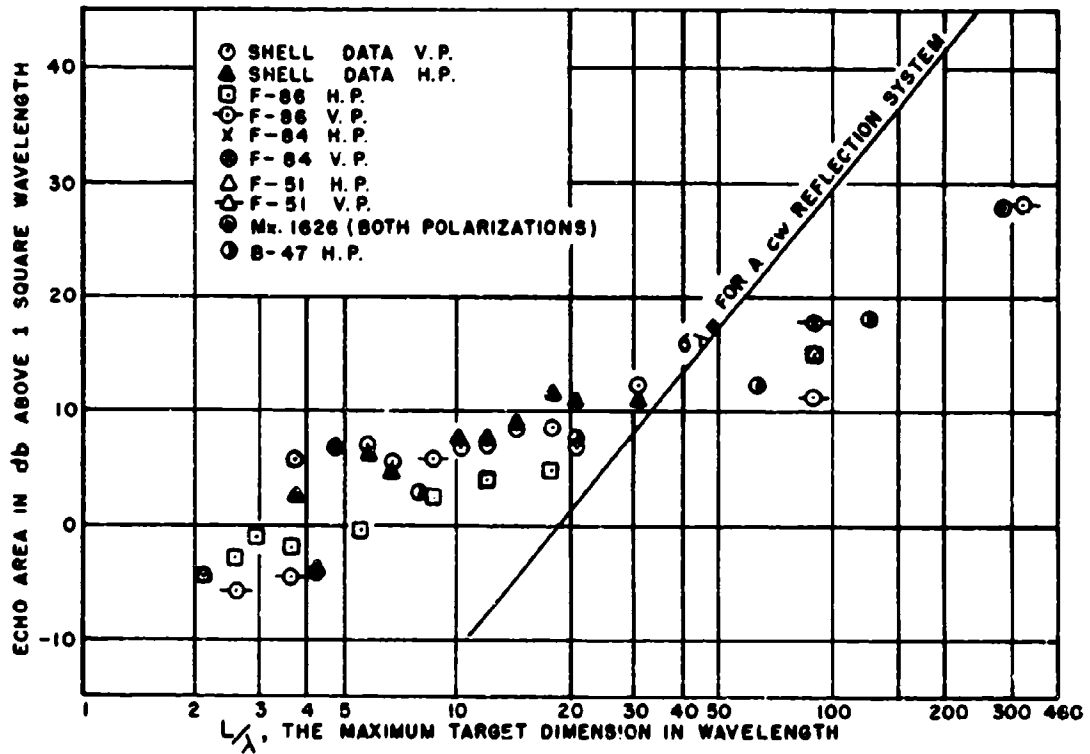


Fig. 5. Median Echo Areas for 0-Degree Elevation Patterns of Artillery Shell and Aircraft Models of Varying Length.

BIBLIOGRAPHY

1. Kouyoumjian, R.G., "An Analysis of Reflection Measuring Systems," Report 444-22, 15 December 1955, Antenna Laboratory, The Ohio State University Research Foundation; prepared under Contract DA 36-039-sc-5506, Signal Corps Engineering Laboratories, Fort Monmouth, New Jersey.
2. Silver, S., Microwave Antenna Theory and Design, M.I.T. Radiation Laboratory Series, Vol. 12, McGraw-Hill Book Co., Inc., New York, 1949, pp. 87-90.
3. Kouyoumjian, R.G., "The Calculation of the Echo Areas of Perfectly Conducting Objects by the Variational Method," Report 444-13, 15 November 1953, Antenna Laboratory, The Ohio State University Research Foundation; prepared under Contract DA 36-039-sc-5506, U.S. Army, Signal Corps Engineering Laboratories, Fort Monmouth, New Jersey.
4. Harrington, R.F., Time-Harmonic Electromagnetic Field, McGraw-Hill Book Co., Inc., New York, 1961, pp. 116-120.
5. Kouyoumjian, R.G., Op. cit., pp. 80-86.
6. Silver, S., Op. cit., p. 199.
7. Polk, C., "Optical Fresnel-Zone Gain of a Rectangular Aperture," IRE Trans. on Antennas and Propagation, Vol. AP-4, January 1956, pp. 65-69.
8. Mentzer, J.R., "The Determination of the Radar Echoing Properties of Objects," Report 444-6, 29 February 1952, Antenna Laboratory, The Ohio State University Research Foundation; prepared under Contract DA 36-039-sc-5506, U.S. Army, Signal Corps Engineering Laboratories, Fort Monmouth, New Jersey.
9. Cohen, M.H., "An Evaluation of Some Aspects of Static Model Radar Echo Measurements," Report 475-17, 17 June 1954, Antenna Laboratory, The Ohio State University Research Foundation; prepared under Contract AF 18(600)-19, Air Research and Development Command, Wright Air Development Center, Wright-Patterson Air Force Base, Ohio.

10. Moranda, P. B. and Rhodes, D. R., "On the Range Effect in Radar Echo Measurements," Report 475-9, 15 April 1954, Antenna Laboratory, The Ohio State University Research Foundation; prepared under Contract AF 18(600)-19, Air Research and Development Command, Wright Air Development Center, Wright-Patterson Air Force Base, Ohio.
11. Rhodes, D. R., "On Minimum Range for Radiation Patterns," Proc. IRE, Vol. 42, September 1954, pp. 1408-1410.
12. Schelkunoff, S. A., Electromagnetic Waves, D. Van Nostrand Co., Inc., New York, 1941, pp. 365-367.
13. Mentzer, J. R., Ibid.
14. Falls, W. A. and Fubini, E. G., "Methods of Measuring Radar Cross Sections, Report No. 380-1, January 1949, Airborne Instruments Laboratory, Inc., Mineola, New York, pp. 5-6.
15. Kouyoumjian, R. G., Op. cit., pp. 104-108.
16. Sherman, J. W., "Properties of Focused Apertures in the Fresnel Region," IRE Trans., Vol. AP-10, July 1962, pp. 399-408.
17. Goodrich, R. F. and Hiatt, R. E., "On Near Zone Antennas," Report No. 2861-1-F, Radiation Laboratory, The University of Michigan Research Institute, Ann Arbor, June 1959.
18. Kouyoumjian, R. G., Op. cit., pp. 74-78, pp. 86-91.
19. Bachman, C. G., et al, "Techniques for Measurement of Reduced Radar Cross Sections," The Microwave Journal, Vol. 6, April 1963, pp. 80-86.
20. Kennedy, P. D., "Equipment and Techniques for the Measurement of Radar Reflections from Model Targets," 1957 IRE-WESCON Convention Record, Part 1, pp. 208-215.
21. Kouyoumjian, R. G. and Yaw, D., "A K-Band Reflection Measuring System," Report 444-20, 15 March 1955, Antenna Laboratory, The Ohio State University Research Foundation; prepared under Contract DA 36-039-sc-5506, U. S. Army, Signal Corps Engineering Laboratories, Fort Monmouth, New Jersey.

MEASURING THE PHASE AND THE AMPLITUDE
OF BACKSCATTERED RADAR ENERGY ON A STATIC RANGE

Norman R. Landry
Electromagnetic Research Laboratory
RCA Missile & Surface Radar Division
Moorestown, New Jersey

ABSTRACT

A pulse system capable of making both phase and amplitude measurements at 1300 megacycles is briefly described. Following a discussion of the phase detectors that are used, some of the stability problems associated with a full-scale pulsed system are explored, with special emphasis on the effects of range background on phase measurements. Also included are discussions of 1) phase versus time delay measurements, and 2) the effect of various centers of rotation on the phase measurements from a given target.

To date, most radar cross-section measurement ranges have concentrated on measuring the amplitude rather than both the amplitude and the phase of backscattered energy. Inasmuch as phase data is very useful in trying to obtain the scattering matrix associated with a particular body, a system capable of measuring both items at 1300 mc has recently been built as a part of DAMP, the Downrange Antimissile Measurement Program under Project DEFENDER (sponsored by the Advanced Research Projects Agency and administered by the Army Missile Command.)

The discussion that follows explores the problems peculiar to phase measurements. It is not meant to ignore amplitude measurements, but it is felt that phase measurements have not been documented as well as amplitude measurements in the radar cross-section literature.

A simplified block diagram of the amplitude and phase measurement system is shown in Figure 1. The transmitted frequency is obtained by mixing the STALO frequency with a crystal controlled 30-mc signal and selecting the proper sideband to be amplified. Characteristics of the preselector are such that the STALO frequency is attenuated 80 db as compared to the transmitter frequency. The RF switch and pulse generator are used to form the low-level RF pulse and the width of the RF pulse is adjustable and is usually set to 0.2 microseconds. The output from the RF switch is fed through two stages of amplification. The first travelling-wave tube amplifier is a Sperry STL-260 and has a power gain of approximately 50 db with an output peak power of up to 30 watts. The second TWT is a Varian VA-131B and has a power gain of approximately 40 db with an output peak power of up to 50 kw of which 5 kw is usually used. The output from the transmitter is fed through the microwave system to the 30-foot diameter L-band antenna. Target returns are mixed with the STALO frequency and then amplified in the gated I.F. amplifier. The 30-mc reference frequency is also amplified in a gated I.F. amplifier and the outputs from the two I.F. amplifiers contain the desired amplitude and phase information. The amplitude and phase detectors extract this information and make it available for any of the recorders (analog and digital) in the recorder complex.

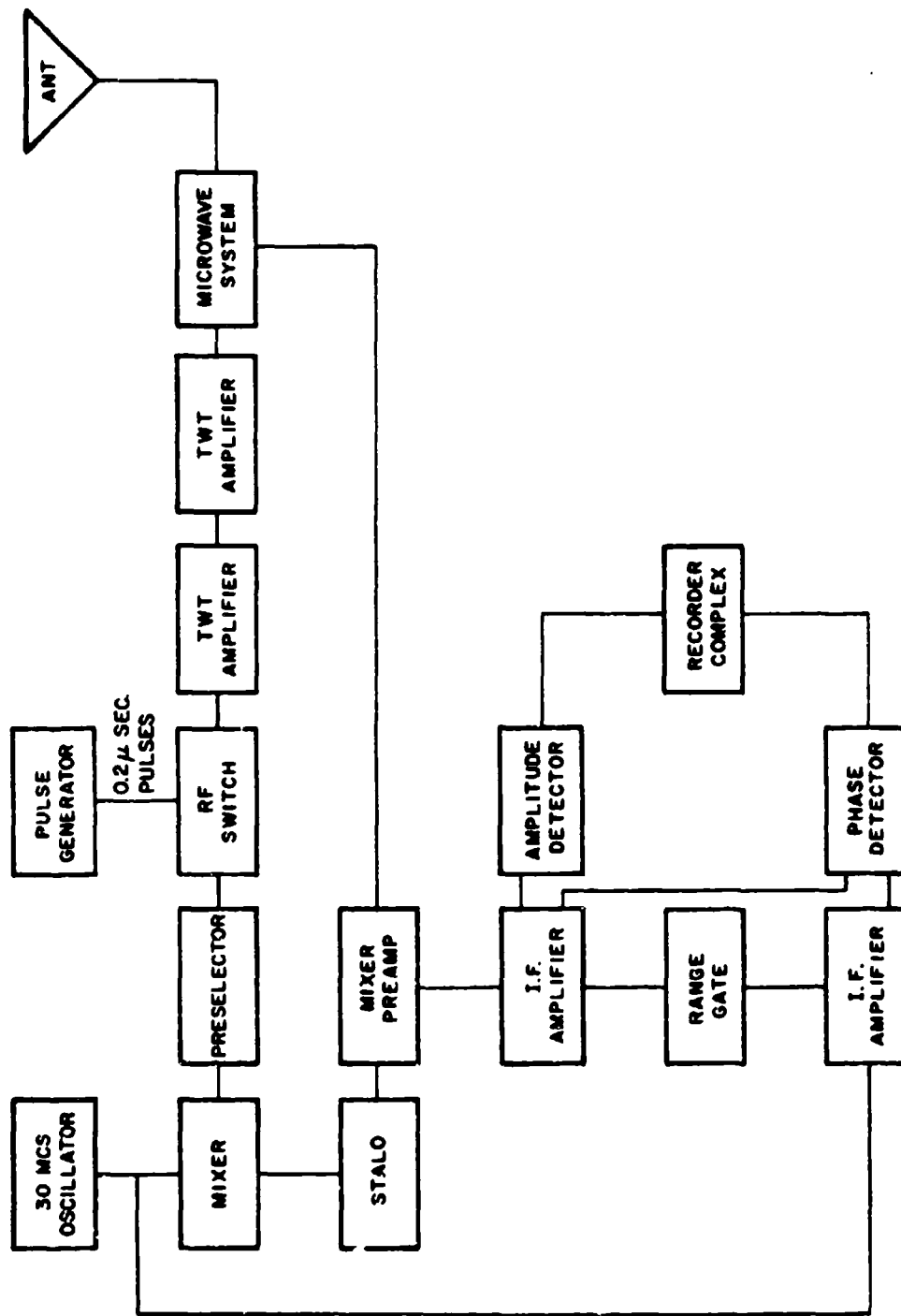
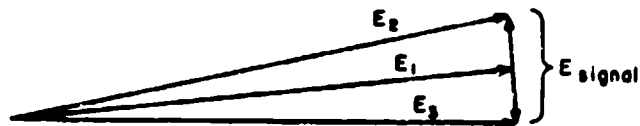
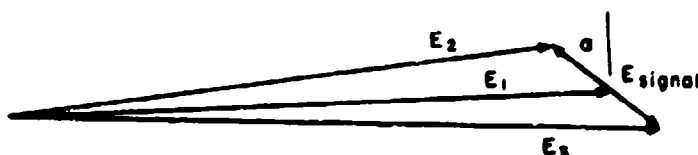


Figure 1. Simplified Block Diagram of Phase Measurement System

In keeping with the idea of discussing those items peculiar to phase measurements, only the phase detector of Figure 1 will be discussed in any detail. A schematic of the basic components of the phase detector is shown in Figure 2. Using phasor diagrams to represent the various voltages, the reference voltage can be depicted as E_1 . The signal voltage is very small compared to the reference and because of the centertapped transformer action adds in quadrature to E_1 when the relative phase between the two signals is zero. See sketch.



As shown, for the case of zero relative phase, E_2 and E_3 are equal in amplitude. The outputs from the half-wave rectifiers will be equal in amplitude and of opposite polarity and the stretched video output from the centertap will have zero amplitude. The case for a forty-five degree relative phase is shown below.



E_2 and E_3 are no longer equal and the stretched video pulses will have some positive amplitude. For E_2 larger than E_3 (for -45 degrees, say) the output pulses would be negative. If E_1 , E_2 , and E_3 are considered as being essentially parallel (E_1 , E_2 , and $E_3 \gg E_{sig}$.) then the amplitude of the output is $E_3 - E_2$, and

$$E_2 \approx E_1 - \frac{E_{sig}}{2} \sin \alpha$$

$$E_3 \approx E_1 + \frac{E_{sig}}{2} \sin \alpha$$

$$E_3 - E_2 \approx E_{sig} \sin \alpha.$$

If the amplitude of E_{sig} is held constant by using the AGC controlled signal, then the output from the phase detector is proportional to the sine of the input phase angle. Note the 180 degree ambiguity in the above sketches. To overcome this ambiguity two phase detectors are used and the reference signal fed into one of

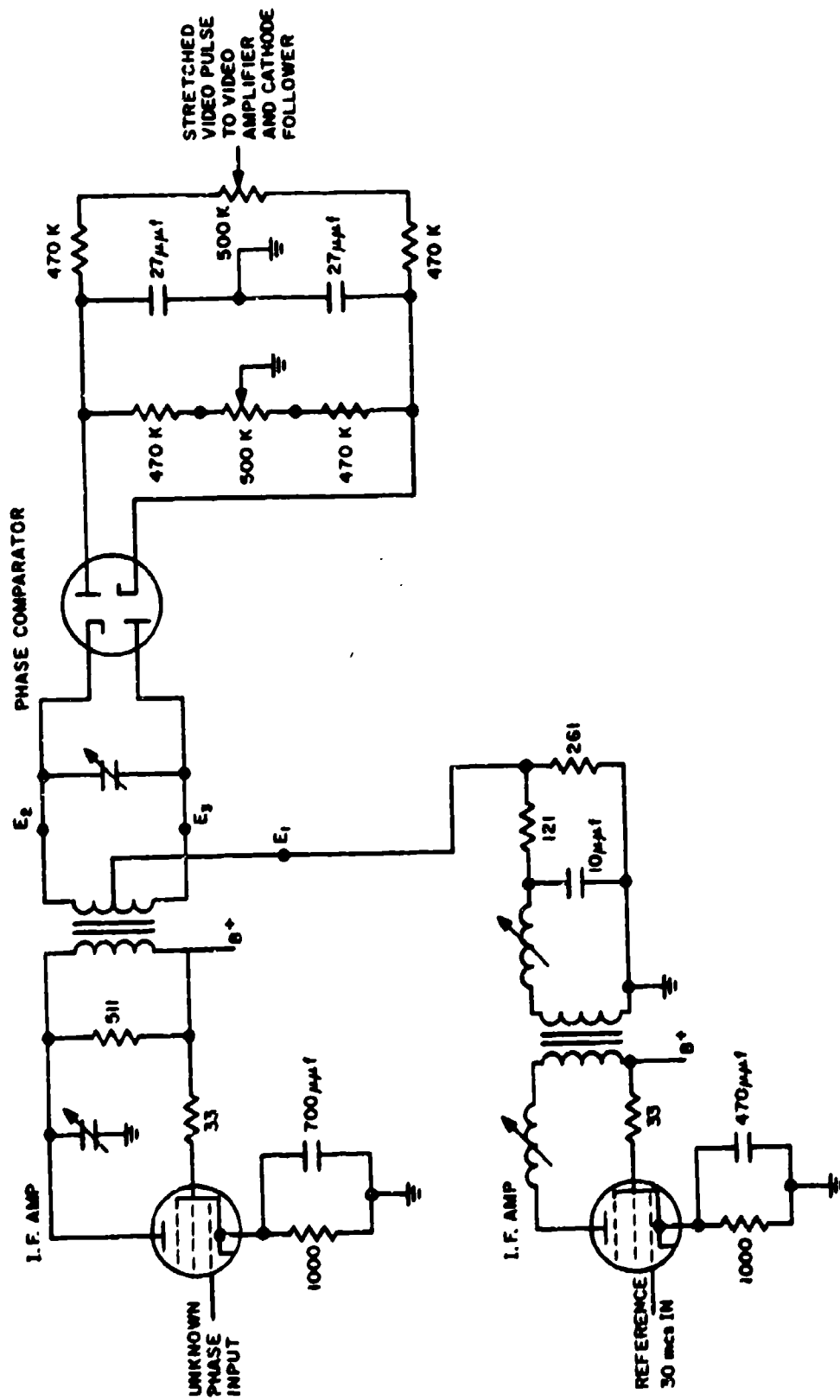


Figure 2. Partial Schematic Diagram of Phase Detector

the phase detectors is phase shifted ninety degrees so that its output voltage is proportional to the cosine of the unknown phase angle. Knowing both the sine and cosine of the angle to be measured, the angle can be unambiguously determined. The stretched video pulses are peak detected and the d-c levels are amplified to a usable level and recorded. In addition, the two d-c levels are fed into an electromagnet chopper and resolver unit and the resolved phase angle is recorded.

A list of the system specifications as applicable to both amplitude and phase measurements is given below.

- 1) Relative phase accuracy of 5.0 degrees rms for a 0.01 square meter target.
- 2) Background cross section of 0.0001 square meters.
- 3) Absolute amplitude calibration accuracy of ± 1.0 db.
- 4) Amplitude measurement accuracy of ± 1.2 db at 0.01 square meters.
- 5) Target aspect angle accuracy of ± 0.1 degrees.
- 6) Target handling capability of 4,000 pounds and approximately 30 feet long.
- 7) Transmit capability of any linear, circular or elliptical polarization.
- 8) Receive capability of any linear, circular or elliptical polarization.
- 9) Transmitter frequency of 1300 megacycles.
- 10) Pulse width of 0.2 microseconds.
- 11) Pulse repetition frequency of 1000 pps.
- 12) Maximum transmitter peak power of 5.0 kilowatts.
- 13) Range gate of 0.2 microseconds.
- 14) Recordings of amplitude and phase on analog and digital magnetic tape and/or rectilinear and polar graphs.

The accuracy of the phase and amplitude data is as given above in the section describing system specifications. Two primary sources of error are from site background and equipment drift. With respect to phase measurements the effects of background have been analyzed analytically and the effects of system drift have been measured and analyzed statistically. The results are given in Table I and the calculations are shown in Appendix A. The phase errors were calculated by assuming that background is fixed in amplitude and phase (a fixed target) and that the phase of the signal voltage is equally likely to be anywhere from 0 to 360 degrees relative to the background at any aspect angle on any given test. The calculations were made for $S/N = 0$ decibels and for very large values of S/N . The condition that gave the largest error was then extrapolated for other values of S/N and the column of RMS error where extrapolation was required has been marked "Approximate". The calculations are still valid if the phase of the background signal varies in a random manner relative to the phase of the target signal. If background takes on the characteristics of noise

TABLE I. BACKGROUND EFFECTS ON PHASE MEASUREMENTS

Signal to Noise db	Maximum Error degrees	Average Error degrees	RMS Error degrees (Approx.)
0	90.0	0.0	52.0
10	18.4	0.0	13.0
20	5.75	0.0	4.06
30	1.81	0.0	1.28
40	.59	0.0	0.42

SYSTEM STABILITY

	Units	10 minute period	20 minute period
Average Maximum Phase Error	degrees	±1.8	±3.1
Standard Deviation of Above Average	degrees	2.2	3.1
Average Standard Deviation of Phase Error Within One Run	degrees	—	0.51
Standard Deviation of Above Average	degrees	—	0.72

(as it tends to do with proper nulling techniques) the phase errors in the RF energy also take on the characteristics of noise. When these signals are processed by peak detecting circuitry, however, these phase errors tend toward the maximum values. Since the peak detection is not perfect, the actual errors will probably be closer to the RMS error.

The system stability section of Table I shows that the average maximum phase error in a 20-minute run is ±3.1 degrees. It must be stressed that this maximum phase error exists only for a very limited target aspect angle and can occur at random. A look at the average standard deviation of phase error within one run will bring out this point. In an average test there can be errors of 3.1 degrees, but their frequency will be associated with the six sigma value of the standard deviation which was determined to be 0.51. For any given test picked at random it can be said that the standard deviation of the phase errors in that test will be less than 2.67 [0.51 + 3 (0.72)] degrees for 998 tests out of 1000. This information was obtained by analyzing 120 pieces of 10-minute data and 60 pieces of 20-minute data. The periods of ten and twenty minutes were chosen because the time for one target rotation is between these two values and because phase stability is only needed during a target revolution since phase differences are read from the data.

Two effects related to phase accuracy that have been noticed in the data that has been recorded are 1) that the phase data from symmetrical targets is very symmetrical and 2) that the phase differences read from the data are a function of the location of the center of rotation on the target. If a target body is immersed in a flat field regardless of the location of the center of rotation and if multipath effects are negligible, the only effect of different centers of rotation is to change the effective range of the target as it is rotated about the different centers of rotation. Having made a phase measurement for a certain center of rotation it is possible to synthesize a phase measurement about a new center of rotation by the following formula.

$$\alpha = \frac{720 \Delta \cos \theta}{\lambda}$$

where

α is the correction angle in degrees

Δ is the amount of translation of the center of rotation and is positive if the center of rotation is moved toward the nose of the target

θ is the target aspect angle and is zero degrees for nose-on

λ is the operating wavelength and must have the same dimensional unit as Δ .

The correction angle, α , is added to the measured phase angle at each target aspect angle and can be positive or negative depending on the sign of the cosine θ . A digital computer program is being prepared to carry out this computation (if desired) on the digital data that will be recorded.

Since the effect of phase variation due to target aspect change and phase variation due to range change (time delay) can be but need not be the same, it had to be determined whether the system was actually measuring phase changes and time delay or just time delay. It was felt that if insufficient bandwidth were available, the phase of the signal in the IF amplifier would be independent of the phase of the RF signal and resultant phase measurements would merely be measurements of the relative times at which the IF amplifier was shocked into ringing. A test was devised to resolve the question and the results proved conclusively that the system measures the phase of the returned energy regardless of what (time or target) has affected the phase. Thus if the phase of the return is affected by the shifting of the center of return or by a change in boundary layer (ablation material, e.g.) the phase system will measure the total change and not only that due to the change in effective range. The test consisted of two parts 1) varying the effective range to the target and 2) holding range constant and varying intra-pulse RF phase. In the first test, the time of the target return was delayed by means of a line stretcher in the transmitter line to the antenna and data of measured phase versus line stretcher position was recorded. In the second test, the time of the echo was maintained constant relative to the reference, t_0 , and the phase of the transmitted signal at t_0 was varied. Again, data was recorded and

when the results of the two tests were compared, it was judged that (within the experimental accuracy described in the system specifications) the two curves were identical. It is thus concluded that the system measures the phase of the RF echo regardless of what has affected the phase.

A sample of a phase measurement is given in Figure 3 and the corresponding amplitude (cross-section) data is given in Figure 4. The target body is a thirty-inch diameter flat plate, has a large U-shaped stiffener on one face and is mounted with a metal shaft. When using the phase data, it must be remembered that phase measurements have meaning only when a change of phase is associated with a change in aspect angle. The phase data can be considered linear for rough approximations and if an arbitrary reference angle of β is associated with the center of the polar graph, then the outside of the polar graph represents $360^\circ + \beta$. Phase angles of α , $2\pi + \alpha$ and in general $2n\pi + \alpha$ are all recorded at the same radial position relative to the center on the graphs. The recording pen flyback at $360^\circ + \beta$ allows the counting of the number of 2π radians that have occurred. A flyback from the outside of the graph toward the inside can be interpreted as saying that an angle of 2π should be added to subsequent readings (another flyback says that 4π should be added etc.) and a flyback from the center of the graph toward the outside can be interpreted as saying that an angle of 2π should be subtracted from subsequent readings. The phase angle for the flat plate varies three $4\pi + \alpha$ where $180^\circ < \alpha < 360^\circ$. A look at $\theta = 0^\circ$ (face on) and $\theta = 180^\circ$ (tail on) shows that the flat plate was not rotated about an axis in the plane of the flat plate. Knowing that it was rotated about an axis parallel to the plane of the flat plate and that the displacement was less than a quarter wavelength, the actual displacement can be calculated from the phase data as being $5/8$ inch. For the radar cross-section plots, the scales are linear, each division is equal to one decibel and the level of one square meter is marked on the graph. For both plots, the angular aspect angle is in degrees and the identification of $\theta = 0^\circ$ (or face on) is marked on the polar graphs.

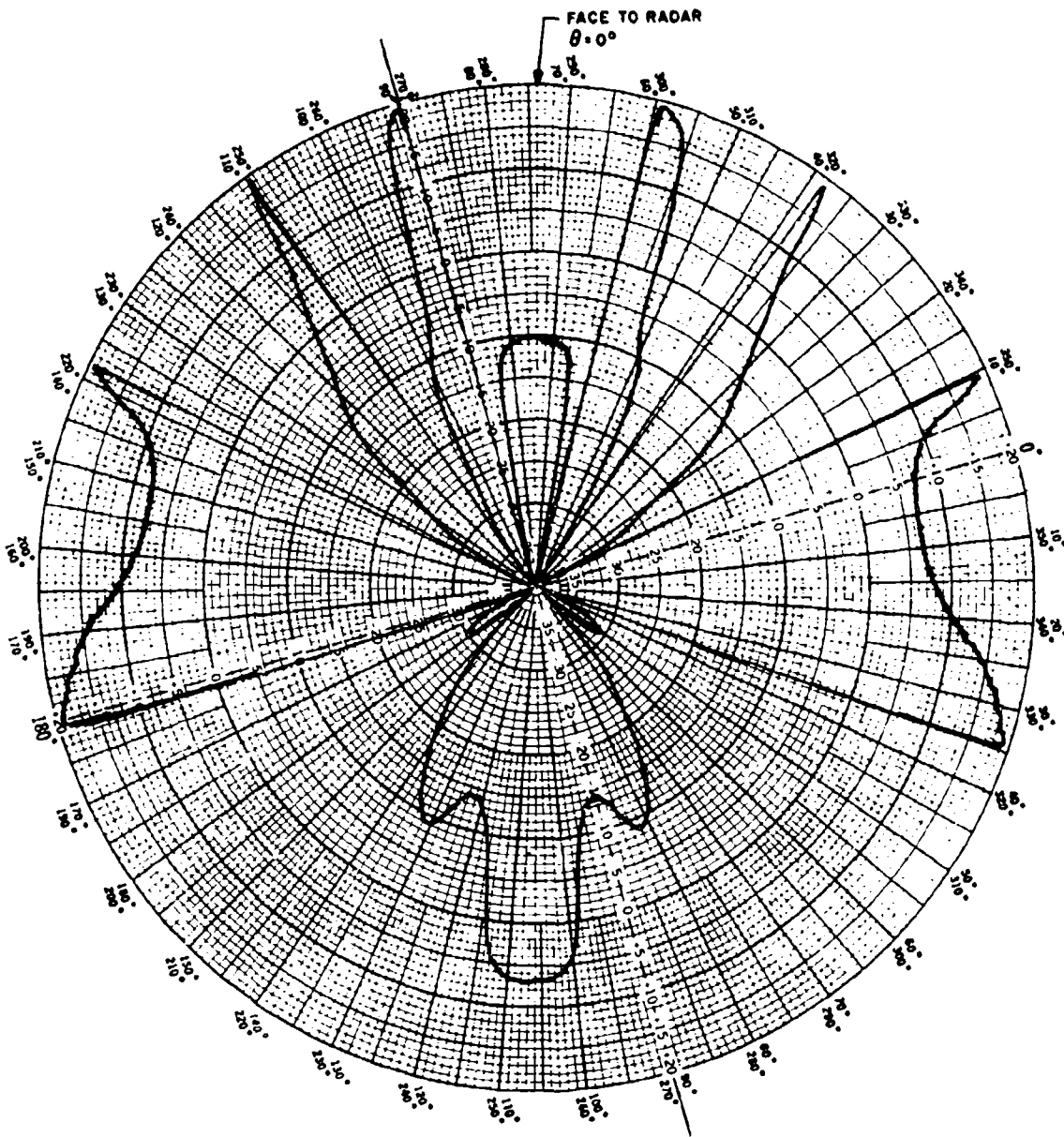


Figure 3. Flat Plate (Phase) 1300 MCS VV Polarization

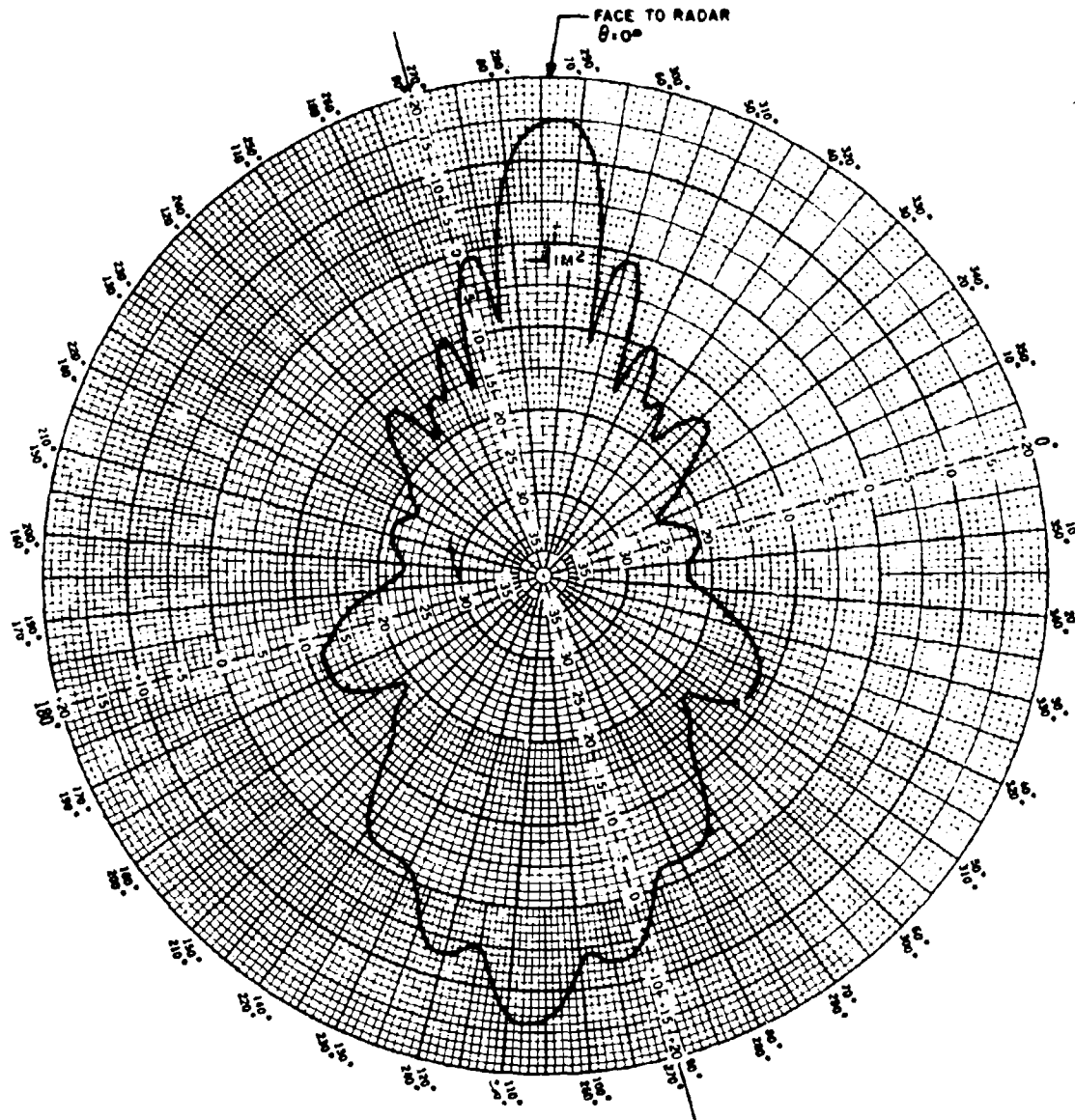


Figure 4. Flat Plate (cross-section) 1300 MCS VV Polarization

APPENDIX A

Background Effects on Phase Measurements

Assumptions:

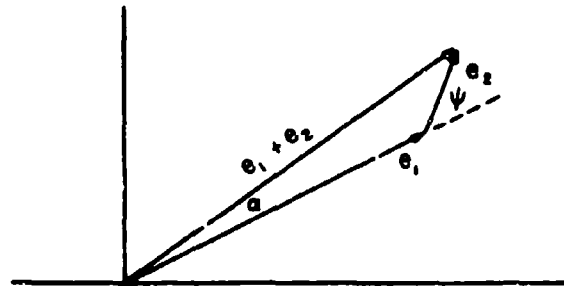
- 1) Background fixed in amplitude and phase.¹
- 2) Relative phase between signal and background voltages equally likely to be anywhere between 0 and 360 degrees

Let e_1 = signal voltage

e_2 = background voltage

ψ = relative phase between signal and background voltage

α = error in phase measurements



then

$$\tan \alpha = \frac{e_2 \sin \psi}{e_1 + e_2 \cos \psi} \quad (\text{A-1})$$

The value of ψ that will make the phase error a maximum can be found by differentiating equation A-1 and setting the resultant equal to zero,

$$\alpha = \tan^{-1} \frac{e_2 \sin \psi}{e_1 + e_2 \cos \psi}$$

¹The phase of the background voltage can be allowed to vary as long as it varies independently from the signal voltage.

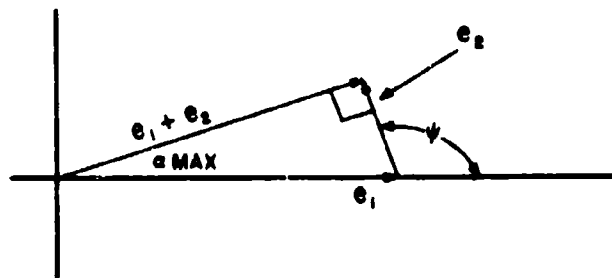
$$\frac{d\alpha}{d\psi} = \frac{e_1 e_2 \cos \psi + e_2^2}{e_1^2 + 2 e_1 e_2 \cos \psi + e_2^2} \quad \text{set} = 0$$

$$e_1 e_2 \cos \psi + e_2^2 = 0$$

or

$$\psi = \cos^{-1} \left(-\frac{e_2}{e_1} \right) \text{ to give } \alpha_{\max}. \quad (\text{A-2})$$

Use of the following sketch



shows that

$$\alpha_{\max} = \sin^{-1} \frac{e_2}{e_1}. \quad (\text{A-3})$$

To study some of the statistical characteristics of the phase error, α , consider the case where the background voltage is much less than the signal voltage. When $e_2 < e_1$ the equation

$$\alpha = \tan^{-1} \frac{e_2 \sin \psi}{e_1 + e_2 \cos \psi}$$

reduces to

$$\alpha = \frac{e_2}{e_1} \sin \psi \quad (\text{A-4})$$

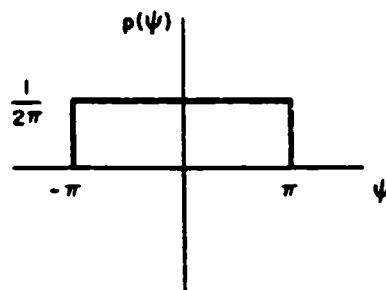
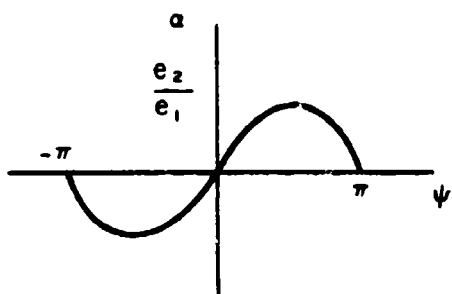
where α is expressed in radians.

From the second assumption on page 156, the probability density function of ψ can be written as follows:

$$p(\psi) = \frac{1}{2\pi} \quad -\pi \leq \psi \leq \pi$$

$$= 0 \text{ otherwise.}$$

The probability density function of α will now be found.



Because of the symmetry of the sine curve about its peak value and because α is a double valued function of ψ

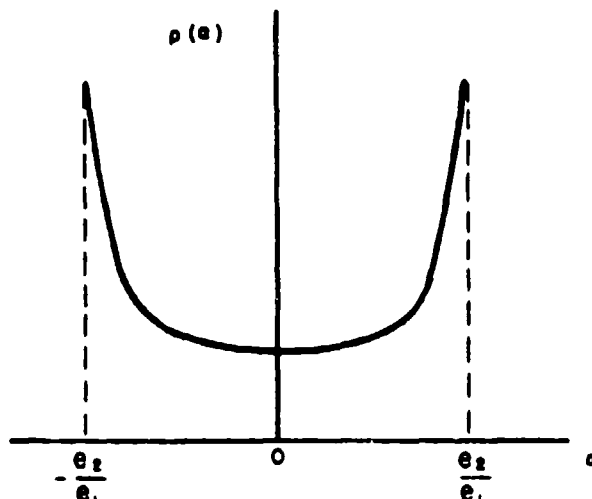
$$p(\alpha) = 2 p(\psi) \left| \frac{d\psi}{d\alpha} \right|$$

$$p(\alpha) = \frac{2}{2\pi} \frac{d}{d\alpha} \left[\sin^{-1} \frac{e_1 \alpha}{e_2} \right]$$

$$p(\alpha) = \frac{1}{\pi \sqrt{\left(\frac{e_2}{e_1}\right)^2 - \alpha^2}} \quad \text{for } |\alpha| < \frac{e_2}{e_1}$$

$$= 0 \quad \text{for } |\alpha| > \frac{e_2}{e_1} .$$

(A-5)



By inspection the mean value of α is equal to zero. The variance of α is equal to the mean square value and is given below.

$$\sigma_{\alpha}^2 = \int_{-\infty}^{\infty} \alpha^2 p(\alpha) d\alpha$$

$$= \frac{1}{\pi} \int_{-\frac{e_2}{e_1}}^{\frac{e_2}{e_1}} \frac{\alpha^2}{\sqrt{\frac{e_2^2}{e_1^2} - \alpha^2}} d\alpha$$

$$\sigma_{\alpha}^2 = \frac{1}{\pi} \left[\frac{\alpha}{\sqrt{\left(\frac{e_2}{e_1}\right)^2 - \alpha^2}} + \frac{\alpha}{2} \sqrt{\left(\frac{e_2}{e_1}\right)^2 - \alpha^2} + \frac{e_2^2}{2e_1^2} \sin^{-1} \frac{\alpha e_1}{e_2} \right]_{-\frac{e_2}{e_1}}^{\frac{e_2}{e_1}}$$

$$\sigma_{\alpha}^2 = \frac{1}{2\pi} \left(\frac{e_2}{e_1}\right)^2 \left[\sin^{-1} 1 - \sin^{-1} (-1) \right]$$

$$\sigma_{\alpha}^2 = \frac{1}{\pi} \left(\frac{e_2}{e_1} \right)^2 \frac{\pi}{2}$$

$$\sigma_{\alpha}^2 = \frac{e_2^2}{2e_1^2}$$

and the standard deviation on RMS value of α is

$$\sigma_{\alpha} = \alpha_{\text{RMS}} = \frac{1}{\sqrt{2}} \frac{e_2}{e_1} = \frac{1}{\sqrt{2}} \alpha_{\text{max}} \text{ for } e_2 \ll e_1. \quad (\text{A-6})$$

As another part of the study consider the case $e_2 = e_1$.

Then

$$\alpha = \tan^{-1} \frac{\sin \psi}{1 + \cos \psi}.$$

Using the facts

$$\sin 2\Phi = 2 \sin \Phi \cos \Phi$$

$$1 + \cos 2\Phi = 2 \cos^2 \Phi$$

$$\tan \alpha = \frac{2 \sin \frac{\psi}{2} \cos \frac{\psi}{2}}{2 \cos^2 \frac{\psi}{2}}$$

or

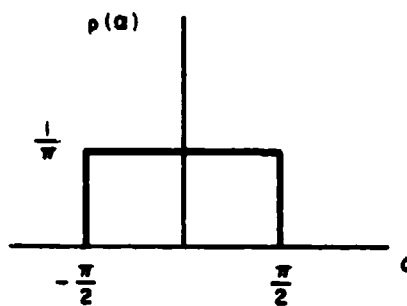
$$\tan \alpha = \tan \frac{\psi}{2}$$

which can be true only if $\alpha = \frac{\psi}{2}$.

It follows that for this case

$$p(\alpha) = \frac{1}{\pi} \text{ for } -\frac{\pi}{2} \leq \alpha \leq \frac{\pi}{2} \quad (\text{A-7})$$

$$= 0 \quad \text{otherwise}$$



Again, the mean value of α is zero by inspection, the variance is found as follows,

$$\sigma_{\alpha}^2 = \int_{-\frac{\pi}{2}}^{\frac{\pi}{2}} \frac{1}{\pi} \alpha^2 d\alpha$$

$$\sigma_{\alpha}^2 = \left. \frac{\alpha^3}{3\pi} \right]_{-\frac{\pi}{2}}^{\frac{\pi}{2}}$$

$$\sigma_{\alpha}^2 = \frac{\pi^2}{12} = \frac{1}{3} \alpha_{\max}^2$$

and the standard deviation or RMS value is

$$\sigma_{\alpha} = \alpha_{\text{RMS}} = \frac{1}{\sqrt{3}} \alpha_{\max} \quad \text{for } e_2 = e_1 \quad . \quad (\text{A-8})$$

To demonstrate that equations A-5 and A-7 are reasonable, the following sketches are offered.

In both sketches equal increments of ψ have been chosen and the vectors $\widehat{e}_1 + \widehat{e}_2$ have been drawn. The distribution of α is constant for $e_1 = e_2$ and for $e_1 = 3e_2$ the distribution is concentrated near the maximum value of α .

The phase errors shown in Table I in the body of the report were calculated as follows:

Maximum Error

Use equation A-3

$$\alpha_{\max} = \sin^{-1} \frac{e_2}{e_1} \quad .$$

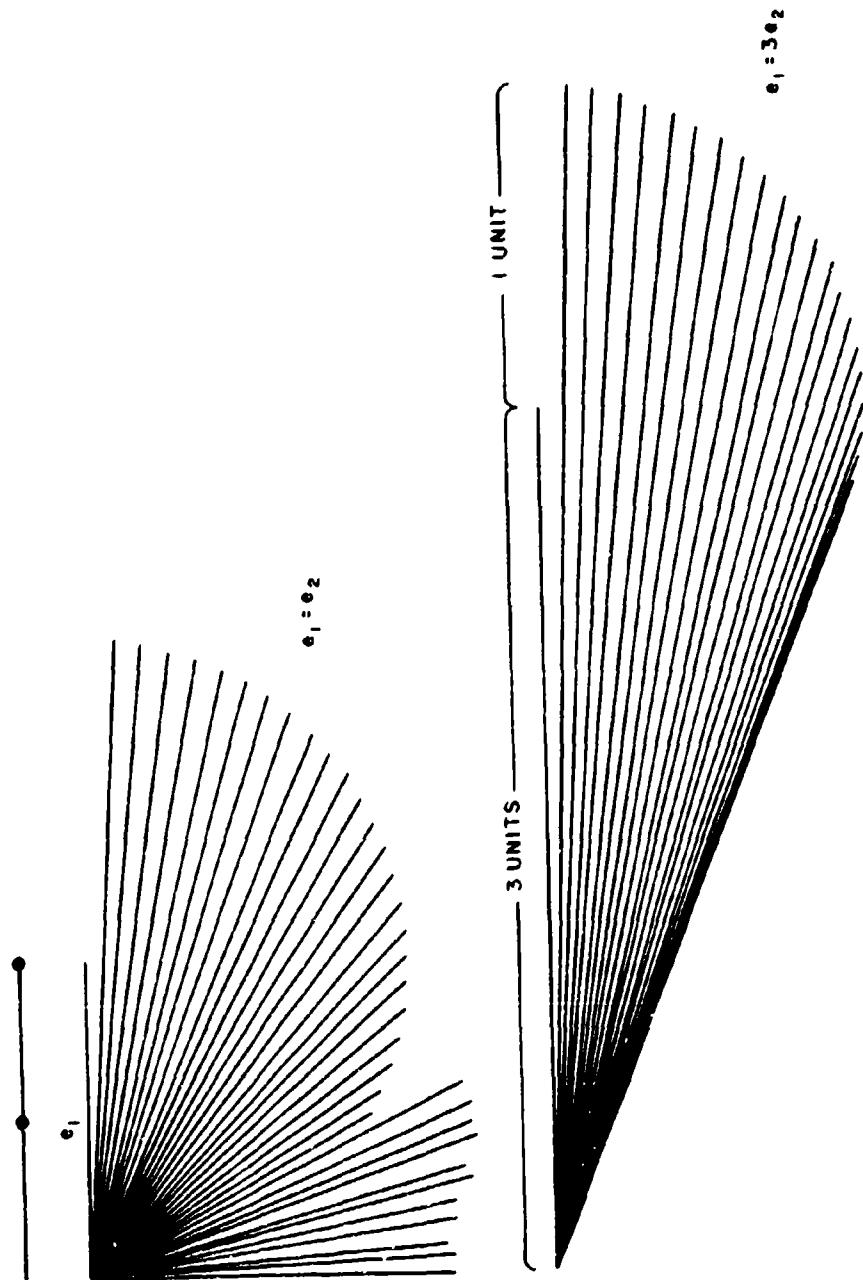


Figure A-1. Phasor Demonstration of Equations A-5 and A-7

Average Error

For $e_2 \ll e_1$ and for $e_2 = e_1$ the mean value of α was found to be zero. With the help of Figure A-1 in this Appendix, these results can be extrapolated for any ratio of $\frac{e_1}{e_2}$. Thus

$$\bar{\alpha} = 0 \text{ for all values of } \frac{S}{N}.$$

RMS Error

$$\alpha_{\text{RMS}} = \frac{1}{\sqrt{2}} \alpha_{\text{max}} \text{ for } e_2 \ll e_1 \text{ by equation A-6}$$

$$\alpha_{\text{RMS}} = \frac{1}{\sqrt{3}} \alpha_{\text{max}} \text{ for } e_2 = e_1 \text{ by equation A-8}$$

Assume the worst case, let $\alpha_{\text{RMS}} = \frac{1}{\sqrt{2}} \alpha_{\text{max}}$ for all cases except $\frac{S}{N} = 1$ and carry out the calculations.

BIBLIOGRAPHY

1. W.B. Davenport, Jr. and W.L. Root, An Introduction to the Theory of Random Signals and Noise. McGraw-Hill Book Company, Inc., 1958
2. F.E. Terman, Electronic and Radio Engineering. McGraw-Hill Book Company, Inc., 4th ed, 1955
3. C.G. Bachman, H.E. King, R.C. Hansen, Techniques for Measurement of Reduced Radar Cross Sections. Microwave Journal, February 1963
4. M.E. Bechtel, Final Report Project ACRE. Cornell Aeronautical Laboratory, Inc., May 1960

SURFACE CURRENTS IN THIN CONDUCTING SHEETS

P. Magoulas, Ph.D., B.Sc. & P.A. Matthews, Ph.D., B.Sc.(Eng.), A.M.I.E.E.
University College, London.

(1) INTRODUCTION

To calculate the field scattered from a conducting obstacle in an electromagnetic field the current distribution in the obstacle must be known. For certain shapes of obstacle it is possible to solve the field equations exactly but in the case considered here, that of a thin flat conducting sheet, illuminated edge on such a formal solution cannot be set up. To evaluate the fields, the current distribution on the sheets has been measured and expressions have been derived from which these distributions may be calculated.

The measurements of the surface currents were carried out using a magnetic loop probe coupled to a bridge detector for measuring relative amplitude and phase. The situation of the sheets relative to the incident field is shown in Figure 1a. The incident field is propagated in the z direction with the electric field in the x or horizontal direction. The sheets lie in the xz plane. Three types of sheet are considered, those finite in both the x and z directions, those finite in the z direction and infinite in the x direction, and those finite in the x direction and semi-infinite in the z direction, that is extending from $z = 0$ to $+\infty$. Measurements have been carried out on rectangular, triangular and circular sheets, and also on cylinders which have an appreciable thickness in the y direction.

For a rectangular sheet currents can be measured parallel to the front edge, parallel to the side edge, longitudinal currents. The currents parallel to the front edge may be divided into two types, those excited in the front edge itself which attenuate rapidly along the sheet and those transverse currents excited further down the sheet which act as a travelling wave along the sheet.

(2) EXPERIMENTAL APPARATUS

The measurements were carried out at a frequency of 3000 Mc/s using the system illustrated in Figure 1b. A Heil tube oscillator radiating from a horn was used to illuminate the obstacle. A reference signal is taken by waveguide from the oscillator to the bridge for measuring amplitude and phase. In the reference arm are level setting and measuring attenuators and phase shifters. A signal from the magnetic loop probe is also coupled to this reference arm. The two signals are mixed in a crystal mixer. The oscillator is modulated at 3 kc/s and the mixer output is taken to a tuned amplifier. Measurements are carried out by setting the position of the probe and then adjusting the calibrated attenuator and phase shift to give a null reading on the output amplifier meter. This is repeated at a number of points to plot out the required field pattern.

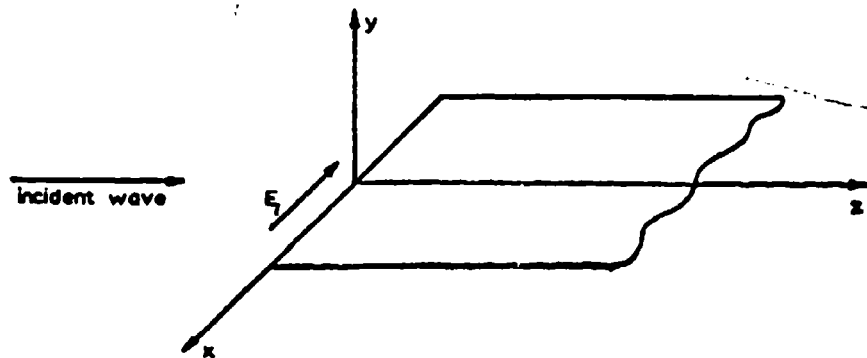


Fig. 1a. Semi-infinite plate.

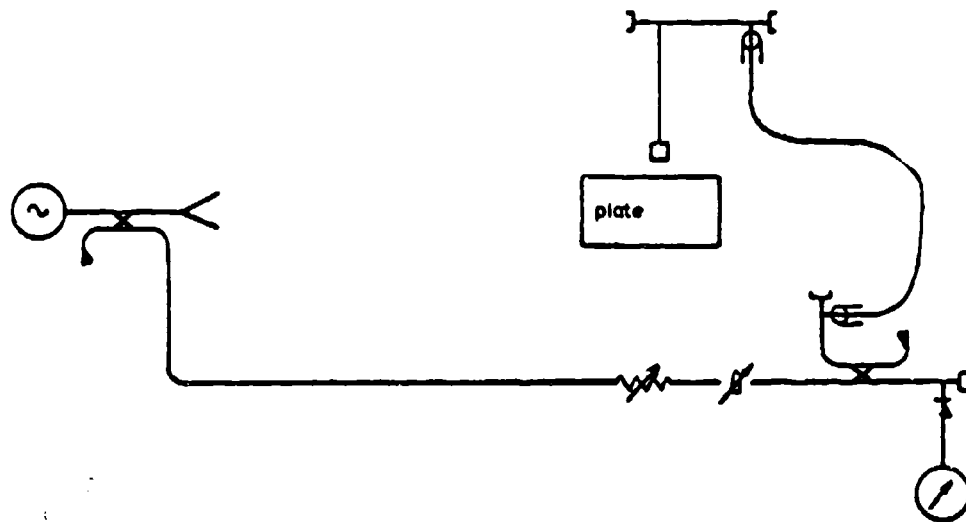


Fig. 1b. Schematic Diagram of apparatus.

The apparatus was set up indoors and to prevent distortion of the field by reflection from neighbouring objects absorbent screens were set up around the region in which the measurements were carried out. The horn was situated sufficiently far from the position of measurement for the field to be substantially plane in that region.

To measure the magnetic field alone a balanced shielded loop was used. This is illustrated in Figure 2.a . This form of loop has the advantage that it is well shielded from electric fields and with the gaps in the outer conductor symmetrically placed in the vertical arm of the loop there is little pick-up from the horizontal electric field. The dimensions of the loop are small compared with the wavelength, having horizontal and vertical dimensions of 2 mm. by 3 mm. If such a loop is held immediately above the conducting sheet the current induced in the loop is proportional to the field through the loop and hence to the current in the surface flowing in the direction of the plane of the loop. If currents are induced in the loop due to the electric field they are in phase in the two vertical arms of the loop. The coaxial lines from the loop are coupled into a waveguide transformer at points $\lambda/2$ apart and so the electric field does not induce any net field into the guide. The currents set up by the magnetic field are 180° out of phase in the two lines and when coupled into the guide set up a wave in the guide.

The efficiency of the loop as a detector of the magnetic field was tested by making measurements on obstacles over which the field distribution could be calculated, e.g. cylinders or wires. The results of such a test are shown in Figure 2.b in which a comparison is made with the measurements of Codis⁶ and with calculated curves.

There is good agreement over the illuminated side of the cylinder. In the shadow region agreement is not so good. It is thought that this may be due to the presence of standing waves in the field in the region of the cylinder.

(3) MEASUREMENTS ON RECTANGULAR SHEETS

3.1. Front Edge Currents

Measurements were made of the current along the front edge of sheets and in wires of the same length. These results are shown in Figures 3.a,b,c. for different lengths together with calculated values of the field. The currents measured along the edge are similar in form to that in wires until the length of the front edge is 2λ . At this length there is a difference in that the current is zero at the centre of the wire but on the sheet it still has a value only half that of the maximum.

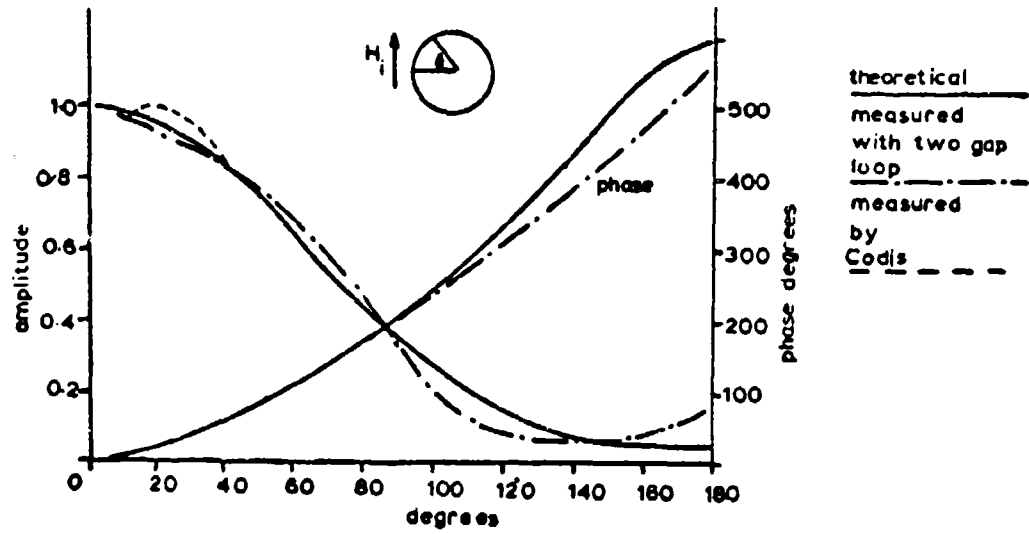
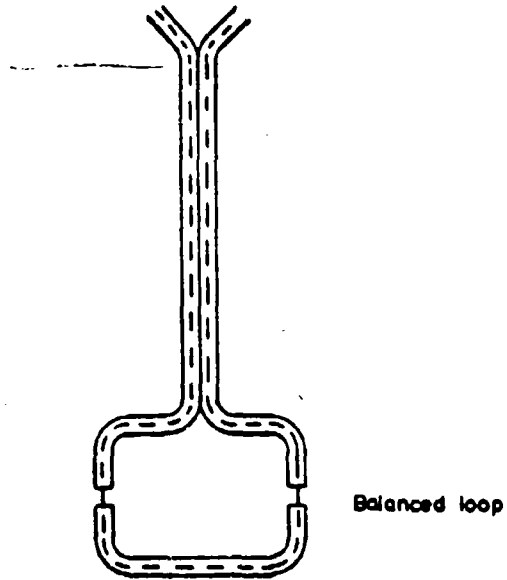


Fig. 2. Balanced loop and measurement on cylinder.

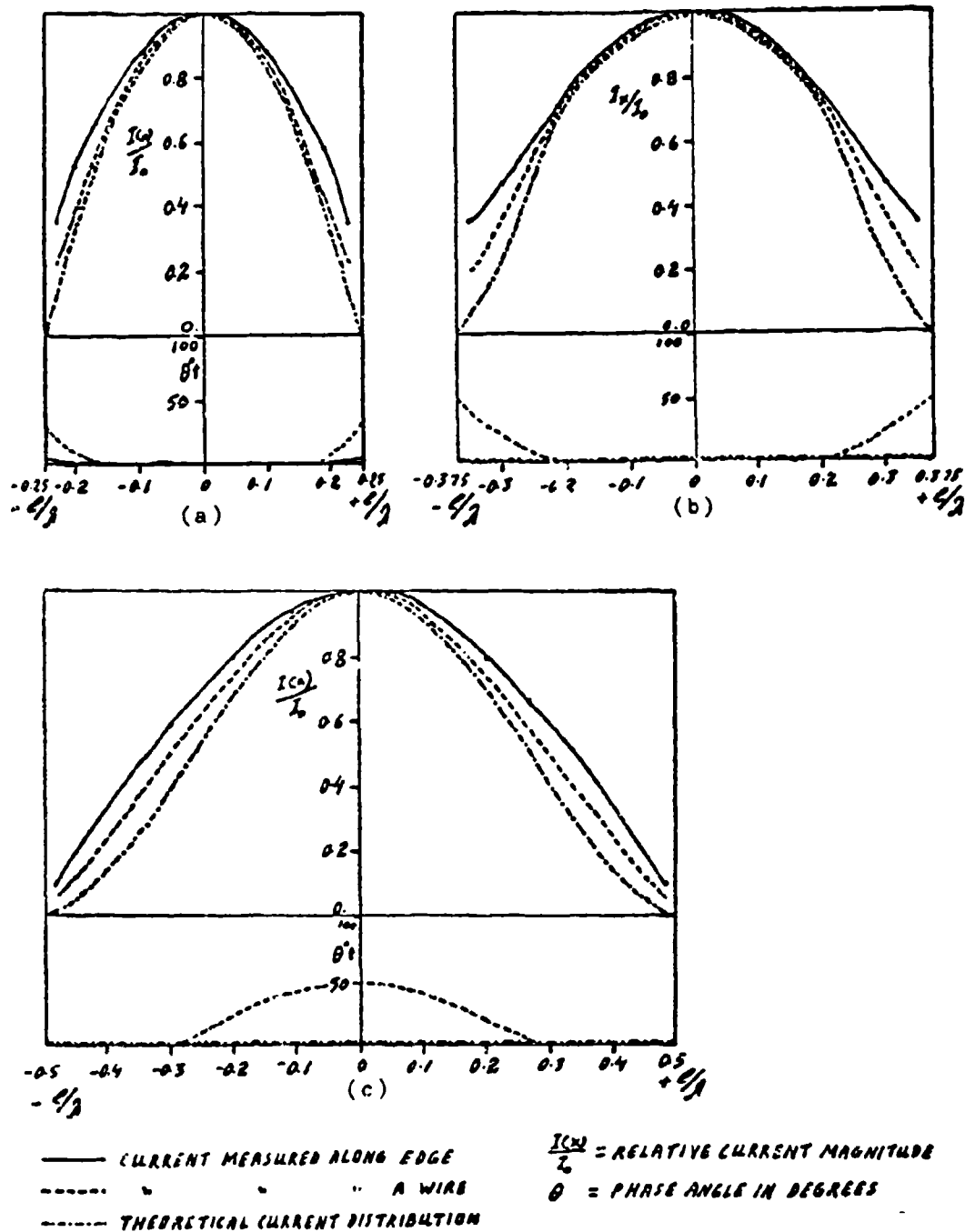


Fig. 3. Measurement of amplitude and phase across the front edge of plates, (a) $1/2\lambda$ (b) $3/4\lambda$ (c) 1λ in width.

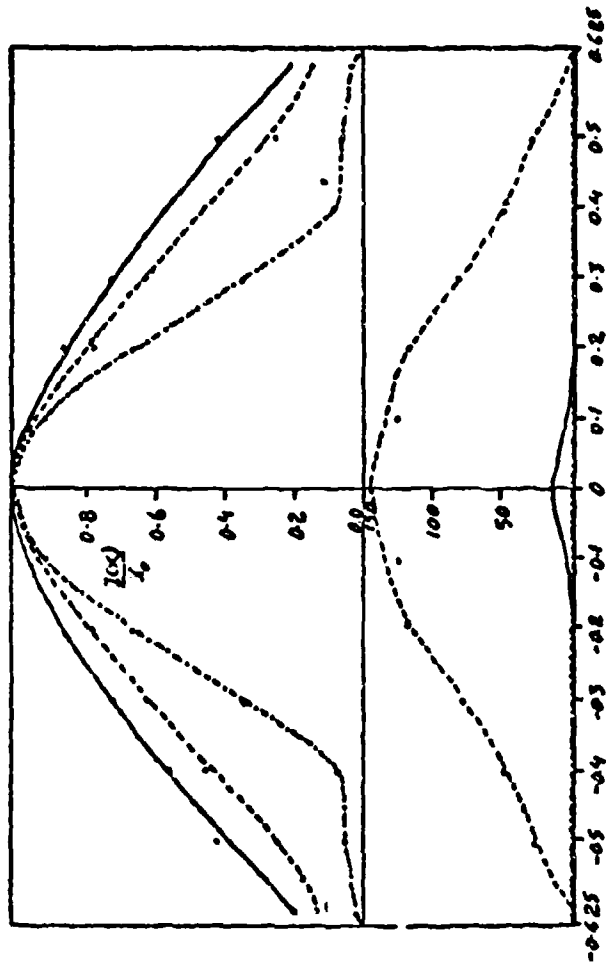


Fig. 3d. Measurement of amplitude and phase across the front edge of a plate $5/4\lambda$ in width.

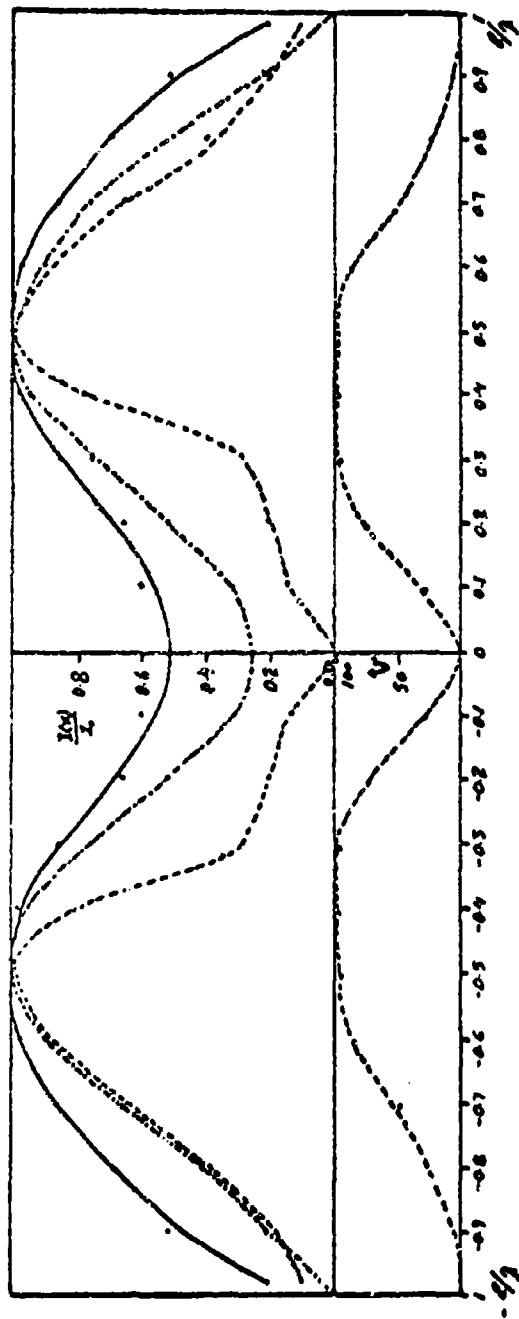


Fig. 3e. Measurement of amplitude and phase across the front edge of a plate 2λ in width.

3.2. Longitudinal currents

The variation in longitudinal current was measured along the side of a sheet 12λ long and one wavelength wide Figure 4a . The field is small in amplitude near the front edge but increases in amplitude along the sheet. There is a marked standing wave pattern along the sheet. When the sheet is terminated with an absorbing screen the standing wave pattern is much reduced and the field has the form of a wave travelling along the sheet. This is confirmed by the measurement of phase (Figure 4b . The variation of the longitudinal field across the sheet is shown in Figure 4c . There is 180° phase change between the currents along one edge of the sheet and the currents along the opposite edge.

3.3. Transverse currents

The transverse component of the current was measured along the sides and centre of the sheet and the results of this measurement are shown in Figure 5a . Near the front edge there is a large current in the centre and little current at the edge, whilst at a point along the sheet the current at the centre falls to a low value and the current in the edge increases. Again it appears that a travelling wave is set up along the sheet. The currents in the front and back edges are similar to those in aeriials. The variation in the transverse component of the current measured across the centre of the sheet is shown in Figure 5b . Again there is 180° phase change in the currents in the two edges.

From these measurements it seems reasonable to consider the theoretical evaluation of these currents in two parts, firstly the currents induced in the front edge of the sheet and secondly the travelling waves set up along the sheet.

4. CALCULATION OF THE FRONT EDGE CURRENT AND BACK SCATTERING FROM THE FRONT EDGE

4.1. Front edge current

The currents in the front edge of the sheet have been calculated following the variational method put forward by Tai⁽²⁾ for cylindrical wires. The front edge of the sheet is shown in Figure 6 . The current is induced in the front edge of the sheet by the incident field E_0 . It is assumed that the current can be regarded as a current filament $I(x')$ along the x axis in the plane $y = 0$ and that the current is scattered along the edges AD, BC. Then for a point x on the edge the distance R from x to x' is given by

$$R = \sqrt{(x-x')^2 + d^2} \quad (1)$$

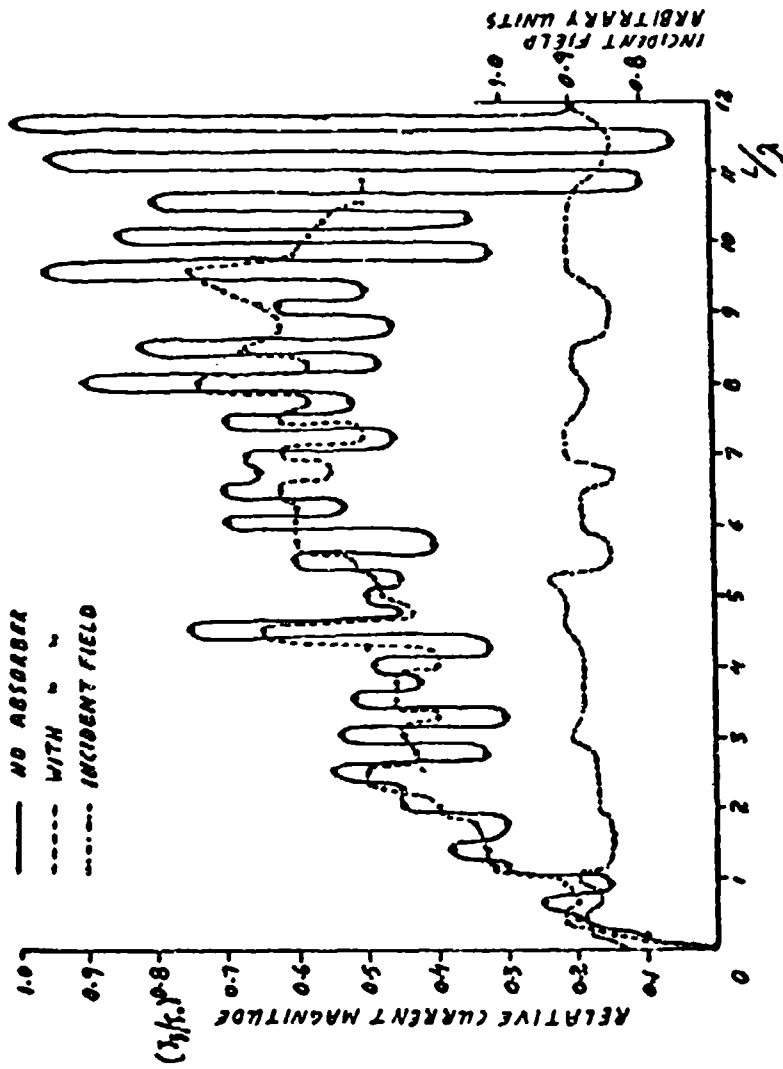


Fig. 4a. Amplitude distribution of longitudinal currents along the side of a rectangular metal plate.

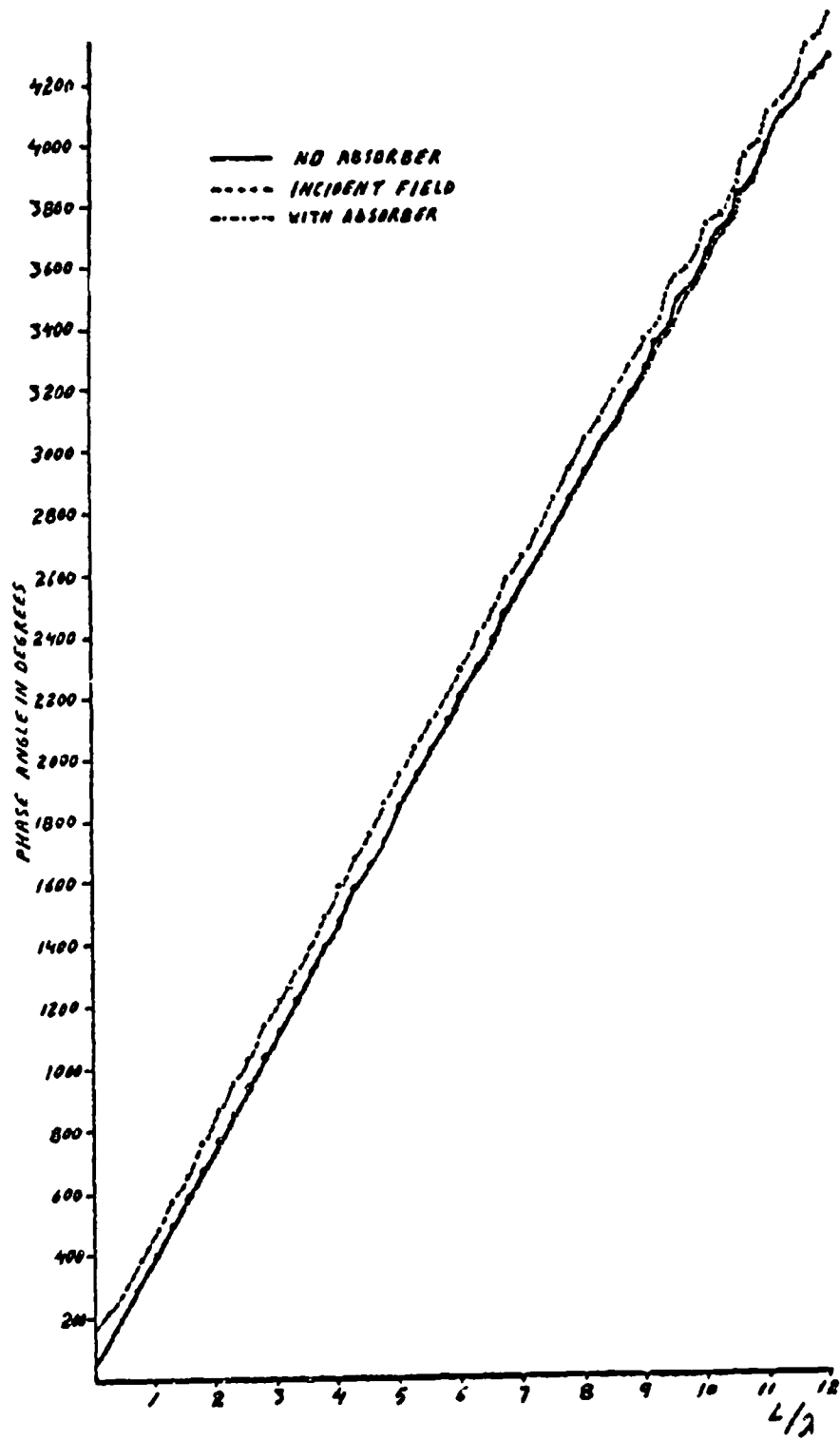


Fig. 4b. Phase distribution of longitudinal currents.

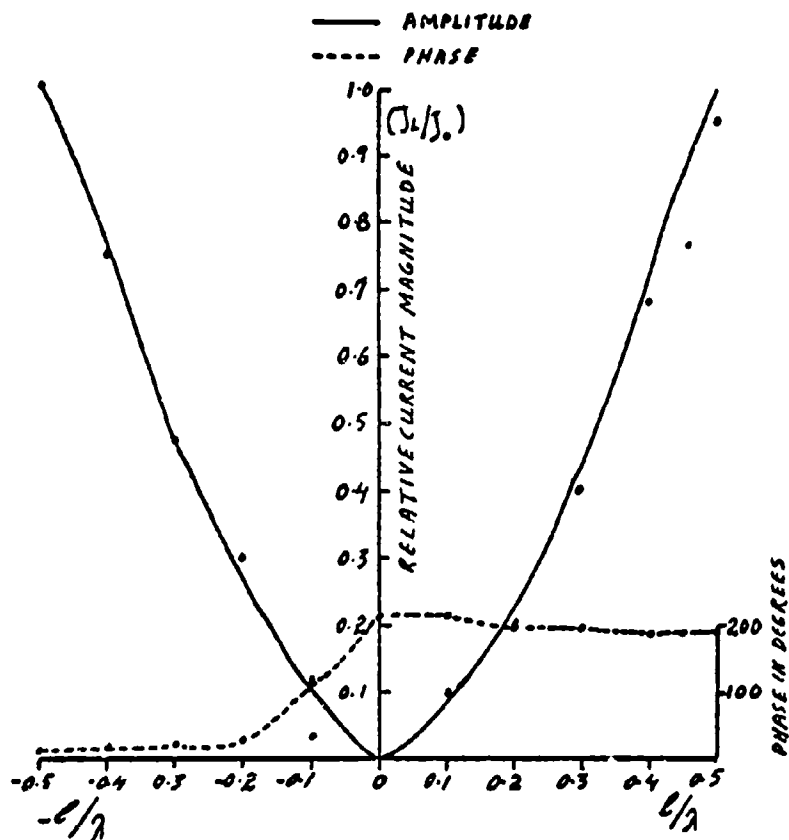


Fig. 4c. Amplitude and phase distribution of the longitudinal current measured across the metal plate.

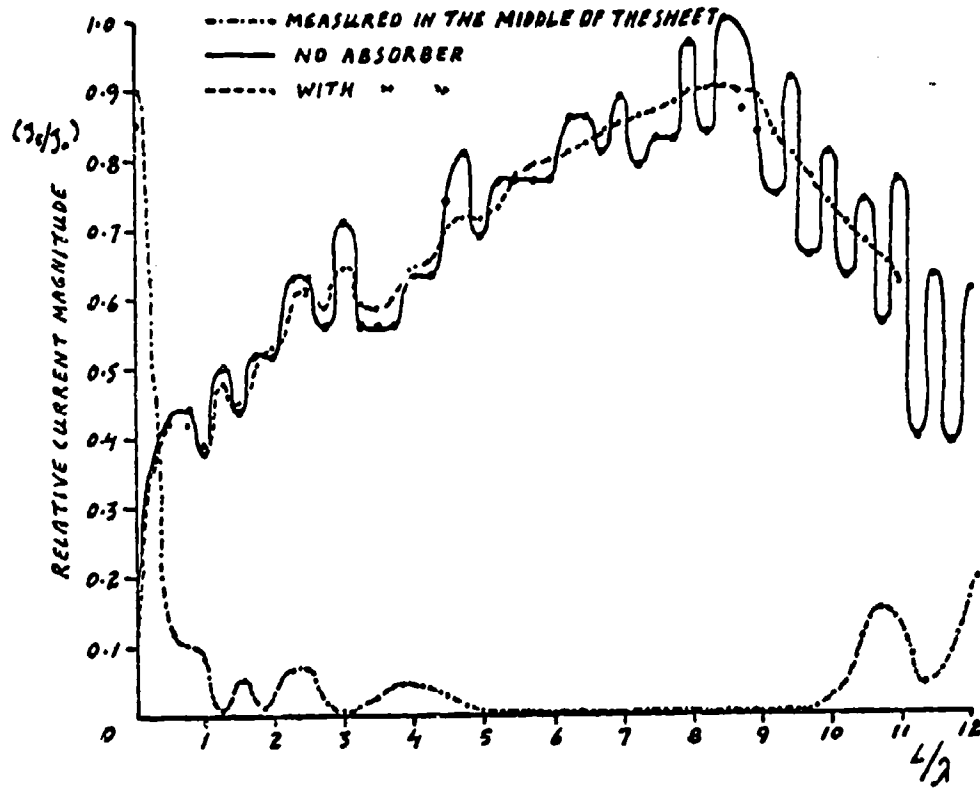


Fig. 5a. Amplitude distribution of the transverse current measured along the side and the centre of the metal plate.

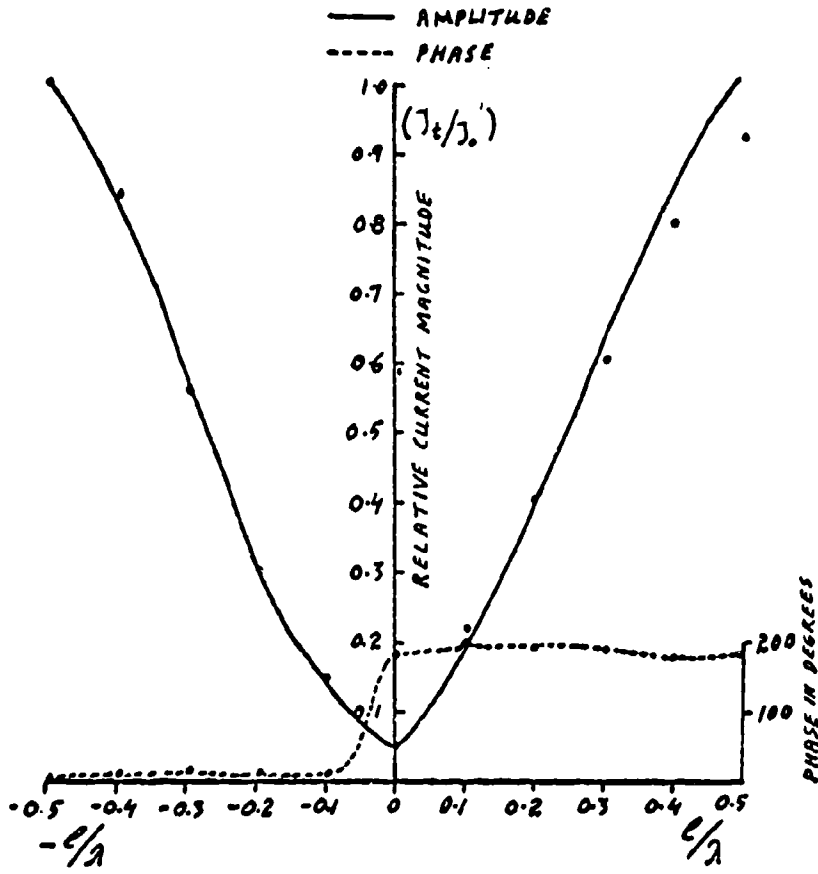


Fig. 5b. Amplitude and phase distribution of the transverse current measured across the metal plate.

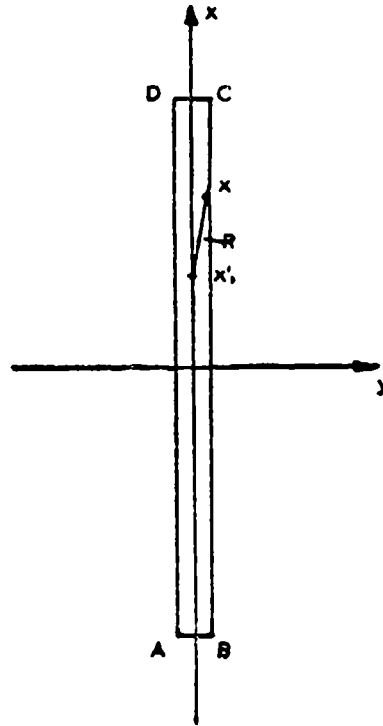


Fig. 6. Front edge of the metal plate.

Now it has been shown that the field E_0 is related to the current $I(x')$ by the relation

$$E_0 = \frac{j\eta k}{4\pi\omega\epsilon} \int_{-l}^{+l} I(x') \left\{ 1 + \frac{1}{k^2} \frac{\partial^2}{\partial x'^2} \right\} \frac{e^{-jkR}}{R} dx' \quad (2)$$

Multiplying by $I(x)dx$ and integrating from $-l$ to $+l$ and then dividing by

$$\left[k \int_{-l}^{+l} I(x) dx \right]^2$$

gives

$$\frac{E_0}{k^2 \int_{-l}^{+l} I(x) dx} = \frac{j\eta \int_{-l}^{+l} \int_{-l}^{+l} I(x) I(x') K(x-x') dx dx'}{4\pi \left[k \int_{-l}^{+l} I(x) dx \right]^2} \quad (3)$$

$$\text{where } K(x-x') = k \left(1 + \frac{1}{k^2} \frac{\partial^2}{\partial x^2} \right) \frac{e^{-jkR}}{R} \quad (4)$$

Then writing

$$S = \frac{k^2 \eta \int_{-l}^{+l} I(x) dx}{4\pi E_0} \quad (5)$$

and

$$\frac{1}{S} = \frac{j \int_{-l}^{+l} \int_{-l}^{+l} I(x) I(x') K(x-x') dx dx'}{\left[k \int_{-l}^{+l} I(x) dx \right]} \quad (6)$$

gives a quantity S which is stationary with respect to small variation in $I(x)$ about the correct value. From a given trial function for $I(x)$ a better value can thus be obtained.

On the front edge two conditions are assumed:

$$\begin{aligned} I(x) &= I(-x) \\ I(l) &= I(-l) = 0 \end{aligned} \quad (7)$$

A current distribution satisfying these conditions is

$$I(x) = I_0 (\cos kx - \cos kl) \quad (8)$$

but this does not agree with the non-zero measured value of the current in the centre of a sheet $l = \lambda$, i.e. 2λ wide and a correction term

$$-\Lambda \cos \frac{kx}{p}$$

may be added where the constant Λ is found through equation (8). P is such that $\cos \frac{kz}{P} = 0$ at $x = \pm l$. Thus

$$\frac{I(x)}{I_0} = \cos kx - \cos kl - \Lambda \cos \frac{kx}{P} \quad (9)$$

Putting the expression into equation (6), and putting the derivative of this with respect to Λ equal to zero as S is stationary, an expression for Λ may be found. This may be expressed as

$$\Lambda = \frac{g_s \gamma_d - \mu \gamma_c}{\gamma_s g_s - \mu \gamma_d} \quad (10)$$

where the expressions are those given in the thesis⁽³⁾ and which may be evaluated in terms of generalised sine and cosine integrals which are tabulated.

When the complex value of Λ has been evaluated the current distributions for values of l from 0 to λ may be calculated. The values of Λ are given in Figure 7. For values of $l > \lambda$ a second approximation must be made as the first approximation again gives zero current at the centre which does not agree with measurements. The actual evaluation of the second and higher approximations becomes increasingly tedious.

The values of current in amplitude and phase calculated by this method have been plotted on the same graphs as the experimental measurements and show a fair agreement.

4.2. Back Scattering from the Front Edge

The scattering cross-section may be defined following King⁽⁴⁾ as

$$\sigma = \frac{\text{total power reradiated from scatterer}}{\text{incident Poynting vector at scatterer}} \quad (11)$$

This is expressed in terms of the incident and scattered electric fields as

$$\sigma = 4\pi R^2 \left(\frac{E_s}{E_0} \right)^2 \quad (12)$$

at a distance R from the scatterer.

Both E_s and E_0 may be expressed in terms of $I(x)$ and S to give

$$\frac{\sigma}{\lambda^2} = \frac{|S|^2}{\pi} \quad (13)$$

The values of S may be evaluated from the calculated current distributions and hence the scattering cross-section of the front edge. This is shown in Figure 8 and is compared with the scattering cross-

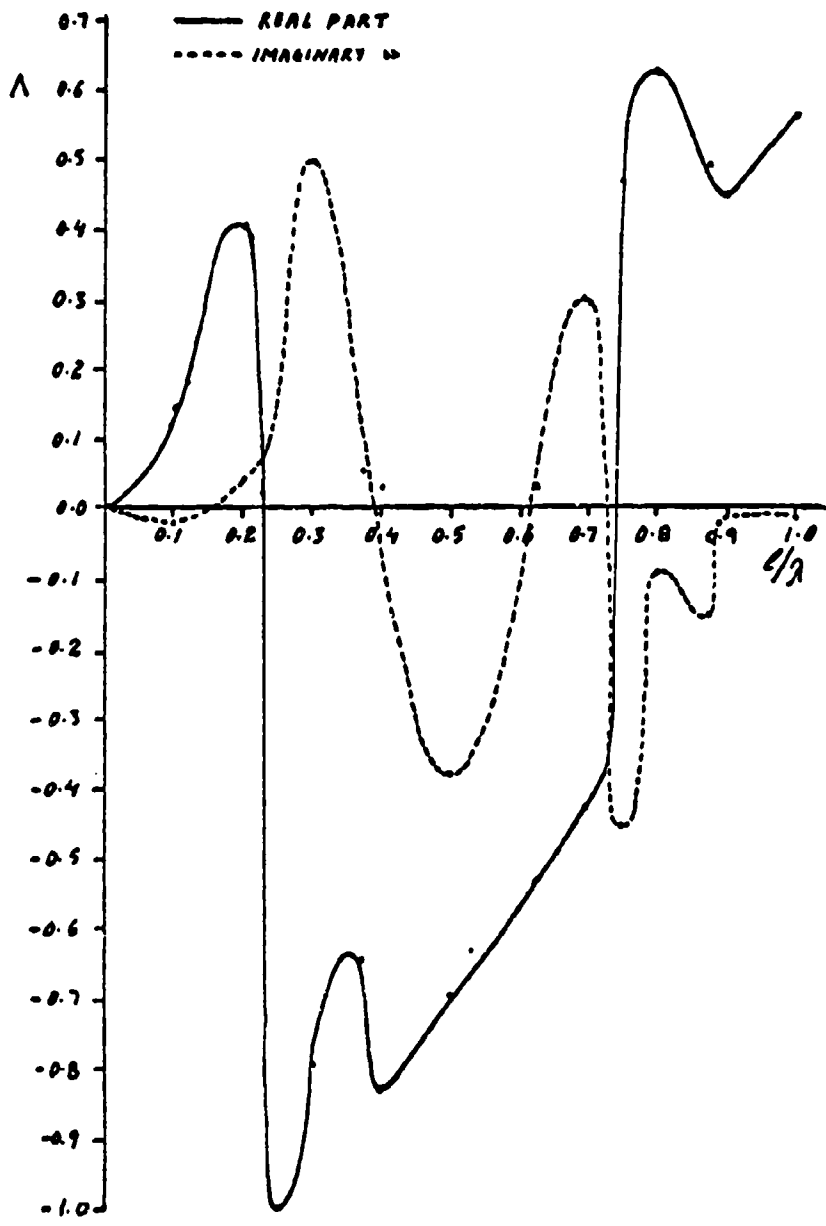


Fig. 7. Graph of the function Λ .

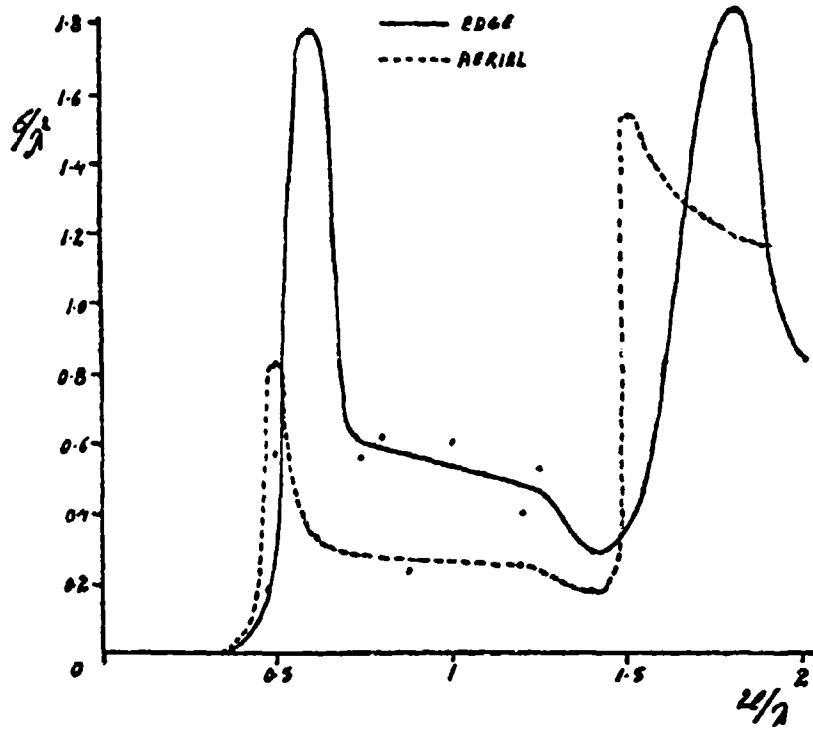


Fig. 8. Back scattering cross-section of the front edge and of a thin wire aerial.

section of wires. Attempts to measure the back scattering by standing wave methods were inconclusive due to the disturbance of the field by surrounding objects.

(5) TRAVELLING WAVES ON THE SHEET

5.1. Surface waves on elliptic cylinders

The travelling waves on the sheet will be analysed by considering them as the limiting case of surface waves on elliptical cylinders. Measurements of the magnetic field above the surface of a thin sheet covered with dielectric confirm the existence of surface waves whilst the field distributions across an elliptic cylinder have the same form as the measured distributions.

An elliptic cylinder of finite conductivity can support both E and A type modes. The excitation of these modes is illustrated in Figure 9a. In (a) the incident electric field is in the direction of the major axis. At points on the surface there are normal and tangential components of E and H. The tangential component H_t will excite TE or H type waves in addition to TM or E type waves. For the E wave the H_t components on the upper side of the cylinder are in anti-phase whilst for the H wave the components of H_n are in phase.

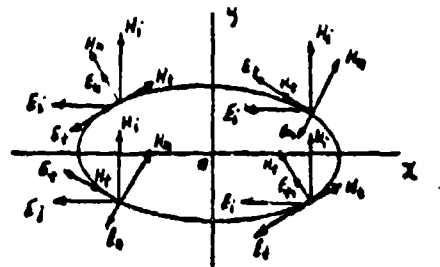
The coordinate system of the elliptic cylinder is shown in Figure 9b. For an incident electric field in the x or $\theta = 0$ direction analysis of the surface wave fields gives

E modes

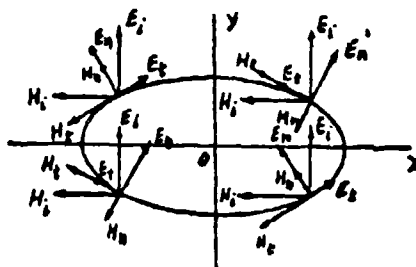
$$\begin{aligned}
 E_z &= A_1 \frac{\cos \theta}{\cosh \mu} e^{-j\beta z} \\
 E_\mu &= A_1 \frac{j k}{\omega^2} \cdot \frac{1}{2} \frac{\sinh \mu}{\cosh^2 \mu} \cos \theta e^{-j\beta z} \\
 E_\theta &= A_1 \frac{j k}{\omega^2} \cdot \frac{1}{2} \frac{\sin \theta}{\cosh \mu} e^{-j\beta z} \\
 H_\mu &= -A_1 \frac{j \omega \epsilon}{\omega^2} \cdot \frac{1}{2} \frac{\sin \theta}{\cosh \mu} e^{-j\beta z} \\
 H_\theta &= A_1 \frac{j \omega \epsilon}{\omega^2} \cdot \frac{1}{2} \frac{\sinh \mu}{\cosh^2 \mu} \cos \theta e^{-j\beta z} \\
 H_z &= 0
 \end{aligned}
 \tag{14}$$

with surface impedance

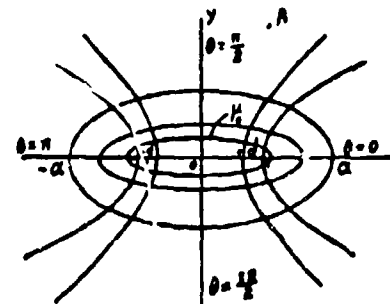
$$\begin{aligned}
 Z_E &= \left(\frac{E_z}{H} \right)_\mu = \mu_0 \\
 &= \frac{j \omega^2 1}{\omega + \tanh \mu_0}
 \end{aligned}
 \tag{15}$$



(a)



(b)



(c)

Figure 9. Analysis of the incident field on an elliptical cylinder for (a) E field along the major axis, (b) H field along the major axis, and (c) coordinate system on elliptical cylinder.

and H modes

$$\begin{aligned}
 H_x &= B_1 \frac{\cosh \mu}{\cosh \mu} e^{-\beta z} \\
 E_y &= B_1 \frac{j\omega\mu_0}{\omega} \frac{1}{\cosh \mu} e^{-\beta z} \\
 E_z &= -B_1 \frac{j\omega\mu_0}{\omega} \frac{1}{\cosh \mu} \cosh \mu e^{-\beta z} \\
 H_y &= B_1 \frac{j\beta}{\omega} \frac{1}{\cosh \mu} \cosh \mu e^{-\beta z} \\
 H_z &= B_1 \frac{j\beta}{\omega} \frac{1}{\cosh \mu} e^{-\beta z} \\
 E_x &= 0
 \end{aligned} \quad (16)$$

with surface impedance

$$\begin{aligned}
 Z_{11} &= \left(\frac{E_y}{H_z} \right)_{\mu = \mu_0} \\
 &= \frac{-j\omega\mu_0 \tanh \mu_0}{\omega} \quad (17)
 \end{aligned}$$

These solutions may be combined to give a composite E-H wave.

Measurements on elliptic cylinders of H_0 and H_z were made both across the cylinder and along the cylinder, with the incident E field along the major axis. These measurements are shown in Figures 10a, b, c, d. The measurements show that a composite E-H surface wave field is set up on the cylinder.

3.2. Surface Wave Measurements on Rectangular Sheets

To confirm the existence of surface waves of both E and H type over rectangular sheets the form of decay of the fields above the surface has been measured. The spread of the field above the surface depends on the surface reactance and to confine the field sheets with dielectric coating have been used in these measurements. The decay of the H_x field was measured over a sheet covered with 1.25 cm. of distrene, whilst the H_z component was measured over a sheet covered with a thickness of 1 cm. of silicone rubber. The measured decay rates are shown in Figures 11a and 11b. The fields fall off as $e^{-\alpha y}$ where for the H_x component over the distrene covered sheet $\alpha = 0.274/\text{cm.}$ and for the H_z component over the silicone rubber covered sheet $\alpha = 0.92/\text{cm.}$

(c) BACK SCATTERING FROM THE SHEET

The back scattering cross-section was defined in equation 11. For the whole sheet this has been calculated as the sum of two contributions, that from currents in the front edge and that from the currents on the surface of the sheet. Due to the finite length of the

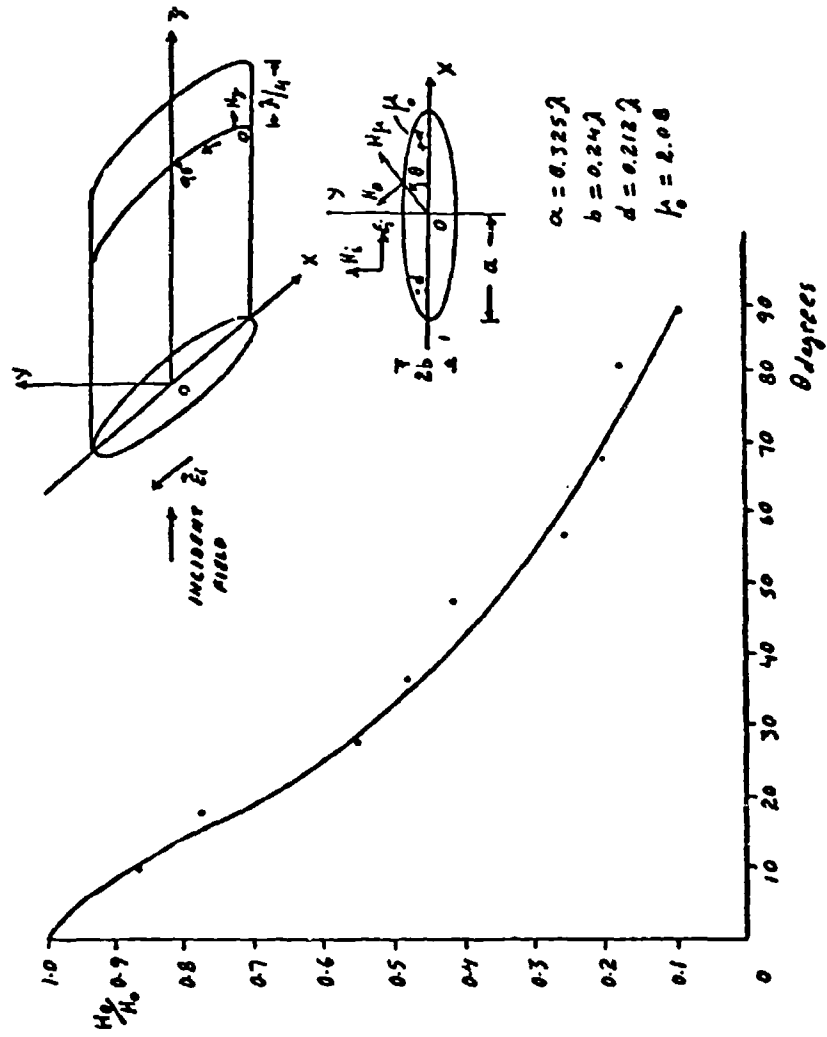


Fig. 10a. Measurement of the H_0 component from 0° to 90° .

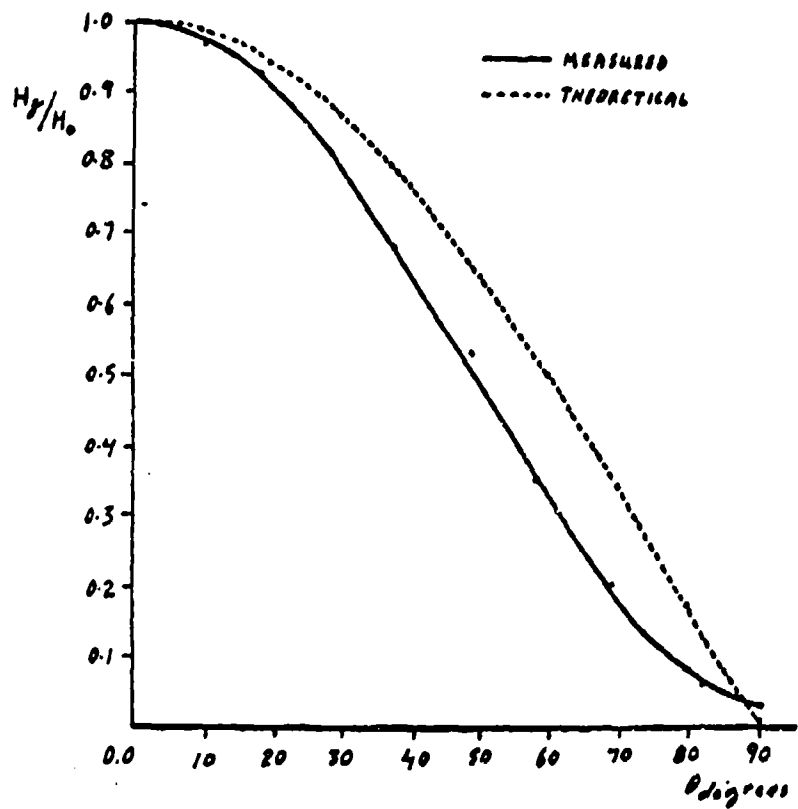


Fig. 10b. Measurement of the H_2 component.

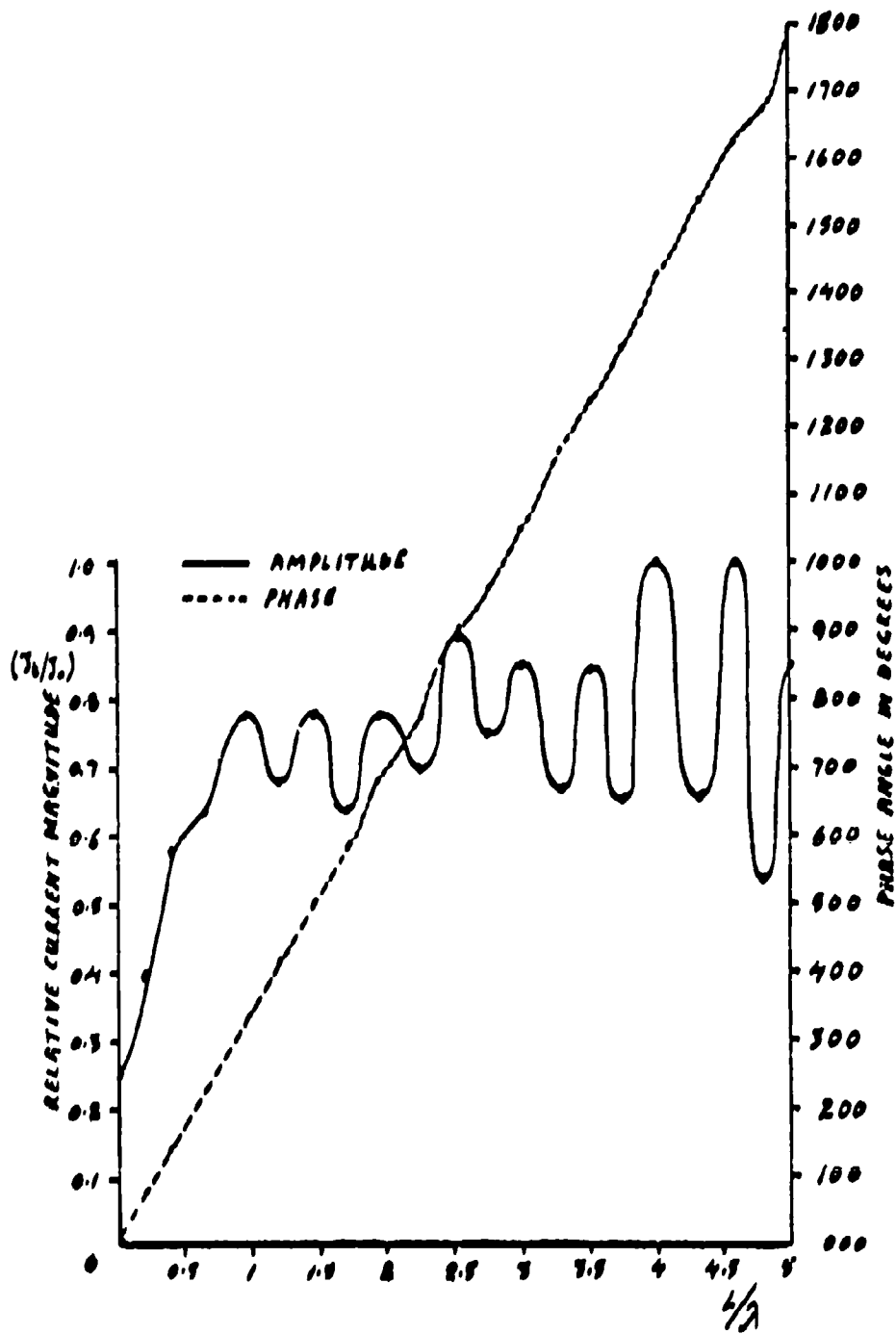


Fig. 10c. Amplitude and phase distribution of the transverse current along the surface of an elliptical cylinder.

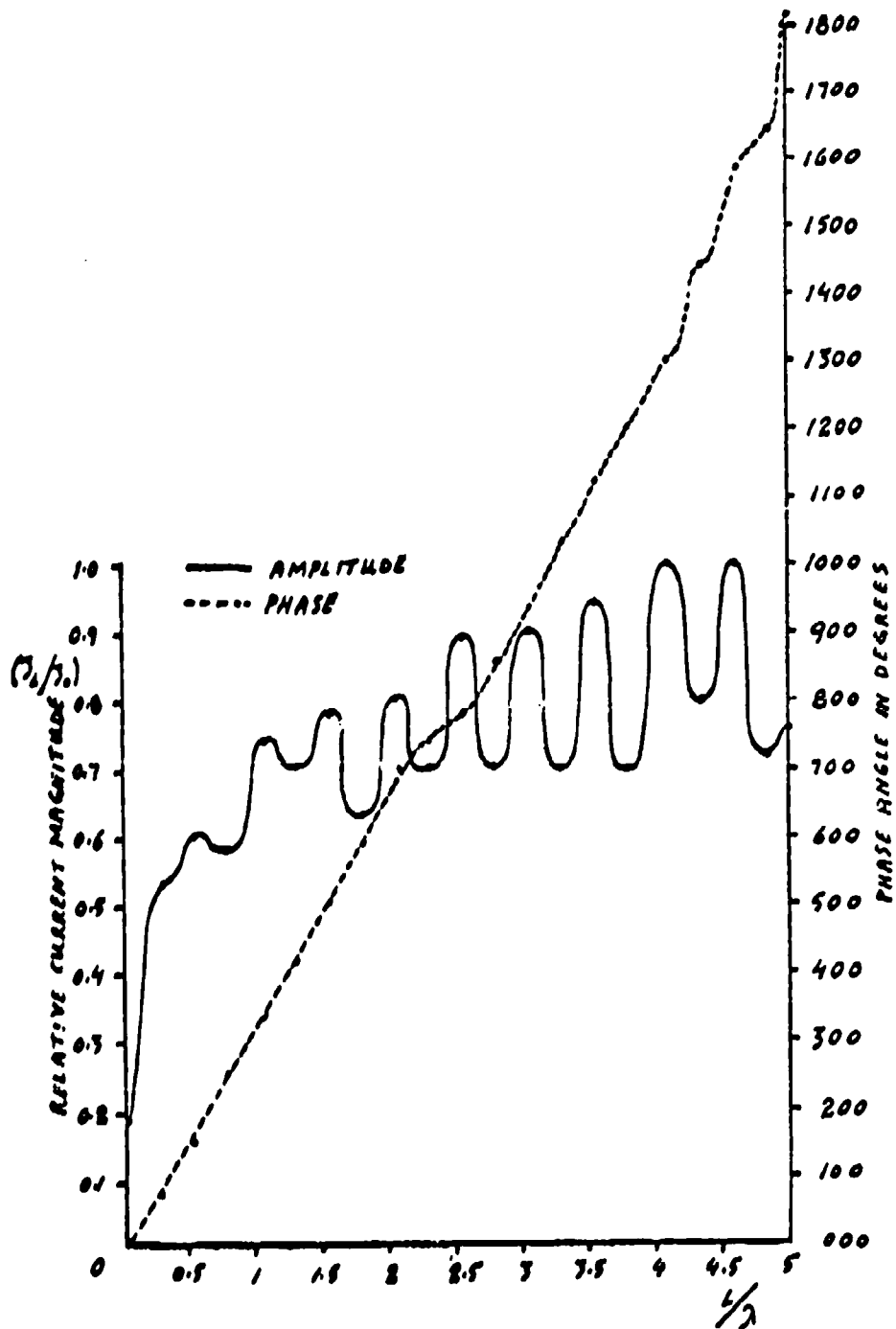


Fig. 10d. Amplitude and phase distribution of the longitudinal current along the surface of an elliptical cylinder.

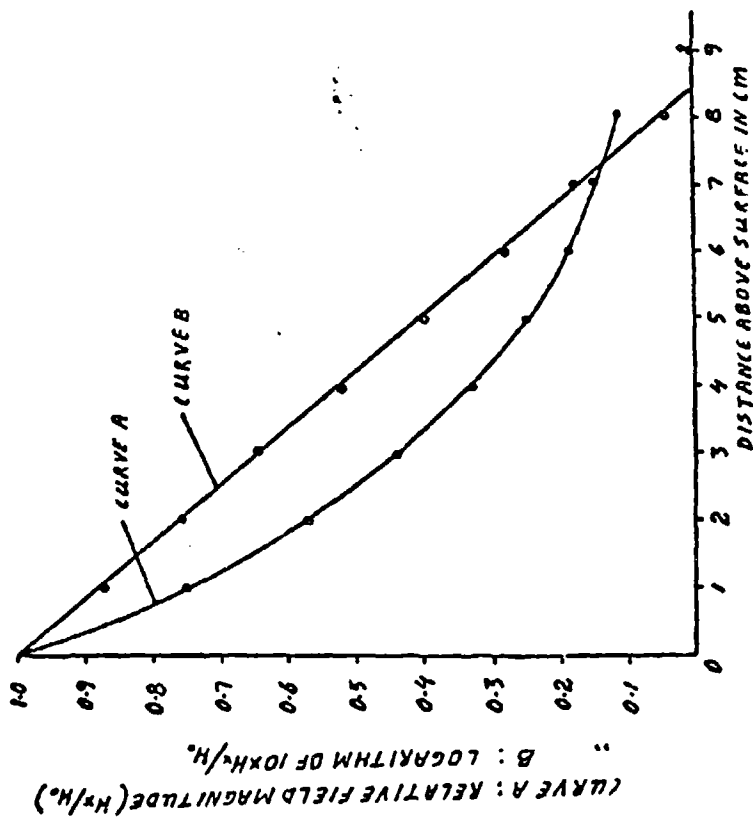
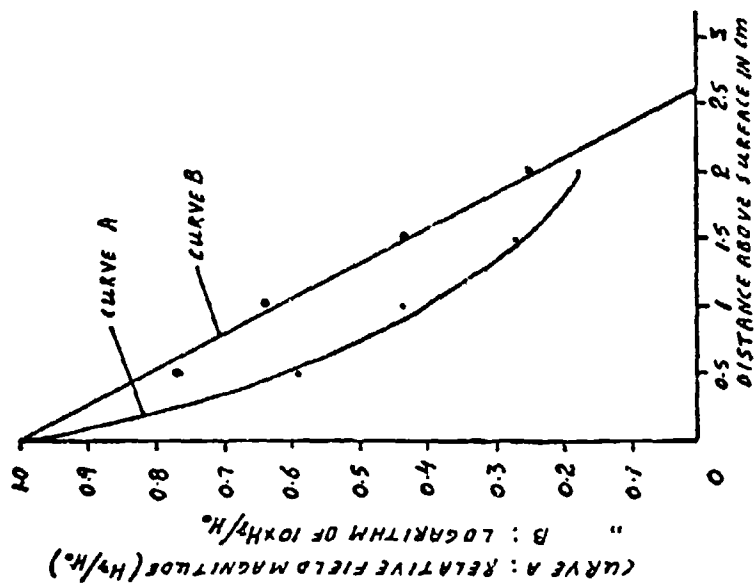


Fig. 11. Decay of H_0 and H_2 above dielectric coated metal plates.

sheet there are travelling waves in both directions on the sheet. The wave reflected at the wave end and travelling back towards the transmitter can contribute towards the total back scattering cross-section. As in the case of the front edge current the back scattering cross-section is calculated from the scattered field. This time the field is due to the currents on the surface of the sheet

$$E_s = \frac{j\eta k}{4\pi} \frac{e^{-jkR}}{R} \iint_S I_t e^{jkz} dz \quad (18)$$

The phase change along the sheet is given by e^{jkz} as the backward travelling wave is being considered. From this value of scattered field the power flux density in the backwards direction can be calculated and the corresponding total reradiated power if the power flux density is assumed constant around the scatterer. Then the back scattering cross-section can be calculated from

$$\sigma = \frac{\text{Equivalent reradiated power}}{\text{Incident Poynting vector}} \quad (19)$$

As both parts of the scattering cross section are evaluated taking the front edge as reference they may be added to give the total scattering cross-section.

When calculating the magnitude of the currents the coupling between the incident field and the waves on the sheet must be known. This has been found experimentally from the measured amplitude distribution and from the measurements of Hey and Senior.⁽⁶⁾ Taking the measured values for a sheet 6.7λ long the constant B, coupling factor, can be found. In practice this value is not constant for short lengths of sheet as the current takes a few wavelengths to build up to a steady value and for short lengths values of B(L) appropriate to the length of sheet may be derived from the measured amplitude distribution. However from the one pair of experimental measurements the scattering cross section can be derived for other lengths of sheet as is shown in Figure 12

(7) CONCLUSION

The measurements made have shown that the currents on rectangular sheets can be considered in two parts, the front edge currents and currents due to travelling waves on the sheet. These travelling waves can have the form of surface waves and the theoretical work on elliptic cylinders shows the current distribution to be expected on flat sheets. From the measured values of current the effective back scattering cross-section of sheets of various lengths can be calculated.

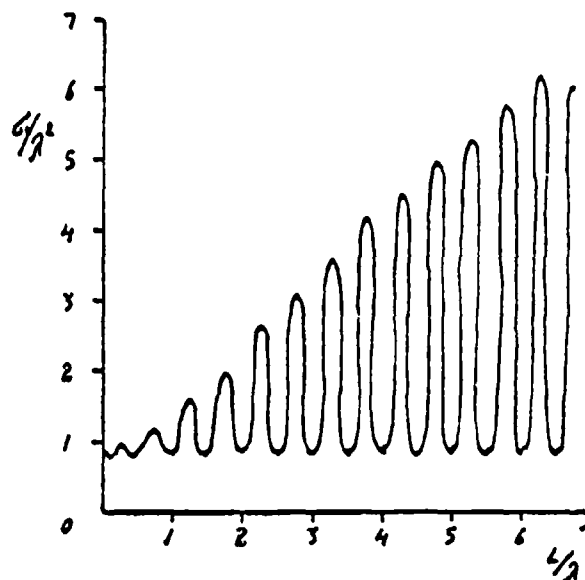


Fig. 12. Back scattering cross-section of metal plates derived theoretically.

ACKNOWLEDGEMENTS

This work has been supported by the Ministry of Aviation, Royal Radar Establishment, Great Malvern, England, and the work has been carried out in the laboratories of the Department of Electrical Engineering, University College London. The authors thank Professor H.M. Barlow for his interest and for the use of the laboratory facilities, and Professor J. Brown for helpful discussions on this work.

REFERENCES

1. W. P. R. King & T. T. Wu, *The Scattering and Diffraction of Waves*, Harvard University Press. 1959.
2. C. T. Tai, "Electromagnetic Back Scattering from Cylindrical Wires." *J. App. Phys.*, 23, 1952, p. 909.
3. P. Magoulas, *A Study of Current Distribution on the Surface of Conducting Sheets in a Microwave Field*. Ph. D. thesis, University of London 1963.
4. C. B. Dunn & W. P. R. King, *Measurement of Surface Current and Charge Distributions on Metal Surfaces at Microwave Frequencies*, Tech Report No. 71. N5, ORI-76, Sept. 1949.
5. J. S. Hey & T. B. A. Senior, "Electromagnetic Scattering by Thin Conducting Plates at Glancing Incidence," *Proc. Phys. Soc.*, 72, 1958, p. 981.

CW MEASUREMENTS OF AN ECHO II
BALLOON IN THE NEAR ZONE

R. K. Ritt
Group Department Head, Applied Sciences
A. W. Wren, Jr.
Group Department Head, Florida Operations
Conductron Corporation

INTRODUCTION

During the months of June and July, 1963, Conductron Corporation performed radar reflectivity measurements on a full-scale Echo II balloon at the main dirigible hangar, Lakehurst Naval Station. The problems connected with efficiently instrumenting for CW measurements in a near zone situation and the treatment of the data were unique and in this paper, we briefly describe the measures taken.

DESCRIPTION OF MEASUREMENT PROCEDURE

A scaffold, 48 feet high, was erected in the Lakehurst NAS main dirigible hangar. Upon this scaffold was constructed a wooden track, 86 feet in length. The track formed a circular arc, 100 feet from the surface of the balloon, which when inflated, had a radius of 67.5 feet. The angle subtended by the arc was 30° . Figure 1 illustrates the relative position of the inflated balloon, the scaffolding, and the hangar interior. Figure 2 illustrates the plan view of the relative positions of the balloon and the scaffolding. At either end of the track was located two standard gain horn antennas, one L-band and one C-band. They were mounted back to back so that by a rotation, either one could be made to point at the balloon, aligned along the balloon radius. These horns were the transmitting antennas, being connected, respectively, to a 1.71 KMC and a C-Band CW source. The sources were located on a platform mounted just beneath the track. A small wooden cart was constructed to move along the track. On the cart, similarly to the transmitting horns, were mounted a third pair of horns. These served as receiving antennas, and were connected to a Scientific Atlanta receiver, located on the deck of the hangar. The coordinates of the recorder chart were db vs. angle. The cart was motor driven, and its position on the track was synchronized to the motion of the recorder chart, so that the angular position of the cart could be made to coincide with the recorded position on the chart. The cable from the receiving antenna to the receiver was slung so that constant cable length could be maintained, independently of cart position. Figure 3 is a sketch of the physical arrangements.

Switching was provided so that all changes of electrical connections and positioning of the receiver cart could be controlled from a console which was constructed and located adjacent to the receiver. Rotation of

800'

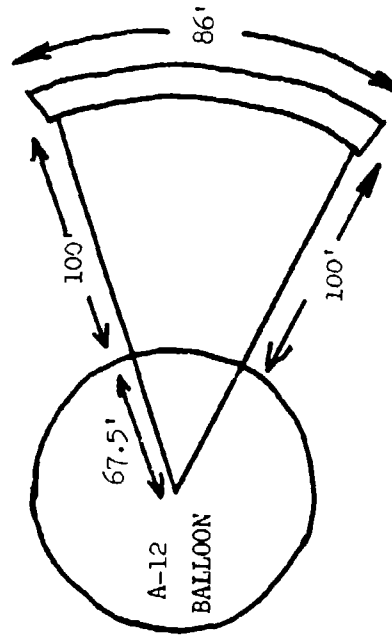


Figure 1 Schematic (Not Scale) Representation of RF Equipment Mounting Relative to the Balloon. An 86' track was constructed on top of a 50' scaffold. Transmitting antennas were located at either end of the track and a moveable cart containing receiving antennas had its position synchronized to the receiver console. Receiver was located on the ground. RF sources were mounted on a platform suspended from and directly below the track (see Figure 3).

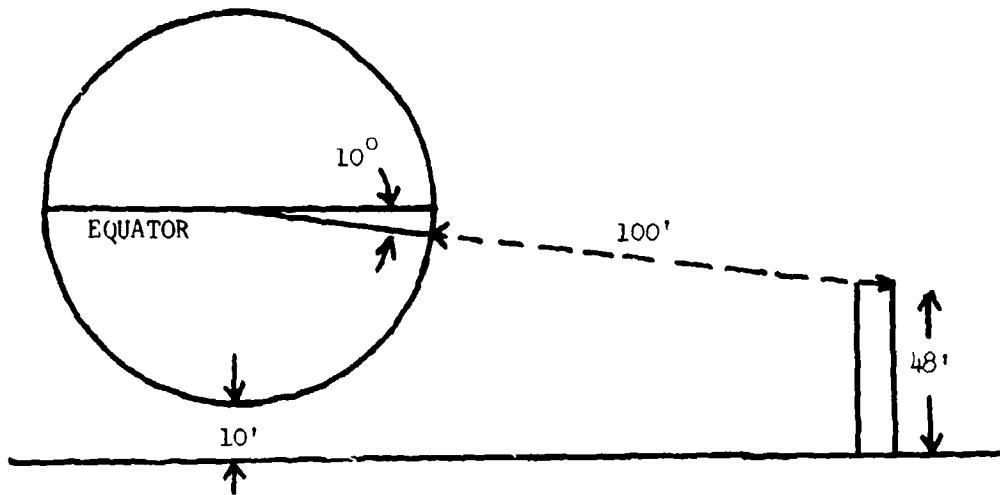


Figure 2 (Not Scale) Plane View of Scaffold-Balloon Configuration. Viewing Aspect for 10° South of Equator

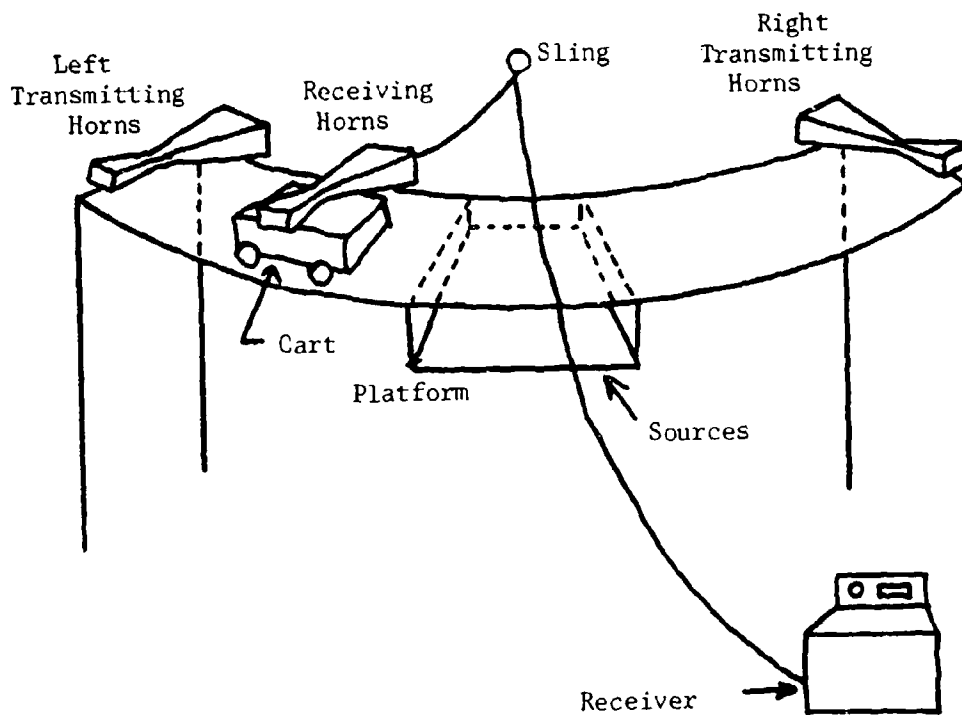


Figure 3 Sketch (Not Scale) of Scaffold Antennas and Receiver Arrangement

the horns was performed by technicians who were located at either end of the track. Tuning and monitoring of the RF sources was performed by a technician located on the source platform. The mounting of the horns was constructed so that axial rotation could be performed, permitting change of polarization.

One hundred feet from the scaffold and on the opposite side from the balloon, a tower was erected, atop of which was placed a flat calibration plate whose position could be remotely controlled and synchronized. During calibration runs the horns were aligned in the direction of the flat plate. Calibrations were performed at 5.85 and at 1.71 KMC. Prior to a test sequence, the C-Band horns were aligned in the direction of the flat plate, with the receiver cart adjacent to the left transmitting horn. All horns were at vertical polarization. The 5.85 source was connected to the left transmitting horn, the flat plate rotated, and a flat plate pattern run off on the recording paper. The voltage source was then connected to the receiver through an attenuator and adjusted so that the receiver pen coincided with the flat plate maximum. A straight line pattern, using this attenuator setting was run. The right transmitter was then connected, a new flat plate pattern recorded, and its maximum compared to the straight line pattern. The attenuator setting was then readjusted so as to lie midway between the two flat plate maximum. This adjustment was maintained throughout the test sequence, and used as the calibration level of measurements at 5.85 and 5.65 KMC. Its nominal value at 5.65 was obtained by computation. The L-Band system was similarly calibrated. At the conclusion of a test sequence, the stability of the source was tested against a flat plate run. For no test sequence was there observed a change in the calibration level.

A test sequence was performed in the following steps:

1. Upon being notified by the test director that the balloon had been inflated to a given pressure level, which was to be maintained throughout the test sequence, the L-Band system was connected and the horns, all polarized vertically, were aligned on the balloon, the receiver cart adjacent to the right transmitter.
2. The right transmitter was connected, and the cart moved to the left, the signal level being recorded.
3. When the receiving horn reached the left most position, the left transmitter was connected, and the receiving horn run to the right. Simultaneously the right transmitter was rotated to horizontal polarization.
4. Upon reaching the right most position, the right transmitter was connected, the receiver run to the left, and the left transmitter rotated to horizontal.

5. Upon reaching the left most position, the left transmitter was connected and the cart run to the right.

6. Upon reaching the right most position, the receiving horn was rotated to horizontal, the right transmitter connected, and the cart run to the left.

7. Upon reaching the left most position, the left transmitter was connected, and the cart run to the right.

8. The recording paper was then calibrated with the secondary standard.

These steps were then repeated for 5.65 and 5.85 KMC. In this fashion, at each frequency, patterns were obtained, which for simplicity, were successively labeled in the following manner:

TRANSMIT RIGHT	VV
TRANSMIT LEFT	VV
TRANSMIT RIGHT	HV
TRANSMIT LEFT	HV
TRANSMIT RIGHT	HH
TRANSMIT LEFT	HH

For any transmit position, the bistatic angle increased from 0° to 30° . The "specular" angle, defined as the bisector of the bistatic angle, increased from 0° to 15° . If the specular angle were redefined to be the angular position on the balloon corresponding to the specular ray, letting, for convenience, the right most position correspond to 0° , then for TRANSMIT RIGHT, the specular angle increased from 0° to 15° , and for TRANSMIT LEFT, it decreased from 30° to 15° .

The balloon was constructed of adjacent gores, each subtending an angle of $180^{\circ}/53 \sim 3.4^{\circ}$. The sector of the balloon corresponding to $0^{\circ} - 15^{\circ}$ contained two adjacent reinforced gores; therefore, the patterns corresponding to TRANSMIT RIGHT represent a specular angle which passes over the reinforced gores, and those corresponding to TRANSMIT LEFT, a specular angle which does not pass over the reinforced gores.

BACKGROUND LEVELS

The radar cross-section of a conducting sphere, 67.5 feet in diameter, is 1335 m^2 , or $31.2 \text{ db} > \text{m}^2$. Following usual practice in cross-section measurements, it was felt that to validate the measurements, the background levels must be maintained at least 10 db and preferably 20 db below this nominal value. The antennas being located 167.5 feet from the center of the 67.5 foot (radius) balloon, the balloon subtended an angle of 44° of the antenna beam. Antenna patterns of the standard gain horns were

measured at the Conductron Range. At 22° , the poorest of the horns (in terms of beamwidth) had a power gain of -12 db relative to its peak. Therefore, any power radiated past the balloon and reflected from the back wall of the hangar was, automatically, 12 db below the specularly reflected power. The background levels in the hangar were found, prior to balloon inflation, by mounting a transmitter on a crane, and transmitting from the nominal location of the center of the balloon. Receiving antennas were also mounted on cranes and moved along the planned position of the receiver track. The data was calibrated and the signal power received was found to be 20 to 30 db below the nominal return from the balloon.

A more serious background effect was direct cross-coupling between the transmitting and receiving antenna. In preliminary tests, there was superimposed upon the cross-section pattern, a sinusoidal oscillation which decreased as the bistatic angle increased. This oscillation occurred in both frequency bands. The period of the oscillation was consistent with side lobe coupling, since the maxima and minima occurred when the antenna separation was such that postulated sidelobes would be, respectively, in and out of phase. In any event, dielectric absorber sheets were placed next to the transmitting antennas, shielding them from the receiving antennas. The result was to eliminate completely the apparent coupling at C-Band, and to reduce it to a maximum of 1.5 db at L-Band. It was not felt that this last residual coupling compromised the data because it was clearly identifiable, and could be taken into account in the analysis and reduction task.

DATA CORRECTION

Each calibration consisted of four measurements. As noted above, a secondary source was adjusted to locate the receiver pen midway between two flat plate maxima before each test series and compared to two flat plate maxima after each test series. Using all of the calibrations so obtained, the mean calibration level at L-Band was 27.5 db and 36.7 db at C-Band. At both bands, the standard deviation was less than $1/2$ db.

Because the antennas were located in the near zone of the balloon, it was necessary to apply the near zone correction to the data. In the next section, the derivation of the near zone correction for a sphere is derived. Taking into account the fact that the bistatic angle 2α is less than 30° , the formula (12) of the next section shows that the measured magnitude of the bistatically scattered field is

$$E^{(m)} = E_0 \frac{a}{2r},$$

where E_0 is the magnitude of the incident field, a is the radius of the sphere, and r is the distance of the antennas from the center of the sphere. If the magnitude of the field backscattered by the calibration plate, is $E^{(c)}$, then

$$E(c) = \frac{1}{\sqrt{4\pi (r-a)^2}} \sqrt{\sigma(c)}$$

where $\sigma(c)$ is the cross section of the calibration plate. But then, the measured cross section $\sigma^{(m)}$ is

$$\sigma^{(m)} = \left(\frac{E^{(m)}}{E(c)} \right)^2 \sigma(c) = (\pi a^2) \left(\frac{r-a}{r} \right)^2.$$

Thus, the true cross section, πa^2 , is

$$\left(\frac{r}{r-a} \right) \sigma^{(m)};$$

for $r = 107.5$, $r - a = 100$

$$\pi a^2 = \left(\frac{r}{r-a} \right)^2 \sigma^{(m)} = (1.07)^2 \sigma^{(m)},$$

or

$$\pi a^2 = \sigma^{(m)} + 4.5 \text{ db.}$$

Thus, the near-field measured cross section must be increased by 4.5 db to obtain the true cross section.

The antenna taper, previously mentioned in connection with background levels has an effect upon the data. At the maximum bistatic angle, that part of the balloon which is most significant for scattering, i.e., that part in the neighborhood of the bistatic angle bisector, is at the 9.5° point of the antenna pattern, with a consequent power loss. The resulting data correction is:

- * 3 db, at L-Band, horizontal polarization,
- * 2.2 db, at L-Band, vertical polarization,
- * 5 db, at C-Band, horizontal polarization, and
- * 4 db, at C-Band, vertical polarization.

These corrections must be applied to the measured cross section at bistatic angles of 30°. For lesser bistatic angles, we interpolated linearly.

NEAR-ZONE BISTATIC SCATTERING BY A SPHERE

The high frequency near-zone bistatic scattering by a perfectly conducting sphere, for a receiver in the illuminated region is considered. For large values of ka , where k is the free space wave number and a is the radius of the sphere, the dominant contribution comes from the region of the specular point with the diffracted field being insignificant. In particular, for the present case ka is the order of 2×10^4 . The near zone

bistatic field can be obtained using the Kline-Luneberg asymptotic expansion, for which the analysis was worked out by Schensted¹ for plane wave incidence on bodies of revolution.

Bistatic Scattering for Plane Wave Incidence

Let a plane wave travel in the direction of the positive z-axis and polarized in the x direction. Consider a sphere of radius a, whose illuminated portion of the surface is given by

$$z = f(\rho) = a - \sqrt{a^2 - \rho^2} \quad (1)$$

where

$$\rho = \sqrt{x^2 + y^2}.$$

The scattered field has the form

$$\underline{E}^s = e^{iks} \sum_{n=0}^{\infty} \lambda^n \underline{E}_n \quad (2)$$

For the case on hand, only the first term given by $n = 0$ need be considered, since the remainder of the expression is the order of $1/(ka)$. The phase factor s is the distance along the incident ray from the $z = 0$ plane to the specular point, plus the distance along the scattered ray from the specular point to observer. See Figure 4; s is the distance $AB + BP$. The leading term of expression (2) has the form

$$\underline{E}_0 = \left(\frac{\rho}{h_\rho h_\phi} \right)^{1/2} (-\cos \phi \hat{\underline{\rho}} + \sin \phi \hat{\underline{\phi}}) \quad (3)$$

where for the observation point P, ρ is the distance of the specular point B from the z-axis. If the bistatic angle ABP is defined to be 2α , then we have

$$\rho = a \sin \alpha. \quad (4)$$

The angle ϕ associated with the position of the observer P is the angle between the $y = 0$ plane and the plane containing the point P and the z-axis. The values of h_ρ and h_ϕ can be found on using Equations 1, 4 and reference 1 to have the form

$$h_\rho = 1 + \frac{2\tilde{s}}{a \cos \alpha} \quad (5)$$

$$h_\phi = a \sin \alpha \left[1 + \frac{2\tilde{s}}{a} \cos \alpha \right]$$

where \tilde{s} is the distance BP. The vectors $\hat{\underline{\phi}}$ and $\hat{\underline{\rho}}$ have the form

$$\hat{\underline{\rho}} = -\sin \phi \hat{\underline{i}}_x + \cos \phi \hat{\underline{i}}_y \quad (6)$$

$$\hat{\underline{p}} = \cos 2\alpha [\cos \phi \hat{\underline{i}}_x + \sin \phi \hat{\underline{i}}_y] + \sin 2\alpha \hat{\underline{i}}_z$$

To complete the picture we need to find \tilde{s} in terms of the angle α and the distance r of the observer from the center of the sphere. It is seen from Figure 4, that

$$\frac{\tilde{s}}{\sin(\theta - \alpha)} = \frac{a}{\sin(2\alpha - \theta)} = \frac{r}{\sin \alpha} \quad (7)$$

Solving the last two equations for $\theta - \alpha$, we have obtained

$$\frac{\sin(\theta - \alpha)}{\sin \alpha} = -\frac{a}{r} \cos \alpha + \sqrt{1 - \left(\frac{a}{r}\right)^2 \sin^2 \alpha} \quad (8)$$

thus giving

$$\tilde{s} = a \left[-\cos \alpha + \sqrt{\left(\frac{r}{a}\right)^2 - \sin^2 \alpha} \right]. \quad (9)$$

Hence combining the above results we obtain

$$\begin{aligned} \sqrt{\frac{D(0)}{D(s)}} &= \left(\frac{\rho}{h \rho h \phi} \right)^{1/2} = \left[\left(1 - 2 \cos^2 \alpha + 2 \cos \alpha \sqrt{\left(\frac{r}{a}\right)^2 - \sin^2 \alpha} \right) \right. \\ &\quad \left. \cdot \left(-1 + \frac{2}{\cos \alpha} \sqrt{\left(\frac{r}{a}\right)^2 - \sin^2 \alpha} \right) \right]^{-1/2} \quad (10) \end{aligned}$$

Relationship Between Near-Zone and Far-Zone Results

Let a transmitter be located at point T (Figure 5). We shall assume that it is sufficiently far away from the sphere so that the specular region lies in the far-zone of the antenna. In addition we shall first assume that locally in the region about the specular point the incident wave can be treated as a plane wave. Let $E_0 \hat{\underline{i}}_x$ be the electric intensity of the incident radiation at the specular point.

The scattered field in the near zone and far zone will be given in Table I, for the following two polarizations. Specifically we shall consider vertical and horizontal polarization, where the incident radiation is respectively polarized perpendicular and parallel to the plane formed by the transmitter, the receiver (previously called the observer) and the center of the sphere. The scattered field for the horizontal and vertical polarization cases are found by setting $\phi = 0$, and $\phi = \pi/2$ respectively in Equations (3) and (6).

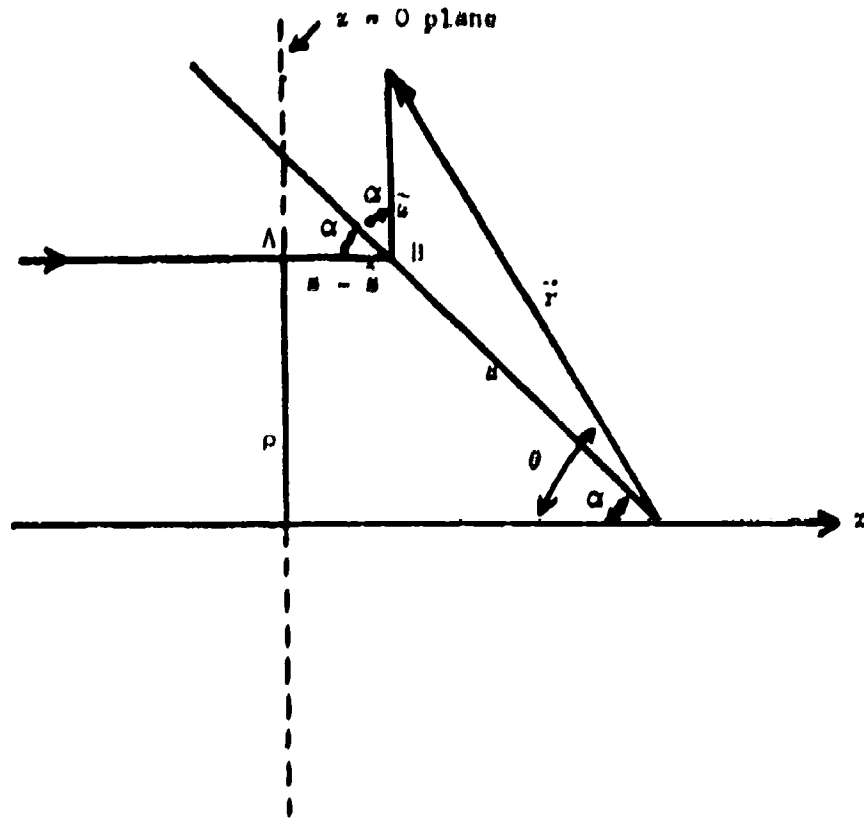


Figure 4 Relationships Among the Geometric Parameters Defined in "Bistatic Scattering for Plane Wave Incidence"

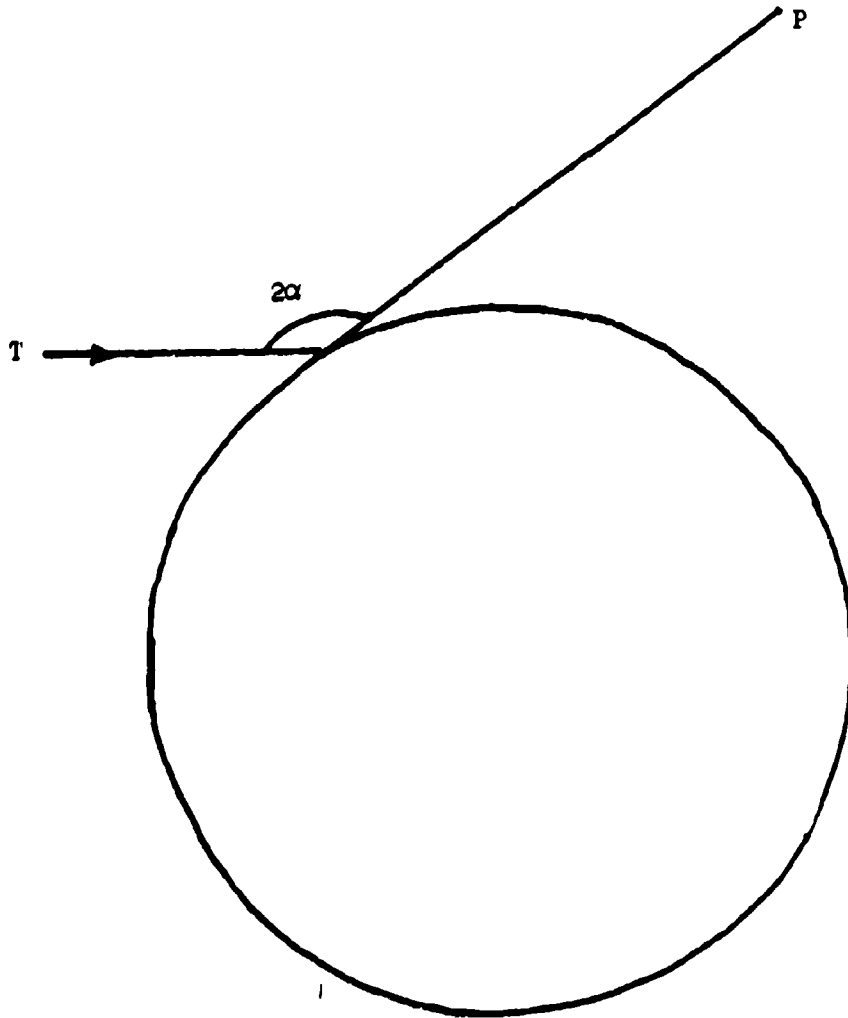


Figure 5 Bistatic Geometry

T = transmitter
P = receiver
 2α = bistatic angle

As seen from Table I, there are no cross-polarization terms. This is because the cross-polarization terms occur in the terms of the series (Equation 2) which have been neglected, and are of lower order by a factor 5×10^{-4} . The angle 2α is the far-zone bistatic angle. To extrapolate far zone results from near zone results this angle must be fixed.

We next come to the question of changing the assumption of plane wave incidence. A more accurate assumption with the transmitter at a finite distance from the sphere is to treat the incidence wave in the neighborhood of the specular point as a spherical wave. The main effect of this is to change the factor $\sqrt{D(O)/D(s)}$ given by Equation (10). For simplicity we will take transmitter and receiver to be the same distance r from the center of the sphere. The "divergence factor" $\sqrt{D(O)/D(s)}$ can be obtained from Fock².

$$\sqrt{D(O)/D(s)} = \frac{a}{2r} \left\{ \frac{\cos \alpha}{M \left(\frac{a}{r} \sin^2 \alpha + \cos \alpha M \right)} \right\} \quad (11)$$

$$\text{with } M = \sqrt{1 - \left(\frac{a}{r} \sin \alpha \right)^2}$$

Thus if a spherical wave is assumed incident, then Table I must be modified in that the near field magnitude (the second column) must be replaced by

$$E_0 \frac{a}{2R} \left\{ \frac{\cos \alpha}{M \left(\frac{a}{r} \sin^2 \alpha + \cos \alpha M \right)} \right\}^{1/2} \quad (12)$$

BIBLIOGRAPHY

1. Schensted, C. E., "Electromagnetic and Acoustic Scattering by a Semi-Infinite Body of Revolution," J. Appl. Phys., 26, 3, 306-308 (1955).
2. Fock, V. A., "Generalization of the Reflection Formulas to the Case of Reflection of an Arbitrary Wave from a Surface of Arbitrary Form", Z.E.T.F., 20, 961-970 (1950).

TABLE I
PLANE WAVE INCIDENCE

INCIDENT POLARIZATION	MAGNITUDE NEAR-ZONE SCATTERED FIELD	MAGNITUDE FAR-ZONE SCATTERED FIELD	POLARIZATION OF SCATTERED FIELD
Horizontal	$E_0 [(1 - 2 \cos^2 \alpha + 2 \cos \alpha L) \cdot (-1 + \frac{2}{\cos \alpha} L)]^{-1/2}$	$E_0 \frac{a}{2r}$	Horizontal
Vertical	Same as Above	Same as Above	Vertical

NOMENCLATURE

r = distance of transmitter from center of sphere

2α = far-zone bistatic angle

$$L = \sqrt{\left(\frac{r}{a}\right)^2 - \sin^2 \alpha}$$

APPLICATION OF SURFACE FIELD MEASUREMENTS TO RADAR CROSS SECTION STUDIES

T. B. A. Senior

Radiation Laboratory, The University of Michigan
Ann Arbor, Michigan

Introduction

When an electromagnetic wave is incident upon a body, a surface distribution of fields or currents is set up which then radiates to produce the scattered field. In some senses, therefore, the surface field is more fundamental than the scattered field; the latter is given in terms of the former by an integral which is relatively simple in the far zone, and consequently, for a given direction of incidence the complete (monostatic and bistatic) field can be derived from the surface field by quadratures. On the other hand, the reverse procedure is not quite so straightforward.

The surface field is the natural product of most integral equation methods for the solution of diffraction problems, and since it is usually more sensitive to minor shape (and material) perturbations than is the scattered field, it provides a stringent check on those approximate techniques which are our only way of treating all but the simplest shapes of body. In addition, however, it has considerable practical importance in itself, even when the ultimate objective is the determination of the scattered field. Many of today's problems in the radar cross section area are concerned with the reduction or enhancement of the field at large distances by modifications to the shape and/or material of the scattering object, and in cases where the field is not dominated by specular reflections, a detailed knowledge of the surface field and of how it is excited is an almost essential prerequisite to any scientific attempt at cross section control. It is certainly essential if near-optimum results are to be achieved.

During the last two years the Radiation Laboratory has given increased attention to the study of surface fields on selected shapes by extensions of the more standard theoretical methods involving physical optics, creeping waves, etc. and by direct measurement of the currents using probes. The latter approach has proved extremely valuable in these investigations, and is already filling a vital role in improving our theoretical tools for the prediction of scattering patterns. With its aid it is a relatively simple matter to discover the direct effect of minor modifications to the shape of a body, and it is expected to prove even more important in later applications to absorbing coatings. It may therefore be appropriate to describe the experimental facility as it exists at the moment, and mention some of the measurements which have been made.

Historical Survey

The use of probes to determine the fields excited on the surface of a conducting object is by no means new. As early as 1938 it was employed by Pippel and Baerner¹ to measure the currents induced by radio antennas on an aircraft structure, and similar work was carried out by Granger and Altman² and Granger and Morita³ soon after World War II. Since 1948 it has been widely exploited by the Cruft Laboratory of Harvard University and many of the improvements in probe design originated there. Reynolds⁴ and Dunn⁵ studied different forms of detection probes and measured the fields on flat conducting plates, and the latter author also considered the effect of elliptical polarization on loop systems. An extensive analysis of loop antennas was later published by King⁶ and still more recently Whiteside⁷ has examined the response of different types of probe to electromagnetic fields. The information provided by this last author is probably sufficient to design and construct any probe necessary for a surface field measurement.

One of the most difficult problems with a probe technique is to avoid stray pick-up in the wires leading from the probe to the detector, and if these wires are kept short the possibility of reflections from the associated equipment is introduced. An attractive way of avoiding both these problems is to use a ground plane and to cut a slot in the body along the trajectory to be followed by the probe. The latter is now below the surface and the lead wires can be taken from the inside of the body through the ground plane to the detector hidden underneath. This method was used by Morita⁸ to study linear antenna elements and a slight variation upon it was employed by Ribblet⁹ in his work on the 'infinite' circular cylinder and the parabolic reflector. Another application of the ground plane system was by Wetzel and Brick¹⁰, whose measurements of the surface field on the shadow portion of an elliptic cylinder confirmed the accuracy of the creeping wave approximation, but for two dimensional objects the parallel plate system becomes appropriate, and this was employed by Row¹¹ and, later, by Plonsey¹².

The obvious disadvantages of all these systems are the necessary restrictions on shape of body, direction of incidence and polarization, and none of them are consistent with a routine type of measurement which would assist in the analysis of scattering from 'practical' (and almost inevitably complex) shapes. One of the few attempts to measure surface fields directly was the limited investigation of flat plates at glancing incidence by Hey and Senior¹³. In some respects the present Radiation Laboratory work is a natural outgrowth of this, and perhaps the major accomplishment is the demonstration that surface fields on three dimensional objects can be measured under reasonably wide circumstances, and with a sufficient degree of accuracy to be of help in studies of scattering phenomena.

Experimental Facility

The facility is housed in a room 13 1/2 ft wide and 100 ft long but the entire operation is confined to a region 25 ft in length. The model to be measured is mounted on a styrofoam pedestal just in front of a shaped absorbing screen composed of high performance absorbing materials, and shielding the traversing mechanism for the probe.

The choice of frequencies has been influenced by two factors: the desire to measure models whose dimensions are comparable or larger than a wavelength, and the necessity of having probes very small in comparison with the wavelength if they are not to disturb the field unduly. The first of these forces one to the higher frequencies if the models are to be of reasonable physical dimensions and this in turn reduces the size of the probe. Ultimately the limit is provided by the difficulties of construction and handling of probes only a few mm in dimension, as well as by the accuracy of positioning, and all of our measurements so far have been carried out at L- and S-band frequencies. It is hoped to add a C-band capability at a later date.

The type of probe depends in part on the field component to be measured. A variety of different types have been investigated including a diode loop, two diodes forming a balanced dipole, and a simple shielded loop. This last has proved convenient for most of our measurements, and several versions have been constructed differing only in size. The latest has a loop 3 mm in outside diameter, which is probably somewhat smaller than the optimum for S-band. This is connected to a piece of rigid coaxial line (Coaxitube, manufactured by the Precision Tube Company) of outer diameter 0.03 in., with inner conductor of diameter 0.01 in. and glass wrap insulation. Because of the relatively high loss in a line of such small dimensions, only a 6 in. length is used and this is attached to a 12 in. length of larger (0.085 in.) diameter Coaxitube. These constitute the support mechanism for the probe. They are maintained in a vertical position perpendicular to the incident field polarization, and coupled at the upper end to a horizontal coaxial line which is coated to reduce surface wave effects. This last rests on a styrofoam beam and passes over the center of the absorbing screen to a vertical tower mounted on the probe positioner. The general arrangement can be seen from Fig. 1.

The mechanism for positioning the probe consists of two coupled horizontal motion lead-screw carriages operating at right angles to one another, and an associated elevating device. The coverage in the horizontal plane is 15 cm by 36 cm, and the latter dimension therefore represents the maximum length of model that can be traversed without repositioning on the pedestal. With this system the probe can be located within 0.2 mm of its intended position in a horizontal plane, but since the vertical alignment is not quite as accurate due to mechanical oscillations, the probe is usually placed in physical contact with the model. To ensure that no conduction currents will flow in this situation,

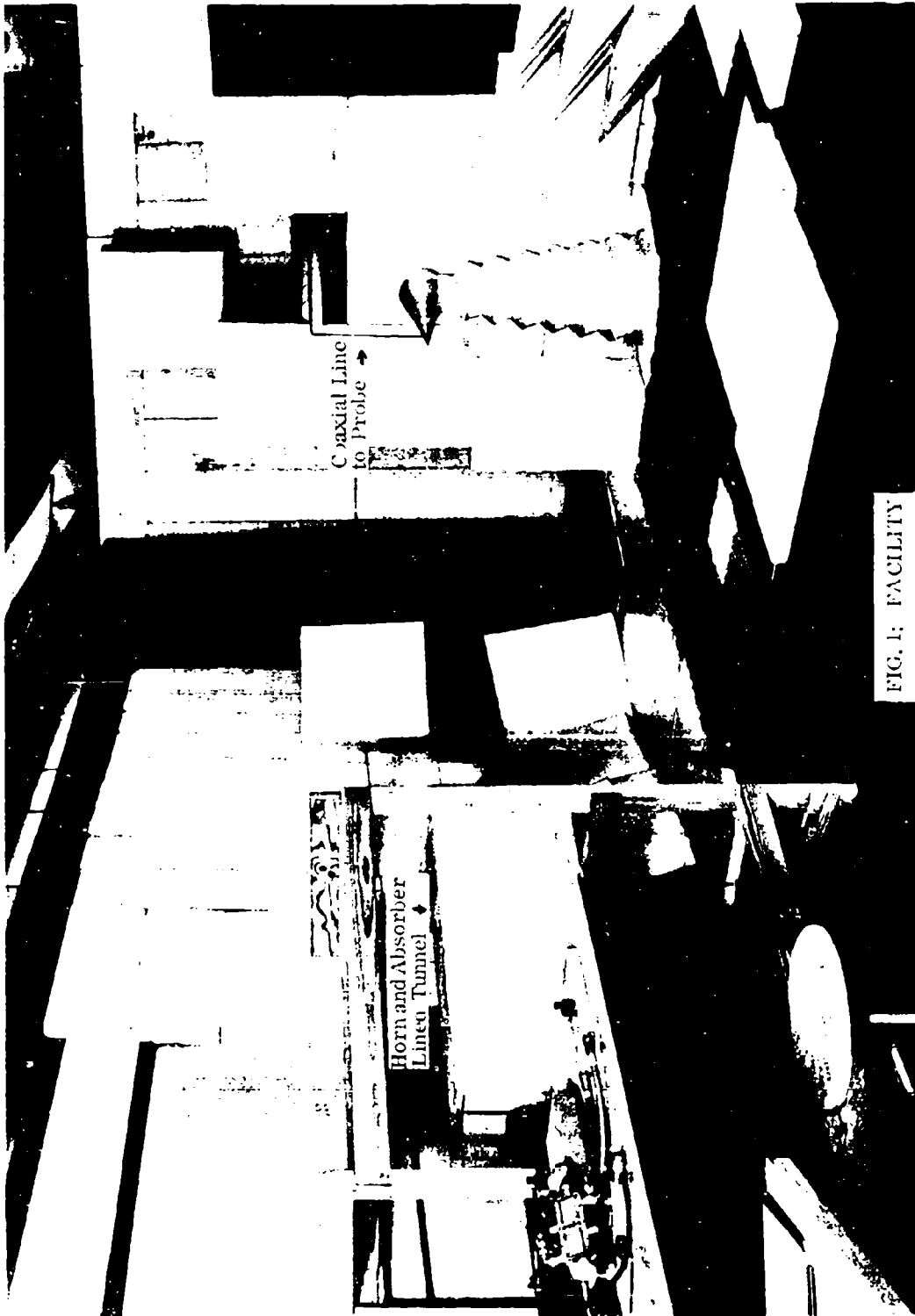


FIG. 1. FACILITY

a bead of epoxy resin is placed at the gap in the loop and filed down on the lower surface to leave a film a few mils in thickness.

The illumination is from a standard gain horn, and to cut down room reflections attributable to the side lobes, an absorbing tunnel 24 in. in length has been attached to the horn aperture. The distance to the center of the model is about 3.5 m, which is not sufficient to provide uniform excitation over the full length of some of the models that have been studied, and for the sphere discussed in the next section the incident field taper is theoretically 0.7db and has been measured as such. The effect can be seen in the data, but to increase the range would decrease still further the level of the signal fed to the receiver. At S-band this is already 80db below a milliwatt. The transmitted power is here some 300 milliwatts, produced by a klystron tube modulated at 1 Kc. The receiver was constructed in the Laboratory from low noise components and has an overall noise level 100db below a milliwatt. A block diagram of the S-band equipment is shown in Fig.2.

Data

In the year that this equipment has been in operation a variety of models has been investigated, and included amongst these are (i) thin wires of up to 3λ in length at end-on and near end-on incidence, (ii) flat plates at glancing incidence, (iii) thin cylinders for over 30 different lengths L spanning the range $0.36\lambda < L < 1.86\lambda$ and for all angles of incidence, but with concentration on broadside aspects, (iv) the same cylinders as in (iii) but with a cavity-backed slot at the center to produce a sequence of reactive loadings, (v) spheres and (vi) cone-spheres at nose-on incidence. It is obviously impossible to do more than give typical results here, and attention will be confined to amplitude⁺ data.

The work on the thin cylinders referred to in (iii) and (iv) above is described in detail by Chen and Liepa¹⁴. The cylinder was constructed so that one basic model was sufficient to embrace the full range of lengths by the insertion of extension pieces and rounded end-pairs of different sizes. The radius was 0.183 in. and all measurements were carried out at a frequency 1.088 Gc. Three samples of the data for broadside incidence on the unloaded cylinder are given in Fig. 3. The upper curve is for the first resonant length, $L = 0.426\lambda$, and the peak value of the current here has been used as the reference level for the amplitudes in the lower curves, in which $L = 0.887\lambda$ and 1.303λ .

Some data for a sphere taken at a frequency of 3.066 Gc is presented in Fig. 4. The probe trajectory is in the equatorial plane containing the incident electric vector, so that in the shadow the field is predominantly the major creeping wave component, and the central point on the rear of the sphere is

⁺ A phase measurement system is still in its trial stages.

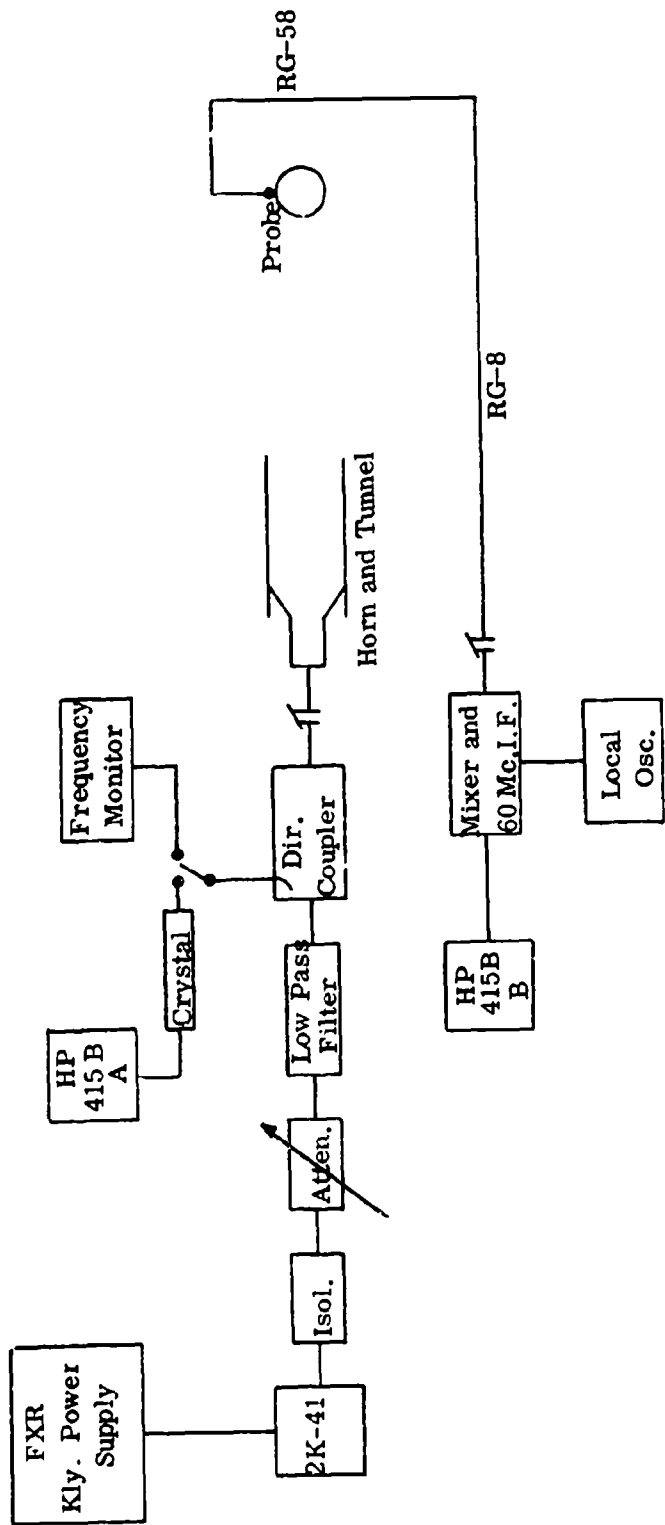


FIG. 2: BLOCK DIAGRAM OF THE S-BAND EQUIPMENT

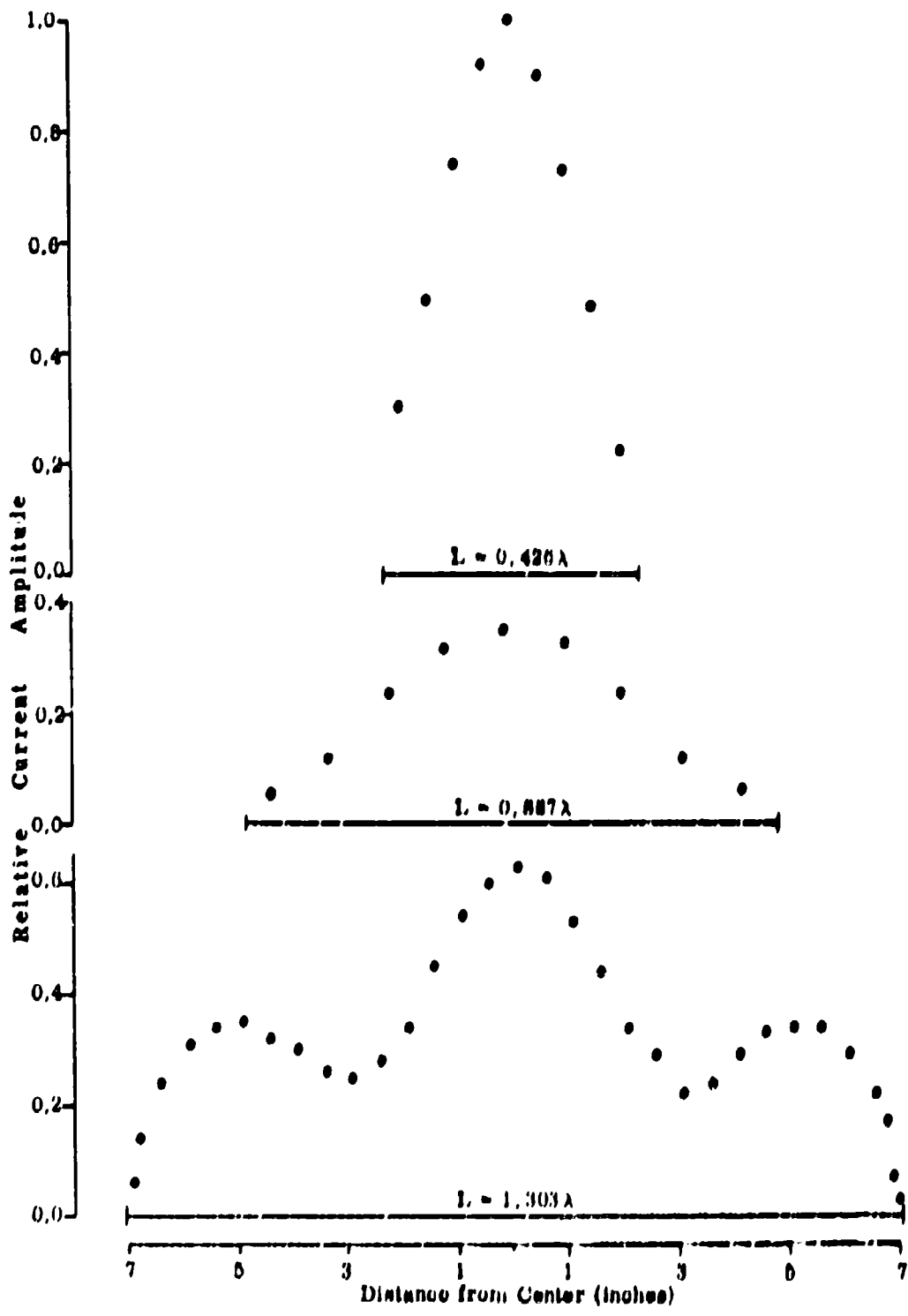


FIG. 3; MEASURED CURRENT AMPLITUDES FOR THIN CYLINDERS

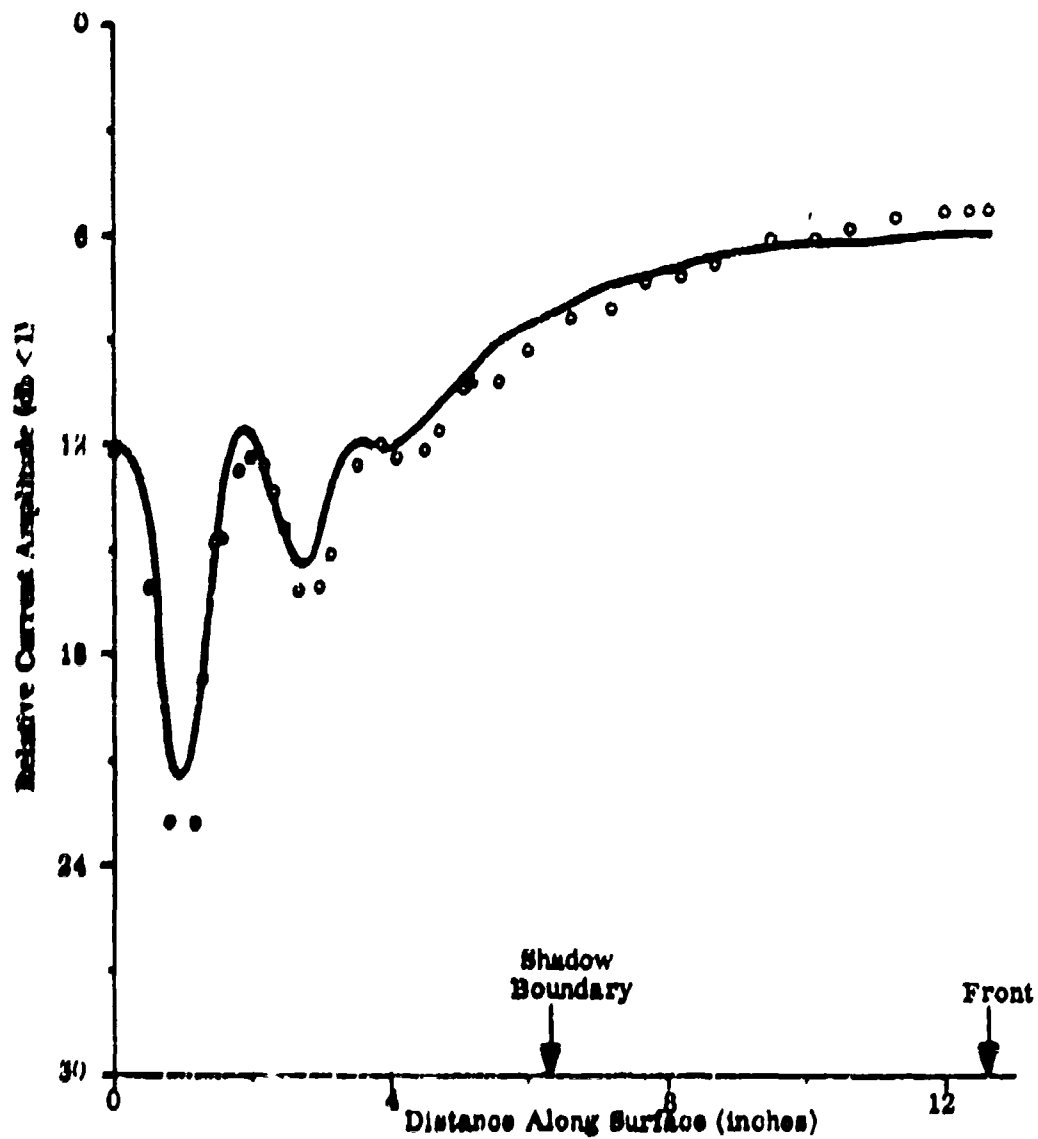


FIG. 4: MEASURED (●●●) AND THEORETICAL (—) CURRENT AMPLITUDES FOR SPHERE

the left-hand end of the horizontal scale. Also shown is the curve computed from the exact Mie series representation of the surface field, and it should be noted that this has been superimposed using the measured value of the incident field in the plane of the support rather than on a 'best fit' basis. The curves are everywhere within 1 db of one another, and the agreement becomes even better if the systematic discrepancy attributable to the incident field taper is subtracted.

Corresponding data for a cone-sphere with vertex angle 30° is shown in Fig. 5. The radius of the spherical cap is identical to that of the sphere used for Fig. 4, and direct comparison of the results now shows the enhancement of the creeping wave component previously deduced¹⁵ from measurements of the nose-on cross section. Its magnitude is such as to remove most of the discrepancy between theory and experiment for the nose-on cross section of a cone-sphere (see, for example, Blore¹⁶), and its origin has been determined. A detailed treatment of cone-sphere scattering, including measured data for both the far and surface fields, will be published shortly.

Acknowledgement

The author is grateful to Mr. V. V. Liepa for the construction and operation of the Facility described in this paper.

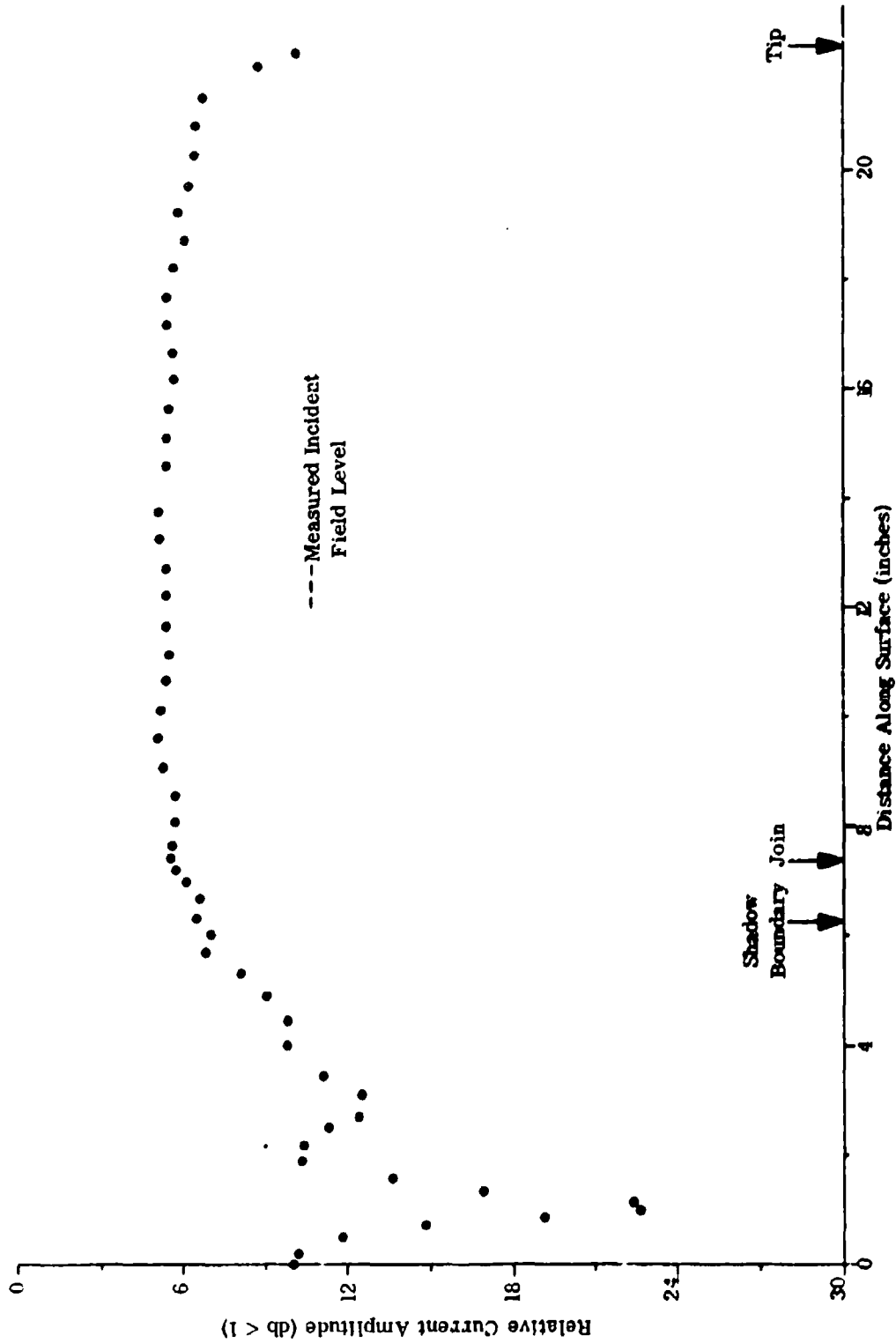


FIG. 5: MEASURED CURRENT AMPLITUDE FOR CONE-SPHERE

References

- 1 Pippel, K. and H. Baerner (1938) "Strom- und Spannungs-Verteilung auf Hoch-frequent Schwingender Flugzeugen," Forschungsbericht No. 915, Flugfunk-Forschungsinstitute, Germany; USAF Translation No. 511.
- 2 Granger, J. V. N. and N. G. Altman (1949) "Full-Scale Aircraft Antenna Measurements," Harvard University Cruft Laboratory Report No. TR-63.
- 3 Granger, J. V. N. and T. Morita (1951), Proc. IRE, 39, p. 932
- 4 Reynolds, D. K. (1948) "Surface-Current and Charge Measurements on Flat Flat Metal Sheets," Harvard University Cruft Laboratory Report No. TR-53.
- 5 Dunn, B. C., Jr. (1949) "On Response of Loops to the Electromagnetic Field," Harvard University Cruft Laboratory Report No. TR-73.
- 6 King, R. W. P. (1957) "The Loop Antenna as a Probe in Arbitrary Electro-magnetic Fields," Harvard University Cruft Laboratory Report No. TR-202.
- 7 Whiteside, H. (1962) "Electromagnetic Field Probes," Harvard University Cruft Laboratory Report No. TR-377.
- 8 Morita, T. (1950), Proc. IRE, 38, p. 898.
- 9 Ribblat, H. J. (1952) "Geometric-Optical Currents," Microwave Development Laboratories Final Report on Contract AF19(122)-167.
- 10 Wetzel, L. and D. B. Briok (1955) "An Experimental Investigation of High Frequency Current Distributions on Conducting Cylinders," Harvard University Cruft Laboratory Report SR-4.
- 11 Row, R. V. (1953), J. Appl. Phys., 24, p. 1448.
- 12 Plonsey, R. (1962). Trans. IRE-PGMMT, MTT-10, p. 214.
- 13 Hey, J. B. and T. B. A. Senior (1958). Proc. Phys. Soc., 72, p. 981.
- 14 Chen, K-M and V. V. Liepa (1964), "The Minimization of the Back Scattering of a Cylinder by a Central Loading," to be published in the Trans. IREK-PTOAP.
- 15 Senior, T. B. A. (1963) "Cross Sections of Nose Cones," The University of Michigan Radiation Laboratory Report No. 6212-1-F. CONFIDENTIAL.
- 10 Blore, W. E. (1963), Proc. IEEE, 51, 1. 1203.

THE TERRAIN SCATTERING PROBLEM*

Robert C. Taylor
Assistant Supervisor
Antenna Laboratory
Department of Electrical Engineering
The Ohio State University
Columbus, Ohio

INTRODUCTION

The basic problem in terrain scattering work is to determine the average radar cross section per unit area (σ_0) for all types of terrain at any frequency, incidence angle, bistatic angle, polarization, and any environment. In recent years the study of lunar and planetary surfaces through their scattering behavior has also become of importance. Thus the converse of the basic problem must be considered; the estimation of the physical properties of the surface from given values of σ_0 .

Two general approaches to the basic problem are to measure the radar cross section of all types of terrain under all conditions, or to calculate the radar cross section theoretically. It is obviously impossible to measure every possible type of terrain under all conditions. This limitation is even more serious for presently inaccessible extra-terrestrial surfaces. A purely theoretical approach which was not validated by experiment would also be of little value. Furthermore, for theoretical models of a surface to be developed, or validated from experiment, precise scattering measurements from controlled surfaces are required. Consequently a combination of experimental and theoretical methods must be used, in which the surfaces can be classified as to type (roughness, loss, etc.).

The first step in the solution of the terrain return problem is always the development of system and measurement techniques that will accurately determine the average radar cross section of terrain. This paper will be concerned with some of the problems encountered in making terrain return measurements, and will describe one practical system that has been found effective.

* The work reported in this paper was supported in part by Grant Number NaG-213-61 between The Ohio State University Research Foundation and National Aeronautics and Space Administration.

CHOICE OF SYSTEM

Airborne vs Land-based

Early work in terrain scattering measurements have emphasized the application of the measurements to the design of high resolution airborne radar systems. Many airborne scattering measurements were made because it had been thought that ground based measurements could not be extrapolated to the airborne case. It has since been shown that for many types of surface, this expectation was unjustified, as ground based measurements can be extrapolated to the airborne case with acceptable accuracy.¹

The main advantage of the ground based system is that it is possible to know exactly what kind of target area is being measured at any given time. This is quite difficult in the airborne system, due to the large area and heterogeneous nature of the surface being illuminated. In addition it is quite difficult to obtain an absolute calibration of the radar system, and the results are often quoted on a relative basis rather than absolute. The cost of obtaining airborne measurements is, compared to ground based measurements, several orders of magnitude greater.

SYSTEM REQUIREMENTS

General

The design of a radar system for terrain scattering measurements is in many ways quite different from the conventional radar systems used to measure the radar cross section of various types of aircraft, missiles, etc., through modelling techniques. This is especially true if the radar scattering is to be measured from natural surfaces, where the radar system must be brought to the target rather than the target brought to the radar, thus requiring the use of a mobile radar system.

Even when the measuring system is a mobile one, some care is necessary in setting up the experiment. It has been found from previous backscattering measurements that 5 fundamental parameters affect the magnitude and characteristics of the terrain return.² These parameters are surface roughness, polarization, complex dielectric constant, incidence angle, and frequency. Since it is not possible to measure the effects of all of these parameters at once, several

measurements of the same surface are required. In order to determine the effects of each individual parameter accurately, care must be taken to ensure that the exact same surface is being measured each time and that the area under investigation is homogeneous. This is more easily accomplished if only a small area of surface is illuminated by the transmitter, since large areas of homogeneous terrain with constant slope are not common.

It has been found from previous work that to obtain an average value for the radar cross section of the terrain requires the averaging of the return from many independent samples of the same terrain.³ This can be accomplished either by measuring many fixed samples of terrain and then averaging the measurements from each sample or by continually moving the transmitter and receiver with respect to the terrain and averaging while the measurements are being made. The latter is preferred since a large amount of effort and time is required to reposition the system for each sample of terrain, using the former method. In addition it has been found that greater accuracy is obtained from the continuous averaging method.

Sensitivity and Dynamic Range

From previous measurements it is known that minimum radar cross sections per unit surface area (σ_0) of -50 db have been measured for the backscattering from smooth surfaces near grazing, whereas the same surfaces near normal incidence exhibit normalized cross sections up to $\sigma_0 \approx +20$ db. These are average values and the instantaneous values may vary ± 10 db from the average. Thus a system dynamic range of at least 90 db is required.

Calibration

The calibration of the radar system is quite important especially if the radar scattering measurements are to be on an absolute basis (in terms of σ , σ_0 or α) rather than a relative basis. The results of the measurements can then be applied universally to any particular application. In addition it is important that the system calibration include the antenna to ensure greater accuracy.

Data Analysis

One problem that is universal in terrain scattering measurements is the data reduction. In many cases the results of the measurements

are not analyzed for days or even weeks. Errors in data taking or equipment malfunctions are not noticed until considerable data has been taken. Thus one important requirement is "instantaneous" data reduction, where the results of the measurements (σ , σ_0 , and α) on an absolute basis, can be checked as the measurements are being obtained.

Mobile CW Doppler Reflection System

Shown in Fig. 1 is a block diagram of the cw Doppler radar system. The system is operated at frequencies of 10, 15, and 35 KMC or any other frequency in this range by changing the RF section of the system. A reference signal is applied to the crystal detector by unbalancing the hybrid tee, thus introducing a small amount of transmitted power into the receiver arm. Because of the relative velocity of the terrain with respect to the antenna, the terrain return signal of constantly changing phase beats in the crystal mixer with the transmitted signal, producing an audio frequency signal. The signal is then amplified by the linear amplifier with variable pass bands to eliminate any undesired signals. The signal is then detected by the square law detector and fed to the electronic integrator and dc recorder. The time base of the integrator is variable and can average the return from the terrain up to periods of 5 minutes. The recorder measures the instantaneous value of terrain return and determines the attenuation to be used in the transmitter to insure square law operation from the detector. It also can provide some information on the fading characteristics and dynamic range of the return.

The antennas used in the system are high-gain pyramidal horns with dielectric lenses designed to give an optimum pattern at the operating range of 20 feet. The effective illuminated area normal to the line of sight transmission is 2.41 ft² for 10 KMC, 2.36 ft² for 15 KMC, and 0.67 ft² for 35 KMC. The complete radar system is installed in a truck and the RF section of the transmitter-receiver is mounted on the end of a 40 foot boom secured to the truck. The Doppler shift in frequency is obtained by driving the truck at a pre-determined speed across the terrain. The speed of the truck is calculated for each angle of incidence so that the Doppler shift in frequency would be an audio signal within the pass bands of the amplifier. The system can transmit and receive vertical, horizontal, and circular polarization.

The calibration of the system is accomplished by measuring the return from either a double or triple bounce corner reflector (dependent upon polarization), the Doppler shift being obtained by rotating the corner on a four-foot arm as shown in Fig. 2. This type of calibration reduces the effects of background noise and the target support since the target must be moving at the required speed to obtain the desired Doppler shift in frequency.

Absolute values of radar cross section can be obtained by a simple slide rule calculation at the end of each measurement. Figure 3 shows the ability of the system to duplicate previous measurements with a precision of better than ± 1 db.

The system can be converted to a bistatic radar for measuring the scattering from simulated surfaces, with the addition of a receiving antenna, and a modulation for the transmitted signal as shown in Fig. 4. In this case the averaging of the return is provided by mounting the surface on a railroad car and moving the car slowly through the beam of the antennas.

Figure 5 shows a representative series of radar backscattering measurements obtained with the cw Doppler system. Figure 6 shows the results of bistatic measurements obtained by converting the Doppler system to a bistatic radar.

CONCLUSIONS

It has been found in terrain scattering work, that to obtain accurate values of σ_0 , several important requirements in system design and techniques must be satisfied. These requirements can be summarized as follows:

1. The radar return from many independent samples of the same terrain must be averaged, preferably a continuous averaging while the measurements are being obtained.
2. The physical characteristics of the exact area of terrain being measured must be known at any instant of time.
3. The area of the surface being measured should be small in order that controlled changes in surface structure can be made accurately.

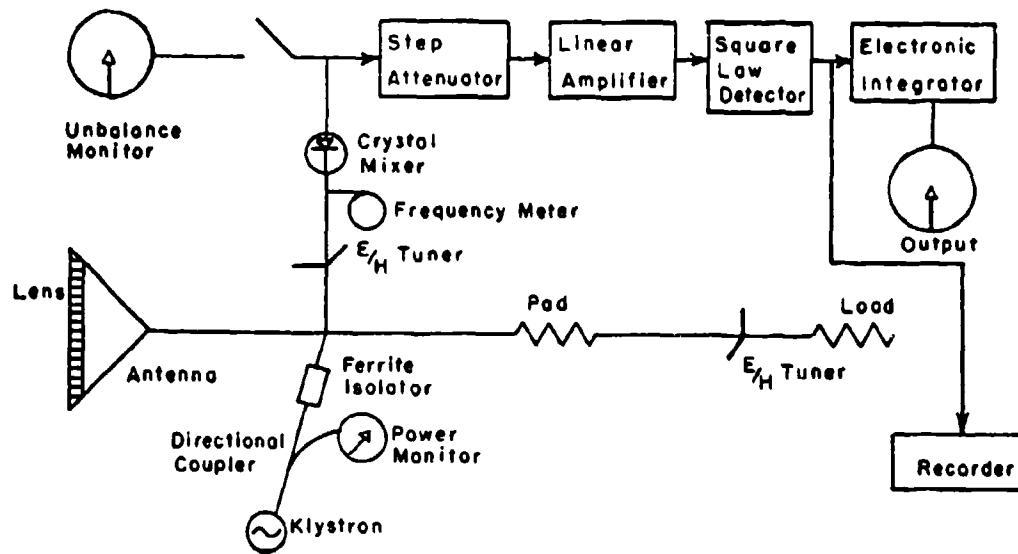


Fig. 1. Block diagram of CW doppler system.

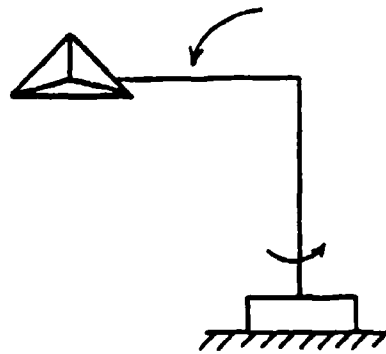


Figure 2. Corner Reflector Calibration

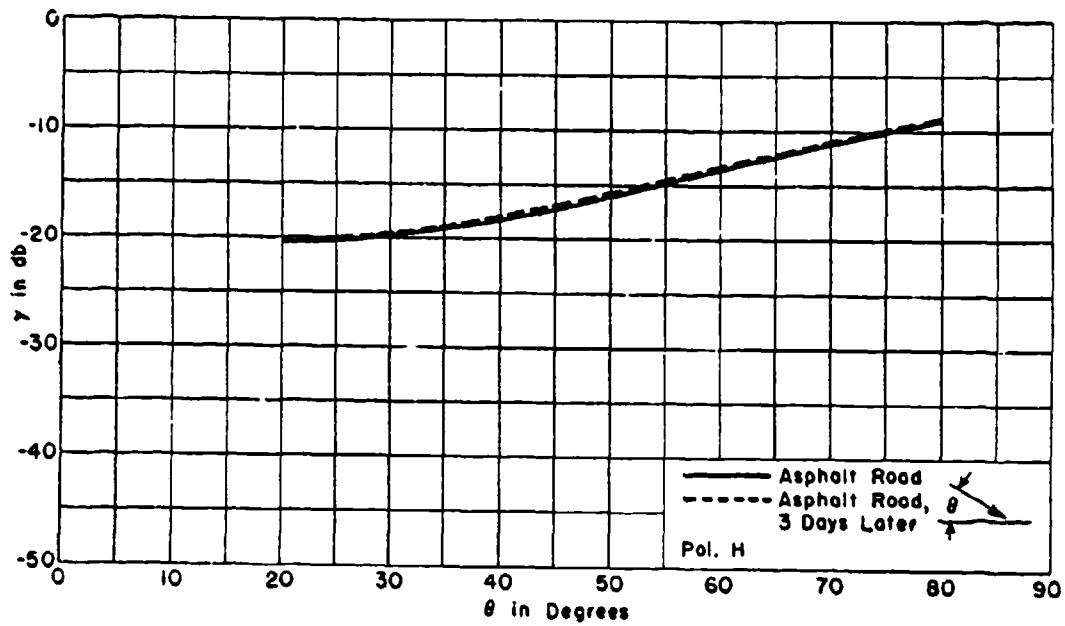


Fig. 3. Accuracy of CW doppler system.

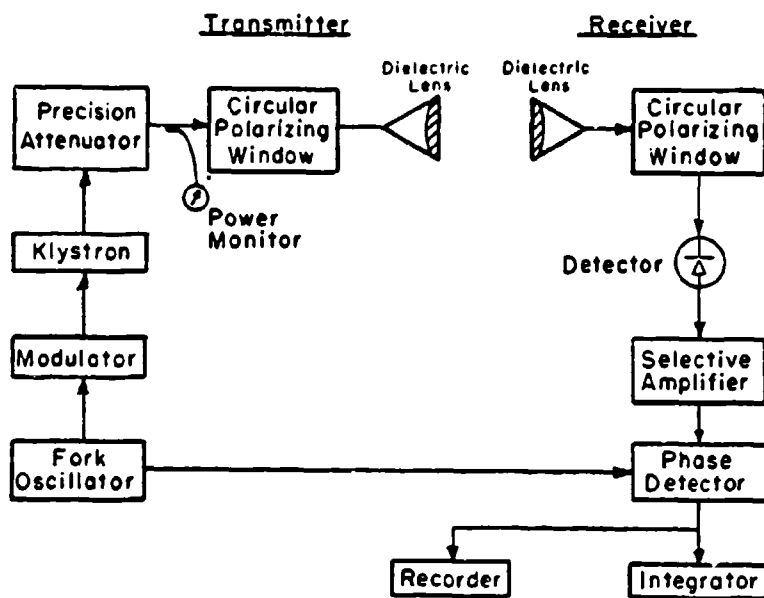


Fig. 4. Block diagram of X-band bistatic radar.

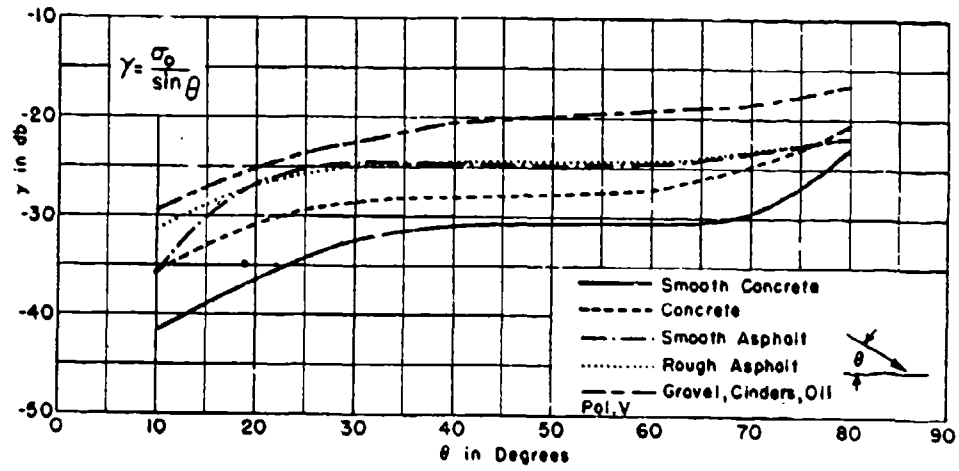


Fig. 5. Contrast of γ for Various Smooth Surfaces at X-band.

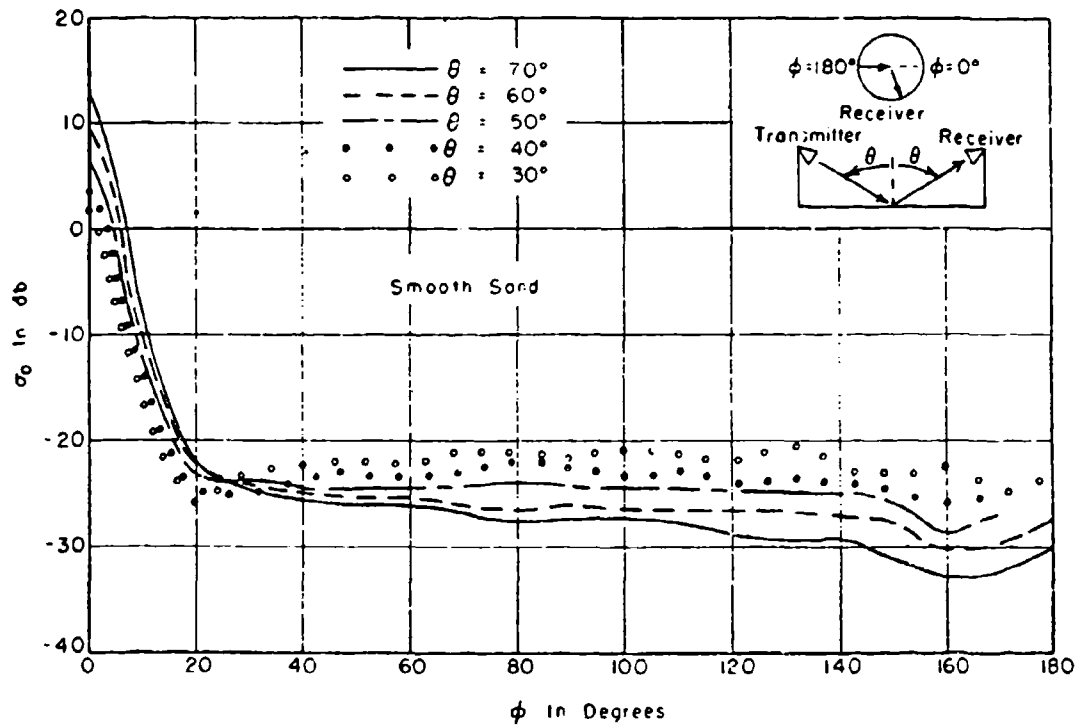


Fig. 6. Bistatic scattering from smooth sand.

4. The surface being measured should be homogeneous and of constant slope.
5. The data analysis should be performed at the time the measurements are being obtained.
6. The complete radar system including the antenna should be calibrated on an absolute basis, in terms of σ_0 , σ , or α .

If the radar scattering characteristics of a surface are accurately known it is possible to apply the results of these measurements to many other problems. It has been found that mathematical models can be developed to predict the scattering not only for one particular surface but for a range of surfaces with a wide variation in complex dielectric constant and surface roughness.⁴ It has also been found that the apparent noise temperature of terrain can be determined from the radar scattering characteristic of the surface.⁵ The effects of terrain environment upon antenna noise temperature can be determined from the scattering characteristics of the terrain surrounding the antenna. It is felt that these applications are only the beginning and that many other important phenomena can be discovered from the radar scattering characteristics of terrain.

REFERENCES

1. Taylor, R. C., Peake, W. H., and Cosgriff, R. L., "Terrain Return Measurements and Applications," Report 694-11, 30 April 1959, Antenna Laboratory, The Ohio State University Research Foundation; prepared under Contract AF 33(616)-3649, Wright Air Development Center, Wright-Patterson Air Force Base, Ohio. Confidential. AD 309 093
2. Cosgriff, R. L., Peake, W. H., and Taylor, R. C., "Terrain Scattering Properties for Sensor System Design (Terrain Handbook II)," Engineering Experiment Station Bulletin, The Ohio State University, EESB 181, \$3.00.
3. Taylor, R. C., "Terrain Return Measurements at K_a -Band," Report 694-6, 15 November 1957, Antenna Laboratory, The Ohio State University Research Foundation; prepared under Contract AF 33(616)-3649, Wright Air Development Center, Wright-Patterson Air Force Base, Ohio. Confidential AD 149 737

4. Peake, W. H. , "Interaction of Electromagnetic Waves with Some Natural Surfaces," Report 898-2, 30 May 1959, Antenna Laboratory, The Ohio State University Research Foundation; prepared under Contract AF 33(616)-6158, Wright Air Development Center, Wright-Patterson Air Force Base, Ohio.
5. Peake, W. H. , and Taylor, R. C. , "Apparent Antenna Temperature at L-Band Over Smooth Surfaces," Report 904-2, 15 December 1959, Antenna Laboratory, The Ohio State University Research Foundation; prepared under Contract DA 18-119ac-533, U. S. Army Signal Procurement Office, Fort George G. Meade, Maryland.
AD 236 186

STUDIES IN RADAR CROSS SECTION MEASUREMENTS

P. H. Ware
Advanced Missile Technology
Douglas Aircraft Company, Inc.

INTRODUCTION

Radar cross section is a measure of the electromagnetic reflection characteristics of a body. This parameter may be described analytically by the relation:

$$\sigma = \lim_{R \rightarrow \infty} 4\pi R^2 \left| \frac{P_r}{P_i} \right| \quad (1)$$

where: σ is the radar cross section
 P_r the scattered power flux density at distance R from the scatterer
 P_i the power flux density in an incident plane wave field.

It is a fact of experience that a large geometric cross section does not necessarily denote a correspondingly large radar cross section; as a matter of fact, there seems to be neither a simple nor obvious relationship between the two. For example, the radar cross section of the mathematical cone seen nose-on is of the order of 10^{-6} meters squared, (πr^2). The exact analytical solution to the radar cross section problem is found to be untractable in all but the very simplest of shapes, i.e., the sphere, etc. The remaining cases, which are, by the way, the ones of most practical interest, remain outside the scope of present-day mathematical techniques.

DISCUSSION

One of the methods of extracting information concerning the radar cross sections of bodies utilizes a continuous wave radar bridge employed against a target mounted in a precision indoor microwave anechoic chamber. In practice, the sensitivity of a continuous wave radar cross section measuring range is determined by the joint effect of two factors: (1) the zero imbalance introduced by equipment imperfections, and (2) a factor which depends on the manner in which the target modifies the illumination of the microwave anechoic chamber. If we can substantially reduce the errors arising out of these factors, we can expect to be rewarded with increased accuracy and precision in our measurements.

The accuracy of any measurement system is dependent upon the ability of the tester to first stabilize and then define the amplitudes and effects of errors inherent in the system. Since the targets of primary interest have been specifically designed to reflect only a very small fraction of the illuminating energy, the first task becomes the design of a transmit-receive system with adequate sensitivity and electrical phase stability characteristics.

Equipment. The equation describing the achievable sensitivity of a CW radar cross section measurements circuit is:

$$\sigma_{\min} = \left[\frac{4\pi R^4 \lambda^2}{A^2 f^2} \right] \cdot \frac{S_{\min}}{P_t} \quad (2)$$

where: R = Propagation Path Length (one way)
 λ = Free Space Wavelength
 A = Antenna Aperture Area
 f = Antenna Efficiency Constant
 S_{\min} = Receiver Sensitivity Threshold
 P_t = Power Transmitted
 σ_{\min} = Minimum Detectable Target Area

The optimum values for the variables in the bracketed quantity are essentially fixed by the criteria for even power illumination of the target and near field requirements. S_{\min} and P_t are both limited by the capabilities of available equipment. In actual practice then, the equation above determines a theoretically achievable goal for the testor when designing and fabricating the microwave circuit.

System isolation is defined as the ratio, expressed in db, of the power at the receiver to the power transmitted when there is no desired target being illuminated.

The theoretically achievable value for "system isolation" is $\frac{S_{\min}}{P_t}$.

The return in a radar cross section measurement range is described by the following equation:

$$\bar{E} = \bar{E}_T + \bar{E}_{ct} + \bar{E}_B + \bar{E}_S + \bar{E}_H \quad (3)$$

where: \bar{E} = Measured relative field strength
 \bar{E}_T = Target relative field strength
 \bar{E}_B = Background relative field strength
 \bar{E}_{ct} = Cross talk relative field strength
 \bar{E}_S = Forward scatter effect from target
 \bar{E}_H = Target holder relative field strength

From the definition for system isolation, we would like to have

$$|\bar{E}| = |\bar{E}_{ct}| + |\bar{E}_B| = S_{\min}$$

when no desired target is being illuminated.

A monostatic or single antenna, transmit-receive circuit was chosen for this test facility, because the bi-static system has an inherent pattern error due to the angular displacement of the two antennas with respect to the normal axis of propagation.

To explain the circuit operation of a monostatic system requires a brief review of the operational principles of the hybrid tee. If all four arms of this device were terminated such that there were no standing waves in the system, the circuit behavior at the tee could be described as follows:

The transmitter power entering arm H is divided equally into arms 1 and 2, and none of the transmitted energy will enter arm E. The reflected or return power entering arm 1 will be divided equally into arms H and E, and none of the return energy will enter arm 2. Since it is impossible to fabricate a perfect hybrid tee or, for the matter, to provide for a perfect termination at all four arms, standing waves are present in the system. The purpose of the 5 or 9 stub tuner in arm 2 is to introduce a mismatch of proper phase and amplitude at the junction of arm H, such that the effects of all system standing waves are cancelled out and maximum isolation is achieved. The theoretically achievable $\frac{S_{\min}}{P_T}$

ratio for the test circuitry which we have so far constructed varies from -115 db to -130 db, and to actually reach this figure and hold it for the period of a test run, it is necessary that the phase stability of the transmitted signal in the waveguide circuitry be of the order of $10^{-8}\lambda$.

The degree of phase stability which can be achieved in any waveguide circuit is directly related to the stability of the test frequency and to the dimensional stability, in all planes, of the waveguide circuit itself.

The frequency stabilizing portion of the test circuit consists of a Synchro Oscillator which phase-locks the test frequency to a crystal reference source which has a long-term frequency stability of one part in 10^{10} (for example, $f = 10^{10} \pm 50$ cps).

The required dimensional stability of the system is achieved by physically isolating it from variations in its thermal and vibrational environment. By careful attention to detail, we have been able to obtain $E_{ct} = S_{\min}$ and to hold it at this value for several hours. If the enclosure surrounding the target is stable mechanically, and the circuit is tuned for maximum isolation with the antenna looking into the empty enclosure, then (because of our over-all system phase stability) the enclosure becomes part of the circuit, and we can tune for $|\bar{E}_B| + |\bar{E}_{ct}| \leq S_{\min}$, thereby reducing $|\bar{E}_B|$ to at least S_{\min} .

Because of our phase and dimensional stability, \bar{E} is no longer time dependent. In other words, should we place a target in the chamber and not move it, \bar{E} would remain at a constant value for a period of time, the duration of which depends upon the long-term stability characteristics of the test setup. This does not mean, however, that $\bar{E} = \bar{E}_t$. Although we may have eliminated the time dependence and reduced all the error quantities to very low values, they nevertheless are contributing in, as yet, an undefined manner to the value of \bar{E} . It is important to note, for example, that after the target has been put in place, the wall reflection is modified due to forward scatter from the target. It has been usual to accept the error caused by this modification of the room reflection and to restrict measurements to targets in which this effect is small. At the

Douglas Radiation Laboratory, we have worked to eliminate this error by a process that we call "traversing". Before delineating this method, let us consider the following:

$$\text{Let } \bar{\Sigma}^2 = \sigma$$

$$\text{so } \sigma = \sigma_t e^{j\beta} + \sigma_{ct} + \sigma_h + \sigma_b + \sigma_s$$

where:

- σ = measured cross section
- σ_t = target cross section
- σ_h = holder cross section
- σ_{ct} = cross talk cross section after system isolation
- σ_b = background cross section after system isolation
- σ_s = forward scatter effect from target

and further, let

$$\sigma = \sigma_t e^{j\beta} + \sigma_v + \sigma_h$$

where

$$\sigma_v = \sigma_{ct} + \sigma_b + \sigma_s$$

and where β = phase angle between Σ_t and Σ_v . One method of accomplishing the above-outlined task is as follows:

σ_v has as many values, at least, as does σ_t and, for most target geometries of interest, σ_t varies with every look angle. It is necessary, therefore, to devise a test procedure such that σ_v is definable for every required look angle. If the angle β can be made to vary from 0° to 360° while recording the value σ , it is possible to define σ_v as the amplitude variation of σ about a fixed value σ_t . If, for every desired look angle, the range to the target is altered by $\frac{\lambda}{2}$, the magnitude and phase of the reflection due to the wall return tends to be constant; however, the phase of the target return changes greatly.

Analytically then, the phase of the return from the target is given by:

$$\beta_1 = \frac{4\pi}{\lambda} R_T$$

- where: β_1 is the phase
 λ is the wavelength
 R_T is the distance between the antenna and the target model.

If now we change R_T by $\frac{\lambda}{2}$, we have:

$$\beta_2 = \frac{4\pi}{\lambda} (R_T + \frac{\lambda}{2}) = \frac{4\pi}{\lambda} R_T + 2\pi$$

and we have changed the phase of the target return by 2π , while keeping the return from the wall essentially constant. Thus, the return signal exhibits a periodic structure with change in range, the amplitude of this periodic term being a measure of the imbalance introduced by the target and the mean value represents the true cross section measured. Analytically, we have:

$$\sigma_t = \frac{\sigma_{\max} + \sigma_{\min}}{2}$$

It should be emphasized at this time that, in addition to the elimination of error as outlined above, this process in effect allows accurate measurements of return signals approaching the magnitude of S_{\min} .

To obtain the required information for every look angle by following this procedure would be tedious to say the least, so the following technique has been employed instead:

The model is rotated and all values of σ recorded. The model is then traversed a distance $\lambda/16$ and the process repeated. A traversing mechanism, instrumented from outside the chamber proper, allows the target model to be altered in range without disturbing the measurement system. This is repeated a total of eight times covering the distance $\lambda/2$ and the nine patterns are all recorded in an overlay fashion on a single sheet of paper.

These data are processed by the 7090 computer to present a tabulation of true radar cross section measured versus aspect angles from 0° to 360° at 1° intervals, in addition to a profile graph of the same parameters. In operation data from the meas. fac. is fed to the computing engineering section, etc. - scale factors, calibration level, etc.

Using the methods outlined above, we have made measurements on a series of spheres shown in Table I. The deviation indicated is within the order of magnitude of our present readout capability. Computer program for conducting spheres is tabulated in increments of $.001 \frac{2\pi}{\lambda} a$ for the range .001 to 10.000.

Figure 1 illustrates the radar return from a common housefly suspended by a single strand of monofilament nylon cord. The average value of the return is approximately 10^{-7} m^2 .

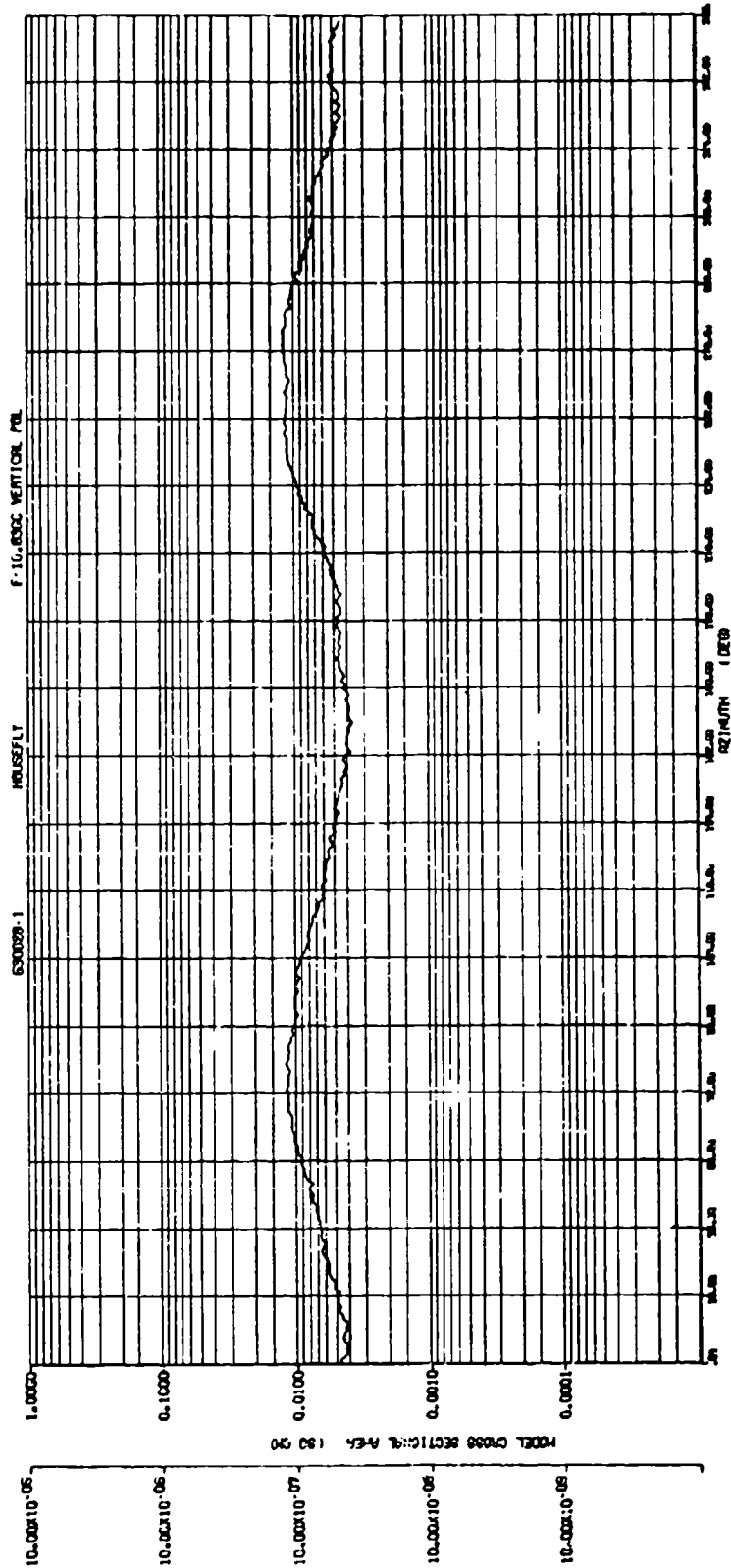


Table I

PRELIMINARY SPHERE CALIBRATION
 AT 5.17 CM IN 70' CHAMBER

Sphere Dia. Inches	Calc. σ cm ²	Meas. σ cm ²	% σ Deviation	Meas. db Level	Calc. db from Ref.	Meas. db from Ref.	db Deviation
5/8	6.032	6.027	0.08	-38.7	-10.9	-10.9	0
3/4	10.417	11.226	7.77	-36.0	- 8.5	- 8.2	.3
2-1/2	47.472	46.780	1.44	-29.8	- 1.9	- 2.0	.1
4.056	74.1496	74.1496	REF	-27.8	0	REF	REF
6.879	271.859	275.466	1.33	-22.1	+ 5.7	+ 5.7	0
10.042	510.973	501.325	1.89	-19.5	+ 8.4	+ 8.3	.1
13.166	878.345	933.543	6.28	-16.8	+10.8	+11.0	.2
15.06	1149.231	1122.625	2.32	-16.0	+11.9	+11.8	.1



PRECISION MEASUREMENT OF THE RADAR SCATTERING MATRIX

J. A. Webb/W. P. Allen
Lockheed-Georgia Company
Marietta, Georgia

ABSTRACT

The radar cross section measurement equipment at Lockheed-Georgia Company is described in this paper, and some of the results of measurements made with resonant dipole chaff are given. This equipment is a quasi-monostatic, cw reflection range operating at X-band. It has one rather unusual feature, in that it utilizes electromechanical servomechanisms to drive a precision microwave phase shifter and a precision attenuator to maintain the receiver output at a null. This technique provides significant advantages over measurements made at intermediate frequencies.

DISCUSSION:

The radar cross-section measurement equipment at Lockheed-Georgia Company is capable of measuring the radar scattering matrix to considerable greater accuracy than that which is normally obtained. There are several factors which contribute to this accuracy, the major ones being (a) a closed loop measurement technique using precision microwave components, (b) the use of an extremely accurate frequency control on the transmitter, and (c) the use of special background compensation techniques. The meticulous care used in setting up and conducting experiments has also contributed significantly to this accuracy.

This equipment is a quasi-monostatic, cw reflection range operating at X-band. A simplified block diagram of the measurement equipment is given in Figure 1. Rotating joints on the transmitting and receiving antennas provide measurement capability at any polarization. A signal leakage path is used to cancel the "background" return. A second signal leakage path is used to cancel the return from the target, to produce a null output from the receiver. Electromechanical servomechanisms drive a precision microwave phase shifter and a precision attenuator in the target cancellation path to maintain the receiver output in a null. The measurement accuracy is therefore determined by the accuracy of these precision microwave components. A second attenuator is used in the target cancellation path as a pad, to set the operating range of the servo-driven attenuator.

A precision potentiometer is located on the shaft of each of the electromechanical servomechanisms to provide output voltage. Two rectangular chart recorders, synchronized to the target azimuth positioner, are used to record the amplitude and phase of the radar scattering parameters.

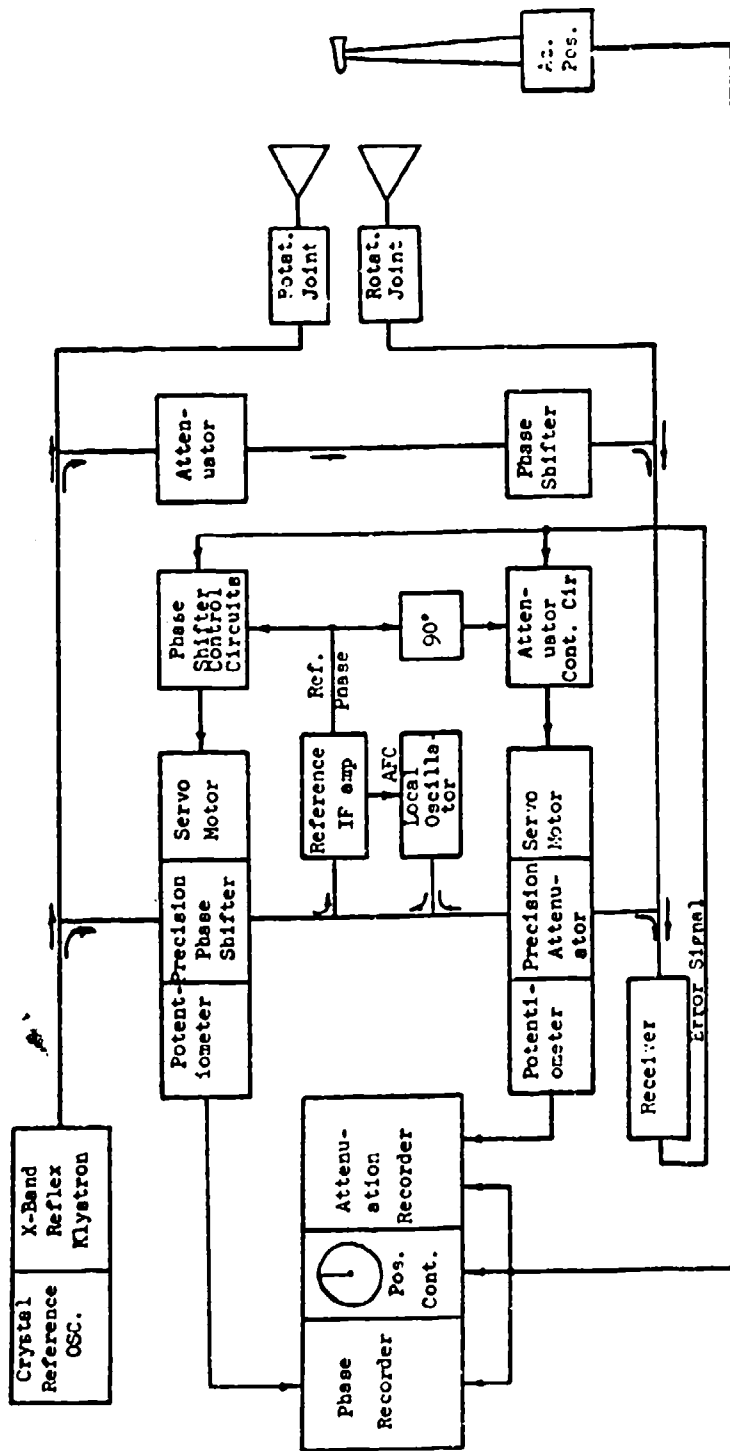


Figure 1. Radar Scattering Matrix Measurement Equipment
at Lockheed Georgia Co.

When measuring the elements of the scattering matrix for any given target, it is necessary to correlate phase shift data obtained at various polarizations. To avoid almost impossible tolerances in target replacement between measurements, the target is not disturbed until all of the elements of the scattering matrix have been measured. This requires that background readings be made before target placement, and that these readings remain constant during a measurement run. Experience has shown that the background will remain constant, provided that the transmitter is sufficiently stable in frequency. To provide this stability, the transmitter is phase-locked to a crystal standard, having a short-term stability of 1 part in 10^8 .

After background cancellation, the residual return from the microwave darkroom is less than the change in return due to the styrofoam model support column, as the column is rotated in azimuth. The mean residual return due to the column is typically -50 to -55 dbsm. The amplitude and phase of the residual column return however can be plotted as a function of azimuth angle, then subtracted from the target return.

This technique of vector subtraction is effective, but the resultant improvement in residual background is not as great as originally anticipated. This is not due to any lack of accuracy in vector measurement and subtraction but to the performance limitations of the darkroom itself.

The static return from a microwave darkroom is generally used to specify darkroom performance. With background cancellation, however, as used in this equipment, the static return from the darkroom is of little interest. What is of interest is the bistatic scattering anomalies caused by the introduction of the target into the darkroom, and the changes in background as the styrofoam column is rotated in azimuth. It was found that bistatic scattering from the room limited the darkroom performance to about -60 dbsm even with vector subtraction of the column return. It was also found that these bistatic scattering anomalies occurred from the back wall of the room, with very little scattering from the sides of the room. As a result of these measurements, improvements in the configuration of the back wall are being planned.

For purposes of system calibration, several highly accurate stainless steel spheres are used. These spheres range in size from 3/16-inch to 3 inches diameter. In addition to providing good calibration reference, these spheres have been used on occasion for darkroom checkout, by rotating the sphere off-center and thereby creating an interference pattern between the reference sphere and the darkroom return.¹ Direct recording of the background return, however, and averaging over 360 degrees azimuth rotation, is considered to be a more desirable technique for microwave darkroom checkout. The rotating sphere method still provides the only technique for evaluating the residual darkroom anomalies after vector subtraction of the column return.

Output data from the servo-driven phase shifter and attenuator are normally recorded on two rectangular chart recorders, synchronized to the target azimuth positioner. These data may also be recorded on magnetic tape and played back either to the chart recorder, or to an analog-to-digital converter, where attenuation and phase shift readings may be made for each 1/2-degree increment of azimuth position change.

Figure 2 is a pictorial view of the measurement equipment. The microwave equipment is located on the table, with the transmitting and receiving antennas extending into the microwave darkroom. Two rectangular chart recorders, the azimuth positioner control and indicator, and the null-monitoring oscilloscope are shown at the right. The servo controls and amplifier are underneath the recorder. Figure 3 is a close-up of the phase shifter servo.

Figure 4 is a view from inside the microwave darkroom, looking towards the back wall. Figure 5 is a forward view, showing the measurement antennas protruding through the microwave absorber. Figure 6 shows the 7-channel instrumentation tape recorder, which is used for multi-channel recording and playback of scattering parameters.

Figure 7 shows the angle synchronizer which is used for synchronizing playback signals from the tape recorder. When converting scattering parameters to digital data, a cam-driven microswitch on the angle synchronizer provides a "read command" pulse for each 1/2 degree change in azimuth angle. When playing back to chart recorders, a synchrotransmitter on the angle synchronizer provides an appropriate signal to synchronize the chart recorders and the azimuth position indicator.

MEASUREMENT DATA:

This equipment has been used to provide input data for use in a digital simulation program. In this simulation program, the vector scattering parameters are used to predict the radar cross-section for any polarization angle, and any orientation of a symmetrical body.

As a check on the validity of this prediction technique, the radar cross-section was predicted, then measured, for an arbitrary incident polarization angle. These tests clearly demonstrate that this prediction technique is valid and that the measurement accuracy is sufficient for prediction of the off-axis scattering characteristics.

Measurements were made of the returns from long thin wires of various lengths, up through the third resonant peak. The resultant data from these measurements are shown in Figure 8. These data represent mean cross-section values, averaged over 180 degrees azimuth angle, and 180 degrees polarization angle. The wire used had a radius of 1.5 mils, representing length-to-radius ratios of 420 to 1260 at the first and third resonant peaks, respectively.

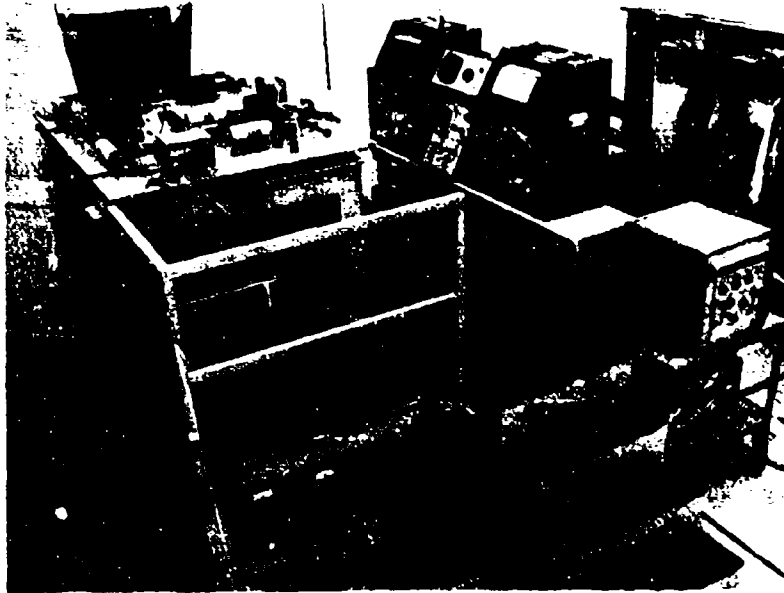


Figure 2. Pictorial view of the radar cross section measurement equipment.

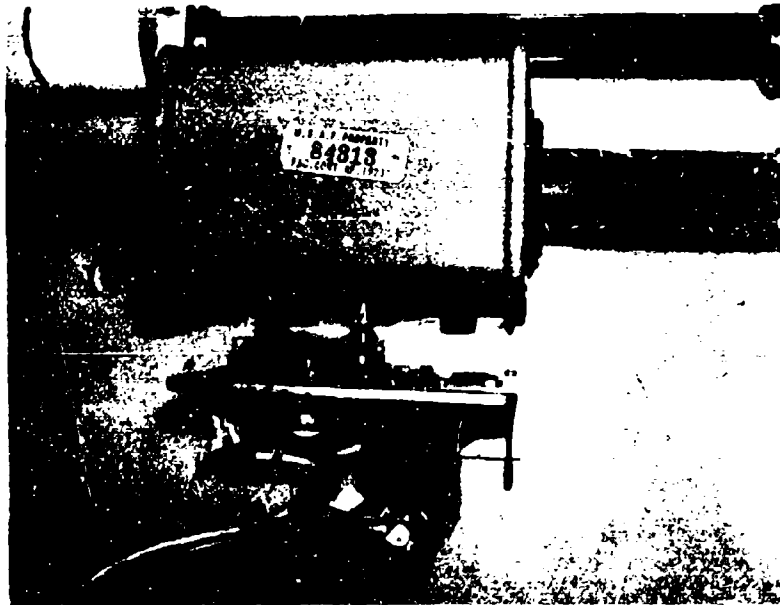


Figure 3. Electromechanical servo driving a microwave phase shifter.

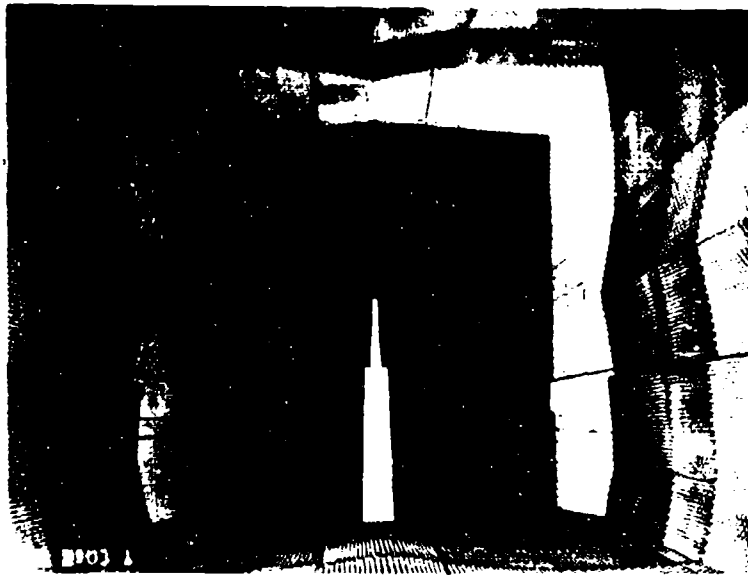


Figure 4. Interior view of the microwave darkroom, looking towards the back wall.



Figure 5. Forward view of the microwave darkroom.



Figure 6. Seven-channel tape recorder used for scattering measurements.

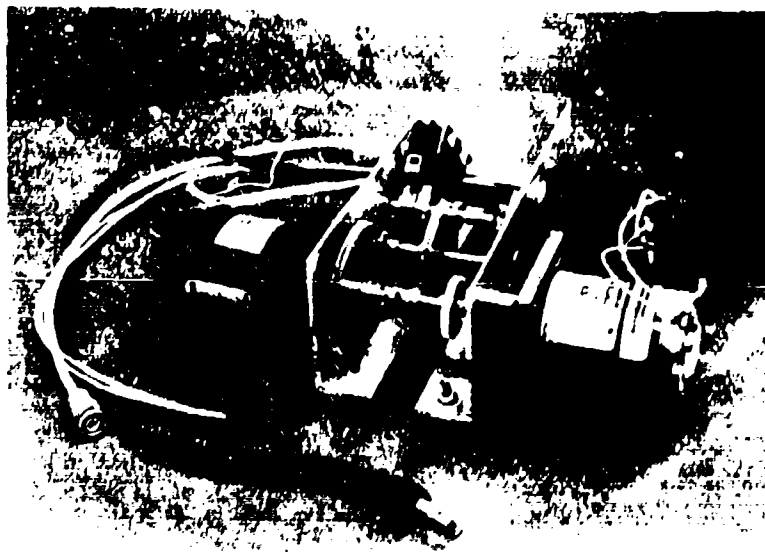


Figure 7. Azimuth position angle synchronizer for analog-to-digital conversion, or for data transfer from tape to chart.

A curve from Van Vleck² representing calculated mean returns from perfectly conducting wires, assuming a constant length-to-radius ratio of 900, is also plotted in Figure 3. It is interesting to note that the best correlation with Van Vleck occurs near the third resonant peak, where the length-to-radius ratios most nearly correspond.

Cassedy and Fainberg³ have shown that the dissipation factor in the wire is also quite important in determining the characteristics of the return. Figure 9 shows calculated peak returns by Cassedy and Fainberg from a perfectly conducting wire and a copper wire, and measured returns from copper wire, compared to measurements made at Lockheed. Cassedy and Fainberg used 1 mil diameter wire at 3000 mc, corresponding to a length-to-radius ratio of 3700, whereas the Lockheed measurements were made at 9375 mc using 3 mil diameter wire, corresponding to a length-to-radius ratio of 420.

Much better correspondence is obtained between the Lockheed measurements and those made by Serracchioli and Lewis at Ohio State University.⁴ The length-to-radius ratio of the wire used by Serracchioli and Lewis was approximately 440 for these measurements, corresponding very closely to the Lockheed measurement conditions. A comparative plot of the Ohio State and Lockheed measurements is given in Figure 10.

The angular distribution of the response of a wire is shown in Figure 11, plotted on a normalized scale, from measurements made at Lockheed. This curve is compared to calculations by Van Vleck, also normalized (Methods A and C, Figure 5). Van Vleck used a wire length-to-wavelength ratio of 0.5 and a length-to-radius ratio of 900, compared to 0.46 and 420 for the Lockheed measurements. Vector subtraction of the column return was used for reducing the background in the Lockheed measurements.

— Measurements made at Lockheed, using 3 mil diameter
 wire at 9375 Mc (length-to-radius ratio of 420 to 1260).
 - - - Calculation from Van Vleck, for length-to-radius ratio
 of 900.

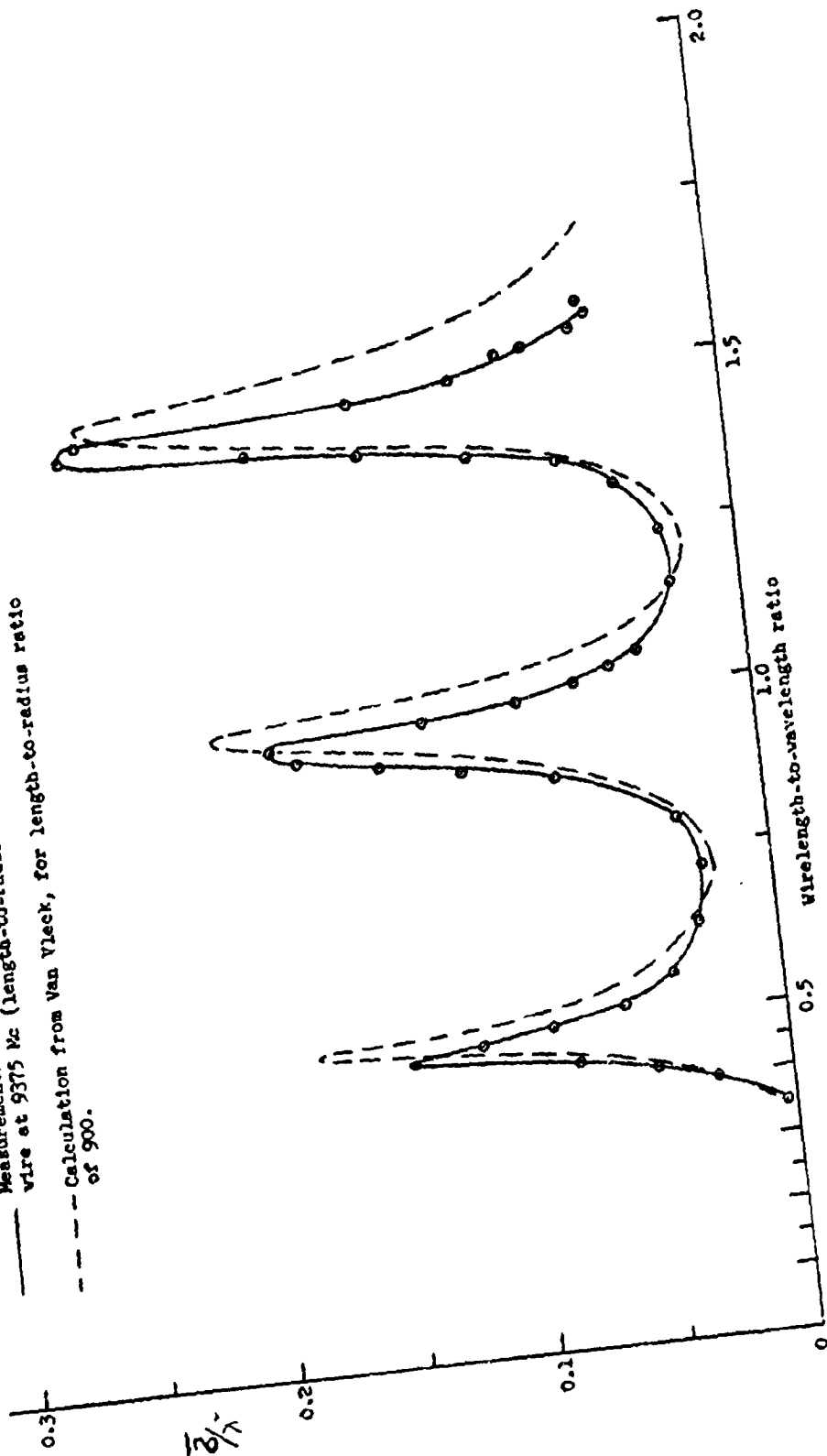


Figure 8. Mean Returns From Thin Wires.

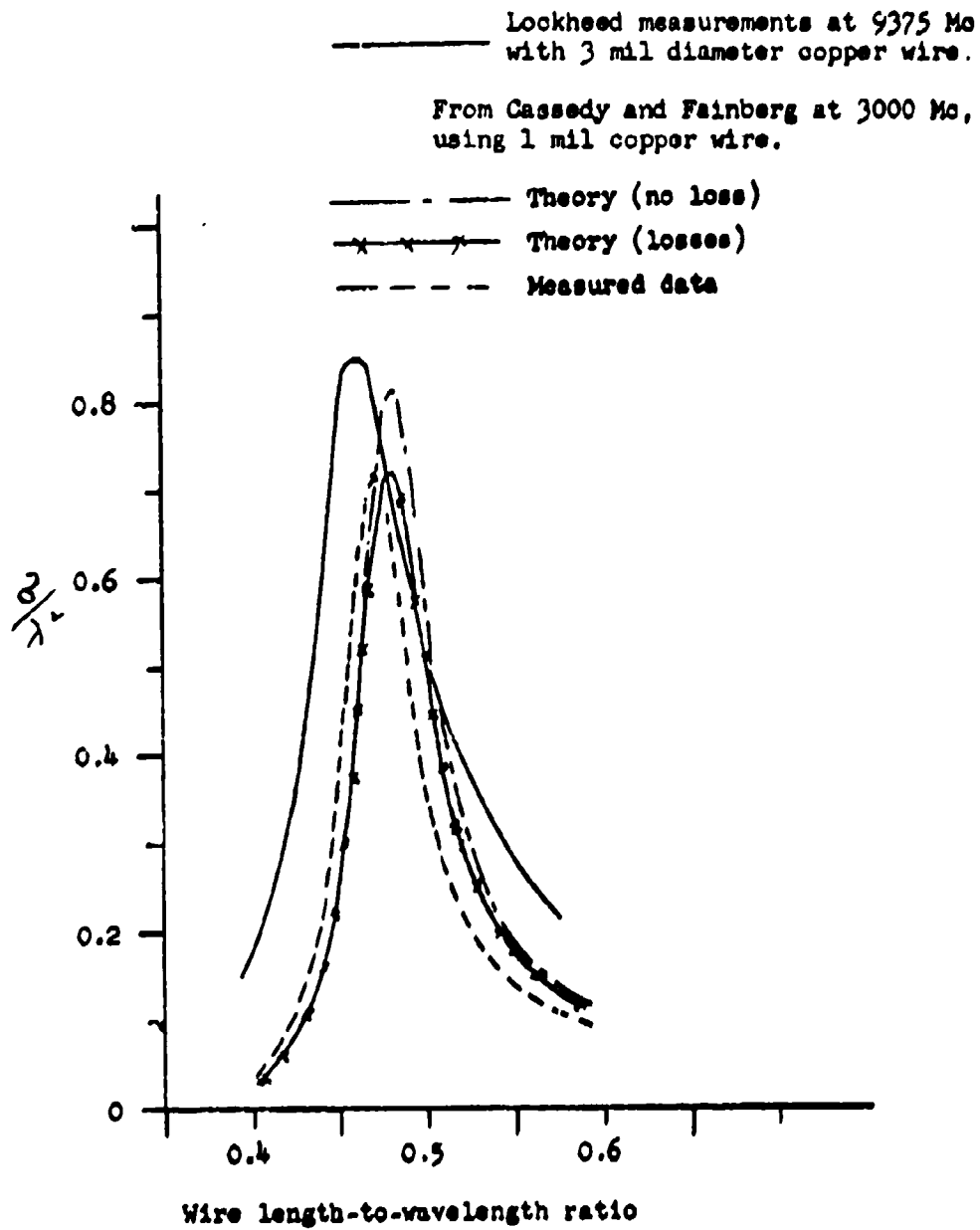


Figure 9. Calculated and Measured Peak Returns for the $\lambda/2$ Resonant Peak.

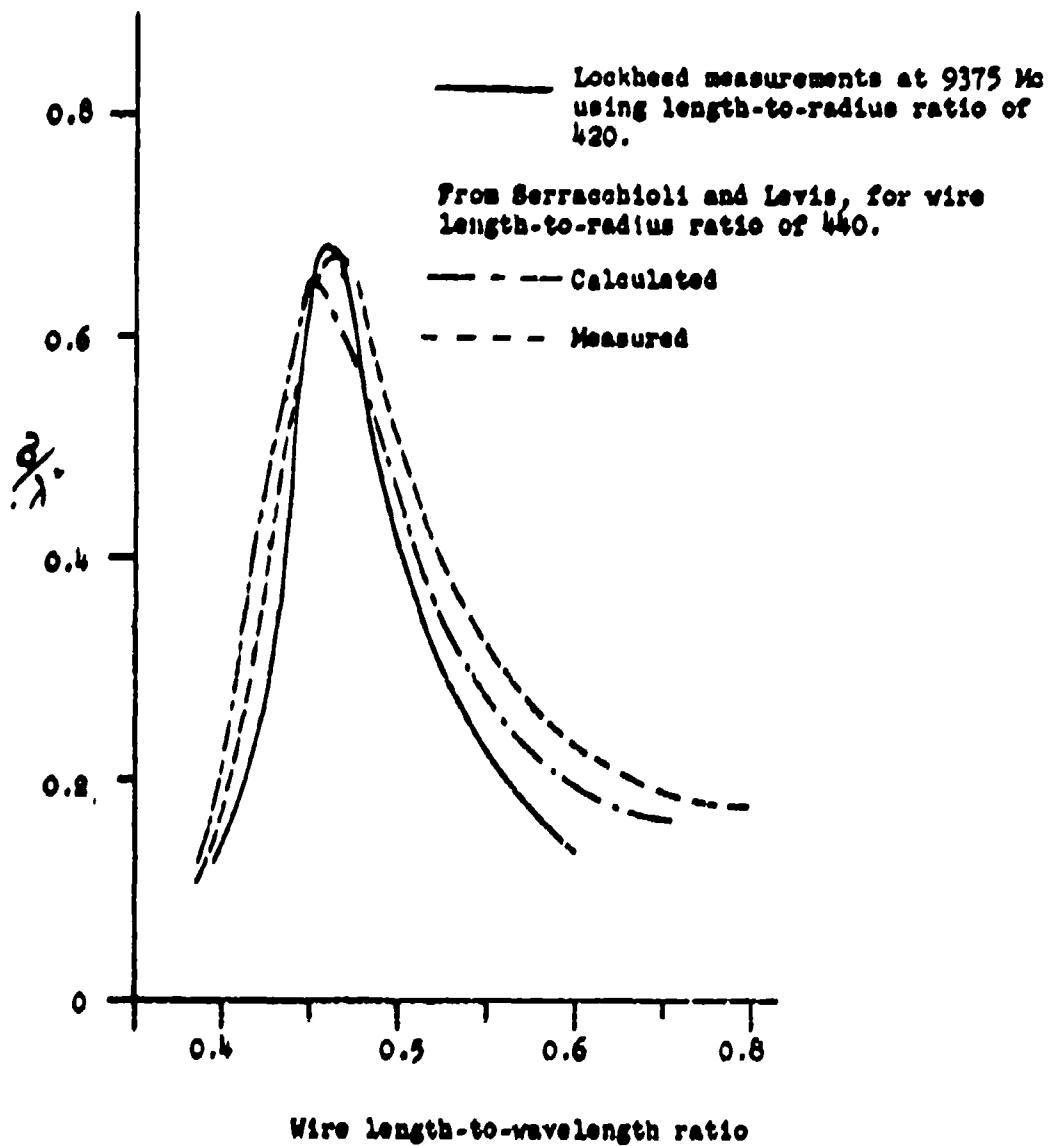


Figure 10. Calculated and Measured Peak Returns for the $\lambda/2$ Resonant Peak.

— Lockheed measurements using 3 mil
wire at 9375 Mc.

- - - Calculated data from Van Vleck.

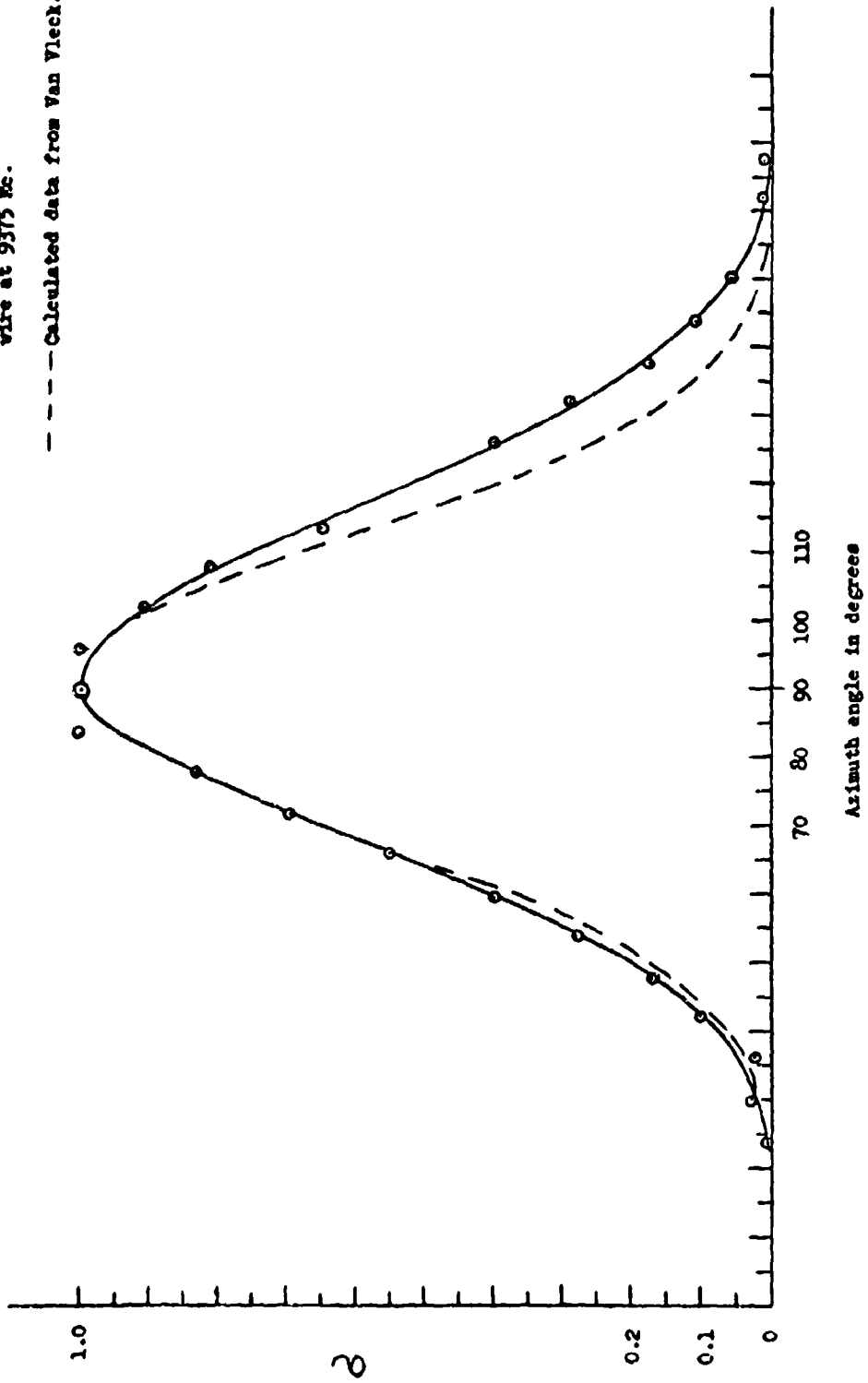


Figure 11. Variation of Cross Section of a Wire With Azimuth Angle.

BIBLIOGRAPHY:

1. Outline of Electrical Evaluation Procedures for Microwave Anechoic Chambers, Emerson & Cuming, Inc., October 1962.
2. Van Vleck, J. H., Black, F., and Hamermesh, M., Theory of Radar Reflection from Wires or Thin Metallic Strips, Journal of Applied Physics, March 1947.
3. Cassedy, E. S., and Fainberg, J., Back Scattering Cross Sections of Cylindrical Wires of Finite Conductivity, IRE Transactions on Antennas and Propagation, January 1960.
4. Serracchioli, F., and Levis, C. A., The Calculated Phase Velocity of Long End-Fire Uniform Dipole Arrays, IRE Transactions on Antennas and Propagation, December 1959.

VERY SMALL RADAR CROSS-SECTION MEASUREMENTS AT UHF

Phillip J. Willcox
Goodyear Aerospace Corporation

ABSTRACT

The Quasi-doppler technique has been used successfully for accurate radar cross-section measurements of the order of the $10^{-5} \lambda^2$ in the UHF band. This presentation includes, in addition to the theoretical discussion of the Quasi-doppler technique, the physical configuration of the test range, with particular emphasis on the determination of range parameters, and the methods employed in data reduction. A review of target support systems contains the description of a unique target mount that virtually eliminates, for certain target configurations, the effect of mount motion on the target return.

THEORY OF THE QUASI-DOPPLER TECHNIQUE

Conventional methods of making radar reflectivity measurements dictate that the background return level be appreciably lower than the level of the target return for reasonable accuracy. The familiar curve reproduced in Figure 1 shows the accuracy that can be insured for a given target to background separation. This is due to the random relative phase between the target return and the background return. This relative phase can be anything from in phase to 180° out of phase; therefore, the target return level accuracy can be no better than the two extremes. For example, the target return level must be nearly 20 db higher than the background for an accuracy of ± 1 db on the measured value. This problem is certainly not unsurmountable if the target to be measured is large in terms of radar cross-section. However, if the target return is very small, the problem of reducing the background to the point at which acceptable accuracy is to be achieved becomes extremely difficult.

This may be readily appreciated by considering the published data on the better radar cross section ranges in the country.¹ Most well designed and carefully constructed ground ranges have an average measured background level of the order of 10^{-6} m^2 . Considering such a range, a target with a radar cross-section of 10^{-4} m^2 would yield a measured return 20 db above background and hence, have a measurement accuracy of ± 1 db. A smaller target, however, would have associated with it a much poorer accuracy figure. By conventional methods then, the size of the target that can be measured with a given accuracy, is seriously limited. This is particularly true at low frequencies such as in the UHF region since the background level is generally higher and more difficult to cancel by conventional cancelling networks.

This limit may be greatly extended by use of the "Quasi-doppler" technique. As the name implies this method employs target motion. If the target is moved slowly in the direction of propagation, the phase of the target return continually varies completing one full period for each half wavelength of target motion. If during this time period, the background level can be assumed to remain fixed in both amplitude and

phase, the net effect is that of a phase changing target return modulating a fixed phase background return. This results in a sinusoidal type recording.

Consider a given target return level of magnitude A and a background return level of magnitude B. The peak power return will result when the target and the background are in phase. This is given by $(A+B)^2$. Similarly, the minimum power return will result when the target and background returns are 180° out of phase and is given by $(A-B)^2$. Then,

$$10 \log \left(\frac{A+B}{A-B} \right)^2 = x \text{ (db)} \quad (1)$$

will yield the peak to null variation of the return in decibels. For any given value of x, the ratios of the peak power level to the target level and to the background level may be computed, i.e., for any given x determine $10 \log (A+B/A)^2$ and $10 \log (A+B/B)^2$ in db. These have been plotted versus x in Figure 2. The first expression yields the level of the target return in terms of the peak, and the second yields the level of the background return in terms of the peak. Notice that if the difference between these curves is plotted as a function of x, the error curve shown in Figure 1 is the result. It is, therefore, evident that the doppler return recording is in fact an actual recording of the error on the target return due to the arbitrary relative phase between the target return and the background return.

DETERMINATION OF RANGE PARAMETERS

The accurate determination of range parameters which will yield an acceptable target illumination precedes any attempt to make a backscatter measurement. Four primary variations must be considered; phase variation over the target aperture, amplitude variation in the horizontal and vertical planes of the target aperture, and the amplitude variation in the longitudinal direction, i.e., in the direction of target motion. Each of these variations will be considered in turn.

Plane Wave Criteria

The ideal target illumination for accurate backscatter measurements would be a perfectly plane wave over the entire target aperture. If a point source is assumed, the degree of "planeness" is a direct function of range length and will determine a minimum range length for any given acceptable phase variation over the aperture. For example, the often used minimum range requirement $R \geq 2D^2/\lambda$, where D is the largest dimension of the target normal to the direction of propagation, yields a phase variation of no greater than $\lambda/16$ over the aperture. For most backscatter measurements, this is assumed to be a reasonable condition. It must be pointed out that this result is based only upon the direct radiation and does not consider the phase effect of energy reflected off the ground or other nearby objects.

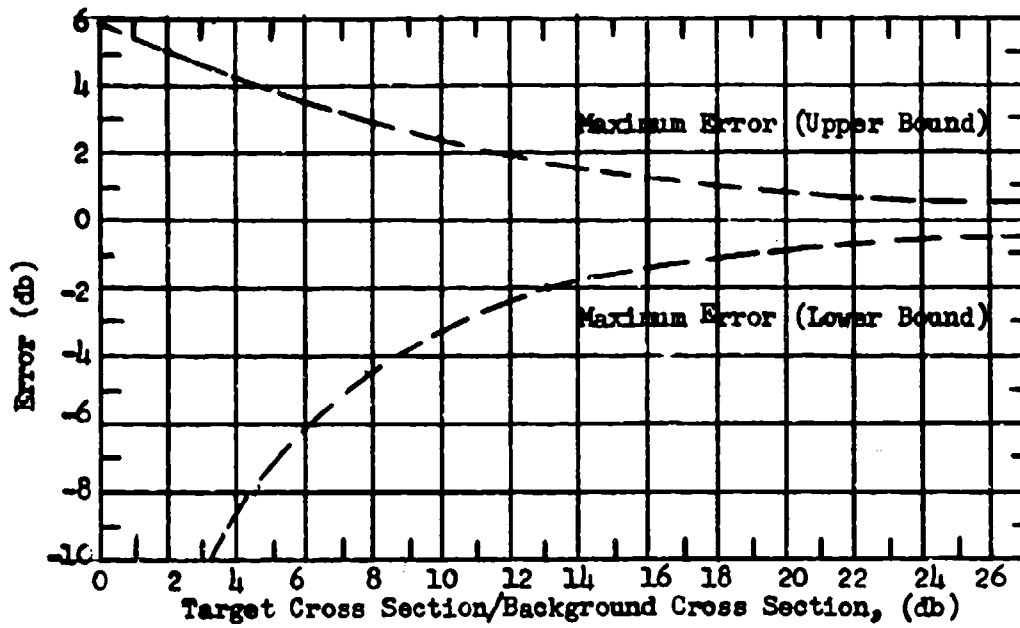
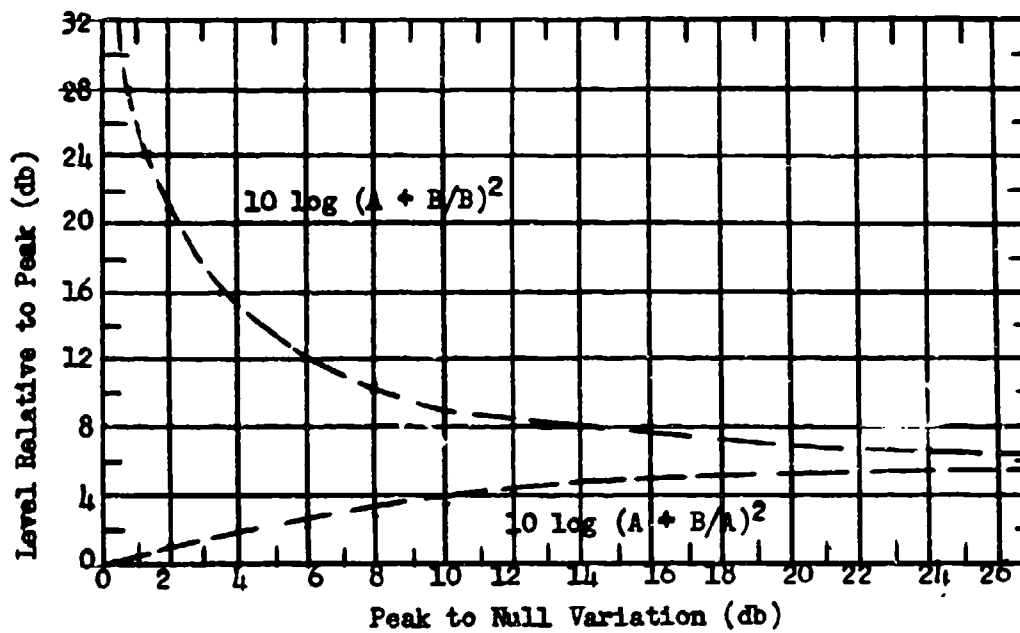


Figure 1 - Error Curve



Note: If $|B|$ is larger than $|A|$ the curves will be reversed.

Figure 2 - Power Level Separation

Amplitude Variation in Longitudinal Direction

Any physical target other than a flat plate will have a significant finite dimension in the direction of propagation. Since the E field decreases in proportion to $1/R$, where R is the distance from the transmitting antenna, it is obvious that the field will differ at points on the target at different distances from the antenna. Consider a target of length L , the nearest part of which is a distance R_A from the antenna and the farthest part of which is a distance R_B from the antenna.

$$\text{Then } R_B - R_A = L. \quad (2)$$

In order to measure the difference in power between the two points, consider the power ratio

$$\frac{P_A}{P_B} = \frac{(E_0/R_A)^2}{(E_0/R_{A+L})^2} = \left(\frac{R_A + L}{R_A} \right)^2. \quad (3)$$

The measured variation in db would then be given by

$$20 \log \left(\frac{R_A + L}{R_A} \right) = \Delta A \quad (4)$$

where ΔA represents the variation in db.

For application to the quasi-doppler technique, the dimension L must consist of the target dimension in the longitudinal direction plus the distance covered by the motion of the target.

Equation (4) may be written

$$R_A = K L \quad (5)$$

$$\text{where } K = \frac{1}{\log^{-1} \left(\frac{\Delta A}{20} \right) - 1}.$$

For any given acceptable value of ΔA , the minimum range required can be easily determined.

Amplitude Variation in the Horizontal Plane

The amplitude variation over the horizontal target aperture will be a function of the transmitter antenna beam width and the range length. For any given target size, the minimum range is determined by the antenna beamwidth for a given allowable variation. In most cases, therefore, the allowable variation in the horizontal plane will dictate the particular antenna to be used.

Amplitude Variation in the Vertical Plane

It has been shown² that when a transmitting antenna is located proximate to the ground such that the grazing angle of the reflected ray is less than 2° , the magnitude of the reflection coefficient is approximately unity for either horizontal or vertical polarization. Similarly, the phase of the reflected ray will be approximately 180° relative to the incident ray for either polarization. For this reason, if the grazing angle can be kept below this value (2°), the far field effect can be considered as being generated by the two element array; i.e., the antenna and its image, considered as two point sources separated by $2h$ where h is the antenna height above ground.

The field strength in the far field from a two element array as a function of elevation angle may be written

$$E(\alpha) = E_0 F(\alpha) \sin \left[\frac{2\pi h}{\lambda} \sin \alpha \right] \quad (6)^3$$

where $F(\alpha)$ is the elevation pattern of the transmitting antenna,
 h is the antenna height above ground,
and λ is the operating wavelength.

For small (2°) grazing angles, it will be assumed that $F(\alpha)$ is constant and normalized to unity over the angles (α) of interest. If x is the target height above ground

$$\sin \alpha \approx \tan \alpha = \frac{x}{R} \quad (7)$$

where R is the range length.

Using this assumption, the far field may be written as a function of the target height x as

$$E(x) = E_0 \sin \left(2\pi hx / \lambda R \right) \quad (8)$$

This then represents the multilobed far field elevation pattern from a transmitting antenna located proximate to the ground. The form of the field is shown by the solid line in Figure 4. The dotted line represents $F(\alpha)$, the far field elevation pattern of the transmitting antenna. If the first lobe of the structure is considered, it is seen that the assumption, that $F(\alpha)$ is constant over the angles of interest, is most valid. The true validity is, of course, dependent upon the beam width in the elevation plane of the transmitting antenna. The far field power pattern may be written

$$P(x) = 20 \log \left(\sin \frac{2\pi hx}{R} \right) \quad (9)$$

The target height x_0 may be fixed at the peak of the first lobe by the condition

$$\frac{2\pi h x_0}{R} = \frac{\pi}{2} \quad (10)$$

which reduces to $\lambda R = 4 h x_0$. (11)

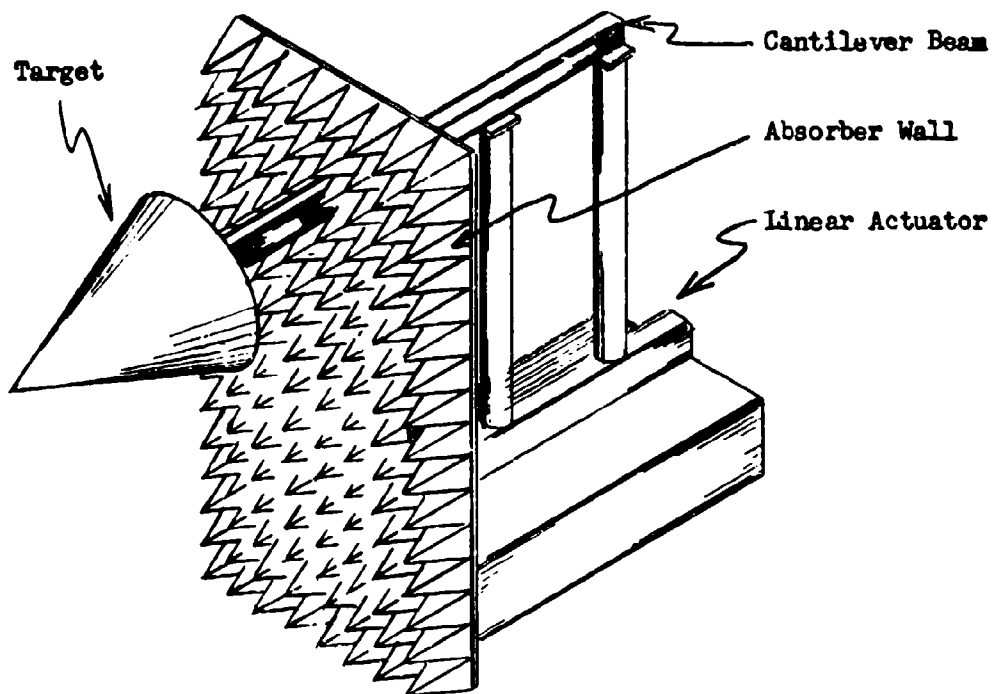


Figure 3 - Quasi-doppler Mount

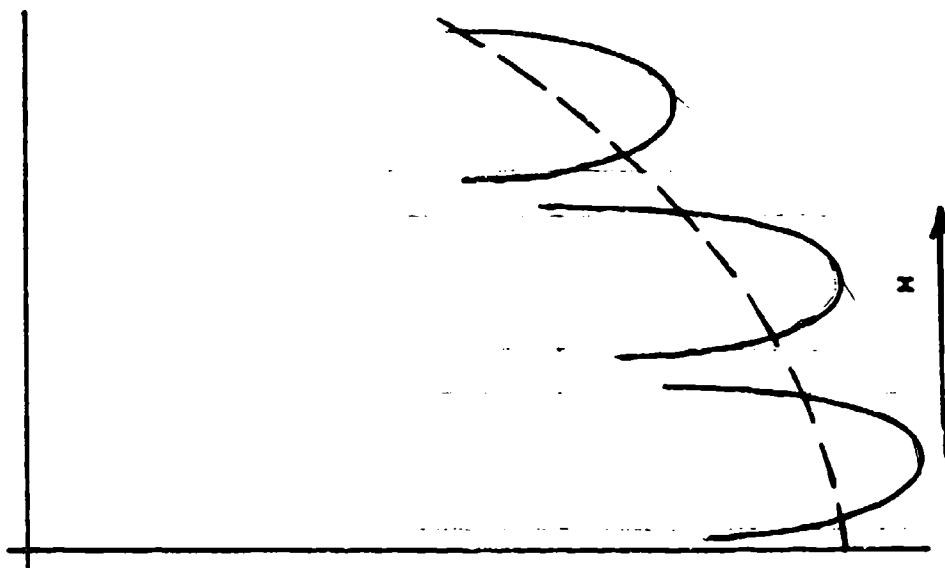


Figure 4 - Power Lobe Structure

Since the range length can be found by other means, e.g., the plane wave criteria and the amplitude variation criteria in the longitudinal direction both yield minimum range values, the range at this point will be a fixed constant. It is left then to uniquely determine the values of h and x_0 for a given acceptable amplitude variation over the vertical target aperture.

Equation (10) applied to the peak of the first lobe becomes

$$20 \log \sin \left(\frac{2\pi h x_0}{\lambda R} \right) = 0 \text{ (db)} \quad (12)$$

Similarly, one may write

$$20 \log \sin \frac{2\pi h x_1}{\lambda R} = A \text{ (db)} \quad (13)$$

where x_1 is the height of the lower edge of the target aperture and A is the power level at this point measured in minus decibels from the peak of the lobe. It is recognized that $(x_0 - x_1)$ is one half, assuming a symmetrical target, of the vertical dimension of the target aperture.

For a given allowable variation (A) at x_1 , the values of h and x_0 may be computed. Solving equation (13) for x_1 yields

$$x_1 = \frac{\lambda R}{2\pi h} \left\{ \sin^{-1} \left[\log^{-1} \left(\frac{A}{20} \right) \right] \right\} \quad (14)$$

Subtracting (14) from (11) and rearranging yields

$$h \Delta x = K \lambda R, \quad (15)$$

where $\Delta x = x_0 - x_1$ and $K = \frac{1}{4} - \left\{ \frac{\sin^{-1} \left[\log^{-1} \left(\frac{A}{20} \right) \right]}{2\pi} \right\}.$

Therefore, once the range has been determined, and the vertical aperture dimension $2 \Delta x$ and the allowable amplitude variation have been determined, a unique antenna height h can be found from equation (15). The unique solution for x_0 is then given by equation (11).

TARGET SUPPORT SYSTEM

The single most obvious problem in the Quasi-doppler technique is that of the motion of the target support. Certainly any structure which supports the target during its motion must also be moving and therefore, will also yield a power return which will effectively add to the target return and contribute to the modulating effect. Various forms of low density and dimensionally small physical structures have been employed with varying degrees of success.

For certain target shapes, a special mount has been devised and successfully employed. Such a mount is shown in diagram form in Figure 3.

It consists of a small cantilever beam extending through a small opening in a very large wall of absorber material. A linear actuator behind the wall moves the beam either toward or away from the transmitting antenna. The target is mounted on the extended end of the beam. Optically, the only motion seen from the antenna is that of the target since the absorber wall is fixed and the target itself hides the beam. Certainly for many targets, such as spheres, or cone spheres which have large forward scattering properties, such a device would not be applicable. However, for certain target configurations, it is well suited.

Consider, for example, a regular cone with a concave base. If the diameter of the base is much larger than the cross section dimension of the cantilever beam, the effect of the beam motion can be considered very small. The diffraction at the edge of the cone base will be appreciable. However, only a very small portion of this will be affected by the motion of the beam. Most of the diffracted energy will instead illuminate the absorber wall which is fixed. Another effect this system introduces is the change in the shadow area on the absorber wall as the target is moved. This could be more significant than the effect of the beam itself. However, if the range length is very large relative to the wavelength, the change in the shadow with target motion of one-half wavelength could be negligible. This will, of course, be a function of the effectiveness of the absorber material itself.

DATA REDUCTION AND ANALYSIS

In order to determine the absolute radar cross-section of any arbitrary target, a reference target of known cross-section must be measured under similar conditions. For this purpose, a simple flat plate can be mounted and moved in the same manner as the test target.

It has been found, however, that a fixed reference located near the test target, but such that its presence does not appreciably perturb the illumination of the target, will serve as a standard reference and also yield additional correlation to the measured data. It must be noted that slightly poorer accuracy will result from using a fixed rather than movable reference. The problem of data analysis can be best understood by considering a typical pattern such as that shown in Figure 5. The curves on the recording are identified as follows:

- 1) Linear Actuator, without target, moved through $\lambda/2$. Fixed reference is not in the field.
- 2) Linear Actuator, with target mounted, moved through $\lambda/2$. Fixed reference is not in the field.
- 3) Linear Actuator, with target mounted, moved through $\lambda/2$. Fixed reference is in the field.
- 4) Linear Actuator, without target, moved through $\lambda/2$. Fixed

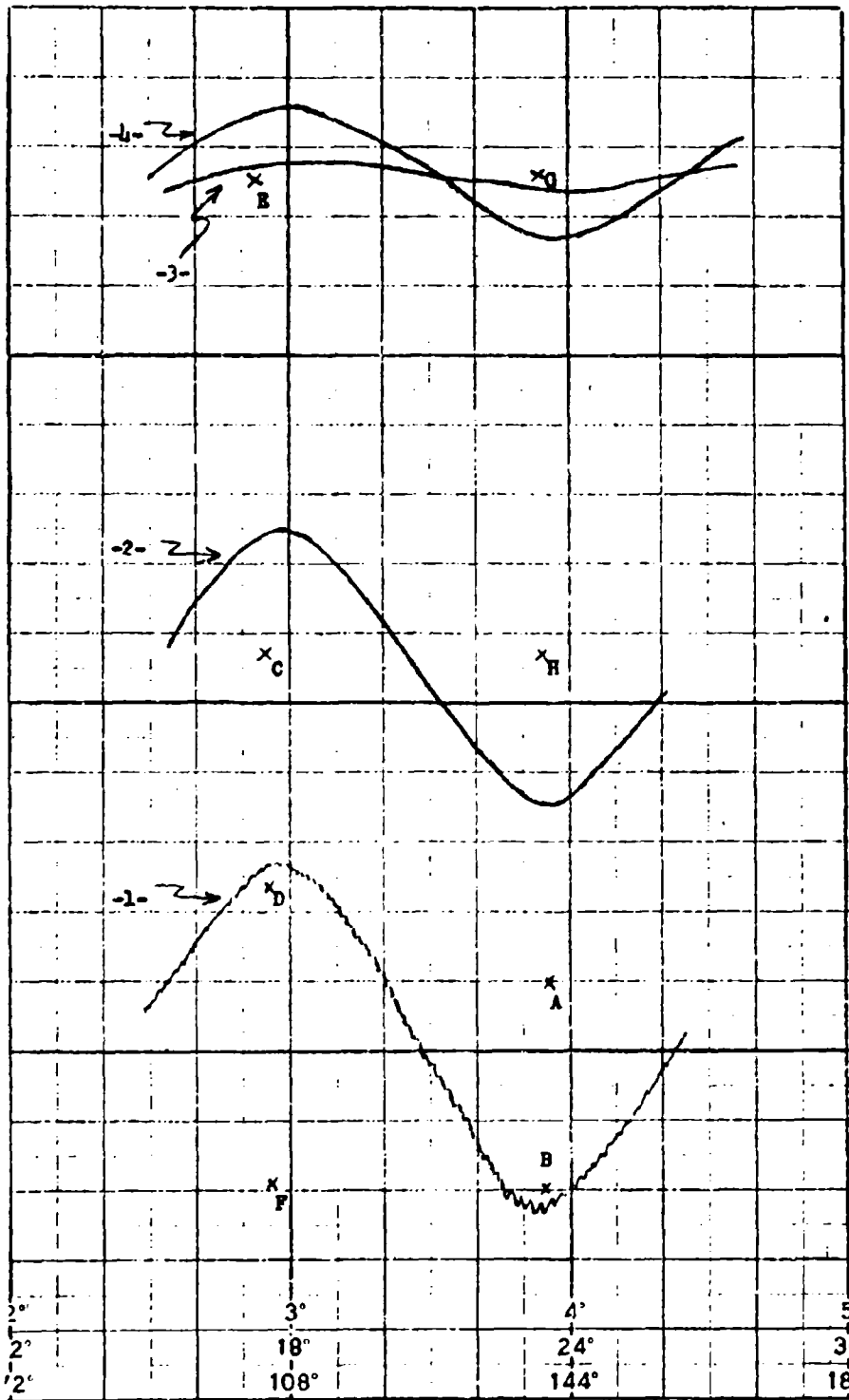


Figure 5 - Typical Quasi-doppler Pattern Recording

reference is placed in the field.

Each recorded curve will yield two levels by use of Figure 2, one being the fixed return and the other being the return from whatever in the field is moving. It is not always obvious which level is which return. This problem can generally be solved, however, by cross correlation between the several curves. To illustrate this, assume that the four patterns were recorded in the order in which they are listed.

Curve 1) shows a 10.0 db peak to null variation. Referring to Figure 2, it is seen that one of the two levels is then 3.6 db down from the peak and the other is 9.4 db below the peak. These are indicated by points A and B respectively. One of these levels represents the average background level, and the other, the return from the moving empty mount. Which level represents which return cannot be determined at this point. Curve 2) has a 8.0 db peak to null variation. This yields one level 3.5 db below the peak and the other 10.2 db below the peak. These levels are labeled C and D respectively. Since one of these levels must represent the target return, and the other, the average background level, it appears at this point as though points D and A must be the average background since they are approximately the same level. This might be sufficient, in certain cases, where only relative measurements are required (such as between different aspect angles). However, for absolute results a suitable reference must also be measured.

Curve 3) recorded with the empty mount moving and fixed reference mounted in the field shows a peak to null variation of 0.7 db. This yields one level 0.4 db below the peak and the other level 29.0 db below the peak. These are indicated by points E and F respectively. One of these levels represents the return from the moving empty mount and the other combined return from the fixed reference and the background added in some random fixed phase. These are indicated by points E and F respectively. Comparison of this with Curve 1.) would point to the fact that points B and F yield the level of the empty mount and point E represents the return from the reference plus background. Additional correlation results from Curve 4). The peak to null variation is 3.6 db yielding one level 1.6 db below the peak and the other 15.6 db below the peak. These are marked G and H respectively. Point G must be the combined return from the fixed sphere and the background and point H that from the target, which agrees with its value as concluded from Curve 2), i.e., point C.

The actual level of the standard reference may now be assigned an accuracy figure determined by its level compared to that of the background. In the example cited, since the reference is approximately 23 db above background, its accuracy is about ± 0.8 db. The accuracy of the absolute measurement of the target is then of the same order. Notice then that a target that yields a return less than 10 db above background which would by conventional measuring methods have associated with it, an accuracy (from Figure 1) of +2.5 to -3.5 db now has a measurement accuracy better than ± 1.0 db.

The method will apply equally well to much smaller targets since the accuracy of the measurements actually depends upon the accuracy that can be given to the measurement of the reference. A suitably large reference can be chosen at will.

PROBLEM AREAS

Many problems encountered in radar cross-section measurements are common to any method or technique employed. Among these are frequency and power stability, target support reflections and target illumination. The first of these can be adequately controlled by use of crystal controlled sources. Continuous frequency and power monitoring systems are suggested as checks during a test operation. Support reflections have been minimized for certain target configurations by the mount described earlier. Proper target illumination has been achieved to within tolerable limits by proper range parameter requirements.

Certain other problems arise in the use of the Quasi-Doppler technique. Among these is the changing shadow effect during target motion. This is minimized by increased range length. Another problem arising from target motion is that of varying aspect angle as the target moves. This can be eliminated, in the monostatic case, by using a single antenna and mounting it at the same height as the target. Proper location of the standard reference in the illumination field is extremely important. Its location must be such that its illumination is essentially the same as the target's (or with a known difference between the two) and also such that the presence of either does not perturb the illumination of the other. Probably the most significant problem yet to be solved is the support structure for targets of any given shape.

ACKNOWLEDGEMENTS

The author wishes to extend his appreciation to all of those who assisted in the measurements research effort. Particular thanks go to J. C. Huber and B. M. Bowman for comments and suggestions, and to F. E. Fischer and W. W. Martin for preliminary theoretical work.

BIBLIOGRAPHY

- 1 Fritsch, P. C., "Survey of Radar Reflectivity Ranges", M.I.T., Lincoln Laboratory, January 1963.
- 2 Kerr, D. E., (Editor), "Propagation of Short Radio Waves", Radiation Laboratory Series, Volume 13, pp. 196-403, McGraw-Hill Book Company, Inc., 1951.
- 3 Cohen, Albert and Molteso, A. W., "The Lincoln Laboratory Antenna Test Range," The Microwave Journal, Volume 4, No. 4, page 57, April 1961.

INDOOR RANGE DESIGN

R. J. Wohlers
Cornell Aeronautical Laboratory, Inc.
Buffalo, New York 14221

ABSTRACT

The successful radar cross-section measurement range requires a unique combination of excellent electronic circuitry and mechanical instrumentation and the minimization of unwanted reflections of electromagnetic radiation from the surrounding environment. Of the three basic factors involved, the most important is control of unwanted reflections, since the degree of precision of control determines the ultimate sensitivity of the entire measurement system. This paper is devoted to the design principles involved in reducing spurious responses associated with the undesired signal returns from physical environment, particularly in regard to indoor facilities.

INTRODUCTION

In general, the perturbations introduced by range environment can be classified into two broad areas:

1. Background cross section, or the inherent return received from the range without a target in place, and
2. Bistatic* interactions, or the coupling between the target and environment.

Of the two, background level is most easily recognized and measured, since it is the residual signal found without a target in place. Bistatic effects, which are more difficult to determine, are not usually considered in terms of range limitation, hence tend to be ignored in range specification.

Both background cross section and bistatic interaction are present in all ranges to some degree, whether indoors or out. However, these effects are usually more noticeable in the indoor case, since the room reserved for measurement behaves in a manner similar to a gigantic microwave cavity. The success of the indoor range thus depends primarily upon the introduction of loss terms in this cavity to achieve a very low Q, as far as the radar is concerned, for all possible targets. In the case of

*The term "bistatic" alone is commonly accepted as referring to a dual antenna radar or radar range system. Throughout this report it is used in conjunction with terminology such as "interactions to denote a multiple reflection path involving the target model. Only once, in Fig. 4, it is used in the "conventional" manner.

continuous wave (CW) measurements, spurious reflections are received continuously, thus the achievement of a sufficiently low room background is completely dependent on physical absorbers. The use of a pulse system permits some of the backwall and target multipath reflections to be partially eliminated by gating.

Basic to solution of the problem is the use of radar absorptive material to achieve the necessary attenuation for the low Q's required. Not only is the choice of material important, but, as in the usual cavity case, so are absorber orientation, geometry and placement. The discussions that follow are devoted to the design principles involved in achieving high performance (high loss) while still observing the desirable engineering goal of economy.

TECHNICAL APPROACH

Of primary concern in indoor range design are the performance characteristics of the materials used for attenuating reflections, since these materials play such a strong role in determining range performance. It is needless to say that the material used should have as high an absorption as possible. This material is usually rated in terms of its absorption at normal incidence.

Just as important as the material's normal incidence reflection coefficient, however, is its behavior for off-normal incidence. Typical of high-performance, commercially available absorbers is an extreme variation of the material's reflection coefficient with angle of incidence. Usually constructed with front surface matching sections of cones, pyramids, etc., the absorber behaves in a decidedly nonspecular manner, with, in some cases, a 40 db increase in reflection coefficient noted for a 20 degree departure from normal incidence.

This effect is displayed in Fig. 1 for K_a band, and Fig. 2 for X-band. The data, presented in terms of median values, were obtained from samples larger than incident beamwidth to insure elimination of edge effects. Each sample was backed with an aluminum plate of the same size as the sample to obtain direct correlation between angular behavior of the plate and sample. The equivalent specular reflection coefficient used as the ordinate on those figures is obtained by dividing power actually received by that which a metallic plate would have produced.

The curves shown in Figs. 1 and 2 clearly illustrate the degree of nonspecular behavior of the material, since total return is given by the product of antenna side-lobe gain squared and effective reflection coefficient. Note that one sample at K_a band, the hair mat material HM 125, had an equivalent specular greater than unity, indicating that a flat metallic plate would have a smaller back-scattered signal at the same incidence angle.

The data presented, typical of materials tested at Cornell Aeronautical Laboratory, clearly shows that optimum range design, predicated on high loss to achieve a very low Q, requires energy incident on the absorber to be nearly normal at all times. As a general rule, the incidence angle should not deviate from the normal incidence case by more than approximately 10 degrees.

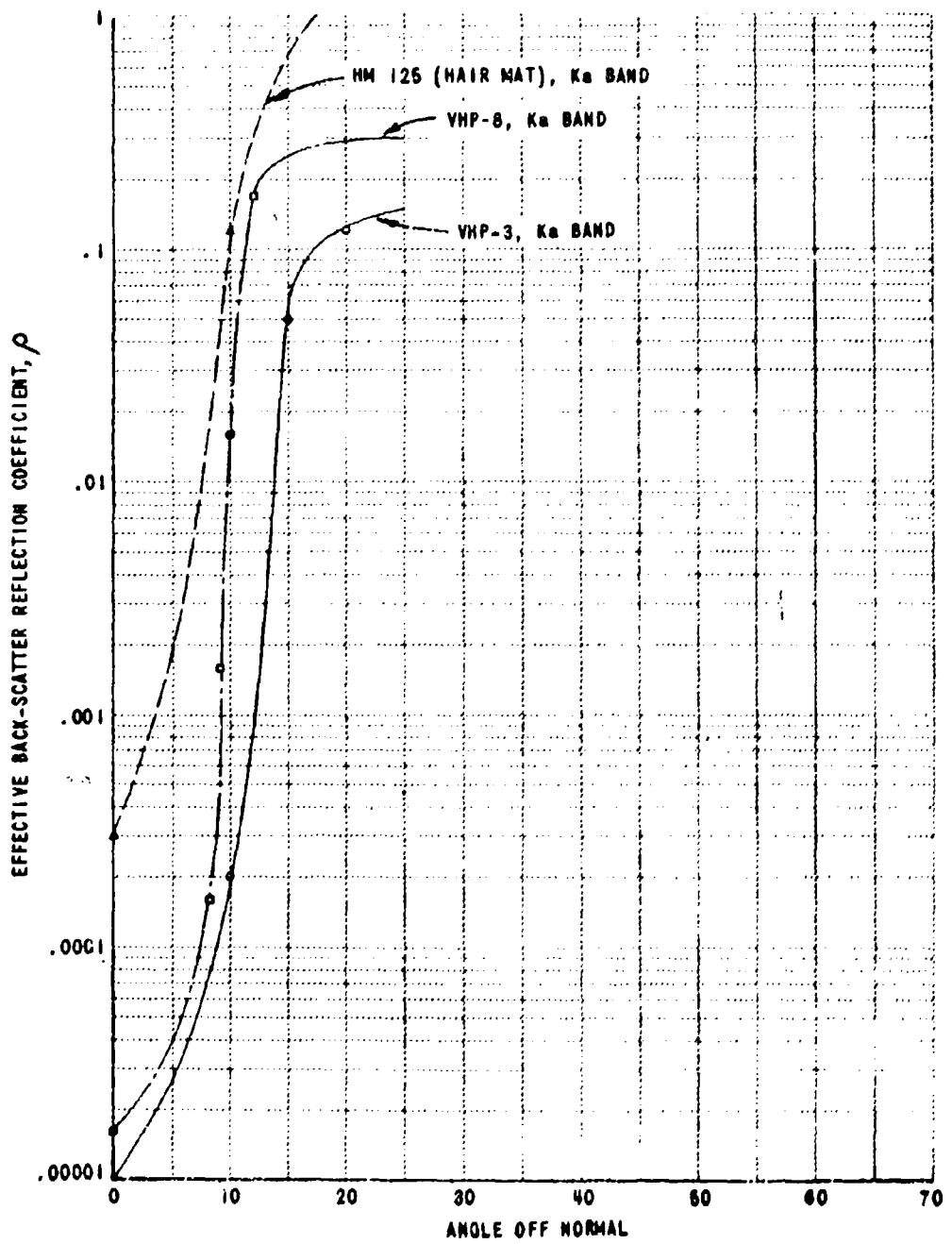


Figure 1 ANGULAR BEHAVIOR OF ABSORBERS, Ka BAND

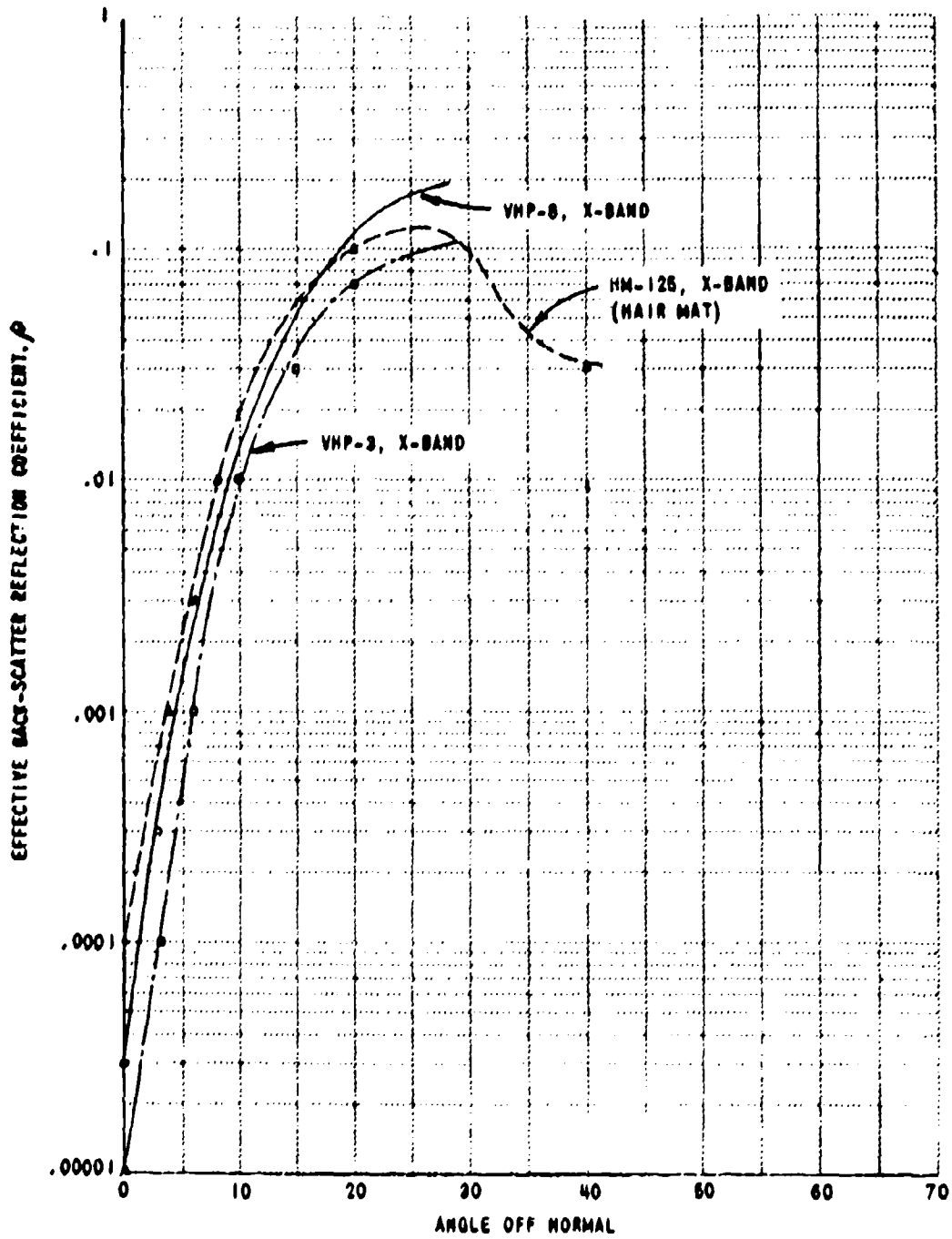


Figure 2 ANGULAR BEHAVIOR OF ABSORBERS, X-BAND

Of importance equal to the use of absorbers within the room to achieve a low effective Q is the actual prevention of some of the transmitted energy from entering the room. For example, the ideal antenna for range application would have a main lobe consistent with the physical aperture employed, while all side lobes would be zero.

This condition cannot be completely met by an antenna structure. It is definitely not approached by normal or conventional antenna practice. The normal antenna exhibits at most -40 db sidelobes, whether a horn or parabolic reflector is employed.

Cornell Aeronautical Laboratory has effected side and back lobe control by the technique illustrated in Fig. 3. This technique uses the original antenna, here called the primary aperture, to illuminate a secondary aperture centered on the main beam axis and located a short distance away from the primary aperture.

A box, lined with radar absorbent material, surrounds primary and secondary apertures. The exit aperture is the same dimension as the primary aperture, while the lining, consistent with the angular behavior of absorbers shown above, is oriented so as to be primarily normal to electromagnetic energy arriving from the feed and primary aperture. From exceedingly simplified considerations, it can be seen that side-lobe energy should be considerably reduced, while main lobe shape and gain remain relatively unperturbed.

Complete design considerations are beyond the scope of the present paper and show that the simplified concept is essentially correct, with the far field given approximately by:

$$E(u) = \int_{-\frac{x_0}{2}}^{\frac{x_0}{2}} f(x) e^{-i k_0 x \sin \alpha} dx \quad \begin{array}{l} \frac{x_0}{z_0} > \tan \alpha \\ \frac{x_0}{z_0} < \tan \alpha \end{array}$$

$$= 0$$

$f(x)$ = antenna aperture distribution

k_0 = propagation constant

x_0 = antenna and box aperture

z_0 = separation between antenna and exit aperture

and assuming a perfect absorber lining the box.

Actual measurements, made with these enclosures, have shown that side-lobe level in the shadow region is given by the product of original side-lobe level and absorber attenuation.

So far the discussion has not differentiated between the two types of measurement apparatus used in indoor ranges, cw and pulse, and has outlined only general methods for reducing extraneous signals. It is well at this point to consider in detail the effect of specific apparatus upon room design.

Figure 4 illustrates the two basic configurations used for cw measurement of radar cross section. Here background cancellation is accomplished

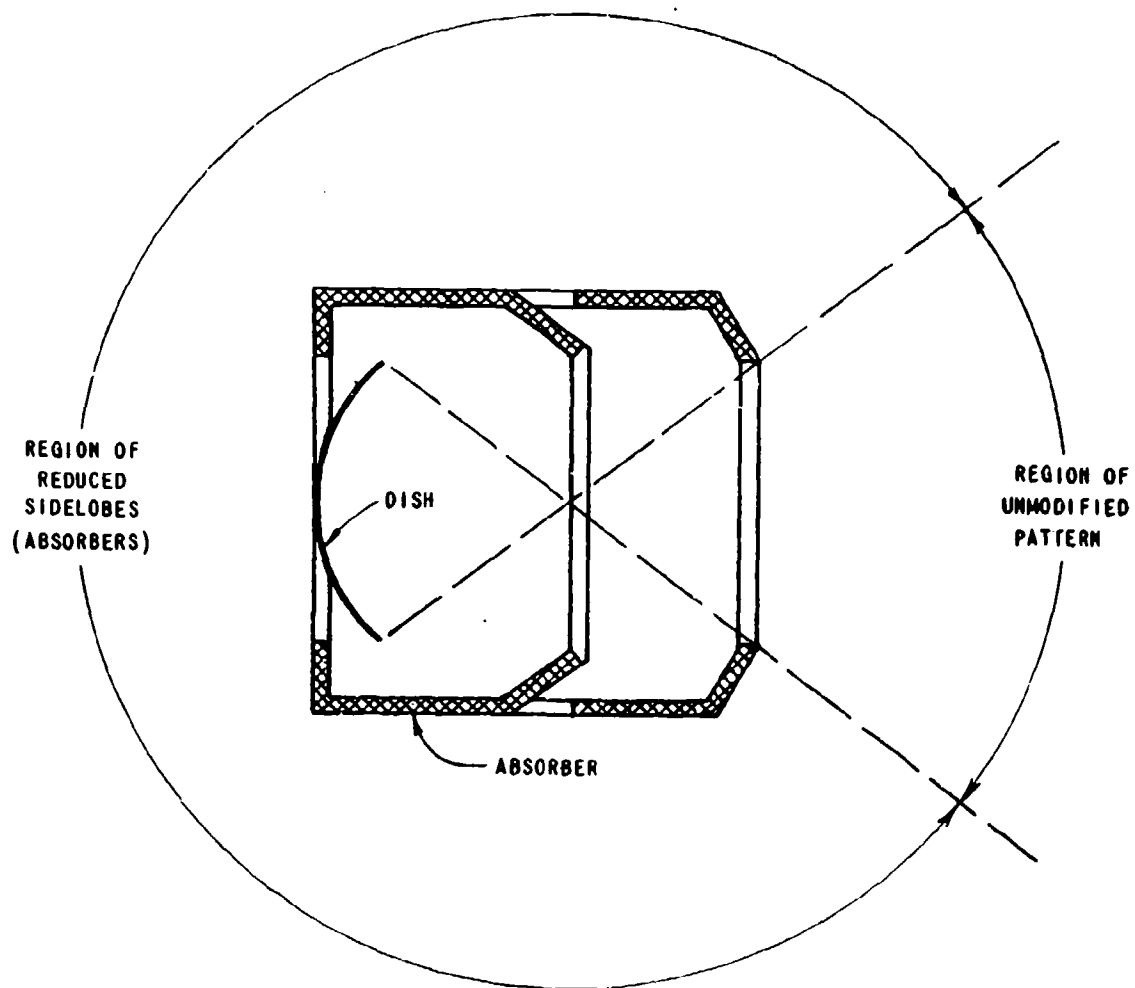
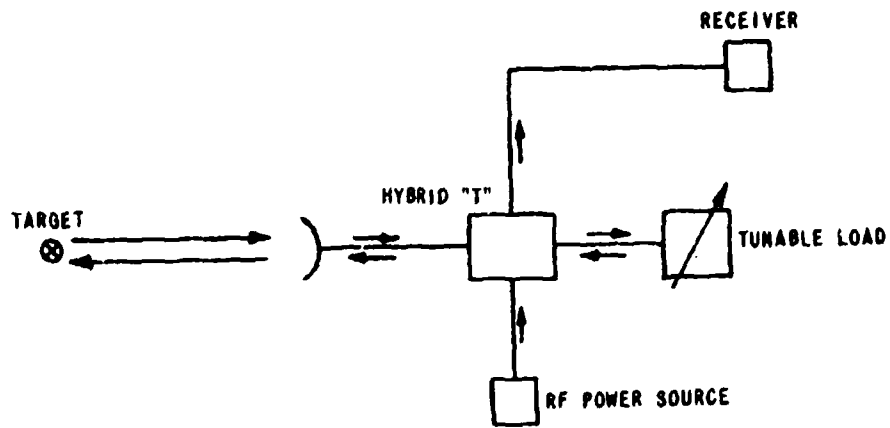
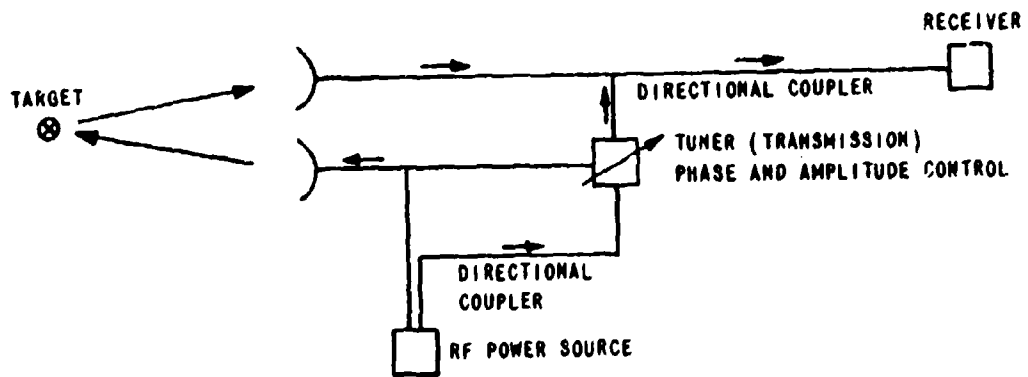


Figure 3 TUNNEL ANTENNA



A. MONOSTATIC (SINGLE ANTENNA) METHOD



B. BISTATIC METHOD

Figure 4 CW RADAR CONFIGURATIONS

by tapping part of the transmitted signal, and with appropriate phase and amplitude adjustment, using this signal to cancel energy returned from the room. Background cancellation is possible for all room configurations, dependent solely upon the frequency stability of the microwave source and compensating network.

Under the assumption of perfect electronic circuitry, it may appear that reduction of the absolute level of background is not a prime concern, since background signal can be balanced out electrically. This is not the case, however, since a large background level implies reflected waves that illuminate the target from the wrong direction and introduces bistatic scattering effects. For the cw case, background and bistatic interactions are interwoven and the multipath reflections cannot be separated from the direct target model reflection. A reduction of background level is required for consequent reduction bistatic coupling.

For the simplest room, a rectangular shape with a radar at one end, a flat wall beyond the target area is lined with absorber to attenuate the transmitted signal that travels beyond the target area (see Fig. 5). The return from the wall is given, in terms of cross section, as:

$$\sigma_w = \rho \pi R_1^2$$

σ_w = wall cross section

ρ = power reflection coefficient

R_1 = range from radar to backwall

Additional returns are also found from antenna sidelobe effects; here side walls are illuminated at glancing incidence, and after multiple reflection, enter the receiving apparatus. In general, such returns are much less than that from the rear wall and can be evaluated only for a particular room size and antenna(s). For purposes of discussion, it can be assumed that the principal source of background is the backstop.

The ratio of power received from the target to that received from the wall is found to be:

$$R_t = \frac{\sigma_T R_2^2}{\pi \rho R_1^2}$$

σ_T = target cross section

R_2 = range to target

Since the wall return can be cancelled to some degree during a measurement period, expressed as a fraction (k_1) of total wall return, the lower limit of effective measurement is given by:

$$\sigma_T = \frac{R_t \pi R_2^2 k_1 \rho}{R_1^2}$$

For a given factor k_1 , denoting the stability of cancellation, and a given R_t , denoting a particular measurement accuracy (usually 100),

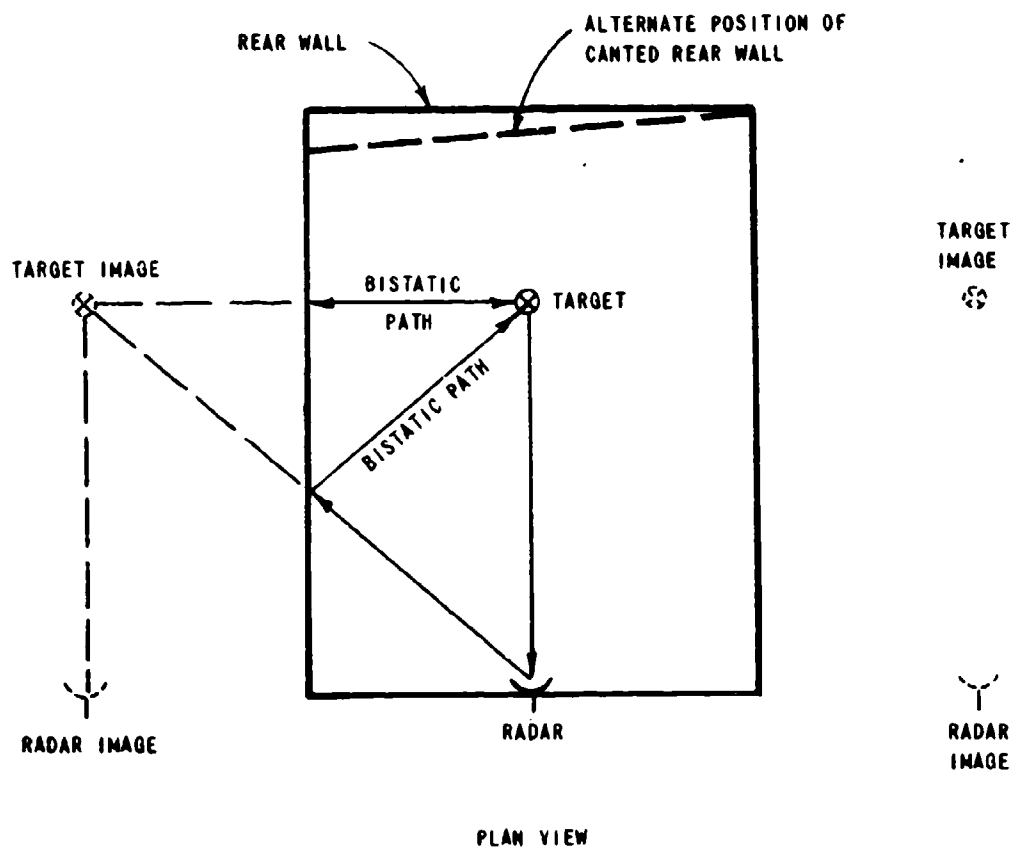


Figure 5 RECTANGULAR DARK ROOM

smaller target cross sections appear to require a larger R_1 . However, R_1 is also a function of R_2 , and an increase in R_2 decreases the allowable value of R_1 . For example, let the room be dimensionally stable, but allow the microwave source to have a limited frequency stability expressed in fractional form as $\frac{d\omega}{\omega}$. Under this condition, the ratio of wall return (in power) to that from the target is given by:

$$\sigma_T = \frac{\pi \rho (4\pi)^2 R_2^4 R_T \left(\frac{d\omega}{\omega}\right)^2}{\lambda^2}$$

and the minimum cross section that can be measured is independent of range to the back wall. In fact, if the far-zone criteria is substituted for R_2 , the minimum cross section that can be measured with 1 db accuracy ($R_T \approx 100$) is

$$\sigma_T = \pi \rho (4\pi)^2 \eta^2 \lambda^2 \left(\frac{d\omega}{\omega}\right)^2 \approx 100$$

1) = target length in number of wavelengths

Three factors thus determine minimum measurable cross section (from the background alone). Those three are the frequency stability of the rf source, target length and absorber efficiency. Figure 6 is a plot of required frequency stability permitting the measurement of a given cross section at a one db measurement accuracy as a function of target length and absorber reflection coefficient.

Some improvement can be noted by slanting the back wall, in which case the minimum measurable cross section is reduced by a factor proportional to the ratio of side-lobe gain to main beam gain squared. However, ρ is also angle dependent, rising for off-normal aspects and limiting the improvement sought. For example, suppose an X-band equipment is used with an antenna beamwidth of 5.3 degrees and a first side lobe 13 db below the main beam gain. Although the return from the wall will be down by 26 db, through the sidelobe reduction of antenna gain, absorber efficiency is also decreased by 26 db (see Fig. 2 for VHP-3), and the net improvement is zero db.

An improvement over the canted wall is possible if the rear wall is made non-planar. For example, let the rear wall be a convex bull's-eye such as a parabola viewed along the axis of symmetry. Then assuming the angle between surface normal to the wall and the incident ray along

* Horns are generally used in cw radar cross section ranges because of their inherently low VSWR, with the horn's high side lobe level tolerated. A much better antenna for this application appears to be the short focus lens, with matching sections, to provide both low VSWR and side lobes. It is not known at this time whether this lens has found application in any range.

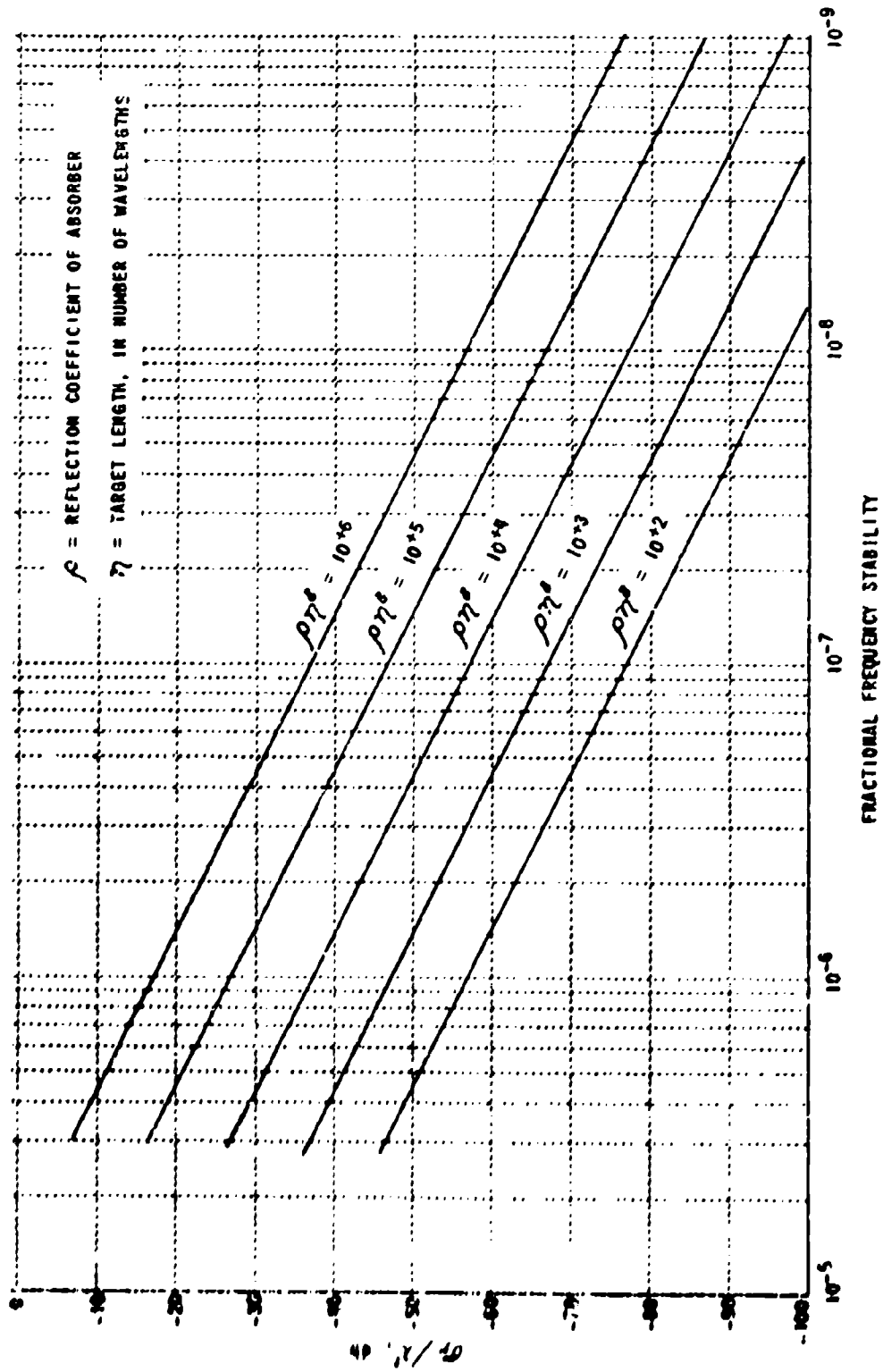


Figure 6 REQUIRED FREQUENCY STABILITY VS TARGET CROSS SECTION

the first pattern null is held to less than 20 degrees, the effective wall cross section is reduced by approximately $.625 \Theta_0^2$, where Θ_0 is the half power beamwidth of the antenna in radians. A 20 db reduction is possible over the flat wall case for antenna beamwidths of less than 7.5 degrees. (See Fig. 7.)* From the foregoing, it can be seen that the combination of an excellent absorber with a source exceedingly stable in frequency usually allows the measurement of almost any target in the cw range. (See Fig. 6). The limitations that do exist lie primarily in bi-static effects.

Figure 5 illustrates the ray geometry for bistatic interaction paths into the receiver. For planar walls, first order multipaths** can be treated most expeditiously in terms of images, as shown. From the figure, the following signals can be denoted:

- E1, the path from transmitter to target, to image, to image antenna (left wall)
- E2, ditto, for right wall
- E3, ditto, for floor
- E4, ditto, for ceiling

These signals will be noted as group one.

- E5, the path from antenna, to target image, to image antenna (left wall)
- E6, ditto, for right wall
- E7, ditto, for floor
- E8, ditto, for ceiling

These signals will be noted as group two.

- E9, the path from antenna, to target, to image antenna (left wall)
- E10, ditto, for right wall
- E11, ditto, for floor
- E12, ditto, for ceiling

These signals will be noted as group three.

- E13, the path from antenna, to target, to image antenna, back wall (the forward scatter case)

For group one interactions, the power contained in extraneous received signals is given by:

$$P_{0n} = \frac{R G^2 \lambda^2 T \sigma_{in}^2 \rho_n}{4\pi (4\pi)^2 R_n^2 R_i^2} = \text{received power}$$

* The shape shown was chosen to obtain a frequency independent return over an extremely wide frequency range. It does not necessarily represent the optimum wall shape for minimum cross section over a limited frequency band.

** It is assumed that two bounce reflections are much smaller than the direct term, hence the major concern is for first-order multipath.

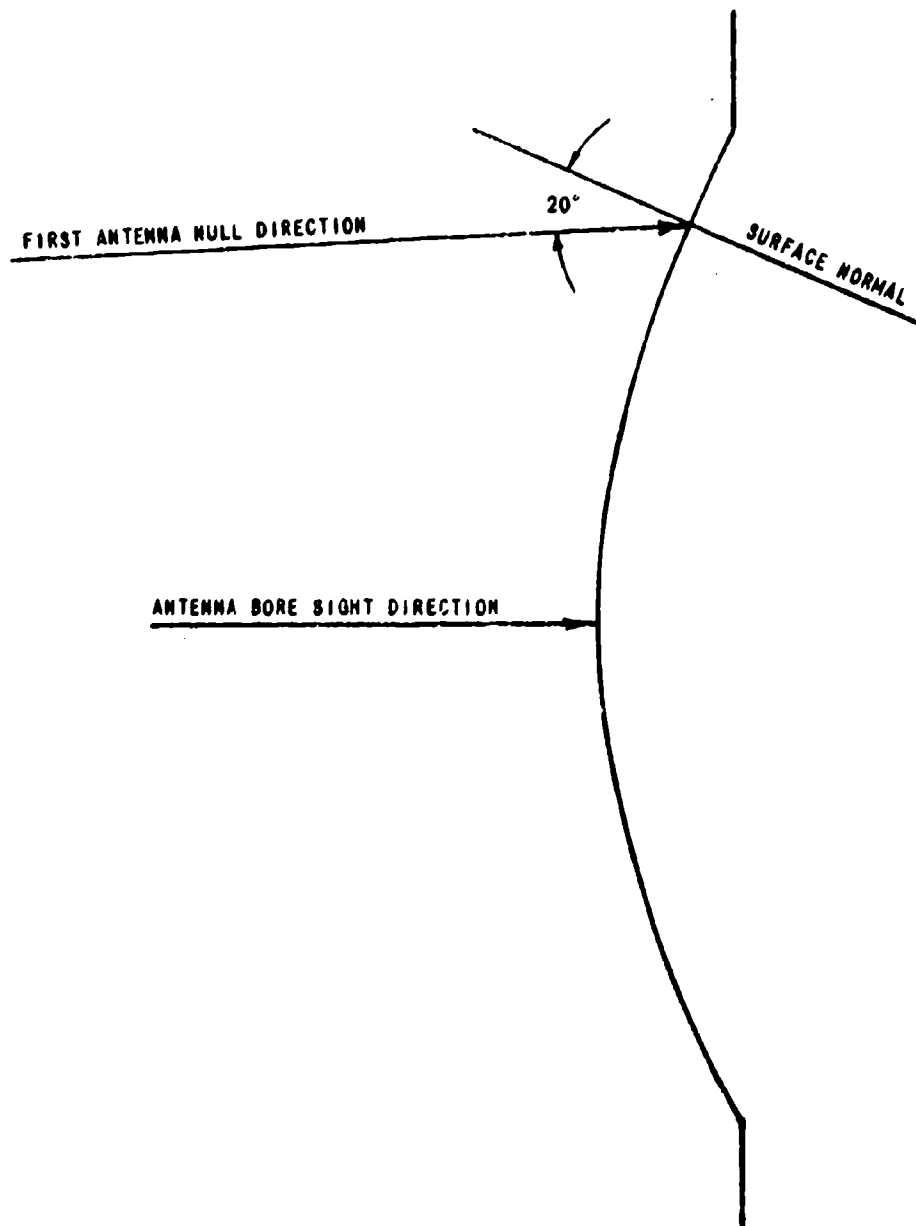


Figure 7 BACKWALL BULL'S-EYE

where $\tau \sigma_{1n}$ = bistatic cross section between target and image, the subscript denoting which wall interaction

R_n = twice the range from target to wall causing interaction

ρ = reflection coefficient of wall causing interaction

Of all the targets considered for measurement in the range, perhaps the most severe in terms of strong bistatic effects is a flat plate. The ratio of bistatic cross section to monostatic cross section for this target is quite high and known, hence it makes an ideal tool for evaluating range performance. Using this target, the ratio of received bistatic power to monostatic power becomes:

$$\frac{P_{bn}}{P_{mn}} = \frac{\tau \sigma_{1n}^2 \rho_n}{4\pi R_n^2 \sigma} = \frac{2\pi^2 l^2 \rho_n}{\lambda^4 R_n^2}$$

assuming a square plate is used in length l .

The usual requirement on accuracy is that $\frac{P_{bn}}{P_{mn}} < 0.01$, for 1 db measurement accuracy. Assuming the target is 10 wavelength on edge ($l=10\lambda$) the required dimension from the wall in question to target area becomes:

$$\frac{R_n}{2} = 2.25 \sqrt{\rho_n} \lambda \times 10^4$$

Using an absorber with $\rho_n = 0.01$, the distance from wall to target is 2230λ , indicating a considerable room size. For example, with a 1 cm wavelength, the necessary room length becomes 148 feet. To obtain a reasonable room size, the absorber would have to equal at least 10^{-4} , at which point room width is a nominal 14.8 feet. Successful room treatment thus requires a circumferential band of high quality absorber material about the target area, of such width as to encompass at least the first lobe of the target pattern (about 2 degrees for a 10λ target).

Group two and three paths are identical, so that the power received (bistatic) is given by

$$P_{bn} = 4 \frac{R_n G G(\theta) \lambda^2 \tau \sigma_{1n} \rho_n}{(4\pi)^2 R_n^2 R_n}$$

where $G(\theta)$ antenna sidelobe gain at angle θ , n denoting the source of interference

$\tau \sigma_{1n}$ = bistatic cross section

R_n = range to image

ρ_n = effective reflection coefficient at the wall

As before, the ratio of bistatic power to monostatic backscatter power is important, hence for the 10λ flat plate:

$$\frac{P_{0n}}{P_m} = \frac{8\pi^2 G(\theta) R_2^2 \rho_n (100)}{G R_n^2}$$

In the general case $R_2 < R_n < 2R_2$ hence the ratio can be assumed to have a value of 1/2 (a pessimistic value). The ratio becomes

$$\frac{P_{0n}}{P_m} = \frac{4\pi^2 G(\theta) \rho_n (100)}{G}$$

With the requirement for $\frac{P_{0n}}{P_m} = 0.01$ (for 1 db accuracy), the side-lobe ratio required of the antennas becomes:

$$\frac{G(\theta)}{G} = \frac{10^{-4}}{4\pi^2 \rho_n}$$

Since the best of absorbers yield a ρ_n of 10^{-3} or higher for angles greater than about 10 degrees, the antenna sidelobe that "looks" at target image must not exceed 2.5×10^{-3} or -26 db. Further reductions are possible to achieve lower sidelobe levels with the tunnel structure previously discussed.

Evaluation of back wall interaction terms cannot proceed with the convenient flat plate target, because the ratio of forward scatter to back scatter is not sufficiently high. Here evaluation must proceed through the use of a target with high forward scatter, but low back scatter. For design purposes, this ratio can be assumed to be 40 db. The ratio of received powers (from bistatic interaction and direct return) is given by:

$$\frac{P_0}{P_m} = \frac{G(\theta) R_2^2 \rho \times 10^4}{G R_1^2}$$

where $R_1 = R_2 + 2\Delta R$, and the distance from target to back wall is ΔR

With a bulged back wall employed $\frac{G(\theta)}{G} < 10^{-4}$ and for a ρ of 10^{-4} , we find $\frac{R_2}{R_1} = 1/3$. Since $R_1 = R_2 + 2\Delta R$, the distance from target to back wall must be no less than $0.366 R_2$.

There is another interaction found with the back wall, the target-target-image path. Assuming a forward to back scatter ratio of 10^4 , the power received from this path for a normal flat wall is:

$$P_0 = \frac{R G^2 \lambda^2 \sigma_t^2 \rho_n \times 10^8}{(4\pi)^2 R_2^4 (4\pi(2\Delta R))^2}$$

The ratio of this power to backscatter power is:

$$\frac{P_b}{P_m} = \frac{\sigma_T \times 10^8 \rho}{4\pi(z_0 R)^2}$$

and, with $\frac{P_b}{P_m}$ required to be 0.01, and assuming $\rho = 10^{-4}$, the required distance between target and backwall becomes:

$$\Delta R = \frac{1}{4} \sqrt{\frac{\sigma_T}{\pi}} \times 10^3$$

Using a bulged wall, the bistatic power return can be reduced by 15 db, and

$$\Delta R = \frac{1}{18} \sqrt{\frac{\sigma_T}{\pi}} \times 10^3$$

If ΔR is assumed $.366R_2$, then the maximum target that can be measured with accuracy is $5.52 \eta^4 \lambda^2 \times 10^{-4}$. * Increasing ΔR to equal R_2 allows measurement of targets as large as $4.8 \eta^4 \lambda^2 \times 10^{-3}$. A nominal choice of $\eta = 10$ (target length = 10λ) yields a target cross section as large as $48 \lambda^2$.

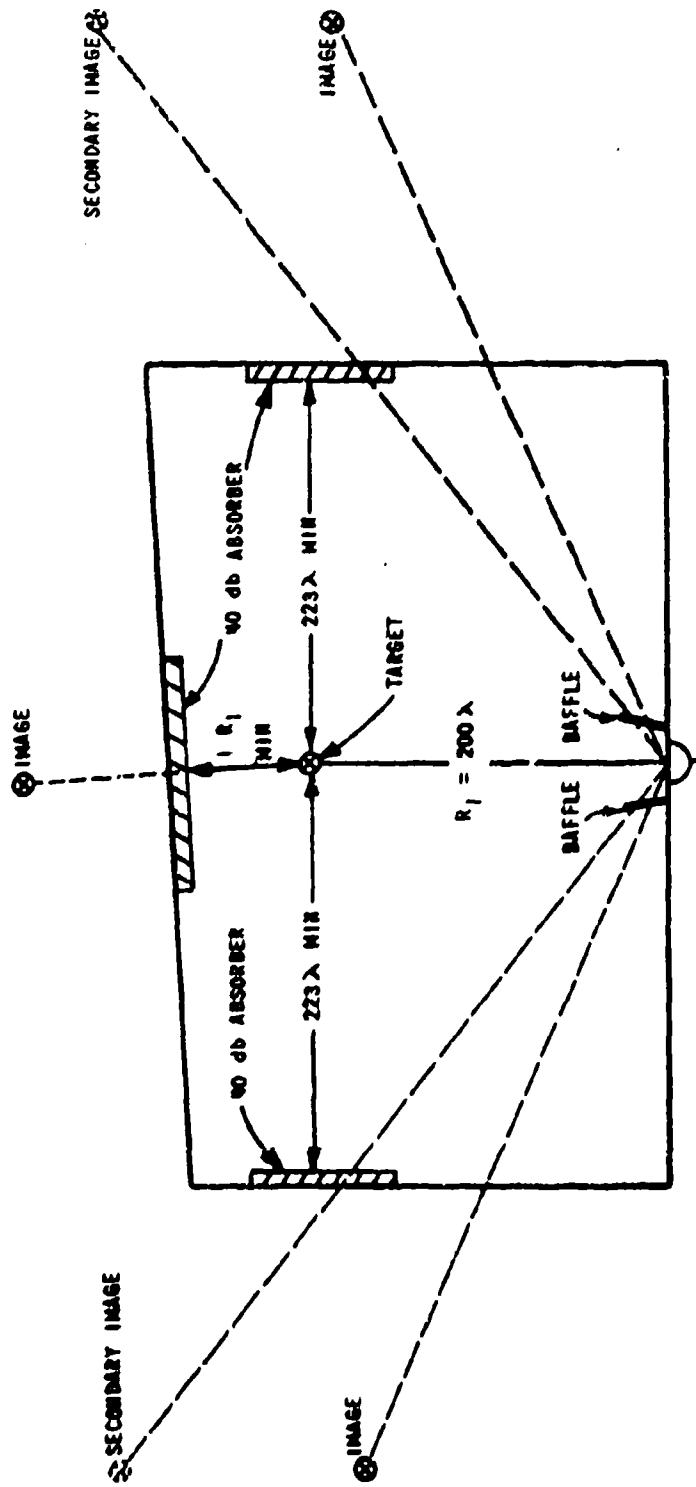
From the analysis presented, evaluating environmental effects, a room can be outlined to satisfactorily measure almost any target, given the specifications of target dimension and expected cross section. Quite surprisingly, the analysis points out that background in itself is not a limiting factor in accuracy; the limitations arise from coupling terms associated between target and environment, a specification that is rarely used for range description.

Using the equations developed, a sample room design can be given. The room is shown in Fig. 8, using a flat back wall. The targets to be measured in this range are 10λ long, with a maximum forward scatter to backscatter ratio of 40 db. Using an rf source having a frequency stability of 1 part in 10^7 over a measurement period, a target of 57 db below λ^2 could be measured. At this level, the measurement limitation lies with the method of target support, a subject not covered in this paper.

Figure 9 and 10 are illustrations of a cw range currently in use at Cornell Aeronautical Laboratory. Operating at K_a band, the design was predicated on targets no longer than 7λ . The asymmetry shown was deliberately introduced to immediately determine bistatic effects on symmetric targets.

The configuration was developed from the design principles outlined in this paper, with certain compromises imposed by budget and space constraints. Originally housed in a room with a height of only 14 feet, the

* This value is based on the far zone criteria of $2 \frac{(\eta \lambda)^2}{\lambda} = R_2$



ALL OTHER ROOM AREAS COVERED WITH 20 db ABSORBER

Figure 8 COMPLETED ROOM

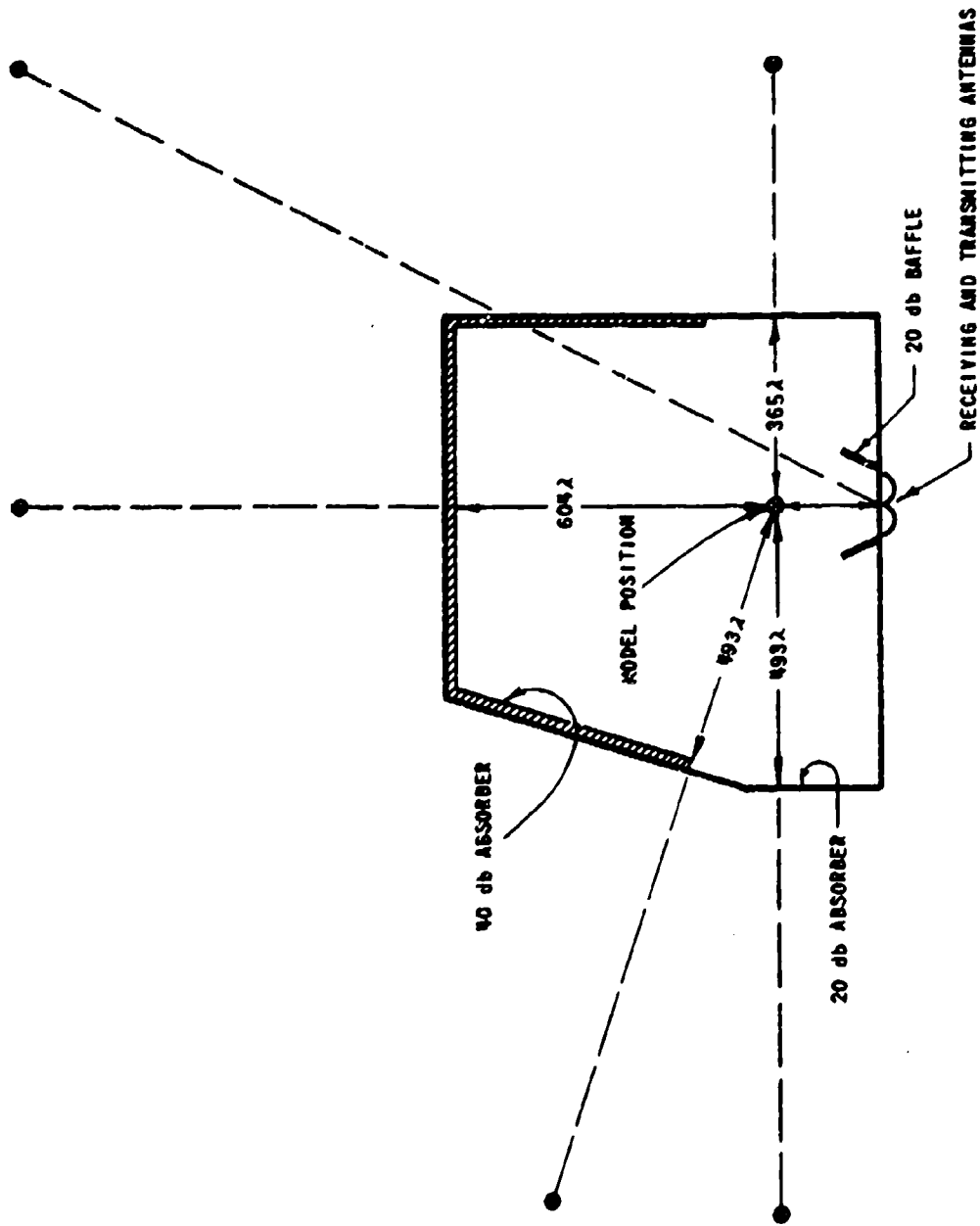


Figure 9 PLAN VIEW - CAL KaCw RANGE

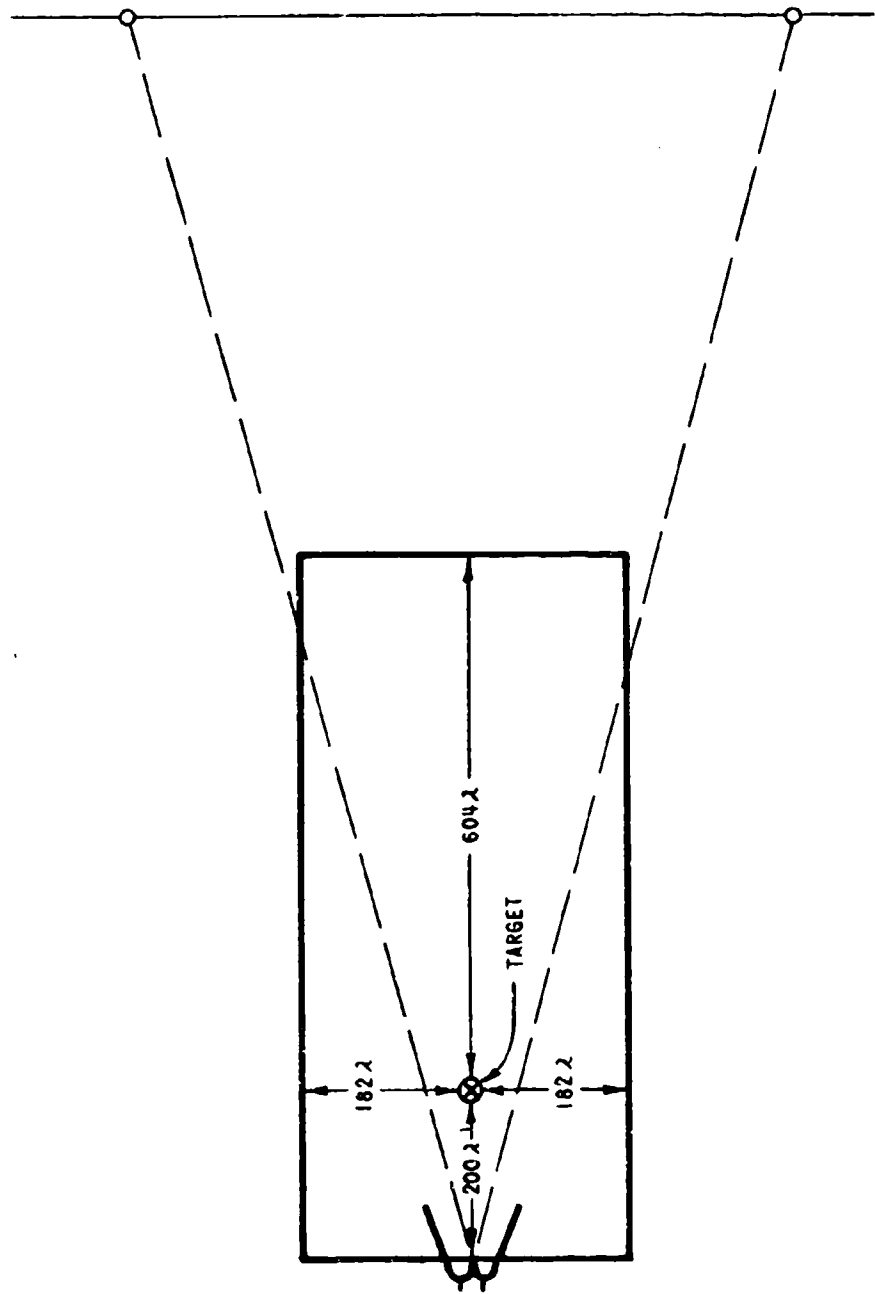


Figure 10 ELEVATION VIEW - CAL K_aC_w RANGE

ceiling is less than the 25 feet indicated as desirable. Although its present location would now permit the increase in height desired, it is felt that this change alone would not warrant the effort required. Major improvements would be effected only by a complete redesign.

The review of possible room modifications revealed that the basic limitations of the rectangular room could not be overcome except through use of higher performance absorber materials. It would be necessary to use materials of 50- to 60-db attenuation and a room of much larger dimensions.

A proposed method for overcoming many of the shortcomings of the rectangular room is found in a configuration that is an extension of the curved back wall. If a continuously curved surface could be provided that had a constant incidence angle with respect to the target area, then a considerable reduction in bistatic interaction could be obtained. That is, the images of target and antenna(s) would be effectively defocused, with a consequent reduction of coupling by the amount of defocusing obtained. Using a 10 degree incidence angle for a 10-wavelength target, approximately 26 db improvement could be achieved.

One method of reducing the interactions is to provide a surface of the type used for reducing backwall reflection: the slightly canted wall. If a continuously curved surface could be provided that had an incidence angle that was always $1\frac{1}{2}$ beamwidths off with respect to a ray from the target area, then a 26 db improvement could be obtained. That is, the target and its image would see each other only through the side lobes of the bistatic pattern, and assuming a flat plate uniformly illuminated, the side lobes would have a gain 26 db less than the main lobe.

The curve satisfying the condition of constant angle with respect to a radius from a fixed point is a logarithmic spiral. Unfortunately, it is not a closed curve, nor does it lend itself to providing the convex surface outlined for a backwall reduction. A compromise solution is shown in Figure 11. Here the room is circularly symmetric about the target-radar axis, with the outer surface a logarithmic spiral starting at the antenna position and continuing to a point where the spiral is parallel to radar boresight. The center of the spiral is located at the target, the spiral constant such that the ray from the target strikes the wall with a 10-degree incidence angle.

From the point where the spiral is parallel to boresight axis, another spiral, of the same constant, is used to close the room. The center of this spiral is located 100λ from the target towards the backwall. The spiral does not completely close the room, however. At the point where incidence angle approaches 7 degrees, the spiral is changed to an arc of a circle, tangent to the spiral. This curve is then faired into the bull's eye backwall. All curves are continuous, at least in first derivative.

The design prevents the target from being illuminated by its image except for a small region on the rear wall, where the circular portion joins the spiral. However, the radius of curvature of this concave surface is small enough, and of sufficiently small angular extent (45 degrees)

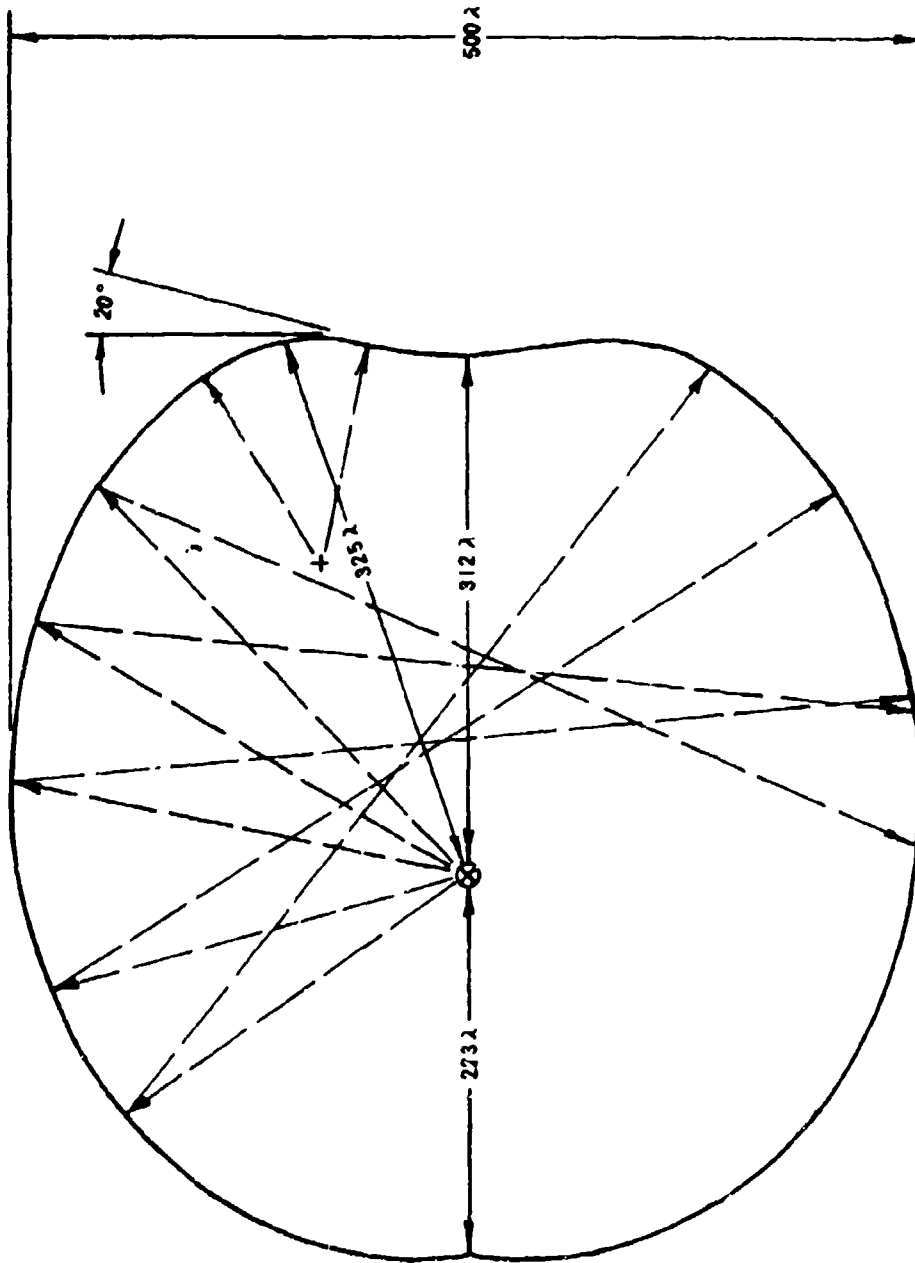


Figure 1: PROPOSED CAL K_a CW DARK ROOM

to effectively defocus reflected energy and again reduce the interaction. It is estimated that the room will be able to measure targets of 10λ length at a level of $10^{-6} \lambda^2$, assuming no support errors.

Presented here have been design considerations for construction of an anechoic chamber to be used with cw radars, with representative examples of rectangular and nonrectangular rooms. What has been implicit in these designs are three principles of design practice that should be carefully observed for any configuration. These are:

1. To obtain maximum absorber efficiency and room performance, incident energy should strike the absorber in a near normal manner, with incidence angle held less than 10 degrees.
2. Absorber should be applied in smooth continuous surfaces, with continuity of at least first derivative preserved. The use of concave "traps" and side wall projections should be deliberately avoided.
3. Concern should be primarily with bistatic coupling, not background per se.

For ranges using pulsed radars, some relaxation in room requirements is possible, since advantage can be taken of electronic circuitry to accomplish both background and bistatic interaction reduction. However, as in the cw case, all absorbers used should be oriented primarily normal to incident microwave energy.

Because the chief advantage of the pulsed system lies in range discrimination, maximum utilization should be made of this characteristic. Figure 12 illustrates this point. The shaded region of the figure shows the region within which a return will be detected by a range-gated receiver system (primary returns). With absorbing fences placed as shown, an effective shield is formed, so that no primary background return is possible and the idealized return of Fig. 13 obtained. The gate in the receiver, opening only in time conjunction with the signal that arises from the target area, thus suppresses the fence returns, while emphasizing the target area return. For a perfect gate, the primary background return is completely eliminated.

In practice, the gate has only a finite isolation and some fence return signal does enter the system. However, the fence signals do not occur in time conjunction with the signal from the target, thus easing the required ratio between fence-return power and target-return power. In most cases, the ratio of target-return power to fence-return power need only be a nominal 6 db to guarantee a 1 db accuracy. The power return from the fences is given by:

$$P_F = \frac{P_T G^2(\theta) \lambda^2 \pi R_f^2 \rho_n q_n}{(4\pi)^3 R_f^4}$$

where $G(\theta)$ = antenna side lobe gain

q_n = range gate suppression ratio, relative to response at center of gate

ρ_n = absorber reflection coefficient

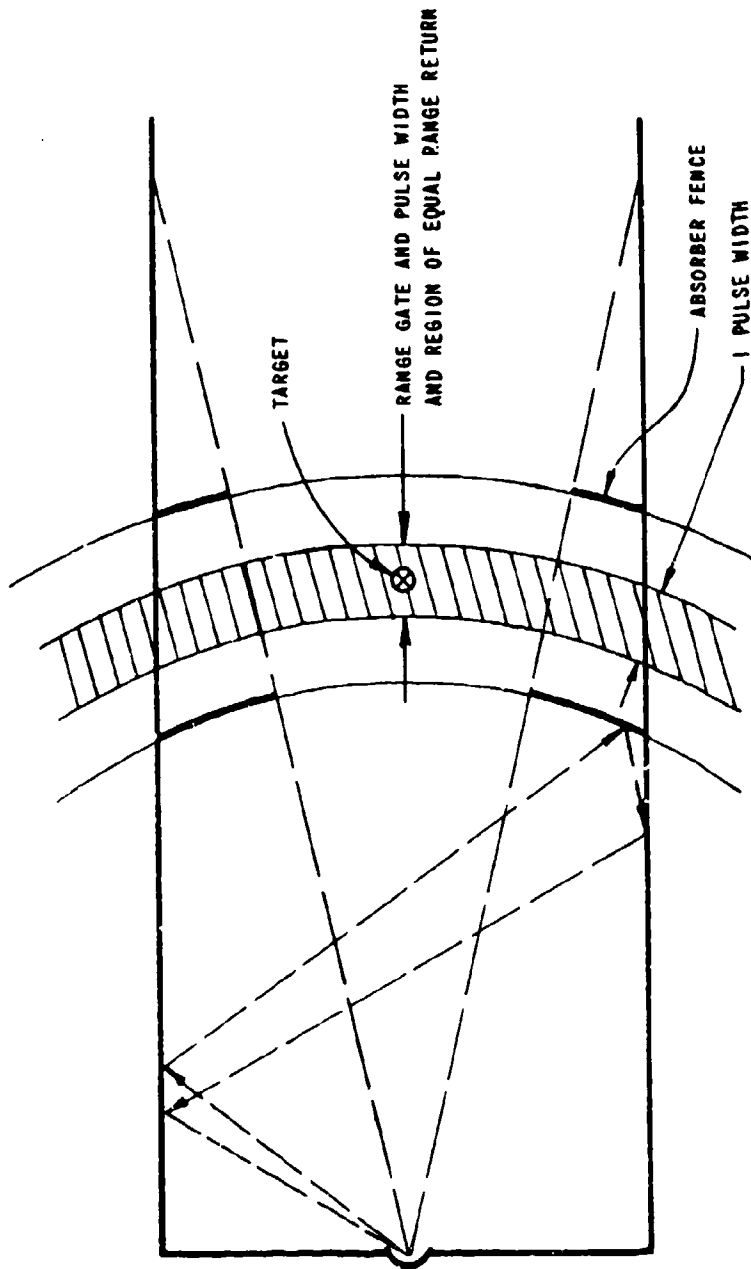


Figure 12 AREAS CAUSING BACKGROUND SIGNAL, PULSE RANGE

R_f = range to fence

The maximum ratio of background signal power to target signal power becomes:

$$\frac{P_f}{P_m} = \frac{G^2(\theta) \pi R_f^2 \rho_n G_n}{G^2 \sigma_T} = 1/4$$

and the lowest target level that can be measured given by:

$$\sigma_T = \frac{4 \pi G^2(\theta) R_f^2 \rho_n G_n}{G^2}$$

For nominal absorbers and range gate suppression, and a common side-lobe level of -30db obtained from parabolic reflectors, it is found that background, first order, can be held to a level that allows measurement to approximately $4.8 \times 10^{-10} \lambda^2$. ($R_f = 2000 \lambda$)

With first order terms such a negligible value, the predominant factor limiting precision of measurement through background is the second order terms that appear in the range gate. That is, the area preceding the fences reflects energy, from antenna side lobes, in such a way that the time path is exactly equal to that of the target area. Such a path is shown in Fig. 12, where it has been assumed a local wall roughness permitted the change in reflection angle shown (local specular surface not parallel to the wall).

Minimization of this source of background can take two courses; either the walls are covered with absorber, an expensive method or the antennas can be modified to obtain better sidelobe control. It is apparent that the ideal case, for the latter treatment, would permit 30 db side lobes incident on the fence, but infinitely low side lobes on adjacent walls of the building. Using the tunnel antennas previously discussed in combination with antennas of -30db side lobe level, the effective side lobe level can be reduced to -70 db. Arranging the tunnels such that the shadow boundary, as previously defined, intersects the fence, it can be seen that approximately 140 db attenuation is possible with a 40 db absorber on the fence. The background from this source (secondary effects) can thus be made negligible (less than $10^{-10} \lambda^2$).

The backwall return, because it too is discriminated against by time gating, also proves negligible, so that the chief concern lies in bistatic interactions.

Figure 13 shows the two primary bistatic paths that are present in the range. From the diagram, it can be seen that with sufficient space, the paths can be so arranged that path length differential is greater than a pulse width. Thus the target-wall-target interaction can be reduced by gate suppression, while the target-wall-receiver coupling can be reduced by the product of antenna side-lobe coupling and gate isolation.

In many cases, the room dimensions are insufficient to allow gate discrimination and target-wall-receiver interaction. Other techniques are

required. Of particular value is the use of the tunnel antenna in conjunction with fence -- here considerable minimization is possible. (see Fig. 14).

For the target-wall-target interaction, the measure of performance is again found in a square flat-plate target. Taking the ratio of interactions received power to monostatic received power, as in the cw case, it is found

$$\frac{P_b}{P_m} = \frac{2\pi^2 l^6 g_n \rho_n}{\lambda^4 R_g^2}$$

where l = edge dimension of the plate
 g_n = gate isolation
 ρ_n = reflection coefficient of the wall
 R_g = gate length, or full room width

Assume the wall is spaced sufficiently for effective gate operation, $g_n = 10^{-7}$ and minimum required $\frac{P_b}{P_m} = 1/4$. Under this condition, even with $\rho = 1$, the interaction term proves negligible. (For example, with a 30 nanosecond gate, operating at Ka band, target size would have to be 100λ before an effect would be noticed.) Application of absorber ($\rho = 10^{-4}$) would allow another order of magnitude in target size.

From an engineering view, elimination of the target-wall-receiver coupling by providing the dimension required for gate discrimination does not seem practical since room size can get quite out of hand.

With a fence required for background reduction, as well as a tunnel antenna, both can be employed effectively here as well. Using fence location so that the ray from target area past the fence edge strikes the ground beneath the receiver, it can be seen that the path is at least one range gate longer than the direct signal. For the signals diffracted around the fence edge, the tunnel provides at least a -70 db attenuation which, in conjunction with diffraction losses, results in approximately -110 db loss (through proper geometry).

The only remaining term of significance is the signal that proceeds from the target, then is diffracted by the fence edge to be received by unmodified antenna sidelobes. This signal is reduced by side-lobe gain and edge diffraction effects. The latter can be held to -40 db or less if the angle between receiver, fence edge, and target is held less than 160° , while antenna side-lobe levels can be obtained of -30 db. As a consequence, this signal can be reduced by 70 db. It is found that a bi-static cross section 50 db higher than the monostatic can be tolerated before a 1 db error in measurement is incurred.

Figure 15 shows the range with absorber fences in place.

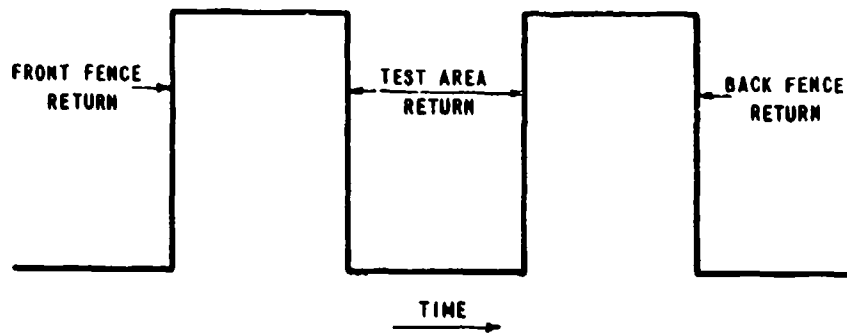


Figure 13 UNGATED RETURN FROM FENCES OF PULSED RADAR RANGE

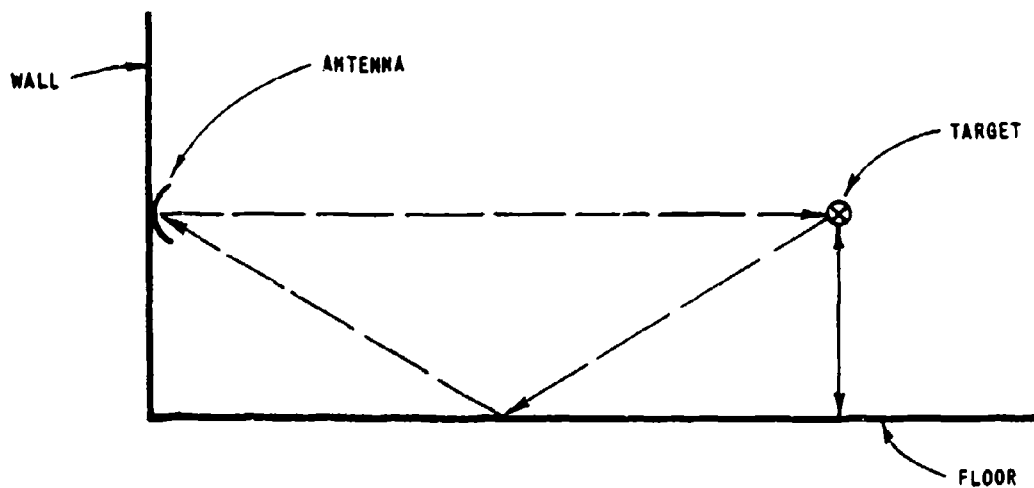


Figure 14 PRIMARY BISTATIC PATHS, PULSE RANGE

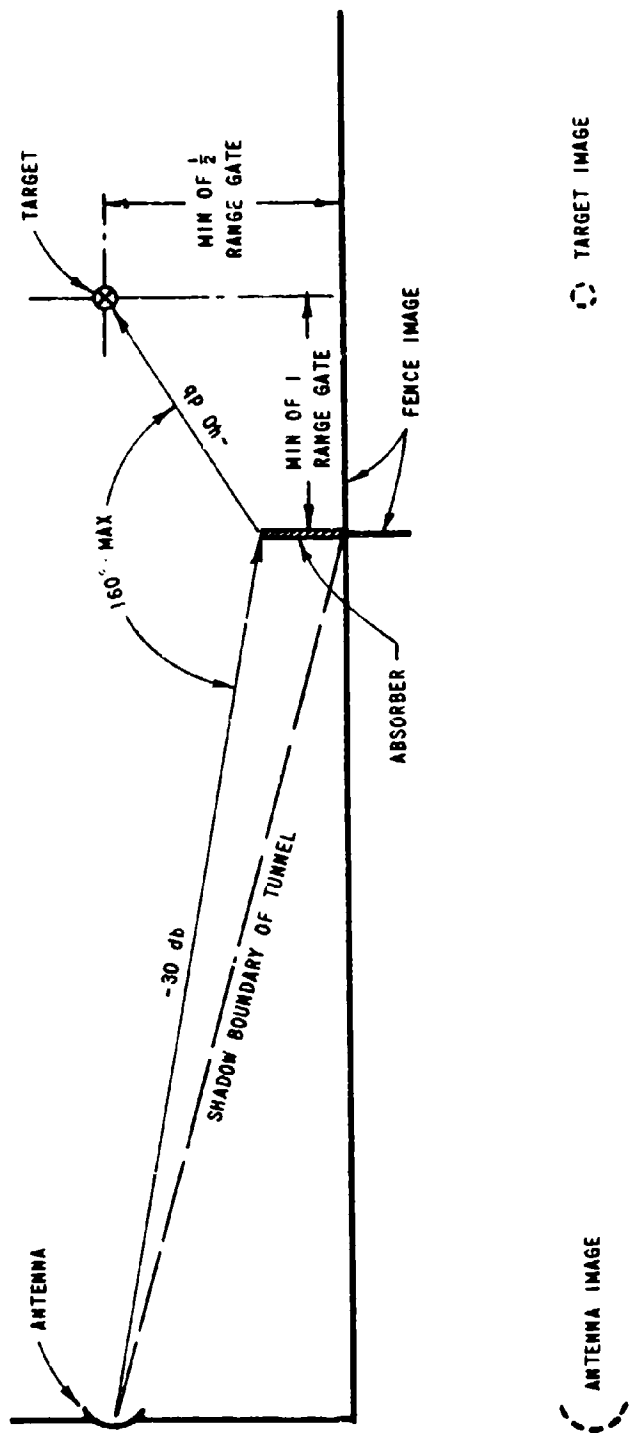


Figure 15 BISTATIC PATH REDUCTION, PULSE RANGE

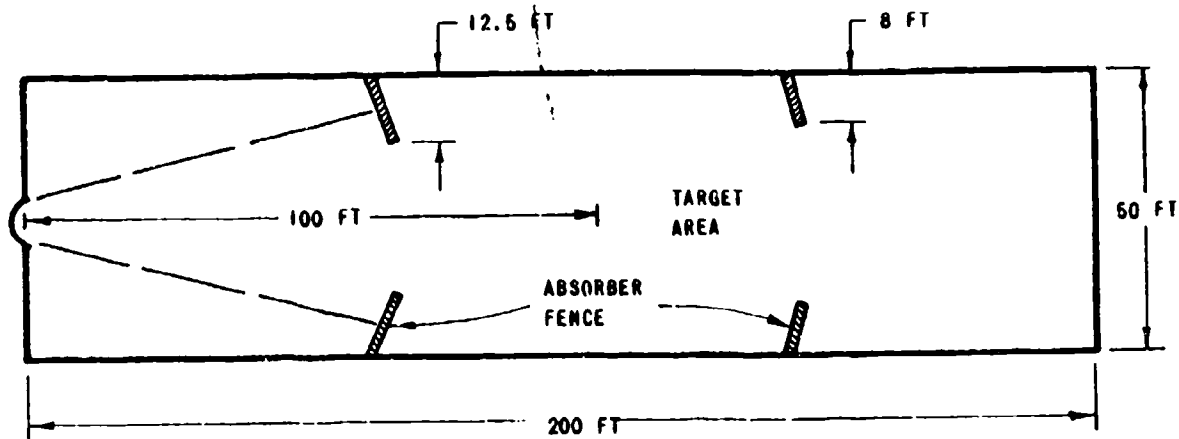
The design principles outlined were employed on the CAL K_a (35 Gc) pulsed range shown in Fig. 16. The only deviation from design principles is found in the tunnel surrounding the antennas, where the shadow angle is less than that stipulated.

Characteristics of this range are:

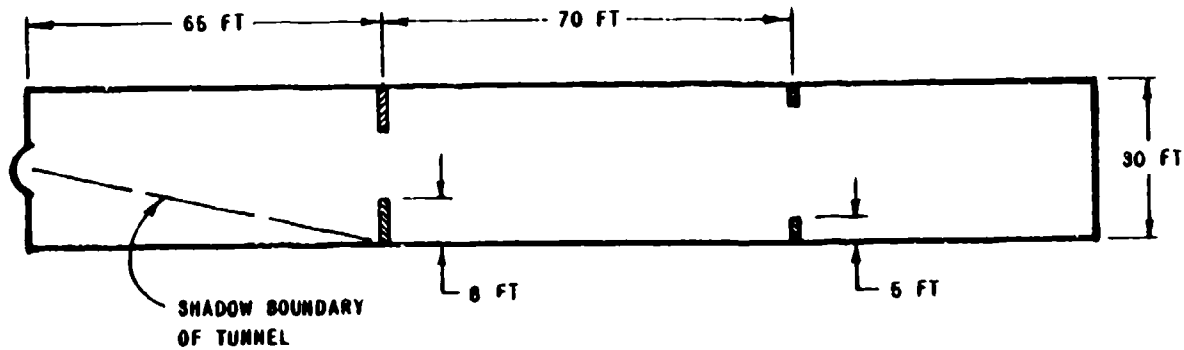
1. Background level - $10^{-5} \lambda^2$, equivalent to receiver noise
2. Bistatic interaction - undetected with a 14" square flat plate.

Figure 17 is the range used for the FM/CW radar, operating at X-band. Almost identical to the K_a pulsed range, this room has properly designed tunnels that holds background to imperceptible levels. Current measurements are not sufficiently sensitive to detect cross interference effects at $10^{-5} \lambda^2$.

The only absorber material used on the ranges is fixed on the fences and backstop, with a total of 3,000 square feet per range. If the room were designed on a cw basis, each would take roughly 10 times as much. Approximately \$300,000 was saved by the design.



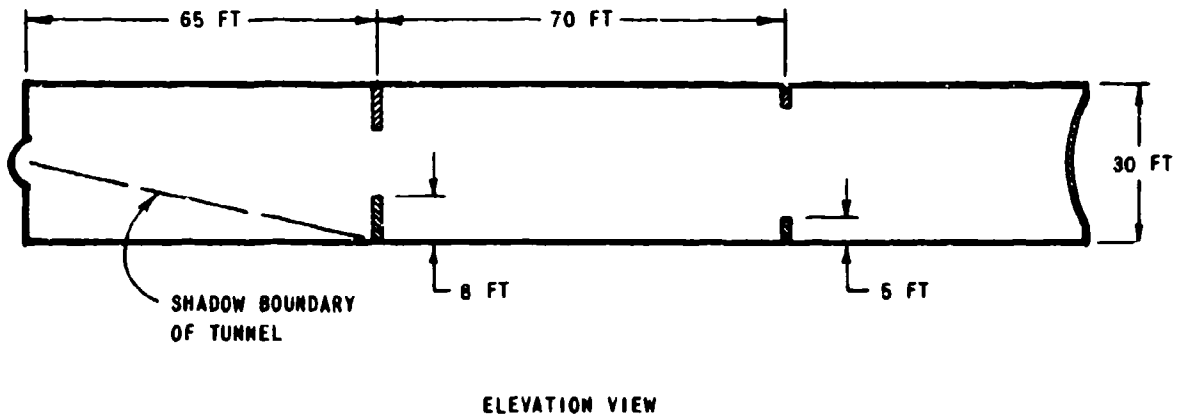
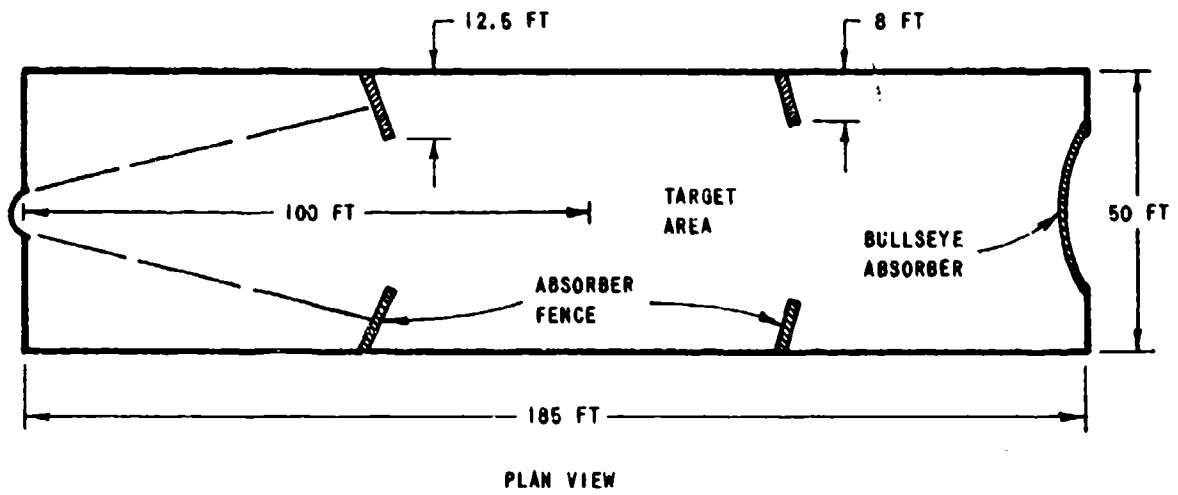
PLAN VIEW



ELEVATION VIEW

ALL WALL FENCES CORRUGATED
METAL EXCEPT ASSEMBLY FENCES

Figure 16 CAL Ka BAND PULSED RADAR RANGE



ALL WALL FENCES CORRUGATED
METAL EXCEPT ASSEMBLY FENCES

Figure 17 CAL XBAND FM/CW RANGE

AN ANALYSIS OF THE POLARIZATION CAPABILITIES OF A GROUND PLANE CROSS SECTION RANGE*

A. W. Wren, Jr., J. A. Green, C. M. McDowell
Conductron Corporation, Ann Arbor, Michigan

ABSTRACT

The problem of measurement of circular polarization components on a ground plane range is considered. If the analysis is restricted to transverse fields, a propagation equation may be derived. This equation is examined and two methods for obtaining circular polarization measurements are deduced. The first method utilizes two orthogonal linear polarizations to obtain the linear scattering matrix which is related to the circular scattering matrix through a unitary transformation. A second method utilizes elliptical polarization to compensate for the effect of the ground plane. With the second method, the circular components may be measured directly. A brief examination of the "depth of field" for the second method indicates a reasonable target space is possible.

THE PROPAGATION EQUATION FOR A GROUND PLANE RANGE

A Dual Channel System

In order to analyze the effect of a ground plane on polarization measurements it is necessary to construct a propagation equation for the ground plane range. The equation so constructed must be descriptive of a system capable of transmitting any selected polarization and receiving any selected polarization. We construct such a system by noting the fact that any plane polarized wave may be expanded in terms of two space orthogonal waves.¹ We consider, therefore, a two-channel system which transmits and receives both a vertical (x component) and a horizontal (y component) polarized component. Since we can obtain any plane polarization by modifying the amplitude and phase of the two space orthogonal components, the addition of phase and amplitude control networks provides the desired system.

In general, the amplitude and phase control network can be described by a diagonal matrix. Thus the transmitted fields may be described by the following matrix equation

$$\begin{vmatrix} E_x^t \\ E_y^t \end{vmatrix} = \begin{vmatrix} A_x^t & 0 \\ 0 & A_y^t \end{vmatrix} \begin{vmatrix} E_x \\ E_y \end{vmatrix} \quad (1)$$

where the superscript indicates the transmitted field and the subscripts x and y indicate the x channel and y channel, respectively. In the same fashion, the received fields are given by

*This work performed under USAF Contract No. AF30(602)-2831.

$$\begin{bmatrix} E_x^m \\ E_y^m \end{bmatrix} = \begin{bmatrix} A_x^r & 0 \\ 0 & A_y^r \end{bmatrix} \begin{bmatrix} E_x^r \\ E_y^r \end{bmatrix} \quad (2)$$

where the superscript r indicates the received field and the superscript m indicates the recorded or measured components.

The Ground Plane Matrix in Rectangular Form

We now describe the effect of the ground plane with a matrix. Let \bar{E}^t be the electric field along the direct ray at the obstacle, \bar{E}^i the field incident on the target, and θ the phase of the specular ray relative to the direct ray at the obstacle. Then

$$E_x^i = \left(E_x^t + \Gamma_x E_x^t e^{-i\theta} \right) e^{-ikR_1} \quad \text{and} \quad E_y^i = \left(E_y^t + \Gamma_y E_y^t e^{-i\theta} \right) e^{-ikR_1} \quad (3,4)$$

where Γ_x = reflection coefficient of the ground plane to horizontal electric field

and Γ_y = reflection coefficient of the ground plane to vertical electric field.

Equations 3 and 4 may be written

$$[E^i] = e^{-ikR_1} [K] [E^t] \quad (5)$$

where

$$[E^i] = \begin{bmatrix} E_x^i \\ E_y^i \end{bmatrix} \quad [E^t] = \begin{bmatrix} E_x^t \\ E_y^t \end{bmatrix}$$

and

$$[K] = \begin{bmatrix} 1 + \Gamma_x e^{-i\theta} & 0 \\ 0 & 1 + \Gamma_y e^{-i\theta} \end{bmatrix}$$

Similarly, if \bar{E}^s is the field scattered directly from the target, then

$$[E^r] = e^{-ikR_1} [K] [E^s] \quad (6)$$

where K is defined above, and

$$[E^r] = \begin{bmatrix} E_x^r \\ E_y^r \end{bmatrix} \quad [E^s] = \begin{bmatrix} E_x^s \\ E_y^s \end{bmatrix}$$

In terms of A, the scattering matrix of the target

$$[E^s] = [A] [E^i] \quad (7)$$

where

$$[A] = \begin{bmatrix} A_{11} & A_{12} \\ A_{12} & A_{22} \end{bmatrix}$$

hence, using Equation 6 in Equation 7,

$$[E^r] = [K] [A] [E^i] e^{-ikR_1} \quad (8)$$

and on further substituting Equation 5 into Equation 8

$$[E^r] = [K] [A] [K] [E^t] e^{-2ikR_1}. \quad (9)$$

By absorbing the phase factor e^{-2ikR_1} into the scattering matrix and using Equation 1 and Equation 2, we obtain the complete matrix equation for the system

$$[E^m] = [A^r] [K] [A] [K] [A^t] [E]. \quad (10)$$

Expanding Equation 10, we obtain

$$\begin{bmatrix} E_x^m \\ E_y^m \end{bmatrix} = \begin{bmatrix} A_{xx}^r A_{xx}^t (1 + e^{-i\theta_{\Gamma_x}})^2 E_x A_{11} + A_{xx}^r A_{xy}^t (1 + e^{-i\theta_{\Gamma_x}}) (1 + e^{-i\theta_{\Gamma_y}}) E_y A_{12} \\ A_{yx}^r A_{xx}^t (1 + e^{-i\theta_{\Gamma_x}}) (1 + e^{-i\theta_{\Gamma_y}}) E_x A_{21} + A_{yy}^r A_{yy}^t (1 + e^{-i\theta_{\Gamma_y}})^2 E_y A_{22} \end{bmatrix} \quad (11)$$

This equation clearly indicates one of the basic problems with the ground plane range. The coefficients for the elements of the scattering matrix are normally determined by calibrating the system with a sphere whose cross section is accurately known. For example, we use a sphere whose cross section is σ_0 , transmit horizontal polarization and receive horizontal polarization. Then $A_x^t = A_x^r = 1$ and $A_y^t = 0$. The scattering matrix for the sphere is, of course, diagonal. Under these conditions we obtain a measure of

$$(1 + e^{-i\theta_{\Gamma_x}})^2 E_x$$

By transmitting vertical and receiving vertical ($A_y^t = A_y^r = 1$ and $A_x^t = 0$) we obtain a measure of

$$(1 + e^{-i\theta_{\Gamma_y}})^2 E_y$$

Now if $\Gamma_x = \Gamma_y$ we would have the system calibrated. However, if this is not the case, we must use some standard depolarization target such as a long thin wire to obtain a measure of

$$(1 + e^{-i\theta_{\Gamma_x}}) (1 + e^{-i\theta_{\Gamma_y}}) E_x \quad \text{and} \quad (1 + e^{-i\theta_{\Gamma_x}}) (1 + e^{-i\theta_{\Gamma_y}}) E_y$$

If we assume that this can be accomplished we are still in difficulty for any polarization which utilizes E_x components simultaneously with E_y components. This difficulty stems from the fact that the calibration factor for the normal component differs from that for the cross-polarized component. It is necessary, then, to consider approaches which circumvent this difficulty.

The Ground Plane Matrix in Circular Form

Equation 10 describes the measuring system in rectangular form. A similar equation exists for the fields described in circular form. We note that the fields in the (x, y) system are related to the fields in a (r, θ) system by a unitary transform.²

$$[E(x, y)] = [U]^{-1*} [E(r, \theta)] \quad (12)$$

where * indicates the conjugate and -1 the inverse. Also, the rectangular scattering matrix is related to the circular scattering matrix by

$$[A] = [U]^{-1} [a] [U]^* \quad (13)$$

Equation 10, without the polarization control networks, is

$$[E^m] = [K] [A] [K] [E] \quad (14)$$

Substituting 12 and 13 in 14, we obtain

$$[E^m(x, y)] = [K] [U]^{-1} [a] [U]^* [K] [U]^{-1*} [E(r, \theta)]$$

Pre-multiply by $[U]$ to obtain

$$[U] [E^m(x, y)] = [U] [K] [U]^{-1} [a] [U]^* [K] [U]^{-1*} [E(r, \theta)]$$

Let

$$[K_c] = [U] [K] [U]^{-1} = [U]^* [K] [U]^{-1*}$$

Then

$$[E^m(r, \theta)] = [K_c] [a] [K_c] [E(r, \theta)] \quad (15)$$

Thus, if we make the two orthogonal channels in the system into a right circular component and a left circular component, we obtain the equivalent equation to Equation 10

$$\begin{bmatrix} E_{rc}^m \\ E_{lc}^m \end{bmatrix} = [A_c^r] [K_c] [a] [K_c] [A_c^l] \begin{bmatrix} E_{rc} \\ E_{lc} \end{bmatrix} \quad (16)$$

LINEAR POLARIZATION

It has been shown in a previous section that the descriptions of the ground plane scattering problem in terms of the linear or the circular components of the electromagnetic fields are simply alternate representations of the same problem as viewed from different coordinate systems. Thus, if the scattering problem is completely specified in the linear polarization basis, it is also specified in the circular polarization basis. The present section deals with the measurement of the scattering matrix in the linear basis; the corresponding matrix in the circular basis can then be obtained analytically by means of the transformation connecting the two systems.

Because of the experimental difficulties involved in making phase measurements, the scattering matrix will be determined by amplitude measurements alone. For the ground plane range with real ground reflection coefficients (see below) this involves a total of eight amplitude measurements. One of these is necessary to determine the properties of the ground plane; the remaining seven yield the five free parameters of the scattering matrix. Since an angle is specified in general by two length measurements, the two redundant measurements can be thought of as necessary to specify the phase angles involved.

When the grazing angle of the specular ray is less than 5° (an angle taken as the upper limit for any range of interest), calculations show that the phases of both the vertical and horizontal ground reflection coefficients are approximately 180° (to within less than 5°) for most soils. Consequently, they are assumed to be real and negative; that is

$$\Gamma_x = -\rho_x \quad \Gamma_y = -\rho_y \quad (17,18)$$

with ρ_x and ρ_y real and positive. Furthermore, if the height of the target and antenna above the ground plane are adjusted so that the first maximum of the incident field occurs on the target, then

$$\theta = \pi. \quad (19)$$

Substituting Equations 17, 18 and 19 into Equation 20 and expanding the matrices, the rectangular components of the measured field become

$$E_x^m = A_{xx}^r A_{xx}^t (1 + \rho_x)^2 A_{11} E_x + A_{xx}^r A_{xy}^t (1 + \rho_x)(1 + \rho_y) A_{12} E_y \quad (20)$$

$$E_y^m = A_{yx}^r A_{xx}^t (1 + \rho_x)(1 + \rho_y) A_{12} E_x + A_{yy}^r A_{yy}^t (1 + \rho_y)^2 A_{22} E_y \quad (21)$$

Using Equations 20 and 21, the measurements required to specify the scattering matrix will now be given. For convenience in notation, the necessary experimental arrangements and the corresponding measured fields will be noted by similar superscripts. As an example, let

$$A^{tl} = \begin{bmatrix} 1 & 0 \\ 0 & 0 \end{bmatrix} \quad A^{rl} = \begin{bmatrix} 1 & 0 \\ 0 & 1 \end{bmatrix} \quad (22)$$

then

$$E_x^{ml} = (1 + \rho_x)^2 A_{11} E_x \quad E_y^{ml} = (1 + \rho_x)(1 + \rho_y) A_{12} E_x \quad (23,24)$$

If the target is replaced by a sphere with scattering matrix

$$A_{ij}^s = s \delta_{ij} \quad (25)$$

then

$$E_x^{msl} = (1 + \rho_x)^2 s E_x \quad E_y^{msl} = 0 \quad (26,27)$$

In a similar fashion, the following measurements can be performed

$$M_1 = \left| \frac{E_x^{ml}}{E_x^{msl}} \right| = \left| \frac{A_{11}}{s} \right| \quad (28)$$

$$M_2 = \left| \frac{E_y^{m2}}{E_y^{ms2}} \right| = \left| \frac{A_{22}}{s} \right| \quad (29)$$

$$M_3 = \left| \frac{E_y^{m1}}{E_y^{ms2}} \right| = \left| \frac{1 + \rho_x}{1 + \rho_y} \frac{A_{12}}{s} \frac{E_x}{E_y} \right| \quad (30)$$

$$M_4 = \left| \frac{E_x^{m2}}{E_x^{ms1}} \right| = \left| \frac{1 + \rho_y}{1 + \rho_x} \frac{A_{12}}{s} \frac{E_y}{E_x} \right| \quad (31)$$

Using the notation

$$E^{mj} = E_x^{mj} + E_y^{mj} \quad E^{msj} = E_x^{msj} + E_y^{msj}$$

$$M_5 = \left| \frac{E^{m1}}{E^{ms1}} \right|^2 = \left| \frac{A_{11}}{s} + \frac{1 + \rho_y}{1 + \rho_x} \frac{A_{12}}{s} \right|^2 \quad (32)$$

$$M_6 = \left| \frac{E^{m2}}{E^{ms2}} \right|^2 = \left| \frac{1 + \rho_x}{1 + \rho_y} \frac{A_{12}}{s} + \frac{A_{22}}{s} \right|^2 \quad (33)$$

$$M_7 = \left| \frac{E^{m3}}{E^{ms3}} \right|^2 = \left| \frac{A_{11}}{s} + i \frac{1 + \rho_y}{1 + \rho_x} \frac{A_{12}}{s} \right|^2 \quad (34)$$

$$M_8 = \left| \frac{E^{m4}}{E^{ms4}} \right|^2 = \left| -i \frac{1 + \rho_x}{1 + \rho_y} \frac{A_{12}}{s} + \frac{A_{22}}{s} \right|^2 \quad (35)$$

Since the elements of the scattering matrix can only be determined to within an arbitrary phase factor, the quantity A_{12} is chosen to be real. From Equations 28 and 29

$$|A_{11}| = |s| M_1 \quad |A_{22}| = |s| M_2 \quad (36, 37)$$

Multiplying 30 by 31,

$$A_{12}^2 = |s|^2 M_3 M_4 \quad (38)$$

Dividing 30 by 31,

$$\left(\frac{1 + \rho_x}{1 + \rho_y} \right)^2 \left| \frac{E_x}{E_y} \right|^2 = \frac{M_3}{M_4}$$

If E_x and E_y are set equal at the time of measurement

$$\left(\frac{1 + \rho_x}{1 + \rho_y} \right)^2 = \frac{M_3}{M_4}$$

Expanding Equations 32 and 34,

$$M_5 = \left| \frac{A_{11}}{s} \right|^2 + \left| \frac{1 + \rho_y}{1 + \rho_x} \frac{A_{12}}{s} \right|^2 + 2 \left| \frac{A_{11}}{s} \right| \left| \frac{1 + \rho_y}{1 + \rho_x} \frac{A_{12}}{s} \right| \cos \theta_1 \quad (39)$$

$$M_7 = \left| \frac{A_{11}}{s} \right|^2 + \left| \frac{1 + \rho_y}{1 + \rho_x} \frac{A_{12}}{s} \right|^2 + 2 \left| \frac{A_{11}}{s} \right| \left| \frac{1 + \rho_y}{1 + \rho_x} \frac{A_{12}}{s} \right| \sin \theta_1 \quad (40)$$

where θ_1 is the angle between A_{11} and A_{12} .

Similarly expanding Equations 33 and 35,

$$M_6 = \left| \frac{1 + \rho_x}{1 + \rho_y} \frac{A_{12}}{s} \right|^2 + \left| \frac{A_{22}}{s} \right|^2 + 2 \left| \frac{A_{22}}{s} \right| \left| \frac{1 + \rho_x}{1 + \rho_y} \frac{A_{12}}{s} \right| \cos \theta_2 \quad (41)$$

$$M_8 = \left| \frac{1 + \rho_x}{1 + \rho_y} \frac{A_{12}}{s} \right|^2 + \left| \frac{A_{22}}{s} \right|^2 - 2 \left| \frac{A_{22}}{s} \right| \left| \frac{1 + \rho_x}{1 + \rho_y} \frac{A_{12}}{s} \right| \sin \theta_2 \quad (42)$$

where θ_2 is the angle between A_{12} and A_{22} . Since all absolute values in Equations 39 to 42 are known, these equations may be solved for $\sin \theta_{1,2}$

and $\cos \theta_{1,2}$ producing an unambiguous determination of all the parameters of the scattering matrix.

One other valuable piece of information which is obtained from the redundant angle measurements should be noted here. Suppose θ_1 or θ_2 is close to zero or π radians. Then Equations 39 and 41 would provide a poor determination of θ , while 40 and 42 would provide the most sensitive determination. The situation is just reversed for θ_1 or θ_2 near $+\pi/2$. Thus, by use of the proper equation, an accurate determination of the magnitude of the phase angle can be made with the equation for the co-function used only to determine the resultant ambiguity sign.

ELLIPTICAL POLARIZATION

While the above section provides an experimental procedure from which all available information about the scattering matrix can be determined, it proves to be overly complicated if only the magnitudes of the elements of the circular scattering matrix are required. This is the case, for instance, in cross section determinations. It would be very desirable if a procedure could be devised to measure these magnitudes in a more direct fashion. One scheme which immediately comes to mind is the application of the procedures given in the above section to the ground plane equation in circular representation. This direct approach is extremely complicated for the circular polarization scheme, however, due to the coupling between the right and left circular components of the field introduced by the ground plane.

An alternative approach is to consider the transmission of an elliptically polarized wave which will nullify the effects of the ground plane. This is, in effect, a pre-emphasis procedure whereby the transmitter and receiver are compensated to remove the effects of the ground plane.

We consider first a system using rectangular components. The basic equation in rectangular form is

$$[E^m] = [A^r] [K] [A] [K] [A^t] [E] \quad (43)$$

A solution of the type sought is evident by inspection. If

$$[A^t] = [A^r] = [K]^{-1}$$

then Equation 43 reduces to

$$[E^m] = [A] [E]$$

which is the free-space equation. Therefore we have succeeded in nullifying the effect of the ground plane.

This is the free-space equation. Consequently, it is a simple matter to measure the magnitudes of the matrix elements. This procedure has no advantage for the determination of the rectangular scattering

matrix since these magnitudes are easily measurable by the methods of the previous section.

In the measurement of the circular matrix, however, there is a distinct advantage. Suppose that it is desired to have a field incident on the target whose rectangular components are

$$E_x^i = E_x \quad E_y^i = +i E_y \quad (44)$$

then if

$$E_x = E_y \quad (45)$$

we have circular polarization incident on the target.

From Equations 1 and 5 it is seen that the fields incident on the target are given by

$$[E^i] = [K] [A^t] [E]. \quad (46)$$

The requirement for right circular polarization incident on the target then is

$$[K] [A^t] = \begin{bmatrix} 1 & 0 \\ 0 & -i \end{bmatrix} \quad (47)$$

Under these conditions the measured fields are

$$\begin{bmatrix} E_x^m \\ E_y^m \end{bmatrix} = [A^r] [K] \begin{bmatrix} A_{11} E_x - i A_{12} E_x \\ A_{12} E_x - i A_{22} E_x \end{bmatrix}$$

Now let $[A^r] [K]$ be the matrix $\begin{bmatrix} 1 & 0 \\ 0 & i \end{bmatrix}$, then

$$E_{\text{mod}}^m = E_x^m + E_y^m = (A_{11} + A_{22}) E_x$$

Using a sphere to calibrate, we measure

$$\frac{|E_{\text{mod}}^{m1}|}{|E_{\text{mod}}^s|} = \left| \frac{A_{11} + A_{22}}{2s} \right| = \left| \frac{a_{12}}{s} \right| \quad (48)$$

A second measurement using $[A^r] [K] = \begin{bmatrix} 1 & 0 \\ 0 & -i \end{bmatrix}$ and a standard target such as a diplane (i.e., a two-bounce target) obtains

$$\frac{|E_{\text{mod}}^{m1}|}{|E_{\text{mod}}^d|} = \left| \frac{(A_{11} - A_{22}) - 2i A_{12}}{2d} \right| = \left| \frac{a_{11}}{d} \right| \quad (49)$$

By transmitting left circular, we obtain $|a_{22}|$ in a similar fashion.

SPATIAL VARIATION OF THE CIRCULARLY POLARIZED FIELDS

It has been demonstrated in previous sections that it is possible to obtain a circularly polarized wave incident upon the target by proper adjustment of the phase and amplitude of the transmitted vertically and horizontally polarized fields. Since the complex ground reflection coefficients as well as the ground plane interference effects vary with grazing angle, the desired field pattern will only be obtained in a limited region of space near the target position. The variation of the field components with consequent deterioration of the desired circularly polarized field will be considered below.

Relative Phase and Amplitude Calculations

The incident fields have been shown to be given by

$$E_x^i = (1 + \Gamma_x e^{-i\theta}) E_x^t e^{-ikR_1} \quad E_y^i = (1 + \Gamma_y e^{-i\theta}) E_y^t e^{-ikR_1} \quad (50,51)$$

where θ is the phase difference between the direct ray and the specular ray, i.e.,

$$\theta = \frac{2\pi}{\lambda} (R_2 - R_1) \quad (52)$$

where R_2 = length along specular ray and R_1 = length along direct ray.

If, in Equations 50 and 51, the reflection coefficients are written in polar form, one has

$$E_x^i = (1 + \rho_x e^{-i\theta_x}) E_x^t e^{-ikR_1} \quad E_y^i = (1 + \rho_y e^{-i\theta_y}) E_y^t e^{-ikR_1} \quad (53,54)$$

where $\theta_x = \theta + \phi_x$ and $\theta_y = \theta + \phi_y$. (55,56)

We wish to calculate the components of the field incident on the target normalized to the corresponding components of the transmitted field; hence to expedite computation, we write Equations 53 and 54 in their polar forms as

$$\frac{E_x^i}{E_x^t} = C_x^i e^{-i\theta_x^i} e^{-ikR_1} \quad \frac{E_y^i}{E_y^t} = C_y^i e^{-i\theta_y^i} e^{-ikR_1} \quad (57,58)$$

where

$$C_x^i = \sqrt{1 + 2\rho_x \cos \theta_x + \rho_x^2} \quad C_y^i = \sqrt{1 + 2\rho_y \cos \theta_y + \rho_y^2} \quad (59,60)$$

$$\tan \theta_x^i = \frac{\rho_x \sin \theta_x}{1 + \rho_x \cos \theta_x} \quad \tan \theta_y^i = \frac{\rho_y \sin \theta_y}{1 + \rho_y \cos \theta_y} \quad (61,62)$$

To obtain an expression for θ in terms of range parameters, it is seen from the principle of images that

$$R_2^2 = (h + h_a)^2 + R^2 \qquad R_1^2 = (h - h_a)^2 + R^2 \qquad (63,64)$$

where h_a = fixed antenna height; h = height of observation point; and R = horizontal distance between the antenna and the point of observation.

On expanding these two expressions by the binomial theorem and substituting the results into Equation 52

$$\theta = 4\pi \frac{h h_a}{\lambda R} + 0 \left[\frac{h h_a}{R^3} (h^2 + h_a^2) \right] \qquad (65)$$

where for $h \ll R$ and $h_a \ll R$, the higher order terms are neglected, giving simply

$$\theta = 4\pi \frac{h h_a}{\lambda R} \qquad (66)$$

When Equation 66 is substituted into Equations 55 and 56, we have, finally at a fixed frequency and for a given soil,

$$\theta_x = 4\pi \frac{h h_a}{\lambda R} + \varphi_x(\psi) \qquad \theta_y = 4\pi \frac{h h_a}{\lambda R} + \varphi_y(\psi) \qquad (67,68)$$

where the functional notation is introduced to emphasize the dependence of the phases φ_x and φ_y on the grazing angle where the grazing angle ψ is determined by

$$\tan \psi = \frac{h + h_a}{R} \qquad (69)$$

We now have all of the relations needed to compute the magnitudes and phases of the incident fields as a function of height above the ground plane. The next topic to be considered is the selection of antenna and target heights.

The most uniform field over the target is obtained when the antenna and target heights are adjusted so that the maximum of the incident field occurs at the center of the target. This means that, at the center of the target, the total phase difference between the direct ray and the specular ray should be an integral multiple of 2π radians, and for minimum antenna and target heights this difference should be exactly 2π radians. Thus, if h_0 is the value of h at the center of the target, then for a given polarization the antenna and target height and the range R are related through Equations 67 or 68 (with θ_x or θ_y replaced by 2π), Equation 69 and the equation of the reflection coefficient. Generally speaking, once two of the factors h_0 , h_a , or R are chosen, the equations given above may be solved graphically or by trial and error for the third factor.

Axial Ratio of the Incident Elliptically Polarized Field

If the transmitted field is adjusted so that the incident field is circularly polarized at the target position, then the phase and

amplitude variations calculated above will in general produce elliptical polarization for field observation points removed from the target center. The ellipticity of the field will be calculated below by evaluating the axial ratio of the incident field as a function of position.

As given in Equations 57 and 58, the rectangular components of the field incident on the target are given by

$$E_x^i = C_x^i e^{-i\theta_x^i} E_x^t e^{-ikR_1} \quad E_y^i = C_y^i e^{-i\theta_y^i} E_y^t e^{-ikR_1} \quad (70,71)$$

If the superscript "o" is used to denote the experimental conditions appropriate to the target center, then in order to produce circular polarization at the center position, the transmitted fields must have an amplitude and phase given by

$$E_x^t = \frac{e^{i\theta_x^{io}}}{C_x^{io}} E^{to} \quad E_y^t = \frac{e^{i(\theta_y^{io} \pm \frac{\pi}{2})}}{C_y^{io}} E^{to} \quad (72,73)$$

In Equation 73, the plus sign is chosen for left circular polarization on the target while the minus sign is chosen for right circular polarization. Choosing $E^{to} = 1$ for convenience, and introducing the notation

$$A_j = \frac{C_j^i}{C_j^{io}} \quad \phi = \theta_j^i - \theta_j^{io} \quad (74)$$

the incident fields become

$$E_x^i = A_x e^{-i(\phi_x + kR_1)} \quad E_y^i = A_y e^{-i(\phi_y \pm \frac{\pi}{2} + kR_1)} \quad (75,76)$$

In real form

$$E_x^i = A_x \cos(\omega t - \phi_x - kR_1) \quad E_y^i = A_y \cos(\omega t \pm \frac{\pi}{2} - \phi_y - kR_1) \quad (77,78)$$

or in terms of the parameters

$$\mu = \omega t - \phi_x - kR_1 \quad \Delta = \phi_x - \phi_y \quad (79)$$

the fields are

$$E_x^i = A_x \cos \mu \quad E_y^i = A_y \cos(\mu + \Delta \pm \frac{\pi}{2}) \quad (80,81)$$

Equations 80 and 81 represent the polarization ellipse. Since the quantities Δ , A_x and A_y can be evaluated from the calculations given in the previous sections, it is a straightforward matter to determine the axial ratio as a function of position.

As an example, the variation of the axial ratio with height is plotted in Figure 1 for the conditions: $h_0 = 10$ feet, range = 500 feet, $\sigma = 0.01$ mho/meter, frequency = 0.5 gcs, $\Gamma_x = -1$.

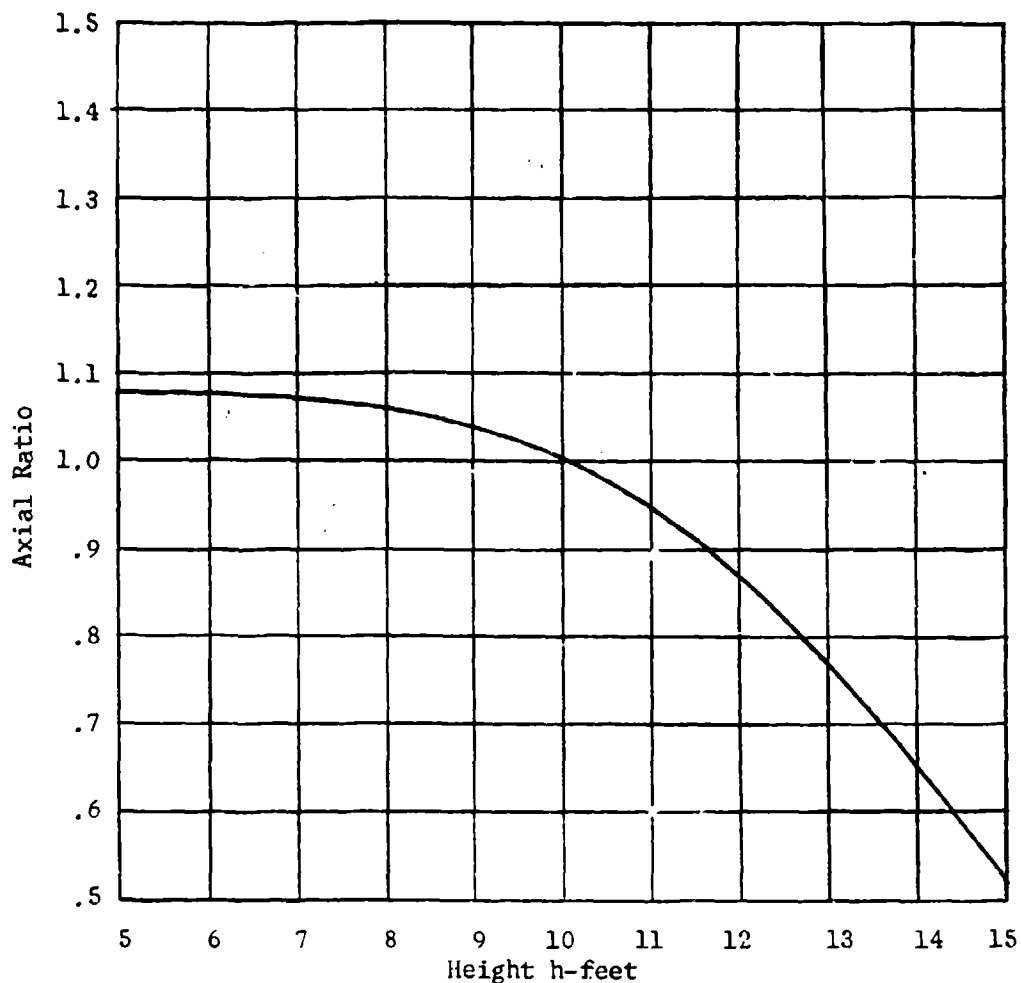


Figure 1. Variation of the Axial Ratio Over the Target

BIBLIOGRAPHY

- ¹ Kales, M. I., "Part III - Elliptically Polarized Waves and Antennas," Proceedings of the IRE, pp. 544-549, (May 1951).
- ² Crispin, J. W.; Goodrich, R. F.; and Siegel, K.M., "A Theoretical Method for the Calculation of the Radar Cross Sections of Aircraft and Missiles," Report No. 2591-1-H, The University of Michigan, Ann Arbor, Michigan, (July 1959).

SECTION III
SPECIAL EQUIPMENT FOR REFLECTIVITY RANGES
Panel Chairman: R.E. Kell

300

PULSED BACKSCATTER RANGE INSTRUMENTATION

A. J. Cann
Director of Engineering
Advanced Development Laboratories, Inc.
Nashua, N. H.

ABSTRACT

The chief reason for using a pulsed radar rather than a CW radar for target cross-section measurements is to discriminate against clutter and feedthrough by range gating. CW systems must use a buckout scheme for this, which has certain disadvantages. Furthermore, when intercept area greatly exceeds scattering cross-section, a buckout system is unsatisfactory. The second reason for using a pulsed radar is to examine the fine structure of the target signature.

A pulsed backscatter range radar is less like a conventional pulsed radar than like an antenna range instrumentation. By taking advantage of the short maximum range and low data rate usually required, we can integrate a great many pulses for each data point, thus attaining high sensitivity with low transmitted power. Non-coherent or post-detection integration is quite inexpensive to implement and can produce considerable gain in the typical application. Coherent or pre-detection integration can produce twice as much gain (in db). Fully coherent operation also permits phase measurements and vectorial cancellation of the target support echo as is being done by Lincoln Laboratory.

Two operating systems are described, one which uses pulse integration and one which does not. The former is designed to plug into a standard antenna pattern recorder, while the latter is designed for high data rate. The difference in cost is striking. Design techniques are discussed, including both coherent and non-coherent integration, suppression of spurious signals, and conditions for range gating and pulse stretching without a noise figure penalty. A design example of very high sensitivity is given.

INTRODUCTION

When CW radar is used for backscatter measurements, the sensitivity is limited, not by transmitter power and receiver noise, but by the stability of the balance obtained in the bridge system for canceling out the clutter or background signal. Furthermore, when a target's intercept area greatly exceeds its scattering cross-section an error is introduced by shadowing of the background signal.¹ Pulse radar has been used to overcome these limitations and also to study the fine structure in range of the target signature.^{1,2,3} But, often, inefficient use of the signal in a brute force design leads to a high transmitted power requirement which raises the cost and introduces a duplexing problem. We shall attempt to show in this paper how a pulsed radar, specifically designed for the backscatter range application, can be quite economical and efficient.

BACKSCATTER RADAR REQUIREMENTS

A pulsed backscatter range instrumentation is less like a conventional pulsed radar than like an antenna range instrumentation. Typical search and tracking radars have a high output data rate requirement. Backscatter range instrumentation, like antenna range instrumentation, can usually be satisfied with an output bandwidth of a few c/s. Therefore, a long integration time can be used, which reduces the average transmitter power required. Secondly, a backscatter range is usually quite short, which permits using a high prf without incurring range ambiguities. The resulting high duty factor reduces the peak power required. In summary, the combination of high prf with long integration time means that many pulses are integrated for each sample of output. The signal to noise ratio of the output data from an optimum receiver depends only on E/N_0 , where E = total signal energy integrated for each data point, and N_0 = noise power per c/s (a measure of receiver quality).⁴ The maximum pulse integration theoretically possible, assuming that the prf is limited only by range, has been derived by Bachman, King, and Hansen¹ as

$$N = \frac{f}{2pk^2} \frac{\Delta \theta}{\dot{\theta}} \quad (1)$$

where f = carrier frequency

p = a constant, usually in the range of 0.5 to 4, depending on the required fine structure

k = target diameter in wavelengths, $\Delta \theta / \dot{\theta}$ = data rate.

For most backscatter range situations N turns out to be a very large number.

Some users may object that in this mode of operation the single pulse signal to noise ratio is so low that an A-scope presentation is useless, and yet they want to study the fine structure, in range, of their target echoes or of clutter on the range. Here again, the low data rate required comes to the rescue. It is not necessary to explore the entire range in one pulse period. A synthetic A-scope display can be made by slowly strobing the range gate out in range and displaying (or recording) the output as a function of range. Essentially the same resolution will be obtained as if high peak power pulses of the same length were being used with a direct video display.* The time required for one complete scan equals the number of range elements divided by the data rate (samples per second).

Another special requirement of backscatter range instrumentation is that of wide dynamic range with good linearity. Typically 40 - 60 db dynamic range is required with a linearity of ± 1 db. In this respect backscatter range radars are more difficult to build, but again, the low data

*Strictly speaking, the synthetic display will be the cross-correlation of the range gate with the video, so that square pulses, for example, would be displayed as triangles whose half-amplitude width is equal to the square pulse width. When a radar is operating at maximum resolution and the pulse shape becomes pseudo-gaussian, the correlation function is still pseudo-gaussian, and wider by a factor of $\sqrt{2}$.

rate minimizes the difficulty. With careful design, a 40 db range can be achieved with fixed bias. To go beyond this, one can take advantage of AGC fed back from a special potentiometer on the recorder. Such a potentiometer is available, for example, on Scientific-Atlanta and Antlab recorders. The potentiometer is energized by several adjustable taps so that the non-linear function required for the AGC voltage can be closely approximated.

OPERATING SYSTEMS

The value of pulse integration is dramatically illustrated by a comparison of two backscatter radars built by Advanced Development Laboratories, Inc. (see Table I). Physical appearance of these radars is shown in Figures 1 and 2. The model 1084 was intended for use with rapidly rotating targets and thus uses no pulse integration. The model 1153 was designed to plug into a standard antenna pattern recorder and takes full advantage of post-detection integration in a narrowband bolometer amplifier. Note that although the 1084 has about 30 db more transmitter power, it has 30 db less receiver sensitivity. Therefore, the overall sensitivity (in terms of space loss) is about the same.

An optimum receiver would use entirely pre-detection integration (fully coherent operation) and would have even greater sensitivity. For example, were the model 1153 made fully coherent it would have 14 db greater sensitivity.

The model 1153 was made for a 2000 ft outdoor range subject to interference from birds and aircraft. Therefore, the rather low prf of 24 Kc/s was used to place the first range ambiguity at at least ten times the range. The transmitter is a klystron whose repeller is pulsed into the mode. Pulse widths well under 100 ns can be obtained in this way. The receiver is a super-heterodyne with a bolometer second detector.

The model 1084 was designed for an indoor range and at its minimum pulse width of 10 ns is capable of a prf of 100 Kc/s, so that some integration could be used. It uses a pulsed TWT chain transmitter and a TWT preamp followed by a crystal video receiver.

TABLE I - COMPARISON OF TWO SYSTEMS

	Model 1084	Model 1135
Frequency Range (Gc/s)	14-18	8.2-12.4
Peak Power (watts)	1000	0.5
Pulse Widths (nanoseconds)	10-100	100
PRF (Kc/s)	0.1-10	24
Tangential Sensitivity (dbm)	-80	-110
Dynamic Range (db)	50	50
Power Consumption (Kw)	4	under 1

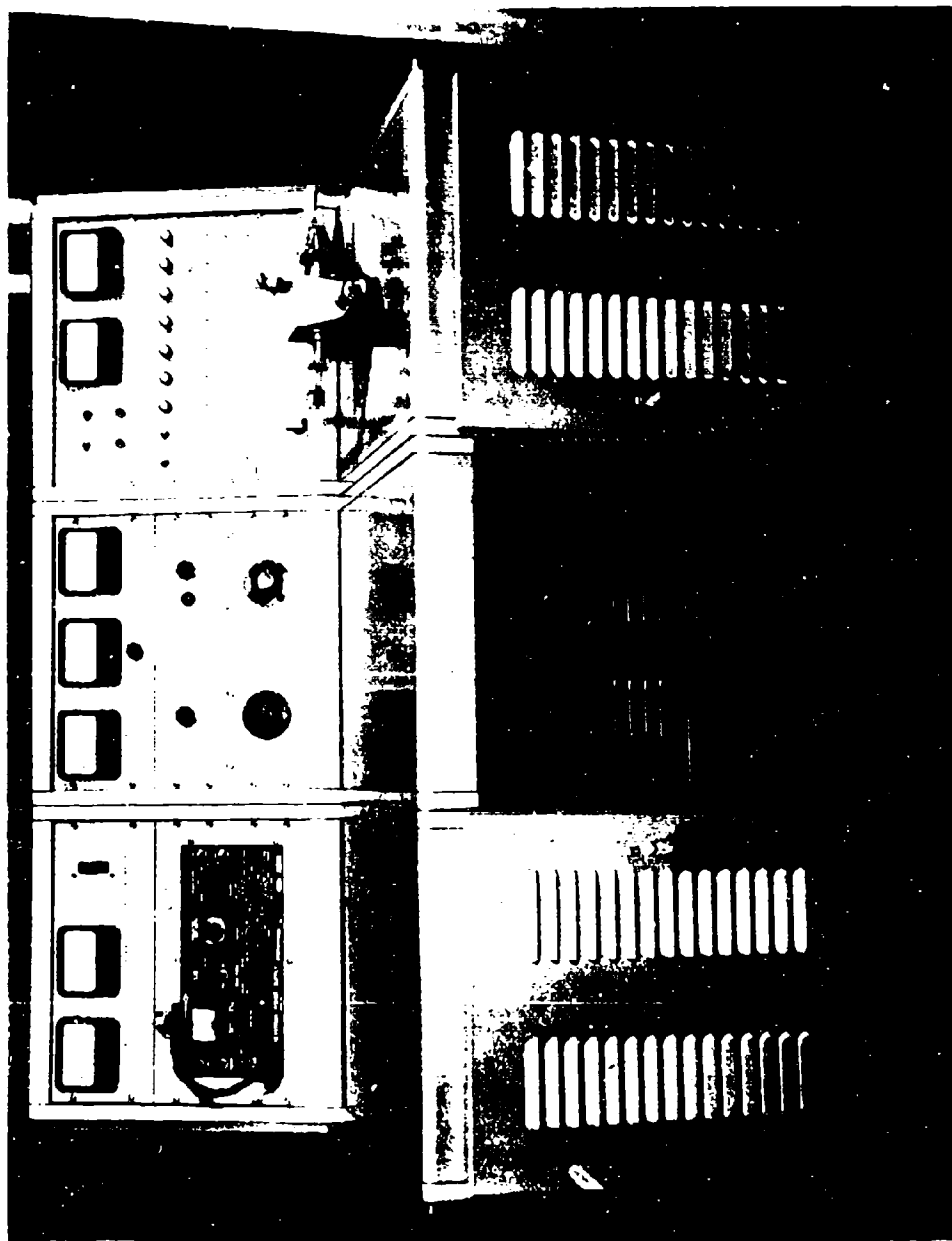


Figure 1. Model 1084 Pulsed Back-scatter Radar

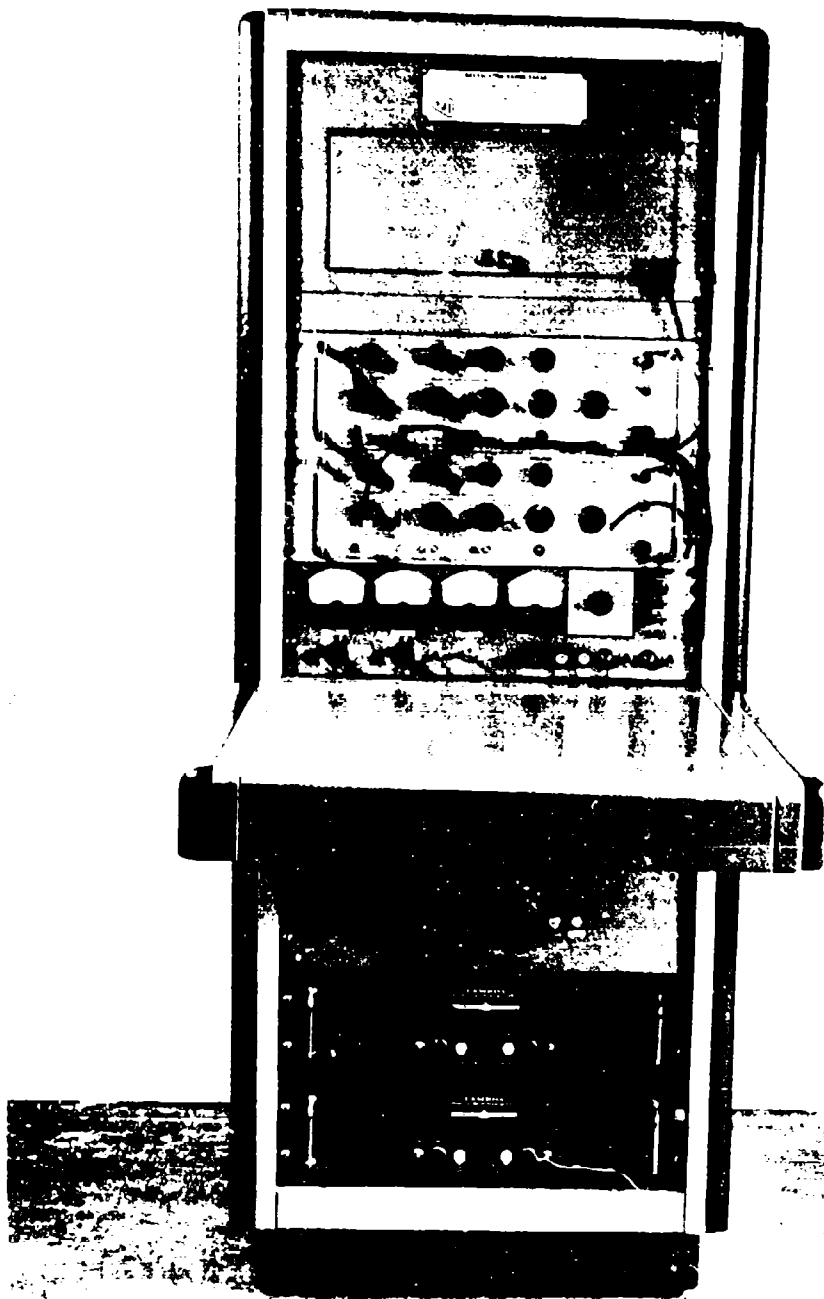


Figure 2. Model 1153 Pulsed Back-scatter Radar

A DESIGN EXAMPLE

To illustrate the techniques discussed in more detail let us design an indoor backscatter range radar system. Both coherent and non-coherent integration will be considered.

Specifications

Let us assume the following specifications:

Frequency	3 Gc/s
Range	25 ft.
Target Area (min.)	10^{-6} sq. ft. (10^{-7} sq. m)
Antenna Gain	30 db
Data Rate	25 Samples/Sec.
Range Resolution	10 ns (5 ft.)

Let us further assume that it is desired to have a 20 db signal to noise ratio with the specified minimum target area. We shall compute the transmitter power required for each case.

Non-Coherent Integration

Consider a system in which the transmitted pulse train is chopped at a 1000 c/s rate, a super heterodyne receiver is used, and the resulting square wave modulated output is detected with a bolometer followed by a 1000 c/s tuned amplifier with a 40 c/s band width. The 40 c/s first order filter will provide the required data rate with over 99% decorrelation between adjacent samples. It will be shown below that range gating, properly done, does not enter into the signal and noise calculations.

The maximum unambiguous prf for 25 ft. is 20 Mc/s. However, to keep the pulse circuitry simple, let us use 1 Mc/s. The integration time of a single-tuned circuit is given by⁶

$$T = \frac{2}{\pi \Delta f} \quad (2)$$

in this case about 0.016 sec. The number of pulses integrated therefore is 16,000. Now, if we assume the predetection signal to noise ratio is very low, the integration gain is given to a good approximation by $\sqrt{16,000} = 126 = 21 \text{ db}^*$. Therefore, the required predetection snr is $20 - 21 = -1 \text{ db}$.

* This is conservative. A more exact analysis is given in Appendix I.

The range equation may now be written:

$$P_t = \frac{kTBF (4\pi)^3 R^4 L_1 L_2 W}{G^2 \lambda^2 \sigma}$$

Thermal Noise	kT		204	db c/sw
Antenna Gain	G ²		60	db
SNR	W		1	db
			<hr/>	
			265	db c/sw
Bandwidth	B	100 Mc/s	80	db c/s
Noise Figure	F		13	db
	(4π) ³		33	db
Range	R ⁴	(25 ft) ⁴	56	db ft ⁴
Modulation Loss	L ₁		3	db
Line Loss	L ₂		3	db
Wavelength	λ ²	(0.3 ft) ²	10	db ft ⁻²
Target Area	σ	10 ⁻⁶ ft ²	60	db ft ⁻²
			<hr/>	
			258	db c/s
			<hr/>	
			265	db c/sw
			<hr/>	
			-7	dbw

= 0.2 watt

Systems designed like this usually require such low transmitter power that duplexing is no problem. Since very short minimum range is often required it is very advantageous to avoid the use of TR tubes or other long recovery devices.

Coherent Integration

Consider a system in which the transmitted pulse train is not chopped, and is coherent (e.g. derived by gating the output of a CW oscillator). Again assume a superheterodyne receiver, and assume that the i.f. output is synchronously detected with a reference frequency 1000 c/s removed. Now, this is not a detection in the communication theory sense; it is merely a translation to a 1000 c/s i.f. Therefore whatever integration occurs in the tuned 1000 c/s amplifier is fully coherent.

The integration gain now is 42 db instead of 21 db so that the transmitter power required is 21 db less. Or conversely, the range can be increased by a factor of 3.35. It will be shown below that the apparatus cost is less than that of a 21 db increase in transmitter power. Of course, it is possible to use still narrower bandwidths, for example a 4 c/s bandwidth will permit a data rate of 2.5 samples/sec and will give 10 db greater sensitivity (5 db in a non-coherent system).

System Design

The discussion of range gating requirements and other details is best carried on in conjunction with examination of the system block diagram shown in Figure 3. To prevent "birdies" and reduce the requirements on gating transient rejection, the prf and all intermediate frequencies are harmonically related, being derived by multiplication and division from a single 60 Mc master oscillator. The klystron oscillator, however, can be freely tuned to any frequency. In a coherent system, insuring that harmonics of the gating transients will appear to have zero doppler shift, we can allow them to be as large as the largest expected signal, it being necessary only to prevent saturation in the receiver. They will not produce any false output. If the frequencies were not locked together, it would be necessary to keep gating transients below system noise level, which would make the range gate design more difficult.

In the non-coherent instrumentation to be described first, however, it is still necessary to keep harmonics of the gating transients below system noise in the i.f. passband, even though they zero beat with the signal. This is because the bolometer and tuned amplifier at the output are sensitive only to total amplitude fluctuations. The 1000 c/s amplitude fluctuation due to a signal smaller than the gating transient will depend on its phase relationship to the gating transient and may even be zero (at 90°).

For a non-coherent system the 1 Mc pulse train is chopped by a 1 Kc square wave, to make bursts of pulses lasting 1/2 millisecond, separated by 1/2 millisecond spaces. These pulses then modulate the TWT which amplifies the output of a klystron. A severed helix TWT should be used, or a diode switch added to reduce leakage between pulses to a level below system noise. Duplexing is partly performed by a circulator.

The received signals are first heterodyned to a rather high i.f., so that sufficient bandwidth can be obtained to pass the major components of the pulse spectrum. A balanced mixer is used only to conserve l.o. power, since at these frequencies it is not needed for noise figure. Before entering the preamp, the signal is passed through a diode switch range gate of moderate attenuation. This is only to reduce the main bang feed-through to a level that permits quick recovery of the preamp. It has already been reduced by the circulator and by limiting in the mixer.

The preamplifier must have enough gain so that average system noise level after range gating will still be about 10 - 20 db above local circuit noise level. When this condition is met, any degree of narrowbanding or pulse stretching is permissible after range gating, without a noise figure penalty. In this case it presents no problem, but in a system with very low duty factor it might require excessive dynamic range of the preamp. In such a case one reduces bandwidth after the first range gate only by a factor equal to the ratio by which peak noise after the range gate exceeds the 10 - 20 db criterion. Then the peak noise in the stretched pulse is still 10 - 20 db above local circuit noise. After further amplification to increase this margin one performs another range gating operation, with an appropriately wider gate. These steps are repeated until average system noise exceeds local circuit noise by 10 - 20 db.

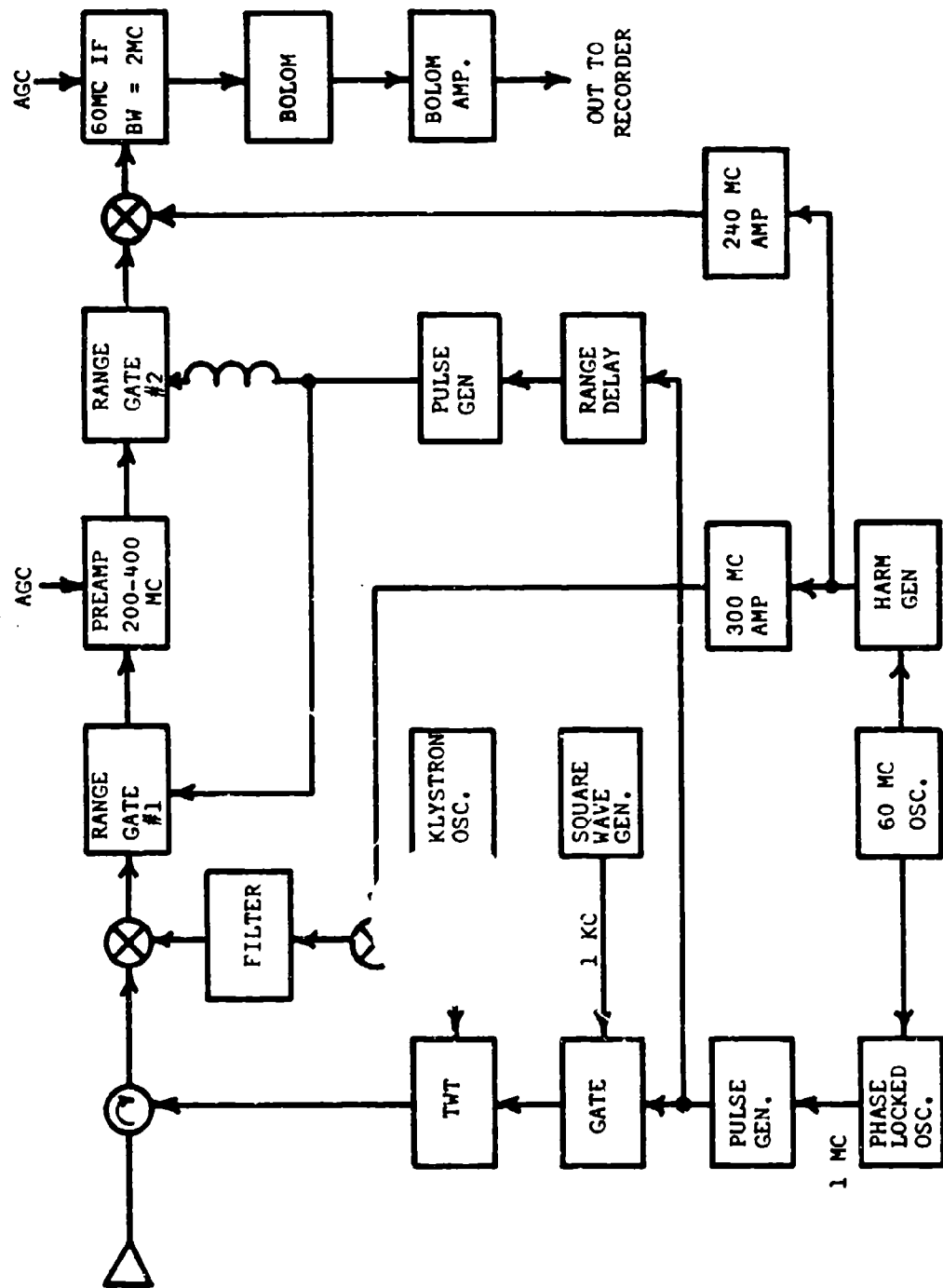


Figure 3 - Block Diagram

The range gate after the preamp must have high enough attenuation to gate out clutter and the remains of main bang feed-through. Were it placed before the preamp, its insertion loss would have raised the system noise figure considerably. After range gating we can translate to a more normal i.f., 60 Mc, with a more normal bandwidth, 2 Mc. The output of this i.f. amplifier drives a bolometer detector. The bolometer output goes through a sharply tuned 1 Kc/s amplifier so that it detects only the modulation on the signal. Post-detection integration is performed in the 40 c/s bandwidth of the bolometer amplifier, as described before.

Coherent, or predetection integration can be added by translating either the transmitted signal or the first l.o. by 1000 c/s to introduce an artificial doppler shift. This can now be detected with a synchronous detector instead of a bolometer, using the 60 Mc oscillator as a reference. Of course, the 1000 c/s square wave modulation is not used in this case. It is important that the frequency offset be produced in the signal or first l.o., and not in the second l.o., the 60 Mc reference, or the prf. Otherwise the harmonics of gating transients would also beat with the reference to produce a false output. The offset can be produced, for example, by serrodyning the TWT.

In order to obtain the full benefits of coherent integration, it is necessary to insure that most of the signal energy is contained in the final bandwidth. Since the typical S-band klystron spectrum is on the order of 100 c/s wide this condition may not be met on a long range. And if a 4 c/s output bandwidth is planned then some form of stabilization is almost surely needed, even on a 25 ft. range. A klystron phase-locked to a harmonic of a quartz oscillator can have a spectrum width of a fraction of a c/s. No such stabilization is required for a non-coherent system, where the predetection bandwidth is typically a Mc/s or more.

Providing a 1000 c/s reference and two quadrature phase detectors after the 1000 c/s amplifier permits measuring signal phase as well as amplitude. This information can be used to cancel the target support signal as has been done by Fritsch at Lincoln Laboratory.

APPENDIX I

Non-Coherent Integration Gain

The previously calculated predetection signal to noise ratio assumed totally non-coherent integration. Actually at the snr obtained, the integration is partly coherent and a more exact analysis should be used.

First, to find the pre-integration snr required, we use not $\sqrt{16,000}$, but 16,000, i.e. 42 db. Thus $20-42 = -22$ db. Now, since the output spectrum of the detector is nearly triangular (at low snr), and 1000 c/s is near the low end (assuming an i.f. band pass of a Mc/s or so), we must have an average snr 3 db less, or -25 db.

From square law detector statistics⁵ we find that to obtain this output snr requires an input snr of -12.5 db. This compares quite favorably with the -1 db snr calculated on the basis of wholly non-coherent integration.

REFERENCES

1. C. G. Bachman, H. E. King, and R. C. Hansen, "Techniques for Measurement of Reduced Radar Cross Sections", Microwave Journal, Feb., March, and April, 1963.
2. R. Honer and R. Hively, "High Resolution Backscatter Techniques", Microwaves, April, 1963.
3. "Subnanosecond Radar Shows High Resolution", Electronics, May 31, 1963.
4. P.M. Woodward, "Probability and Information Theory", McGraw Hill, 1956, p. 87.
5. S. O. Rice, "Mathematical Analysis of Noise", BSTJ, 23, pp 282 - 332, 1944, and 24, pp 46 - 156, 1945, and 27, pp 109 - 157 (1948).
6. "Detection of Pulsed Signals With a Narrow Band Filter, Detector, and Integrator", Report R-42, Control Systems Laboratory, University of Illinois, May, 1953.

ACKNOWLEDGMENT

The author gratefully acknowledges the help received from many of his colleagues, particularly K. Dollinger, M.E. Mehron, and R.M. Stetson, and stimulating discussions with P. Fritsch of Lincoln Laboratory.

THE HUGHES BACK SCATTER MEASUREMENT RADAR AND RECORDING EQUIPMENT

James D. Carlson
Member, Technical Staff
Hughes Aircraft Company
Radar Division
Fullerton, California

INTRODUCTION

This paper will describe in detail some of the problems encountered and the solutions derived during the instrumentation and operation of the short pulse, back scatter measurement range at the Ground Systems Group of the Hughes Aircraft Company at Fullerton, California. The emphasis in this paper will be on problems common to short pulse systems in general, and on the signal processing and data recording techniques that have been developed in conjunction with the Hughes system.

This range has been in operation for more than a year, and although excellent results have been obtained in the measurement of numerous test objects, some of the techniques that have been employed could be improved. This paper will attempt to point out these areas and to prescribe possible improvements.

SHORT PULSE MEASUREMENTS

Short pulse radar measurements are an ideal method for evaluating the radar cross sections of various geometric configurations and for determining the effects of coating materials, since the short pulse radar return permits identification of the scattering points directly as to magnitude and position on the test object. A short pulse radar is in general a radar whose pulse width, or range resolution cell, is small with respect to the range dimension of the object being measured. Therefore, each scatter point and specular area on the test object will scatter back to the receiver a discrete pulse which will be identifiable on the display. A typical short pulse radar system would have a transmitted pulse width of 1 nanosecond, which would correspond to an r-f signal bandwidth of 1000 mc/s or a range resolution cell of 0.5 foot. It is this high degree of range resolution that makes the short pulse radar so valuable as a tool, but it also imposes some severe requirements on the system instrumentation as to stability and bandwidth. The synchronization circuitry in the radar system must be extremely stable so that correlation of the return with a test object can be made to a high degree of precision. The spectrum of the pulse must not be distorted in transmission or reception so that the shape of the detected signal envelope will not be widened with consequent loss in range resolution. Methods of data processing must be employed that are capable of handling the wide bandwidth of the detected signal envelope as well as the wide dynamic range of signal amplitudes that are to be expected from typical

targets. In addition, range ambiguities in the form of side lobes of the main pulse originating from reflections and distortions in the component parts of the system must be eliminated, or at least reduced below the level of any anticipated return from the test object.

HUGHES SHORT PULSE RADAR

The Hughes radar is shown in block diagram form in Figure 1, together with a photograph illustrating the relatively small size of the installation. The specific information on some portions of the system is omitted for security reasons.

Transmitter

In the transmitter, a signal is generated and amplified in a traveling wave amplifier that is gated "on" only at the time of transmission, so that the amplifier's noise is not introduced into the receiver during the time of desired signal reception.

Receiver

Due to the wide signal bandwidths associated with short pulse radar returns, it is desirable to perform as much amplification as is possible at r-f so that inherently broad band amplifiers, such as traveling wave tubes, may be employed and the problems found in broad bandwidth, high gain video amplifiers may be circumvented. Since octave bandwidth traveling wave amplifiers are commonly available, no bandwidth reduction of the receiver signal will be encountered, even though several stages of amplification are cascaded. The noise figure of the receiver should be as low as possible to take full advantage of the available signal-to-noise ratio, and the receiver should have sufficient output power to ensure that a wide dynamic range of signal amplitudes can be handled.

The receiver used in the Hughes radar consists of three cascaded traveling wave amplifiers. This receiver, together with the transmitter, defines the magnitude of the noise level seen on the display. This noise level corresponds to the return which would be received from a 10^{-6} square meter target located on the range. The radar system is then capable of recording (with a 10 db signal-to-noise ratio) a 10^{-5} square meter test object located on the range.

Detector

The requirements placed on the video detector in the short pulse radar are very stringent, and it is therefore one of the components which must be selected with great care. It must provide a good match to the r-f signal over the band of interest, have sufficient video bandwidth to assure faithful reproduction of the detected signal envelope, provide

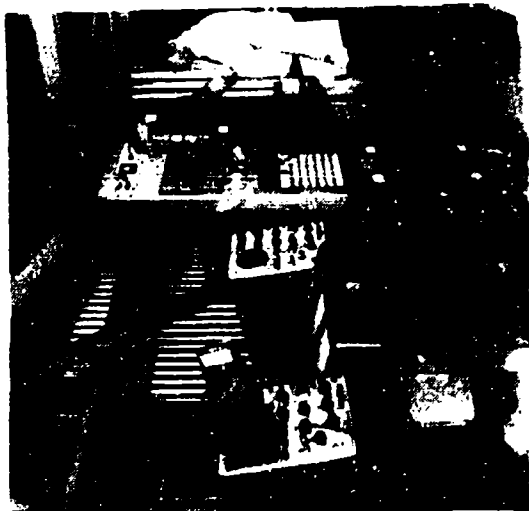
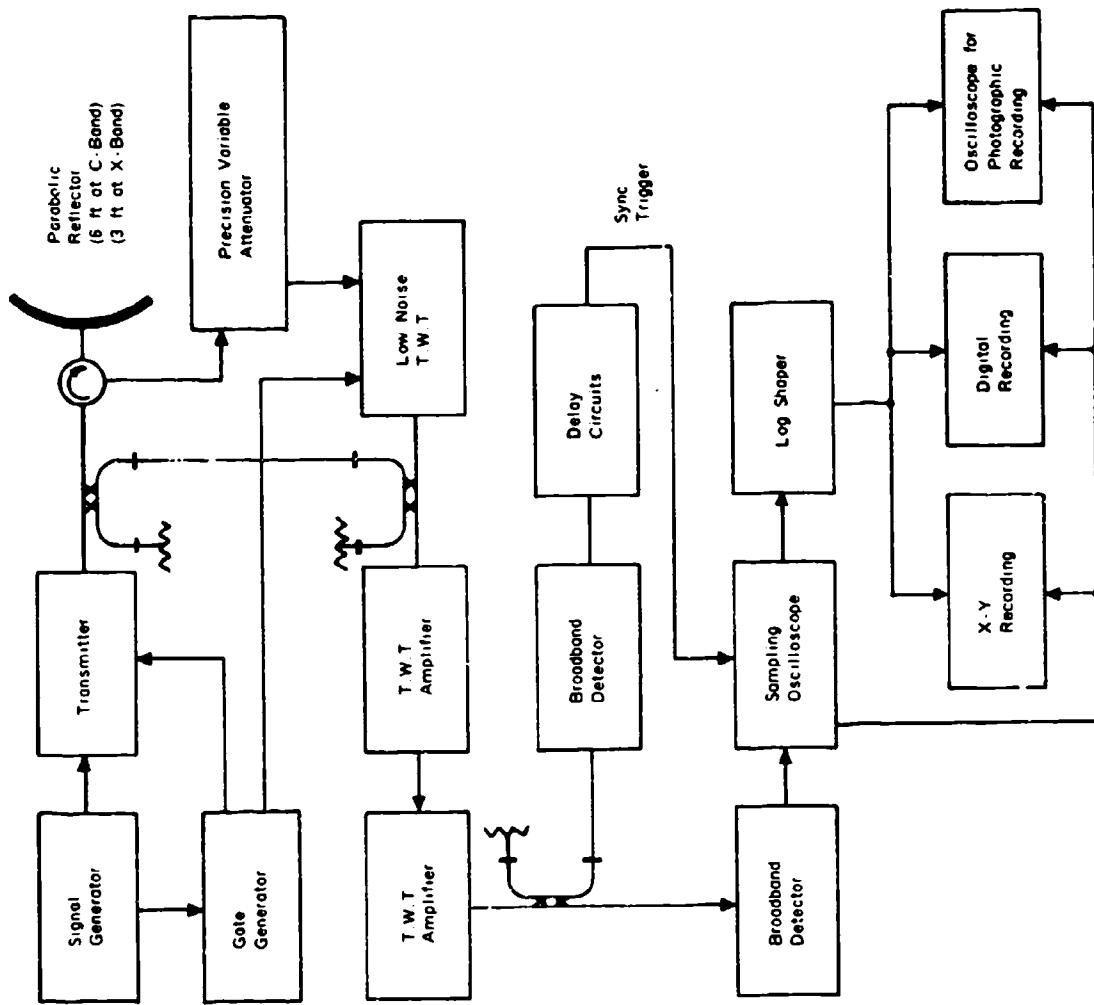


Figure 1. Measurement Radar and Recording System

sufficient video voltage to the display so that a minimum of video amplification is required, and have a predictable transfer function or "law". Commercially available detectors fall short of these requirements, notably in the area of video bandwidth.

A detector mount was constructed for use with the Hughes system by incorporating a 1N23 mixer diode in a modified General Radio coaxial mixer assembly. The r-f input was terminated resistively in 50 ohms, and the diode was mounted normal to the center conductor. Most of the lumped capacity of the video side of the diode was removed and was replaced by the distributed capacity of a length of coaxial cable which was used for the video transmission line. This video cable was terminated in 50 ohms at the display to complete the detection circuit. Measurements were made of VSWR at the r-f input to the detector mount and, while it was rather high (approximately 1.8 to 1), it was fairly constant over the band, thereby implying a constant reflection coefficient. Since a reflection from this point could be re-reflected by a system discontinuity and appear as a false target on the display, a coaxial isolator was added at the detector input to terminate any reflections. The short pulse saturation level of the diode in this mount was measured and the diode was found to be capable of delivering 1.5 volts into the 50-ohm load. The video bandwidth of the mount is excellent. No degradation in output pulse width has been observed for r-f input pulses of up to 2000 mc/s bandwidth (0.5 nanosecond pulse width).

Work is presently in progress on the design and construction of wide band detector mounts using both silicon and tunnel diodes. Considerably improved rectification efficiency should be obtainable with tunnel diodes due to their intrinsically lower series resistance (which is on the order of 100 ohms) as compared to 5000 ohms for the silicon point contact diodes that have been used.

DATA DISPLAYS

The dynamic range of the magnitudes of the returns from a test object may be very great, and it would be most desirable if the radar were capable of instantaneously displaying radar cross sections from 10^3 to 10^{-5} square meter without distortion. Such is not the case since, if the receiver gain is set high enough so that the 10^{-5} square meter target is discernible, the 10^3 square meter target will saturate the receiver. Conversely, if the receiver gain is reduced such that the 10^3 square meter radar cross section target just brings the receiver to saturation, the 10^{-5} square meter target will be undiscernible on the display.

This, then, gives rise to two criteria for the radar. The first criterion is the dynamic range of signals, or of radar cross sections, that the system can handle. The smallest radar cross sections which

can be displayed are determined by the noise figure of the receiver and the transmitter power level, and the largest are limited by receiver saturation. Larger radar cross sections can be accommodated by adding attenuation to the receiver input. The second criterion, which is considerably more restrictive, is the instantaneous dynamic range of the display. It is determined by the range of voltages that may be seen on the display at a usable level, which in turn is determined by the detector's transfer function or "law" and the physical size of the display. Figure 6 shows the transfer characteristic of the detector used in the Hughes system. If the detector is driven to a high peak power level, well above the square law region, amplitude compression of the signal will occur which will in effect increase the usable dynamic range of the display. In the Hughes system it was desired to have an instantaneous dynamic range of 30 db; therefore, operation in this region of the detector was chosen. The ability to accommodate a wide range of target magnitudes was implemented by the addition of a calibrated attenuator at the receiver input. With this attenuator set to zero, the system sensitivity will be a maximum. The receiver operating point is held at this level during all measurements by adjusting the input attenuator so that the peak of the incoming signal corresponds to a reference on the display. Since the radar cross section corresponding to the reference level is known, any incoming signal magnitude can be determined by using the attenuator setting to correct the reference level.

The data, in the form of a short pulse signature, must be displayed for observation and equipment adjustment on a device that is capable of handling the wide video bandwidth involved. Since the range-gated Type A display is the most useful for range measurements, it was employed in the Hughes system. In this type of display the target amplitude is shown versus the sector of range which the target occupies. Two basic instruments will give this type of display and have sufficient bandwidth to handle the video information: the traveling wave oscilloscope and the sampling oscilloscope.

The traveling wave oscilloscope uses a slow wave structure in the cathode ray tube to deflect the beam, thereby achieving very high deflection speeds. It is a real time device; that is, it gives one sweep for each transmitted pulse, thereby displaying the instantaneous signature of the target. The primary disadvantage of this instrument is its very low deflection sensitivity, requiring about 10 volts for a deflection of one centimeter, and the small size of the display, typically 2 by 4 centimeters. Photographic techniques may be used to increase the effective size of the display, but video amplification is necessary to obtain a usable input signal level. A wide bandwidth, solid state video amplifier capable of a 20 volt output was constructed at Hughes to allow the use of this instrument with the Hughes system; however, it was found that the versatility of the sampling oscilloscope far outweighed the limited advantage of the real time display for most measurement purposes.

The sampling oscilloscope constructs a display by consecutively sampling the video information on a periodic basis. Since it requires many radar returns to construct a single complete display, a transformation from real time to a much longer time base is performed in the instrument. This is particularly advantageous for radar signature measurements because the horizontal and vertical components of the display are available as low frequency waveforms and may be processed with conventional narrow bandwidth techniques. The sampling oscilloscope also offers very high voltage sensitivity at the input so that no video amplification is required. The main disadvantage of this instrument is that since many samples are required to make up a single display, any target motion during the display time will show up as distortion of the target's signature. However, for high pulse repetition frequencies and stable target orientation configurations, this effect is negligible. Therefore, a sampling oscilloscope was chosen as the primary display device for the Hughes radar. Figure 2 shows the return from a 9.500-inch calibration sphere displayed on a sampling oscillograph.

DATA RECORDING TECHNIQUES

The initial means of data recording used with the Hughes radar was an X-Y plot, the X coordinate being range and the Y coordinate return magnitude. The sampling oscilloscope provides outputs that are suitable for use with a conventional X-Y plotter.

Because the power-to-voltage transfer function of the detector is very nonlinear, it was desired to shape the voltage to the Y coordinate input to modify the scale factor for a logarithmic display. A simple diode shaper was used to perform this scale factor modification. The resulting plots of the radar signature data were made on 11 x 17 inch graph paper with typical horizontal scale factors of from 1 to 3 feet of range per inch and a vertical scale factor of 5 db per inch below the reference level. Figure 3 shows the data format. The signature recorded is that of the 9.500 inch diameter calibration sphere.

In addition to displaying the radar signature, it is necessary that a range reference be provided to relate the signature to the test object for scatter point correlation. This can be accomplished by triggering the display from a very stable trigger which is precisely delayed from the transmitted pulse. This was implemented in the Hughes system by sampling the transmitted pulse and introducing it into the receiver. By passing this sync pulse through the receiver the effects of the traveling wave tube transit time variations, which can be considerable, are eliminated. This signal is then picked off the output of the receiver through a directional coupler, detected, and delayed in a coil of coaxial cable whose electrical length is equal to the two-way range distance to this test object before being applied to the display. The accuracy obtained in correlating a single return with its scatter point on the object has been observed over an extended period to be within 1.5 inches.

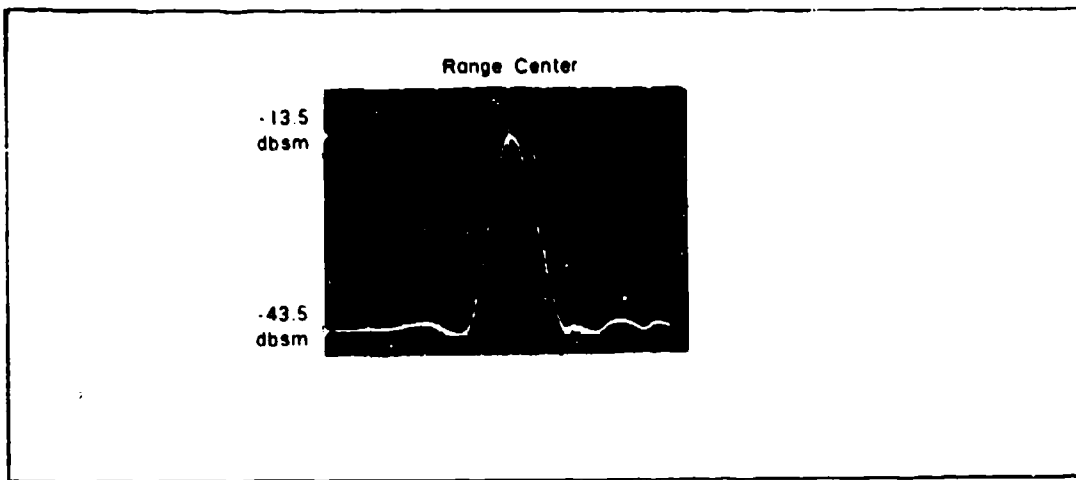


Figure 2. 9.500-Inch Calibration Sphere

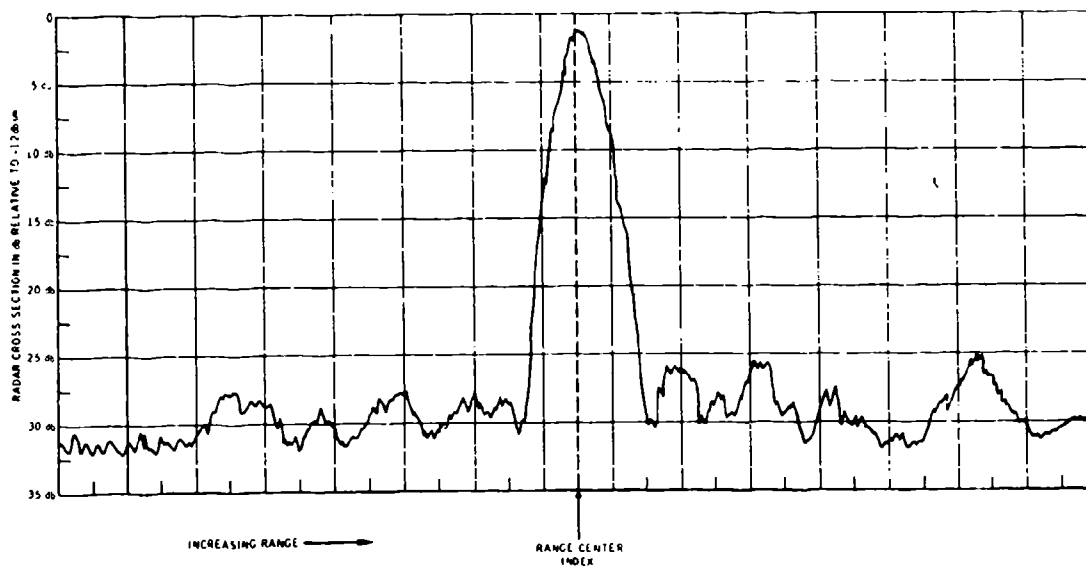


Figure 3. Short Pulse Radar Return From a 9.500-Inch Diameter Sphere

While X-Y plotting as a method of data recording has been used with considerable success at the Hughes facility, it becomes a rather time-consuming process when large amounts of data are to be recorded. Each target position requires setting the input attenuator, recording this magnitude on the graph, and making the actual X-Y plot (which consumes about 10 seconds of tracing time). To reduce the time involved for this portion of the operation, a photographic recording system is currently being implemented.

The X output from the sampling oscilloscope and the output from the amplitude shaper are applied to a large-screen oscillograph. This display is then photographed with a 16mm camera using one frame for each target aspect position. Setting the input attenuator, which is at present a manual operation, will be replaced with an automatic technique. A block diagram of the mechanization is shown in Figure 4. In this technique the manual attenuator at the receiver input will be replaced with an electronically variable attenuator which will be controlled by a voltage shaper and amplifier chain such that the amount of attenuation set into the attenuator will be directly proportional to the input voltage. The target return signal at the receiver output will be peak-detected and the peak level stored in an operational integrator. This voltage will then be applied to the attenuator at the receiver input and used to set the recorder reference level. In addition, a number that indicates the amount of voltage that is applied to the attenuator will be set into the data channel on the recording camera and photographed with the target return. Therefore, each frame on the film will contain all the information necessary to describe the target signature for a particular target position. This recording system is adaptable to manual or mechanical target positioning and offers a method of obtaining a large amount of target data in a minimum amount of recording time and at minimum cost.

The automatic recording system may also be modified to obtain the data directly in a digital form on tape or punched cards. The mechanization is shown in Figure 5. Data taken in this form are ideally suited for use in computers with a minimum amount of manual processing. The data unit that defines each target position must contain the target aspect angle, polarization of the signal, target magnitude reference level, the range reference index, and the magnitude of the return as a function of range. The information corresponding to target designation, aspect angle, and polarization may be placed on the tape by manually operated punch keys or automatically by means of suitable switching circuits, depending mainly on whether manual or automatic target positioning is used. The horizontal scale on the sampling oscilloscope, which indicates range, is divided into range increments or cells. This may be easily accomplished on the sampling oscilloscope by converting the stepped horizontal sweep that is used in constructing the sampled display into a series of pulses by differentiating it. Each pulse then

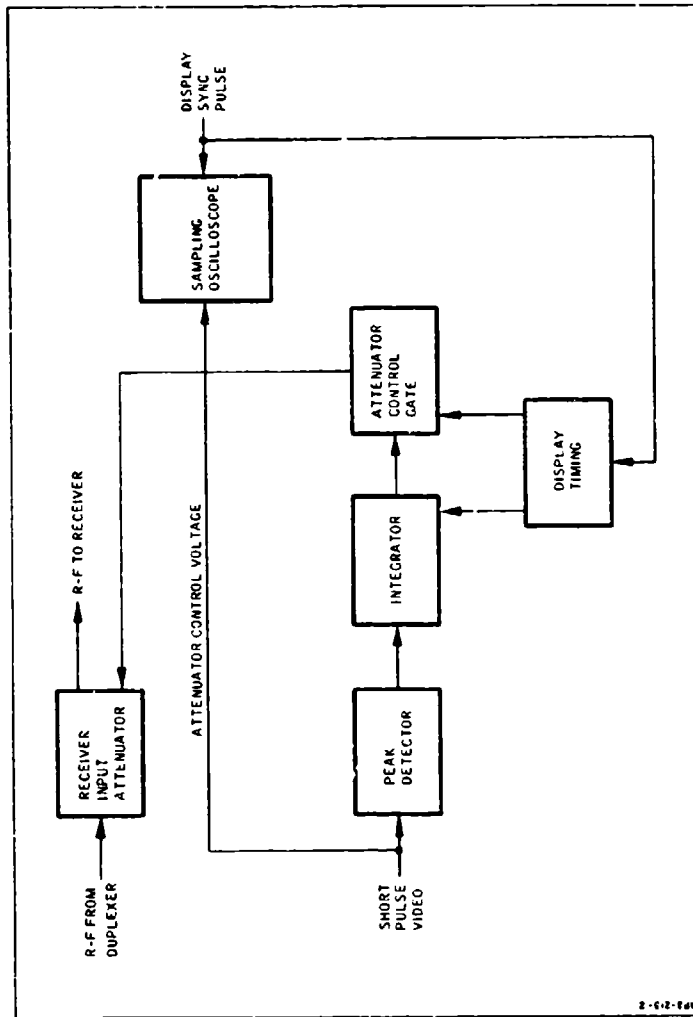


Figure 4. Automatic Scale Factor Adjustment Block Diagram

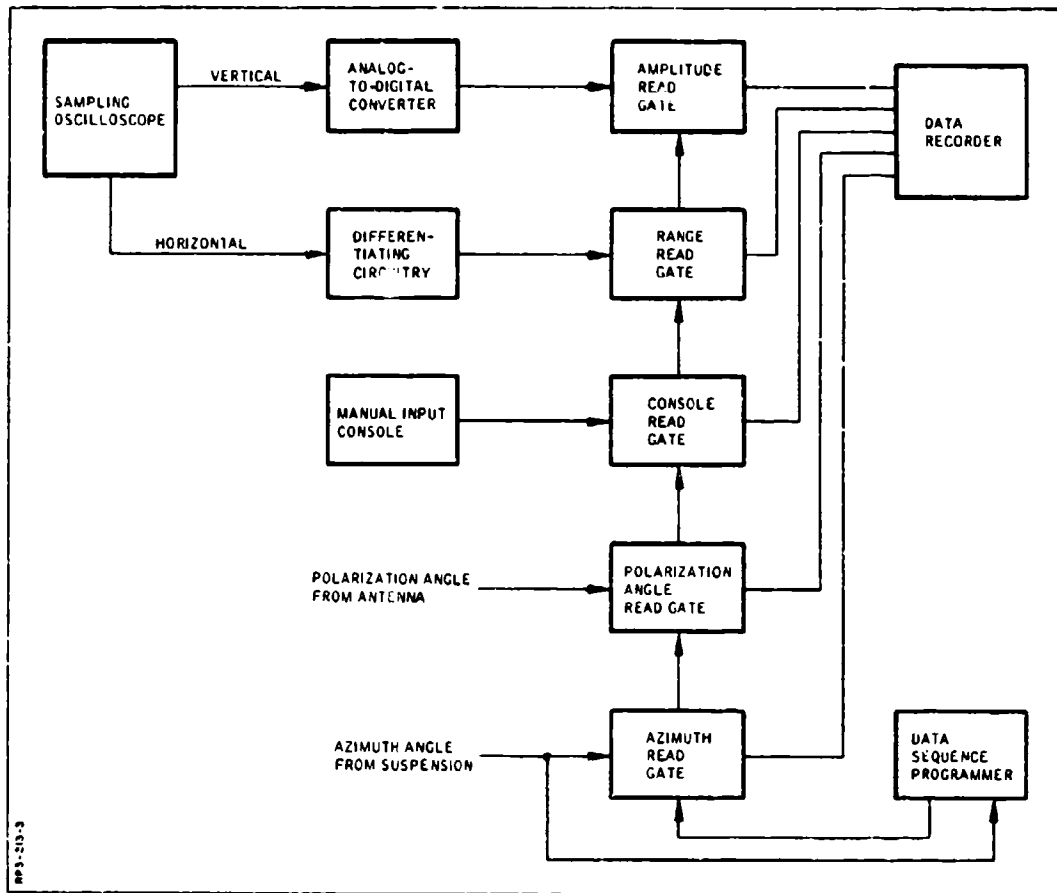


Figure 5. Data Digitizer

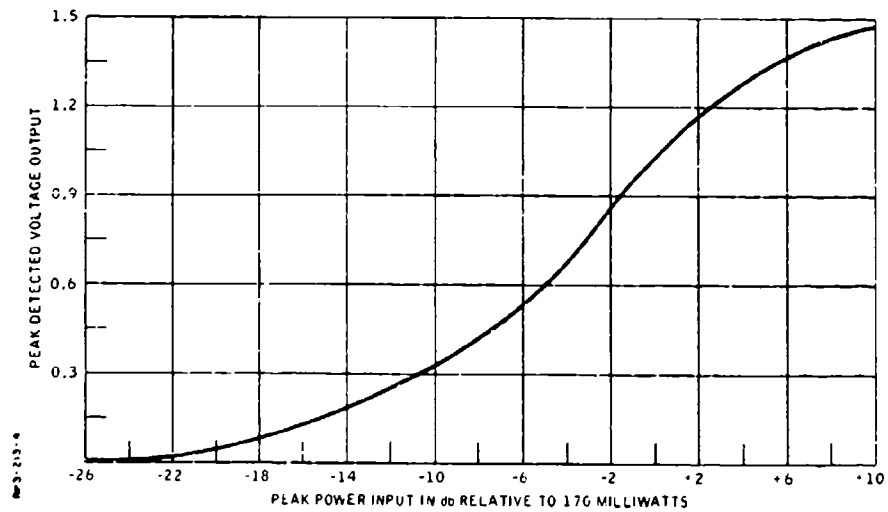


Figure 6. Wideband Crystal Detector Transfer Characteristic

defines the start of a range increment, and the number of range increments in the total display may be determined by the samples per division control on the oscilloscope. The vertical output, which comes from the signal shaper, is introduced into an analog-to-digital converter which gives a numerical output proportional to the vertical voltage input. The range increment pulses are recorded on the tape and concurrently cause the output of the analog-to-digital converter to be written on the tape. The tape will therefore contain one magnitude reading for each range increment pulse. The number of range increments should be chosen such that at least 10 occur during each range cell as defined by the resolution (or pulse width) of the radar. This will allow reasonably good reconstruction of the target return from the digitized data. In the Hughes system, the range displayed on the sampling oscilloscope for a large target is 15 feet. The horizontal scale on the oscilloscope contains 10 divisions, so that a sampling rate of 30 samples per division will give a total of 300 samples in 15 feet of 20 samples per foot.

SUMMARY

The Hughes short pulse radar has been used with considerable success to obtain radar cross section data from a wide range of test objects. The use of the sampled display as a vehicle for data recording has proved to be most satisfactory because it permits a number of recording methods to be employed. Consideration is now being given to the addition of precision phase measurement equipment to the system so as to allow the measurement of the relative phase between individual scatter point returns. This added information will permit correlation between the short pulse return from a test object and the CW or long pulse return, extending the usefulness of short pulse measurement data.

*A METHOD OF PHASE MEASUREMENT
FOR PULSED RADAR SYSTEMS

Bernd Falk, Design Specialist
General Dynamics/Fort Worth

ABSTRACT

This paper contains a description of a phase measuring technique in which feedback principles are used. A feedback loop around the entire IF system is used to eliminate the errors and nonlinearities that would result from simple phase detection of the IF output. Several amplitude and phase plots of typical radar targets are presented. Application of the equipment to the direct measurement of the scattering matrix and background subtraction are briefly discussed.

INTRODUCTION

The need for measurement of radar cross section amplitude is well established. The measurement of phase on a radar cross section range enables the determination of other significant target and range parameters. The most significant applications are (1) subtraction of the background returns and (2) determination of the scattering matrix. Encouraging results have been obtained from experiments designed to allow subtraction of background returns from measured cross section.

In order to describe the scattering properties of a target completely, an infinite number of polarizations relative to target orientation are required. Phase measurement techniques may be employed to determine coefficients of the scattering matrix directly. From the scattering matrix, the cross section of arbitrary polarizations may be determined. By using direct phase measurement, three sets of runs are required to determine the scattering matrix. At this writing, experiments are being planned to verify scattering matrix techniques.

TECHNICAL APPROACH

Figure 1 is a block diagram of the phase and amplitude measuring instrumentation. The received signal is mixed with a local oscillator signal to obtain a 60-megacycle IF signal. Following the IF amplifier is a range gate which allows only echoes at the desired target range to be gated through the circuit. The gated pulses are detected and stretched in a boxcar circuit to provide an output voltage which is proportional to the echo signal strength.

A standard 60-megacycle pulsed signal is injected into the IF system at a time sufficiently delayed after main bang that no target echoes are received. This pulsed signal is fed through a precision, servo-driven attenuator to the input of the IF system. The range gate and boxcar

*All rights reserved

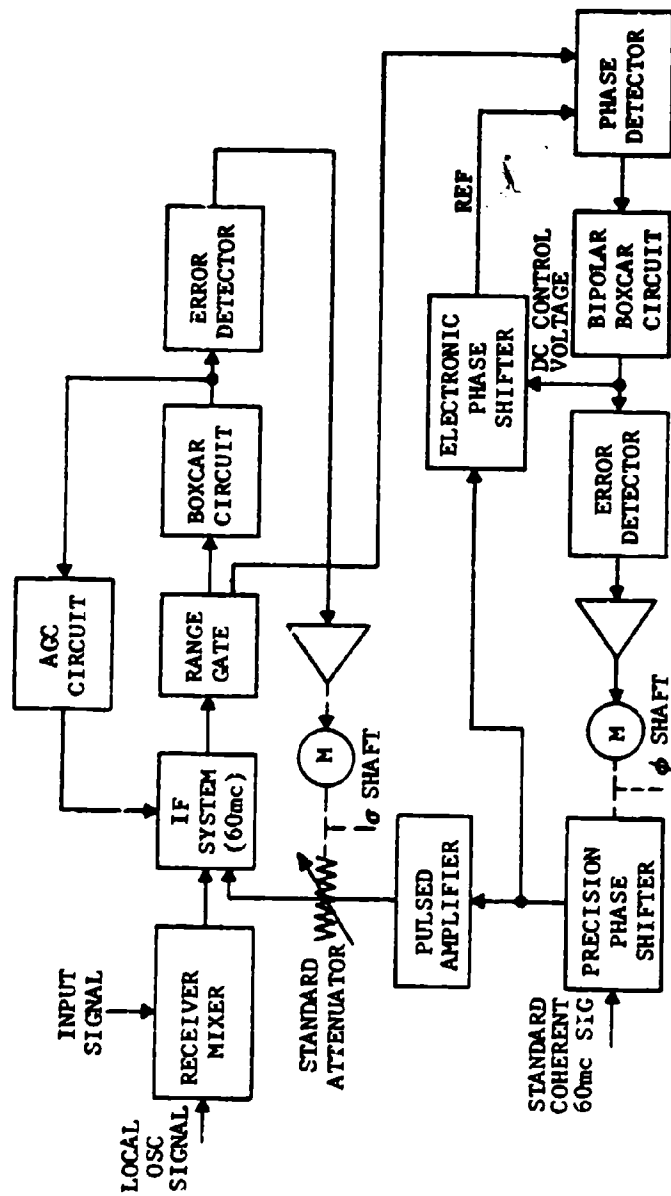


Figure 1. Phase Measurement System Block Diagram

circuits act on this pulsed signal in the same way as they act on the target echo signal. Output of the boxcar circuit is now a rectangular wave if the amplitude of the echo and reference signal are not equal. The amplitude of this rectangular wave is proportional to the difference between the amplitude of the echo and standard signals.

This rectangular wave is fed to an error detector circuit in which it is demodulated and used to generate a servo-drive correction voltage which is proportional to the amplitude difference between the echo and the standard signals. This correction voltage is fed to the servo motor which drives the precision reference attenuator until the amplitude of the standard and target echo signals are equal. Potentiometers and a digital shaft encoder are connected to this shaft to read out σ .

The technique used in the phase-measuring equipment is based on the principle of comparing the signal phase with the phase shift produced by a precision phase shifter. A servo loop is used to make the two phase shifts identical. Since range gating is effected at the intermediate frequency, phase information is preserved through the range gate. The 60-megacycle IF which results from the input signal is fed to the phase detector circuit and compared with the reference 60-megacycle signal. The output of the phase detector is a positive or negative pulse depending on whether the IF signal is in phase or out of phase with the phase detector reference. A bipolar boxcar circuit is used to stretch this pulse. The amplitude of the boxcar output voltage is proportional to the phase difference of the IF and reference signal.

The standard pulse is also processed through the phase channel to produce a rectangular wave output from the bipolar boxcar circuit in which the amplitude is proportional to the phase difference between the echo and the standard signal. The polarity of the rectangular wave will be proportional to the phase error sense. This rectangular wave is processed in the error detector, as previously described, and is used to drive a servo motor. The motor will operate until the phase of the standard pulse and the echo signal are equal. Potentiometers and shaft encoders may be connected to the motor shaft to serve as phase readout mechanisms.

The reason for the inclusion of the electronic phase shifter is not immediately apparent. If it were omitted, phase would still be measured independently of IF phase shift since both echo and reference signals pass through identical circuitry. However, it is possible for the circuit to operate about a false null. This application may result from phase shifts in the IF and gating circuits. This false null can be brought about by cumulative phase shifts in the IF system. The forward loop gain of the servo loop depends on the relative phase of the signal and the reference at the phase detector. Use of the electronic phase shifter assures that the phase detector always has a reference which is in the required phase. This operation is accomplished by sampling the output of the bipolar boxcar circuit and adjusting the

reference phase for a zero average voltage at the bipolar boxcar output.

FREQUENCY STABILIZATION

On an outdoor range, range length is usually long relative to wavelength. Therefore, small changes in frequency will cause relatively large changes in the received signal phase. For the worst case, frequency stabilities in the order of 1 part in 10^7 are required. Frequency stabilization of the transmitted frequency is achieved by phase-locking a microwave signal source to a quartz crystal oscillator by use of one of the recently introduced oscillator synchronizers.

The frequency determining circuitry is shown in Figure 2. A microwave oscillator is frequency-stabilized by the synchronizer. The output signal of the oscillator is used as the receiver local oscillator signal. Transmitted frequency is derived from the local oscillator signal by use of a "side-stepping" technique. The 60-megacycle oscillator provides signals for the sidestep mixer as well as for the phase-measuring loop, to ensure that the system is completely coherent.

TYPICAL DATA

Figure 3 is a representation of phase measurements made on a large sphere mounted on a styrofoam column approximately 11 centimeters from the axis of rotation. Theoretically, a sine wave should be traced out as shown. A maximum error in the order of 6 degrees is indicated for this run. Both range and equipment errors are present in this type of measurement.

The application of phase measurements to background subtraction is shown in Figures 4 through 7. In each case, a run is made to plot the amplitude and phase of the background and the styrofoam column as the column is rotated one turn. The target is then mounted atop the column, and the run repeated. If it is assumed that the target and the background add linearly, the true target cross section may be determined by performing a vector subtraction as indicated below:

$$\sigma_{\text{Target}} = \sigma_{\text{(Target + Background)}} - \sigma_{\text{Background}}$$

The results obtained with a 2-inch sphere are shown in Figures 4 and 5. No attempt was made to reduce initial background level. Target and background signals were almost equal. Consequently, large variations were present in the measured return (background + target). Computed target return is also shown. The degree to which cross section variations are smoothed out is one measure of the usefulness of the subtraction technique. Cross section obtained after subtraction agrees with the theoretical value of the sphere to within $\pm 1/2$ db. Subtraction results obtained with a 30-degree sphere-cone are shown in Figures 6 and 7. In the nose-on region, background returns were larger than the target.

CONCLUSIONS

The feasibility of making phase measurements on a pulsed ground plane radar range has been demonstrated. An experimental program is continuing in the areas of background subtraction and scattering matrix.

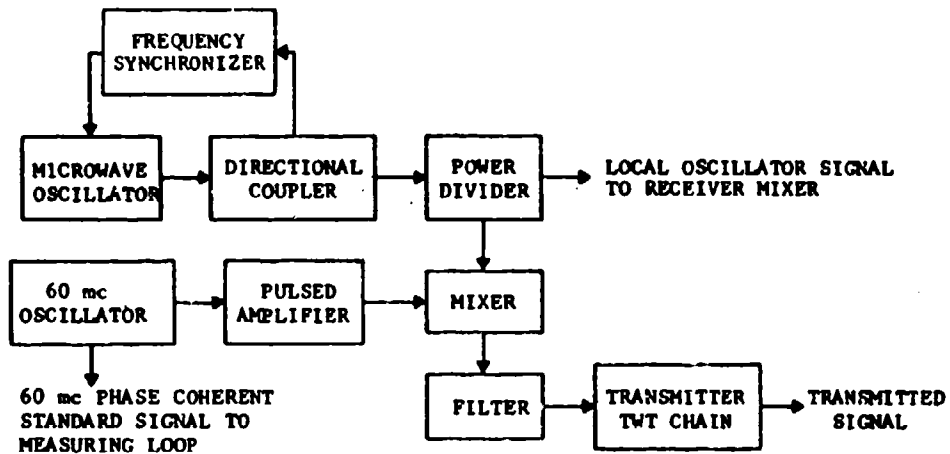


Figure 2. Frequency Determining Circuits

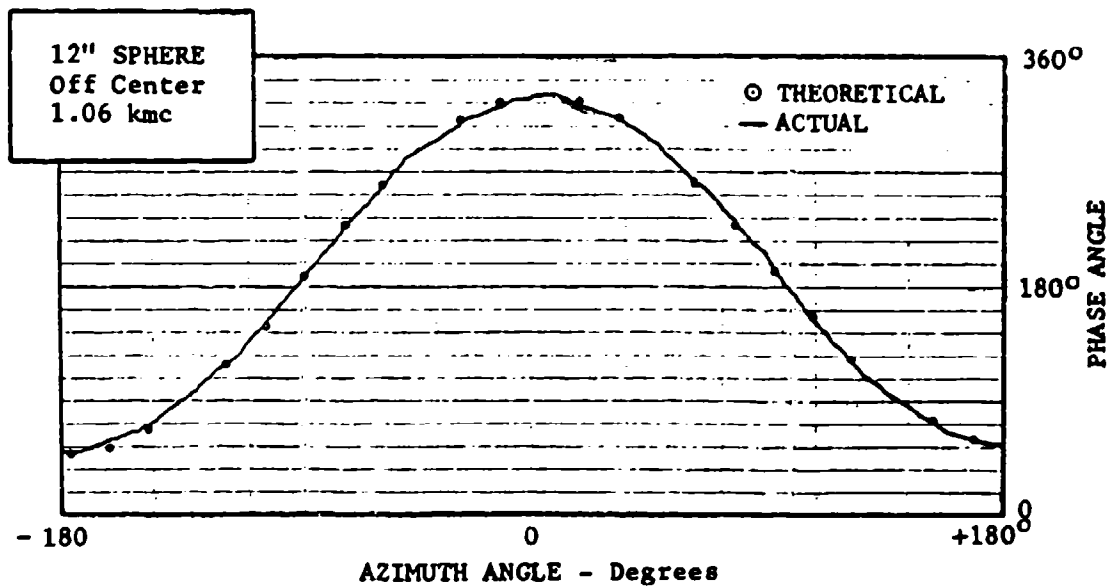


Figure 3. Phase Measurement of Off-Center Sphere

2" SPHERE

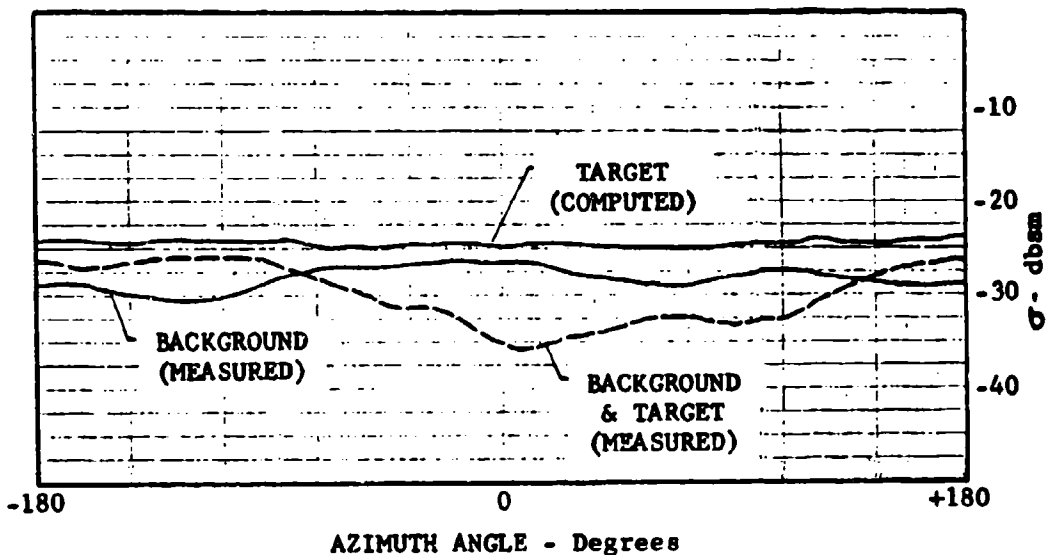


Figure 4. Amplitude Plot - 2" Sphere

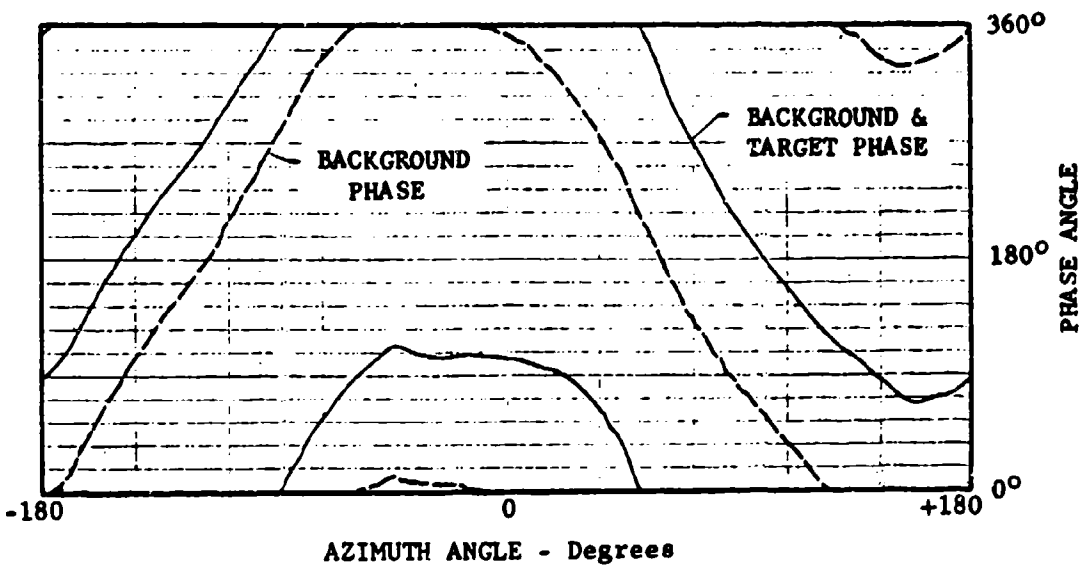


Figure 5. Phase Plot - 2" Sphere

30° SPHERE CONE

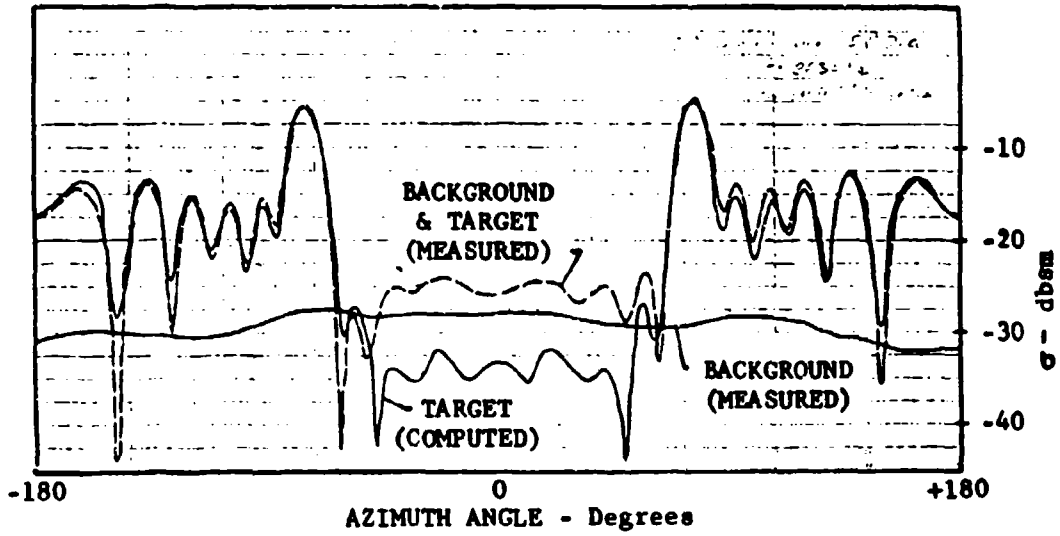


Figure 6. Amplitude Plot - Sphere Cone

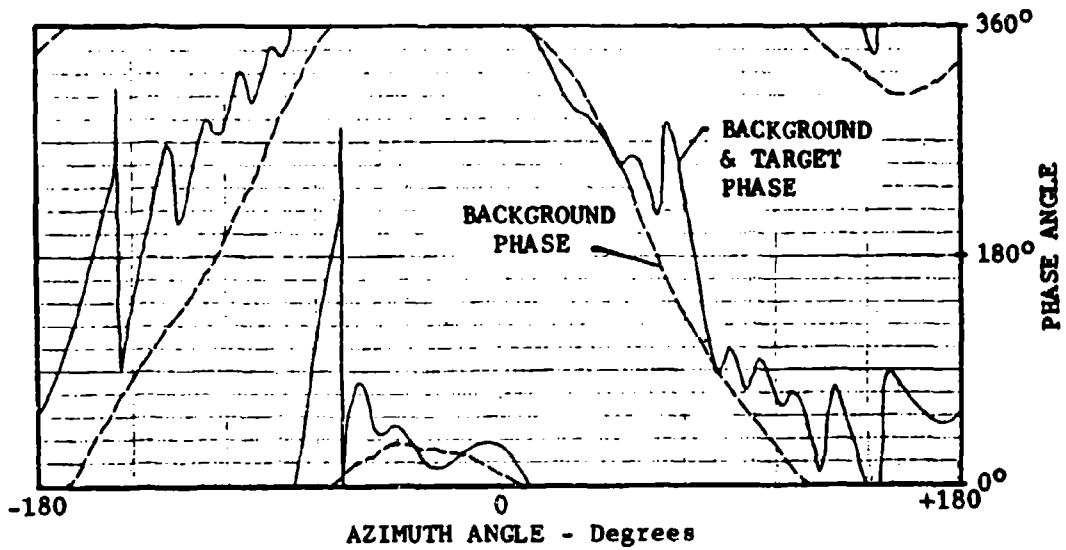


Figure 7. Phase Plot - Sphere Cone

RF PHASE STABILITY REQUIREMENTS FOR BALANCED CW REFLECTOMETERS

William D. Fortner, Senior Electronics Engineer
Micronetics Incorporated

ABSTRACT

An analysis is presented which indicates the critical dependence of the background cancellation capability of a CW reflectometer on the frequency stability of the transmitter as well as the mechanical stability of both the microwave circuitry and the environment.

The importance of using an antenna with an exceedingly low VSWR in a truly monostatic CW system is emphasized. The desirability of equalizing and minimizing (insofar as possible) the length of background signal paths and nulling signal paths is shown.

The bearing of the analysis on both CW reflectometer design and CW range design is discussed briefly.

INTRODUCTION

Balanced CW reflectometers (CW reflectometers employing background cancellation) represent one of the oldest and most widely used instrumentation schemes for performing RCS measurements. This instrumentation technique is relatively inexpensive and is conceptually simple.

This type of reflectometer is subject to several well known limitations¹. Its use is most appropriate to a restricted class of target-wavelength combinations which includes VHF and UHF measurements involving relatively large targets as well as higher frequency measurements involving physically small targets.

The effectiveness with which a background signal can be cancelled depends firstly on the degree to which the background is independent of the target and secondly on the phase stability of the transmitted signal, the stability of the environment, and the mechanical stability of the radar components¹.

The analysis of an idealized "equivalent circuit" model and the discussion which follows, indicates the critical dependence of background cancellation capability on the factors listed in the foregoing paragraph and suggest some expedients for optimizing the performance of the Balanced CW Reflectometer.

RF PHASE STABILITY ANALYSIS

Equivalent Circuit

The idealized equivalent circuit to be analyzed is shown in Figure 1a. The signal propagating around the long loop, Path #1, is taken to be analogous to a background signal encountered on a reflectivity range. The signal propagating across the short loop, Path #2, is the nulling signal. An alternate equivalent circuit is shown in Figure 1b. Figure 1a represents a dual antenna (quasi-monostatic or bistatic) reflectometer. Figure 1b represents a single antenna reflectometer. As far as the analysis is concerned, the two circuits are identical provided the assumptions listed below are made.

Assumptions

The following simplifying assumptions are made:

1. Perfect directivity of directional couplers shown in Figure 1a.
2. Perfect isolation of the E and H arms of the magic tee in Figure 1b.
3. A discrete source of background interference.
4. Free space propagation velocity.

The first two assumptions may result in optimistic numerical results. The third is an obvious oversimplification. Its only justification is simplification if an outdoor range is being considered, but in the case of an anechoic chamber, it is acceptable as a "worst case" provided the differential length between Path #1 and Path #2 is taken to be approximately twice the chamber length. (In general, the background will be due to N loops of various lengths with N very large.) The fourth assumption is realistic for the case where Path #1 is a free space path and is much longer than Path #2.

Basic Relations

Let E_1 and E_2 be the field strengths of the signals propagating along Path #1 and Path #2 respectively.

$$\begin{aligned} E_1 &= |E_1| e^{j\omega t - \gamma z_1} \\ E_2 &= |E_2| e^{j\omega t - \gamma z_2} \end{aligned} \tag{1}$$

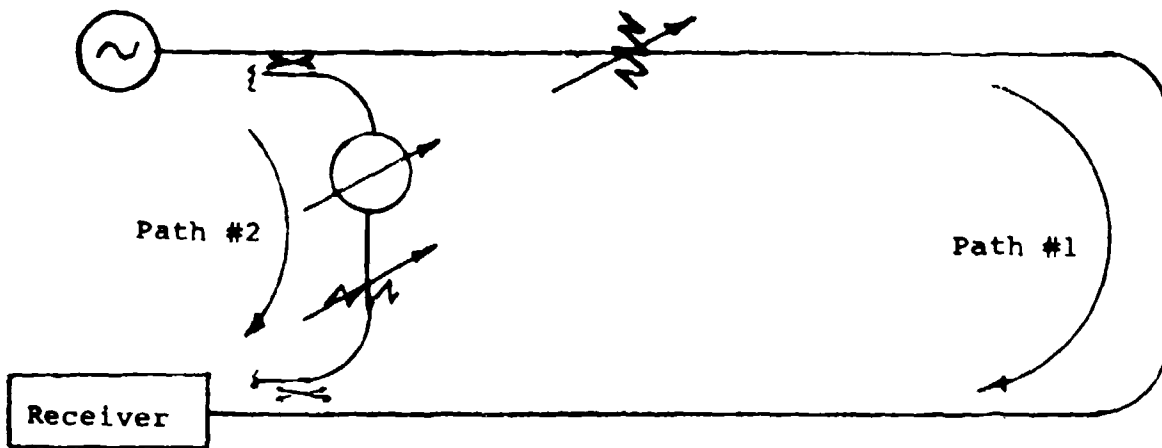


Figure 1a. Equivalent Circuit for Dual-Antenna Balanced CW Reflectometer and Range

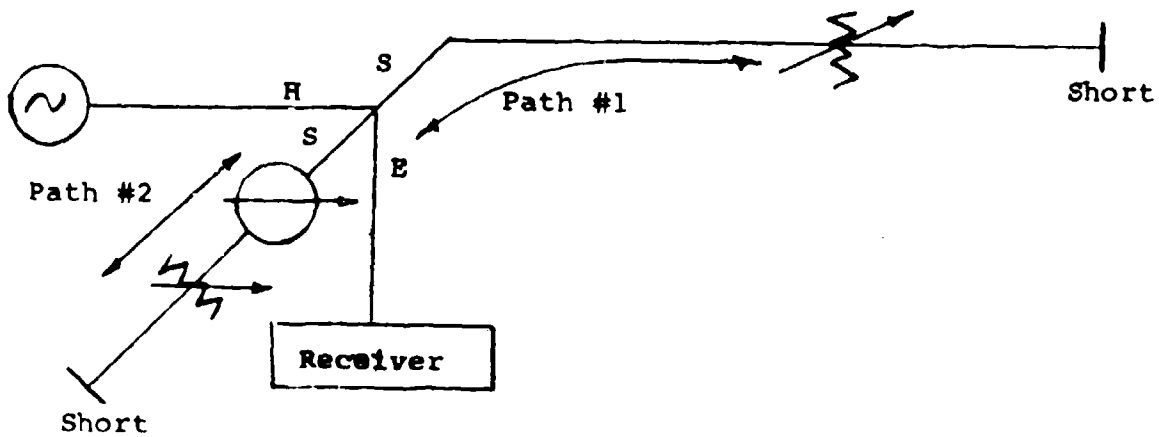


Figure 1b. Equivalent Circuit for Single Antenna Balanced CW Reflectometer and Range

Where γ is the conventional propagation constant

$$\gamma = \alpha + j\beta \quad (2)$$

Separating the phase terms

$$\begin{aligned} E_1 &= \left[|E_1| e^{j\omega t - \alpha z_1} \right] e^{-j\beta z_1} \\ E_2 &= \left[|E_2| e^{j\omega t - \alpha z_2} \right] e^{-j\beta z_2} \end{aligned} \quad (3)$$

Let

$$\begin{aligned} |E_1| e^{j\omega t - \alpha z_1} &= E_{O1} \\ |E_2| e^{j\omega t - \alpha z_2} &= E_{O2} \end{aligned} \quad (4)$$

Then equations (1) and (3) can be rewritten

$$\begin{aligned} E_1 &= E_{O1} e^{-j\beta z_1} \\ E_2 &= E_{O2} e^{-j\beta z_2} \end{aligned} \quad (5)$$

The level of the "background reflection" can be adjusted to any appropriate value via the attenuator in Path #1. Cancellation is achieved by adjusting the attenuator and phase shifter in Path #2 so that E_2 is equal in amplitude and in counterphase with E_1 .

In general, the total field strength, E_t , at the detector is the sum of E_1 and E_2 .

$$E_t = E_1 + E_2 \quad (6)$$

The resultant power, P , is proportional to $|E_t|^2$.

$$P \propto |E_t|^2 = E_{O1}^2 + E_{O2}^2 + 2E_{O1}E_{O2} \cos[\beta(z_1 - z_2)] \quad (7)$$

For complete background cancellation, $E_{O1} = E_{O2}$ and

$$P \propto 2E_{O1}^2 \left\{ 1 + \cos[\beta(z_1 - z_2)] \right\} = 0 \quad (8)$$

Meaning, for the non-trivial case, that

$$\cos[\beta(z_1 - z_2)] = -1 \quad (9)$$

Let

$$z_1 - z_2 = L \quad (10)$$

and let

$$\beta(z_1 - z_2) = \frac{2\pi}{\lambda} L = \frac{2\pi L}{c} f = \phi \quad (11)$$

It is convenient to let

$$2 \left[1 + \cos \phi \right] = \xi_0 \quad (12)$$

which may appropriately be called the quieting factor; the zero subscript indicates that free space propagation velocities are involved.

By equations (8), (9) and (12), it is necessary that

$$\xi_0 \Big|_{\min} = 0 \quad (13)$$

for complete background cancellation. This can be true only if

$$\phi = \phi_0 = (2n-1)\pi = \frac{2\pi L}{c} f_0, \quad n = 1, 2, 3... \quad (14)$$

by (12) and (13).

It is now desirable to determine how sensitive null degradation is to incidental frequency modulation, frequency drift, and spurious spectral content of the transmitter output. Differentiate (11)

$$\frac{d\phi}{df} = \frac{2\pi L}{c}$$

or in incremental form

$$\Delta \phi = \frac{2\pi L}{c} \Delta f. \quad (15)$$

Hence, when a frequency shift is introduced, the quieting factor becomes

$$\xi_0 = 2 \left[1 + \cos (\phi_0 + \Delta \phi) \right] \quad (16)$$

or, in view of (14),

$$\xi_0 = 2 \left[1 - \cos \Delta \phi \right] \quad (17)$$

Rearranging (17)

$$\cos \Delta \phi = 1 - \frac{\xi_0}{2} \quad (18)$$

The series expansion for $\cos \Delta \phi$ is

$$\cos \Delta \phi = 1 - \frac{(\Delta \phi)^2}{2!} + \frac{(\Delta \phi)^4}{4!} \dots \quad (19)$$

For the situation of interest $\Delta \phi \ll 1$ so that all terms past the second in equation (19) will be insignificant. It then follows from (18) and (19) that

$$\xi_o = (\Delta \phi)^2 = \frac{4\pi^2 L^2}{c^2} (\Delta f)^2. \quad (20)$$

Figure 2 is a graph of ξ_o versus Δf . If an anechoic chamber reflects a known amount of power into the receiver, then the amount of quieting necessary to reduce the background to a specific level can be determined via the radar range equation

$$\frac{P_r}{P_t} = \frac{G^2 \lambda^2 \sigma}{(4\pi)^3 R^4}. \quad (21)$$

Hence, the maximum allowable frequency deviation of the RF transmitter can be determined from equation (20) or Figure 2.

Sample Analysis - Phase Stability

Assume an anechoic chamber situation as described below:

- | | | |
|---|--|------|
| a. Chamber length | $l = 20$ meters | |
| b. Background cross-section referenced to a range of 6 meters | $\sigma_B \Big _{R=6 \text{ meters}} = -20$ dbsm | |
| c. Reflectometer antenna gain | $G = 30$ db | (22) |
| d. Measurement frequency | $f_o = 10$ Gc. | |
| e. Receiver sensitivity | $P_{r \text{ min}} = -95$ dbm | |
| f. Cross-section to be measured | $\sigma_{\text{min}} = -60$ dbsm | |
| g. At a range of | $R = 15$ meters | |
| h. With a signal-to-background ratio | $\frac{\sigma_{\text{min}}}{\sigma_B} = 14$ db | |
| i. Receiver signal-to-noise ratio | $\frac{S}{N} = 14$ db | |

It is necessary to find the required

transmitter power: $P_t = ?$

quieting factor: $\xi_o = ?$

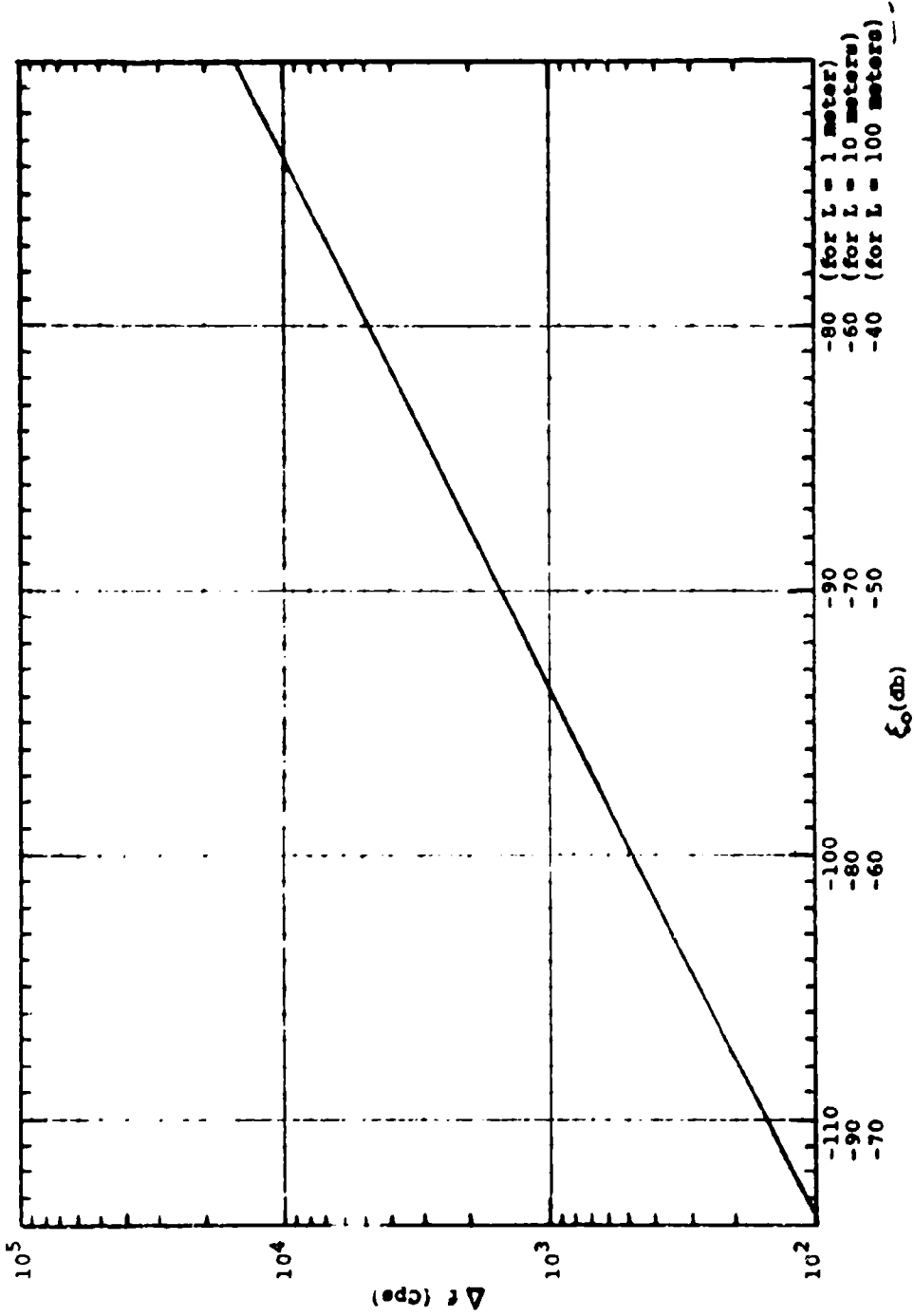


Figure 2. Δf versus ξ_0

and the corresponding maximum allowable

frequency deviation: $\Delta f = ?$

The radar range equation reads

$$\frac{P_r}{P_t} = \frac{G^2 \lambda^2 \sigma}{(4\pi)^3 R^4} \quad (23)$$

Substituting conditions (22) b, c, d and g into (23) and converting to decibel notation, one finds that the ratio of received power (due to background reflections) to transmitted power, P_{rB}/P_t , is

$$\left. \frac{P_{rB}}{P_t} \right|_{\text{uncompensated}} = -55 \text{ db.} \quad (24)$$

The maximum allowable background level, $\sigma_B \Big|_{R=15}$, by (22) f and h, is

$$\left. \sigma_B \right|_{R=15} = -74 \text{ dbsm.} \quad (25)$$

The required compensated ratio of P_{rB} to P_t can be calculated by substituting conditions (22)c through h into the radar range equation yielding

$$\left. \frac{P_{rB}}{P_t} \right|_{\text{compensated}} = -125 \text{ db.} \quad (26)$$

The difference between (26) and (24) is the required value for the quieting factor.

$$\left. \xi_o \right|_{\text{required}} = -70 \text{ db.} \quad (27)$$

The receiver signal-to-noise ratio, by (22) i, is to be 14 db so

$$P_t = +30 \text{ dbm} = 1 \text{ watt.} \quad (28)$$

If $\xi_o = \text{constant}$, then $L \Delta f = \text{constant}$ in equation (20). Hence, it is simple to interpolate from the $L = 1$ meter scale or the $L = 10$ meter scale of Figure 2 in order to find the necessary quieting factor for any other L .

For $L = 10$ meters and $\xi_o = -70$ db, Figure 2 indicates that

$$\Delta f = 1.5 \times 10^3 \text{ cycles/sec.} \quad (29)$$

The L of interest is about 40 meters (twice the chamber length) so for $\xi_o = -70$ db,

$$L_1 \Delta f_1 = L_2 \Delta f_2$$

$$10 \times (1.5 \times 10^{-3}) = 40 (\Delta f_2)$$

$$\Delta f \Big|_{\max} = 390 \text{ cps.} \quad (30)$$

Recapitulating

$$P_t = +30 \text{ dbm} \quad (28)$$

$$\xi_o = -70 \text{ db} \quad (27)$$

$$\Delta f \Big|_{\max} = 390 \text{ cps} \quad (30)$$

for the conditions of equation (22).

Values of Quieting Factor for Waveguide Systems

Equation (15) was derived on the assumption that only free space propagation velocity was encountered. When the expression for waveguide propagation velocity is substituted for c in equation (11), differentiation yields

$$\frac{d\phi}{df} = \frac{2\pi L}{c \sqrt{1 - \left(\frac{f_c}{f}\right)^2}} \quad (31)$$

Figure 3 is a graph of $1/\sqrt{1 - (f_c/f)^2}$ versus f/f_c over the range of f/f_c representing the standard waveguide bandwidth for the TE_{01} mode. It demonstrates that the factor $1/\sqrt{1 - (f_c/f)^2}$ varies between 2.1 at the low end of the band and 1.42 at the high end of the band. Furthermore, it is clear that, for the values of Δf which might be encountered ($\Delta f/f_o < 10^{-6}$), the value of $1/\sqrt{1 - (f_c/f)^2}$ will remain essentially constant. So it is justifiable to write

$$\Delta \phi = \frac{2\pi L}{c} \frac{\Delta f}{\sqrt{1 - \left(\frac{f_c}{f_o}\right)^2}} \quad (32)$$

and

$$\xi_g = (\Delta \phi)^2 = \frac{4\pi^2 L^2 (\Delta f)^2}{c^2 \left[1 - \left(\frac{f_c}{f_o}\right)^2\right]} \quad (33)$$

The subscript, g, indicates that waveguide propagation velocities are involved. Figure 4 is a plot of ξ_g/ξ_o versus f/f_c for the range of f/f_c representing the standard waveguide bandwidth for the TE_{01} mode.

VSWR Problems

When a single antenna CW reflectometer is used, the VSWR may be a significant source of "background interference". Figure 5, a graph of P_r/P_t versus VSWR, will demonstrate this point.

Consider

$$\text{VSWR} = 1.1, \quad (34)$$

an excellent value in the context of general antenna practice. Figure 5 indicates that

$$\left. \frac{P_r}{P_t} \right|_{\text{uncompensated}} = -26 \text{ db} \quad (35)$$

The required value of P_r/P_t was stated by equation (26) to be

$$\left. \frac{P_{rB}}{P_t} \right|_{\text{compensated}} = -125 \text{ db} \quad (26)$$

Hence, the required value of ξ_g is

$$\xi_g = -99 \text{ db.} \quad (36)$$

Assume a differential path length between the VSWR path and the balancing path = 1 meter,

$$L = 1 \text{ meter.} \quad (37)$$

By Figure 4,

$$\frac{\xi_g}{\xi_o} = 4 \text{ db.} \quad (38)$$

Hence, the equivalent value of ξ_o is

$$\xi_g - \xi_o \Big|_{\text{equiv.}} = -103 \text{ db.} \quad (39)$$

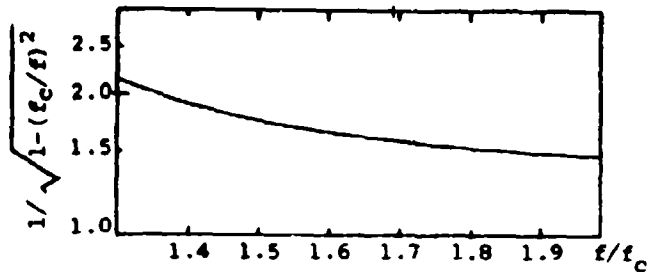


Figure 3

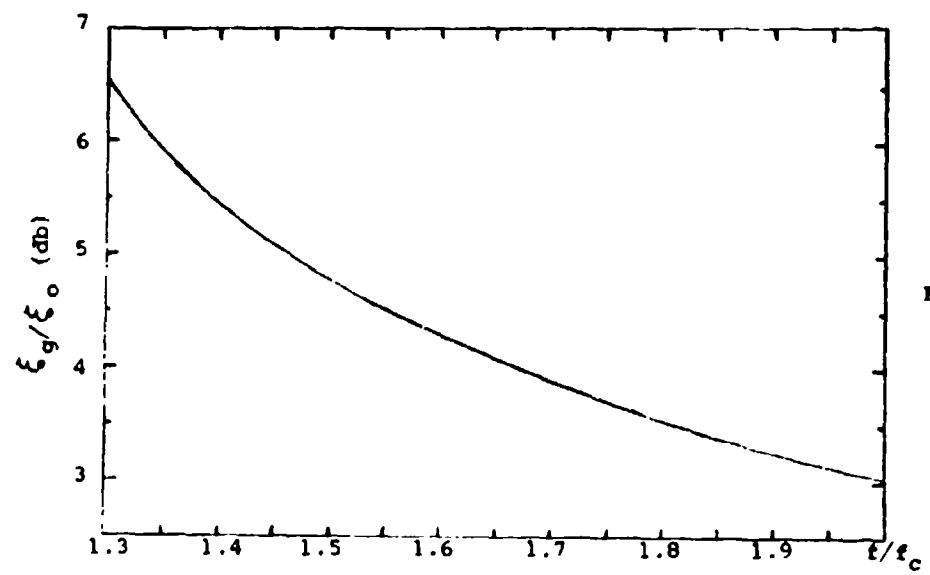


Figure 4

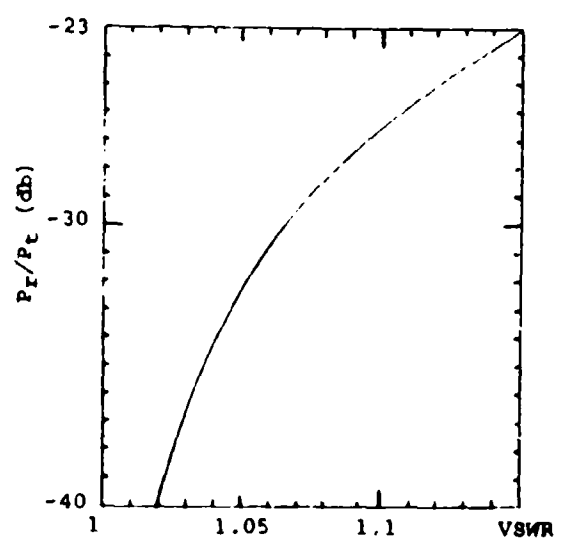


Figure 5

From Figure 3, one finds that

$$\Delta f \Big|_{\max} = 340 \text{ cps} \quad (40)$$

a value slightly more stringent than that imposed by the reflection from the chamber itself. The value of $L = 1$ meter can normally be bettered considerably with careful reflectometer layout.

MECHANICAL STABILITY ANALYSIS

The manner in which L affects RF phase stability requirements is indicated by equations (20) and (33).

The manner in which thermal expansion and similar mechanical instabilities will affect background cancellations is also interesting.

Note that

$$\phi = \frac{2\pi L f}{c} \sqrt{1 - \left(\frac{f_c}{f}\right)^2} \quad (41)$$

Phase shift due to change of differential path length is given by

$$\Delta \phi = \frac{2\pi f_0}{c} \sqrt{1 - \left(\frac{f_c}{f_0}\right)^2} \Delta L \quad (42)$$

So

$$\xi_g \Big|_{\text{mech.}} = \frac{4\pi^2 f_0^2}{c^2} \left[1 - \left(\frac{f_c}{f_0}\right)^2 \right] (\Delta L)^2 \quad (43)$$

Sample Analysis - Mechanical Stability

Consider a reflectometer as follows:

$$f = 10 \text{ Gc.} \quad (44)$$

$$L = 1 \text{ meter.}$$

The coefficient of expansion for brass is approximately

$$\epsilon = 2 \times 10^{-5} / \text{C}^\circ. \quad (45)$$

Hence, for RG-52/U waveguide,

$$\Delta L = 2 \times 10^{-5} \text{ m/C}^\circ \quad (46)$$

$$(\Delta L)^2 = 4 \times 10^{-10} (\text{m/C}^\circ)^2$$

With the result

$$\xi_g = -51.5 \text{ db} \quad (47)$$

which is 47.5 db worse than the value of ξ_g specified by equation (36).

This example indicates emphatically that L should be minimized, and that temperature control of the environment of the reflectometer may sometimes be necessary.

CONCLUSIONS AND RECOMMENDATIONS

Equations (20), (33) and (43) indicate the dependence of background cancellation capability on

- a. Transmitter RF phase stability
- b. System geometry
- c. System mechanical stability.

The simplified analysis may reasonably be applied to anechoic chamber scattering range design and operation.

The analysis indicates that

- a. Chamber design should strive to minimize uncompensated background level.
- b. Δf should be as small as reasonable.
- c. Line lengths should be minimized.
- d. Environmental temperature control is desirable.
- e. Mechanical vibration should be minimized.

The approach to minimizing line lengths and L within the waveguide network is straight forward.

Features of chamber design which would tend to minimize uncompensated background level include:

- a. Longitudinal baffles (perhaps controversial).
- b. Extremely high performance absorber.
- c. Dimensions as large as practicable.

A back wall which can be opened out during fair weather is reportedly used by Conductron with favorable results. If a back wall must be tolerated, it is possible to minimize the L involved in cancelling its reflection by making the section of the wall which intercepts half of the incident power conveniently and remotely moveable along the direction of the incident beam. The target should be mounted as far from the back wall as the minimum range criterion permits and should, of course, be centered in the antenna beam.

BIBLIOGRAPHY

1. C. G. Bachman, H. E. King and R. C. Hansen, "Techniques for Measurement of Reduced Radar Cross Sections", Parts I, II and III, The Microwave Journal, Vol. VI, No. 2, 3 and 4, February, March and April, 1963.

NANOSECOND PULSE SCATTERING SYSTEMS

Robert R. Hively, Vice President
Micronetics Incorporated

ABSTRACT

A description of the pulsed radar scattering systems in use at Micronetics is presented, with some discussion of the gated receiver and the handling of data. In addition, the low cross section model mounts used by Micronetics will be described.

PULSED RADAR SYSTEMS

Transmitters

The pulsed transmitters in use at Micronetics are generally categorized according to pulse duration as long pulse, intermediate pulse, and short pulse transmitters.

Long Pulse The term "long pulse" refers to the pulse length relative to the length of the model being measured. All long pulse radars use magnetrons as the basic r.f. source, and the magnetrons are driven by a line type or hard tube modulator. The magnetron tube types and their pulse durations are as follows:

<u>Frequency Band</u>	<u>Pulse Duration (Nanoseconds)</u>	<u>Magnetron Type</u>
L	200	Raytheon 5J26
C	250	RCA 6521
X	100	Western Electric 725A
K _u	250	Raytheon QK400
K _a	250	Microwave Associates 5789

These pulse durations are long enough that the target being measured is immersed in an essentially CW field, and they are short enough to enable accurate range gating within the confines of the range. The modulation techniques used are quite conventional and will not be described further in this paper. The peak transmitted power in each case is a nominal 500 watts and the pulse repetition frequency normally used is 1000 pulses per second.

Intermediate Pulse The intermediate pulse duration available at Micronetics is 10 nanoseconds at X-band,

with a maximum peak power output of 25 kilowatts. The basic r.f. source for the 10 nanosecond pulses is the X-band magnetron-modulator combination used for long pulse measurements. The pulses generated by the magnetron are 100 nanoseconds in duration with a peak power of about 50 kilowatts and a rise time of slightly less than 10 nanoseconds. To obtain a fast rise time on the main bang pulses, it was necessary to slightly degauss the magnetron's magnet. These pulses are then fed into a high power ferrite limiter with a 10 nanosecond reaction time. For the first 10 nanoseconds of duration of the main bang, the ferrite limiter causes about 3 db loss to the signal, and after 10 nanoseconds, it reaches subsidiary resonance and absorbs the remaining power in the pulse. The result is an inexpensive source of 10 nanosecond pulses at a moderately high power level. This technique was developed as Micronetics-sponsored research, and acknowledgment is given to Dr. M. T. Weiss for helpful discussions and references.¹

The major function of 10 nanosecond pulses is their inherent reduction in background noise when measuring low cross section models whose physical length is much less than 10 feet. Since the background noise of the Micronetics range is below 10^{-7} square meters with long pulses, the 10 nanosecond pulses have not found wide usage. They would, however, find good application for indoor ranges where background noise is a problem.

Short Pulse The short pulse durations used at Micronetics have the following characteristics:

<u>Freq. Band</u>	<u>Duration (Nanoseconds)</u>	<u>Peak Power (Watts)</u>	<u>PRF (Pulses Per Second)</u>
L	0.4	0.5	100 to 100K
X	0.4	0.5	100 to 100K
X	0.7	100	500 to 2000

The pulses having durations of 0.4 nanosecond are generated by a variation of a technique described by Pulfer and Whitford². The technique basically amplifies the r.f. components of a short video pulse to provide a short r.f. pulse. The video pulse is fed into the r.f. input of a traveling wave tube, and a 0.4 nanosecond r.f. pulse results. These pulses are usable at repetition rates variable up to 100K pulses per second, and the peak power can be amplified with off-the-shelf traveling wave tubes. Pulses have been generated by this technique at L, S, C, and X-bands.

The pulse described in the above list with a duration

of 0.7 nanosecond is simply the spike leakage through a TR tube. The peak power level is 100 watts and the pulse repetition rate is determined by the magnetron-modulator source; normally 1000 pulses per second. Photographs of this pulse are contained in a paper in Session VI of this symposium titled "Sub-Nanosecond Pulse Methods Of Radar Cross Section Measurement".

Receivers

The receivers used by Micronetics are variations of a basic unit. At L-band, the receiver consists of a precision attenuator, a low-noise TWT, a one watt TWT, a PIN modulator³, a filter, a detector, and a recording device. In all other frequency bands the attenuators are replaced by attenuators for the appropriate band, and a mixer (with local oscillator power) is inserted ahead of the L-band low noise TWT. The balance of the system then becomes an IF system with L-band as the IF frequency. The PIN modulator is used to provide a 100 nanosecond range gate that is adjustable in range.

Long Pulse For long pulse reception, the filter described under "Receivers" is a narrow band pass filter to limit the noise power at the L-band r.f. or IF frequency. The detector is a bolometer and the recording device is a rectangular chart recorder.

Intermediate or Short Pulse For the 10 nanosecond pulse duration and the sub-nanosecond pulses, the filter is removed from the receiver since greater receiver bandwidth is required. The detector is normally a special germanium diode in a special mount. This detector is designed to have good transient (or instantaneous broad band) response. The detected signal is then displayed on a sampling oscilloscope and data is obtained either manually from the scope display, photographically from the scope display, or on a chart recorder driven by the deflection voltages of the scope. It is also possible to record these intermediate and short pulse signals on a rectangular chart recorder. This is accomplished by using an AGC loop between the oscilloscope and the one watt TWT, and using a portion of the AGC signal to drive the recorder. With this signal, range gating to six inches has been achieved.

The bandwidth requirements for the short pulse receiver are quite stringent. The measured spectrum of the sub-nanosecond pulse reveals that it is triangular in shape with a spectrum about 700 megacycles wide at the half power points. The significant spectrum, however, is about 1000 megacycles

wide and this requires that all components in the receiver have at least a 1000 megacycle bandwidth to prevent distortion of the pulses.

Duplexing

In all scattering radars used at Micronetics, duplexing is accomplished using a ferrite circulator at the antennas and the PIN modulator in the receiver to provide 120 or more db isolation between the transmitter and receiver. The only exception is the bistatic range where space duplexing is used by physical separation between the transmitting and receiving antennas.

LOW CROSS SECTION MOUNTS

Styrofoam

Cylindrical styrofoam columns are normally used as support structures for models of relatively high radar cross section at Micronetics. In an attempt to reduce the specular return from the styrofoam columns, several were placed in a lathe and circumferential grooves of various depths were cut. As one would expect, a reduction of cross section of about 12 db resulted. While this provided much better mounts with very little reduction in strength, it was still not adequate for some measurements that are desired. The lowest cross section obtained to date for a 16-inch diameter shaped column is 10^{-4} square meters at X-band. It is now planned to cut a series of grooves with resonant dimensions in a styrofoam column to determine the effect at a fixed frequency.

Nylon Cord Suspension

A suspension system has just been installed and tested at Micronetics, and the preliminary results are excellent. This system consists of a pair of telephone poles at a range of 150 feet from the antennas, with nylon support cords on top and nylon position cords attached to the bottom of the model. The poles are set so they are inclined 20 degrees away from the antennas. Care has been taken to insure that no part of the system is perpendicular to the radar line-of-sight. As of the end of December, the system has been evaluated only at X-band and one set of low cross section measurements has been made. The background contribution due to the nylon cords is 10^{-5} square meters when the main nylon cord is hanging vertically, but drops to below 10^{-7} square meters when the cord is tilted at a small angle. Evaluation at other frequencies will be made early in 1964.

BIBLIOGRAPHY

1. W. F. Krupke, T. S. Hartwick, and M. T. Weiss, "Solid-State X-Band Power Limiter", IRE Transactions on Microwave Theory and Techniques, Vol. MTT-9, No. 6, November 1961.
2. J. K. Pulfer and B. G. Whitford, " A Simple Method of Generating Nanosecond Pulses at X-Band", Proceedings of IRE, Vol. XLIX, No. 1, May 1961, p 968.
3. Hewlett-Packard Model No. 8714A Modulator.

THE AUTOMATIC RECORDING OF EFFECTIVE RADAR CROSS SECTION

Charles W. Matthis, Jr., Research Engineer
The Boeing Company, Airplane Division-Wichita Branch

A plotter that records the average value of radar cross section of targets at the same time that the instantaneous value is recorded was designed for use with existing Scientific-Atlanta radar reflectivity range measurement equipment. The term "average value" as used here is the integral of the square root of the target radar cross section as a function of aspect. The equipment is capable of plotting the average radar cross section over a 40 DB range in amplitude in increments of 2 degrees, 5 degrees, and 10 degrees target aspect. Recording the average value electronically reduces the time required for manual reduction of instantaneous data to average or median values. The plotter is particularly useful in the analyses of comparative data between model configurations.

INTRODUCTION

The signatures of the instantaneous monostatic radar cross sections recorded on backscatter ranges are as varied as there are varied geometries utilized as targets. These variations in recorded cross section will range from the essentially straight line of the sphere to a rapidly scintillating return depending upon the complexity (number of scattering sources on the target) and the ratio of the length to wavelength of the scattering elements.

Unless one is interested in the derivation of empirical equations, or in the comparison of theory to measured values, the instantaneous recorded radar cross section of complex targets such as aircraft is normally smoothed to an effective radar cross section. We shall consider effective radar cross section of an aircraft as that value of cross section which can be converted into a probable radar detection range for the aircraft in question.

RADAR DETECTION PROBABILITIES

One form in which the radar range equation may be written is:

$$R_{\max} = \sqrt[4]{\frac{P_T G^2 \lambda^2 \sigma_e}{(4\pi)^3 P_R}}$$

This equation generally assumes that the radar cross section of the airplane, the only factor not associated with the radar, is a constant. The radar cross section actually scintillates and changes radically in value from moment to moment. Radars tend to respond to the average of the scintillations over the time of illumination for at least one scan.

The reasons for the fluctuation in the radar cross section of an aircraft are the rapid changes in aspect during flight at which the radar observes the target and the rapid change in radar cross section with aspect. The causes for the changes in aspect are as follows:

The aircraft changes its geometrical relationship to the radar as it moves along its path in a curved earth coordinate system.

Air turbulence and the match of the autopilot or pilot to the aircraft response characteristics causes the aircraft to oscillate about its own pitch, roll, and yaw axis. This results in changes of aspect with respect to the radar.

Bending in the airframe causes changes in radar cross section as seen by the observing radar.

DATA SMOOTHING TECHNIQUES

There are several methods of smoothing the instantaneous recorded data to a value more representative of that observed by radar systems. Two techniques which should be mentioned are the average radar cross section and the median radar cross section.

Average Radar Cross Section

The average radar cross section, perhaps the most meaningful way to express effective radar cross section, is simple in concept but difficult to obtain using manual techniques. To obtain the average, the data must first be converted from the logarithmic scale normally used to record the instantaneous cross section to linear values and then averaged.

Median Radar Cross Section

The median radar cross section has been more universally used to smooth recorded data because of the relative ease with which the median value can be obtained. Since the logarithm of a quantity increases with the magnitude of the quantity, the median value of the recorded logarithmic plot is equivalent to the median value of the linear data. In practice, the median value over a specified interval may be obtained by inspection. When a sharp rise or drop occurs in the radar cross section within a given interval, the median value will not follow the rapid change as well as the average. A

detailed examination of median and average radar cross sections of aircraft performed by McDonald and Strattan¹ showed that the differences in the two values are not large and the two values are considered to be reasonably compatible.

AVERAGE FIELD VOLTAGE INTEGRATOR

Several technicians are required to process the output from a single reflection range to obtain median radar cross section plots from the recorded instantaneous plots utilizing manual methods. A need was apparent for a device that would automatically smooth the data to a value representative of effective cross section at the same time permitting retention of the instantaneous plot.

Dr. Larry Clayton and Mr. George M. Potter of Scientific-Atlanta² designed and built an integrator, the Scientific-Atlanta Model SP-173 Average Field Voltage Integrator, which is used to automatically average, over each of a number of angular sampling increments, the detected signal from the receiving antenna on the Boeing-Wichita Radar Reflection Range³. The averaged value of field voltage for each increment is step-plotted on a slightly modified antenna pattern recorder. A graph of the amplitude of the integrated signal versus angular orientation is produced. This output may be described by the equation:

$$\sigma_{AVE} = 20 \log \left| \frac{1}{\Delta \theta} \int_{\theta}^{\theta + \Delta \theta} \sqrt{\sigma} d\theta \right|$$

Sampling increments were provided for 2, 5 and 10 degree intervals.

The input to the Average Field Voltage Integrator is obtained from a modified potentiometer in the recorder used to plot the instantaneous radar cross section. One section of the ganged potentiometer serves as the normal balance potentiometer for the instantaneous value recorder while the second section is energized with a constant dc voltage from the integrator unit and develops a dc output which is proportional to the field voltage of the receiving antenna.

A synchro-driven sample-pulse generator controls the sampling and plotting processes over selectable angular increments. In addition, pulses from the sample-pulse-generator section are used to develop an indication of positioner speed.

As the dc signal from the potentiometer is integrated, a similar integration is performed upon a constant dc voltage. The stored output of this secondary integrator is used as a reference voltage

for the pen-function amplifier used in the average-value pattern recorder which is the output device for the integrator unit. The secondary integrator accomplishes an automatic compensation for variations in sample-pulse rate.

When a sample pulse is generated, the following sequence is initiated (see block diagram in Figure 1):

- (1) The attained values of the primary and secondary integrators are stored.
- (2) Both integrators are reset and allowed to begin a new integration cycle.
- (3) The pen-servo amplifier of the average-value recorder is energized, thus allowing the pen to assume a position as dictated by the previously stored values from the primary and secondary integrators. After a sufficient time for plotting, the pen-servo amplifier is de-energized.
- (4) All control circuits are returned to an initial state to await the next sample pulse.

The output recorder thus develops an average-value recording of the detected signal from the receiving antenna.

COMPARISON OF DATA

A scaled model of an aircraft was measured on the reflection range. At the same time that the instantaneous radar cross section was recorded the Average Field Voltage Integrator was used to obtain an average plot of the radar cross section. The median radar cross section was obtained manually from the instantaneous plot. A comparison of the average and the median plots obtained is presented in Figure 2.

CONCLUSIONS

Anytime the instantaneous recorded radar cross section of a target is altered in an attempt to smooth the data, information is lost. The significance of this loss must be weighed against the advantages obtained by the smoothing while considering the intended use for which the data was obtained.

The use of an average field voltage integrator similar to the one herein described is considered to give data useful in determining target detection against radar systems and for the comparison of data obtained from different model configurations.

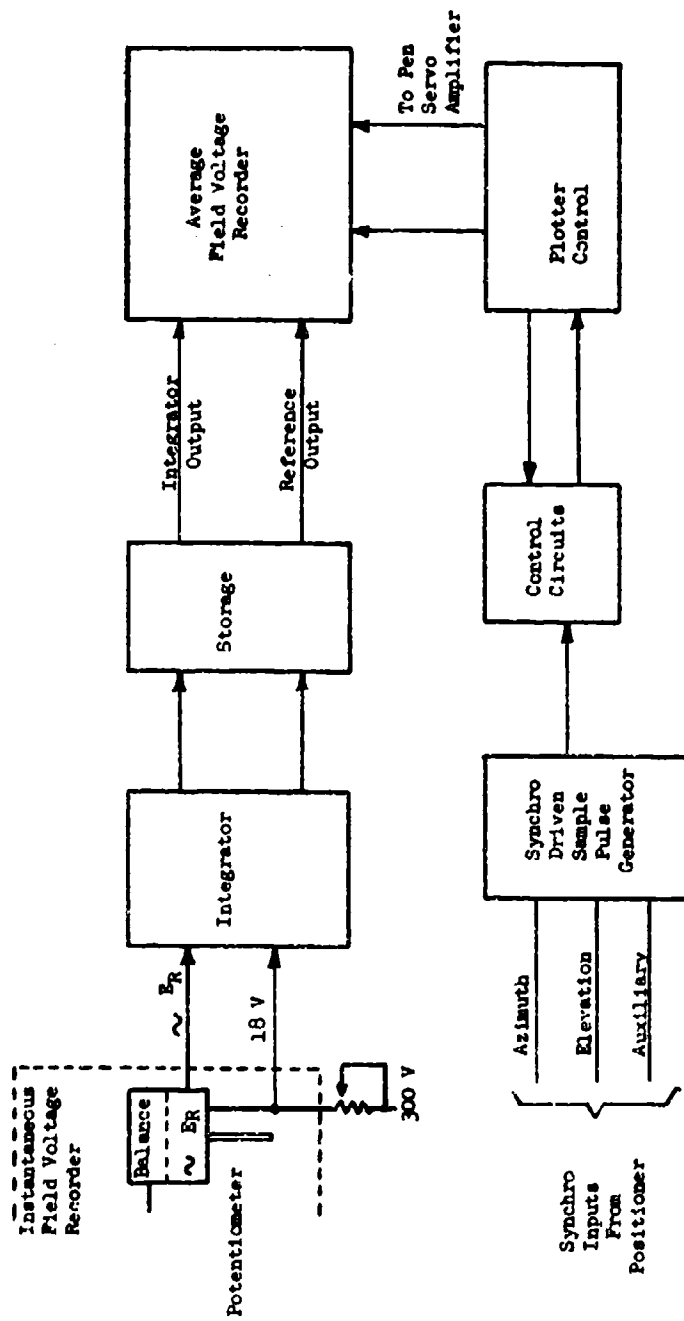


Figure 1. Block Diagram
Average Field Voltage Integrator

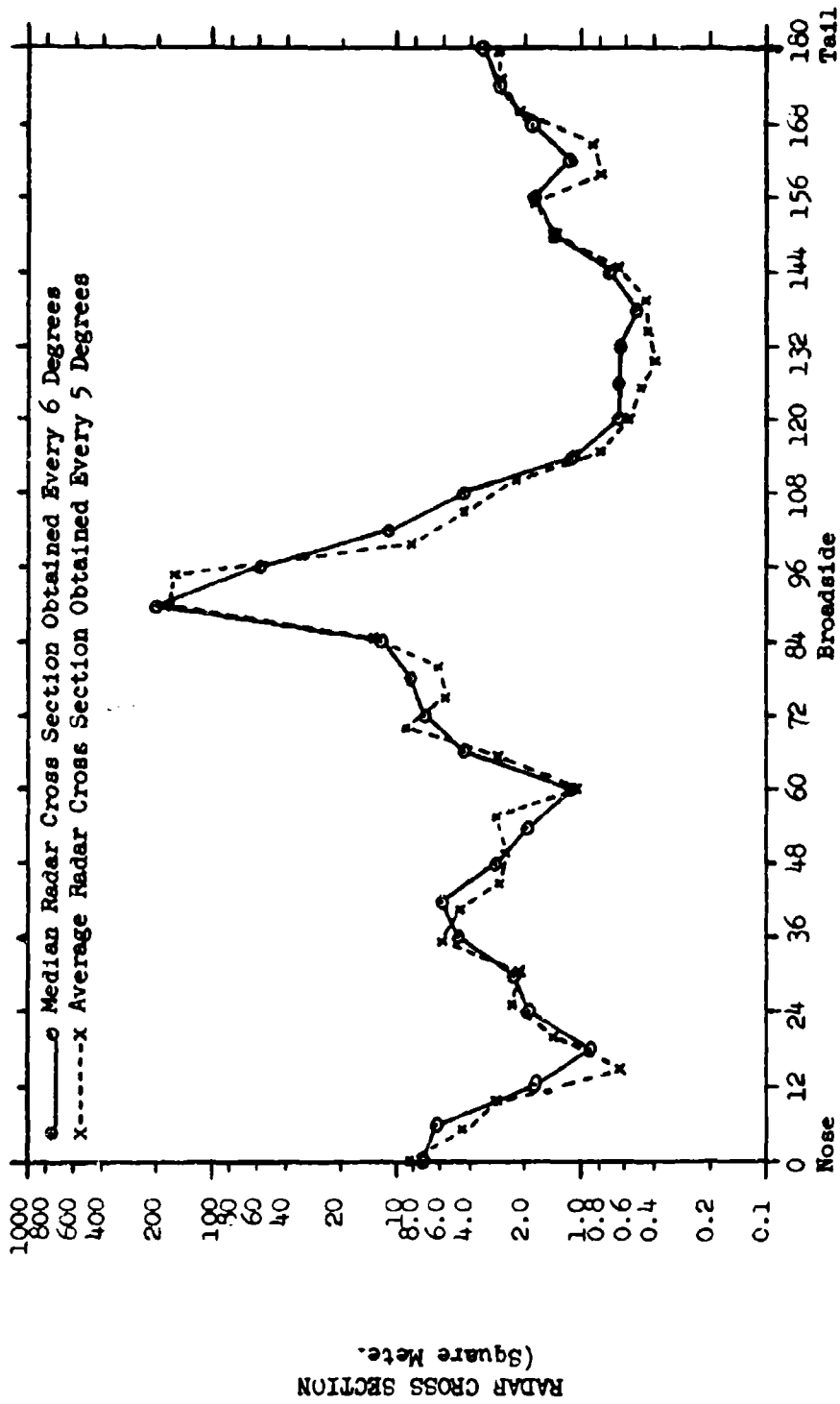


Figure 2. Comparison of Median and Average Radar Cross Section

BIBLIOGRAPHY

1. McDonald, Frank and Robert D. Strattan, "Characteristics of the Median Radar Cross Section of Reflectors as a Function of Frequency (U)", Engineering Report EMD/ER-EMR-750, The Boeing Company, 29 January 1963 (Confidential).
2. Instruction Manual, Model SP 173 Average Field Voltage Integrator, Scientific-Atlanta, Inc., February 1963.
3. "Radar Cross Section Research and Development Capability," Document D3-4225-1, The Boeing Company, January 1963.
4. Kennedy, Peter D., "Memorandum on Advanced Techniques For Radar Reflectivity Data Analysis," Report 601-18, The Ohio State University Research Foundation, April 1, 1957.

ACKNOWLEDGEMENT

A note of personal appreciation is extended to the members of the Electromagnetic Radiation Group for their assistance in obtaining the data from which this paper was prepared.

*A METHOD OF STATIC RADAR CROSS SECTION
MEASUREMENT FOR PULSED RADAR SYSTEMS

J. M. Murchison, Group Engineer
General Dynamics/Fort Worth

ABSTRACT

This paper contains a description of a unique receiving system for the measurement of radar cross section by use of a pulsed radar. The receiver incorporates a closed loop servo system wherein the target echo and a reference signal are compared and the amplitude of the reference signal is adjusted until it is equal to that of the echo signal. The reference signal is introduced at the IF frequency and is adjusted by use of a motor-driven wave guide "beyond-cutoff" type of attenuator. Reference signal attenuation is directly related to echo signal amplitude when the system is at null, and the shaft position of the reference attenuator therefore represents the relative radar cross section.

INTRODUCTION

Since the determination of static radar cross section involves the illumination of a target with a microwave source and the recording of the reflected energy as a function of aspect angle, some unusual and stringent requirements are placed on the receiving system. Amplitude variations of the reflected signal can be of such a magnitude that the dynamic range of the receiving and recording equipment must be in the order of 50 db. In addition, pulsed systems must be capable of operation through a suitable bandwidth, and means of selecting the desired reflection (range gate) must also be provided. The receivers commonly used for antenna pattern measurements are not suitable since they are designed for use with CW or square wave signals and are characterized by rather limited sensitivity. The simple recording of the peak pulse amplitude of a receiver output would limit the dynamic range to that of the receiver with a fixed gain setting.

Two systems designed to circumvent the above mentioned problems are in common use. One system incorporates a receiver similar to those used in tracking radars (Figure 1). In this receiver, the AGC voltage is recorded as a measure of received signal amplitude. The dynamic range of this receiver can be well in excess of the required 40 to 50 db, but the linearity and stability are not suitable for many applications since they are functions of the AFC characteristics of the IF amplifier. Another system incorporates an attenuator which is placed in the RF input to the receiver (Figure 2). As determined by the AGC, receiver output voltage is maintained at a constant level by means of a servo system which is used to drive an RF attenuator. This system is capable of stable operations and linear measurement, but it has the disadvantage of operating at a fixed signal-to-noise

*Patent rights reserved

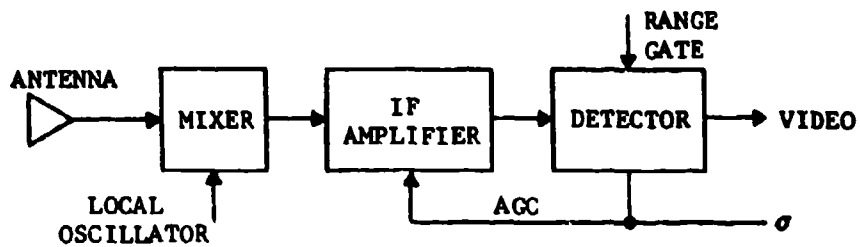


Figure 1.

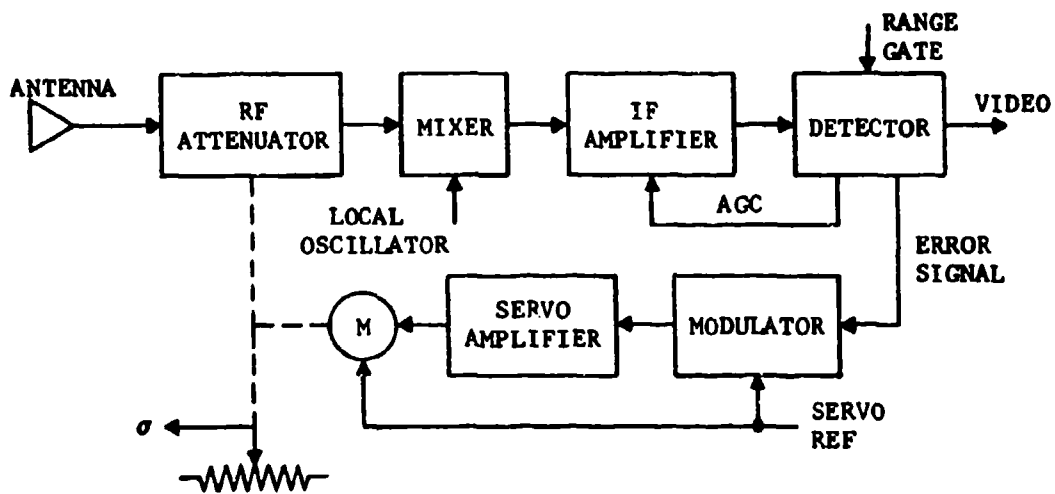


Figure 2.

ratio, and different attenuators must be provided for each frequency or band of operation.

In the spring of 1961, the Aerosystems Laboratories at General Dynamics/Fort Worth developed a new receiving system for broadband radar cross section measurements. This system, known as "The Sigma Servo System," operates over a frequency range determined only by the choice of mixers and local oscillators; it has a stable, linear, dynamic range of 50 db. The amplitude of the received signal is available in the form of a shaft position; consequently, digital and analog output data are available on the basis of the transducers used in a particular operation. The receiver is range-gated and may be operated with signal and gate pulse widths as low as 0.1 second.

THE SIGMA SERVO RECEIVER

Description

A simplified block diagram of the sigma servo receiving system is shown in Figure 3. The receiver is a superheterodyne which incorporates hybrid mixers and passive preselection. Received signals are heterodyned to the IF frequency before comparison with the reference signal. No RF amplification is used so that all active devices subject to gain variations or limited dynamic range are included in the feedback loop. The reference pulse is coupled to the IF amplifier input along with the mixer output. The time relation of the transmitted pulse and other signals in the system are shown in Figure 4. A PRF of 1000 pulses per second, with a resulting interpulse period of 1000 microseconds, may be chosen for the discussion of system operation. The reference pulse occurs at one-half of the interpulse period (500 microseconds) which corresponds to a radar range of approximately 40 miles. As shown in Figure 4, the range gate is opened alternately to pass first the desired echo (target pulse) and then the reference pulse to the recycling peak detector. The local oscillator is turned on immediately after "main bang" and off before the reference pulse time (1) to preclude the possibility of undesired echos which can cause interference with the reference signal and (2) to reduce IF saturation. The detector output may have an ac component that is essentially a square wave in which the amplitude is proportional to any difference between the amplitude of the reference signal and that of the echo signals. The phase of this square wave is compared to the echo and reference gate times (as phase), and it will be of one phase when the echo is larger and of a different phase (180 degrees) when the reference is larger. The detector output also has a dc component that is proportional to received signal strength. The dc output is delayed and fed back to the IF gain control line to maintain the desired IF and detector levels. The ac component is fed to a phase-sensitive demodulator; the output of the demodulator is a dc voltage proportional in polarity and magnitude to any difference between the reference and echo signals. This voltage is converted by

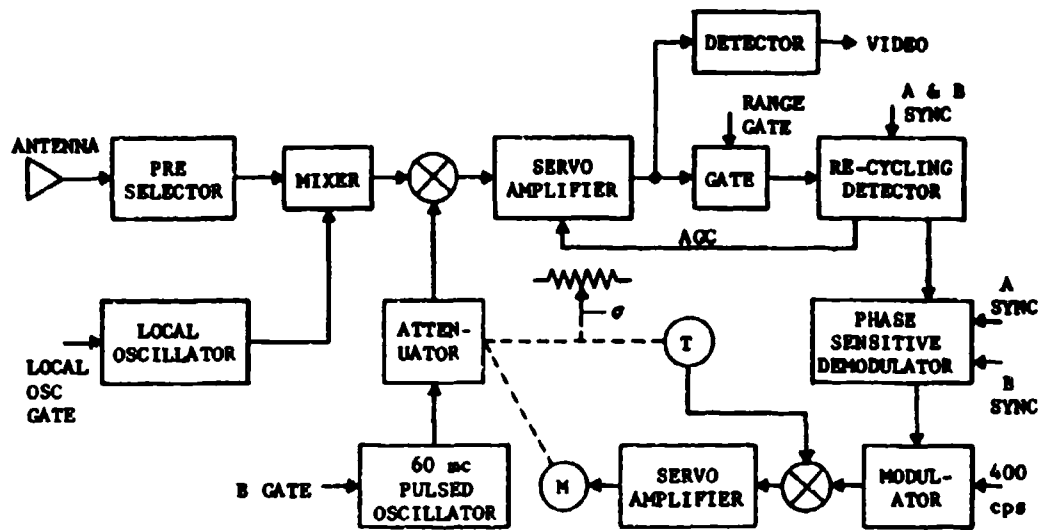


Figure 3. Sigma Servo Receiver

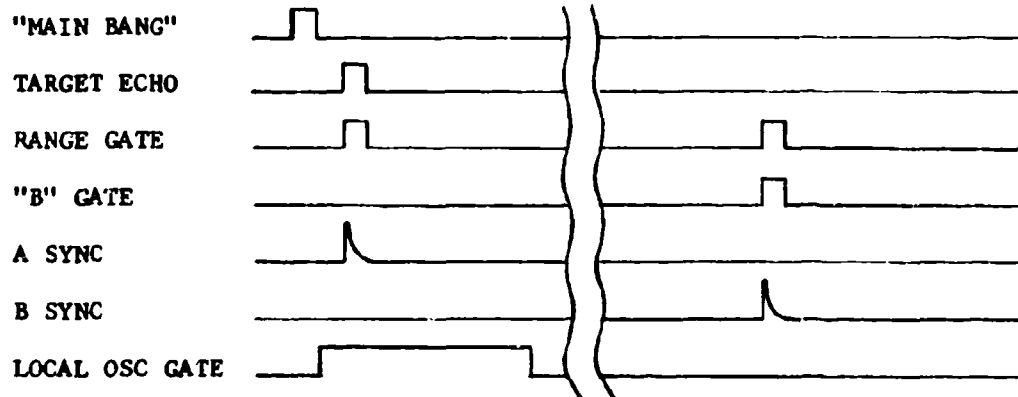


Figure 4. Timing Diagram

means of a synchronous modulator to a 400-cycle per second error signal that causes the reference attenuator servo motor to drive in such a manner as to reduce the error to zero. Any difference between the reference and echo signals causes an error signal and a compensating movement by the reference attenuator; therefore, reference attenuation is a continuous measure of the magnitude of the received signal. Transducers placed on the drive shaft of the reference attenuator provide both analog and digital outputs.

Design Considerations

The Reference Attenuator. In effect, the sigma servo receiver is a high-speed, automatic, power ratio meter. The reference attenuator is used as the standard, and the linearity and stability of this device determines that of the system. The attenuator is a waveguide-beyond-cutoff type of unit. The insertion loss of the attenuator is approximately 15 db beyond that point at which attenuation is a linear function of travel. Since the attenuator is operated at a fixed frequency (60 megacycles), both the input and output couplers are tuned to resonance and loaded to obtain the desired 50-ohm impedance. Aside from linearity and stability, which are inherent in this type of attenuator, the main requirement placed on the reference attenuator is that of low driving torque to permit rapid changes in attenuation. Attenuators used in the sigma servo receivers were specially designed in the Aerosystems Laboratories at General Dynamics/Fort Worth.

IF Amplifiers. Operation of the sigma servo receiver is predicated on the assumption that the IF amplifier and subsequent detection circuitry react in exactly the same manner to the echo and reference signals. The use of this approach imposes several rather severe requirements on the IF amplifier; the first of which is that of fast recovery. The receivers at General Dynamics/Fort Worth are operated in conjunction with 1000-watt transmitters on a quasi-monostatic, ground plane range. In practice, it has been found that "main bang" may result in a receiver input of up to +10 dbm, which is more than sufficient to cause complete saturation. Desirable operating ranges are such that target echos may occur as soon as 0.4 microsecond after "main bang," and the IF circuitry must be designed so that recovery is complete within this interval. Dynamic range is another consideration. A 50-db operating range, coupled with a possible requirement for 20-db minimum signal-to-noise ratio, indicates that the receiver must operate over a range of 75 db above noise without pulse distortion. Distortion that would be tolerable in a typical radar system is not acceptable in a system where peak pulse amplitude is of interest. Still another consideration is "Miller Effect" since a change in either center frequency or band pass characteristics of the IF as a function of signal level will almost invariably produce different effects on the reference and echo signals, and there will be a corresponding degradation in system linearity.

Gate Circuitry. A high-level IF range gate was chosen for the sigma servo receiver. General Dynamics/Fort Worth has had extensive experience with various methods of range gating in connection with radar simulation activities, and choice of a high-level IF gate was indicated by a consideration of recovery time, gate width, and the requirement for a 120-db on-to-off ratio with a minimum of gating pulse leakage. A high on-to-off ratio (referred to the receiver input) is readily achievable with a high-level gate since at this point the gate ratio is only required to exceed the dynamic range of the preceding IF stages. Gating pulse leakage is held to a minimum through the use of low gain between the gate and the detector, and leakage is well below receiver thermal noise without any special balance or threshold adjustments.

SYSTEM PERFORMANCE

System performance characteristics are summarized in Table I.

TABLE I - PERFORMANCE CHARACTERISTICS

Frequency coverage	Determined by RF components
Sensitivity	Typically 96 dbm
IF noise figure	2.0 db
Bandwidth	10 mc
Bandpass	Gaussian
Pulse width	.1 microsecond
PRF	500 to 5000 pps
Gate width	.1 microsecond
Recovery time	.4 microsecond
Dynamic range	50 db
Linearity	± 5 db
Maximum response	120 db/second
Outputs	Analog and digital

Figures 5 and 6 are typical linearity curves for the sigma servo receiver. Figure 5 was obtained by positioning the range gate to select a large fixed target and recording the signal variations produced by a precision attenuator placed in series with the receiver input. During

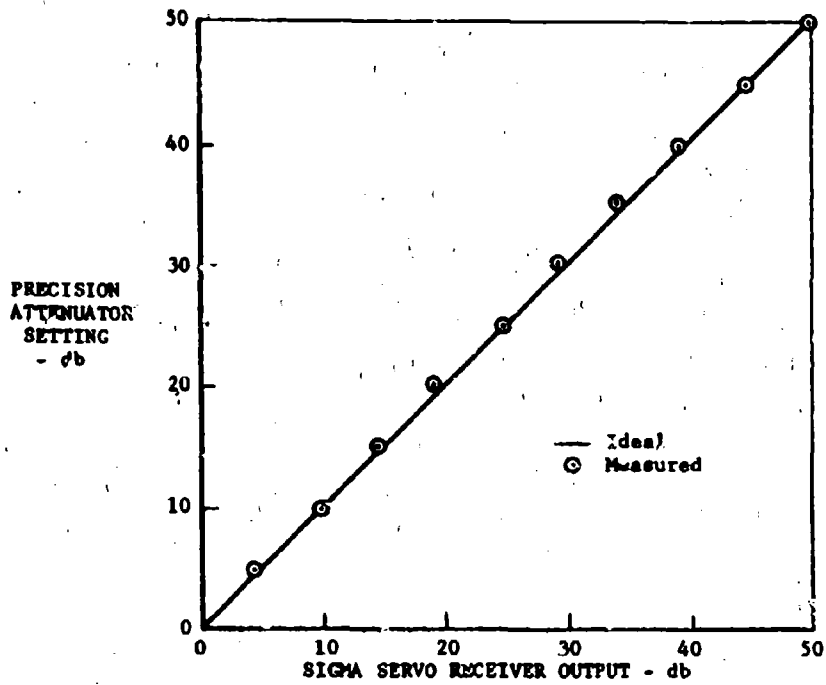


Figure 5. Receiver Linearity

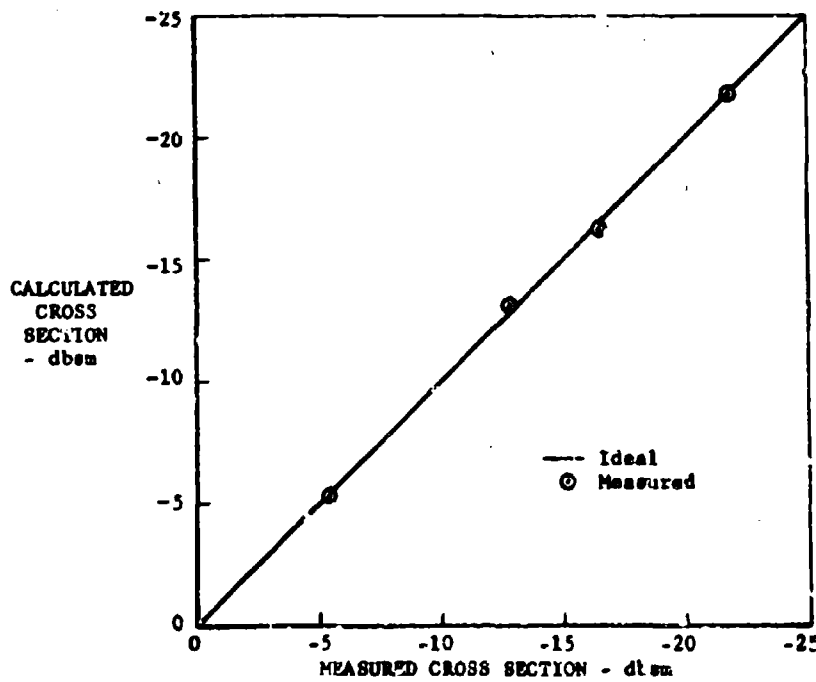


Figure 6. System Linearity

this particular test the absolute level of input varied between -75 and -25 dbm. Figure 6 is the plot of a series of calibration spheres which demonstrates the linearity obtainable in overall measurement. Recordings from which this data was obtained were made at a range of 500 feet and a frequency of 1.7 gigacycles.

System response to a step input of 10 db is shown in Figure 7. Damping can be adjusted to any desired value by varying loop gain and rate feedback. For damping factors between .5 and 1.0, the velocity error is typically less than 0.5 db/100 db/second.

Figure 8 is a typical vehicle cross section data plot obtained with the sigma servo receiver. The vehicle was a small, approximate sphere-cone test object, and the measuring frequency was 1.2 gigacycles. Azimuth rotation rate was approximately .25 RPM, and the pattern was retraced as a demonstration of system stability and the ability to repeat previous measurements with a high degree of accuracy.

SUMMARY

The sigma servo receivers have been in constant use for over two years on the General Dynamics/Fort Worth Radar Cross Section Range. No more than a normal amount of routine maintenance has been needed for these receivers, and their initial cost has been more than offset by the accuracy of data and ease of operation. The basic technique of the sigma servo receiver has been adapted to the square wave system used in the anechoic chamber at General Dynamics/Fort Worth, and it has proven completely successful in this application. It is readily apparent that the technique could be used for antenna pattern measurements and would offer a considerable improvement in sensitivity and stability over conventional techniques. The application would be quite similar to that in the anechoic chamber where recording sensitivities in the order of -125 dbm have been realized. Other applications of the sigma servo receiving system are being investigated in the Aerosystems Laboratories at General Dynamics/Fort Worth, and patents have been applied for for this and related techniques.

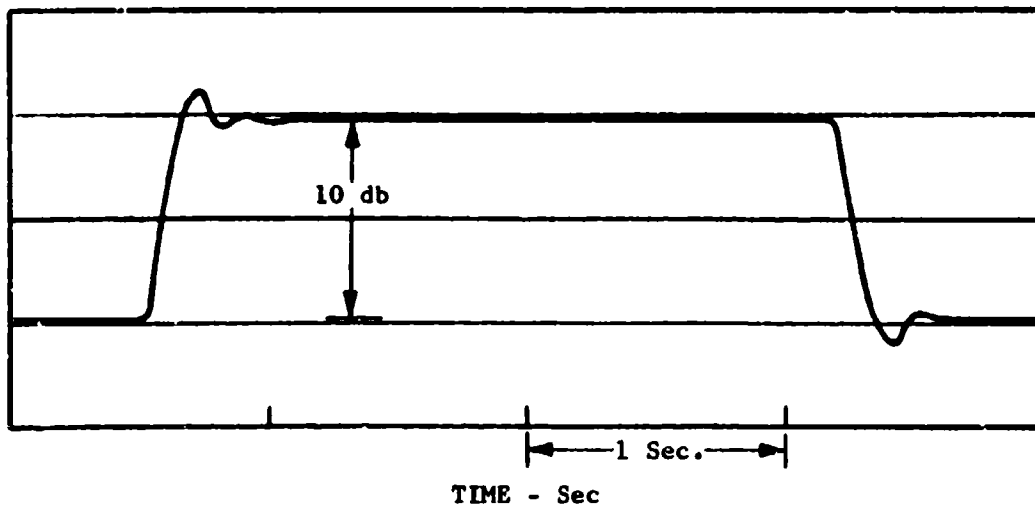


Figure 7. Response to 10db Step Input

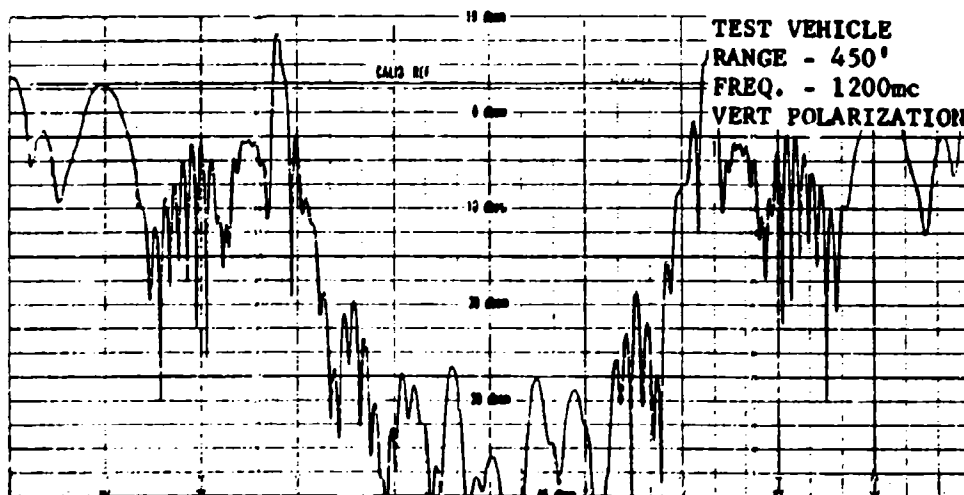


Figure 8. Typical Data

POLARIZATION ASPECTS OF RADAR REFLECTIVITY MEASUREMENTS

R. D. Tompkins
U. S. Naval Research Laboratory
Washington, D.C. 20390

ABSTRACT Current interest in polarization diversity radars requires a better understanding of the target influence on polarization coupled with an awareness of the potential of polarization diversity for target identification, signal enhancement, and clutter rejection. This paper will briefly review the introduction of the polarization scattering matrix into the radar range equation, discuss some of its implications and applications, and describe some measurement techniques and components which can be used to determine this matrix.

INTRODUCTION The polarization of a wave backscattered by a radar target constitutes an important part of the information contained in the return. A knowledge of this information is important from the standpoint of fixed polarization radars in that a portion of the amplitude noise appearing in the received signal can be ascribed to polarization variations. This point is particularly apparent from some of the data presented by Olin and Queen elsewhere in this journal¹. This knowledge is perhaps even more important from the standpoint of the more sophisticated polarization diversity radar techniques now being considered if the full potential of polarization information for target identification, signal enhancement, and clutter rejection are to be realized.

Some of the implications of polarization in radar will be discussed in briefly reviewing the influence of the polarization scattering matrix on the radar equation. Applications will be cited, and some measurement techniques and components which can be used to determine the polarization scattering matrix will be described.

THE POLARIZATION SCATTERING MATRIX In 1948 Sinclair² introduced a modification to the radar echoing area term in the radar range equation to take into account the polarization transformation properties of an arbitrary radar target. He related the scattered, or returned field, E^r , to the incident, or transmitted field, E^t , by the equation

$$E^r = KAE^t, \quad (1)$$

where K is a function of the range to the target and A is the polarization scattering matrix of the form

$$A = \begin{bmatrix} a_{11} & a_{12} \\ a_{21} & a_{22} \end{bmatrix} \quad (2)$$

The term a_{jk} is a function of the target aspect and the radar frequency and is generally complex. In the radar case, where the same antenna is used for transmitting and receiving, $a_{12} = a_{21}$. It was assumed in the development that the target was at a sufficient distance from the radar that the incident field could be represented by a plane wave.

Kennaugh³ later extended the analysis to include the concept of null polarizations and its application to target classification. In his work, Kennaugh showed that there are two particular polarizations which, when used to illuminate an arbitrary target, will be back-scattered as the orthogonal, or null, polarization. In the fixed polarization radar case this means that the backscattered energy would be rejected at the antenna and the signal level would be zero. The relationship of these null polarizations with respect to each other provides a classification basis. For instance, the two null polarizations may coincide. In this case, the backscattered polarization will always be the same regardless of the incident polarization. Since a thin wire gives such a return, Kennaugh refers to targets in this class as linear targets. It should be noted, however, that the return from a linear target need not be a linear polarization. In another class called isotropic targets, the two null polarizations are orthogonal to one another. An example of this class is a sphere which has circular null polarizations. A third class is called symmetrical targets. Here the null polarizations have equal axial ratios but are of opposite sense. Any target having a plane of symmetry containing the radar line of sight will fall into this class. Finally, Kennaugh refers to a general class of targets which have null polarizations which do not fit any of the above restrictions.

In most polarization analyses the basic polarization concepts are established by considering the linear components of an elliptically polarized wave; the resolution into circular components is usually mentioned only in passing. There is advantage, however, in thinking in terms of circularly polarized (CP) components. The reasoning behind this is associated with the accepted terms defining the state of polarization, namely, axial ratio, orientation angle, and sense. Using circular components, the axial ratio is a function of the amplitudes of the two components according to the relation

$$\text{Axial Ratio (db)} = 20 \log \frac{E_L - E_R}{E_L + E_R} \quad (3)$$

with the larger CP component determining the sense. The orientation angle is solely a function of the phase relationship between the CP components. The practical and analytical utility of this approach lies

in this parameter independence. Another feature which is perhaps of equal importance to reflectivity measurements has come out of a recent analysis by Brown⁴ which develops the transformations between scattering matrices based on linear and circular components, and which investigates the effects of target rotation about the radar line of sight. In this work, it is shown that target rotation about the radar line of sight (when the target is illuminated with circular polarization) will cause a phase shift in the same sense CP component of the backscattered signal which does not appear in the opposite sense component of the return. The amount of this phase shift is equal to twice the angle of rotation of the target, with the direction being determined by the sense of the illuminating signal and the direction of rotation of the target.

APPLICATIONS From theory it is known that a radar target generally depolarizes a wave incident upon it and that this depolarization can be predicted from a knowledge of the polarization scattering matrix of the target. Since the elements of the matrix are a function of frequency, target shape, target aspect and target motion, a knowledge of their values and variations has potential in devising polarization control and measurement techniques for signal enhancement and target classification. The form of the display of these elements for optimum utilization of polarization data is currently under study by various investigators. Copeland⁵ has suggested a method for representing the return polarization from a target as a combination of two components, one of which represents the return from a sphere and the other which represents the return from a linear target. The relationship between these two components, which is the key to his classification technique, is obtained from a study of the complex voltage received from a radar with a rotating linearly polarized antenna.

Huynen⁶ has proposed a measurement technique on the basis of changes in null polarizations of a target as the aspect is varied. By means of a special plotting technique he obtains the null polarizations on the basis of the amplitude relationships of the return using four different illumination polarizations. The special feature of this approach is that the data is in terms of the target parameters only and is not dependent on the radar frame of reference.

Before these techniques can be applied to the practical radar case more information is needed on the spectral components of the target return, the relationship of the amplitudes in the components of the returned polarization, and the significance of phase of these components. Dynamic data is needed on known targets so that appropriate signal processing and presentation techniques can be developed to aid in target classification. Currently, Olin and Queen¹ are obtaining polarization data on dynamic targets. Their system yields, in part, orthogonal linear and orthogonal circular components of the received signal on a pulse-to-pulse basis for selected illuminating polarizations.

MEASUREMENT TECHNIQUES AND COMPONENTS The continuing efforts to utilize the dimension of polarization to gather more information about radar targets justify increased attention to polarization in radar reflectivity measurements. Two useful components, the polarimeter⁷ and the polarization resolver⁸, are available for the instantaneous measurement of wave polarization. Both are based on the trimode turnstile junction^{9,10} shown in Fig. 1. The following properties characterize this novel 7-port junction:

- a. Complete isolation between the circular and coaxial ports,
- b. equal amplitude and in-phase coupling of a signal from the coaxial port to the four rectangular ports, and
- c. equal amplitude and out-of-phase coupling between opposing rectangular ports and a signal in the co-linear mode in the circular guide.

Consider a wave of arbitrary polarization incident on the junction through the circular waveguide. One linear component will couple to a pair of opposing rectangular ports; the orthogonal linear component will couple to the remaining pair. If now crystal mixers connected in a balanced arrangement are attached to the rectangular ports and a local oscillator signal is injected into the coaxial port, the orthogonal linear RF components will be heterodyned down to some intermediate frequency (IF). Since the phase and amplitude relationships of the IF signals are the same as the orthogonal components of the incident RF wave, the received polarization state is defined at a lower, more convenient, frequency. The block diagram of this polarimeter, shown in Fig. 2, indicates these outputs being applied to the orthogonal deflection plates of an oscilloscope where the display will be a Lissajou pattern directly depicting the wave polarization. The signals can also be applied to computational circuitry for direct calculation of the polarization matrix elements. In this application, Olin¹¹ has shown that at least two measurements are necessary for a complete determination of the matrix. The measurement consists of illuminating the target with a given polarization and measuring the backscattered polarization and then repeating the measurement with orthogonal illumination. These two measurements must be separate and distinct, taken either at different times or at different frequencies. Since the scattering matrix is a function of aspect and frequency, the separation must be small enough to insure no significant variation in matrix elements.

In the form described, the matrix elements will be obtained in terms of the linear components. A simple modification of the polarimeter will permit obtaining the matrix elements in linear components and circular components simultaneously. The modification consists of inserting a quadrature hybrid between a pair of adjacent rectangular ports of the trimode turnstile junction and the crystal mixers as indicated in Fig. 3. The 90 degree phase shift inherent in the hybrid performs the required transformation from linear to circular components. Through the use of this polarization resolver the display mentioned

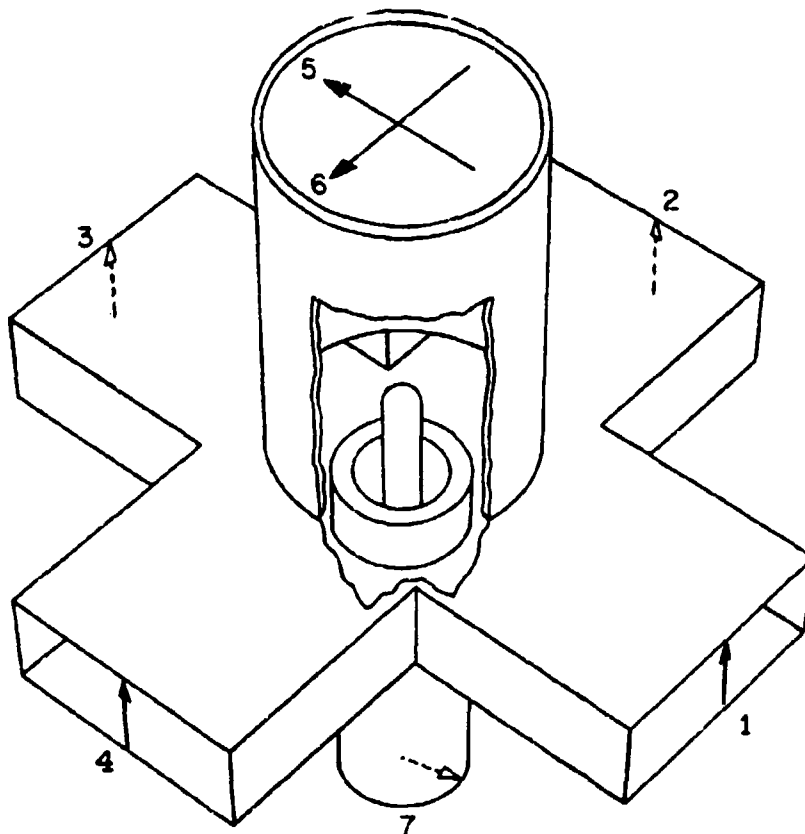


Figure 1. Trimode Turnstile Junction

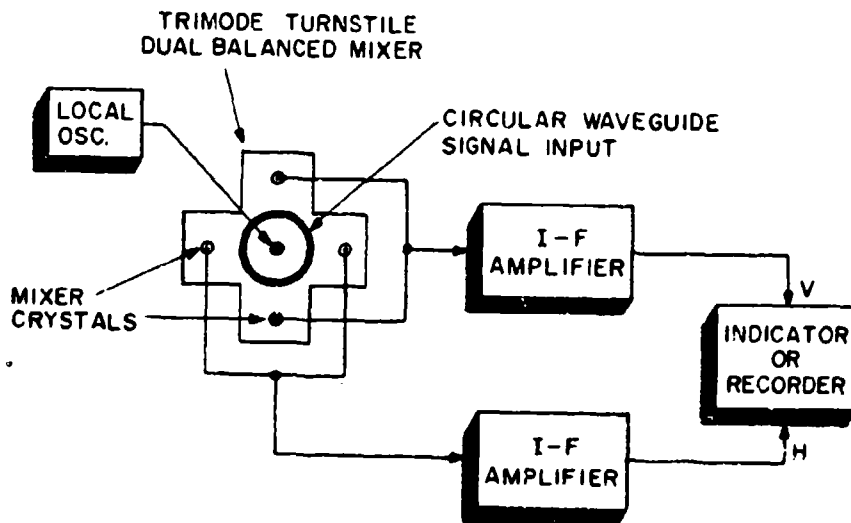


Figure 2. Instantaneous Polarimeter

above can be obtained and at the same time the phase shifts described by Brown can be investigated.

The measurement of phase is, of course, an important part of the polarization measurement. This phase measurement can be made at RF but to do so generally requires rather complicated waveguide circuitry which may reduce operational bandwidth. For reflectivity measurements an effective method involves generating a stable IF low enough in frequency to permit the measurement of phase with available phase meters. To this end a novel frequency translator has been developed for use in a cw measurement system to provide a local oscillator signal.¹² The device, mechanical in nature, utilizes a low mass dipole rotating in a waveguide in front of a short circuit. The device operates in the following manner. Referring to Fig. 4, a signal of frequency f_0 is applied to the input of a circulator. The signal passes through a dual-mode, rectangular-to-circular transducer and is converted to circular polarization by means of the quarter wave plate. The phase of this circularly polarized signal upon reflection from the dipole-short circuit combination will be a function of the position of the dipole. Thus as the dipole rotates at a continuous rate the phase will also vary at a continuous rate which is twice the rotation rate of the dipole. The reflected signal, now at frequency $f_0 \pm 2f_r$, is separated from the input in the circulator. Characteristics of the device feature a low insertion loss, typically less than 0.5 db, with suppression of the carrier and unwanted sideband in excess of 35 db over a 12% band in X-band. Greater suppression is obtainable at a sacrifice in bandwidth. With this device a stable IF at frequencies up to 800 cps can be developed thus permitting audio frequency phase measuring techniques to be utilized.

In the applications described, control of the illuminating polarization is required as well as the measurement of the backscattered polarization. The independence of control of axial ratio and orientation angle implicit in the concept of circular components can be very useful in this area. The basic component for polarization control is a two port circularly polarized antenna. Energy into one port of this device will cause the radiated signal to have one sense of circular polarization, while excitation of the other port will generate the opposite sense. The form can be quite varied ranging from a spiral with a port at the center and one on the periphery, to a conical horn coupled through a quarter wave plate to a dual mode transducer. This type of antenna can be incorporated into the circuit shown in Fig. 5. The variable power divider will determine the amplitude relationship between the CP components thus establishing the axial ratio of the radiated wave. The setting of the differential phase shifter will determine its tilt angle. Ports A and B will always represent orthogonal polarizations for any setting of the circuit variables. The generation of a rotating polarization can be accomplished in two ways. First, the differential phase shift can be varied in a continuous manner causing the polarization to rotate. If the rate of rotation is to be constant

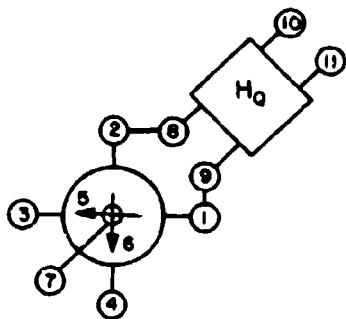


Figure 3. Polarization Resolver

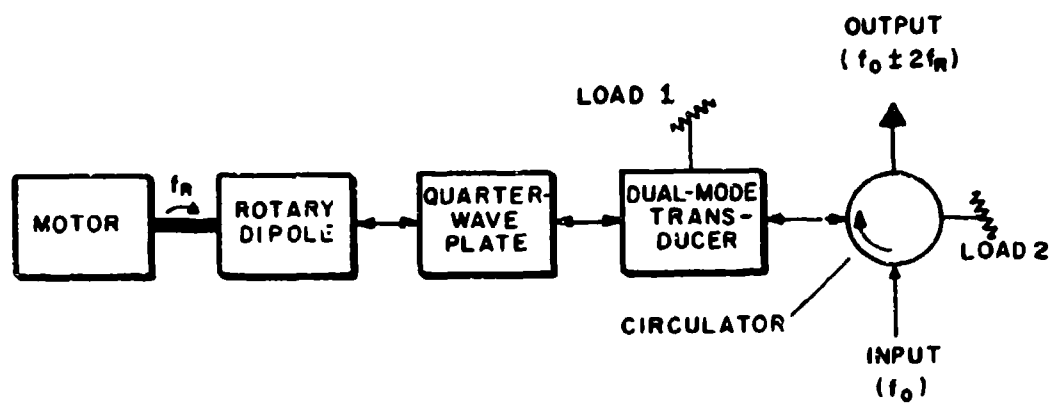


Figure 4. Frequency Translator

then another technique can be utilized.¹³ Recognizing the fact that a constant rate of change of phase can be expressed as another frequency, it is possible to inject a signal at frequency f_1 into port A and a signal at frequency f_2 into port B and thus generate a signal whose polarization is rotating at a rate equal to one-half the difference between the two input frequencies. The axial ratio of the rotating polarized wave will, of course, be a function of the relative amplitudes of the two CP components. When the two components are equal, a rotating linearly polarized wave results.

A polarization simulator has also been developed for the study of polarization phenomena. Although not a measurement device, the instrument is a useful tool for the study of the effects of changes in target illumination and characteristics under controlled laboratory conditions. The simulator is basically an audio frequency analog computer which has been designed to solve Eq. (1). A block diagram of the system is shown in Fig. 6. The transmitter has two outputs representing orthogonal components of the radiated signal. The phase and amplitude relationships of these two signals can be varied so that the output will represent any desired polarization. These outputs are then applied to a network which represents the target polarization scattering matrix. The network parameters are adjustable so that the elements of any matrix, written either in linear or circular components, may be dialed in. The outputs of the target network represent the polarization of the backscattered wave and are available in both linear and circular components. These "backscattered" signals may be viewed directly on an oscilloscope as a polarimeter display, or they may be applied to a receiver whose antenna polarization can be varied, or they may be applied to other display or computational circuitry for additional analysis.

SUMMARY AND CONCLUSIONS The significance of polarization as it applies to radar reflectivity measurements has been reviewed and some techniques and components for measuring the polarization characteristics of targets have been briefly described. With this theory and measurement capability, the polarization parameters of a target (scattering matrix, null polarization, etc.) can be completely determined. The lack of definitive data in the area of polarization measurements makes it difficult to state which of these parameters has the most potential in the utilization of polarization as an aid to classification or enhancement. The continuing collection of polarization data, especially on dynamic targets, will, with a careful study of the relationships of the received quantities, permit the determination of the optimum form of data presentation and processing.

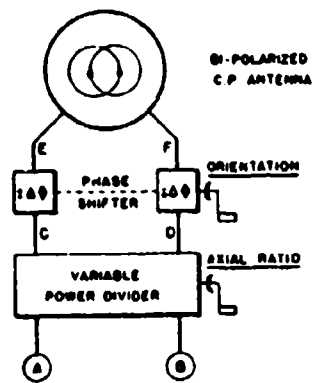


Figure 5. Polarisation Controller

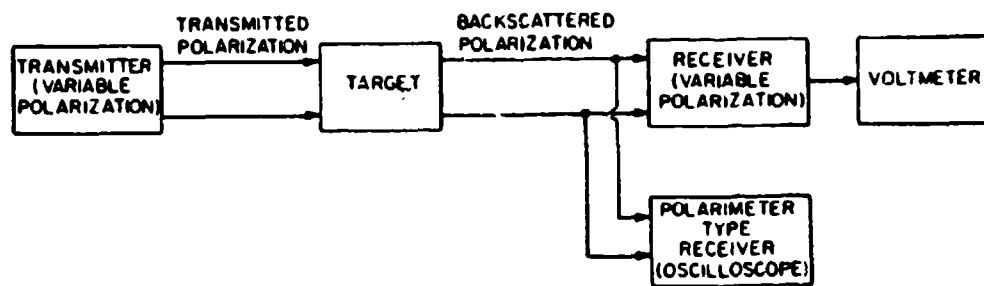


Figure 6. Polarisation Simulator

REFERENCES

1. I. D. Olin and F. D. Queen, "A Multi-Band Polarization Diversity System for Dynamic Radar Cross-Section Studies," Radar Reflectivity Measurements Symposium Record, April 1964.
2. G. Sinclair, "Modification of the Radar Range Equation for Arbitrary Targets and Arbitrary Polarization," Ohio State University, Antenna Laboratory Report 302-19, Sept. 1948.
3. E. M. Kennaugh, "Polarization Properties of Radar Reflections," Ohio State University, Antenna Laboratory Report 389-12, March 1952.
4. H. A. Brown, "The Radar Target Scattering Matrix in Linearly and Circularly Polarized Components for Target Aspect Changes around the Line of Sight," NRL Memorandum Report No. 1474, January 1964.
5. J. R. Copeland, "Radar Target Classification by Polarization Properties," IRE Proc. 48:1290-96, July 1960.
6. J. R. Huynen, "A New Approach to Radar Cross Section Measurements," IRE Convention Record, Part 5, pp 3-11, 1962.
7. P. J. Allen and R. D. Tompkins, "An Instantaneous Microwave Polarimeter," IRE Proc. 46:172-183, July 1959.
8. P. J. Allen and I. D. Olin, "A Four Component Polarization Resolver for Microwaves," NRL Memo Report 1086, April 1960.
9. R. S. Potter, "The Analysis and Matching of a Trimode Turnstile Waveguide Junction," NRL Report 4670, Dec. 1955.
10. R. S. Potter, "Multiple Mode Excitation of the Trimode Turnstile Waveguide Junction," NRL Report 4802, August 1956.
11. I. D. Olin, "A Note on Measurement of Polarization Transformation Properties of Radar Targets," NRL Memo Report 1046, May 1960.
12. Report of NRL Progress, pp 43-44, March 1962.
13. P. J. Allen, "On Generating a Rotating Polarization," IRE Proc. 48: 941, May 1960.

SECTION IV

MODELS, MODEL SUPPORTS, SPECIAL MATERIALS

Panel Chairman: E.M. Kennaugh

374a

REFLECTING PROPERTIES OF AIRCRAFT MATERIALS
AT 0.6943 AND 1.06 MICRONS USING PULSED LASERS

Stephen E. Barber
Electronic Engineer
Michelson Laboratory
U. S. Naval Ordnance Test Station
China Lake, California

ABSTRACT

The reflectivity of aircraft materials when illuminated by light at 0.6943 and 1.06 microns wavelength is discussed in this paper. Quantitative results of the return at different angles and the absolute reflectance are given. In addition some work on optical cross-section measurements is discussed.

INTRODUCTION

The invention of laser light sources, with properties previously unavailable at these frequencies has stimulated considerable interest in the use of optical frequencies for radar functions. Optical devices are limited in their possible uses by high atmospheric transmission losses, however, the well collimated beam combined with the small physical size possible for equipment could prove useful as a supplement to present radar systems.

At optical frequencies (10^{15} cps) the necessary size of a radiating antenna for a given watts per cm^2 at the target can be considerably reduced. In addition it is possible, within the limits of tracking capabilities, to keep the beam size the same as or smaller than the target size. This means a large reduction in background echoes and also a reduction in required power since there is then no penalty imposed by the inverse square law for the transmitted beam.

REFLECTIVITY STUDIES

In order to determine practical design considerations for an optical radar system it is necessary to learn something of the targets. We have made studies to determine what sort of return it is possible to obtain from naval aircraft targets. As part of this study we have made measurements of the reflectivity of aircraft materials, using as radiation sources the two most common solid state laser materials, ruby with output at 0.6943 microns wavelength and neodymium with output at 1.06 microns wavelength.

In order to make these measurements, a 15' long optical bench was built. The laser head was mounted at one end with a beam splitter and a detector to monitor the output. The monitor is necessary since the output of the laser is a function of a number of variables, and particularly

of the heating of the laser rod. At the other end of the optical bench is a quarter-circle arm which carries the measuring detector. This arm has a 4 ft. radius. The sample to be illuminated was placed at the center of this radius. The samples consisted of 6 x 6 in. squares of aircraft skin material painted with typical aircraft paints. Three samples were used, a light grey, a dark grey, and a fluorescent orange.

The ruby used for the measurements at 0.6943 microns was a 2" x $\frac{1}{2}$ " rod with multilayer dielectric reflecting coatings on both ends. The rod for 1.06 microns was a 2" x $\frac{1}{2}$ " neodymium doped glass with one end totally internal reflecting and a 98% reflecting dielectric coating on the other. Both rods were used in a 2" major axis elliptical cavity.

Measurements were first made to show the curve of the distribution of the reflected light with angle from normal incidence to 80°. This was made by determining the ratio of the return from the target at the various angles to that from a front-surface mirror at 0°. This gave the relative reflected signal distribution over 80° of the circumference of a 4 ft. circle. The graphs in Figures 1 and 2 show these results for the 3 samples and 2 wavelengths involved.

In order to obtain numbers for the absolute reflection it was necessary to integrate the reflectance curves of Figures 2 and 3 over the surface of a hemisphere of radius r (the target to detector distance) whose base plane lies in the plane of the sample plate, the center of the plate coinciding with the center of the base plane. The upper half of this hemisphere is shown in Figure 3.

The numerical integration is based upon the assumption that the reflection is essentially constant over the incremental angle $\Delta\sigma$ shown in Figure 3, so that it is nearly constant over the area included in spherical zone A. The area of the curved surface of this zone may be shown to be

$$A = 2\pi r^2 [\cos \sigma - \cos(\sigma + \Delta\sigma)]. \quad (1)$$

As the aperture of the detector moves through the angle $\Delta\sigma$ it sweeps out a finite area. This area is

$$a = \omega r \Delta\sigma \quad (2)$$

where ω is the diameter of the detector aperture and $\Delta\sigma$ is in radians. This area is shown in Figure 3.

The area under the reflectance curve may be approximated by a quantity I, which represents the area under the curve between σ and $\sigma + \Delta\sigma$. If $\Delta\sigma$ is a small increment (2° was used for the present calculations), I may be taken as

$$I = \Delta\sigma (R_\sigma + R_{\sigma + \Delta\sigma})/2 \quad (3)$$

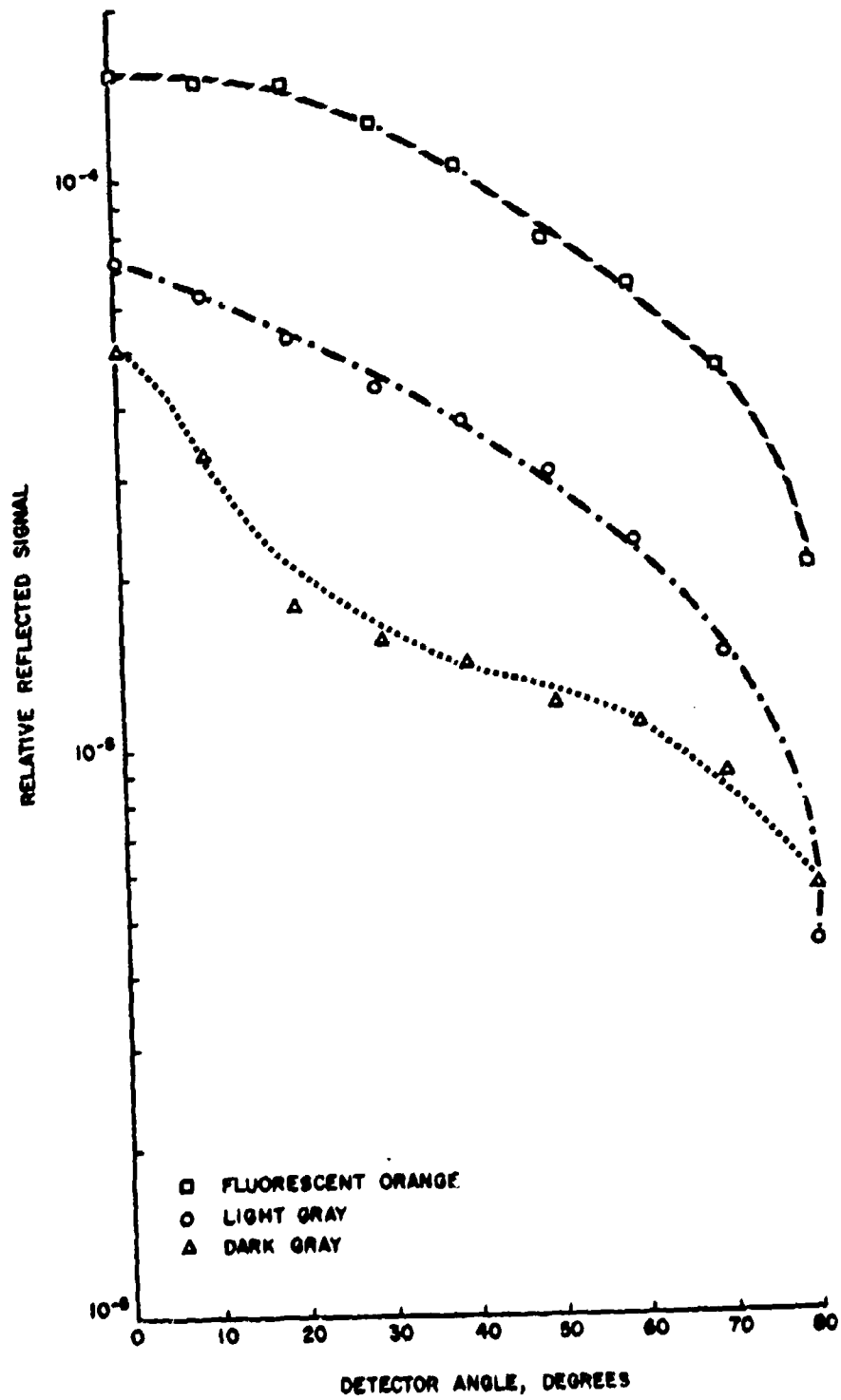


Fig. 1. Reflectance vs. Angle at 0.6943 μ

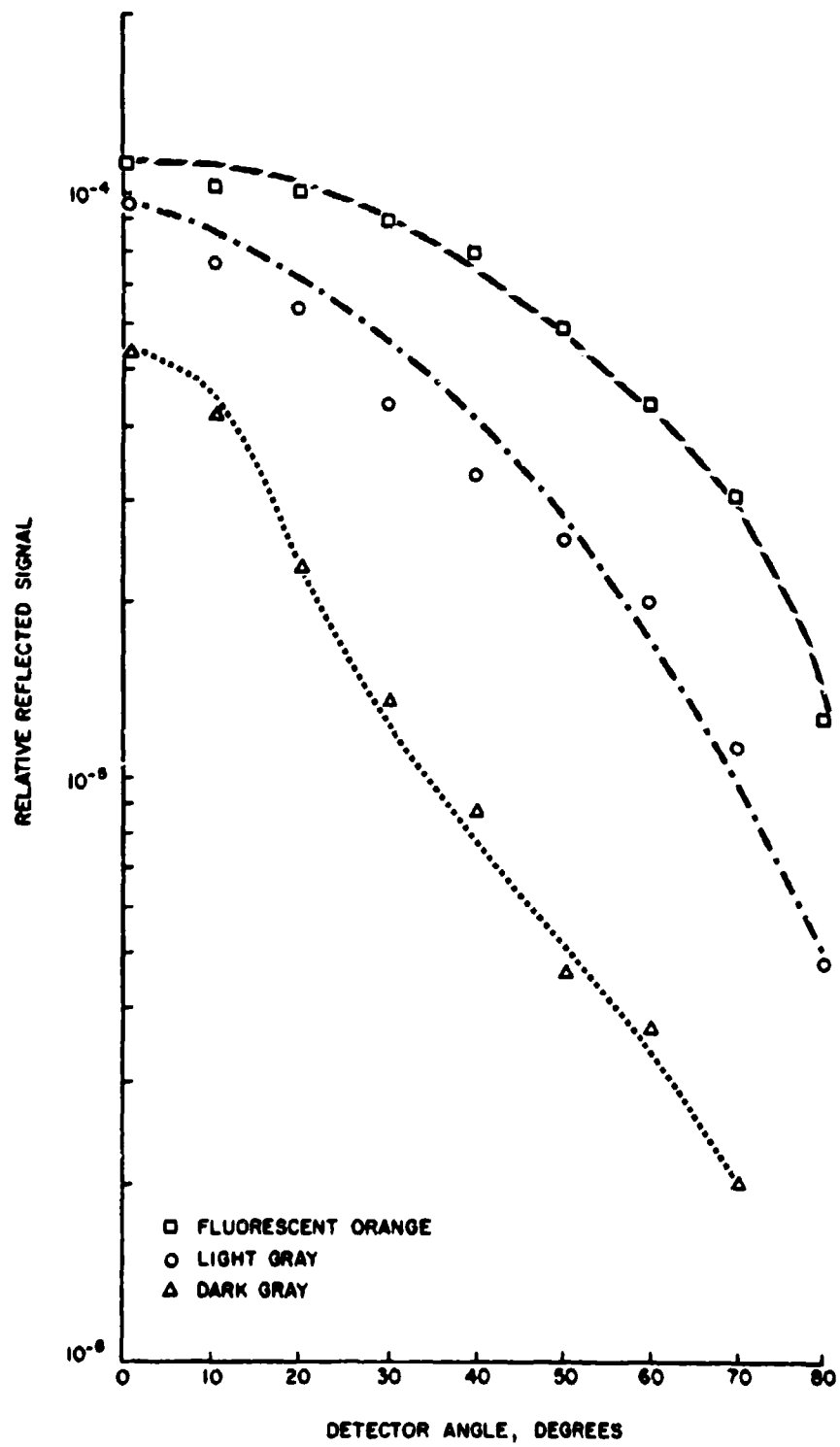


Fig. 2. Reflectance vs. Angle at 1.06μ

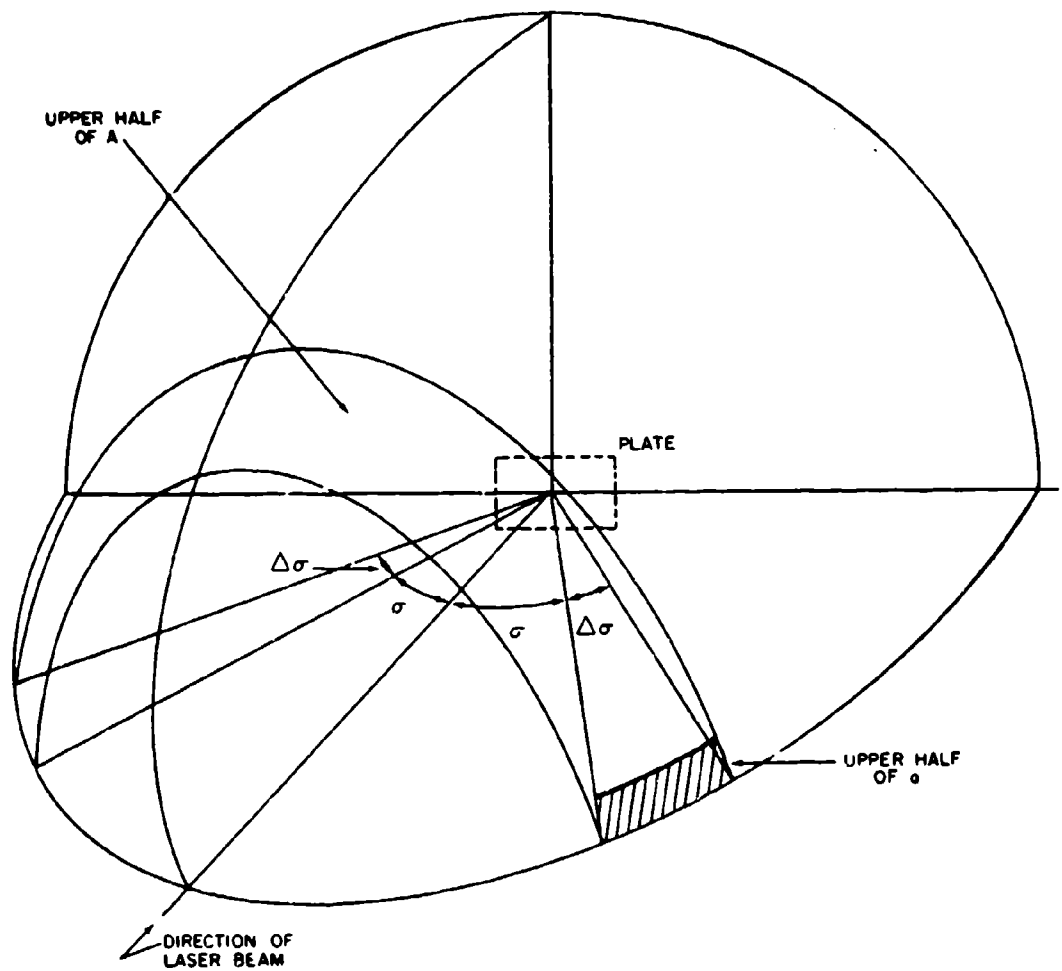


Fig. 3. Diagram for Calculation of Absolute Reflectance

where $\Delta\sigma$ is in degrees. This yields an accurate value for I because the detector subtends an angle of close to 1° in the σ direction. Thus if drawn accurately the graphs of reflectance would not be smooth curves, but rather a series of steps of 1° width. I is the sum of the heights of the steps in the increment $\Delta\sigma$, and I is finite because the number of steps is finite. Since the width of each step is 1° , I is numerically approximated by the height of the curve at the mid point of $\Delta\sigma$; this is what is implied by equation (3).

The total reflectance may be found from these quantities as follows:

$$R_T = \sum_{\sigma = 0^\circ}^{\sigma = 90^\circ} \frac{I A}{a} \quad (4)$$

This is physically interpreted as

$$R_T = \sum \frac{\text{total reflectance over } \Delta\sigma}{\text{sampling area}} \times \text{area over which the reflectance is nearly constant.}$$

The total reflectances were calculated to be as follows:

<u>Paint</u>	<u>R_T at 6943 Å</u>	<u>R_T at 1.06μ</u>
Light grey	0.37	0.37
Dark grey	0.11	0.11
Orange	1.07	0.77

Obviously the orange paint did not reflect more light at 6943 Å than it received. The actual result was probably close to but less than one and the above result represented a small cumulative error. The difference in reflectance of the orange paint at the two wavelengths is possibly a function of the fluorescence, perhaps the 1.06 micron quanta are not able to trigger the fluorescence.

OPTICAL CROSS-SECTION STUDIES

In addition to the reflectivity measurements, some studies have been made of the effective cross-section of naval aircraft. The results of these measurements are classified and hence will not be given; however the methods used may be of some interest.

These measurements were made on scale models of naval aircraft. The models were painted with light grey paint except for the stainless steel sections and the tailpipe. These were painted with chrome and velvet black paints respectively.

In order to simulate the relative size of the beam on an actual aircraft the following arrangement was used. The laser head, utilizing a 2" x 1/2" ruby rod, was mounted at right angles to the desired beam path, and a beam splitter placed in front of it for the monitor pulse. A 30 mm focal length converging lens was placed in the beam 30 mm in front of the

focal point of a 12.5 inch diameter spherical mirror. An optically flat 45 degree mirror was placed between the lens and the large mirror. The light reaching the target was then a 12.5 in. diameter circle of collimated light. (See Figure 4).

To obtain the measurements of the cross-section the following method was used. Measurements were first made of the return from the background, which was velvet black with a reflectance of 2%. Measurements were then made of the return from a flat grey painted piece of metal of known area. After correcting the background for the area blocked by the metal, the background return was subtracted from the readings for the painted metal to give its actual return. The models were then placed in the beam and readings taken for various orientations. These readings were also corrected for background return. The ratio of the return from the plate and the return from the model gave the ratio of the areas. An equivalent flat area for the model was then calculated from this. These results were then scaled up to full aircraft size.

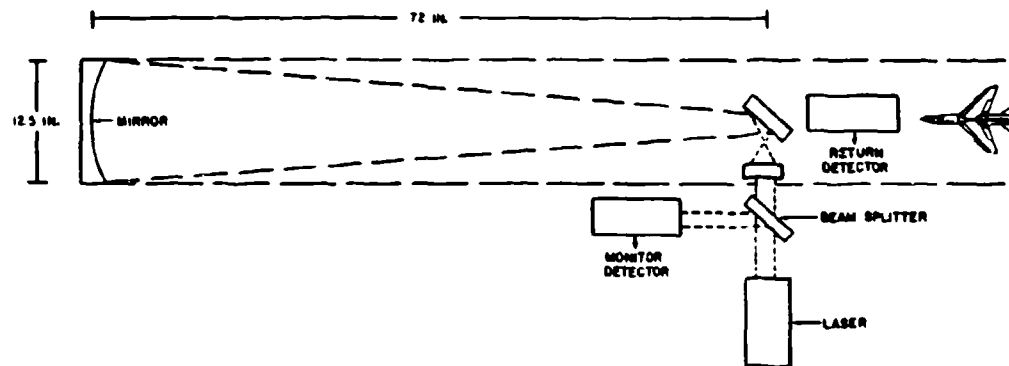


Fig. 4. Equipment Diagram of Optical Cross-section Measurements

MICROWAVE BACK-SCATTERING FROM SUPERSONIC
LABORATORY PLASMA STREAMS

A.I. Carswell and M.P. Bachynski
RCA Victor Research Laboratories
RCA Victor Company, Ltd.
Montreal, Canada

ABSTRACT

The scattering of electromagnetic waves by supersonic plasma streams has been studied in the laboratory in a radio frequency, low density (0.1 to 10 Torr static pressure) plasma tunnel. Measurements have been concerned with the aspect dependence of microwave back-scattering from cylindrical supersonic plasma flow fields and with the back-scattering of microwaves from turbulent supersonic plasma streams.

The amplitude of the signal back-scattered from supersonic plasmas in argon has been measured as function of the angle of incidence at frequencies of 10Gc (x-band) and 25Gc (k-band) and comparisons made with back-scattering from dielectric and metal rods of the same geometry as the plasma stream. The scattering depends critically on the ratio of plasma frequency to incident radio frequency, the aspect angle, the polarization (for small diameter columns compared to a wavelength) and the nature of the flow itself. For laminar flowing plasmas, similar scattering characteristics to dielectric rods are obtained and only slight fluctuation of the scattering amplitude occurs.

When the plasma is turbulent, it is possible to have variations in the back-scattered signal arising from the turbulence which are as large or larger than the variations arising from the aspect angle dependence of the return. A frequency analysis has been made of the random amplitude modulation imposed by the turbulence to the back-scattered microwave signal. The frequency content of the back-scattered signal appears very similar at both 10Gc and 25Gc frequencies and is predominantly in the audio range (0-10Kc) decreasing monotonically with increasing frequency.

INTRODUCTION

The ionized wake found behind a space vehicle moving at hypersonic velocities within a planetary atmosphere provides a significant target from which radar signals can be reflected. A detailed knowledge of the radar scattering cross-section can provide information on the wake and indeed on the vehicle itself, thus providing a means of detection (and possibly discrimination) of such vehicles as they enter the atmosphere.

The dependence of the scattering cross-section of the wake on the vehicle and space environment is complicated by the large number of parameters which are involved. These include the electron density in

the wake (or more accurately the plasma frequency relative to the radar frequency ω_p/ω), the polarization of the incident signal, the geometry of the scattering path (aspect angle θ), the dimension of the wake (diameter and length in wavelengths - d/λ and l/λ) and on the nature of the flow surrounding the vehicle (characterized perhaps by some Reynolds number). Furthermore, the above parameters may vary in space and time and be complicated by additional factors such as the collisional (attenuation) effects of the wake plasma, the non-uniform electron distribution (both radially and longitudinally) in the wake, thermal non-equilibrium conditions of the plasma and ablation from the vehicle itself. It thus becomes exceedingly difficult to uniquely interpret radar scattering cross-section measurements if the scattering environment cannot be accurately specified.

Consequently, measurements made in suitable laboratory systems in which many of the parameters can be controlled can yield considerable information of value for the interpretation of free-flight radar scattering cross-section measurements. Because of the large number of parameters involved, exact scaling of all the geometric, aerodynamic and electromagnetic properties of the full-scale system is not possible. However, the laboratory experiment can, in general, be designed to simulate some specific important aspect of the full scale problem.

A laboratory experiment designed for the study of microwave scattering from supersonic plasma flow-fields has been conducted. The experimental system consisting of a low density plasma tunnel¹ which provides rf excited supersonic plasma flow streams has been described elsewhere in the Symposium Record. This paper is concerned with the measurements of microwave back-scattering from supersonic flowing plasma streams obtained in this plasma tunnel and with their interpretation in terms of current theories of radar scattering.

BACK-SCATTERING FROM LAMINAR PLASMA STREAMS

When a plasma moves under conditions where the flow is laminar, the plasma can generally be considered as a dielectric with a well-defined geometry which is determined by the specific flow conditions. Otherwise the effects of the flow do not manifest themselves in the electrical properties of the plasma. The plasma electrical properties can then be described in terms of a dielectric coefficient K where:

$$K = 1 - \left(\frac{\omega_p}{\omega}\right)^2 \frac{1}{1 + j(\nu/\omega)} \quad (1)$$

and (ν/ω) is the ratio of collision frequency to radar frequency.

In order to calculate the back-scatter from a laminar plasma of a given geometry resort can usually then be made to the large body of literature on scattering and diffraction by bodies of smooth geometrical shape choosing the contour which most nearly approximates the plasma in question. The major requirement is a model which is simple enough to permit ready

analytical computation but still sufficiently accurate to describe the physical situation.

Some insight into the back-scattering properties of a plasma can be gained by first briefly considering back-scatter from a plane surface. The back-scattering cross-sections σ from a plane surface whose dimensions are not too small compared to wavelength and which is located a distance r from the source (and receiver) is given by²:

$$\sigma = \frac{k^2}{\pi} \cos\theta \cos\phi \left| \iint_A \Gamma e^{-j2k \vec{r} \cdot \vec{n}} dA \right|^2 \quad (2)$$

where: θ is the angle between direction of incidence and the normal to the reflecting surface,
 n is the unit normal to the reflecting surface,
 k is the wave number ($2\pi/\lambda$),
 Γ is a reflection coefficient determining the reduction of the field (both phase and amplitude) at the reflecting surface.

A note of explanation regarding the factor Γ is in order. In a perfect conductor Γ is unity. At normal incidence Γ is the usual Fresnel coefficient if only a single surface is involved in the reflection. If more than one surface is involved (say a layer of plasma) then Γ is the reflection coefficient determined by solving the boundary value problem. Typical values for Γ for a layer of uniform plasma for an electromagnetic wave normally incident on the plasma³ are shown in Fig. 1.

For a plane rectangular surface of dimensions $a \times b$ for a wave incident from the polar directions θ, ϕ when the reflection coefficient of the surface (or layer) is constant over the area, the back-scattering cross-section is given by:

$$\sigma(\theta, \phi) = \frac{(ka)^2 (kb)^2}{\pi k^2} \cos\theta \cos\phi \Gamma^2 \left[\frac{\sin(ka \sin\theta \cos\phi)}{ka \sin\theta \cos\phi} \right]^2 \times \left[\frac{\sin(kb \sin\theta \sin\phi)}{kb \sin\theta \sin\phi} \right]^2 \quad (3)$$

The cross-section thus exhibits a diffraction pattern over angle which is the same as for a modified aperture of twice its dimensions (due to twice the phase variation in back-scatter compared to forward scatter).

A model more appropriate for the interpretation of scattering from plasma flow fields as encountered in missile re-entry is that of a uniform plasma cylinder. Exact solutions exist for both perfectly conducting^{2,4} and dielectric cylinders⁵⁻⁹. It is significant to note that the scattering cross-section is now dependent on the orientation (polarization) of the incident electromagnetic field. The major difficulty is one of

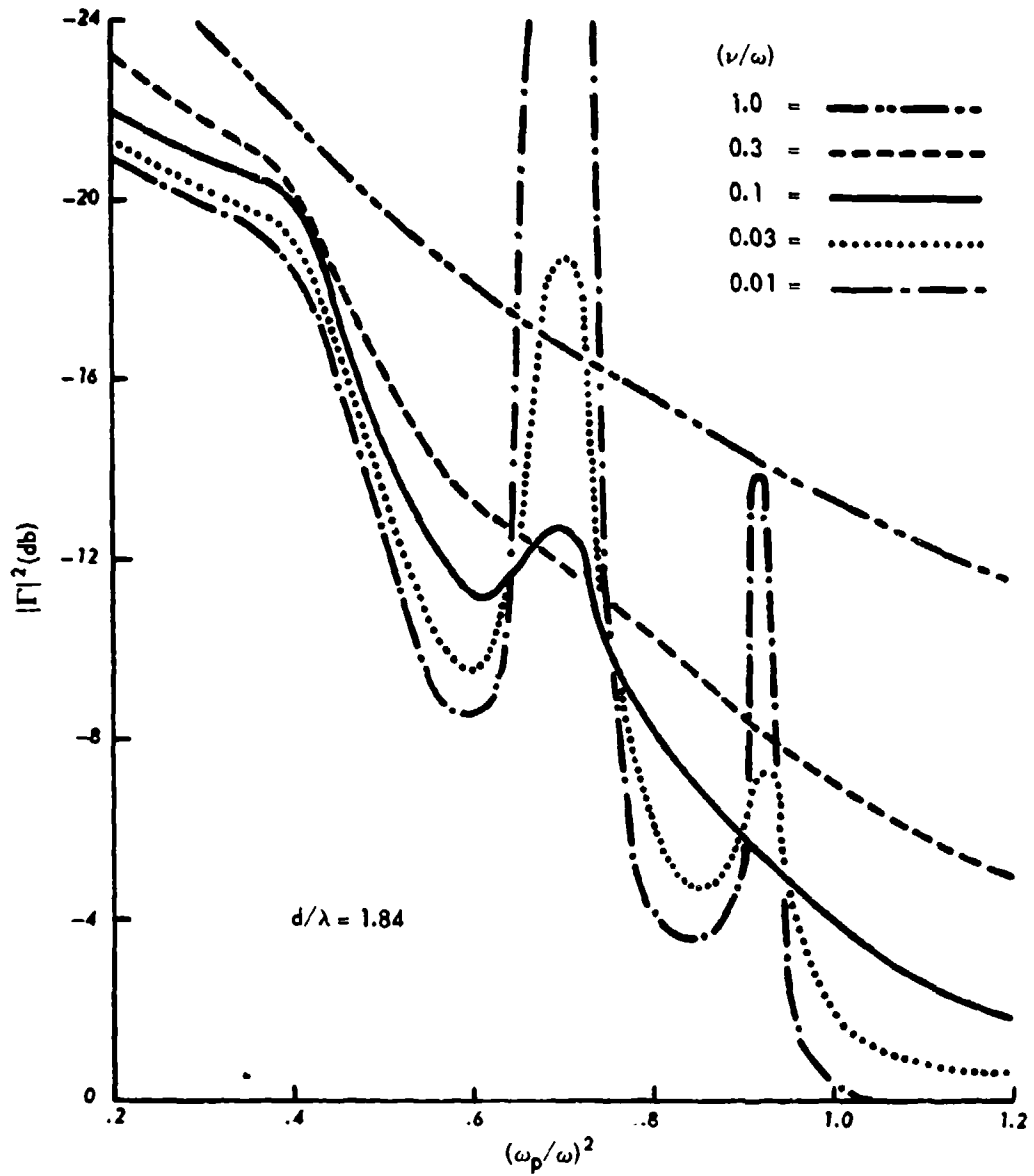


Figure 1. Power Reflected from a Plasma Slab 1.84λ Thick for Various Values of the Collision Frequency.

numerical evaluation since the solutions are generally in terms of slowly converging infinite series. These approaches have been widely used in the analysis of radar scattering from meteor trails (see for example Ref. 10). Two limiting cases are of interest which enable a simplification of the computations to be attained. These are the underdense case: $(\omega_p/\omega)^2 \ll 1$ where the radar return can be considered as a summation of the scattering of individual electrons and we obtain:

$$\sigma \propto n^2 \text{ or } \left(\frac{\omega_p}{\omega}\right)^4$$

where: n is the electron density of the plasma cylinder.

In the overdense case, $(\omega_p/\omega)^2 \gg 1$, the plasma approaches a metallic cylinder and we obtain:

$$\sigma \propto \left(\frac{\omega_p}{\omega}\right)^{\frac{1}{2}}$$

For a cylinder, the scattering is independent of ϕ and carrying out the integration in a similar manner to that which was used in obtaining Eq.(3) leads to:

$$\sigma(\theta) = kaL^2 \cos\theta \left[\frac{\sin(kL \sin\theta)}{kL \sin\theta} \right]^2 \Gamma_c^2 \quad (4)$$

where: a is the radius and L the length of the cylinder, and Γ_c is a phenomenological factor which indicates the reduction of the field strength upon reflection compared to a perfect reflector.

Back-scattering of microwaves from supersonic plasma streams has been studied in the laboratory for both overdense and underdense plasmas. The aspect angle dependence of back-scattering is found to obey the dependence predicted by Eq.(4) (at least for overdense streams) as shown in Fig. 2. Fig. 2(a) shows a typical variation of the back-scattered signal from a metallic rod and Fig. 2(b) the variation of the back-scattered signal from a stream of plasma moving at Mach 2 under laminar flow conditions. Both measurements were made under identical conditions (same L , etc.) at 10Gc and for this frequency the plasma was essentially overdense. Back-scattering measured from an underdense plasma is shown in Fig. 3. The dependence on aspect angle is somewhat similar to that for the overdense case but the signal levels are markedly reduced (as would be the case for a dielectric cylinder) and asymmetries are apparent. (These asymmetries are discussed later).

The model of a uniform cylinder is often not accurate enough to determine scattering from a laminar flowing plasma and a non-uniformity in

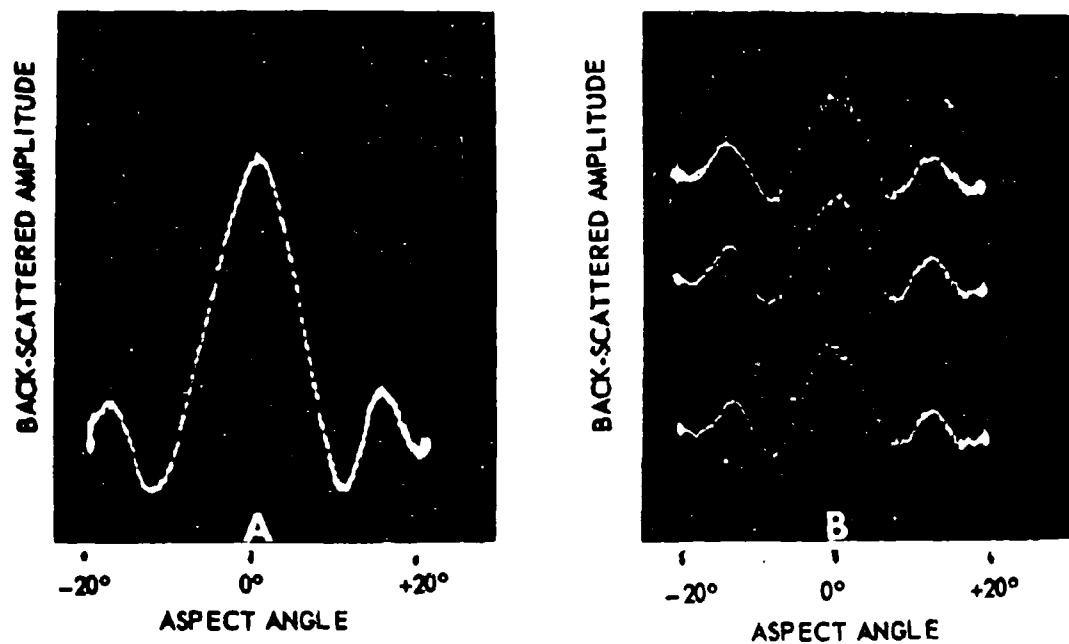


Figure 2. Sample Displays of the Aspect Angle Variation of a Microwave Signal (9.4Gc) Back-scattered from Cylinders 15cm Long. (A) $\frac{1}{2}$ inch Diameter Metal Rod (B) Laminar Supersonic Jet.

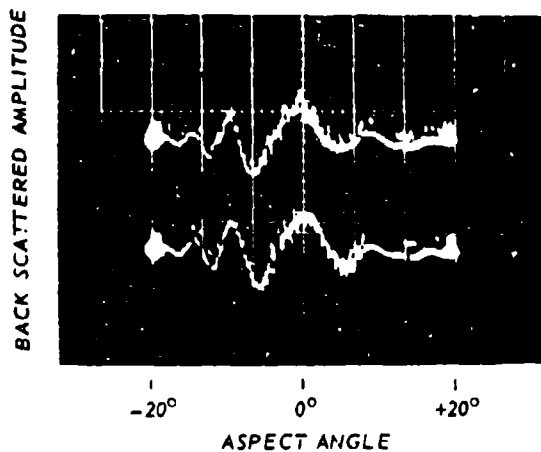


Figure 3. Sample Displays of the Aspect Angle Dependence of a 24Gc Microwave Signal Back-scattered from an Underdense Plasma Jet.

the spatial variation of the plasma is introduced. A number of solutions^{8,11,12} for scattering from a plasma cylinder with a radial variation of electron density (or dielectric constant) are available although the computational difficulties are usually severe. Consequently, numerical results are available mainly for normal incidence and for the electric field polarized along the direction of the cylinder axis. (No cross-polarization fields which should be present at oblique incidence⁸ have thus been evaluated). For overdense cylinders, the following considerations are appropriate. If the electron density near the surface is sufficiently high then the scattering of electromagnetic waves is predominantly a surface effect and the non-uniform variation has no influence on the back-scattered signal so the highly overdense case can still be considered as a metallic cylinder. If the plasma becomes overdense only over an interior portion of its volume which is surrounded by an underdense region of plasma, then the model of a metallic cylinder (interior region) encompassed by a dielectric (i.e. two concentric cylinders, the interior metallic, the exterior of dielectric) can be used to describe the scattering. When this is the case the scattering from both regions must be taken into account. Because of the complexity of the problem in this case, it is difficult to find a unique combination of parameters which will predict the scattering cross-section measured for a given plasma system at a single frequency.

If the non-uniform plasma is underdense, then scattering of electromagnetic waves can be considered due to individual electrons. For a small cylinder ($a/\lambda \ll 1$), the phase variation of the waves scattered from different electrons is insignificant and the important parameter then becomes the total number of electrons per unit length of the cylinder. For large a/λ ratios this phase variation must be taken into account when summing the scattering by individual electrons. If we write the dielectric constant of a plasma with a radial distribution of electron density as:

$$K = 1 - \left(\frac{\omega_{p0}}{\omega} \right)^2 \frac{1}{1 + j\nu/\omega} f\left(\frac{r}{a}\right) \quad (5)$$

where: $f(r/a)$ is the variation of the electron density with radius r over a cylinder of radius a so that $f(0) = 1$
 ω_{p0} is the plasma frequency at the centre of the cylinder ($r/a = 0$).

Then for $a/\lambda \ll 1$

$$\sigma \approx 2\pi \omega_{p0}^2 \int_0^a f(r/a) r dr \quad (6a)$$

Taking the phase variation into account gives:

$$\sigma \approx 2\pi \omega_p^2 \int_0^a f(r/a) \left(\int_0^{2\pi} e^{-j2kr \cos\theta} d\theta \right) r dr$$

$$\approx 2\pi \omega_p^2 \int_0^a f(r/a) J_0(2kr) r dr \quad (6b)$$

These expressions must be evaluated for each radial distribution of the electron density. It is important to note that Eq.(6) can give a fairly good first approximation for the scattering cross-section for small values of ω_p/ω and is far simpler to calculate than the exact expression. (For a homogeneous cylinder Eq.(6b) is found to hold approximately even for ω_p/ω approaching one.)

It is also apparent that even for this simple case a measurement of σ cannot give unambiguous information about the electron density and its distribution. A wide range of distributions having different maximum electron densities and different effective radii can give the same value of radar cross-section. This indicates the need of utilizing at least two radar frequencies simultaneously to study plasmas in which spatial variations of the electron density exist.

The effects of variations of the electron density along the length of the cylinder of plasma (longitudinal variation) are more difficult to predict and to calculate since the problem becomes three-dimensional. The plasma now effectively becomes a tapered cylinder. The effect of such a plasma is easier to measure than to calculate and in fact Fig. 3 shows the back-scattering characteristics of a plasma whose electron density (as determined by probe measurements¹³) decreases with length. This effect results in the pronounced asymmetry in the maxima and minima variation with aspect angle increasing the maxima when the aspect angle is such that the denser region is nearer the receiver and decreasing the maxima when the reverse is true. Comparison of these measurements with back-scatter from tapered dielectric rods shows good agreement.

Thus far, the back-scattering from a plasma under laminar flow conditions has been described solely on the basis of a dielectric cylinder. The only plasma property involved has been its effective dielectric coefficient. This model, however, is not sufficiently accurate to explain certain phenomena which arise because of the more complex behaviour of plasma. One striking example of the limitation of the "effective" dielectric coefficient representation of the plasma occurs for a cylindrical plasma when $a/\lambda \ll 1$ and the incident field is polarized normal to the axis of the cylinder.

Under these conditions it has been found that the plasma column

exhibits "resonances" (often called the Tonks-Dattner resonances) in its absorption and scattering properties as the electron density of the plasma is varied. Calculations¹⁴ using the effective dielectric coefficient model of the plasma show that a resonance behaviour will only result when the electric vector is transverse to the column axis and when a/λ is small. However, this theory predicts only a single resonance whereas the experiments exhibit a resonance pattern comprised of a main resonance and a series of secondary peaks which occur at electron densities lower (and in some cases higher) than the main peak. Attempts to describe the secondary resonances on the basis of the physical properties of the plasma have only recently begun to prove successful. It appears from this work that in the "resonance" range of electron densities the coupling of the transverse electromagnetic waves with the longitudinal waves in the plasma must be included in the theory. This has been done recently for cylindrical plasmas^{13,14} and agreement with experiment has been obtained. Using this theory it is demonstrated that the observed spectrum of secondary resonances depends very strongly on the (radial) distribution of electron density in the plasma.

It was suggested by Herlofson¹⁴ that this resonance effect (which is actually an enhancement of the radar return) should be apparent in radar returns from meteor trails under the proper conditions. This fact appears to be verified by recent work such as that reported by Billam and Browne⁷ who have detected resonances in the back-scattered signal for an incident wave having the electric field transverse to the axis of the meteor trail. Since the structure of the resonance spectrum obtained in this way provides (in principle at least) information about the electron density and its spatial distribution in the trail, it is of considerable interest to examine the dependence of the resonance characteristics on re-entry parameters.

Studies of this resonance phenomena have been performed using both steady mercury discharge tubes and supersonic plasma jets. Sample results are shown in Figs. 4 and 5 for a microwave frequency of 9.4 Gc. Fig. 4 shows typical resonances obtained in the radar return from a cylindrical mercury discharge tube as the current (electron density) is varied. Fig. 5(a) shows sample signals back-scattered from a supersonic plasma jet¹³. (The fluctuations in the signal carried by turbulence in the flow are apparent and this effect will be discussed later.) These results show the resonances for the transverse polarization. No such resonances are observed for the longitudinal polarization in agreement with the theory. It is of interest to compare these results with those for a typical meteor trail obtained by Billam and Browne as shown in Fig. 5(b). Comparison of Figs. 5(a) and (b) shows the marked similarity of the laboratory results to the meteor measurements. Measurements in a two-phase supersonic mercury plasma tunnel¹³ have also shown evidence of the resonance effect. Fig. 6 shows sample results of this work for flow velocities of the order of Mach 3. By comparing such results with the resonances measured in simple mercury discharge tubes (e.g. Fig. 4) it is possible to derive apparent λ/d ratios

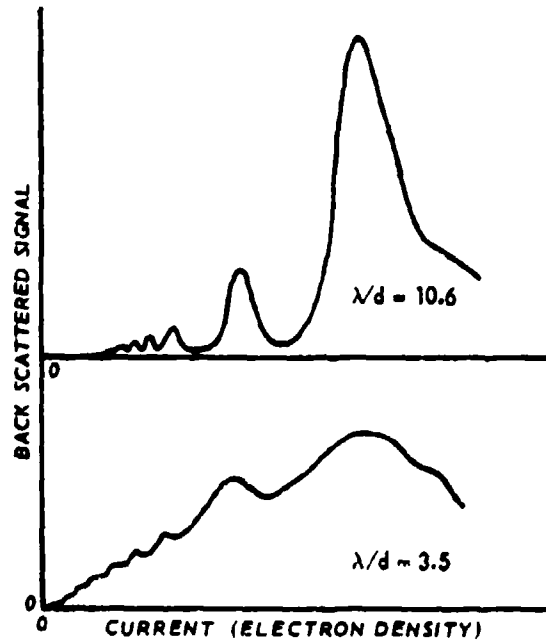


Figure 4. Sample Resonances Observed at X-band ($\lambda = 3.19\text{cm}$) in the Back-scattering from Mercury Tubes of Diameter d .

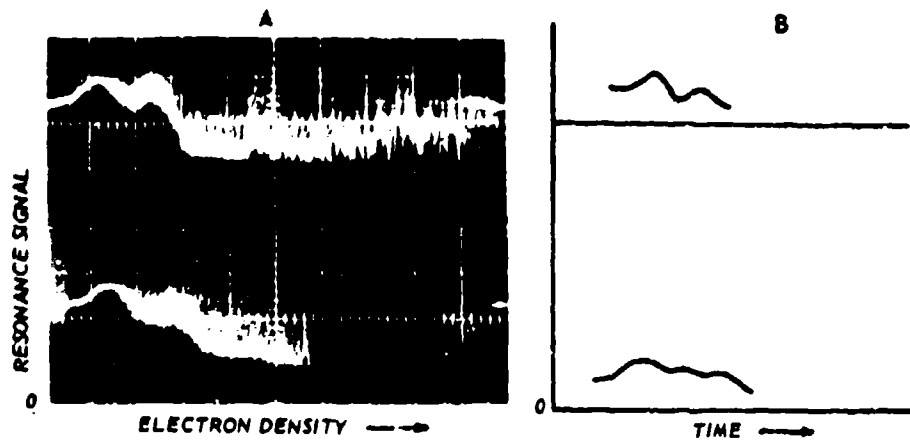


Figure 5. Resonance Effects in Back-scattering from Plasma Flow-Fields. (A) Scattering from a Supersonic Plasma Jet in the Laboratory¹² (B) Scattering from a Meteor Trail in the Atmosphere¹⁷.

for the jet and these have been found to be of the order of magnitude of the visible stream diameter. Simultaneous measurement of the forward and back-scattered component (as shown in Fig. 6) in such a laboratory study provides further insight into the interaction involved. Because of the difficulties encountered in measuring and controlling the plasma stream the resonance measurements thus far have provided only semiquantitative data. The results do appear to indicate, however, that more detailed studies are warranted.

BACK-SCATTERING FROM NEARLY LAMINAR PLASMA STREAMS

When conditions are such that the flow departs only slightly from being laminar, small scale fluctuations begin to occur in the plasma stream. The plasma stream can no longer be treated as a uniform cylinder but a model whereby the plasma is considered to consist of a uniform cylinder with rough surfaces becomes more appropriate. The idea of surface roughness can be used to take into account the small scale fluctuations by means of a phenomenological scattering coefficient ρ_s which is the ratio of the reflection coefficient of the rough cylinder to the reflection coefficient of the smooth cylinder. The resulting scattering cross-section is the scattering cross-section of the smooth cylinder multiplied by the scattering coefficient.

The major problem is then the analytical form for the scattering coefficient. For the situation where scattering elements are equally probable at any level from the lowest to the highest of the rough surface and neglecting multiple scattering and diffraction effects, Beckmann⁹ gives for scattering in the principal (specular) direction:

$$\rho_s = \left[p + (1-p) \frac{\sin^2 a}{a^2} \right]^{\frac{1}{2}} \quad (7a)$$

where: $a = kh \sin \gamma$,
 $h =$ maximum vertical height of the scattering irregularities,
 $\gamma =$ grazing angle = 90° minus the angle of incidence,
 $p =$ probability of occurrence of scattering element which scatter in the principal direction.

For back-scatter at normal incidence ($\gamma = \pi/2$) we have:

$$\rho_s = \left[p + (1-p) \frac{\sin^2 kh}{(kh)^2} \right]^{\frac{1}{2}} \quad (7b)$$

In addition, Beckmann gives a probability distribution for the scattering coefficient determining the bounds within which a given percentage of a large number of measured points should lie.

For back-scattering in directions other than normal incidence, the

scattering coefficient has a Rayleigh distribution.

Experimental measurements of back-scattering from nearly laminar flowing columns of plasma are shown in Fig. 7. The notable feature of the back-scattered signal is its reduced amplitude relative to the purely laminar flow under similar conditions although the envelope of the variation with aspect angle remains much the same as before. A fluctuating signal (depending on the deviation from a uniform flow) is superimposed on the return from a laminar column. Comparing Eq.(7b) with the experimental measurements leads to values of the scattering coefficient (ρ_s) of approximately 0.7, the height of irregularities (h) of the order of $\lambda/4$ and a probability of occurrence of scattering elements for back-scatter at normal incidence (p) of about $1/6$. All appear to be reasonable values. As yet, the scattering coefficient for other than normal incidence has not been analysed to determine if it follows a Rayleigh distribution.

MICROWAVE BACK-SCATTERING FROM TURBULENT PLASMA STREAMS

When turbulence occurs in the plasma flow, the plasma characteristics will be random functions of time and position. The exact nature of the turbulence is exceedingly difficult to ascertain since theories of turbulence even in the conventional fluid dynamics sense are at best restricted to ideal incompressible fluids. When these are complicated with compressibility, electrical conductivity and particle production and loss processes it is quite hopeless to expect quantitative results from existing analyses. In a plasma, if the charged particles are closely coupled to the neutral particles, and the motion of the neutrals is predominantly determined by the fluid flow (the plasma velocity is the velocity of the neutral particles) then the turbulence would be of an aerodynamic type. This should be the case for a slightly ionized plasma moving at high velocities. The onset and degree of turbulence would then be functionally dependent on a parameter of the neutral gas flow such as the usual Reynolds number R where

$$R = VL/\beta$$

where: β is the ratio of viscosity to gas density
 V, L are a characteristic velocity and length respectively.

The exact dependence of the turbulence on the Reynolds number is, however, not clear. On the otherhand, for a highly-ionized flowing plasma, space charges and currents may predominate in determining the plasma characteristics and the plasma turbulence is more in the nature of instabilities. The form of the instability would then depend on the type of space charge forces which manifest themselves in the plasma. This is the type of turbulence of great interest in studies of controlled thermonuclear fusion and will not be treated further here.

Very little work has been done on the intermediate case of high

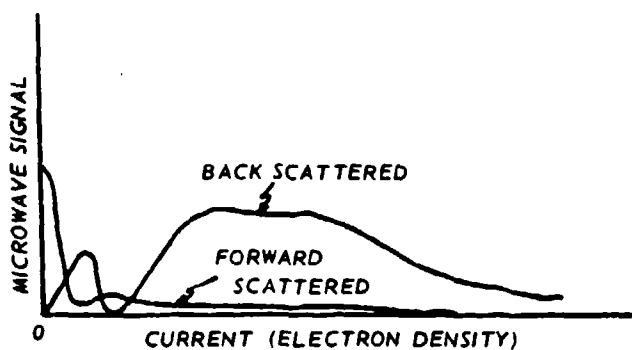


Figure 6. Sample Resonance Effects Observed in X-band (9.4Gc) Scattering From a Mach 3 Mercury Plasma Jet.

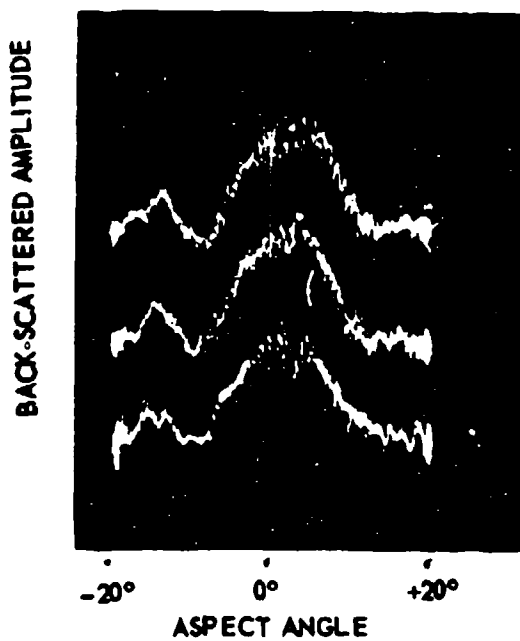


Figure 7. Sample Displays of the Aspect Angle Dependence of 9.4Gc Microwaves Back-scattered from a Turbulent Plasma Jet.

density of charged particles and large neutral velocity.

The temporal and spatial variations of the plasma characteristics due to turbulence should be reflected in the characteristics of the electromagnetic signal back-scattered from such a plasma. One would normally expect that the scattering at directions off normal incidence would be enhanced while the normal incidence back-scattering would be reduced. The scattering of electromagnetic waves by turbulent fluctuations has been studied extensively in connection with tropospheric scatter propagation. Adapting the results of such studies to back-scattering from underdense turbulent plasmas the scattering cross-section is given by:

$$\sigma = \frac{k^4}{16\pi^2} \iiint_V \frac{\langle \Delta K^2 \rangle}{K^2} e^{-j2(\vec{k} \cdot \Delta \rho)} C(\Delta \rho) dV \quad (8)$$

where: ΔK is the fluctuation in the dielectric constant K ,

$$C(\Delta \rho) = \frac{(\Delta K(\rho))(\Delta K(\rho + \Delta \rho))}{\langle \Delta K^2 \rangle} \quad \text{is the correlation function between position } \rho \text{ and } \rho + \Delta \rho \text{ within the scattering volume.}$$

The scattering cross-section can also be defined in terms of a spectrum function $S(k)$ where:

$$S(k) = \int_V e^{-j2(\vec{k} \cdot \Delta \rho)} C(\Delta \rho) \frac{\langle \Delta K^2 \rangle}{K^2} dV \quad (9)$$

so that:

$$\sigma = \left(\frac{\pi^2}{\lambda^4} \right) S(k) .$$

Depending upon the correlation function or spectrum function various values of the scattering cross-section are obtained. A general dependence of the scattering cross-section¹⁹ is of the form:

$$\sigma \propto \frac{\omega^4}{\omega^r}$$

where, r is a number which depends upon the respective theory (and hence nature of the correlation function) (r varies from 4 to 11). Thus for back-scatter one should have a direct frequency dependence.

For an overdense trail it is difficult to formulate a suitable analytical model for comparison with experiment, other than the surface roughness considerations presented earlier.

The back-scattering of electromagnetic waves from a turbulent plasma has been measured in the laboratory facility. A typical behaviour of the back-scattered signal with time is shown in Fig. 8, while a typical display of the frequency content of the turbulent signal is shown in Fig. 9. Since the degree of ionization in the laboratory plasma is low the turbulence is expected to be dominated by the flow of neutrals. The fluctuations of the charged particles in position and time is determined by the neutrals and hence the microwave back-scattering should give an indication of the turbulence of the neutral flow. These conclusions are substantiated by comparisons of these results with hot wire anemometer measurements²⁰ in a neutral gas which show a similar frequency spectrum of turbulence. Further measurements which are in progress are necessary in order to be able to make analytical comparison with Eqs. 8 and 9. These include direct measurement of the correlation function by means of electrical probes and focused microwave beams and studies of the frequency dependence of the back-scatter cross-section.

CONCLUSION

The present investigation has provided microwave back-scattering measurements from supersonic plasma flow-fields of relatively well-defined properties and has provided new information on several aspects of the scattering process. This type of information is essential in the interpretation of radar returns from full scale re-entry bodies.

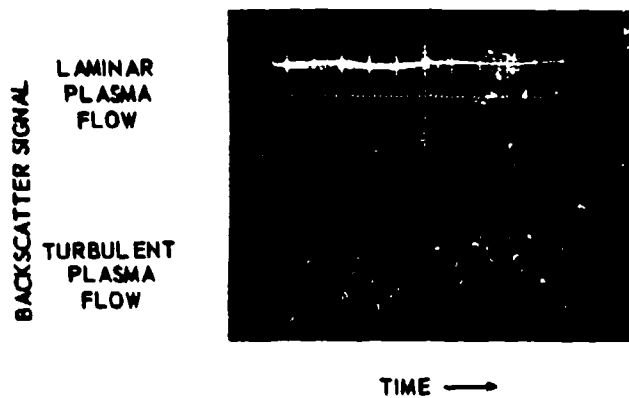


Figure 8. Broadside Return of X-band (9.4 Gc) Microwave Scattered from a Plasma Jet Showing the Difference Between a Laminar and Turbulent Flow (Time Scale is 1 milliseo/div.)

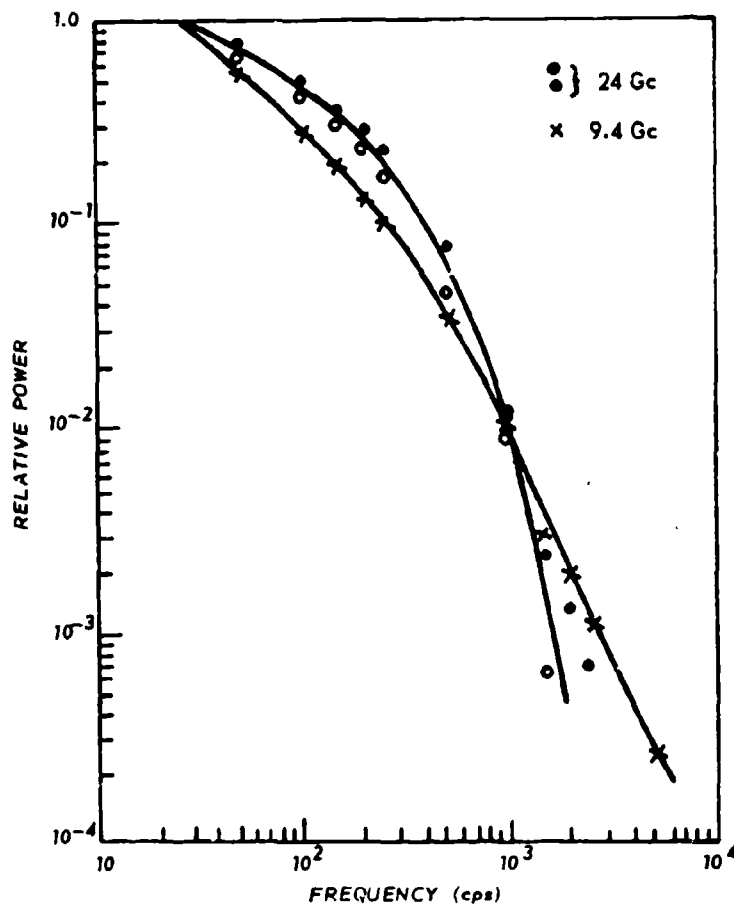


Figure 9. Frequency Content of the Fluctuating Microwave Signals Back-scattered from a Turbulent Plasma Jet.

REFERENCES

1. A.I. Carswell, "Radio Frequency Excited Plasma Tunnel for Laboratory Studies of Supersonic Plasma Flow-Fields", Rev. Sci. Instr. 34, 1015 (1963).
2. D.E. Kerr, "Propagation of Short Radio Waves", MIT Radiation Lab. Series, Vol. 13, McGraw-Hill (1951).
3. M.P. Bachynski, K.A. Graf, "Electromagnetic Properties of Finite Plasmas", RCA Review, March (1964).
4. J.R. Wait, "Electromagnetic Radiation from Cylindrical Structures" Pergamon Press, New York (1959).
5. J.R. Wait, "Scattering of a Plane Wave from Cylindrical Dielectric Cylinder at Oblique Incidence", Can. J. Phys. 33, 189 (1955).
6. J.R. Wait, "Some Boundary Value Problems Involving Plasma Media", J. Res. NBS 65B, 137 (1961).
7. C. Froese, J.R. Wait, "Calculated Diffraction Pattern of Dielectric Cylinders at Centimetre Wavelengths", Can. J. Phys. 32, 775 (1954).
8. C.M. de Ridder, L.G. Peterson, "Scattering from a Homogeneous Plasma of Infinite Length", MIT Lincoln Lab. Rep. 312G-4 (1962).
9. R.G. Kouyoumjian, L. Peters, D.T. Thomas, "A Modified Geometrical Optics Method for Scattering by Dielectric Bodies", IEEE Trans. AP11, 690, Sept. (1963).
10. J.S. Greenhow, A.C.B. Lovell, "The Upper Atmosphere and Meteors" in 'Physics of the Upper Atmosphere', ed. J.A. Ratcliffe Academic Press (1960).
11. C.M. de Ridder, S. Edelberg, "Scattering from Plasma Cylinders with Radial Variations in Electron Density", Proc. of Symposium on Plasma Sheath, Plenum Press (to be published).
12. T.H. Lee, "Back-Scattering of Electromagnetic Waves by Inhomogeneous Plasma Wakes", Lockheed Missile & Space Company, Rep. LMSC 657225-II, July (1963).
13. A.I. Carswell, "Microwave Scattering from Supersonic Plasma Flow-Fields", RCA Victor Res. Report 7-801-24, Jan. (1963).
14. N. Herlofson, "Plasma Resonances in Ionospheric Irregularities" Arkiv för Fysik 3, 247 (1951).

15. J.C. Hickel, J.V. Parker, R.W. Gould, "Resonance Oscillations in a hot Non-Uniform Plasma Column", Phys. Rev. Lett. 11, 183 Sept. (1963).
16. A. Dattner, "Experiments on Plasma Resonance", Ericsson Technics 19, 1 (1963).
17. E.R. Billam, I.C. Browne, "Characteristics of Radio Echoes from Meteor Trails IV : Polarization Effects", Proc. Phys. Soc. B69, 98 (1956).
18. P. Beckmann, "New Approach to the Problem of Reflection from a Rough Surface", Acta Technica CSAV 2, 311 (1957).
19. D.K. Bailey, R. Bateman, R.C. Kirby, "Radio Transmission at VHF by Scattering and other Processes in the Lower Ionosphere" Proc. IRE 43, 1181 (1955).
20. B. Franzen, W. Fuchs, "Use of the Corona Discharge for Measurements of Turbulence", Proc. IV Intl. Conf. on Ionization Phenomena in Gases, North Holland, Amsterdam (1960).

THE SPIN-DROP METHOD OF MEASURING
MODEL RADAR CROSS SECTION

Peter C. Fritsch

Lincoln Laboratory,*

Massachusetts Institute of Technology

The common and time-honored method of measuring radar cross section on static ranges involves the positioning of the test object ("model") by means of some mechanical support. Typical examples in the past have included styrofoam or other plastic columns or cantilevers, nylon or dacron dielectric strings and even metallic structures "shielded" by microwave absorber. By these means the model is ultimately connected mechanically to the ground, often through a rotating or other positioning mechanism, or to the ceiling of the room, or to support towers of some sort or other.

It has long been realized that these supports are apt to have an undesirable effect on the test results, for they tend to modify both the incident field and the reflected field. In the case of rigid supports, their backscatter cross section can be measured directly; if the latter approaches the cross section of the test object, one will naturally view the results of any measurements with scepticism. In the case of supports which are held in place by the model to which they are attached, even this crude evaluation appears to be precluded. In any case, measuring the perturbation of the reflected field (which is likely to include multiple-bounce effects) seems to us impossible.

The principle of the solution is clear: since supports are bothersome, they must be done away with altogether. The immediate implication is that the model must consequently be in free fall during the measurement. There are many ways in which this principle could be implemented, including some in which forces are imparted to the model before radar measurements are started, in such a way as to minimize or cancel displacement of the model. Examples which have received consideration include tossing the model upward, in order to make the measurement when zero velocity is reached at the apogee of the trajectory, and balancing the force of gravity by a magnetic field, or some other force field. We have chosen to let the model fall as dictated by gravity imparting to it simultaneously a mechanical torque so as to make the model spin about the trajectory (Fig. 1). The principal purpose of the spin is to let the radar "see" a rapid succession of aspect angles; however, it is believed that the spin also tends to stabilize the object through a gyroscopic effect. For reasons now apparent, we have dubbed this particular free-fall technique of radar reflectivity measurement the "Spin-Drop" method.

The spin-drop principle has been implemented in our laboratory by

*Operated with support from the U. S. Air Force.

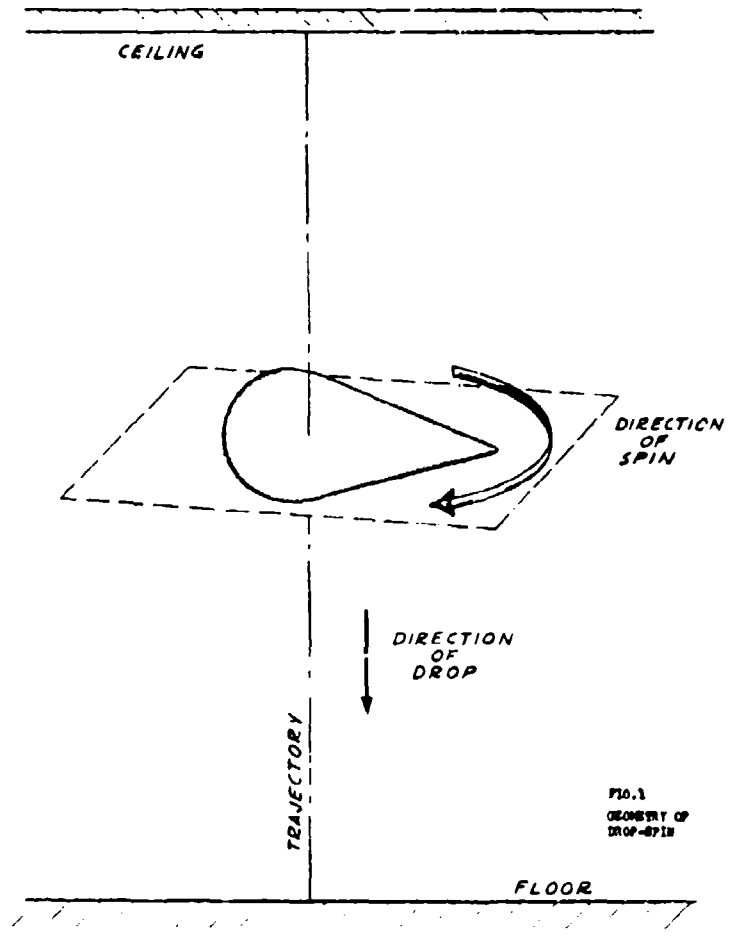


FIG. 1
GEOMETRY OF
DROP-SPIN

attaching a drill press to the ceiling of the room. A face plate attached to the spindle carries a cradle particularly made for a specific model (Fig. 2). A rubber band slung beneath the model holds it firmly in place pressed against the cradle. After the spindle of the drill press has reached full speed (2000 r.p.m., in our case), the rubber band is released and the model falls, spinning about its center of gravity, into a box filled with shock-absorbing material.

To date, we have dropped several models up to 8 inches in length and several pounds in weight. Multiple flash exposures taken against background of vertical strings (Fig. 3) show that the axis of the model stays within 1° of horizontal throughout the drop. Frames from a high-speed motion picture (Fig. 4) further prove that the model separates from the cradle in a clean fashion.

In order to insure that the model drop straight down, instead of following an unpredictable path to the possible detriment of men and machine, it has been found necessary to balance the rotating mass (face plate, cradle, and model all together) accurately. This is accomplished with the aid of a balancing machine (Fig. 5) capable of indicating imbalance to 0.01 inch-ounce. Balancing is then accomplished by motion of the cradle containing the model relative to the face plate, and by adjusting movable weights within the face plate assembly.

The distance through which the model falls is about ten feet; the antenna beam of a K_u -band c.w. radar is pointed so as to intersect this vertical trajectory half-way down. The beam-width in the plane of the trajectory is about one foot; this then determines the rotational speed required in order that the model make at least one revolution within the beam. A rotational speed of 2000 rpm corresponds to a period of approximately 30 milliseconds per revolution; an 8 inch long object at a wavelength of $1/3$ inch is about 25 wavelengths long, hence its sidelobes will be of the order of one degree wide. Assuming that one cycle of bandwidth suffices to reproduce one such lobe, the recording bandwidth required is approximately 360 cycles per 30 milliseconds, or 10 kc. Two or more cycles of bandwidth per sidelobe will yield correspondingly finer data, hence 20 or 30 kc of bandwidth are to be preferred.

Such recording bandwidths are near the upper frequency limit of oscillographs (e.g., Minneapolis-Honeywell Visicorder), and while these were used at first (Fig. 6), we have more recently used direct oscilloscope photography (Fig. 7) and analog tape recording. In the first instance, a photoelectric circuit was set up so that its light beam was interrupted by the falling model a known distance above the antenna beam. This triggered a delayed sweep (Tektronix oscilloscope Model 545) which was photographed by a Polaroid camera. The photographs shown in Fig. 7 were so obtained; they represent (a) the low cross section region of a sphere-cone, and (b) a series of traces produced by dropping a sphere through the antenna beam;



Figure 2. View of Drop-spin Apparatus Mounted Below Ceiling

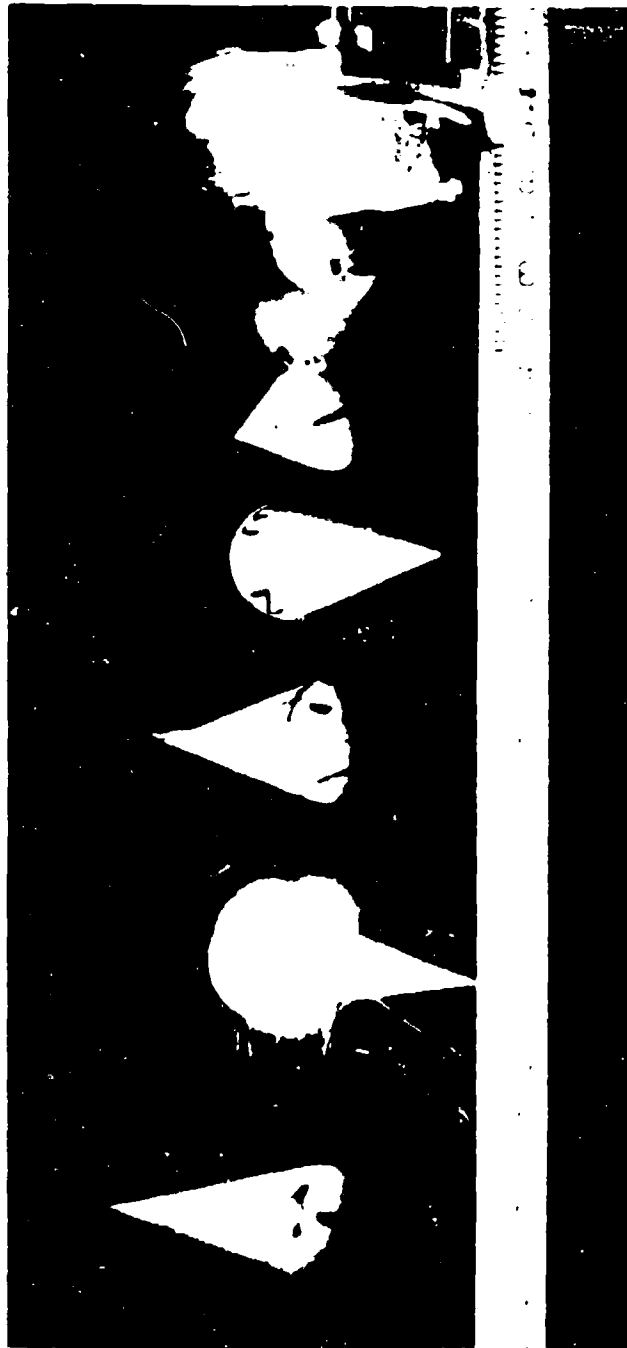


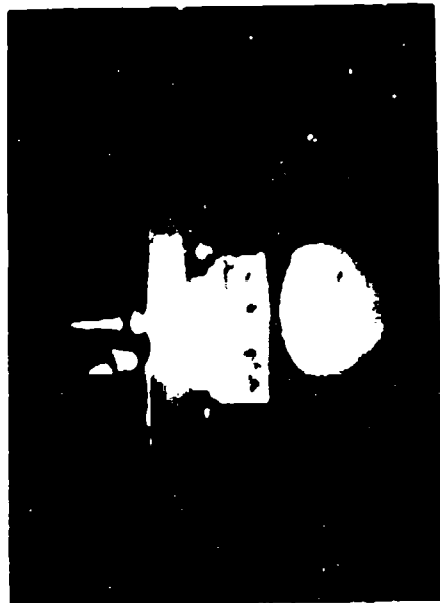
Figure 3. Multiple-flash Photo of Model During Spin-drop



FRAME



FRAME



FRAME



FRAME

Figure 4. Four Frames from High-speed Movie Showing Launch Phase of Spin-drop.

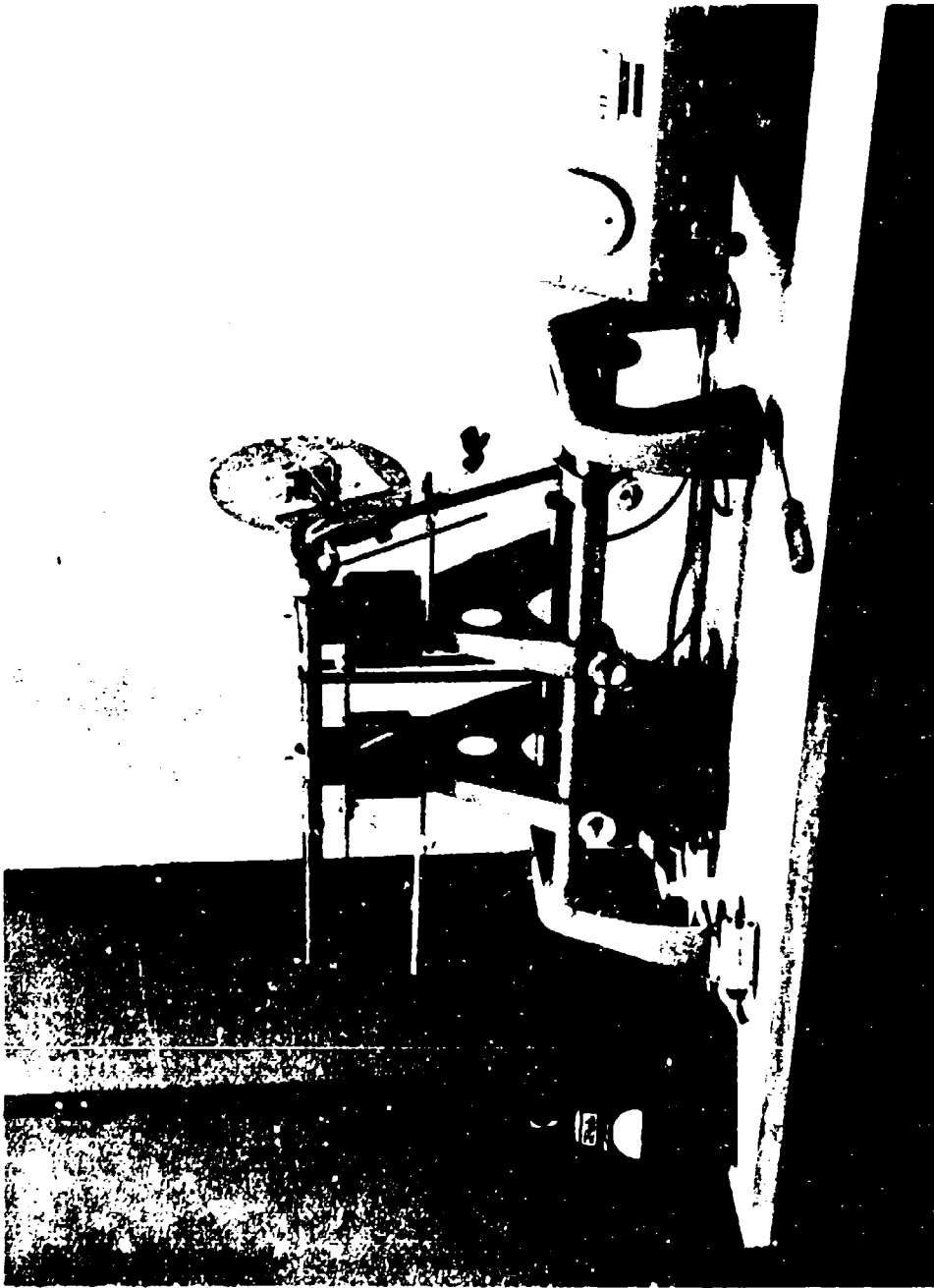


Figure 5. Balancing Machine with Face Plate and Model in Place

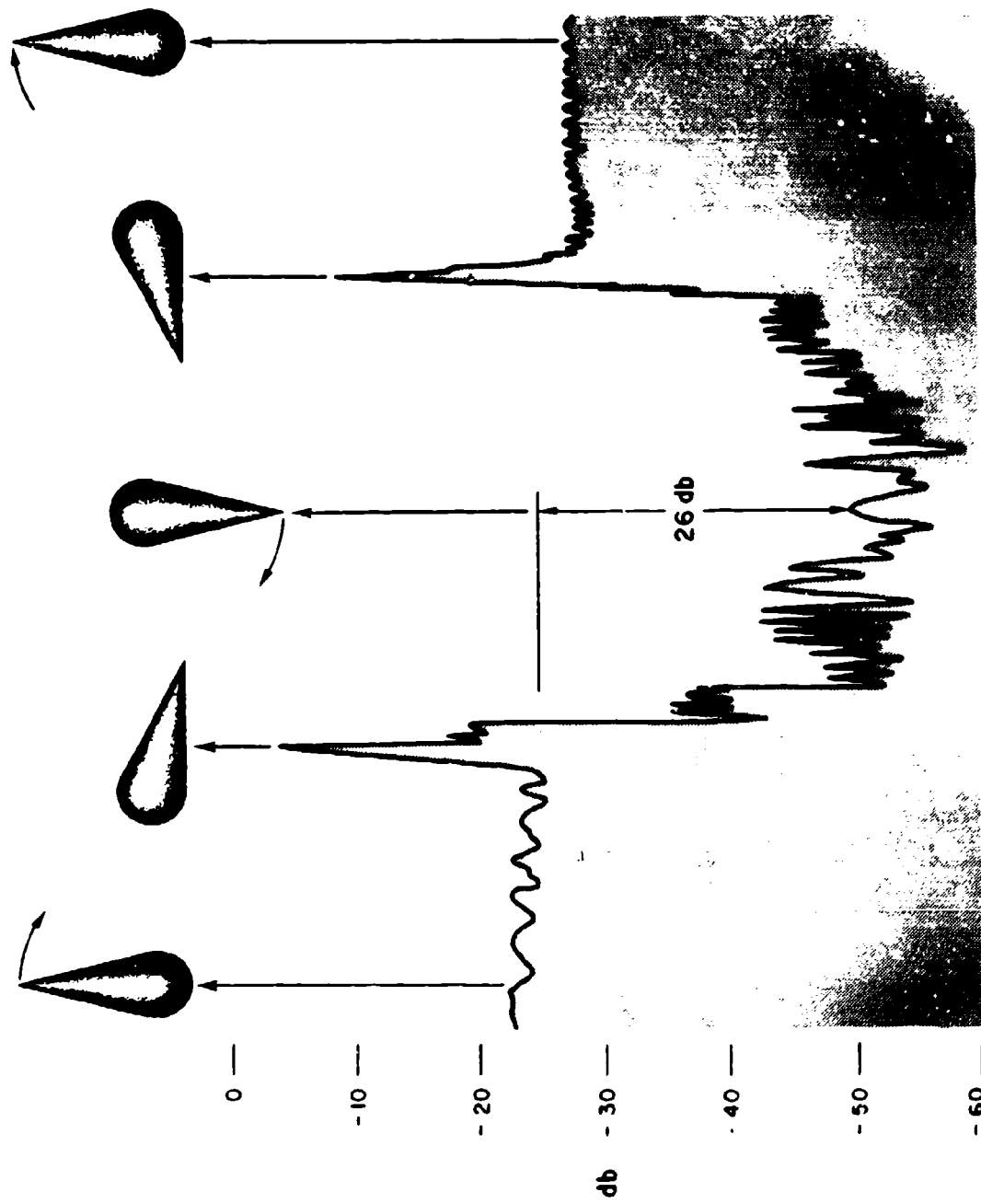


Figure 6. Redrawn Trace of Drop-spin Result (Original Drawn by Oscillograph)

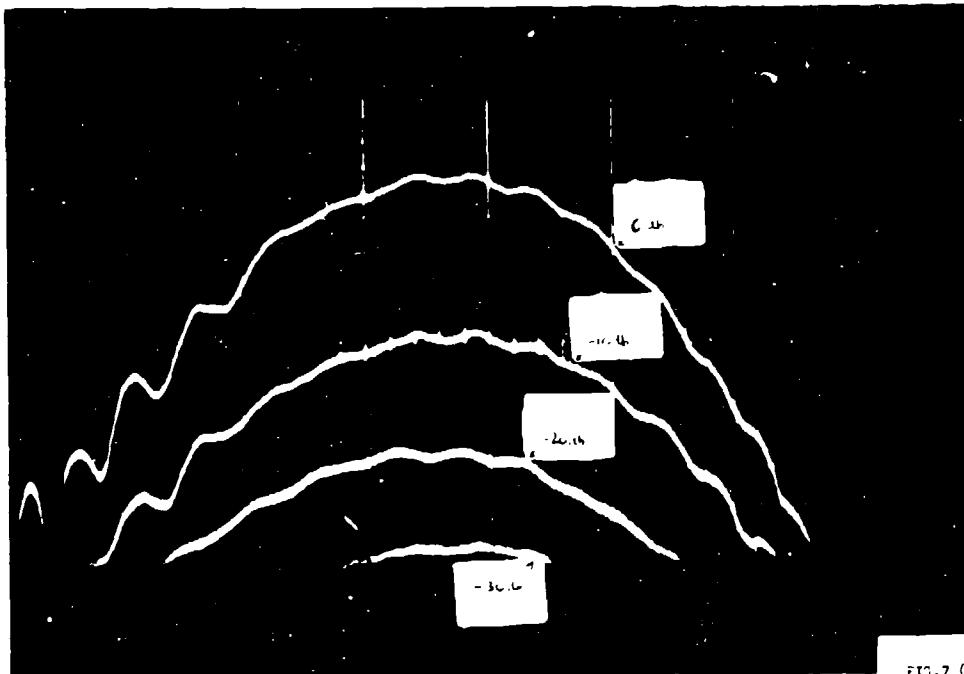


FIG. 7 (a)

OSCILLOSCOPE PHOTO
OF DROP-SPIN RESULT
(SPHERE WITH 0.10
20,30 ATTENUATION)

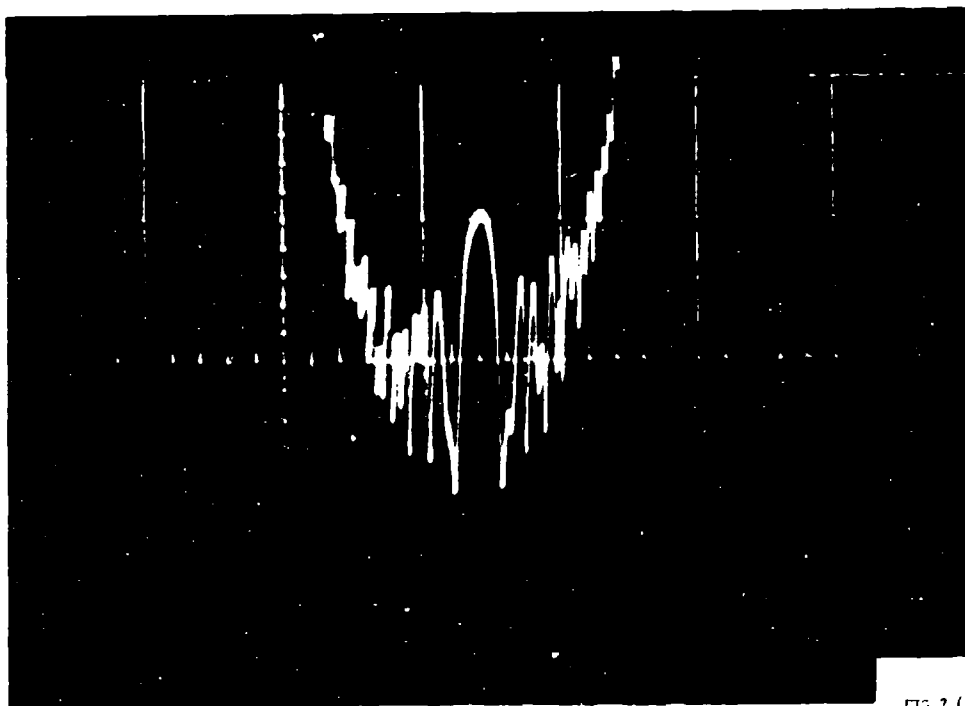


FIG. 7 (b)

OSCILLOSCOPE PHOTO
OF DROP-SPIN RESULT
(SPHERE-CONE)
for vert. scale, see

the sphere in question had a backscatter cross section of one square wavelength, the successive traces being produced by inserting 10, 20, and 30 db of attenuation ahead of the receiver. The amplitude calibration can thus be seen to be about 10 db per square (one centimeter in the original size photo); the sweep speed was 5 milliseconds per square (centimeter). We have recently constructed a device which will store several spheres and drop them, one by one, on command, as a convenience for rapid amplitude calibration. Angular calibration is less easy, and in fact, we have not faced up to it since it seems relatively unimportant. For the time being, we have contented ourselves with assuming that uniform angular speed permits uniform division of one cycle of rotation into 360 degrees.

Another recording method, and one which appears to be the most flexible, has been by use of a Consolidated Electrodynamics Corporation Model PR 3300 FM magnetic tape recorder. The wide range of available tape speeds can be used to record at high speed, to play back later at reduced speed into a relatively narrow-band graphic recorder. We have used tape speeds of 60 and 1-7/8 inches per second to obtain reasonably satisfactory traces on a Sanborn strip chart recorder, which has an upper cutoff frequency about 100 cps. By repeating the recording/playback process, multiplying the tape speed step-down ratios each time, one could perhaps eventually obtain data in a form suitable for a very narrow band recorder.

All our experiments with spin-drop to date have been carried out using a K_u band C.W. radar. While no nearby supports now interfere with the scattering from the model, other more distant objects, such as the walls of the anechoic chamber, continue to obtrude as before. To further isolate the model from such effects, it is necessary to employ a measuring instrument capable of discriminating against the background, such as a pulsed radar. We consequently plan to attempt spin-drop measurements soon with the use of a K_u band pulsed coherent radar. And finally, as models grow in size and weight, future mechanical improvements will become necessary, especially in redesigning the model release mechanism.

Thanks are due to Messrs. W. C. Erwin, F. B. Magurn, D. F. Sedivec, and D. G. Stuart who have all contributed materially to the development described.

A METHOD OF MEASURING SMALL RADAR CROSS SECTIONS BY
DIGITAL VECTOR-FIELD SUBTRACTION

F. E. Heart and P. C. Fritsch

Lincoln Laboratory,*

Massachusetts Institute of Technology

The measurement of very small radar cross sections is limited by receiver noise, amplitude and phase stability of the radar, background level, and by unwanted cross section contributions from target support structures. Most notable, and hardest to deal with, of these contributions is the effect of the target support structure.

Often, the cross section of these supports is sufficiently high to completely mask the low cross section region of the target. Because of this effect, it becomes increasingly difficult to properly evaluate target shapes and nearly impossible to further reduce the cross section of these shapes experimentally. An additional unwanted contribution is the effect of support coupling. The target under test may couple to the column if a significant portion of the target surface comes in contact with the column, and the coupling will tend to increase as the dielectric constant of the column material becomes higher.

If the coupling between the support and the target has negligible effect on the cross section of the target, then it should be feasible to measure the amplitude and phase of the return of the column, and separately that of column plus target, subtract the fields, and thereby obtain what would be the return of the target in the absence of a supporting structure. With this technique, the necessity of reducing the cross section of the supporting structure is somewhat decreased, allowing the measurement of larger and heavier low cross section targets. The foregoing idea has been implemented at Lincoln Laboratory; as a result, we have obtained a substantial reduction in the interference contribution of the support structure. First, the support structure is rotated through a full revolution, and a digital recording is made of the amplitude and phase of the reflected energy as a function of support structure azimuth. Then the experiment is repeated with the target in place on the support structure. The two recordings are then processed in a digital computer to obtain the vector difference as a function of azimuth. This process provides a substantial increase in the ability to measure true target phase and amplitude as a function of azimuth. A secondary benefit of this approach is the convenience of digital processing to obtain output presentations of the data in more useful forms.

The experimental system is illustrated in Fig. 1. A shaft encoder was installed on the rotatable support turntable of the backscatter range, Fig. 2, equipped with a phase-locked C.W. K_a -band radar. Azimuth from the

*Operated with support from the U. S. Air Force.

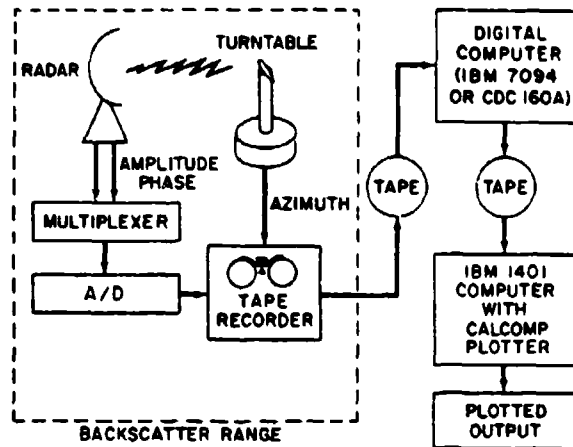


Fig. 1. Schematic of Apparatus Used for Vector-Field Subtraction Method

turntable, along with amplitude and phase from the radar, are recorded on a slow-speed, IBM-format, digital magnetic tape recorder. Amplitude and phase are sampled approximately 50 times per second, and azimuth is sampled approximately 10 times per second. When the support structure rotates at 1 rpm, data is obtained at approximately 1/10 degree intervals of turntable azimuth. Experimental vector subtraction programs were written for the IBM 7094 computer and the CDC-160A computer. Computer outputs were obtained on an intermediate magnetic tape, and these results were then plotted by use of a Calcomp plotter driven by an IBM 1401 computer. The experimental implementation employed several stages in order to make use of the existing laboratory computational facilities; if this technique were to be used on a routine basis, a more natural thing might be to employ a computer and a plotter connected in real time to the backscatter range.

At K_u -band, low cross section shapes commonly exhibit RCS of -10 to -20 $\text{db}\lambda^2$.* It is generally accepted that the target cross section should be approximately 20 db higher than the radar return of the support structure for good evaluation of the target characteristics. This means that the support structure return should be at least -30 $\text{db}\lambda^2$ in the low cross section region of the target under test.

Figure 3 presents an illustration of the type of preliminary results obtained. Figure 3(a) shows the cross section of a styrofoam column as a function of azimuth; Figure 3(b) represents the cross section of a sphere-cone (cone half-angle = 15° , $k_a = 17.35$) as measured with this model emplaced atop that column. Note how the low cross section region of the model is totally masked by the return from the column. (The phase angle corresponding to the above amplitude records was also measured but is not displayed here.) After the vector subtraction described earlier had been

* (i.e., 10 to 20 db below $\sigma = \lambda^2$).



Fig. 2. View of K_q Band Radar and Auxil. Equipment

performed, the results shown in Fig. 3(c) were obtained. Observe here the relative symmetry of the function, and the fact that the amplitude of the critical nose-on region of the model now lies 10 to 20 decibels below the amplitude of the column. The resultant phase (after vector subtraction) is shown in Fig. 3(d). Observe here also the relative symmetry of the net phase result. This symmetry, however, will prevail only if the target is placed symmetrically within the illuminating field, and only if the axis of azimuth rotation lies in the plane of symmetry of the target.

That such promising results have been obtained at millimeter wavelengths, where even very small mechanical deflections (e.g., of the column) will cause relatively large errors in phase measurement, leads us to believe this method will be even more profitable to apply at lower frequencies. This, in turn, suggests that the digital subtraction method of low radar cross section measurement may be most useful for large objects measured at the lower frequencies, typically a task of full-scale reflectivity ranges. Measurements results are also expected to be improved by the use of pulse instead of C.W. methods in order to be able to gate out unwanted returns of objects other than the column.

The aid rendered by A. J. Yakutis and E. J. Peters in the instrumentation area, W. R. Crowther and O. V. Fortier in the computer programming, and D. F. Sedivec in both, is gratefully acknowledged.

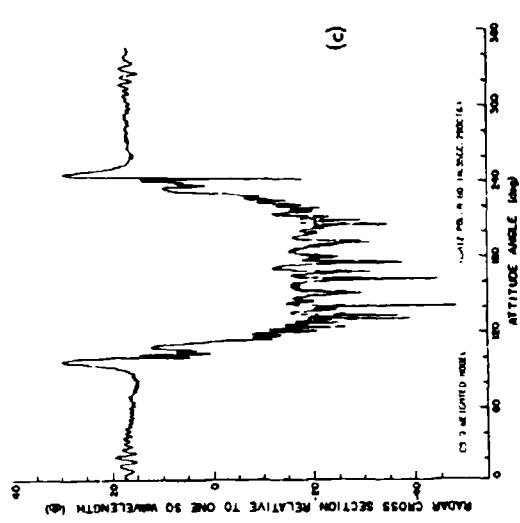
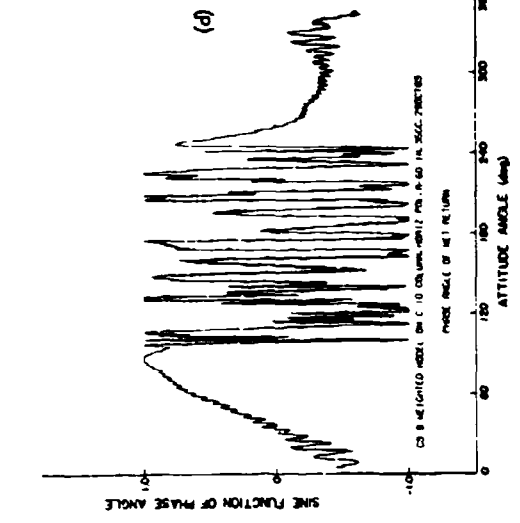
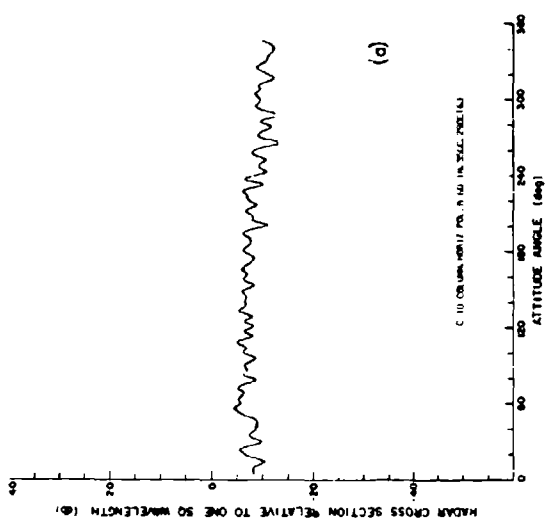
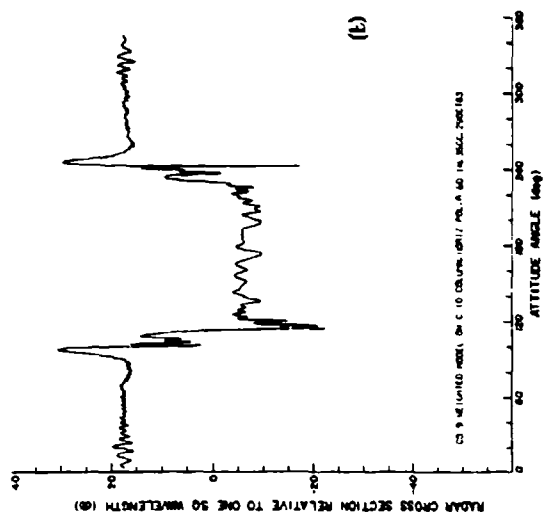


Fig. 3. Plots of:
 (a) Amplitude of Column vs. Azimuth
 (b) Amplitude of Column plus Model vs. Azimuth
 (c) Calculated Amplitude of Model
 (d) Calculated Phase of Model

RADAR CROSS-SECTION MODEL FABRICATION AT CORNELL AERONAUTICAL LABORATORY

John E. Hopkins
Cornell Aeronautical Laboratory, Inc.
Buffalo, New York 14221

ABSTRACT

Problems and techniques of model fabrication are discussed. The need for lightweight models to permit using supports with small radar reflection is noted. The merits of wooden models are mentioned, and precautions which must be taken in working with these models are presented.

INTRODUCTION

The Cornell Aeronautical Laboratory indoor cross-section ranges operate in the X and K_a bands and are used primarily for making measurements on scaled models. If the measurements are to indicate accurately the results which can be expected on full-scale targets, it is necessary that all significant target characteristics be preserved in the design and fabrication of the scaled models. This paper provides a brief review of the model construction materials and practice which have been examined and used at this Laboratory.

Model Requirements

Two factors have been found of prime importance in modeling practice. One of these factors is model cost, since the expenditure on models of the more elaborate targets may exceed all other costs of an experimental program. The other factor is model weight, which must be kept low for targets with small radar cross-section.

The interrelation between model weight and observable radar cross-section arises through need for minimizing radar scattering by the target support. The support which has proven most satisfactory at the Cornell Aeronautical Laboratory consists of two or more thin dielectric strings. The radar cross section of these strings causes unwanted signal to interfere with the target signal. The unwanted signal is approximately proportional to the fourth power of string diameter.^{*} The strength varies with the square of diameter, so that the reduction in support interference which can be obtained by reducing model weight and thus both tensile strength and string diameter is evident.

^{*}The fourth power relationship is predicted theoretically. Experimental studies have yielded an exponent of 3.86.

Materials for Handling

Early versions of lightweight models were made using solid aluminum, which has a density of about 0.1 pound/inch³. As improvements in equipment capability permitted the reliable measurement of smaller radar cross-section, the need for more delicate support mechanisms became apparent. Models were lightened somewhat by using magnesium (approximately 0.066 pound/inch³) and, where external model contour allowed it by internal hollowing. Hollow magnesium models generally weigh from one-third to one-half as much as their solid aluminum equivalents.

Several techniques for constructing still higher models were then studied. These included the use of foamed plastics and of molded plastic shells. The models subsequently were covered with highly conductive silver paint. Although such techniques offer promise of future development, we have not found them fully satisfactory and they have not as yet been generally employed at CAL.

Machined balsa wood was also tried for model construction. It was found that its grain texture is not well suited to the precision machining commonly required. Furthermore, balsa wood is not dimensionally stable and the conductive silver coating frequently cracks when subjected to varying temperature and moisture conditions.

The material finally chosen and currently being used for the construction of models is well cured, close-grained white pine. Other woods have not been investigated since white pine, which is commonly used for pattern material, has been found to be fairly stable, relatively easy to machine, inexpensive and readily available.

For the construction of very small models and of model appendages, aluminum is a satisfactory material. Aluminum or magnesium is also used generally when it is necessary to cover conducting surfaces with materials having special physical properties such as dielectric coatings, etc.

Method of Fabrication

Wooden models are generally constructed of a laminate in order to minimize tendencies toward warpage and splitting. Initial machining results in a slightly oversize model, the surface of which is then thoroughly impregnated with a lacquer sealer. The sealer serves the dual purpose of improving the wood stability and of providing a better surface for final machining. After final machining, an automobile sanding surface lacquer is applied which gives the model a hard finish. The latter is then carefully sanded to produce an extremely smooth surface. Finally, the model is sprayed with highly conductive silver paint. This paint is applied in several thin coats in order to assure uniformity as well as maximum surface conductivity.

Precautions

Certain precautions in handling these models are necessary. Care must be taken not to rub off any of the conductive surface. Also, wooden models are much more subject to surface denting, than are those made of metal. On the other hand, if such damage does occur, the wooden model can be repaired much more easily.

Prolonged storage of the wooden models and/or subjecting them to relatively large changes in ambient temperature is very likely to result in the occurrence of hairline cracks in the conductive surfaces.

The presence of even very minute surface discontinuities must be avoided, especially where a dielectric (wood, plastic, etc.) is the material used for construction of the model base. If such discontinuities do exist, then the non-metallic medium inside the metallic surface can be excited by energy radiated through the cracks. The reradiation which may then result is likely to give a significant contribution to the observed radar cross section. In order to illustrate this point, two examples from our own experience are worth noting.

In the first instance, the target was a smooth, symmetrical body normally having a "nose-on" cross section of about $10^{-0.7} \lambda^2$ and a minimum value of the cross section envelope of about $10^{-2.5} \lambda^2$ between the nose-on and specular aspects. When a hole .040 inch diameter was deliberately introduced in one side of this body, the minimum value of the cross section envelope between nose-on and specular aspects on that side of the body increased by 13 db to about $10^{-1.2} \lambda^2$.

In a second case, a body having an original radar cross section of approximately λ^2 at X-band was observed, after fairly prolonged storage, to have developed fine crazing marks, less than .005 inches wide. A measurement of the body in this condition was compared to a measurement taken after the surface had again been prepared carefully to be continuously conductive. Differences in the cross section of at least 10 db were observed.

The presence of these discontinuities is therefore unacceptable and it is desirable to keep the models in a constant temperature, constant humidity environment to minimize crazing. Even when such care is taken, it is advisable in the case of a model which has been stored for some time to perform the relatively inexpensive precautionary task of refinishing the conductive surface.

Because of the relative ease in handling of wood, the method of model construction just described has been found economically attractive even in cases of relatively high cross-section targets where close weight control is not particularly essential.

SUMMARY

For modeling targets of small radar cross section and of appreciable physical size, the experience at Cornell Aeronautical Laboratory has shown that wooden models painted with conducting silver paint are satisfactory. They combine light weight with economy in fabrication. The wooden models must be treated and stored with some care and must be refinished occasionally. The effect of maltreatment or careless storage may be to damage the skin of the model, which can have major effect on the radar cross section.

METAL-SPRAYED FIBERGLAS RADAR TARGET MODELS

Forest M. Hudson
Senior Engineering Designer
Hughes Aircraft Company
Radar Division
Fullerton, California

INTRODUCTION

In January, 1962 Hughes Aircraft Company became actively engaged in performing ultra-short pulse radar signature measurement studies. Among the radar target models of various geometries which were required for the measurement programs, five were comparatively large and complex in shape (see Figures 1 through 4). A major requirement was to produce these targets at minimum cost while maintaining desired electrical and mechanical specifications. This paper covers the design approach and the subsequent solution to the problem.

SPECIFIC REQUIREMENTS

During the signature studies, the targets were to be suspended in the radar test range from a single point located at their linear centers. This scheme would permit positioning at any specific aspect angle with respect to the radar antenna boresight line. The targets were to be held in position by means of a system of three or four light (0.03 inch diameter) Dacron stabilization lines which would run from the target to a tiedown circle on the ground. The circle would have 360 anchor points spaced at 1-degree increments.

The targets were required to be of minimum weight so that the size of the lines used for target suspension and positioning would exhibit the smallest possible radar cross section. Another requirement was to obtain a metal surface with a maximum resistivity of 5 micro-ohms per cubic centimeter. It was also necessary that the metal surface be as free as possible of electrical discontinuities. The size of holes for attaching the suspension elements was correspondingly held to a minimum.

FLAME METAL-SPRAYING

The key to the choice of a structural material for the targets was the flame metal-spraying process used in other areas of industry, but not widely employed in the field of electronics. Flame metal-spraying makes possible the use of many low cost nonmetals such as glass, paper, plastics, etc., in applications where conductivity or electrical reflectivity of metallic surfaces are required. Of particular interest for this application were the versatile and easily fabricated plastic fiberglass laminates.



Figure 1. 2-Foot Diameter Sphere



Figure 2. 32-Inch Truncated Cone



Figure 3. Spherically Truncated Cone Approximately 8 Feet Long (Target has three interchangeable tips of different point radii)

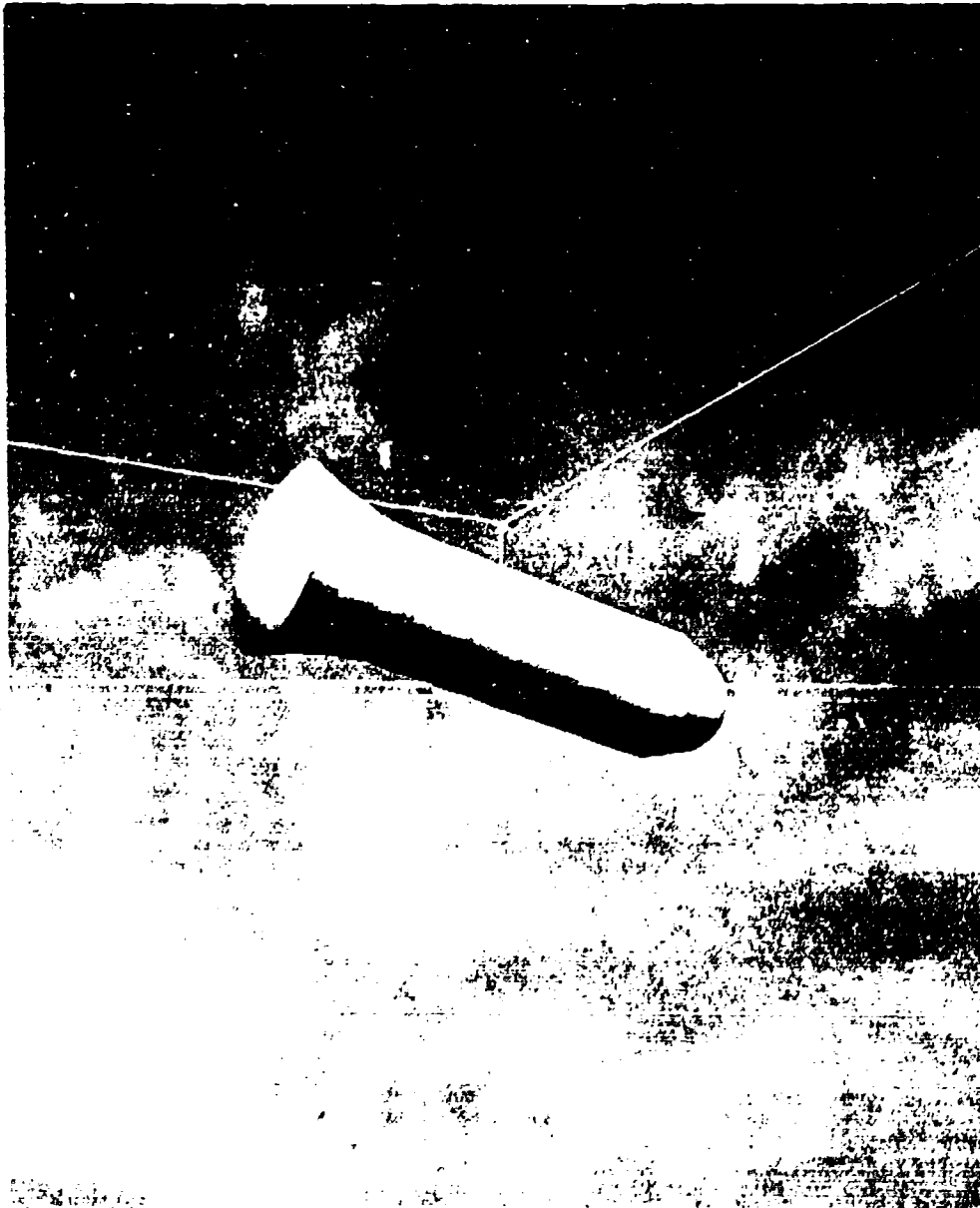


Figure 4. Signature Model Approximately 12 Feet Long

Spraying Process

The flame metal-spraying process is a means by which metal powders or wire are atomized in an oxy-acetylene flame and sprayed by compressed air onto the receiving surface in much the same way as paint is sprayed.

Sandblasting is usually employed to provide a rough and clean surface to facilitate film adhesion. The metal droplets flatten when striking the surface, and interlock with irregularities of the base material and with each other. Heat produced by the molten droplets is quickly dissipated by the compressed air due to the low mass of material involved (proper spraying techniques permit some metals to be sprayed directly onto the human hand without causing discomfort). The costs for metal-sprayed surfaces range from \$0.05 to \$0.20 per mil, per square foot.

Electrical Properties of Sprayed Metal Surfaces

The conductivity of the sprayed metal surface is largely dependent on film thickness and the spraying technique. Too much heat increases the oxides content of the film, thereby reducing conductivity; too little heat gives the film poor mechanical properties. Using a spraying technique with optimum heating, a 3-mil thick aluminum film will exhibit a conductivity 80 to 90% of that characteristic of the basic metal.

Experimental investigation reveals that samples with a film of approximately 3-mil average thickness and approximately 90% surface coverage reflect 99% of incident energy. Radar cross section measurements revealed that the measured cross section of a 2-foot diameter metal-sprayed sphere compared favorably with the theoretical cross section calculations within a ± 1 db measurement tolerance.

FIBERGLAS PLASTIC LAMINATES

It can be seen that flame metal-spraying makes available a broad selection of structural nonmetals for the construction of radar targets. Epoxy-based fiberglass has a higher strength-to-weight ratio than that of aluminum, and in many cases costs less to fabricate, particularly in the case of compound curved surfaces. In addition, the method avoids surface discontinuities such as the welded seams or fasteners required in sheet metal fabrication.

Other advantages include resistance of the materials to corrosion, and (although the surface is inherently dent-proof and mar-proof) easy and cheap repair of damage.

FIBERGLAS FABRICATION

Fiberglas products are fabricated in many ways, ranging from hand lay-up, through methods in which the materials are sprayed, to the complex filament winding processes. By far the simplest and cheapest method for most requirements is the hand lay-up process, which employs an epoxy resin that cures at room temperature.

Although only one target of any given type was required for this program, the method allows any number of copies of a particular shape to be produced from the same molds. A master pattern of the desired target shape was first constructed; a wooden framework covered with wire cloth on which casting plaster could be applied to obtain the finished shape was satisfactory for most cases. If a target were symmetrical about an axis, the master pattern could be shaped by turning against a profiling tool.

Castings were taken from the master pattern, providing negative molds in which the fiberglas was subsequently laminated. Ribs and stringers were installed for strength as required. (Such members can be made of any structural material such as wood or metal, or can be formed of fiberglas.)

Hardware required for suspension or handling was molded into the target parts where necessary. Weights were installed in some of the targets to move the center of gravity into conjunction with the linear center, so that a level attitude would be achieved when the target was suspended in the test range.

Target parts were assembled and joined with additional resin and fiberglas. The finished seams resulted in smooth, unbroken surfaces. Corrections to exact tolerances were easily made by building up or removing fiberglas and resin in the pertinent areas.

COST COMPARISON

The costs involved in the fabrication of equivalent fiberglas and aluminum targets are exemplified by a spherically terminated cone approximately 12 feet long, and 8 feet at its greatest diameter. Sphericity tolerances were ± 0.06 inch for the large end and ± 0.03 inch for the small end. Tolerance for the length and major diameter of the cone was ± 0.06 inch. (As a basis for tolerance comparison, $1/16$ wavelength at 5 kilomegacycles, C-band, is 0.147 inch.)

The cost of the fiberglas tooling, including master pattern and castings, was \$1450.00. Material costs were approximately \$830.00, and labor was \$1400.00. The total cost of the completed target thus was \$3680.00.

The same target fabricated from aluminum would have consisted of a welded internal framework of extruded aluminum ribs and stringers. The spherical surfaces would have been spun from aluminum sheet, and the conical surfaces would have been aluminum sheet riveted to the internal framework. The spherical ends would have been welded onto the conical surface, and all seams and rivets of the target would have been welded and ground. The estimated fabrication costs for the aluminum target are as follows:

Small spherical end (spinning)	Material	\$ 60.00
	Tooling	480.00
	Labor	320.00
Large spherical end (spinning)	Material	100.00
	Tooling	3200.00
	Labor	800.00
Internal structure	Material	200.00
	Labor	1600.00
Skin for cone	Material	320.00
	Labor	1200.00
Total		<u>\$8280.00</u>

The total cost for the aluminum target does not reflect a possible additional \$800.00 to \$1000.00 for hand rework labor due to distortion of the skin during the welding processes.

CONCLUSION

The five targets required for the signature study program were successfully fabricated at a relatively low cost with the metal-sprayed fiberglass process. All targets were produced within tolerances similar to those of the cost comparison example. The following tabulation shows the targets that were made and the production cost of each.

<u>Target</u>	<u>Cost, \$</u>
2-foot diameter sphere (Figure 1)	335.00
32-inch truncated cone (Figure 2)	415.00
8-foot spherically terminated cone, including three interchangeable tips (Figure 3)	981.00
12-foot signature model (Figure 4)	2600.00

ANTENNA SCATTERING MEASUREMENTS*

D. L. Moffatt
Research Associate
Antenna Laboratory
Department of Electrical Engineering
The Ohio State University
Columbus, Ohio 43210

INTRODUCTION

It is sometimes required that one experimentally obtain the monostatic or bistatic echoing area of loaded scatterers, i. e., targets which have one or more pairs of terminals with associated loads. Often such measurements are desirably if not necessarily made using modelled targets. The purpose of this paper is to present systematic measurement procedures developed at The Ohio State University Antenna Laboratory for the evaluation of the scattering properties of such targets. The interpretation of model measurements is described, but the measurement procedures given are equally applicable to modelled or full scale targets. We restrict ourselves to a scatterer with a single pair of terminals located on a transmission line supporting a single propagating mode.

ANTENNA SCATTERING

A basic expression for the field scattered by a loaded target as a function of its load impedance has been developed by a number of authors.^{1,2,3,4} These results show that, in general, knowledge of the transmitting and receiving properties of the target are not sufficient to predict the scattered field. Usually additional information such as the scattered field for an open or short-circuited load is required. The form of this expression which we have found to be most useful was developed by Green⁵

$$(1) \quad E^S(\theta, \phi, Z_L) = A(\theta, \phi) + B(\theta, \phi) \Gamma(Z_L),$$

* The work reported in this paper was supported in part by Contract AF 33(616)-8039 between Air Force Avionics Laboratory, Research Technology Division, Wright-Patterson Air Force Base, Ohio and The Ohio State University Research Foundation.

where θ and ϕ are spherical coordinates defining the direction of the scattered field, $Z_l = R_l + j X_l$ is the load impedance, $Z_a = R_a + j X_a$ is the input impedance and the modified current reflection coefficient is given by

$$(2) \quad \Gamma(Z_l) = \frac{Z_a^* - Z_l}{Z_a + Z_l}$$

The asterisk (*) denotes complex conjugate. Equation (1) holds for a single component of the scattered field and for a fixed frequency, polarization, and aspect of the incident field. The terminal plane is on a transmission line supporting a single propagating mode so that the input impedance (Z_a) and load impedance (Z_l) may be uniquely defined. Equation (1) separates the scattered field into a component independent of the load impedance ($A(\theta, \phi)$) and a component dependent on the load impedance ($B(\theta, \phi) \Gamma(Z_l)$). It is evident that

$$(3) \quad A(\theta, \phi) = E^s(\theta, \phi, Z_a^*) = \frac{1}{2} [E^s(\theta, \phi, -jX_a) + E^s(\theta, \phi, j\infty)] ,$$

and

$$(4) \quad B(\theta, \phi) = \frac{1}{2} [E^s(\theta, \phi, -jX_a) - E^s(\theta, \phi, j\infty)] .$$

It is also possible to express $B(\theta, \phi)$ in terms of antenna parameters⁵

$$(5) \quad B(\theta, \phi) = \frac{-j\omega\mu}{8\pi R_a} \text{hr}(\theta, \phi) (\underline{\text{hr}} \cdot \underline{E}^i) \frac{e^{-j\beta R}}{R} ,$$

where \underline{E}^i is the incident field, $\underline{\text{hr}}$ the vector height and hr a scalar component of $\underline{\text{hr}}$. Equation (5) demonstrates that the load dependent component of the scattered field has the same pattern as the transmitting pattern of the antenna.

For a fixed direction of the scattered field (θ_0, ϕ_0), the variation of the scattered field with load impedance may be graphically represented conveniently on a Smith chart. Normalizing Eq. (1) by $B(\theta_0, \phi_0)$,

$$(6) \quad \frac{E^s(\theta_0, \phi_0, Z_L)}{B(\theta_0, \phi_0)} = \frac{A(\theta_0, \phi_0)}{B(\theta_0, \phi_0)} + \Gamma(Z_L) \quad .$$

Referring to Fig. 1 (coordinates u, v in Fig. 1 will be utilized later), the scattered field as a function of load impedance is proportional to the distance yx , where y_0 is a vector representing the load independent component $= A(\theta_0, \phi_0)/B(\theta_0, \phi_0)$ and ox is the modified reflection coefficient $= \Gamma$. The relative phase of the scattered field is given by the angle oyx . For an arbitrary scatterer, the point y may lie inside, outside, or on the rim of the chart. For passive loads, $|\Gamma|$ is always ≤ 1 . Thus point x for passive loads is always inside or on the rim of the chart. As the load Z_L is varied, y_0 remains fixed and x wanders over the interior (lossy loads) and rim (reactive loads) of the chart. The corresponding changes in yx and angle oyx yield the change in amplitude and phase of the scattered field.

ANTENNA MODELS

A diagram of a receiving antenna is shown in Fig. 2a. Region I is the ambient medium surrounding the antenna, region II is a transition from free space to a transmission line, i. e., the antenna. Region III is a transmission line on which a single mode propagates and region IV is an ideal load. As shown in Fig. 2a, Eq. (1) may be used at any terminal plane defined in region III.

Suppose a second antenna was constructed which was intended to be either a practical geometrical model (same ambient medium in model and prototype) or a full scale duplicate of the antenna in Fig. 2a. Such an antenna is shown in Fig. 2b. The linear, passive, bilateral two-port shown in Fig. 2b is introduced to account for any differences between either the full scale antenna and its duplicate or the actual model and a valid practical model. It should be noted that although the devices in Fig. 2 have been termed antennas, in the general case they could represent a complex radar target with an attached antenna system.

Introduction of the two-port in Fig. 2b requires some explanation. In the case of models, we assume that with strict attention to scale factor and conductivity effects the physical antenna configuration and a short section of transmission line can be properly modelled. The

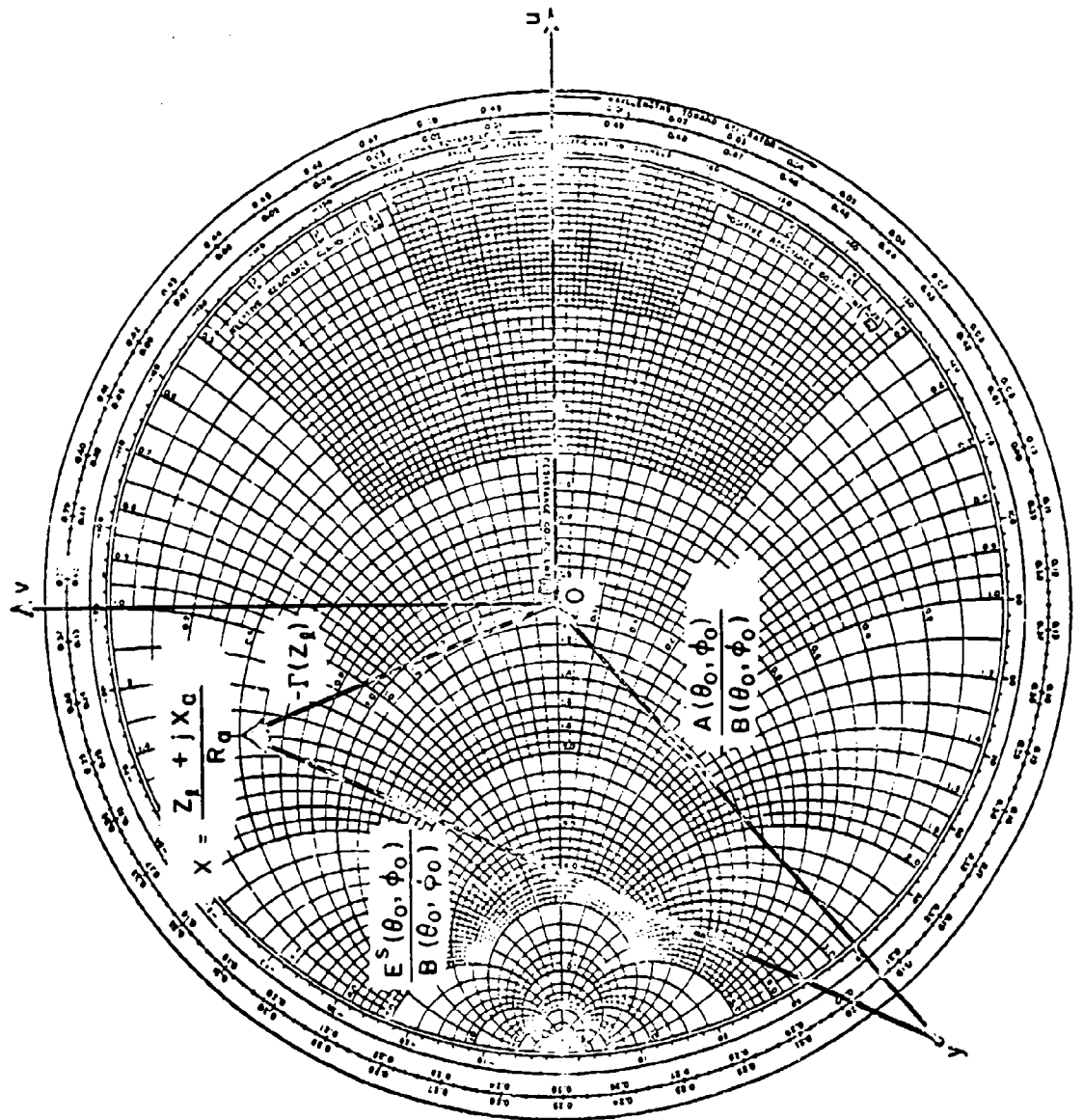


Figure 1. Geometrical Representation of Antenna Scattering.

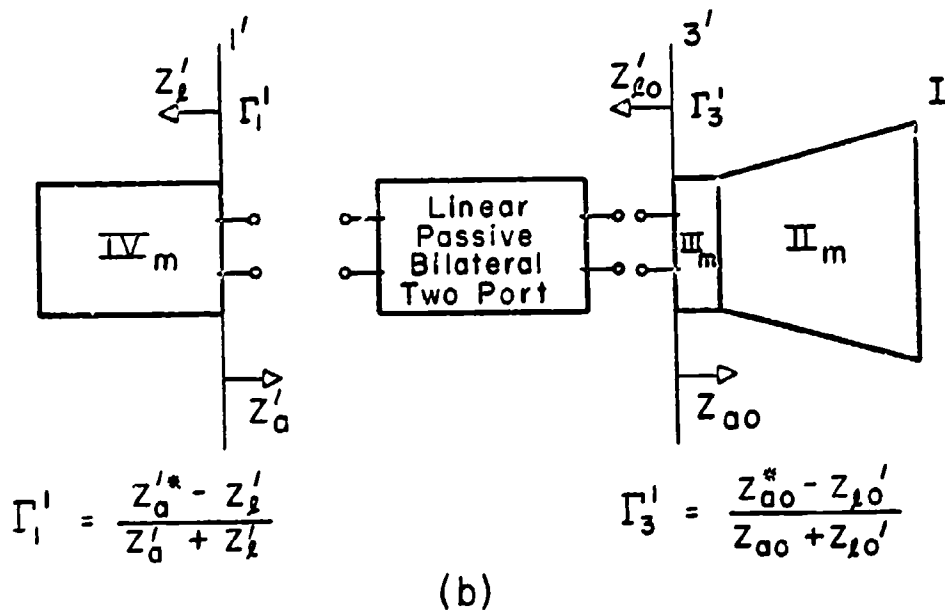
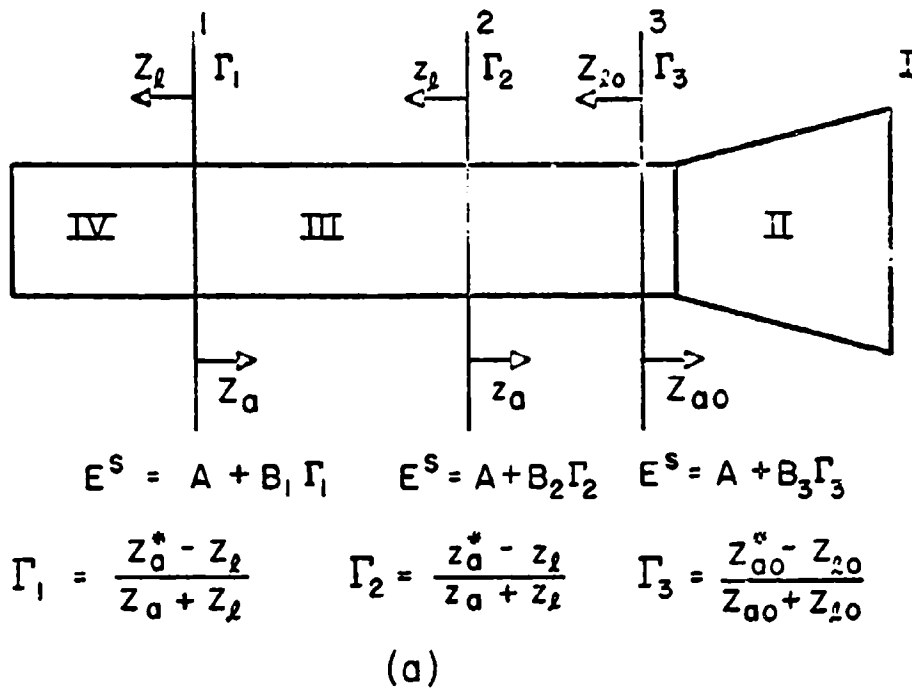


Figure 2. Diagrams of Receiving Antenna.

transmission line and load will often be encapsulated within a radar target and not readily accessible, and any leads to the target could interfere with the scattering measurements. For this reason, a programmed type load capable of either stepping to various pre-selected reactances or varying continuously from $j\infty$ to $-j\infty$ is used. It is not feasible to construct a modelled version of this load because of component size and loss considerations. Also a different load would be required for each scale factor. Thus in the model the two-port is deliberately introduced and becomes a transition section from the modelled line to the programmed load. In the case of the full scale duplicate antenna, some type of transition may still be necessary to attach the programmed load. Barring this, slight differences could also occur in the transmission line leading to the load.

In general then either deliberately or inadvertently an unknown two-port exists between the load terminals 1^2 and antenna terminals 3^1 of the antenna in Fig. 2b. To the right of terminal plane 3^1 we assume either an exact duplicate antenna or a valid geometrical model. Insofar as the antenna characteristics are concerned, the validity of this assumption could be established by comparing input impedances, receiving patterns, etc. at terminal planes 3 and 3^1 . The existence of the two-port could then be established by corresponding measurements at terminal planes 1 and 1^1 . Finally, a calibration of the two-port would permit proper identification of loads at terminal plane 3^1 and one could proceed with the measurement procedures to be described. In the case of full scale antennas, such an approach is straightforward. For models, however, although this approach is entirely feasible it would involve construction of an additional transition section as well as modelled loads. In the following section an alternative procedure involving one two-port measurement rather than a complete calibration and requiring only the construction of a modelled open circuit load is described.

Much of the preceding discussion is idealized in the sense that we have assumed complete knowledge of the prototype antenna. In many instances one may be dealing with an experimental model version of an antenna on a complex structure for which no full scale information is available. In such a case, the burden of proof would rest with the full scale experimenter. He would be forced to ensure his antenna parameters agreed with those of the model before utilizing the model measurements.

MEASUREMENT PROCEDURES

The measurement procedures to be described are designed to permit the prediction of the echoing area of a loaded target for any load from a basic set of measurements. They also enable one to separately identify the load dependent and load independent components. While the application is not stressed here, it should be noted that the techniques for determining the input impedance and gain of an antenna from scattering measurements can be extremely useful in cases where exterior leads strongly influence the antenna parameters.

Consider first the full scale antenna. Equations (3) and (4) demonstrate that when phase measuring facilities⁶ are available, measurement of the input impedance and the scattered field with the antenna terminated in two particular reactive loads suffices to predict the scattered field and echo for any load at any measured aspect. Usually only echo facilities are available. Let the antenna be oriented at a fixed aspect and terminated in a reactive load variable from $j\infty$ to $-j\infty$. Varying the reactive load over its complete range we record the maximum, minimum, and average cross-sections. That is, from Eq. (1) we measure

$$(7) \quad \left\{ \begin{array}{l} \sigma_{\max}(\theta_0, \phi_0) = K |B(\theta_0, \phi_0)|^2 \left[\left| \frac{A(\theta_0, \phi_0)}{B(\theta_0, \phi_0)} \right| + 1 \right]^2 \\ \sigma_{\min}(\theta_0, \phi_0) = K |B(\theta_0, \phi_0)|^2 \left[\left| \frac{A(\theta_0, \phi_0)}{B(\theta_0, \phi_0)} \right| - 1 \right]^2 \\ \sigma_{\text{avg}}(\theta_0, \phi_0) = \frac{\sigma_{\max}(\theta_0, \phi_0) + \sigma_{\min}(\theta_0, \phi_0)}{2} \\ \qquad \qquad \qquad = K |B(\theta_0, \phi_0)|^2 \left[\left| \frac{A(\theta_0, \phi_0)}{B(\theta_0, \phi_0)} \right|^2 + 1 \right] \\ \overline{\sigma_{\max}}(\theta_0, \phi_0) = K |B(\theta_0, \phi_0)|^2 \end{array} \right. ,$$

where K is the calibration constant of the range and $\overline{\sigma_{\max}(\theta_0, \phi_0)}$ is the maximum cross section when the microwave bridge of our echo range is misnullled such that $\sigma_{\min}(\theta_0, \phi_0)$ is equal to zero. Given these measurements, the input impedance, gain of the antenna at θ_0, ϕ_0 , and the diagram of Fig. 1 for θ_0, ϕ_0 can be determined. The justification and details of these procedures are given in a series of reports by Garbacz.^{7, 8, 9} For our present purpose we are primarily interested in the determination of the input impedance from scattering measurements,⁷ which requires only the first three measurements of Eq. (7).

Now consider the duplicate or modelled antenna in Fig. 2b. It can be shown that the modified reflection coefficients at terminal planes 1' and 3' are related as

$$(8) \quad \Gamma_3^i = a + b \Gamma_1^i \quad ,$$

and that

$$(9) \quad \begin{aligned} a &= r + s \\ b &= r - s \end{aligned} \quad .$$

The quantities r and s can be expressed in terms of the four pole impedance parameters of the two-port and Z_a^i .¹⁰ It is not unreasonable to assume that the transition from modelled line to the load is essentially lossless. In this case $r = -s$

$$(10) \quad \begin{aligned} a &= 0 \\ |b| &= 1 \end{aligned} \quad ,$$

and

$$(11) \quad \Gamma_3^i = - \frac{Z_a^i - j X_{22}}{Z_a^i + j X_{22}} \Gamma_1^i \quad ,$$

where X_{22} is the reactance looking into the two-port from terminal plane 1' with an open circuit at terminal plane 3'. Thus it is possible to transfer a meaningful quantity through the two-port by utilizing the measurements of Eq. (7) to determine Z_a^i and making

one measurement on the two-port. As a consequence one bench measurement; requiring a quarter wavelength of shorted model line, permits us to work entirely from terminal plane 1'. Note that we have no knowledge of Z_{l0}' , nor is it possible to determine Z_{a0} by this method. But knowing Γ_3' is sufficient to permit us to completely determine the scattering properties of the antenna.

In the following we assume that the measurements of Eq. (7) to determine Z_a' and the bench measurement of X_{22} have been made. We note that

$$(12) \quad \left\{ \begin{array}{l} \Gamma_3' \left| \begin{array}{l} Z_l' = D_1 \\ \end{array} \right. = 1 \\ \Gamma_3' \left| \begin{array}{l} Z_l' = D_2 \\ \end{array} \right. = -1 \\ \Gamma_3' \left| \begin{array}{l} Z_l' = D_3 \\ \end{array} \right. = j1 \\ \Gamma_3' \left| \begin{array}{l} Z_l' = D_4 \\ \end{array} \right. = -j1 \end{array} \right.$$

where

$$D_1 = -j \left[\frac{|Z_a'|^2 - X_{22} X_a'}{X_a' - X_{22}} \right]$$

$$D_2 = -jX_{22}$$

$$D_3 = -j \left[\frac{|Z_a'|^2 - X_{22} (R_a' + X_a')}{X_a' - R_a' - X_{22}} \right]$$

$$D_4 = -j \left[\frac{|Z_a'|^2 - X_{22} (X_a' - R_a')}{X_a' + R_a' - X_{22}} \right]$$

When the two-port is not present, i. e., for the full scale antenna these reactive loads become

$$\begin{aligned}
 D_1 &= -jX_a \\
 D_2 &= j\infty \\
 (13) \quad D_3 &= -j(R_a + X_a) \\
 D_4 &= j[R_a - X_a]
 \end{aligned}$$

If K is the calibration constant of the echo range and p is the modelling scale factor, the echoing area of the prototype antenna for reactive loads is given by

$$\begin{aligned}
 (14) \quad \sigma(\theta, \phi, Z_f) &= Kp^2 [|A(\theta, \phi)|^2 + |B(\theta, \phi)|^2 \\
 &\quad + 2|A(\theta, \phi) B(\theta, \phi)| \cos \{ \beta(\theta, \phi) - \alpha \}] ,
 \end{aligned}$$

where $\beta(\theta, \phi)$ is the phase angle between A and B and α is the phase angle of Γ .

$$(15) \quad \left| \frac{A(\theta, \phi)}{B(\theta, \phi)} \right| = - \frac{1 + \sqrt{\frac{\sigma_{\max}(\theta, \phi)}{\sigma_{\min}(\theta, \phi)}}}{1 + \sqrt{\frac{\sigma_{\max}(\theta, \phi)}{\sigma_{\min}(\theta, \phi)}}}, \quad \begin{aligned} &+ |A/B| > 1 \\ &- |A/B| < 1 \end{aligned}$$

$$(16) \quad \frac{\sigma_{\max}(\theta, \phi)}{p^2} = \sigma_{\text{avg}}(\theta, \phi) + \frac{\sigma(\theta, \phi, D_1) - \sigma(\theta, \phi, D_2)}{2 \cos \beta(\theta, \phi)} ,$$

$$(17) \quad \frac{\sigma_{\min}(\theta, \phi)}{p^2} = \sigma_{\text{avg}}(\theta, \phi) - \frac{\sigma(\theta, \phi, D_1) - \sigma(\theta, \phi, D_2)}{2 \cos \beta(\theta, \phi)} ,$$

$$(18) \quad \frac{\sigma_{avg}(\theta, \phi)}{p^2} = \frac{\sigma(\theta, \phi, D_1) + \sigma(\theta, \phi, D_2)}{2}$$

$$(19) \quad \beta(\theta, \phi) = \tan^{-1} \left[\frac{\sigma(\theta, \phi, D_3) - \sigma(\theta, \phi, D_4)}{\sigma(\theta, \phi, D_1) - \sigma(\theta, \phi, D_2)} \right]$$

Thus from echo measurements of the antenna terminated in the four reactive loads of Eq. (12) (models) or Eq. (13) (full scale) the echo area of the antenna for any passive load at any measured aspect can be predicted. When the relative magnitude of the load dependent and load independent components is not known, the ambiguity in sign in Eq. (15) is removed with a fifth echo measurement with the antenna terminated in an arbitrary known lossy load. In utilizing the geometrical representation to predict the echo for an arbitrary load

$$(20) \quad \sigma(\theta_0, \phi_0, Z_L) = \left[\frac{|xy|}{|oy| + 1} \right]^2 \sigma_{max}(\theta_0, \phi_0).$$

The measurements just described have the advantage that only reactive loads and possibly one known arbitrary lossy load are required. Some of the mathematical operations however are non-linear which precludes averaging or smoothing the measured data before reduction. A linear procedure is also possible as explained below.

Referring to Fig. 1, the echo area as a function of load is proportional to the square of the line length yx , where y is a fixed point and x varies with the terminating impedance. This construction holds for a single orientation of the antenna and for a fixed polarization and frequency. The construction can be generalized to cases where the aspect, frequency, or polarization of the transmit-receive antennas is varied,^{5,11} in which case a slightly more complicated construction applies to the average echo area as a function of load impedance. This change merely adds a constant to the square of the length yx to obtain the average echo area. Viewed in this sense, the problem of measuring the scattering properties of an antenna reduces to the determination of the point y , the appropriate scale factor and, for the case where average quantities are sought, an additive constant.

Utilizing the uv coordinates of Fig. 1, the echo area as a function of load impedance can be written

$$(21) \quad \sigma(u_x, v_x) = K_1 [(u_y - u_x)^2 + (v_y - v_x)^2 + K_2],$$

where K_1 is the scale factor, K_2 is the additive constant, (u_x, v_x) represents the point x and (u_y, v_y) represents the point y. Note that K_2 would be zero for a fixed aspect and polarization. Choosing the four particular loads

$$(22) \quad \begin{aligned} \sigma(0, 1) &= K_1 [1 + u_y^2 + v_y^2 - 2v_y + K_2] \\ \sigma(1, 0) &= K_1 [1 + u_y^2 + v_y^2 - 2u_y + K_2] \\ \sigma(0, -1) &= K_1 [1 + u_y^2 + v_y^2 + 2v_y + K_2] \\ \sigma(0, 0) &= K_1 [u_y^2 + v_y^2 + K_2] \end{aligned}$$

and setting

$$(23) \quad \sigma(u_x, v_x) = \sum_{i=1}^4 \lambda_i \sigma(u_i, v_i),$$

$$(24) \quad \begin{aligned} \lambda_1 + \lambda_2 + \lambda_3 + \lambda_4 &= 1 \\ \lambda_1 + \lambda_2 + \lambda_3 &= u_x^2 + v_x^2 \\ \lambda_1 - \lambda_3 &= v_x \\ \lambda_2 &= u_x \end{aligned}$$

Thus

$$(25) \quad \begin{aligned} \lambda_1 &= \frac{1}{2} [u_x^2 + v_x^2 - u_x + v_x] \\ \lambda_2 &= u_x \\ \lambda_3 &= \frac{1}{2} [u_x^2 + v_x^2 - u_x - v_x] \\ \lambda_4 &= 1 - u_x^2 - v_x^2 \end{aligned}$$

Clearly the echo area of an antenna, either averaged or not averaged, can be obtained from a linear combination of the echo areas measured for four particular load impedances. Note that a conjugate matched load is required. In the case of models, a conjugate match for Z_a^1 is required and Eq. (11) is used to obtain the required reactive terminations.

CONCLUSIONS

The echoing area of an antenna as a function of its load impedance can be predicted from echo measurements with the antenna terminated in four particular loads. Both linear (requiring a conjugate matched load) and nonlinear (requiring only reactive loads) operations are possible. Modelling techniques for the evaluation of antenna scattering properties can be used, and a single bench measurement eliminates the necessity for modelling the load impedance and a portion of transmission line.

REFERENCES

1. Stevenson, A.F., "Relations Between the Transmitting and Receiving Properties of Antennas," *Quarterly of Applied Mathematics*, Vol. 5, January 1948.
2. Morita, T., "Measurements of Current and Charge Distributions on Cylindrical Antennas," *Proc. IRE*, Vol. 38, p. 898, 1950.
3. Hu, Y.Y., "Backscattering Cross-Section of a Center Loaded Antenna," *PGTAP*, Vol. AP-6, January 1958.
4. King, R.W.P., The Theory of Linear Antennas, Harvard University Press, Cambridge, Mass., p. 467, 1956.
5. Green, R.B., "The Effect of Antenna Installations Upon the Echo Area of an Object," Report 1109-4, 29 September 1961, Antenna Laboratory, The Ohio State University Research Foundation; prepared under Contract AF 33(616)-7386, Aeronautical Systems Division, Wright-Patterson Air Force Base, Ohio. AD 274 041

- (6) Garbacz, R. J. and Eberle, J. W., "Measurement of Time Quadrature Components of a Scattered Field," 1960 IRE-WESCON Convention Record, Part 1, August 1960.
- (7) Garbacz, R. J., "The Determination of Antenna Parameters by Scattering Cross-Section Measurements. I. Antenna Impedance," Report 1223-8, 30 September 1962, Antenna Laboratory, The Ohio State University Research Foundation; prepared under Contract AF 33(616)-8039, Aeronautical Systems Division, Wright-Patterson Air Force Base, Ohio. AD 286 760
- (8) Garbacz, R. J., "The Determination of Antenna Parameters by Scattering Cross-Section Measurements. II. Antenna Gain," Report 1223-9, 30 November 1962, Antenna Laboratory, The Ohio State University Research Foundation; prepared under Contract AF 33(616)-8039, Aeronautical Systems Division, Wright-Patterson Air Force Base, Ohio. AD 297 953
- (9) Garbacz, R. J., "The Determination of Antenna Parameters by Scattering Cross-Section Measurements. III. Antenna Scattering Cross Section," Report 1223-10, 30 November 1962, Antenna Laboratory, The Ohio State University Research Foundation; prepared under Contract AF 33(616)-8039, Aeronautical Systems Division, Wright-Patterson Air Force Base, Ohio. AD 295 031
- (10) Moffatt, D. L., "Determination of Antenna Scattering Properties from Model Measurements," Report 1223-12, In preparation.
- (11) Green, R. B., "The General Theory of Antenna Scattering," Report 1223-17, 30 November 1963, Antenna Laboratory, The Ohio State University Research Foundation; prepared under Contract AF 33(616)-8039, Research Technology Division, Wright-Patterson Air Force Base, Ohio.

THE EFFECT OF FINITE CONDUCTIVITY ON RADAR CROSS SECTIONS*

Leon Peters, Jr.
Associate Supervisor
Antenna Laboratory
Department of Electrical Engineering
The Ohio State University
Columbus, Ohio 43210

INTRODUCTION

The radar cross section of metallic bodies is usually obtained by considering the conductivity to be infinite. This paper considers the changes in the radar cross section when the conductivity is not infinite. These changes are based on physical mechanisms and the change in radar cross section is readily obtained by slide rule computations.

The first case to be considered is the sphere. The boundary value solution of an electromagnetic wave scattered by a spherical shape was originally obtained by Mie.¹ In order to apply this solution to spheres of finite conductivity, it is necessary to introduce Bessel functions of complex argument. This may be done using modern digital computers but is expensive and this approach cannot be readily applied to most other shapes. One of the purposes of this paper consists of presenting a method by which the radar cross section of the perfectly conducting sphere can be modified readily to estimate the radar cross section of the sphere with finite conductivity. The method given is applicable to other shapes whose radar cross section is due to a specular reflection and to a creeping wave. The first approximation to be used consists of multiplying the radar cross section of the metallic body by the square of the Fresnel reflection coefficient. The attenuation of the creeping wave due to the finite conductivity is also treated by means of a simple approximation which yields reasonable reduction of this contribution. Attempts to determine the change in phase of the creeping wave component due to the finite conductivity have not been successful.

* The work reported in this paper was supported in part by Contract AF 33(616)-8039 between Air Force Avionics Laboratory, Research Technology Division, Wright-Patterson Air Force Base, Ohio and The Ohio State University Research Foundation.

The above method is applicable if there are no significant internal reflections such as would be the case for lossy dielectric bodies, i.e., dielectric bodies with small conductivity. The modified geometrical optics^{2,3,4,5} method would yield readily the appropriate echo area for such bodies.

The echo area of long thin targets may be estimated by considering the target to be a thin traveling wave antenna excited in the dominant mode by the incident field.^{6,7,8} It is first assumed that the target is a receiving antenna which couples energy from the field to a fictitious antenna terminal pair. Any mismatch at these terminals reflects a portion of this energy which is reradiated by the target. The echo area of such a target is given by

$$(1) \quad \sigma = \gamma^2 \frac{G^2(\theta, \phi)}{4\pi} \lambda^2$$

where γ is the voltage reflection coefficient at the terminals,

$G(\theta, \phi)$ is the gain function of the equivalent antenna,

θ, ϕ are the usual polar coordinates and

λ is the wavelength.

Previously it has been assumed that the equivalent antenna is lossless and hence the gain equals the directivity. If the conductivity is infinite and the body is smooth only the lowest order TM mode or the principal mode can exist. The directivity of the equivalent antenna for this dominant mode is readily computed and the radar cross section is then obtained from Eq. (1). Targets whose echo area have been computed using this method include a long thin rod,⁶ an ogive and a styrofoam clad rod.⁸

New modes may be introduced by placing a dielectric shell on the body or by a rough surface⁸ or by a lower conductivity. The case of the dielectric shell and corrugated surface⁸ have been considered previously. The boundary value problem needs to be solved to treat the case for finite conductivity and then the calculation would parallel the previous case. Consideration of the

loss mechanism caused by the finite conductivity for the principal mode is to be introduced in the present paper.

HIGH CONDUCTIVITY SPHERES

It is suggested that the radar cross section of the perfectly conducting body may be used to approximate the radar cross section of certain bodies whose conductivity is not infinite. The first order approximation to be proposed⁹ is

$$(2) \quad \sigma = R^2 \sigma_{\infty}$$

where σ = radar cross section

σ_{∞} = radar cross section of the perfectly conducting body of the same size and shape.

$$(3) \quad R = \frac{1-n}{1+n} = \text{Fresnel reflection coefficient and}$$

n = the complex index of refraction.

The complex index of refraction n is defined by

$$(4) \quad \begin{aligned} \gamma &= j \beta_0 n = j \beta_0 \sqrt{\epsilon_r} = \sqrt{j \omega \mu s + \omega^2 \mu \epsilon'} \\ &= j \omega \sqrt{\mu \epsilon_0} \sqrt{\epsilon_r' + j \frac{s}{\omega \epsilon_0}} \end{aligned}$$

where γ = propagation constant

ω = angular frequency

ϵ' = dielectric constant

ϵ_r' = ϵ'/ϵ_0

ϵ_0 = dielectric constant of free space

s = conductivity

μ = permeability

$\beta_0 = \omega \sqrt{\mu \epsilon_0}$ = phase factor of free space and

$\epsilon_T = \epsilon_T' - j \epsilon_T''$ = the complex dielectric constant.

The complex dielectric constant

$$(5) \quad \epsilon_T = n^2 = \epsilon_T' - j \frac{s}{\omega \epsilon_0}$$
$$= \epsilon_T' (1 - j \tan \delta)$$

where $\tan \delta = \text{loss tangent} = \frac{s}{\omega \epsilon'}$

The approximation of Eq. (2) assumes that all of the energy transmitted into the body is absorbed.⁹ The remainder of the energy is then reflected by the body acting as though it is a perfect conductor.

The results of this approximate solution are compared in Figs. 1, 2, 3, and 4 with those obtained from the boundary value solution for four cases; $\epsilon_T = 0 - j 0.1$, $0 - j 1.0$, $0 - j 4.0$ and $\epsilon_T = 42.6275 - j 41.2692$. The first three cases are for a wave incident on a lossy plasma sphere with a frequency equal to the plasma cut-off frequency. The final case is the water sphere computed by Herman and Battan.¹⁰ These cases do not satisfy the usual condition of a perfect conductor given by $s/\omega \epsilon \gg 1$ and were chosen as examples simply because they were available.^{3, 10}

This first order approximation may be improved by considering the reflection mechanisms individually. The specular component of scattered fields is readily calculated by multiplying the scattered field obtained from geometrical optics by the square of the reflection coefficient or

$$(6) \quad \sigma_{sp} = R^2 \sigma_{opt}$$

where σ_{sp} = specular component of radar cross section and

σ_{opt} = geometrical optics radar cross section of the perfectly conducting body.

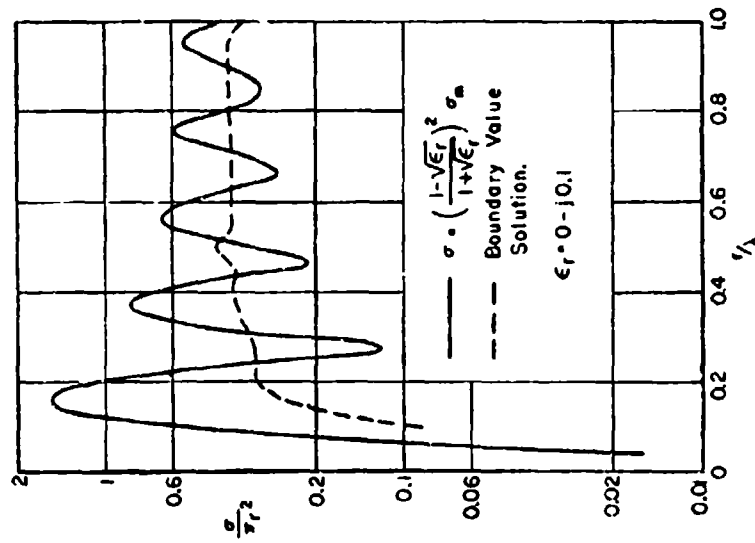


Fig. 1. Radar cross section of lossy sphere with negligible creeping wave component.

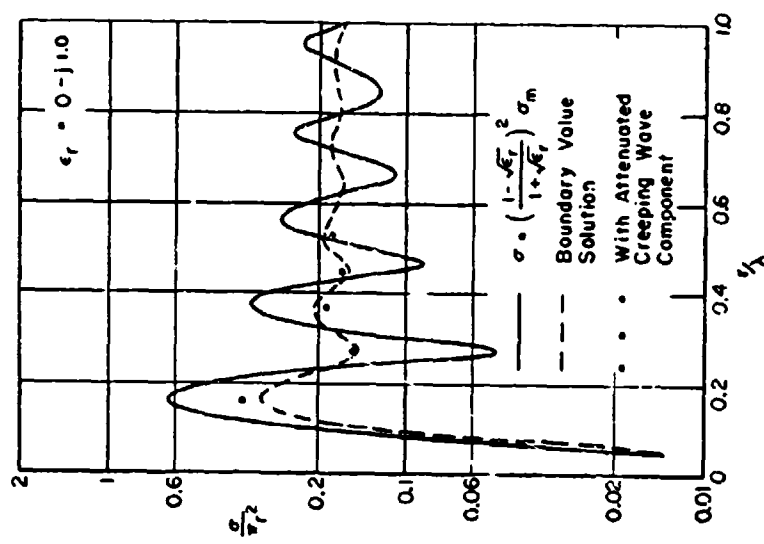


Fig. 2. Radar cross section of lossy sphere with small creeping wave component.

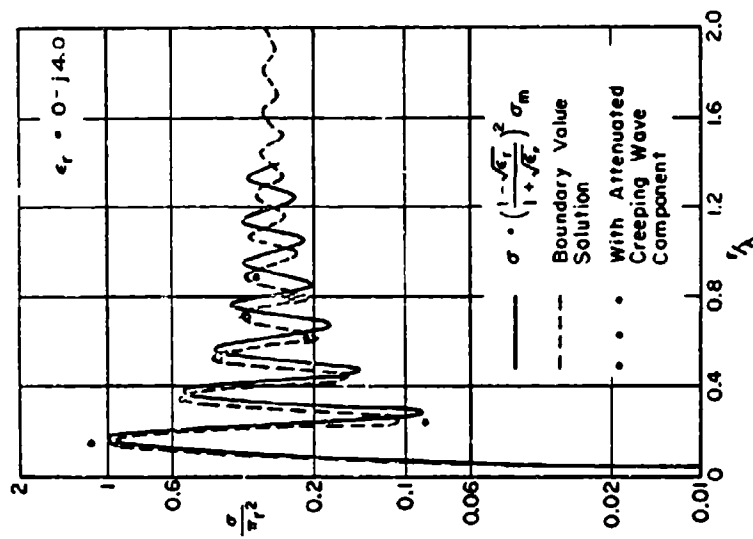


Fig. 3. Radar cross section of lossy sphere with large creeping wave component.

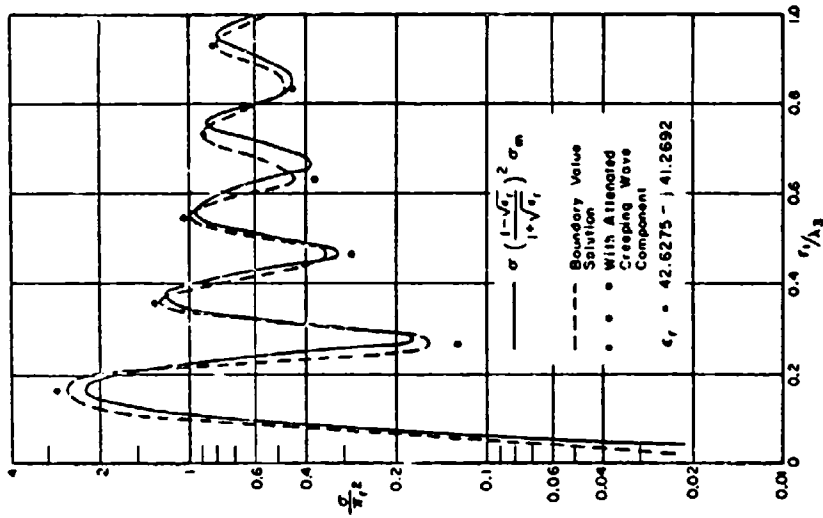


Fig. 4. Radar cross section of a water sphere.

The geometrical radar cross section for a sphere is the well known

$$\sigma_{\text{opt}} = \pi r^2$$

where r is the radius of the sphere. This equation is valid for this component for all radii exclusive of the region of Rayleigh scattering.

The magnitude of the component of the scattered field due to the creeping wave can be found from the maximum and minimum values of radar cross section of the perfectly conducting sphere. For the radii where these maxima occur, the specular component and creeping wave component are in phase. This yields

$$(7) \quad \sqrt{\sigma_{\text{cw}}} = \sqrt{\sigma_{\text{max}}} = \sqrt{\sigma_{\text{opt}}}$$

where σ_{cw} = component of radar cross section due to the creeping wave and

σ_{max} = maximum radar cross section.

Similarly

$$(8) \quad \sqrt{\sigma_{\text{cw}}} = \sqrt{\sigma_{\text{opt}}} - \sqrt{\sigma_{\text{min}}}$$

where σ_{min} = minimum radar cross section.

Note that σ_{cw} is a function of radius.

The creeping wave field is attenuated by absorption in addition to attenuation by radiation if the conductivity is not infinite. The absorption attenuation factor is taken approximately to be equal to the attenuation factor of a wave traveling along the interface illustrated in Fig. 5. The attenuation factor for this case is¹¹

$$(9) \quad \alpha = \beta_0 \frac{\omega \epsilon_1}{2\sigma_2}$$

where β_0 = phase factor of ambient medium
 ϵ_1 = relative dielectric constant of the ambient medium and
 s_2 = conductivity of the body.

The attenuation factor is $\alpha = 10\pi, \pi, \pi/4, \pi/41.2692$ nepers per wavelength for ϵ_r equal to $0 - j 0.1, 0 - j 1.0, 0 - j 4.0$ and $42.6275 - j 41.2692$ respectively. The path of the creeping wave contributing to the monostatic radar cross section is illustrated in Fig. 6. Its path length is simply πr . The approximate radar cross section may be written as

$$(10) \quad \sigma_{\max} = \sqrt{R^2 \sigma_{\text{opt}}} + \sqrt{\sigma_{\text{cw}} e^{-\alpha \pi r}}$$

and

$$(11) \quad \sigma_{\min} = \sqrt{R^2 \sigma_{\text{opt}}} - \sqrt{\sigma_{\text{cw}} e^{-\alpha \pi r}}$$

where σ_{\max} is the maximum radar cross section

σ_{\min} is the minimum radar cross section of the lossy sphere.

This method has been used to obtain values for the maxima and minima for the four cases. The results are indicated in Figs. 2, 3, and 4. The attenuation of the creeping wave is sufficient that its contribution is negligible for $\epsilon_r = 0 - j 0.1$ and this is in agreement with the exact solution shown in Fig. 1. The agreement between this approximate solution and the exact solution is remarkable for all cases except for the nulls of Fig. 4. This deviation probably occurs because the exact radar cross section may not have been computed at the precise radius at which the null occurs.

It is to be emphasized that the radii associated with these computed values has not been obtained from the approximation. To date no successful method has been obtained for determining the change of the phase of the creeping wave component due to the finite value of the conductivity.

The radar cross section of a class of targets is due to the reflection of the creeping wave at a discontinuity. This class of target may also be treated if the conductivity is finite provided that the reflection mechanism for the perfectly conducting body of the same shape is known.

LOSSY DIELECTRIC SPHERE

It has been shown that the modified geometrical optics method may be used to determine the radar cross section of lossless dielectric bodies. This method may also be used to determine the radar cross section of lossy dielectric bodies. Since the modified geometrical optics method has been described adequately elsewhere, only the factors introduced by loss are to be discussed.

The various reflection coefficients are modified due to the presence of the conductivity. The reflection coefficients may be obtained simply by replacing ϵ_r for the lossless¹² case by the complex value given by Eq. (5).

The modified geometrical optics method treats rays that undergo internal reflections which contribute to the radar cross section. Several of these are illustrated in Fig. 7. If the medium becomes lossy, these rays are attenuated by an amount $e^{-\alpha d}$ where α is the attenuation factor for a plane wave propagating in such a medium given by the real part of Eq. (4) and d is the path length of the ray. As either α or d becomes large the contribution from such components become negligible. This would lead to a radar cross section similar to that of Fig. 1. As the conductivity is increased further the creeping component becomes significant yielding radar cross sections similar to those of Figs. 2, 3, and 4. These changes may also occur simultaneously.

The phase factor may also be changed from the free space value and is now the imaginary part of Eq. (4). Computation of the phase of the scattered field is essentially in order that the total scattered field be determined.

RADAR CROSS SECTION OF LONG THIN BODIES OF FINITE CONDUCTIVITY

The radar cross section long thin bodies may be determined by the methods outlined in the introduction. Since this case has been reduced to an antenna problem the fields radiated by the long thin antenna excited in the principal mode are to be considered when the conductivity is finite. The current distribution of this traveling wave now has the form

$$(12) \quad I(z) = I_0 e^{-\gamma z}$$

where the coordinate system is illustrated in Fig. 8.

$$\gamma = \alpha + j\beta = \alpha + j \frac{\beta_0}{p}$$

α = attenuation factor of a wave

β = phase factor of the wave

$p = \frac{v}{c}$ = the relative phase velocity

v = velocity of the wave

c = velocity of a wave in free space

β_0 = phase factor in free space.

Walter¹³ obtains the far field radiated by this antenna as

$$(13) \quad E_\theta = \frac{j \omega \mu I_0 e^{-jkr}}{4\pi r} e^{-\frac{\alpha L}{2}} \sin \theta \left[\frac{e^{(j\beta_0 \cos \theta - \gamma) \frac{L}{2}} - e^{-(j\beta_0 \cos \theta - \gamma) \frac{L}{2}}}{j \beta_0 \cos \theta - \gamma} \right]$$

Equation (13) may be written in the form

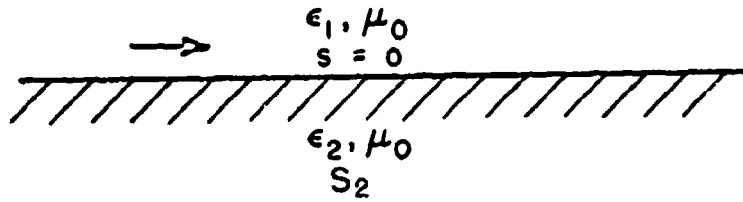


Fig. 5. Wave propagating along lossy interface.

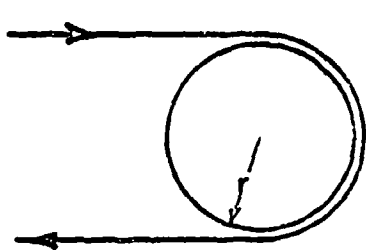


Fig. 6. Creeping wave path.

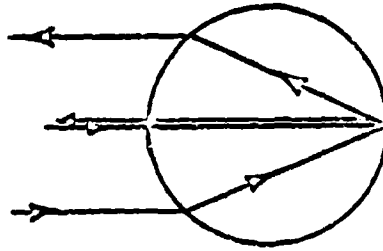


Fig. 7. Several significant internally reflected rays for a dielectric sphere.

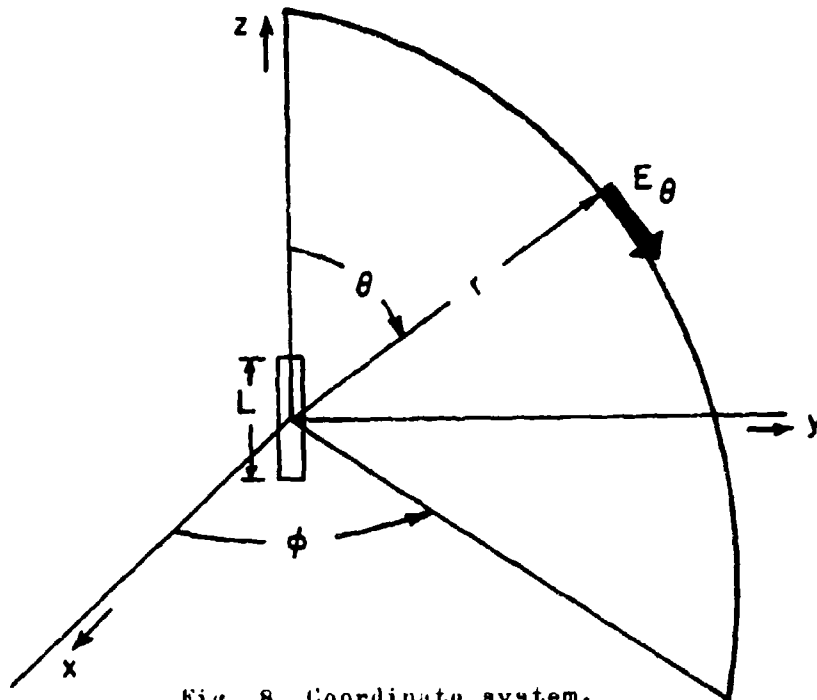


Fig. 8. Coordinate system.

$$(14) \quad E_{\theta} = \frac{pk e^{-\frac{\alpha L}{2}} \sin \theta \sinh \left[\frac{j \beta_0}{p} (p \cos \theta - 1) - \alpha \right] \frac{L}{2}}{j \beta_0 (p \cos \theta - 1) - \alpha_0 p}$$

If the conductivity is large, but not infinite, Eq. (14) may be approximated by

$$(15) \quad E_{\theta} \approx \frac{jkp e^{-\frac{\alpha L}{2}} \cosh \frac{\alpha L}{2} \sin \theta \sin \left(\frac{\beta_0}{p} (p \cos \theta - 1) \right)}{j \beta_0 (p \cos \theta - 1) - \alpha_0 p}$$

If $\beta_0(p \cos \theta - 1) \gg p \alpha_0$, Eq. (15) becomes

$$(16) \quad E_{\theta} \approx jkp \left(e^{-\frac{\alpha L}{2}} \cosh \frac{\alpha L}{2} \right) \left(\frac{\sin \theta \sin \left(\frac{\beta_0}{p} (p \cos \theta - 1) \right)}{\beta (p \cos \theta - 1)} \right)$$

which now is of the form

$$E_{\theta} \approx k p (\text{loss factor}) (\text{pattern factor})$$

Furthermore the pattern factor is identical to the pattern factor for $\alpha = 0$ provided p does not change significantly due to the finite value of conductivity. For small attenuation factors, the relative phase velocity is not changed significantly and the pattern factor remains unchanged.

The condition $\beta_0(p \cos \theta - 1) \gg p \alpha_0$ must be satisfied for the first major maxima or for $(\beta_0/p) (p \cos \theta - 1) L/2 = \pi/2$. If the condition is satisfied for this lobe it will also be satisfied for the remainder of the pattern. Thus the required condition takes the form $\pi/L \gg \alpha_0$.

Since the pattern given by Eq. (16) is identical to that obtained when α equals zero, there is no need to determine the directivity once it has been found for the lossless case. It is only necessary to find the change in the relative magnitude of E_{θ} as a function of the attenuation factor, i.e., to evaluate the loss factor. The attenuation factor for the cylindrical shape¹⁴ may be obtained from the boundary value solution of a wave traveling along the cylinder.

Measurements⁶ reported for a steel and silver rod of the same dimensions show a 5 db difference in the magnitude of their respective radar cross sections but the pattern shape is essentially the same for both cases. The rod is 19 1/2 inches long and 1/8 inch in diameter. The radar wavelength is 1/2 inch. Computations of the radar cross section for these two cases show no significant difference. However the relative permeability of the steel¹⁵ rod which is not known was taken as unity. Its value which is considerably larger than unity is needed to determine the attenuation factor. This measurement does indicate the validity of the suggested approach, i. e., the use of Eq. (16) to obtain the change in radar cross section. It also demonstrates that the cross section may be obtained with reasonable accuracy from the lossless case for ordinary conductors when the relative permeability is unity.

Decreasing the conductivity would next require that fields given by Eq. (16) be used. Carbon is an example of a material for which this may be the case.

Decreasing the conductivity still further would require that fields given by Eq. (14) be used. This would necessitate a new derivation of directivity and require a numerical integration. Some observations may be made however by expanding Eq. (14) in the form

$$E_{\theta} \approx \frac{-kp e^{-\frac{\alpha L}{2}} \cosh \frac{\alpha L}{2} \left[e^{-j \frac{\beta_0}{p}} (p \cos \theta - 1) \right] \sin \theta}{j \beta_0 (p \cos \theta - 1) - \alpha_0 p}$$

since $\sinh \alpha L/2 \approx \cosh \alpha L/2$ for large $\alpha L/2$. The pattern factor is now of the form

$$\frac{\sin \theta}{\sqrt{[\beta_0 (p \cos \theta - 1)]^2 + (\alpha_0 p)^2}}$$

Thus the directivity is greatly decreased. It would be further decreased by a decreased value of p due to the presence of the lower conductivity.⁸ In addition the loss factor $e^{-\alpha L/2} (\cosh \frac{\alpha L}{2})$ would be very small. Thus such radar cross sections due to traveling waves would not be significant for such materials as the usual radar absorbers.

There also exists the possibility of exciting higher order modes as the conductivity is further reduced. This treatment of high order modes is best considered from the opposite extreme, i. e., the dielectric with a small conductivity. Means of treating the radar cross section of dielectric rods has been treated previously.¹⁶ Introduction of loss in the computation of radar cross section would parallel the methods discussed above. It is also of interest to note that surface roughness can also cause higher order modes to be excited. The pattern due to this type of mode may have a maximum value in the endfire direction similar to that of the dielectric rod antenna. This is shown to be true for the case of a threaded rod both by theory and experiment.⁸

CONCLUSIONS

Methods of obtaining the radar cross sections of bodies of finite conductivity have been discussed. Several of these methods require knowledge of the radar cross section of the perfectly conducting body of the same shape.

The radar cross section of many bodies is due to a specular reflection and a creeping wave component. A first order approximation consists of simply multiplying the radar cross section of the perfectly conducting body by the square of the Fresnel reflection coefficient. This is reasonably valid for many cases. This approximation is not valid if the creeping wave is significantly attenuated. A means of determining the absorption attenuation factor has been given and has been shown to yield accurate radar cross section values for the maxima and minima of the sphere with finite conductivity. The method does not yield the radii at which they occur. This method should be applicable to bodies of other than spherical shape.

The application of the modified geometrical optics method for dielectric bodies with small conductivity has been discussed. In particular the considerations necessary to treat this case have been described.

The effect of loss on the radar cross section due to traveling wave modes has been treated. The change in radar cross section should be small for usual conducting bodies. This mode should be negligible for bodies of smaller conductivity such as absorbers. Higher order modes introduced by low conductivity require treatment to obtain the radar cross section paralleling that of the dielectric rod.

BIBLIOGRAPHY

1. Mie, G., "Beitrage zur Optik Truber Medien, Speziall Kollordaler Metallosungen," Ann. Physick, vol. 25, p. 377, 1908.
2. Kouyoumjian, R.G., Peters, L., Jr., and Thomas, D. T., "Modified Geometrical Optics Method for Scattering by Dielectric Bodies," Transactions of Professional Technical Group on Antennas and Propagation, Institute of Electrical and Electronic Engineers, November 1962.
3. Third Annual Summary Report, Report 1116-43, September 1963, Antenna Laboratory, The Ohio State University Research Foundation; prepared under Contract AF 19(604)-7270, Air Force Cambridge Research Laboratories, Bedford, Mass.
4. Thomas, D. T., "Scattering by Plasma and Dielectric Bodies," Report 1116-20, August 1962, Antenna Laboratory, The Ohio State University Research Foundation; prepared under Contract AF 19(604)-7270, Air Force Cambridge Research Laboratories, Bedford, Mass. AD 286 854
5. Kawano, T. and Peters, L., Jr., "An Extension of the Modified Geometrical Optic Method for Radar Cross Section of Dielectric Bodies," Report 1116-39, 15 November 1963, Antenna Laboratory, The Ohio State University Research Foundation; prepared under Contract AF 19(604)-7270, Air Force Cambridge Research Laboratories, Bedford, Mass.
6. Peters, L., Jr., "Endfire Echo Area of Long Thin Bodies," IRE Transactions on Antennas and Propagation, pp. 133-139, January 1958.
7. Peters, L., Jr., and Green, R. B., "Echo Area of the Plasma Coated Sphere," Journal of Planetary and Space Science, July 1961.

8. Peters, L., Jr., "Echo Area Properties of Bodies Due to Certain Traveling Wave Modes," Report 777-19, 18 May 1960, Antenna Laboratory, The Ohio State University Research Foundation; prepared under Contract AF 33(616)-5341, Wright Air Development Division, Wright-Patterson Air Force Base, Ohio. AD 239 936
9. Peters, L., Jr., "Radar Cross Section of Plasma Bodies in the Vicinity of Plasma Resonance," Report 1116-35, August 1963, Antenna Laboratory, The Ohio State University Research Foundation; prepared under Contract AF 19(604)-7270, Air Force Cambridge Research Laboratories, Bedford, Mass.
10. Herman, B.M., and Battan, L.J., "Calculations of Mie Back-Scattering of Microwaves from Ice Spheres," Quarterly Journal of the Royal Meteorological Society, No. 372, pp. 223-230, April 1961.
11. Ramo, S. and Whinnery, J.R., Fields and Waves in Modern Radio, John Wiley and Sons, Inc., New York, p. 291, 1947.
12. Richmond, J. H., "Electromagnetic Field and Optic Theory," Chapter 2 of "Techniques for Airborne Radome Design," McGraw-Hill Book Co., Inc., New York, p. 31, September 1957. AD 142 001
13. Walter, C. H., Traveling Wave Antennas, to be published by McGraw-Hill Book Co., Inc., New York.
14. Stratton, J.A., Electromagnetic Theory, McGraw-Hill Book Co., Inc., New York, p. 529, 1941.
15. Ibid, p. 508.
16. Peters, L., Jr., "Echo Area of Satellite Wakes Acting as Dielectric Rod Antennas," Report 1116-3, 31 January 1961, Antenna Laboratory, The Ohio State University Research Foundation; prepared under Contract AF 19(604)-7270, Air Force Cambridge Research Laboratories, Bedford, Mass. AD 254 857

DIELECTRIC PROPERTIES; DATA AND MEASUREMENT TECHNIQUES

Paul E. Rowe
Eino J. Luoma
Elery F. Buckley

Emerson & Cuming, Inc.
Canton, Massachusetts

ABSTRACT

The selection and use of dielectric materials in the microwave industry continues to baffle many engineers and scientists. Materials which exhibit substantial dielectric losses or very high values of dielectric constant, for example, are not well understood. The variation of dielectric properties with frequency seems to be a complete enigma to all but a few people who have had occasion to study this behavior. The measurement of dielectric properties at microwave frequencies is usually regarded as a major chore to be left strictly to the experts. As the range of available dielectric properties broadens, however, in artificial dielectrics and in mixtures of natural dielectrics, applications of these materials in both full-scale and model studies will oblige technical personnel in ever-increasing numbers to become more familiar with dielectric properties and their measurement.

This paper has the dual purpose of reviewing the range of available dielectric properties and of summarizing recent advances in the techniques of measuring dielectric properties, all in the hope of enhancing to some degree the understanding and the application of dielectric materials. We do not have time to discuss the theories of artificial or mixture dielectrics, or to include any thorough discussion of the theory of measurement of dielectric properties. We do hope that the reader will appreciate upon scanning Section I that a tremendous variety of dielectric properties can be combined with a wide range of physical characteristics, and that it is often possible to tailor dielectric properties to one's liking. Similarly we trust that Section II will convince the reader that many long-standing limitations on measurement ease and accuracy are gradually disappearing.

I. DIELECTRIC PROPERTIES

A. Low-Loss Dielectrics

A large variety of low-loss dielectrics are presently available for applications. Dielectric constants vary from 1.02 for very low density polystyrene foam to 230 for sintered strontium titanate. Available materials with higher dielectric constants are generally lossy.

Table I lists room temperature dielectric constants and loss tangents of several low-loss materials. An idea of the effect of frequency on dielectric properties of such materials may be gleaned from the following data of VonHippel¹:

<u>Material</u>	<u>Frequency cycles per second</u>	<u>K'</u>	<u>Tan d</u>
Polythene A-3305 (DuPont)	1×10^7	2.25	0.0003
	3×10^9	2.25	0.0003
	1×10^{10}	2.25	0.0004
	2.5×10^{10}	2.24	0.00067
TAM Ticon MC (Magnesium Titanate)	1×10^7	13.9	0.0004
	3×10^9	13.8	0.0017
	1×10^{10}	13.8	0.0028
	2.5×10^{10}	13.7	0.0065
TAM Ticon T-J (Rutile)	1×10^7	96	0.0003
	3×10^9	96	0.00034
	2.5×10^{10}	91	0.0033

The dielectric properties of lossless dielectrics vary much less with frequency than do those of lossy dielectrics. For this reason modeling can usually be accomplished using the low-loss dielectrics to be employed on the end item.

Often more than one material will have dielectric properties suitable for a given application. Choice of the material to be employed will depend on one or more other characteristics. These include.

1. Temperature stability (physical)
2. Density
3. Physical strength
4. Machinability
5. Cost

TABLE I
 LOW-LOSS DIELECTRICS
 (Values of tan d are multiplied by 10⁴)

Material	Frequency Gc	k'	tan d	Maximum Continuous Use Temperature, °F (based on physical properties)
<u>Ceramics</u>				
Fused Quartz ^{*a}	10	3.78	1.0	2400+
Alumina High Purity ^{*b}	8.6	9.40	1.8	3000+
Eccofoam Q-F ^c	8.6	1.2	10	1800+
Eccofoam Q-G	8.6	1.4	5	1800+
Eccofoam Q-R	8.6	1.7	5	1800+
Eccofoam LM-45A ^c	8.6	2.0	80	1000+
Eccoceram QC ^c	8.6	2.8	20	2500
Eccoceram SM-25 ^c	8.6	3.0	40	2000
Eccoceram 21 ^c	8.6	7.0	60	2500
Eccofo HIK ^{**c}	8.6	1.5 thru 10.0	3 thru 10	2000+
Eccoceram HiK ^c	8.6	5.0 thru 9.0	10	1500+
<u>Plastics</u>				
Eccofoam PS ^c	8.6	1.02 thru 2.1	2 thru 5	175
Eccofoam SH ^c	8.6	1.04	1	275+
Eccofoam SH ^c	8.6	1.12	3	275+
Eccofoam SH ^c	8.6	1.25	10	275+
Eccofoam 300L ^c	8.6	1.3	20	300+
Eccofoam 300L ^c	8.6	1.5	30	300+
Eccofoam 300L ^c	8.6	2.0	60	300+
Eccofoam 300L ^c	8.6	2.5	100	300+
Eccofoam 300L ^c	8.6	3.0	150	300+
Eccofoam HiK 625D ^c	8.6	2.5	130	400+
Eccofoam HiK 625D ^c	8.6	3.6	160	400+
Eccofoam HiK 625D ^c	8.6	3.5	180	400+
Eccofoam HiK 625D ^c	8.6	4.0	190	400+
Eccofoam HiK 625D ^c	8.6	5.0	230	400+
Eccofoam HiK 625D ^c	8.6	6.0	270	400+
Eccofoam HiK 625D ^c	8.6	7.0	300	400+
Eccofoam SR ^c	8.6	1.3	30	500+
Polyethylene ^{*d}	8.6	2.38	1.6	
Stycast LoK ^c	8.6	1.8	9	400+
Eccostock HT3003 ^c	8.6	2.2	3	500+
Eccostock CPE ^c	8.6	2.4	7	350+
Stycast 0005 ^c	8.6	2.5	5	260+
Stycast HiK ^c	8.6	3 thru 15	20	215
Stycast HiK 500F ^c	8.6	3 thru 25	10 thru 25	500

Footnotes: a. General Electric
 b. Kearfoot
 c. Emerson & Cuming, Inc.
 d. Marlex 50 Monsanto

* data of VonHippel
 ** granular powders

Several other considerations may also enter into the selection. Very often one or more desirable characteristics will have to be neglected in order to obtain more necessary properties. All of these properties cannot be discussed in this paper.

An approximate high temperature at which the material will retain physical properties is listed for most of the materials in Table I. VonHippel¹ shows the effect of temperature on the dielectric properties of many low-loss materials. For most low-loss materials the variation of dielectric constant with temperature is much less at microwave frequencies than at lower frequencies.

B. Lossy Dielectrics

The study of lossy dielectrics is much more complicated than the study of low-loss dielectrics. In low-loss dielectrics the goal is usually the preparation of materials of given dielectric constants having the lowest possible loss tangents. With lossy dielectrics the dielectric constant and loss tangent are interdependent variables which must be controlled. It may be required, for example, to prepare a series of materials with a given dielectric constant and widely different loss tangents. Furthermore, when dielectric properties of a low-loss dielectric are known at a given frequency, one can be fairly certain that these properties will be similar over quite a range of frequencies. The dielectric properties of lossy dielectrics change rather rapidly with frequency. This can be observed from the data on lossy dielectric liquids listed in Table II and the data on lossy dielectric solids listed in Table III.

Lossy dielectric liquids are extremely limited in their use since their dielectric properties change rapidly with temperature. This effect is attributed for the most part to the change in viscosity of the liquid which in turn affects the ease of rotation of the molecular dipoles. Carbon-containing solids most probably achieve their loss tangents from resistance to movement of electrons through semi-conductive chains. For this reason the effect of temperature on such solids should be different than the effect on liquids. Temperature effects on lossy dielectric solids should be studied.

The use of carbon in the preparation of lossy dielectric solids has definite advantages. Carbon is a chemical element. It would appear therefore to be a simple material which can be characterized quite readily. This is far from the case. As every schoolboy knows carbon is available in three forms: diamond, graphite and amorphous carbon. But even this is a great simplification where electrical properties are concerned. Individual particles of different industrial carbons have various amorphous carbon-graphite proportions, particle sizes, particle shapes and porosities. Most materials sold as carbon contain significant proportions of other elements. These variables and others affect the electrical properties of carbon-containing dielectrics. Although the wide variety of available carbons tends to complicate the

TABLE II - LOSSY DIELECTRIC LIQUIDS

Material	300 Mc		3.0 Gc		10.0 Gc	
	k'	tan d	k'	tan d	k'	tan d
Ethanol*	22.3	0.27	6.5	0.25	1.7	0.368
n-Propanol*	16.0	0.42	3.7	0.67	2.3	0.090
Ethyl polychloro- benzene*	3.84	0.14	2.7	0.126	2.55	0.660
(β) Chloro 2, 5 di- chlorobenzene*	5.18	0.11	3.31	0.324		
Aroclor-1232 a*	3.10	0.190	2.75	0.103	2.65	0.059
Pyranol-1467 ^b *	3.19	0.150	2.84	0.120	2.62	0.074
Dichloropentanes ^c #40	7.57	0.084	6.81	0.198		
Halowax Oil 1000 ^d *	4.67	0.05	3.52	0.25	2.99	0.190
Ethylene Glycol*	39	0.16	12	1.0	7	0.78
n-Butanol*	11.5	0.55	3.5	0.47		
Methanol*	30.9	0.08	23.6	0.64	8.9	0.81
Aqueous NaCl(.3Molal) [†] 71		2.4	69.3	0.435	52	0.605
Water*	77.5	0.016	76.7	0.157	55	0.540

Footnotes: * data of VonHippel¹
a. monochlorobiphenyl
b. chlorinated benzenes and diphenyls -- General Electric
c. Sharples
d. mixed chloronaphthenes

TABLE III - LOSSY DIELECTRIC SOLIDS

Material	300 Mc		3.0 Gc		10.0 Gc	
	K'	Tan d	K'	Tan d	K'	Tan d
Pyralin ^a			3.74	0.165	3.32	0.131
Catalin 500 Base ^b			4.77	0.125	4.43	0.130
Plascon Melamine (← cellulose) ^c	5.79	0.154	4.93	0.103	4.6	0.110
Melmac 1077 ^d			4.8	0.09	4.7	0.10
Selenium Multicrystals ^e	11.0	0.25	10.4	0.154	7.5	0.11
Steak Bottom Round ^f	50	0.78	40	0.30	30	0.40

	1.0 Gc		3.0 Gc		8.6 Gc	
	K'	Tan d	K'	Tan d	K'	Tan d
Eccosorb PMA ^{**}	2.7	0.14	2.5	0.10	2.5	0.10
Eccosorb PMB ^{**}	5.9	0.53	4.6	0.44	3.8	0.33
Thiokol PRI [†]	20.5	0.26	17.1	0.23	8.4 [†]	0.22 [†]
Thiokol S [†]	17.0	0.30	14.8	0.36	8.5 [†]	0.40 [†]
Polystyrene 70% } *	11.0	0.23	9.1	0.25	8.8 [†]	0.11 [†]
Carbon 30% ^g						
Polystyrene 50% } *	25.9	0.73	20.8	0.56	19.4 [†]	0.28 [†]
Carbon 50% ^g						
Eccosorb HF 2050 ^{**}	10.0	0.1			10.0	0.1
Eccosorb HF 1000 ^{**}	15	0.2			15.0	0.2
Eccosorb HF 853 ^{**}	40	0.6			20.0	0.3
Eccosorb HF 680 ^{**}	50	0.8			25	0.4
Eccosorb HF 155 ^{**}	90	1.0			30	0.5
Eccosorb VF ^{**}	76.0	0.60	48.5	0.76	40.4	0.36

Experimental Materials^{**}

(a) Polyurethane foams (open celled) coated with carbon films						
Sample A	1.68	0.56	1.33	0.31	1.24	0.22
Sample B	1.90	0.96	1.51	0.56	1.36	0.39
Sample C	2.51	0.67	1.89	0.50	1.43	0.40
(b) Coated foam embedded in epoxy resin						
Sample D	4.27	0.45	3.64	0.25	3.29	0.21
(c) Moldings containing carbon and phenolic resin						
Sample E	8.95	0.36	7.18	0.27	6.34	0.22
Sample F	24.8	0.82	15.6	0.59	12.2	0.45
Sample G	56	1.18	23.6	1.01	14.6	1.06
(d) Carbon-loaded ceramic foams						
Sample H	2.08	0.020	2.11	0.018	2.16	0.033
Sample I	3.32	0.046	2.98	0.036	2.85	0.059
Sample J	7.28	0.182	6.45	0.231	5.65	0.255
Sample K	17.02	0.938	10.58	0.673	9.97	0.717

^aCellulose nitrate, 25% Camphor, DuPont

^bCatalin

^cLibby-Owens-Ford

^dAmerican Cyanamid, 25% alpha pulp, Zn stearate

^eThiokol, 100 pts. polysulfide copolymer of bis (chloroethyl) formal and ethylene dichloride, 60 pts. carbon blacks

^fThiokol, 100 pts. polysulfide polymer of bis (chloroethyl) formal, 60 pts. carbon blacks

^gCabot's #9

[†]VonHippel data¹

^{**}Emerson & Cuming, Inc.

[†]10 Gc measurement

study of carbon-containing dielectric, this same variety permits the preparation of lossy materials having greatly differing dielectric properties. Most of the solids listed in Table III contain a form of carbon.

In order to obtain a high loss tangent at a reasonably low dielectric constant it appears to be necessary to have semi-conductive chains of carbon throughout the dielectric. The following example may illustrate this:

Sample I - A mixture of RTV silicone and graphite containing 27.4 weight per cent graphite was blended and then allowed to cure at room temperature. The cured sample had the following dielectric properties:

<u>Frequency</u>	<u>1.0 Gc</u>	<u>3.0 Gc</u>	<u>8.6 Gc</u>
K'	14.8	15.5	15.1
Tan d	0.090	0.050	0.067

The specific resistance of the sample was over 10^6 ohm-cm.

Sample II - A more conductive carbon was mixed with granular phenolic molding powder. The mixture which contained 2.4 weight per cent carbon was molded into a disc which yielded the following dielectric properties:

<u>Frequency</u>	<u>3.0 Gc</u>	<u>8.6 Gc</u>
K'	10.15	6.70
Tan d	0.85	0.60

The sample had a specific resistance of 258 ohm-cm.

The higher loss tangent of Sample II is attributed to the semi-conductive chains through the sample which are demonstrated by its lower specific resistance.

The above example also points out another often observed phenomenon. Higher loss tangent materials usually show a greater change of dielectric properties with frequency than do lower loss tangent materials.

Open cell matrices coated with carbon-resin films are interesting dielectrics. Such materials often yield high loss tangents and low dielectric constants. For example, one sample of carbon-resin coated foam had a dielectric constant of 1.40 and a loss tangent of 1.77 at 5.6 Gc. By varying the cell size of such foams one may prepare materials having similar dielectric constants and widely

varying loss tangents. The following data was taken at 11.3 Gc from samples having similar carbon-resin films:

<u>Cell Size</u> <u>pores per inch</u>	<u>K'</u>	<u>Tan d</u>
10	1.29	0.827
30	1.31	0.600
80	1.33	0.242
100	1.32	0.197

Embedding such foams in low-loss dielectrics results in materials with increased dielectric constant and decreased loss tangent. Varying the carbon film in such a composite has a great effect on the loss tangent and a small effect on the dielectric constant. Variation of the dielectric constant of the embedding medium has the reverse effect.

Using the techniques described above and others it is possible to prepare materials with a wide range of dielectric constants and loss tangents. Actually it appears possible to tailor-make a material to a given dielectric constant and loss tangent at a given frequency. A possible exception is high-dielectric-constant high-loss materials. These have not yet been thoroughly studied.

As pointed out previously, lossy materials show variation of dielectric properties with frequency (dispersion). This may prove particularly discouraging in the modeling of absorptive materials. A given lossy dielectric is expected to have far different properties at the modeling frequency than at the frequency of final use. A material may probably be prepared which has the same dielectric properties at the modeling frequency as the final-use material has at the use frequency. It is highly unlikely, however, that both materials will have similar variation in dielectric properties through their respective frequency ranges. For this reason, it will most probably be necessary to prepare several models to permit the use of modeling techniques over a frequency range.

A program which may lead to improved control of the variation of dielectric properties of lossy materials with frequency is under way at Emerson & Cuming, Inc.

The complicated study of magnetic dielectrics is considered beyond the scope of this paper.

11. MEASUREMENT TECHNIQUES

A. Introductory

It is the purpose of this section of this paper to bring the reader up to date on some recent developments in the art of measuring microwave dielectric properties. The basic methods used in these techniques, as set forth in References such as 1, 2, and 3, have not changed. Recent developments are in the nature of refinements and development of tools for more rapid data reduction.

Closed system microwave dielectric measurements are made either in a shorted transmission line (waveguide or coaxial) or cavity. This paper discusses some advances in data reduction for the shorted-waveguide dielectrometer.

Free-space microwave dielectric measurements are made either with interferometers or reflectometers. This paper discusses some refinements in interferometry as well as some improvements in data reduction for interferometers.

Before entering into the detailed discussion of these advances in dielectrometer and interferometer techniques, a few general observations about their relative merits are in order. The dielectrometer method, being a closed system, is the more accurate of the two, provided the sample fits precisely into the transmission line, and is homogeneous. On the other hand, with care, measurement accuracy good enough for most applications can be obtained with a free-space interferometer. In addition, with the interferometer, the problem of sample fit is eliminated and an effective or average answer is obtained in a more sensible fashion for the non-homogeneous sample, because, in contrast with reflection measurements, insertion measurements give the same result regardless of which face of the sample receives the incident energy. Nor should it be overlooked that the dielectrometer measurement is, in most cases, a destructive test because of the necessity of having a small sample, whereas, the interferometer permits measurements to be made non-destructively on the slab of dielectric intended for the required application.

Both dielectrometer and interferometer measurements are the substitution type. That is to say the dielectric sample is substituted for a standard, usually air, during the measurement. And, the measurements consist of making a comparison between the effect of the dielectric sample vs. the effect of the standard on the signal being detected, both as to its phase and amplitude. With the dielectrometer, the phase and loss information are derived from the standing wave pattern and the data reduction is handled as an impedance - propagation constant problem. With the interferometer the phase and loss are read directly on precision phase shifters and attenuators, and the data reduction is handled as a problem in the geometric optics of the passage of a plane wave through a flat sheet of infinite area.

The most difficult part of the data reduction problem in both cases involves the implicit solution of a transcendental equation involving complex variables. Since the explicit solution is the one readily obtainable, the problem is overcome in both cases by plotting curves or computing tables of a large number of solutions for the explicit case.

At this point it is appropriate to discuss the advances in dielectrometer and interferometer techniques in the following two separate sections.

B. Dielectrometer

Dielectrometer measurements have for many years been burdened with the necessity for a lengthy, time-consuming computation program to extract the dielectric constant and loss tangent from the raw data which consisted of null shift and width of a standing-wave minimum. For the low-loss case it has been possible by certain approximations and by plotting a few additional curves to shorten this computation. Some laboratories have established programs for computers with which it is possible to feed the raw data into the computer with the dielectric constant and loss tangent becoming the computer output. This approach has the disadvantage of requiring the scheduling of computer time.

Because of the number of parameters involved in the data reduction, there has been an apparent reluctance to plot curves or prepare tables which permit the complete conversion directly from null shift and null width into dielectric constant and loss tangent. Rather, the transcendental-complex number part of the conversion has been narrowed to use of tables or graphs for the following complex functions:

$$\tanh z, \frac{\tanh z}{z} \text{ and } \frac{\coth z}{z}.$$

For the low-loss case, at the expense of losing only a little accuracy, the complex transcendental functions can be approximated by using the real functions

$$\frac{\tan x}{x} \text{ and } \frac{\cot x}{x}.$$

One advance in this data reduction problem is the establishment at Emerson & Cuming, Inc. of new sets of tables which do indeed permit, for non-magnetic samples, the complete direct conversion of null shift and null width into dielectric constant and loss tangent for either the short-circuit or open-circuit case. Figures 1 and 2 are sample pages respectively from these tables.

An interesting development in this work was that, contrary to the expectations of many engineers faced with this data reduction problem, the actual physical magnitude and number of solutions required for excellent versatility in the tables does not turn out to be at all prohibitive. As shown in the sample pages, the sample thickness parameter, which was expected to be the most troublesome, was disposed of simply by always pairing two tables on a page with electrical sample thicknesses at and just above the chosen nominal thickness. This permits ready interpolation or extrapolation for any thickness near the nominal thickness. All length parameters are normalized with respect to wavelength, thus universalizing the use of any table to any frequency, although the appropriate physical thickness for a table computed for a given electrical thickness does change with frequency. The primary tables are for the coaxial case. For the waveguide case, the coaxial tables can still be used provided the ratio of sample thickness to waveguide wavelength is made equal to the thickness-to-wavelength ratio for which the coaxial tables were computed. In this case, since the dielectric constant and loss tangent obtained from the coaxial tables are not the true values, they must be converted into the true values by use of a second table, a sample page from which is given in Figure 3.

For the more general case, where the sample may be magnetic, and where the conversion involves going from four known values (the null shift and width for both open- and short-circuit cases) to four unknown values (dielectric constant, dielectric loss tangent, magnetic permeability, and magnetic loss tangent), it is not possible to do the data reduction in one step. Nevertheless, there has been established at Emerson & Cuming, Inc. a procedure involving the use of four universal tables which take most of the labor out of the conversion. Figures 4, 5, 6, and 7 are sample pages from each of these tables respectively. Table IV is a lab. sheet which directs the data reduction. Desk calculations intermediate between look-up in one table and use of the next table in the sequence of operations are reduced to simple addition and subtraction. The tables can be used for the non-magnetic case as well as the magnetic case. In the non-magnetic case, the number of tables required is reduced to two. It is estimated that the speed of data reduction by use of this scheme for lossy samples, either magnetic or non-magnetic, is increased by at least a factor of four over the old method which used $\tanh z$ graphs.

In summary, for all methods, increased accuracy will result by use of tables wherever possible, since mathematical manipulations are reduced to simple arithmetic steps.

C. Interferometer

Interferometer measurements have for many years been limited to determination of dielectric constant for low-loss, non-magnetic samples. This was because there was no convenient way of converting the measured insertion loss and insertion phase delay into dielectric constant and loss tangent. Within the past year this obstacle has been

FOR WAVELENGTH DIELECTRIC CONSTANT, (1) USE GUIDE WAVELENGTH IN COAX TABLES, (2) LOOK UP C_1 (DIELEC. CONST.) AND T_1 LOSS TANGENT) IN COAX TABLES, (3) FIND TRUE VALUES, D_2 AND T_2 , FROM TABULATION BELOW.

COAX WAVELENGTH / GUIDE WAVELENGTH = 0.581400

01	02	T2/T1												
1.00	1.000	.3160	1.02	1.007	.3625	1.04	1.016	.3669	1.06	1.020	.3512	1.08	1.027	.3555
1.10	1.076	.3597	1.12	1.061	.3635	1.14	1.067	.3679	1.16	1.074	.3720	1.18	1.081	.3760
1.20	1.048	.3799	1.22	1.076	.3830	1.24	1.081	.3874	1.26	1.088	.3915	1.28	1.095	.3955
1.30	1.101	.3990	1.32	1.100	.4026	1.34	1.105	.4069	1.36	1.110	.4110	1.38	1.116	.4150
1.40	1.155	.4189	1.42	1.142	.4203	1.44	1.149	.4237	1.46	1.155	.4271	1.48	1.162	.4304
1.50	1.169	.4337	1.52	1.176	.4370	1.54	1.183	.4402	1.56	1.189	.4436	1.58	1.196	.4465
1.60	1.203	.4606	1.62	1.210	.4527	1.64	1.216	.4558	1.66	1.223	.4590	1.68	1.230	.4617
1.70	1.237	.4667	1.72	1.243	.4674	1.74	1.250	.4705	1.76	1.257	.4733	1.78	1.264	.4761
1.80	1.270	.4789	1.82	1.277	.4817	1.84	1.284	.4846	1.86	1.291	.4871	1.88	1.297	.4898
1.90	1.303	.4926	1.92	1.311	.4951	1.94	1.318	.4976	1.96	1.325	.5002	1.98	1.331	.5027
2.00	1.336	.5053	2.02	1.343	.5077	2.04	1.352	.5102	2.06	1.359	.5126	2.08	1.365	.5151
2.10	1.372	.5175	2.12	1.379	.5198	2.14	1.385	.5222	2.16	1.392	.5245	2.18	1.399	.5268
2.20	1.406	.5291	2.22	1.412	.5315	2.24	1.419	.5338	2.26	1.426	.5360	2.28	1.433	.5382
2.30	1.430	.5401	2.32	1.446	.5423	2.34	1.453	.5446	2.36	1.460	.5468	2.38	1.466	.5490
2.40	1.473	.5507	2.42	1.480	.5527	2.44	1.487	.5548	2.46	1.494	.5568	2.48	1.500	.5588
2.50	1.507	.5607	2.52	1.516	.5627	2.54	1.521	.5647	2.56	1.527	.5666	2.58	1.534	.5685
2.60	1.541	.5706	2.62	1.549	.5725	2.64	1.556	.5744	2.66	1.561	.5763	2.68	1.568	.5781
2.70	1.575	.5796	2.72	1.581	.5814	2.74	1.588	.5832	2.76	1.595	.5849	2.78	1.602	.5867
2.80	1.600	.5886	2.82	1.615	.5902	2.84	1.622	.5919	2.86	1.629	.5936	2.88	1.635	.5952
2.90	1.642	.5959	2.92	1.649	.5986	2.94	1.656	.6002	2.96	1.663	.6018	2.98	1.669	.6034
3.00	1.676	.6050	3.02	1.683	.6066	3.04	1.690	.6082	3.06	1.696	.6098	3.08	1.703	.6113
3.10	1.710	.6128	3.12	1.717	.6144	3.14	1.723	.6159	3.16	1.730	.6174	3.18	1.737	.6189
3.20	1.746	.6204	3.22	1.750	.6218	3.24	1.757	.6233	3.26	1.764	.6247	3.28	1.771	.6262
3.30	1.777	.6276	3.32	1.786	.6290	3.34	1.791	.6304	3.36	1.798	.6318	3.38	1.805	.6332
3.40	1.811	.6345	3.42	1.818	.6359	3.44	1.825	.6372	3.46	1.832	.6386	3.48	1.838	.6399
3.50	1.845	.6412	3.52	1.852	.6425	3.54	1.859	.6438	3.56	1.866	.6451	3.58	1.872	.6464
3.60	1.879	.6477	3.62	1.886	.6489	3.64	1.892	.6502	3.66	1.899	.6514	3.68	1.906	.6527
3.70	1.913	.6539	3.72	1.919	.6551	3.74	1.925	.6563	3.76	1.933	.6575	3.78	1.940	.6587
3.80	1.966	.6599	3.82	1.973	.6611	3.84	1.980	.6623	3.86	1.987	.6635	3.88	1.994	.6646
3.90	1.980	.6657	3.92	1.987	.6669	3.94	1.994	.6680	3.96	2.001	.6691	3.98	2.007	.6702
4.00	2.016	.6713	4.02	2.021	.6725	4.04	2.028	.6736	4.06	2.035	.6747	4.08	2.041	.6757
4.10	2.060	.6768	4.12	2.055	.6778	4.14	2.061	.6789	4.16	2.068	.6799	4.18	2.075	.6810
4.20	2.082	.6820	4.22	2.088	.6830	4.24	2.095	.6841	4.26	2.102	.6851	4.28	2.109	.6861
4.30	2.115	.6871	4.32	2.122	.6881	4.34	2.129	.6891	4.36	2.136	.6901	4.38	2.143	.6910
4.40	2.149	.6920	4.42	2.156	.6930	4.44	2.163	.6939	4.46	2.170	.6949	4.48	2.177	.6958
4.50	2.181	.6968	4.52	2.190	.6977	4.54	2.197	.6986	4.56	2.205	.6996	4.58	2.210	.7005
4.60	2.217	.7016	4.62	2.224	.7025	4.64	2.230	.7034	4.66	2.237	.7043	4.68	2.244	.7052
4.70	2.261	.7059	4.72	2.257	.7068	4.74	2.264	.7076	4.76	2.271	.7085	4.78	2.278	.7094
4.80	2.284	.7102	4.82	2.291	.7111	4.84	2.298	.7119	4.86	2.305	.7128	4.88	2.312	.7136
4.90	2.310	.7145	4.92	2.317	.7153	4.94	2.324	.7161	4.96	2.332	.7169	4.98	2.339	.7177
5.00	2.352	.7186	5.02	2.359	.7194	5.04	2.366	.7202	5.06	2.373	.7210	5.08	2.379	.7218
5.10	2.388	.7225	5.12	2.393	.7233	5.14	2.399	.7241	5.16	2.406	.7249	5.18	2.413	.7257
5.20	2.420	.7266	5.22	2.426	.7272	5.24	2.433	.7279	5.26	2.440	.7287	5.28	2.447	.7294
5.30	2.456	.7297	5.32	2.463	.7304	5.34	2.469	.7311	5.36	2.476	.7318	5.38	2.481	.7325
5.40	2.487	.7332	5.42	2.494	.7338	5.44	2.501	.7345	5.46	2.508	.7351	5.48	2.514	.7357
5.50	2.521	.7372	5.52	2.528	.7378	5.54	2.535	.7384	5.56	2.541	.7390	5.58	2.548	.7397
5.60	2.555	.7409	5.62	2.562	.7416	5.64	2.568	.7423	5.66	2.575	.7429	5.68	2.582	.7436
5.70	2.589	.7435	5.72	2.595	.7442	5.74	2.602	.7448	5.76	2.609	.7454	5.78	2.616	.7460
5.80	2.623	.7474	5.82	2.629	.7480	5.84	2.636	.7486	5.86	2.643	.7492	5.88	2.650	.7498
5.90	2.656	.7508	5.92	2.663	.7514	5.94	2.670	.7521	5.96	2.677	.7527	5.98	2.684	.7533

FIGURE 3

COLLECTION TABLE ONE

U	V	U	V	U	V	U	V	U	V	U	V	U	V
1.7249	-0.4720	1.1014	-0.3020	0.7704	-0.3700	0.7509	-0.5000	0.6595	-0.5000	0.5466	-0.5000	0.4	0.0010
1.8344	-0.4619	1.2798	-0.4627	0.9400	-0.4841	0.7507	-0.4493	0.6496	-0.4920	0.5763	-0.4935	0.0010	0.0010
1.6139	-0.0000	1.0451	-0.4371	0.8788	-0.4682	0.7501	-0.4787	0.6591	-0.4837	0.5663	-0.4871	0.0010	0.0010
1.4887	-0.0000	1.0457	-0.4372	0.8789	-0.4683	0.7502	-0.4788	0.6592	-0.4838	0.5664	-0.4872	0.0010	0.0010
1.3332	-0.0000	1.0778	-0.3758	0.7742	-0.4370	0.7481	-0.4576	0.6570	-0.4679	0.5656	-0.4742	0.0010	0.0010
1.3222	-0.0000	1.0659	-0.3523	0.8708	-0.4218	0.7465	-0.4471	0.6561	-0.4600	0.5650	-0.4677	0.0010	0.0010
1.2642	-0.0000	1.0525	-0.3279	0.8668	-0.4070	0.7446	-0.4366	0.6550	-0.4521	0.5643	-0.4614	0.0010	0.0010
1.2151	-0.0000	1.0380	-0.3035	0.8621	-0.3928	0.7425	-0.4266	0.6539	-0.4443	0.5635	-0.4530	0.0010	0.0010
1.1727	-0.0000	1.0237	-0.2791	0.8574	-0.3786	0.7404	-0.4166	0.6528	-0.4365	0.5626	-0.4448	0.0010	0.0010
1.1352	-0.0000	1.0094	-0.2546	0.8527	-0.3644	0.7383	-0.4067	0.6517	-0.4287	0.5617	-0.4366	0.0010	0.0010
1.1017	-0.0000	0.9952	-0.2300	0.8480	-0.3502	0.7362	-0.3967	0.6506	-0.4209	0.5608	-0.4284	0.0010	0.0010
1.0698	-0.0000	0.9810	-0.2054	0.8433	-0.3360	0.7341	-0.3867	0.6495	-0.4131	0.5600	-0.4202	0.0010	0.0010
0.9998	-0.0000	0.9668	-0.1808	0.8386	-0.3218	0.7320	-0.3767	0.6484	-0.4053	0.5591	-0.4120	0.0010	0.0010
0.9224	-0.0000	0.9526	-0.1562	0.8339	-0.3076	0.7299	-0.3667	0.6473	-0.3975	0.5582	-0.4038	0.0010	0.0010
0.8451	-0.0000	0.9384	-0.1316	0.8292	-0.2934	0.7278	-0.3567	0.6462	-0.3897	0.5573	-0.3956	0.0010	0.0010
0.8017	-0.0000	0.9242	-0.1070	0.8245	-0.2792	0.7257	-0.3467	0.6451	-0.3819	0.5564	-0.3874	0.0010	0.0010
0.7583	-0.0000	0.9100	-0.0824	0.8198	-0.2650	0.7236	-0.3367	0.6440	-0.3741	0.5555	-0.3792	0.0010	0.0010
0.7149	-0.0000	0.8958	-0.0578	0.8151	-0.2508	0.7215	-0.3267	0.6429	-0.3663	0.5546	-0.3710	0.0010	0.0010
0.6715	-0.0000	0.8816	-0.0332	0.8104	-0.2366	0.7194	-0.3167	0.6418	-0.3585	0.5537	-0.3628	0.0010	0.0010
0.6281	-0.0000	0.8674	-0.0086	0.8057	-0.2224	0.7173	-0.3067	0.6407	-0.3507	0.5528	-0.3546	0.0010	0.0010
0.5847	-0.0000	0.8532	0.0160	0.8010	-0.2082	0.7152	-0.2967	0.6396	-0.3429	0.5519	-0.3464	0.0010	0.0010
0.5413	-0.0000	0.8390	0.0414	0.7963	-0.1940	0.7131	-0.2867	0.6385	-0.3351	0.5510	-0.3382	0.0010	0.0010
0.4979	-0.0000	0.8248	0.0668	0.7916	-0.1798	0.7110	-0.2767	0.6374	-0.3273	0.5501	-0.3300	0.0010	0.0010
0.4545	-0.0000	0.8106	0.0922	0.7869	-0.1656	0.7089	-0.2667	0.6363	-0.3195	0.5492	-0.3218	0.0010	0.0010
0.4111	-0.0000	0.7964	0.1176	0.7822	-0.1514	0.7068	-0.2567	0.6352	-0.3117	0.5483	-0.3136	0.0010	0.0010
0.3677	-0.0000	0.7822	0.1430	0.7775	-0.1372	0.7047	-0.2467	0.6341	-0.3039	0.5474	-0.3054	0.0010	0.0010
0.3243	-0.0000	0.7680	0.1684	0.7728	-0.1230	0.7026	-0.2367	0.6330	-0.2961	0.5465	-0.2972	0.0010	0.0010
0.2809	-0.0000	0.7538	0.1938	0.7681	-0.1088	0.7005	-0.2267	0.6319	-0.2883	0.5456	-0.2890	0.0010	0.0010
0.2375	-0.0000	0.7396	0.2192	0.7634	-0.0946	0.6984	-0.2167	0.6308	-0.2805	0.54			

TABLE 5. REFLECTIVITY COEFFICIENTS

S	0.0500		0.1000		0.1500		0.2000		0.2500		P
	R	T	R	T	R	T	R	T	R	T	
0.0000	1.0000	0.0000	1.0000	0.0000	1.0000	0.0000	1.0000	0.0000	1.0000	0.0000	0.0000
0.0001	0.9999	0.0001	0.9999	0.0001	0.9999	0.0001	0.9999	0.0001	0.9999	0.0001	0.0001
0.0002	0.9998	0.0002	0.9998	0.0002	0.9998	0.0002	0.9998	0.0002	0.9998	0.0002	0.0002
0.0003	0.9997	0.0003	0.9997	0.0003	0.9997	0.0003	0.9997	0.0003	0.9997	0.0003	0.0003
0.0004	0.9996	0.0004	0.9996	0.0004	0.9996	0.0004	0.9996	0.0004	0.9996	0.0004	0.0004
0.0005	0.9995	0.0005	0.9995	0.0005	0.9995	0.0005	0.9995	0.0005	0.9995	0.0005	0.0005
0.0006	0.9994	0.0006	0.9994	0.0006	0.9994	0.0006	0.9994	0.0006	0.9994	0.0006	0.0006
0.0007	0.9993	0.0007	0.9993	0.0007	0.9993	0.0007	0.9993	0.0007	0.9993	0.0007	0.0007
0.0008	0.9992	0.0008	0.9992	0.0008	0.9992	0.0008	0.9992	0.0008	0.9992	0.0008	0.0008
0.0009	0.9991	0.0009	0.9991	0.0009	0.9991	0.0009	0.9991	0.0009	0.9991	0.0009	0.0009
0.0010	0.9990	0.0010	0.9990	0.0010	0.9990	0.0010	0.9990	0.0010	0.9990	0.0010	0.0010
0.0011	0.9989	0.0011	0.9989	0.0011	0.9989	0.0011	0.9989	0.0011	0.9989	0.0011	0.0011
0.0012	0.9988	0.0012	0.9988	0.0012	0.9988	0.0012	0.9988	0.0012	0.9988	0.0012	0.0012
0.0013	0.9987	0.0013	0.9987	0.0013	0.9987	0.0013	0.9987	0.0013	0.9987	0.0013	0.0013
0.0014	0.9986	0.0014	0.9986	0.0014	0.9986	0.0014	0.9986	0.0014	0.9986	0.0014	0.0014
0.0015	0.9985	0.0015	0.9985	0.0015	0.9985	0.0015	0.9985	0.0015	0.9985	0.0015	0.0015
0.0016	0.9984	0.0016	0.9984	0.0016	0.9984	0.0016	0.9984	0.0016	0.9984	0.0016	0.0016
0.0017	0.9983	0.0017	0.9983	0.0017	0.9983	0.0017	0.9983	0.0017	0.9983	0.0017	0.0017
0.0018	0.9982	0.0018	0.9982	0.0018	0.9982	0.0018	0.9982	0.0018	0.9982	0.0018	0.0018
0.0019	0.9981	0.0019	0.9981	0.0019	0.9981	0.0019	0.9981	0.0019	0.9981	0.0019	0.0019
0.0020	0.9980	0.0020	0.9980	0.0020	0.9980	0.0020	0.9980	0.0020	0.9980	0.0020	0.0020
0.0021	0.9979	0.0021	0.9979	0.0021	0.9979	0.0021	0.9979	0.0021	0.9979	0.0021	0.0021
0.0022	0.9978	0.0022	0.9978	0.0022	0.9978	0.0022	0.9978	0.0022	0.9978	0.0022	0.0022
0.0023	0.9977	0.0023	0.9977	0.0023	0.9977	0.0023	0.9977	0.0023	0.9977	0.0023	0.0023
0.0024	0.9976	0.0024	0.9976	0.0024	0.9976	0.0024	0.9976	0.0024	0.9976	0.0024	0.0024
0.0025	0.9975	0.0025	0.9975	0.0025	0.9975	0.0025	0.9975	0.0025	0.9975	0.0025	0.0025
0.0026	0.9974	0.0026	0.9974	0.0026	0.9974	0.0026	0.9974	0.0026	0.9974	0.0026	0.0026
0.0027	0.9973	0.0027	0.9973	0.0027	0.9973	0.0027	0.9973	0.0027	0.9973	0.0027	0.0027
0.0028	0.9972	0.0028	0.9972	0.0028	0.9972	0.0028	0.9972	0.0028	0.9972	0.0028	0.0028
0.0029	0.9971	0.0029	0.9971	0.0029	0.9971	0.0029	0.9971	0.0029	0.9971	0.0029	0.0029
0.0030	0.9970	0.0030	0.9970	0.0030	0.9970	0.0030	0.9970	0.0030	0.9970	0.0030	0.0030
0.0031	0.9969	0.0031	0.9969	0.0031	0.9969	0.0031	0.9969	0.0031	0.9969	0.0031	0.0031
0.0032	0.9968	0.0032	0.9968	0.0032	0.9968	0.0032	0.9968	0.0032	0.9968	0.0032	0.0032
0.0033	0.9967	0.0033	0.9967	0.0033	0.9967	0.0033	0.9967	0.0033	0.9967	0.0033	0.0033
0.0034	0.9966	0.0034	0.9966	0.0034	0.9966	0.0034	0.9966	0.0034	0.9966	0.0034	0.0034
0.0035	0.9965	0.0035	0.9965	0.0035	0.9965	0.0035	0.9965	0.0035	0.9965	0.0035	0.0035
0.0036	0.9964	0.0036	0.9964	0.0036	0.9964	0.0036	0.9964	0.0036	0.9964	0.0036	0.0036
0.0037	0.9963	0.0037	0.9963	0.0037	0.9963	0.0037	0.9963	0.0037	0.9963	0.0037	0.0037
0.0038	0.9962	0.0038	0.9962	0.0038	0.9962	0.0038	0.9962	0.0038	0.9962	0.0038	0.0038
0.0039	0.9961	0.0039	0.9961	0.0039	0.9961	0.0039	0.9961	0.0039	0.9961	0.0039	0.0039
0.0040	0.9960	0.0040	0.9960	0.0040	0.9960	0.0040	0.9960	0.0040	0.9960	0.0040	0.0040
0.0041	0.9959	0.0041	0.9959	0.0041	0.9959	0.0041	0.9959	0.0041	0.9959	0.0041	0.0041
0.0042	0.9958	0.0042	0.9958	0.0042	0.9958	0.0042	0.9958	0.0042	0.9958	0.0042	0.0042
0.0043	0.9957	0.0043	0.9957	0.0043	0.9957	0.0043	0.9957	0.0043	0.9957	0.0043	0.0043
0.0044	0.9956	0.0044	0.9956	0.0044	0.9956	0.0044	0.9956	0.0044	0.9956	0.0044	0.0044
0.0045	0.9955	0.0045	0.9955	0.0045	0.9955	0.0045	0.9955	0.0045	0.9955	0.0045	0.0045
0.0046	0.9954	0.0046	0.9954	0.0046	0.9954	0.0046	0.9954	0.0046	0.9954	0.0046	0.0046
0.0047	0.9953	0.0047	0.9953	0.0047	0.9953	0.0047	0.9953	0.0047	0.9953	0.0047	0.0047
0.0048	0.9952	0.0048	0.9952	0.0048	0.9952	0.0048	0.9952	0.0048	0.9952	0.0048	0.0048
0.0049	0.9951	0.0049	0.9951	0.0049	0.9951	0.0049	0.9951	0.0049	0.9951	0.0049	0.0049
0.0050	0.9950	0.0050	0.9950	0.0050	0.9950	0.0050	0.9950	0.0050	0.9950	0.0050	0.0050

FIGURE 5

DELECTRICAL TABLE TYPES

S	E	S	E	S	E	S	E	S	E	S	E
0.0010	2.7663	0.0100	0.2832	0.1010	-0.1518	0.1510	-0.4078	0.2010	-0.5879	0.2510	-0.7313
0.0020	2.3350	0.0200	0.2709	0.1020	-0.1500	0.1520	-0.4120	0.2020	-0.5910	0.2520	-0.7318
0.0030	2.0069	0.0300	0.2587	0.1030	-0.1482	0.1530	-0.4162	0.2030	-0.5967	0.2530	-0.7364
0.0040	1.9038	0.0400	0.2468	0.1040	-0.1460	0.1540	-0.4203	0.2040	-0.5993	0.2540	-0.7389
0.0050	1.7817	0.0500	0.2352	0.1050	-0.1445	0.1550	-0.4244	0.2050	-0.6024	0.2550	-0.7414
0.0060	1.6836	0.0600	0.2237	0.1060	-0.1430	0.1560	-0.4285	0.2060	-0.6055	0.2560	-0.7439
0.0070	1.5975	0.0700	0.2124	0.1070	-0.1415	0.1570	-0.4326	0.2070	-0.6086	0.2570	-0.7463
0.0080	1.4625	0.0800	0.2014	0.1080	-0.1400	0.1580	-0.4366	0.2080	-0.6117	0.2580	-0.7488
0.0090	1.3975	0.0900	0.1905	0.1090	-0.2003	0.1590	-0.4407	0.2090	-0.6147	0.2590	-0.7513
0.0100	1.3004	0.1000	0.1798	0.1100	-0.2061	0.1600	-0.4448	0.2100	-0.6178	0.2600	-0.7537
0.0110	1.2598	0.1100	0.1692	0.1110	-0.2119	0.1610	-0.4488	0.2110	-0.6208	0.2610	-0.7562
0.0120	1.2254	0.1200	0.1589	0.1120	-0.2177	0.1620	-0.4528	0.2120	-0.6238	0.2620	-0.7586
0.0130	1.1934	0.1300	0.1487	0.1130	-0.2235	0.1630	-0.4568	0.2130	-0.6268	0.2630	-0.7610
0.0140	1.1662	0.1400	0.1387	0.1140	-0.2293	0.1640	-0.4608	0.2140	-0.6298	0.2640	-0.7635
0.0150	1.1423	0.1500	0.1288	0.1150	-0.2351	0.1650	-0.4648	0.2150	-0.6327	0.2650	-0.7659
0.0160	1.1212	0.1600	0.1191	0.1160	-0.2409	0.1660	-0.4687	0.2160	-0.6357	0.2660	-0.7683
0.0170	0.9926	0.1700	0.1095	0.1170	-0.2468	0.1670	-0.4727	0.2170	-0.6386	0.2670	-0.7708
0.0180	0.9462	0.1800	0.1001	0.1180	-0.2528	0.1680	-0.4767	0.2180	-0.6416	0.2680	-0.7732
0.0190	0.9118	0.1900	0.0908	0.1190	-0.2588	0.1690	-0.4807	0.2190	-0.6445	0.2690	-0.7756
0.0200	0.8797	0.2000	0.0816	0.1200	-0.2648	0.1700	-0.4847	0.2200	-0.6474	0.2700	-0.7780
0.0210	0.8481	0.2100	0.0726	0.1210	-0.2708	0.1710	-0.4887	0.2210	-0.6503	0.2710	-0.7804
0.0220	0.8185	0.2200	0.0637	0.1220	-0.2768	0.1720	-0.4927	0.2220	-0.6532	0.2720	-0.7828
0.0230	0.7907	0.2300	0.0549	0.1230	-0.2828	0.1730	-0.4967	0.2230	-0.6561	0.2730	-0.7852
0.0240	0.7645	0.2400	0.0463	0.1240	-0.2888	0.1740	-0.5007	0.2240	-0.6590	0.2740	-0.7876
0.0250	0.7397	0.2500	0.0377	0.1250	-0.2948	0.1750	-0.5047	0.2250	-0.6619	0.2750	-0.7899
0.0260	0.7164	0.2600	0.0293	0.1260	-0.2998	0.1760	-0.5087	0.2260	-0.6648	0.2760	-0.7923
0.0270	0.6945	0.2700	0.0210	0.1270	-0.3048	0.1770	-0.5127	0.2270	-0.6677	0.2770	-0.7946
0.0280	0.6740	0.2800	0.0127	0.1280	-0.3098	0.1780					

overcome for non-magnetic materials. The solution was the computation of extensive tables of insertion loss and insertion phase vs. dielectric constant, loss tangent, incidence angle, thickness-to-wavelength ratio, and polarization. Reference 5 describes these tables. Figure 8 is a sample page from these tables. It had been suspected that the insertion loss measurement on thin flat sheets would not have sufficient sensitivity for good loss tangent determination. Actually it turns out that for lossy materials with a thickness of the order of one-half wavelength the loss tangent determination is as accurate as with a dielectrometer. For low-loss materials with the same thickness the measurement accuracy of loss tangent is not as good as on the dielectrometer and is ± 0.001 or $\pm 3\%$ whichever is greater.

Encouraged by the success with the interferometer measurements, attempts were made to extend the free space measurement art into other variations. Potentially, there are several measurable reflection-transmission parameters for a flat sheet in free space. At normal incidence, they are: insertion loss, insertion phase delay, reflection loss, reflection phase, reflection loss with the sample metal-backed and reflection phase with the sample metal-backed. If oblique incidence is considered, such as 45° incidence as in the interferometer tables, there are in addition four other parameters: insertion loss and insertion phase delay for perpendicular and parallel polarization. For the non-magnetic case, with only two values, dielectric constant and loss tangent to be determined, it should be sufficient to measure any two of the ten parameters listed. Eliminating parallel polarization at 45° , because it does not place the electric field in the plane of the sample, there are still eight potentially measurable parameters from which any pair could be chosen. Attempts to develop an accurate measurement technique for free space by use of these concepts are proceeding, but have not succeeded as of this writing mainly because of difficulties in making accurate reflection measurements in free space. To date, these experiments have been limited to attempts to measure reflected power. Possibly better performance will be achieved with reflection phase.

Extension of the free-space measurement to the magnetic case has not as of this writing, been undertaken.

Another program which grew out of the initial success with the interferometer was the development of techniques for using the instrument to check non-destructively the degree of homogeneity of a flat dielectric sheet. This is described fully in Reference 4.

These measurements were all made at 45° incidence using perpendicular polarization to keep the electric field in the plane of the sample. The new variation in measurement technique developed was the capability of reducing the measurement area (inspection zone) for a given single measurement to a minimum. The minimum is an area of approximately one square wavelength. As the measurement is normally made, using standard 15 db gain horns, the

inspection zone is approximately 16 square wavelengths in area. The technique which permitted reduction of the inspection zone to one square wavelength was the use of special small-aperture horns with a minimum of spacing between them, just enough to permit insertion of the sample between the horns at 45° incidence. The small aperture was achieved by dielectric loading of an open-end waveguide, thus making possible an aperture which was about three-fourths that of the waveguide cross section. At 8.6 Gc, for example, with a sample one foot square, it was possible to layout 100 inspection zones, each one inch square with a one inch uninspected border all around the periphery. This border was maintained to minimize edge effects. In addition, to further minimize edge effects guards were used whenever the inspection zone was within 3 inches of the edge of the sample. These guards consisted of dielectric slabs of about the same dielectric constant and thickness as the sample being measured and were placed along the edge of the sample to be guarded. To verify the accuracy of the interferometer in the homogeneity measurement, 10 samples were cut out at random points from each of 3 sample slabs and measured in a shorted-waveguide dielectrometer. Correlation within 2% was maintained between the interferometer and dielectrometer dielectric-constant measurements, with two-thirds of the measurements agreeing within less than 1%. As a by-product of this exercise it was established that a homogeneity level of less than 3% variation in dielectric constant at 8.6 Gc can be held in loaded plastics at the 4 and 6 dielectric-constant level. In the corresponding unloaded plastics, at a 2.5 dielectric-constant level, the variation is less than 1%. Measurements of the homogeneity that can be achieved in glass are now in progress.

TABLE IV - DIELECTROMETER LAB SHEET

Sample Identification _____

Name _____
 Date _____
 Time _____

Sample Thickness _____
 Guide Wavelength _____

Frequency (Gc) _____
 Free-Space Wavelength _____

$(.5)n - (\Delta X + S + .25)$

$(.5)n - (\Delta X + S)$

$X_o =$ _____
 $W_o =$ _____
 Table One
 $U_o =$ _____
 $V_o =$ _____

$X_s =$ _____
 $W_s =$ _____
 Table One
 $U_s =$ _____
 $V_s =$ _____

$P = U_o + U_s =$ _____
 $Q = V_o + V_s =$ _____

$A = U_o - U_s =$ _____
 $B = V_o - V_s =$ _____

$S =$ _____
 Table Three
 $E =$ _____

Table Two
 $C =$ _____
 $D =$ _____

$R = C + E =$ _____

$F_e = R + P =$ _____
 $G_e = D + Q =$ _____
 Table Four and Five
 $K_e =$ _____
 $T_e =$ _____

$F_m = R - P =$ _____
 $G_m = D - Q =$ _____
 Table Four and Five
 $K_m =$ _____
 $T_m =$ _____

After waveguide conversion, if necessary,

$K_e =$ _____
 $T_e =$ _____

$K_m =$ _____
 $T_m =$ _____

NOTE: To find K_e and T_e by the short-form procedure, ignore Table Two and Three and use $F_e = 2P$, $G_e = 2Q$, in Table Four.

REFERENCES

1. VonHippel, A. R. , "Dielectric Materials and Applications, " 1954, The Technology Press of M. I. T. and John Wiley and Sons, Inc.
2. Redheffer, R. M. , "The Measurement of Dielectric Constants, " Chapter 10 of Techniques of Microwave Measurements, M. I. T. Radiation Laboratory Series, Vol. 11, pp. 591-606, McGraw Hill Book Co., Inc., 1947
3. Hope, H. R. and Bayless, W. W. , "Microwave Dielectric Measurements at High Temperatures, " Technical Memorandum No. 577, Hughes Aircraft Company, ASTIA Document No. AD207804, June 1958
4. Luoma, E. J. and Volk, M. C. , "Measurement of Dielectric Homogeneity With a Microwave Interferometer, " Final Report on Subcontract No. 285 under Prime Contract AF19(628)-500 by Emerson & Cuming, Inc. for M. I. T. Lincoln Laboratory
5. Preliminary Technical Bulletin 30-2-2, Ecco Interferometer Tables, Emerson & Cuming, Inc., Canton, Massachusetts

ACKNOWLEDGMENTS

1. The work on improvements in the dielectrometer and interferometer art was accomplished in part under Contracts AF33(616)-7047 and AF33(657)-11139 with Mr. William F. Bahret of the Aeronautical Systems Division serving as the Air Force Project Engineer.
2. The work on extension of the interferometer technique to homogeneity measurements was sponsored under Subcontract No. 285 of Prime Contract No. AF19(628)-500 by the M. I. T. Lincoln Laboratory with Dr. Peter Fritsch of the Lincoln Laboratory serving as the sponsor's project engineer.
3. The dielectrometer and interferometer conversion tables were developed by Professor Samuel J. Mason of M. I. T. serving as consultant to Emerson & Cuming, Inc. Computations were carried out on the IBM 7090 data processing system.

NANOSECOND PULSE SCATTERING FROM EXTENDED LABORATORY TARGETS*

H. S. Rothman, H. Guthart and T. Morita
Stanford Research Institute
Menlo Park, California

ABSTRACT

Through the use of an X-band (9.4 Gc) radar with a pulse width of one nanosecond, pulse broadening and interference effects in the reflected electromagnetic signal have been studied. This paper is concerned with scattering from targets of simple configuration such as an array of dipole scatterers as well as a metal cylinder. The backscatter from a simplified ionized target in the form of an extended laminar-plasma column has also been investigated and the measured results compared with calculations based on a homogeneous model approximation. The initial diagnosis of the ionized constituents of a turbulent flame has been completed using an electrostatic ion probe and a microwave electron probe, and the results are presented.

INTRODUCTION

The radar data from field measurements programs show that during the altitude regime of the re-entry, when ionization is produced about the vehicle in the form of a plasma sheath and plasma trail, the character of the scattered return from the re-entry vehicle is considerably different from that expected from the bare body; an enhancement of the scattered return is observed, resulting in an appreciable increase in the received signal. During this period of backscatter cross-section enhancement, large pulse-to-pulse amplitude fluctuations are noticed and significant pulse broadening of individual received pulses is observed.¹

In succeeding sections, an experimental laboratory electromagnetic scattering program will be discussed. The program examined X-band pulses of nanosecond width reflected from a variety of scattering targets to aid in the explanation of the characteristics of radar backscatter observed in field measurement programs. The targets consisted of dipole arrays in free space and in dielectric rods. By adjusting the number and spacing of scattering elements, any degree of interference can be achieved.

* The work reported in this paper was supported by the Advanced Research Projects Agency, under Contract SD-103 under ARPA Order No. 281-62.

The scatter from columns, both metallic and ionized shall next be considered. The ionized laminar column was first diagnosed using Langmuir probes and microwave transmission measurements. The X-band scattering measurements shall then be compared with calculations based on a homogeneous model approximation.

Finally, the initial diagnosis of the ionized constituents of a turbulent flame shall be discussed and the results presented.

SCATTERING FROM EXTENDED TARGETS

Interference is a well known phenomenon that is manifested throughout the electromagnetic spectrum. For example, in optics when two objects are brought close together, their images overlap and interfere, producing light and dark rings. Similarly, if two scatterers of pulsed microwave energy are brought close enough together, the scattered pulses will overlap and interfere. The "resolving power" of the microwave pulse is determined by the pulse length and the group velocity of the pulse in the ambient medium. For example, if a millimicrosecond-long, square pulse is propagating in free space, then the energy of such a pulse is spatially distributed over a width of $30 \text{ cm} = (3 \times 10^{10} \text{ cm/sec})(10^{-9} \text{ sec})$, where $3 \times 10^{10} \text{ cm/sec}$ represents the group velocity in free space. As a consequence, if two scatterers are separated by some distance less than 15 cm, the scattered pulses overlap and the resultant pulse will have an interference pattern and an extended length. Let an electromagnetic pulse $\pi(t)$ propagating in the positive-x direction be incident on an extended radar target. The axis of the target is the x axis, and the electromagnetic backscatter cross section as a function of axial distance is $\sigma(x)$. Define the backscattered radar signal to be $f(t)$. In general $\sigma(x)$ and $f(t)$ represent voltage functions that contain amplitude and phase information, and $f(t)$ is given by

$$f(t) = \int_{-\infty}^{\infty} [\sigma(x)e^{-2j\beta x}] \pi \left(t - \frac{2x}{u} \right) dx \quad (1)$$

$$\text{where } f(t) = |f(t)| e^{-j\theta(t)}$$

$$\sigma(x) = |\sigma(x)| e^{-j\theta(x)}$$

u = Group velocity of pulse with respect to the target

β = Propagation constant along target.

Equation (1) indicates that the observed signal (amplitude and phase) is the convolution of the target cross section [inclusive of the phase factor, $\exp(-2j\beta x)$] with the incident pulse.

Scatter From Dipole Arrays

One of the simplest target configurations is that of an array of dipoles in free space. For simplicity, let $\sigma(x)$ represent the back-

scatter cross section of an array of two dipoles separated by a distance d , i.e.,

$$\sigma(x) = \sigma_0 \delta(x) + \sigma_0 \delta(x - d) \quad (2)$$

where $\delta(x)$ is the Dirac δ -function. The geometry of this configuration is shown in Fig. 1. The dipoles are arrayed along the x axis. The incoming pulse $\pi(t)$ is propagating in the positive- x direction and the backscattered signal $f(t)$ is triangular in amplitude and uniform in phase; then

$$\pi(t) = \left\{ \begin{array}{ll} 0 & t < -\frac{\tau}{2} \\ \frac{2}{\tau} \left(t + \frac{\tau}{2} \right) & -\frac{\tau}{2} < t < 0 \\ -\frac{2}{\tau} \left(t - \frac{\tau}{2} \right) & 0 < t < \frac{\tau}{2} \\ 0 & \frac{\tau}{2} < t \end{array} \right\} . \quad (3)$$

Using Eq. (1) and observing, in free-space, that $u = c$, the velocity of light

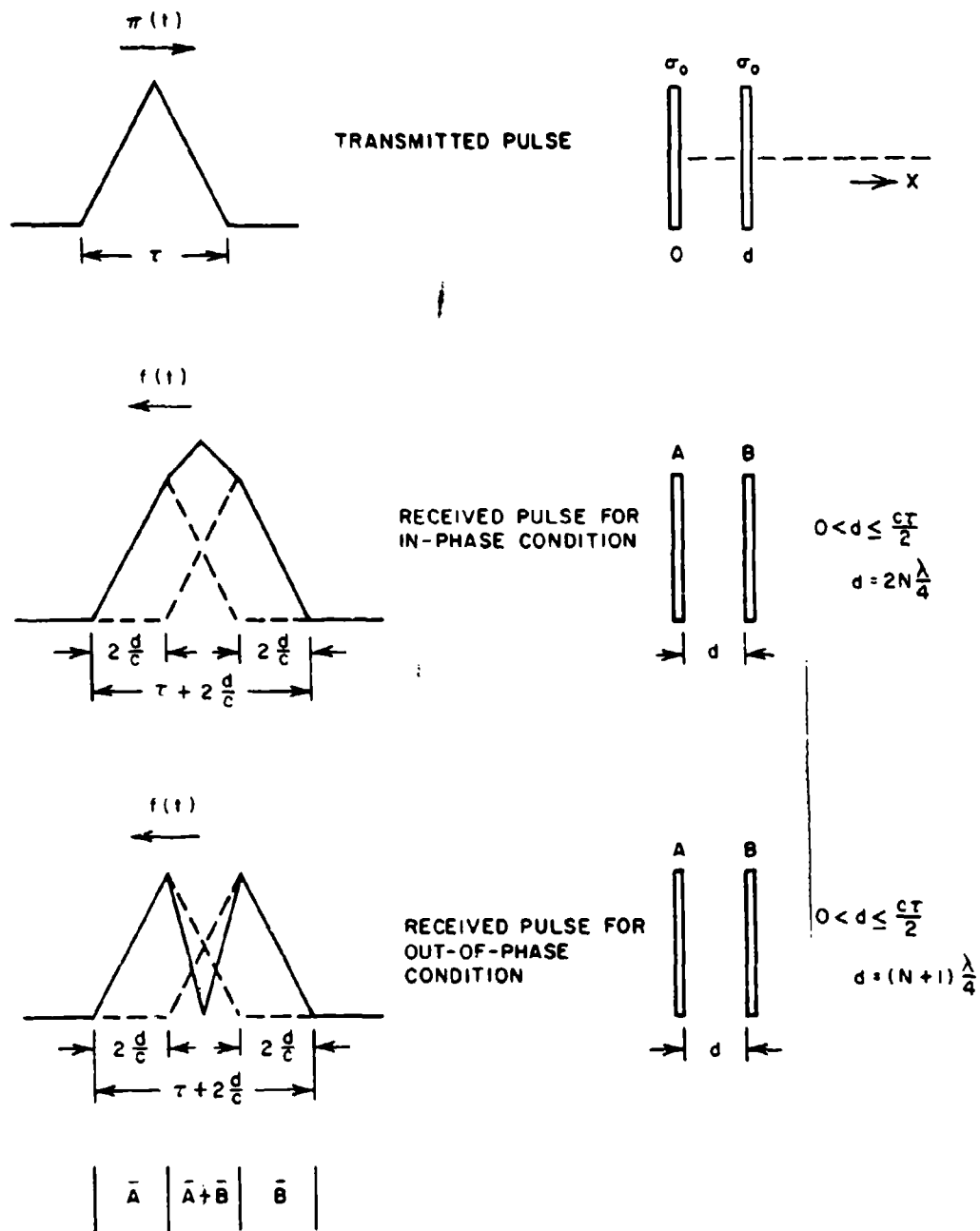
$$f(t) = \int_{-\infty}^{\infty} [\sigma_0 \delta(x) + \sigma_0 \delta(x - d)] e^{-j2\beta x} \pi \left(t - \frac{2x}{c} \right) dx .$$

Substituting for $\pi(t - 2x/c)$ and carrying out the integration,

$$f(t) = \sigma_0 \pi(t) + \sigma_0 \pi \left(t - \frac{2d}{c} \right) e^{-2j\beta d} . \quad (4)$$

If $d > c\tau/2$, then $f(t)$ is simply two triangular pulses with a peak-to-peak separation of $(2d/c)$ seconds. When $d < c\tau/2$, the two pulses interfere and the pulse amplitude as a function of time depends on βd , the relative phase between the scatterers. Two of the possible configurations for $f(t)$ are shown in Fig. 1 for the condition $d < c\tau/2$ and for $(2\beta d)$, an odd or even multiple of π radians. The total pulse width is consequently greater than the transmitted pulse width by $(2d/c)$ seconds. The first $(2d/c)$ seconds of the return pulse represents scatter from the first dipole, and the final $(2d/c)$ seconds represents scatter from the second dipole alone. In the overlap region or the center portion, the amplitude represents the vector sum of the scatter from both dipoles.

To demonstrate these simple concepts of pulse stretching, the scatter from an array of dipoles in free-space and in a dielectric rod was measured.



A-3657-88

Figure 1 Received Pulse Amplitude From Two Discrete Scatterers (Theoretical).

Figure 2 is a photograph of the scattering range employed in the measurements described in the following sections. In this photograph the horns are mounted on an "H" frame (horizontal in the photograph), which is pivoted at the sides of the chamber. The calibration sphere shown is located at a distance of 28 inches from the horns and in line with the horns. With this arrangement, the angle of incidence between the central ray of the antenna pattern and a vertical plane through the array can be varied through ± 25 degrees.

Also visible in Fig. 2 is absorbing material (developed by Goodrich and designated as Type VHP) mounted in the rear of the chamber, on portions of the top and bottom of the chamber and on the door, to reduce the extraneous background scattered signals in those regions which are within the resolution cell of the scattering object; Hairflex absorbing material (developed by Emerson & Cuming) is also wrapped around the interior waveguide circuitry to eliminate stray radiation.

In order to observe pulse-width broadening of the returns from the targets produced in the laboratory, a nanosecond- (10^{-9} seconds) pulse-width, X-band (9.4 Gc) radar was assembled. With a transmitted pulse width of one nanosecond, a range resolution of 6 inches is obtained. Since the radar will be used to examine scattering from a thermal plasma produced in a low-pressure chamber shown in Fig. 2 and described later in the paper, the scattering range was assembled inside this chamber. The short pulse will enable separation of the desired scattering from the target situated inside the chamber from the extraneous background scattering signals produced by reflections within the chamber.

The technique employed to generate the pulse is the same as that used by Convair in their short-pulse transmission system.² A block diagram of the nanosecond-pulse radar appears as Fig. 3. With this instrumentation, the pulse generated is triangular in shape with a peak output of about 1000 watts. The pulse rises to its peak amplitude in slightly more than 1.5 nanoseconds, has a base width of 3 nanoseconds, and a half-power width of one nanosecond.

On the range, cross sections as low as 0.8 cm^2 (8×10^{-5} square meters) can be measured at 28 inches from the antennas with a 6 db ratio of desired scattered signals to extraneous background scattered signals.

An array consisting of a 0.66-inch (0.52-wavelength) dipole scatterer and 0.63-inch (0.50-wavelength) dipole scatterer was positioned in the range and adjusted for constructive, quadrature, and destructive phase addition between the two scatterers. The results are shown in Fig. 4. The correlation of the calculated and experimental results for the quadrature and in-phase conditions is very good, especially in regard to the over-all pulse length. The extended width of the out-of-phase waveform is attributed to scatter from the array that specularly scatters from the walls of the chamber into the receiving horn. The multipath scatter becomes apparent only for arrays with small cross section. There is some time resolution of the multiple

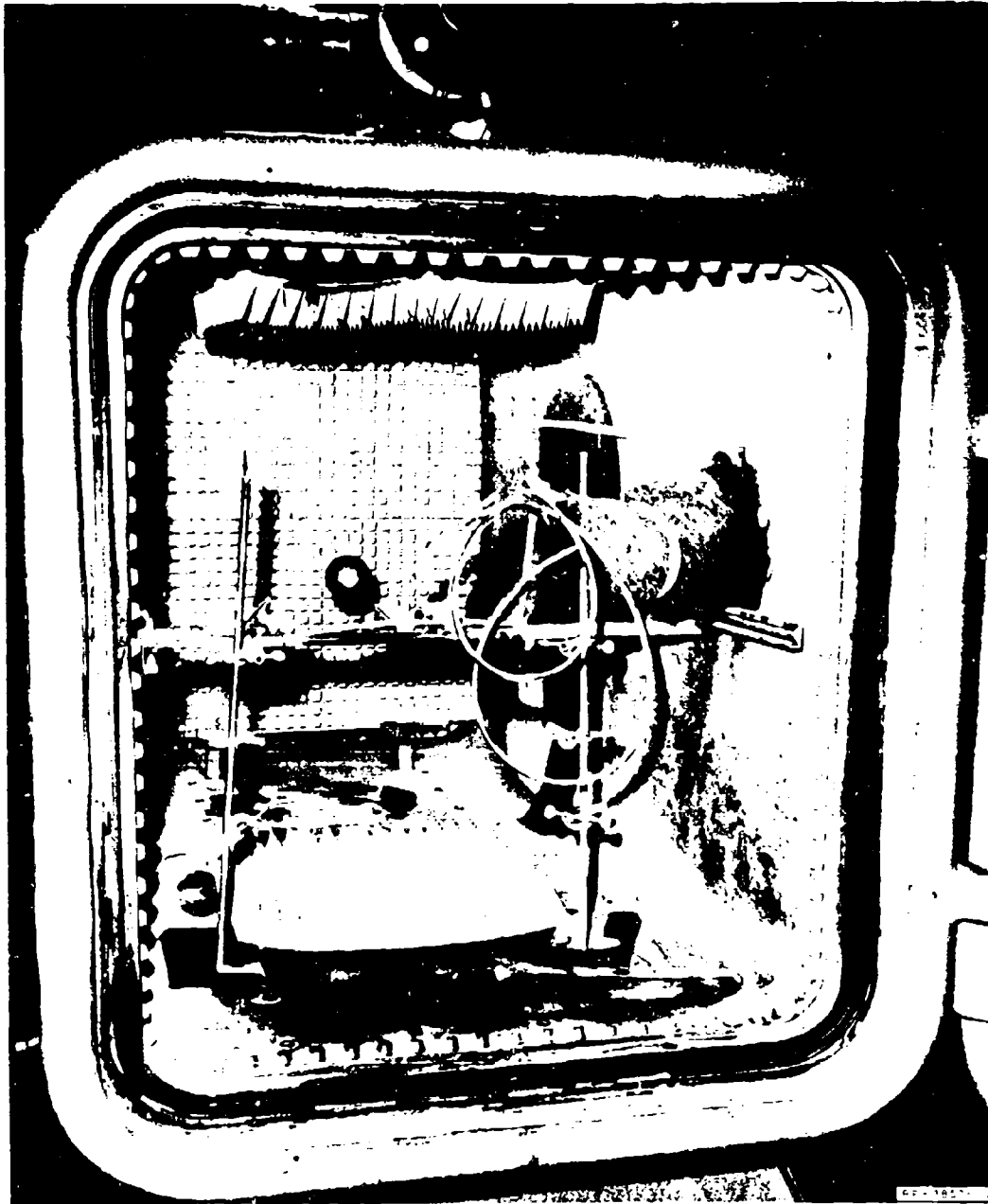


Figure 2 Photograph of Scattering Range Within Low-Pressure Chamber.

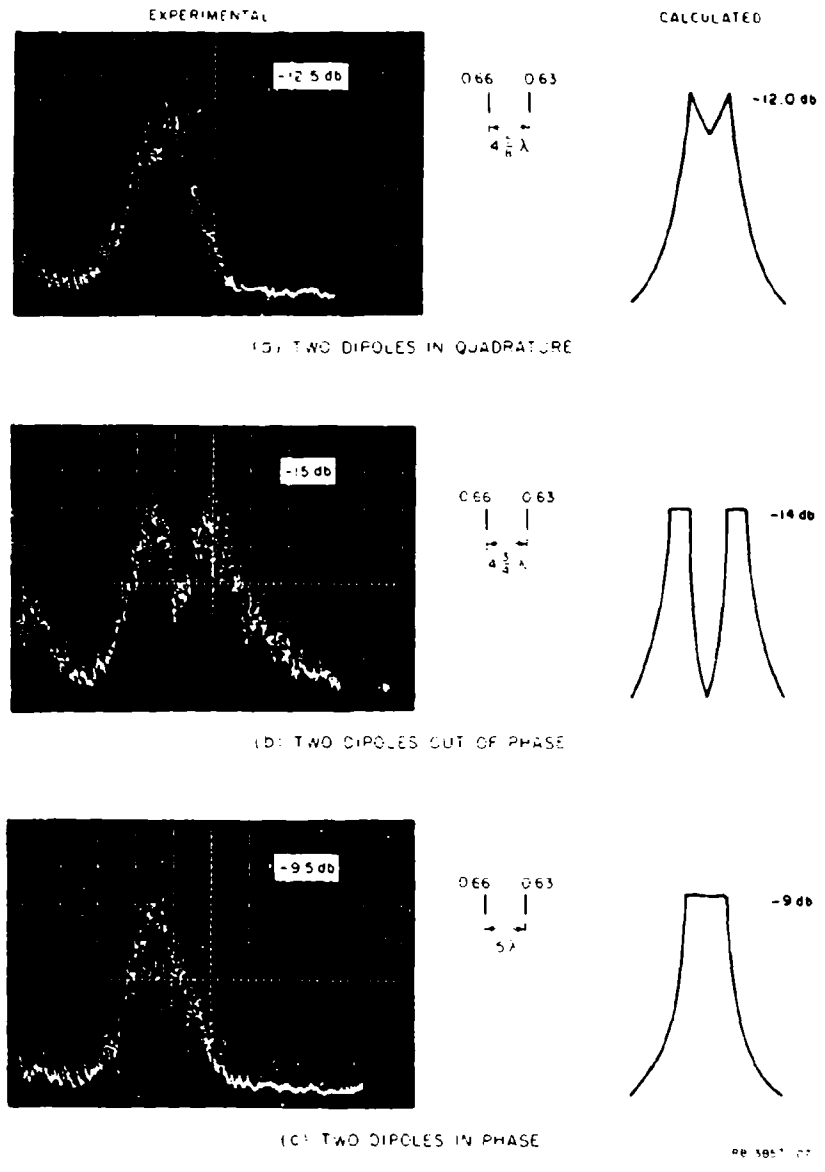


Figure 4 Received Pulse Amplitude From Two Interacting Discrete Scatterers (Experimental).

scatter in that the path length of this ray is greater than that of the direct ray, so that the stretching of the pulse occurs on the trailing edge. The correlation of the peaks and central null of the experimental and calculated waveforms in the out-of-phase condition is quite good.

In Fig. 4 the ordinate is linear in power and each abscissa division corresponds to 1 nanosecond; therefore, a sampling point occurs every 0.01 nsec. The db ratings in the upper corners of the oscilloscope pictures refer the indicated signal amplitude to the backscattered signal from a 4-inch-diameter metal sphere at a range of 28 inches from the transceiving horns. At 0.375 Gc, the sphere cross section is 74.5 cm².

Before examining the results of the backscatter measurements from a dielectric rod, let us briefly consider the nature of wave propagation along the rod. The dielectric rod is one of a class of structures capable of guiding an electromagnetic wave. The rod can support a propagating mode that is intimately bound to its surface. The field is characterized by an exponential decay away from the surface and has the usual propagation function $e^{-j\beta z}$ along the axis. For this reason, the solution to the wave equation is called a surface wave and the rod may be called a surface waveguide. At discontinuities in rod configuration, radiation takes place. The tendency toward radiation in a dielectric rod is turned to advantage when the rod is used as an end-fire antenna.

The mechanism of backscatter for the surface mode of the dielectric rod is described by the following sequence. A fraction of energy from the incident plane wave is coupled into the surface-wave mode and then propagates down the rod unattenuated (lossless dielectric rod). The amount of coupling to the rod is proportional to the gain of the rod as an antenna, which is in turn dependent on the rod length. At the far end of the rod, a fraction of the incident surface-wave energy is reflected as a surface wave, and a fraction is transmitted as radiation. When the reflected wave is incident on the near end of the rod, a fraction is again radiated.

The backscatter signal detected by the nanosecond radar from a 12.6-inch-long, 0.5-inch-diameter polyrod whose axis is rotated 10° with respect to the direction of propagation of incident energy is shown in Fig. 5. In this and succeeding polyrod measurements, the ends of the rod have been partially metallized to enhance the over-all backscatter signal as well as to enhance the direct scatter from the end relative to the surface-wave scatter. The first (left) pulse of Fig. 5 represents scatter from the end of the polyrod and the second (right) pulse indicates surface-wave scatter. The peak-to-peak separation is 3 nanoseconds, corresponding to an 18-inch free-space separation of scatterers. The actual physical separation is 12.6 inches. Consequently the group velocity along the rod is approximately two-thirds the speed of light, which is in agreement with the theoretical calculations.

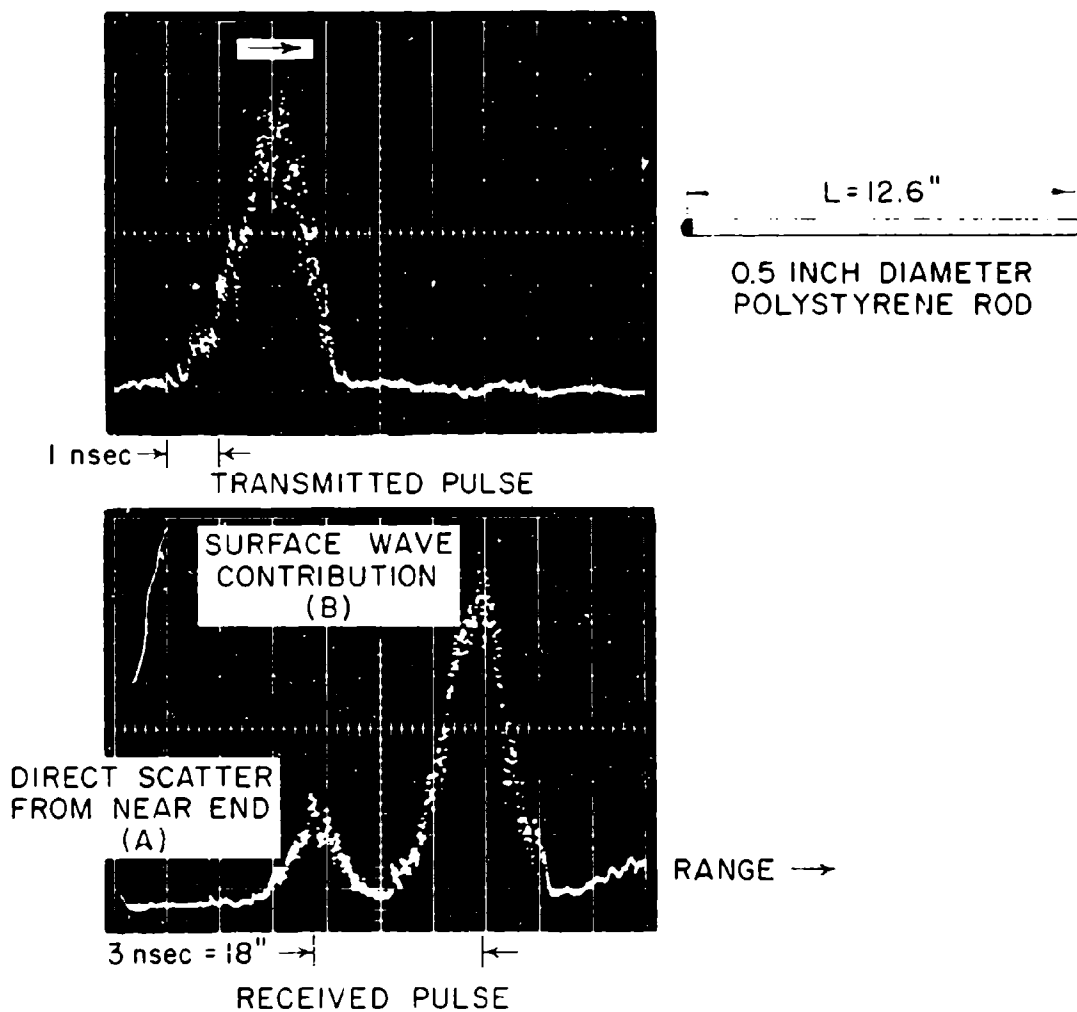


Figure 5 Scattered Return From a Smooth Dielectric Cylinder.

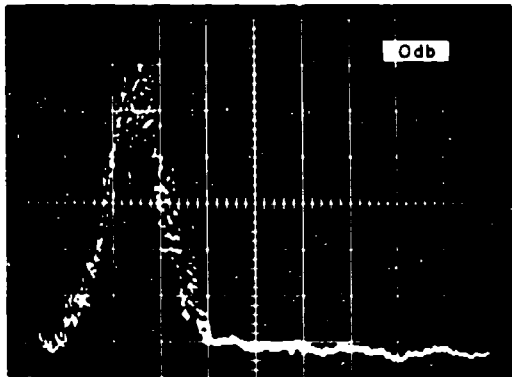
In a final sequence of measurements, the scatter from a lucite rod loaded with dipoles was measured. The sequence of backscattered energy from the dipole-loaded rod is shown in Fig. 6. In Figs. 6(a) and 6(b) the calibration pulse and the scatter from the unloaded rod is shown. In Fig. 6(c), the scatter from the rod plus a 0.29-inch dipole 3.495 inches (three surface-wave wavelengths) from the near end is shown. Since the dipole scatter is in phase with that from the near end, the initial pulse scatter is enhanced. Figure 6(d) shows the backscatter from a configuration similar to the previous case but where the dipole scatter is out of phase with respect to the initial pulse, thereby almost cancelling this initial scatter. In Figs. 6(e) and 6(f) a 0.40-inch dipole was added so that scatter in phase with the initial direct scatter, and the 0.29-inch dipole was adjusted for the in-phase and the out-of-phase conditions. This sequence was repeated in Figs. 6(g) and 6(h) for different locations of the two dipoles.

Scatter From a Metal Cylinder

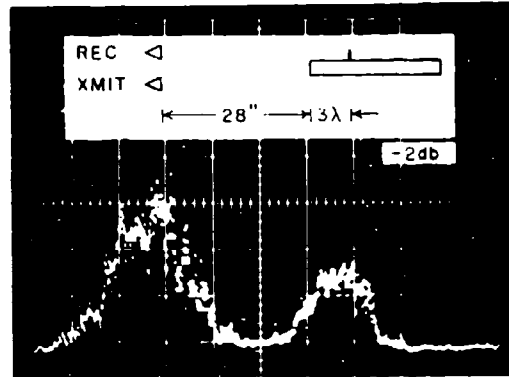
The next extended scattering target to be considered was a long metallic cylinder. Due to the wide illumination of the cylinder by the transmitting antenna inside the low-pressure vessel, which is used as the scattering range, the receiving antenna is not in the far zone of the scattering column ($R < 2L^2/\lambda$, where R is range, L is the length of the column illuminated by the transmitting antenna, and λ is the wavelength). As a result, the scatterer is illuminated with a phase variation that lags the phase at the point on the column that is the shortest distance from the antenna (referred to as the specular point).

Since the receiving antenna is in the Fresnel region of the scatterer and the illumination of the specular region by both antennas varies with incidence angle the backscatter cross section will be modified. Calculations for the backscatter cross section of a metallic cylinder for $2\pi a/\lambda \gg 1$ (where a is the radius) including the phase curvature, antenna pattern and illumination by the short pulse were made using the expressions given in Reference 3. The resulting cross section for a 1-1/2 inch radius metallic cylinder relative to the calculated cross section of a 2-inch radius calibration sphere is plotted in Fig. 7. Also shown in this figure are the experimental results obtained from this type of cylinder placed in the chamber. As seen by the figure, the scattering measurements agree to within 1 db of the calculated backscatter results for all values of angle of incidence (the angle between the central ray of the antenna pattern and the column axis), α , chosen.

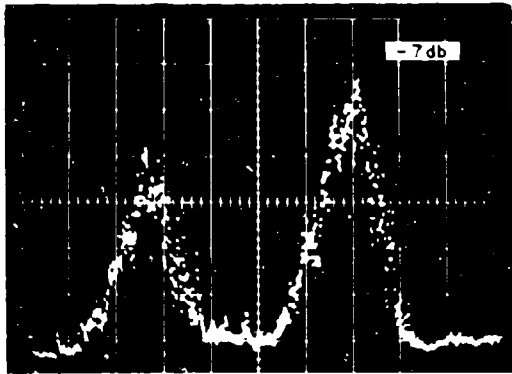
The level of the broadened portion of the backscattered return from an extended laminar target is greater than 10 db below the level of the portion from the specular region. However, the dynamic range of the sampling oscilloscope is only about 6 db. Hence to observe the pulse width broadening from a long metallic cylinder the specular region was shadowed and measured experimentally with the nanosecond pulse width radar inside the low-pressure chamber. The resultant theoretical return not including the finite bandwidth of the receiver is plotted in Fig. 8.



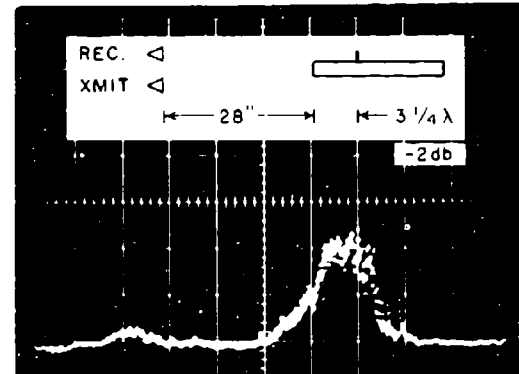
4" DIAMETER SPHERE
(a)



17.6" LUCITE ROD + 0.29" DIPOLE
(c)



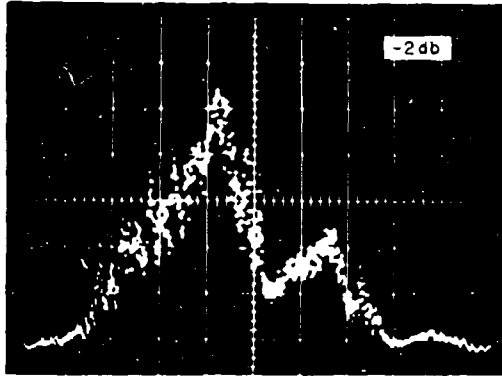
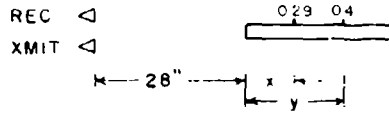
17.6" LUCITE ROD
(b)



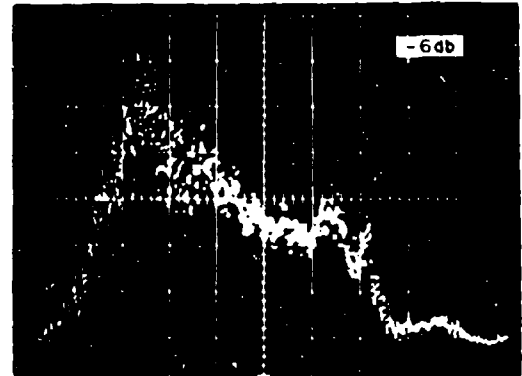
17.6" LUCITE ROD + 0.29" DIPOLE
(d)

RB-3857-102

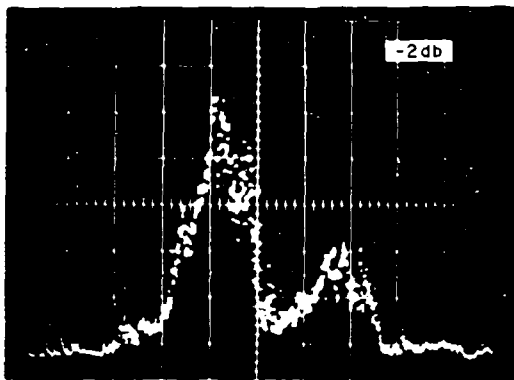
Figure 6 Scattered Return From A Dielectric Cylinder Loaded With Dipoles.



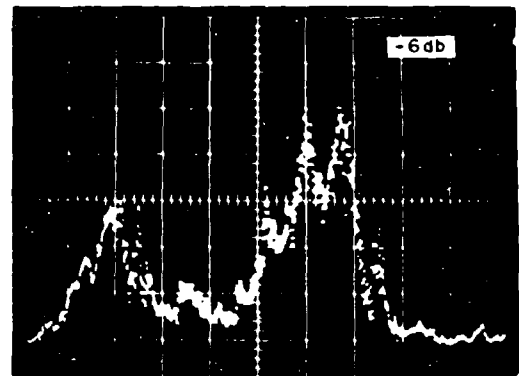
17.6" LUCITE ROD + 0.29" DIPOLE + 0.4" DIPOLE
 $x = 3.50$
 $y = 7.99$
 (e)



17.6" LUCITE ROD + 0.29" DIPOLE + 0.4" DIPOLE
 $x = 5.83$
 $y = 11.65$
 (g)



7.6" LUCITE ROD + 0.4" DIPOLE + 0.29" DIPOLE
 $x = 3.76$
 $y = 7.99$
 (f)



17.6" LUCITE ROD + 0.29" DIPOLE + 0.4" DIPOLE
 $x = 6.12$
 $y = 11.65$
 (h)

PB-3857-103

Figure 6 Continued.

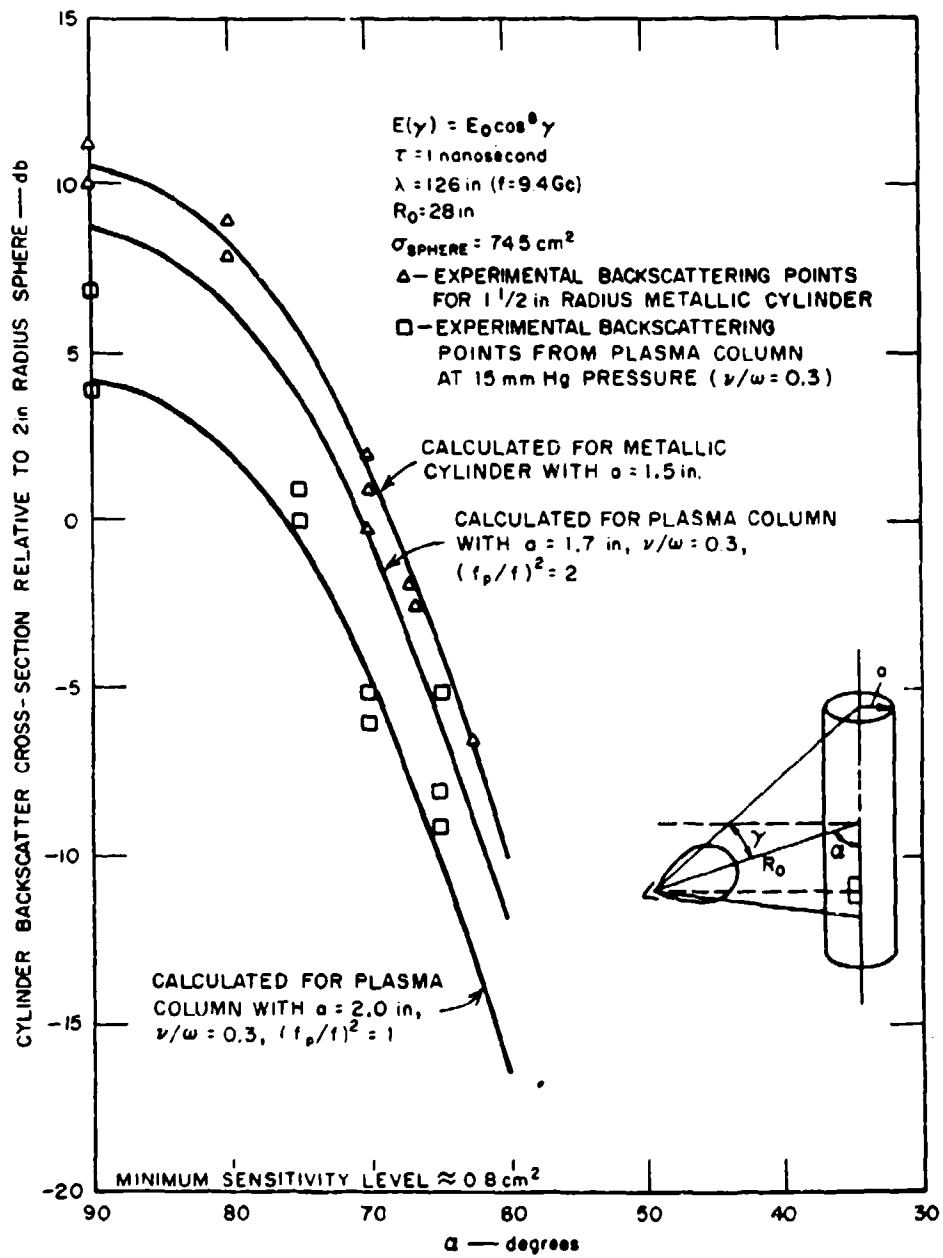
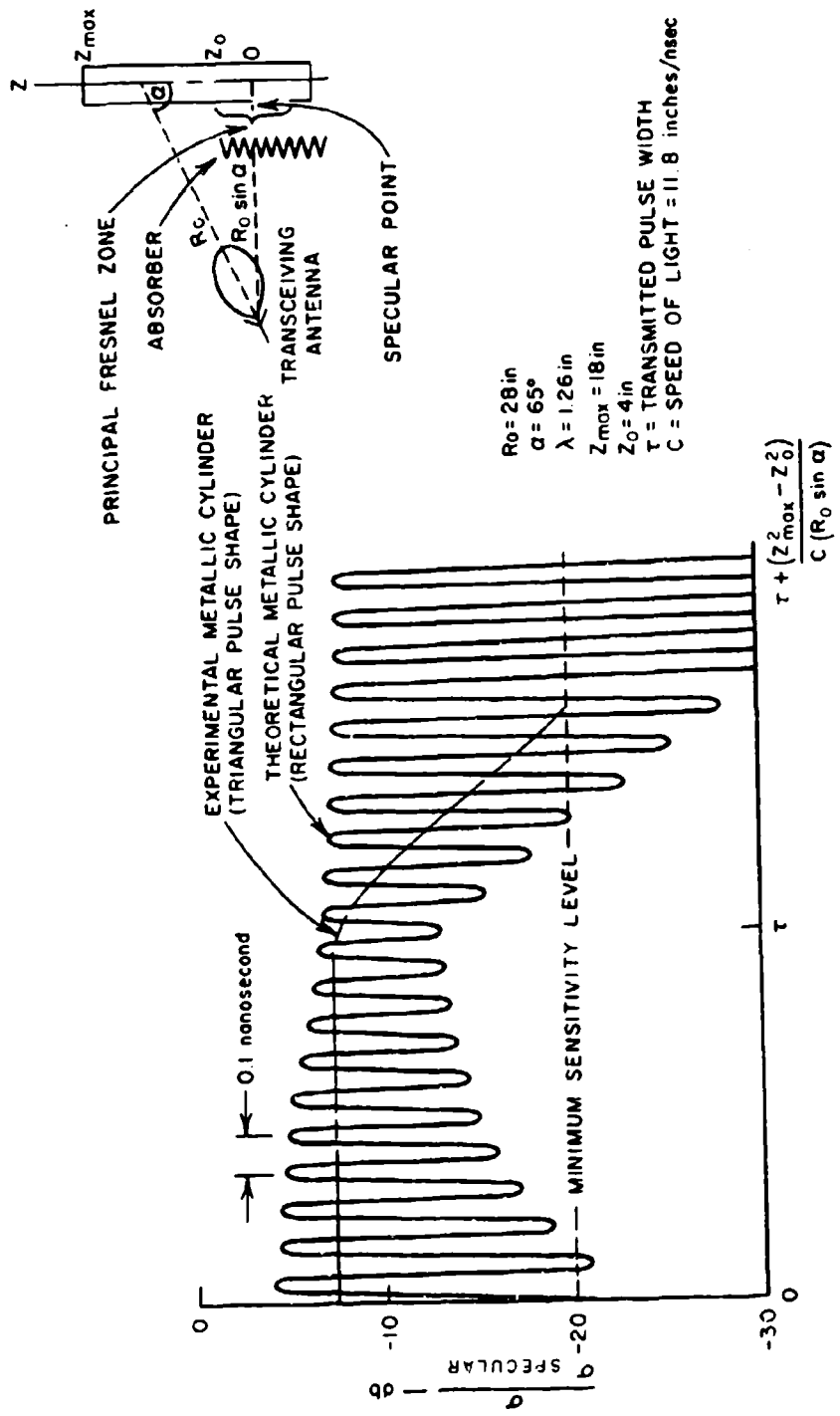


Figure 7 Backscatter Cross Section From An Extended Target.



DA - 3957-152

Figure 8 Backscatter Pulses From An Extended Cylindrical Target With The Principal Fresnel Zone Scattered.

At $t = 0$, the leading edge of the transmitted pulse is coincident with the edge of the shadowed region. When the pulse completely illuminates the first higher order Fresnel zone ($t \approx 0.05$ nsec) a peak in the return is observed and when the first and second zones are illuminated ($t \approx 0.1$ nsec) the return decreases by about 15 db since the amplitude of the scattering from the second zone is almost equal to that of the first zone but 180 degrees out of phase with it. Since the phase of the scattered contribution from adjacent zones differs by π radians, the backscattered return will be a maxima when an odd number of zones are illuminated and a minima when an even number are illuminated. However, since the amplitude of the contribution from the highest order Fresnel zones decreases as we move away from the specular region, the cross section reaches an asymptotic value, when the pulse fully illuminates the cylinder, of about 10 db below the specular return.

After times greater than τ , the pulse is no longer spread over the whole cylinder, but rather the illumination gradually moves towards the uppermost portion of the cylinder. As successive higher-order zones are no longer illuminated, the cross section also begins decreasing with an oscillatory behavior. When the contribution from the zone closest to the specular region is not received, the cross section dips slightly since it is only a small fraction of the total region now illuminated. However, as contributions from the additional higher-order zones are not received the oscillatory behavior of the cross section becomes more pronounced since the backscattered energy from the recent shadowed zone is becoming a larger fraction of the total contribution. This continues until time

$$\tau + \frac{(z_{\max}^2 - z_0^2)}{c(R_0 \sin \alpha)}$$

when the trailing edge of the pulse is coincident with the top of the cylinder; $R_0 \sin \alpha$ is the range to the specular point, z_{\max} is the length of the cylinder from the specular point, z_0 is the half length of the principal Fresnel zone and c is the speed of light. In the calculations, the cylinder length $z_0 + z_{\max}$ was chosen as 22 inches. The effect of changing the cylinder length compresses the time scale between time τ and the time at which the pulse no longer illuminates the cylinder. The effect of including a finite receiver bandwidth into the calculations would be to smooth out the oscillatory behavior of the theoretical waveform by damping the frequency components greater than the receiver bandwidth. From Fig. 8 we see that the mean level of the broadened portion of the return varies from approximately 10 to 20 db below the specular returns. Hence, the sensitivity of the receiver will determine the observable amount of pulse-width broadening.

In the laboratory, the specular region of a 1-1/2-inch-radius metallic cylinder was covered with microwave absorbing material so that the same conditions as in the calculations were met. The results obtained using the nanosecond-pulse-width radar described previously are shown in Fig. 8; to determine the extent of the pulse broadening,

the received return pulses from the cylinder were compared with those obtained from the calibration sphere. Even though theoretical results do not take into account the frequency response of the receiver or the triangular shape of the transmitted pulse, the correlation of the levels of the experimental and calculated waveforms is quite good. From the experimental scattering measurements, it is seen that the peak level of the return was 7.5 db below the measured specular return of the metallic cylinder when the principal Fresnel zone was not shadowed. The broadened portion of the return dropped off somewhat faster than the calculations indicate; due to background scattering within the chamber, we were only able to observe a pulse broadening of 0.6 nanoseconds. These discrepancies may be due in part to the fact that the calculations do not take into account the variation in the angle of arrival of the rays of the pattern incident on the cylinder, but rather assumes that they are all perpendicular to the axis. For the conditions chosen, the angle of arrival varies from about 80° for the ray that intersects the edge of the principal Fresnel zone down to about 55° for the ray that intersects the edge of the cylinder. As a result, we might expect an additional reduction in the contributions from the higher-order zones furthest away from the specular point. Therefore, the peak level of the return should be closer to the initial level of the pulse or closer to the specular level and the effective length of the scatterer should be decreased or i.e., the broadened portion should drop off more rapidly.

Scattering From Plasma Columns

The final scattering configuration to be considered is the plasma column. The first such column to be considered is the laminar-plasma column. Since scattering from this column has been treated in the literature,⁴ the experimental results can be compared with the theoretical calculations to demonstrate the capabilities of the plasma diagnostic techniques. The second plasma column is the turbulent column on which only the preliminary diagnostic results can be reported.

Laminar Columns

The experimental technique used to obtain an extended ionized column, from which scattering measurements could be made, was to form a thermally generated plasma by burning premixed ethylene-oxygen in the low-pressure vessel. The gas equipment is depicted in Fig. 9. The burner consists of six aluminum rings 1/2-inch high by 5-1/2 inches OD by 4-1/2 inches ID, between each of which is inserted a fine mesh stainless steel screen to diffuse the gases so that at the burner top a uniform velocity exists across the burner surface. Flames can be sustained within the chamber over a 5-to-40 mmHg pressure range. Since the electron density concentration produced by the flame would make the column below critical (plasma frequency, f_p , less than the radio frequency, f , where $f_p = 9 \times 10^3 \sqrt{N}$ and N is the concentration in el/cc) at the illuminating frequency of 9.4 Gc, the flame was seeded with potassium chloride (KCl).

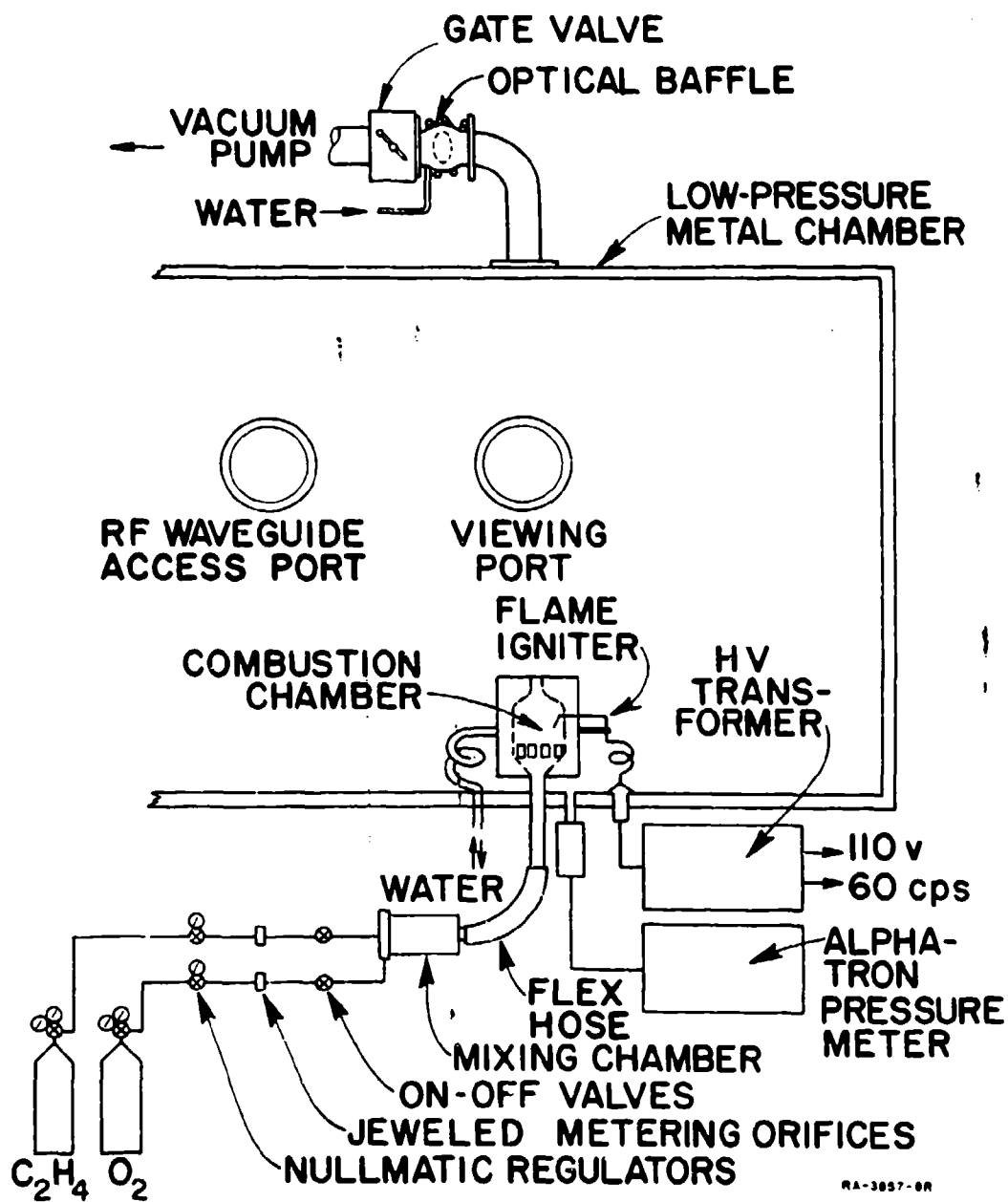


Figure 9 Low-Pressure Flame Apparatus.

The diagnostic tools used to determine the electromagnetic properties of the thermally generated plasma are a microwave bridge and an unbalanced electrostatic ion probe. The microwave bridge determines the attenuation and phase shift of a microwave signal transmitted through the partially ionized hot gases in the flame from which the average electron density and collision frequency, ν , along the transmission path can be determined. Since the desired electron concentration in the flame is on the order of 10^{12} el/cc or greater for a column thickness of approximately 10 cm, the diagnostic measurements were carried out at frequencies in the K-band (18.0 to 26.0 Gc) region.

The bridge is formed with the signal transmitted through the flame as one leg and through a waveguide network comprising a precision attenuator and phase shifter as the other. Since similar diagnostic measurements with dielectric rods have shown the validity of the plane-wave assumptions, we use the phase shift and attenuation of the microwave signal through the flame and the expressions for the phase constant and attenuation constant of a plane wave propagating through a homogeneous ionized plasma to determine the average angular plasma frequency and collision frequency of the flame.

The electrostatic coaxial probe measures the positive ion saturation current collected when it is immersed in the plasma column with the inner electrode charged with respect to the outer electrode.

The collecting surface of the probe for the positive ions is made of 0.010-inch diameter iridium wire 0.250 inch long, while the surface for collecting the electrons is made of tantalum tubing 0.250 inch long. A piece of alumina tubing is used both as a dielectric spacer between the iridium wire and the tantalum tubing and as a dielectric sleeve around the tantalum tubing. All of these materials are required for the probe to withstand the high temperature (2000°K) and caustic environment of the seeded flame. If the probe radius is larger than several Debye lengths and small compared with the ion-mean-free path, the current arriving at the probe is given by⁵

$$i_+ = 0.4 A n_+ e (2k T_e / M_+)^{1/2} \quad (5)$$

where A is the inner probe electrode area, n_+ is the ion density, e is the charge of an electron, k is Boltzmann's constant, T_e is the electron temperature, and M_+ is the ion mass. A more complete discussion of probe measurements is given by Taylor.⁶

This method of measuring the electron density requires an independent measurement or estimate of the electron temperature. The temperature of the gases above the flame was measured using the sodium line reversal technique.⁷

The diagnostic measurements carried out within the low-pressure chamber were taken at a pressure of 15 mmHg. The radial electron density concentration was measured with the ion probe at distances of 3, 8, 14, 20, and 26 inches from the burner surface, while at 20 inches the average collision frequency and electron density was measured with the microwave bridge. From previous measurements the electron temperature was estimated at 2000°K.

The axial electron density variation as measured by the probe and the corresponding current drawn with a bias of -45 volts and a load resistor of 1000 ohms are shown in Fig. 10, while the normalized radial density variation is shown in Fig. 11. These plots were obtained by drawing smooth curves through the measured data points. From these figures, it can be shown that for z (the axial distance above the burner) between 8 and 20 inches, the electron density varies approximately as

$$N(r, z) = 2.5 \times 10^{13} \left(\cos \frac{\pi r}{D} \right)^{-(z/D)+4.8} \exp \left(-\frac{z}{10} \right) \text{ el/cc,}$$

where r is the radial distance in inches and D is approximately 6 inches.

With this variation the column for distances above the burner z , between 4 and 22 inches appears cylindrically stratified for electron densities up to the critical density N_c [N_c equals $(f/9)^2 \times 10^{12}$ el/cc for f , the frequency in Gc]. For z between 6 and 16 inches, the stratifications extend up to $2 N_c$. In these portions of the column, the radial separation between each of these three contours of $0.5 N_c$, $1.0 N_c$, and $2.0 N_c$ is approximately a quarter wavelength at 9.4 Gc.

The average collision frequency ν_c and electron density measured by the microwave bridge for z of 20 inches at a pressure of 15 mmHg was $2 \times 10^{10} \text{ sec}^{-1}$ and $2.7 \times 10^{12} \text{ el/cc}$, respectively. With this value of collision frequency, $\nu/\omega = 0.3$ for the X-band nanosecond radar. This rather high value of collision frequency results from the fact that for the temperature encountered in the flame the collision frequency is probably largely determined by collisions between electrons and water molecules, since in this energy range the collision cross section for water is much larger than the other combustion products.

The axial electron density as measured by the probe is about 10% higher than the average value of electron density as measured by the microwave bridge. To determine the credibility of this result, the attenuation expected from a homogeneous plasma slab whose width equals the antenna separation of the bridge was calculated and compared with the attenuation expected from the same width plasma slab but including the radial variation measured by the probe. From these calculations the axial density as measured by the probe should be approximately 30% higher than the average density as measured by the microwave bridge. At a frequency of 22 Gc for the radial electron distribution measured at 20 inches is $\cos^{1.5} \pi r/6$; hence, the calculated and experimental results agree to within 20%.

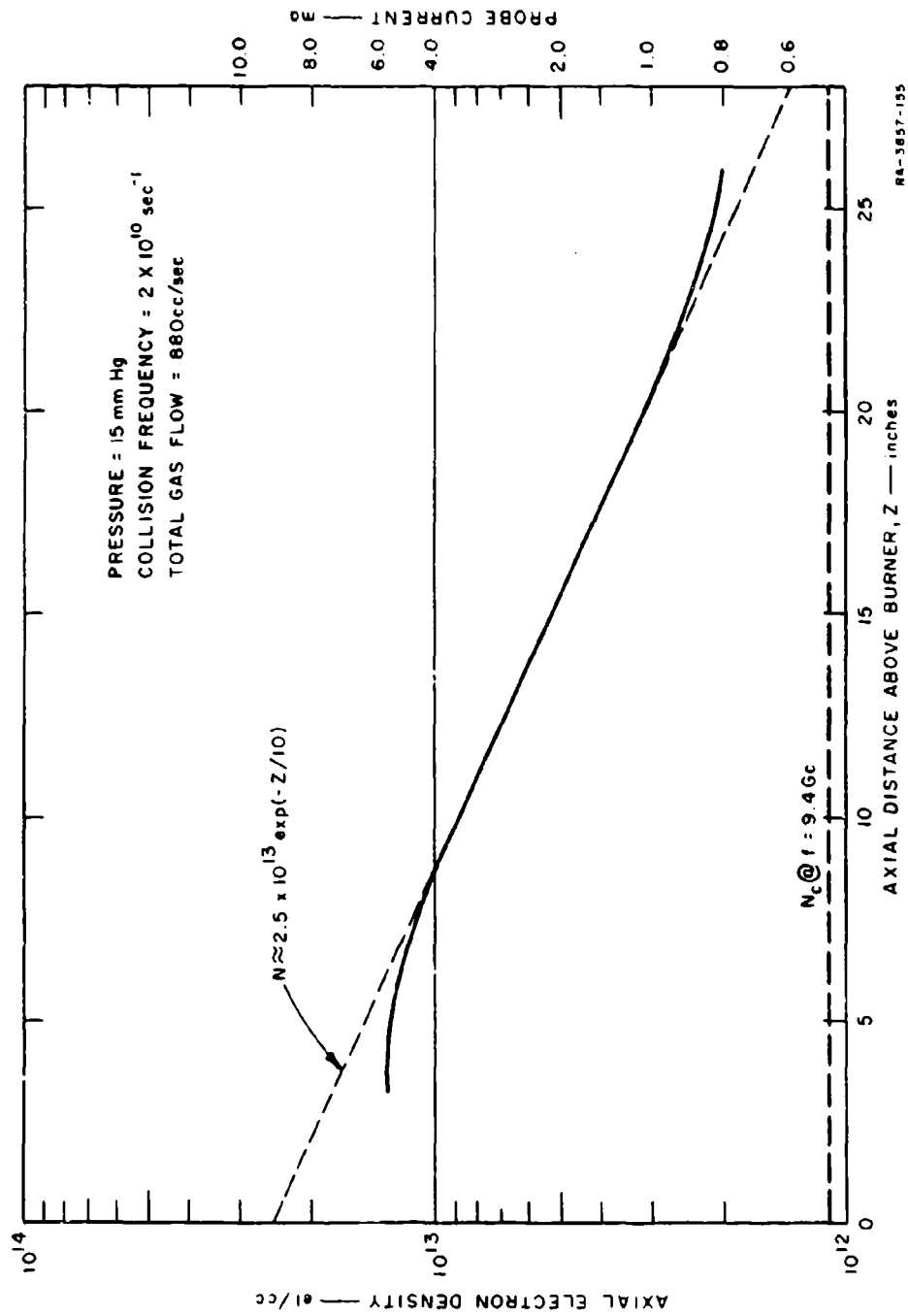


Figure 10 Measured Axial Electron Density In A Laminar Plasma Column.

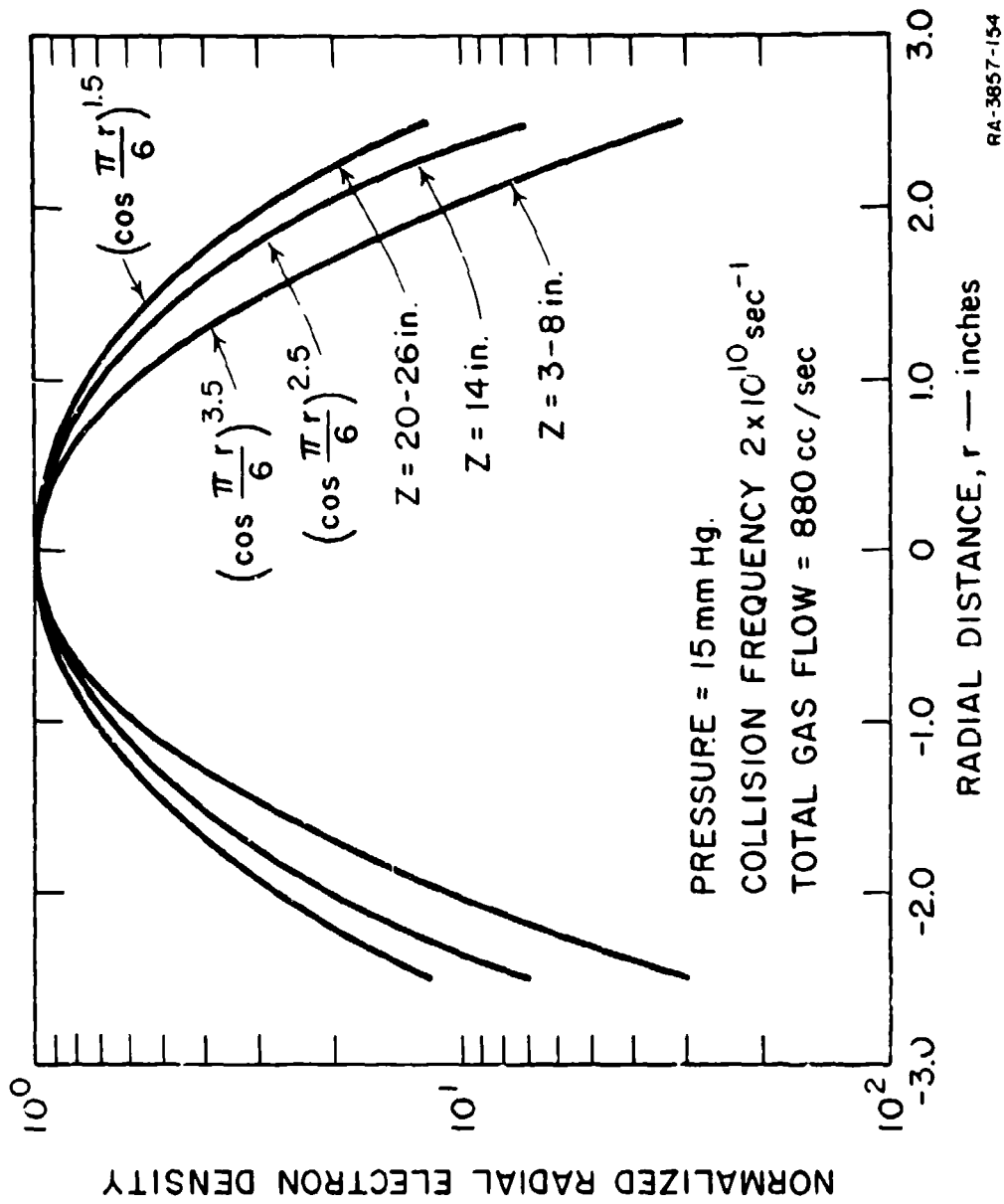


Figure 11 Measured Radial Electron Density In A Laminar Plasma Column.

The scattering measurements were carried out at a pressure of approximately 15 mmHg. The measured backscatter cross section from the column as a function of the angle of incidence is shown in Fig. 7. Along with these data points are the theoretical curves of the backscatter cross section for two homogeneous plasma columns, one whose electron density equals $N_c [(f_p/f)^2 = 1]$ and radius equals that of the critical density stratification found in the experimental column ($a_c = 2$ inches) and another whose electron density equals $2N_c [(f_p/f)^2 = 2]$ and radius equals that of the twice critical density stratification ($a_{2c} = 1.7$ inches).

The plasma model used to approximate the plasma column of the laboratory was an infinitely long ionized cylinder with a homogeneous complex dielectric constant. Using the formulas of Wait⁴ and King et al.⁸, the cross section of plasma columns such as studied here has been calculated using IBM library subroutines to calculate the Bessel and Neumann functions for complex arguments.

The cross section of the region of the plasma column between z of 2 and 22 inches is approximately equal to that calculated for a homogeneous column of critical electron density and whose radius equals that of the critical density stratification found in the experimental column. To see whether this result is reasonable, let us consider by using a plane wave theory approximation the contribution to the scattering by the electron density concentration in the column at radii less than and greater than the critical radius. From plane wave theory we find that (1) due to the high attenuation constant of the medium at 9.4 Gc within the critical contour (6.0 db/cm) there is no effective scattering from the regions within the critical contour and we can assume that for radii less than the critical radius, the column appears homogeneous with an electron density equal to the critical value; (2) the signal scattered by the critical contour would be reduced by about 1.5 db in transversing the underdense region twice. On this basis, the expected return should be about 1.5 db below the curve calculated for a 2-inch-radius critical column.

However, this does not take into account the incremental scattering from the electron density concentration outside of the critical contour. Since the radial separation between the contours of $0.5 N_c$ and N_c is less than a quarter wavelength, the backscattered energies from this radial portion of the column have in-phase components. This will tend to produce a scattered return above that expected from the critical contour alone and closer to the calculated value for the homogeneous column of critical density.

The pulse-width-broadening effects were observed in scattering measurements made on an extended metallic cylindrical scatterer with its principal Fresnel zone shadowed. These broadening effects were observable because the peak level of return was about 13 db above the minimum sensitivity level. However, the peak of the scattered returns from the plasma column with its principal Fresnel zone shadowed is only 3 db above the minimum sensitivity level. Hence, we were only

able to observe that the peak level of the return was 8.5 db below the measured specular return; this level compares very well with the calculated value.

Turbulent Columns

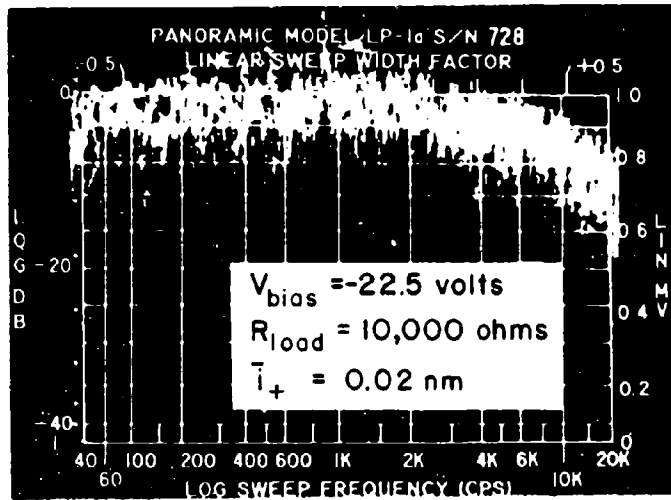
In the laboratory an extended turbulent plasma was formed by seeding the premixed ethylene-oxygen flame in the combustion chamber and then exhausting through an expansion nozzle into a low-pressure vessel. The measurements reported were made at an ambient pressure of 16 mmHg, a combustion chamber pressure of 32 mmHg and a mass flow of 0.002 lbs/sec. Under these conditions the velocity and Reynolds number at the nozzle exit are approximately 3000 feet/sec. and 3.0×10^3 .

The density fluctuations of the ionized particles were measured by an unbalanced probe. When the probe is used to measure the spectrum of the ion fluctuations the inner electrode is biased negatively with respect to the outer electrode and the probe response is given by Eq. (5).

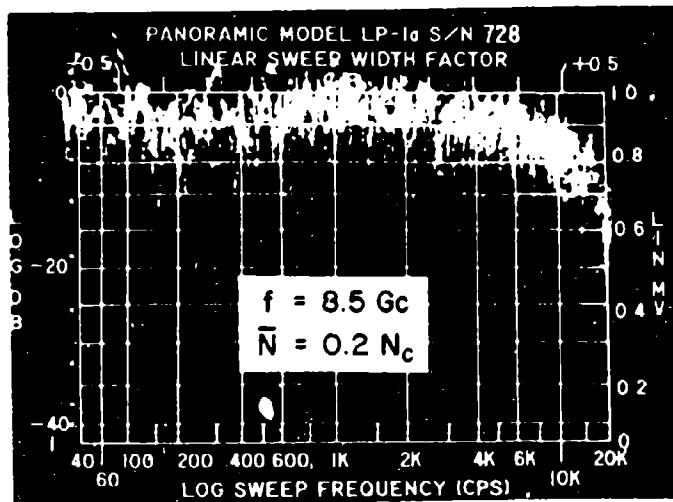
When the probe is used to measure the spectrum of the electron fluctuations it is excited from a CW microwave source through a tee junction and the signal reflected from it is observed with a crystal detector. Since the length of the dipole is small compared to the wavelength, it behaves like a capacitive reactance. The region of the electrostatic field is approximately defined by the radial electrode separation. If the electron concentration in the plasma medium is much less than the critical concentration, N_c , ($N_c = f^2/81 \times 10^{-3}$ el/cc where f is in cycles/sec) variations in the impedance of the dipole are linearly related to variations in the electron density. Thus fluctuations in the reflected signal from the dipole are a measure of the fluctuations in the electron density surrounding the probe.

To obtain the frequency spectrum of the fluctuation ion or electron density, the output from the probe was fed into a Panoramic sonic analyzer Model LP-1a. This instrument scans the frequency range from 40 to 20,000 cycles/sec. in one second. The average fluctuation was obtained by photographing a number of traces from the display tube by multiple exposure. Figure 12 is a photograph of a typical display of the one-dimensional ion spectrum.

From measurements of the spectral distribution of charged particles measured by the probe in its dual capacity, it is seen that the electron and ion fluctuations have identical spectrums in the thermally produced plasma. The frequency characteristics of the ion saturation current at various points downstream from the nozzle was obtained from other intensity-modulated photographs and plotted in Fig. 13; a line with a slope corresponding to $f^{-5/3}$ has been included in the figure. These curves have been normalized to unity at a frequency of 100 cycles/sec.



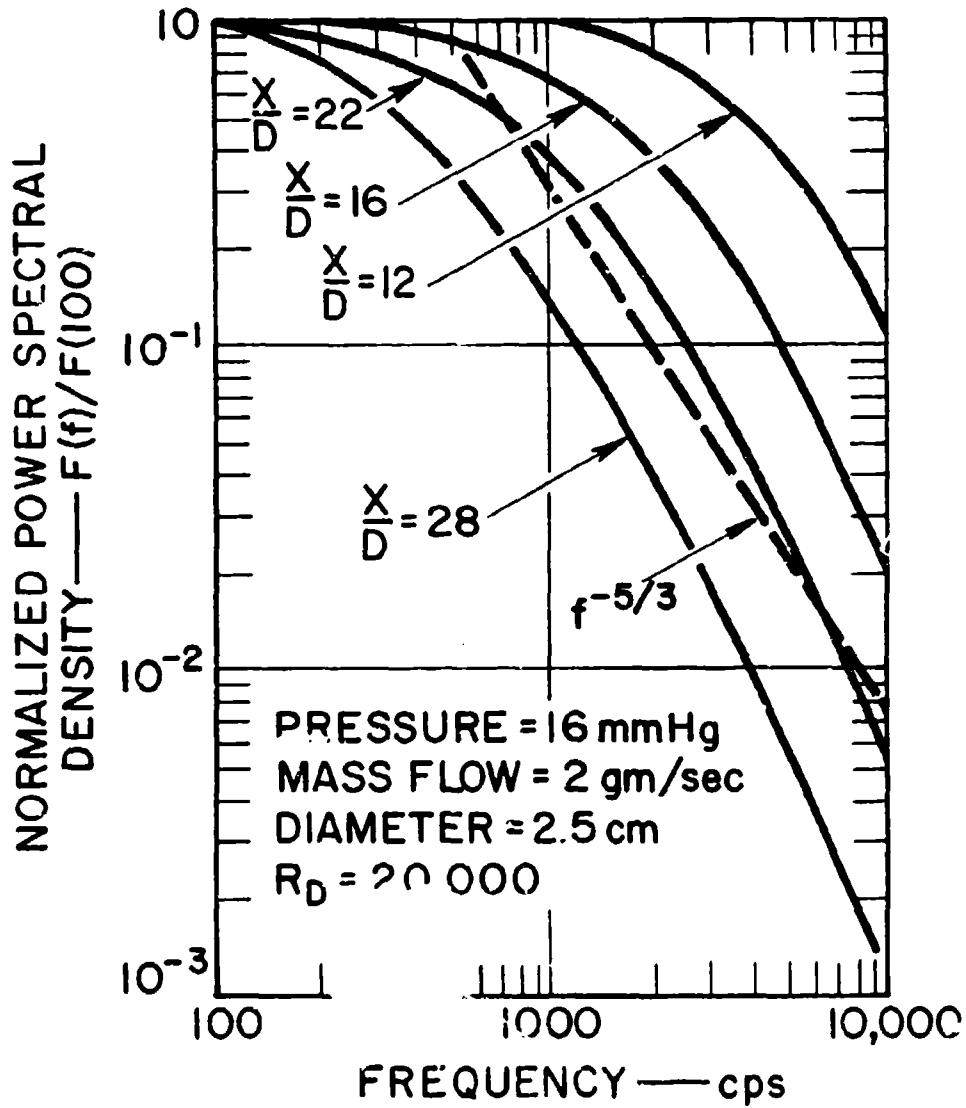
ION PROBE



ELECTRON PROBE

RP-3857-176

Figure 12 Spectrum Of The Ionized Density Fluctuations At A Point 12 Nozzle Diameters Downstream From The Exit Of A 2.5 CM Diameter Sonic Nozzle Exhausting Into A Pressure of 16 mmHg.



RA-657541-48R

Figure 13 Spectrum Of Ion Density Fluctuation.

From Fig. 13 it is seen that the one-dimensional spectrum of the positive ion fluctuations for various positions downstream of the nozzle follow an identical power law. The normalized power spectral density, $F(f)/F(100)$, where f is the frequency in cycles/sec., is found to be represented rather well by the expression $(1 + c^2 f^2)^{-1}$, where c is $2\pi \lambda / U$ for values of $F(f)/F(100)$ greater than $0.1 (cf < 3)$. The corresponding spatial correlation function would be $\exp(-[2\pi/cU]x_1)$ where U is the mean velocity in the x_1 direction; going downstream from $x/D = 12$ to 28 , c goes from 3×10^{-4} to 2.5×10^{-3} sec. For values of cf greater than 3 the measured spectrum falls below the values given by the expression $(1 + c^2 f^2)^{-1}$. This same result (although it related to the spectrum of the turbulent velocity components) was obtained from measurements made by Liepmann⁹ for grid Reynolds number of the order of 10^4 . On the other hand, the spectrum at $x/D = 22$ approximates the Kolmogoroff spectrum ($f^{-5/3}$) over the frequency range from 600 to 10,000 cycles/sec.

Preliminary velocity measurements indicate that the mean flow velocity 16 diameters downstream is approximately 500 feet/sec. With this velocity and a value for c of 7.0×10^{-4} sec. obtained from the measured ion spectrum, an average eddy size of $3/4$ inch is inferred. This work is more fully described in Reference 10.

CONCLUSIONS

The results obtained from the scattering from the extended targets have shown how extremely sensitive the backscattered pulse is to the separation between scatterers. However, these results and the calculations presented from representative targets have shown that the base width of the backscattered pulse is an excellent measure of the total length of the scatterer when there is a high signal-to-noise ratio.

The backscattering measurements from the laboratory produced laminar-plasma column have shown that the laboratory produced laminar-plasma column is a coherent scatterer. A comparison between the experimental results and the calculated results, which incorporate the measured electrical parameters from the column, shows that the column scatters electromagnetic energy that is polarized with the electric vector along the column axis in the same manner as a homogeneous column of critical density with the column radius equal to that of the critical radius. Finally, in the thermally produced turbulent flame, the electron and positive ion fluctuations have identical spectra.

BIBLIOGRAPHY

1. "Re-Entry Physics and Project PRESS Programs," Semi-Annual Technical Summary Report to ARPA, 1 January 1961 - 30 June 1961, MIT Lincoln Laboratory (August 1961).
2. Final Report, "Short Pulse Signature Study," (U), Report No. ZN-526, RADC-TR-61-154, Convair San Diego, Convair Division, General Dynamics Corporation (July 1961). SECRET
3. J. R. Metzner, Scattering and Diffraction of Radio Waves (Pergamon Press, London and New York, 1955).
4. J. R. Wait, "Some Boundary Value Problems Involving Plasma Media," J. Research National Bureau of Standards 65E, No. 2, pp. 137-150 (April-June 1961).
5. F. F. Chen, "Use of Electrostatic Probes in Plasma Physics," IRE Trans. NS-8, No. 4 (October 1961).
6. W. C. Taylor, "The Use of Ion Probes For Diagnosing Re-Entry Plasmas," Technical Report 11, SRI Project 3857, Contract SD-103 Under ARPA Order 281-62, Stanford Research Institute, Menlo Park, California.
7. A. G. Gaydon and H. G. Wolfard, Flames: Their Structure, Radiation and Temperature, Chap. X (Chapman and Hall, Ltd., London 1960).
8. R. W. P. King and T. T. Wu, The Scattering and Diffraction of Waves (Harvard University Press, Cambridge, Mass., 1959).
9. H. W. Liepmann, J. Laufer, and K. Liepmann, National Advisory Committee for Aeronautics, Technical Notes No. 2473 (1951).
10. H. S. Rothman, H. Guthart and T. Morita, "Measurement of the Spectrum of Ion and Electron Density Fluctuations In A Thermally Produced Turbulent Plasma" (U), AMRAC Proceedings, Vol. IX, Part 1. UNCLASSIFIED.

SURFACE ROUGHNESS AND TOLERANCES IN MODEL SCATTERING EXPERIMENTS

T. B. A. Senior

Radiation Laboratory, The University of Michigan

I. INTRODUCTION

The effect of surface finish on the scattering behavior of a target is a subject on which a variety of diverse opinions have been expressed, but for which there is very little definitive information available. Nevertheless, it is a matter of considerable importance in model scattering experiments, particularly those where a large number of similar models are required to investigate the size (or frequency) characteristics of the return. The cost of fabricating the models can then be high, and it is clearly uneconomic to specify a degree of surface finish or overall tolerance better than is necessary to ensure an accurate determination of the scattering.

If a given surface is perturbed a small amount, the change in the scattering cross section is a function not only of the type of perturbation but also of the scattering from the original base surface. This in turn introduces a dependence on aspect, polarization and frequency, and it is obviously impossible to estimate the minimum construction requirements which will be satisfactory in all cases. It therefore comes as no surprise that experimentalists have erred on the side of safety by seeking the best finish that can reasonably be achieved. Primich, for example, stated in 1959 that the models used at DRTE were constructed with an rms surface finish better than 12 microinches, which implies a high degree of competence on the part of the machinists. He added that "if the surface is allowed to get rougher than, say, 20 or 30 microinches, we can normally detect a change in echoing area," but in contrast for the overall dimensions a tolerance of 10^{-3} inches was regarded as sufficient. Similar requirements were imposed at both the Royal Radar and Royal Aircraft Establishments in England, and a summary of the RAE view has been given by Dawson (1960). For low cross section objects of cone-sphere type the importance of having no ridges or kinks was emphasized, and from a study of data obtained with many models constructed with varying degrees of accuracy it was concluded that surface roughness can be important when the object is large in comparison with the wavelength. On the other hand, with smaller models (base radii less than 3λ) no effects were observed on going from a roughish surface to a shiny mirror-like finish. As a result of this study all later models were constructed with a surface roughness of no more than 30 microinches, equivalent to $2 \times 10^{-6}\lambda$ at the X-band wavelength used by RAE, and it seems that a factor in this choice was the desire to have the rms amplitude less than the skin depth.

Valuable as these conclusions are, it would appear that they are largely based on isolated measurements carried out on bodies which, through faulty manufacture, turned out to have some specific form of surface irregularity. In many cases the irregularity was discovered only after inspection of a scattering pattern, and usually no further experiments were made to discover the variation as a function of frequency, polarization, aspect, etc. Because of the stray effects which all measurements are prone to in this area, care is necessary to avoid giving undue weight to a single observation, but in the absence of controlled experiments to examine in detail the scattering produced by selected types of surface perturbation, we have to draw what conclusions we can from the limited data available.

In the following paragraphs an attempt is made to provide a few general statements about the effect of surface perturbations based on our experiences in the Radiation Laboratory. The dimensions of the perturbations are assumed small in comparison with those of the base surface and usually, but not always, small in comparison with the wavelength. The perturbations may take the form of deformations (e. g. a sphere into a spheroid of small ellipticity) pertinent to overall tolerance criteria, ridges or grooves (as at the join of a badly constructed cone-sphere) or random roughness (as might occur in a casting process), and brief remarks are made about each class. For simplicity, attention will be confined to metallic bodies. If the surface is non-metallic, or coated with a dielectric or absorbing material, the effect of irregularities tends to be reduced, and this is consistent with Dawson's hypothesis about the size in relation to the skin depth.

To keep the discussion as general as possible, bodies will be categorized according to the nature of the return from the unperturbed surface at different aspects and frequencies. The cases to be distinguished are those in which the return is (i) volume-dominated, (ii) specular and (iii) the result of singularity (tip, edges, etc) or surface wave contributions, and the consequences of surface perturbations in the three cases are considered in Section 2 through 4. The final section is concerned with experimental studies of random roughnesses.

II. VOLUME-DOMINATED BEHAVIOR

At sufficiently low frequencies a finite body appears only as a singularity in the field and the Rayleigh scattering law then applies. With an accuracy which is adequate for most purposes, the back scattering cross section is

$$\sigma = \frac{4}{\pi} k^4 V^2 F^2$$

where k is the propagation constant ($= 2\pi/\lambda$), V is the volume and F is a shape factor dependent on the length-to-width ratio (Siegel, 1958, 1963). Any

surface irregularity is now tantamount to a 'singularity on a singularity' and is negligible in its effect on σ . Since F is a slowly varying function, any slight deformations of shape are also unimportant, as are small changes in the volume resulting from a relaxation of the overall tolerances.

III. SPECULAR BEHAVIOR

Any body will produce a specular return at some aspect if the frequency is high enough, and in most cases such a return will dominate all other contributions. If a portion of the surface is plane and normal to the incident field direction, the corresponding back scattering cross section is

$$\sigma = \frac{4\pi A^2}{\lambda^2} \quad (1)$$

where A is the area. Similarly, for a section of a circular cylinder of radius a and length \mathcal{L}

$$\sigma = \frac{2\pi \mathcal{L}^2 a}{\lambda} \quad (2)$$

and for curved area with (finite) principal radii of curvature R_1 and R_2 ,

$$\sigma = \pi R_1 R_2 \quad (3)$$

All of these are high frequency approximations, and in spite of the differing wavelength dependence the formulae go over continuously one into another. If, for example, $A = \mathcal{L}b$ and the surface is now bent in the direction of the b dimension to form a section of a circular cylinder whose rim is displaced a distance δ relative to the middle of the element, the cross section will remain essentially unchanged until δ exceeds the value $\lambda/16$. The radius a of the cylinder is then $2b^2/\lambda$ and equations (1) and (2) give identical results, but as δ increases beyond $\lambda/16$ equation (2) must be used, and the cross section falls off as $\delta^{-1/2}$. The transition from equation (2) to equation (3) is similar.

Of the above cross sections the flat plate one is potentially the largest, and can be equalled only by a return from a similar flat surface or aperture. Any perturbation of the surface is more likely to degrade this return than to increase another until its size is comparable. If the scattering region is uniformly perturbed, the extent to which the cross section is affected can be deduced from the preceding discussion. Thus, for example, a plate 10λ on the side can be bent into an arc subtending $3-1/2^\circ$, or tilted through an angle $2-1/2^\circ$, before the cross section is reduced by 1 db. Corresponding data for

curved surfaces can be obtained from equations (2) and (3), and all suggest that a relatively loose tolerance ($\sim 10^{-2}\lambda$) would be satisfactory for most purposes.

If the perturbations can be likened to a regular series of ridges and furrows whose depth δ is small in comparison with the wavelength, the change in the back scattering cross section can be estimated using results for corrugated surfaces. The analysis for a plane sheet (Senior, 1959) shows that to a first order the corrugations are equivalent to a voltage reflection coefficient $J_0(2k\delta)$, which will reduce the back scattered energy by less than 1 db if $\delta < 0.1\lambda$. On the other hand, from the solution for a corrugated cylinder (Clemmow and Weston, 1962) it is seen that to a first order the effective surface of reflection is displaced to lie along the top of the corrugations, leading to an increase in the return from a convex body, and partially compensating for the smaller scattering from each element.

In the case of more general perturbations which can be modelled by a random distribution of irregularities of small slopes and amplitude, an alternative approach is to represent the surface by a smooth but imperfectly conducting one whose impedance is defined in terms of the statistical properties of the irregularities (Senior, 1961). If the roughness is such that $k\ell$, $k\xi_0 \ll 1$ where ℓ and ξ_0 are the scale and amplitude respectively, the surface impedance η is almost purely imaginary, but as the scale increases, η assumes a resistive part as well. The latter can be attributed to diffuse scattering which, in the back scattering direction, is indistinguishable from absorption. Since the impedance increases the cross section of a large sphere by a factor $|1-\eta|^2$, the roughness will serve to increase the return as long as $k\ell \ll 1$ and is equivalent to reflection at a surface of larger radius. As $k\ell$ approaches unity, however, the cross section may fall below the smooth sphere value depending on the magnitude of $\arg \eta$.

In view of these results it would appear that only the most severe roughness can produce a noticeable effect on a specular return, and this has been confirmed by experiments carried out with a rough sphere at a series of different frequencies. The experiments were described by Hiatt et al (1960), and the data, together with some more recently obtained, is summarized in Section 5. As an example of the findings, a roughness of amplitude 0.037 cm and scale 0.101 cm produced an average increase in cross section of only 0.02 db at X-band. The standard deviation was 0.4 db and the maximum change observed was 1.5 db. When the wavelength was decreased to 1.3 cm the corresponding values were 0.41, 1.04 and -3.9 db, which shows how rapidly roughness becomes important as its relative scale increases. At this frequency, however, $\xi_0 \sim 0.03\lambda$ and $\ell \sim 0.1\lambda$, with actual bumps having dimensions greater by a factor 2 or more, and one would hardly conceive of using such a surface to represent a smooth body.

It is therefore tempting to conclude that extremely smooth surfaces are not as essential as had been supposed, and both theory and experiment suggest

that an rms surface finish good to $10^{-3}\lambda$ should be more than adequate for all measurements of specular contributions. Theoretically, however, there is a danger in adopting this as a criterion because of the possibility that even slight roughness may so effect the side lobes of a specular return as to produce a sizable contribution at aspects where the smooth body provided none. Similarly, if a smooth body had two specular contributions which cancelled one another at some aspect, roughness could modify this cancellation. Any discussion of modelling ultimately leads to the question of the accuracy with which a scattering pattern must be reproduced, and obviously the deep minima are the most susceptible to perturbation effects, but because of the approximations inherent in any theoretical study of roughness, such degradations of a pattern can only be investigated experimentally. Some pertinent data is presented in Section 5.

IV. SINGULARITY AND SURFACE WAVE BEHAVIOR

Two of the commonest types of contributor to the back scattering cross section are singularities (edges, tips, etc) and surface (travelling or creeping) waves. A singularity is essentially a place where the surface or one of its derivatives changes rapidly within a small fraction of a wavelength, and any direct return is therefore local in origin. This is in contrast to a surface wave contribution, which is generally produced by waves which have travelled some distance around the body, and which is consequently more susceptible to the cumulative effect of small perturbations. In both cases, estimates of the cross section are usually based on high frequency approximations, but the results have also found application in the upper half of a resonance region defined in terms of the overall dimensions of the body.

To determine the influence of perturbations on these forms of scattering it is convenient to concentrate on a particular body, and the cone-sphere is ideal for this purpose. At nose-on and near nose-on aspects the dominant sources of return are the join of the cone and sphere and the creeping waves which have traversed the rear. The former is a degenerate version of a circular edge or rim, and measurements of the overall cross section at closely-spaced frequencies have shown that the return from the join is in reasonable agreement with the predictions of physical optics. For the creeping wave contribution, however, the agreement is not quite so good, and for base radii one to two wavelengths the magnitude appears to exceed that for a sphere of the same size by a db or two. Direct measurements of the surface field intensity have confirmed this enhancement, and the effect may be due to an 'overflow' of the travelling wave supported by the cone.

At precisely nose-on incidence ($\theta = 0$) the cross section associated with the tip is

$$\sigma_t = \frac{\lambda^2}{16\pi} \tan^4 \alpha \quad (4)$$

where α is the half-cone angle, and for most α of practical interest this cross section is insignificant in comparison with the return

$$\sigma_j = \frac{\lambda^2}{16\pi} \sec^4 \alpha \quad (5)$$

attributable to the cone-sphere join. As θ increases away from zero, σ_j decreases according to the factor

$$\left\{ J_0(2ka \cos \alpha \sin \theta) \right\}^2,$$

where a is the radius of the spherical base. The appearance of the Bessel function J_0 is characteristic of the return from a ring, and it is now trivial to investigate the consequences of an angular displacement of the join relative to the axis of the body. However, a more probable inaccuracy in a model is a failure to match precisely the first derivatives of the surface in this region. If δ is the angle between the tangents to the cone and sphere at this point, the physical optics cross section becomes

$$\sigma'_j = \frac{\lambda^2}{16\pi} \sec^4 \alpha \left| 1 + 2ika \cos \alpha \tan \delta \right|^2 \quad (6)$$

(Senior, 1963), and for any non-zero value of δ the second term will predominate at sufficiently high frequencies. Taking, for example, $\delta = 1^\circ$, the second term will exceed the first if $a \cos \alpha > 4.6\lambda$, and with further increase of frequency the cross section will approach the constant value

$$\pi (a \sec \alpha \tan \delta)^2 \quad (7)$$

instead of decreasing in accordance with equation (5).

It is believed that errors in matching the sphere to the cone have been responsible for many of the discrepancies in experimental data, particularly in those measurement programs where a large number of models were employed. Nevertheless, the importance of good construction in this region should not be exaggerated, and if the rear of the body were still spherical in spite of the non-zero value of δ , an overall surface tolerance of $10^{-2}\lambda$ would be enough to ensure that the return from the join was not out by more than 1 db at any frequency.

Because of the large area of surface on the sides of the cone, it might be imagined that at nose-on and near nose-on incidence a small amount of roughness could generate a signal comparable to that from the join. That this is not

so can be seen by postulating a dense collection of identical hemispheres of radius ϵ . The number of such protuberances on the cone itself is then $(a/\epsilon)^2 \cos \alpha \cot \alpha$. If there is no shadowing and each provides one quarter of the Rayleigh cross section of the corresponding sphere, the net return is

$$\sigma_r = \frac{9\pi}{4} \sin \alpha (k\epsilon)^4 a^2.$$

Hence

$$\frac{\sigma_r}{\sigma_j} = 9 \operatorname{cosec} \alpha (k\epsilon \cos \alpha)^4 (ka \cos \alpha)^2 \quad (8)$$

which is comparable to unity only for large roughness, very large ka or extremely small α . In this last case the assumption of no shadowing is clearly inappropriate and if, for example, $\alpha = 7-1/2^\circ$, $ka = 20$ and $k\epsilon = 0.05$ (extreme roughness), the ratio is about 0.1.

For a roughness which is random but statistically uniform in character an alternative approach is to represent its effect using an impedance boundary condition. If the scale and amplitude are small in relation to the wavelength, the appropriate impedance η does not differ substantially at grazing and normal incidence. The former is a reasonable approximation for the sides of the cone at nose-on aspects and Weston (1960) has shown that at high frequencies σ_t and σ_j are both increased by a factor $|1 - \eta(\sin \alpha + \operatorname{cosec} \alpha)|^2$, but since η is purely imaginary for small scale roughness, the factor is almost unity in most practical cases in spite of the term involving $\operatorname{cosec} \alpha$. Thus, for example, with $k\ell = 0.2$ and $k\zeta_0 = 0.05$, $\eta \sim 0.01i$, and even for $\alpha = 7-1/2^\circ$ the predicted increase in cross section is less than 1 percent.

This same method can also be used to estimate the change in any creeping wave contribution. For a smooth cone-sphere the 'theoretical' creeping wave cross section at nose-on incidence is greater than σ_j by a factor 2 when $ka \sim 10$ and is equal to σ_j when $ka \sim 18$. At higher frequencies σ_j dominates, but the value of ka at which this situation obtains is increased due to the enhancement of the creeping waves. If the spherical portion of the body is now roughened in such a way that an impedance boundary condition is applicable, the main effect is to increase fractionally the apparent radius of the cap, and therefore force the wave to describe a larger path. In addition, some attenuation can be expected resulting from scattering of the wave in its passage, but analyses suggest that the total change in the back scattering cross section is entirely negligible for roughnesses of order $10^{-2}\lambda$ or less. The measured data on rough cone-spheres does not disagree with this conclusion.

For travelling waves, an estimate of the effect of roughness is harder to come by because of the absence of a precise theory for the dependence of these waves on the parameters of the unperturbed body. There is, however, no evidence to indicate that they are more sensitive than creeping waves.

Although the above analyses are neither rigorous nor all embracing, they do give some information about the probable influence of surface finish on the behavior of low cross section shapes, and on this basis it would seem that a finish good to $10^{-3}\lambda$ should be more than satisfactory for most (if not all) model measurements. As in the case of specular returns, however, this criterion has been arrived at by considering only the dominant features of the scattering pattern, and any imperfections in surface or tolerance will clearly affect the minima to a greater extent. To see what changes can be expected in these portions of the pattern, experimental data is essential, and some pertinent results are presented in the next section.

V. A MEASUREMENT PROGRAM

In early 1960 an experimental study of surface roughness was undertaken partly to confirm the applicability of the surface impedance approach to random roughness, but also to obtain some direct measurements of the effect of roughness on the back scattering behavior of selected objects. To begin with, attention was confined to a large sphere and the results were reported by Hiatt et al (1960). The program was then allowed to lapse, but was resurrected in late 1961 and has been pursued intermittently ever since.

The rough sphere employed in the initial experiments was approximately 10 inches in diameter and was cast in aluminum a hemisphere at a time. It was found that the casting process could be modified to provide an acceptable degree of relatively uniform roughness, and this is the method by which all of the models were constructed. The mean radius a of the sphere turned out to be 12.86 cm, the total depth d of a typical bump from crest to trough (approximately twice the rms amplitude ξ_0) was 0.07 cm, and the total width w (rather than the width between 3 db points required for the specification of the scale \mathcal{L}) was 0.3 cm. The measurements of d and w were made with a vernier caliper and though there were variations from point to point on the sphere, the above values are typical of those obtained not only for this one body but for all of the rough models used.

A close-up photograph of the surface is given in Hiatt et al (1960), which reference also contains a description of the experimental technique. At three frequencies in the S, X and K-band ranges the cross section was recorded as a function of rotation angle, 0° through 360° , for a variety of different positions of the hemispheric join relative to the plane normal to the direction of incidence. The traces were compared with those for a companion smooth sphere of almost identical size, and at frequencies where roughness was found to have an effect the differences in cross section were tabulated and analyzed. At the two higher

frequencies the data was reinforced with 'point by point' measurements obtained by constructing a grid on the surface of the sphere and directing the antenna beam successively at each of these points, and at X-band the program was enlarged to include measurements taken at ranges from 16 feet down to 6 inches. Since the publication of the Hiatt paper, results have been obtained with a still higher (K_a -band) frequency, and the relative values of the sphere parameters in the four cases are listed in Table I.

TABLE I: SPHERE PARAMETERS

Freq. (Gc)	λ (cm)	ka	d/λ	w/λ
2.87	10.5	7.73	7×10^{-3}	3×10^{-2}
9.70	3.09	26.1	2×10^{-2}	10^{-1}
22.97	1.31	62.0	6×10^{-2}	2×10^{-1}
31.97	0.938	86.2	8×10^{-2}	3×10^{-1}

At S-band the roughness had no perceptible effect. The cross section was almost constant as a function of rotation and nowhere differed by more than 0.2 db from the level appropriate to a smooth sphere of the same diameter. When the frequency was increased to X-band, however, the roughness became apparent and the traces oscillated about the smooth sphere value with peak deviations as much as 1 db. Nevertheless, the average change in cross section was infinitesimal, which is in accordance with the theoretical prediction. As expected, there was no statistically significant range dependence. At the two highest frequencies, the roughness was playing a major role. The dimensions of the bumps were now such that they could act singly, or in combinations of a few at a time, to produce individual features in the traces, and quite large variations were observed. Portions of sample traces at the four frequencies are reproduced in Figure 1, and in Table II the fractional changes in cross section are

TABLE II: RELATIVE CROSS SECTION OF ROUGH SPHERE

Freq. (Gc)	aver. σ_R/σ_S	st. dev. σ_R/σ_S	no. of readings	max. σ_R/σ_S	min. σ_R/σ_S
2.87				<0.2 db	-0.1 db
9.70	0.02 db	1.10	1272	1.5 db	-0.8 db
22.97	0.41 db	1.27	1488	2.3 db	-3.9 db
31.97	-0.09 db	0.263	541	2.4 db	-6.4 db

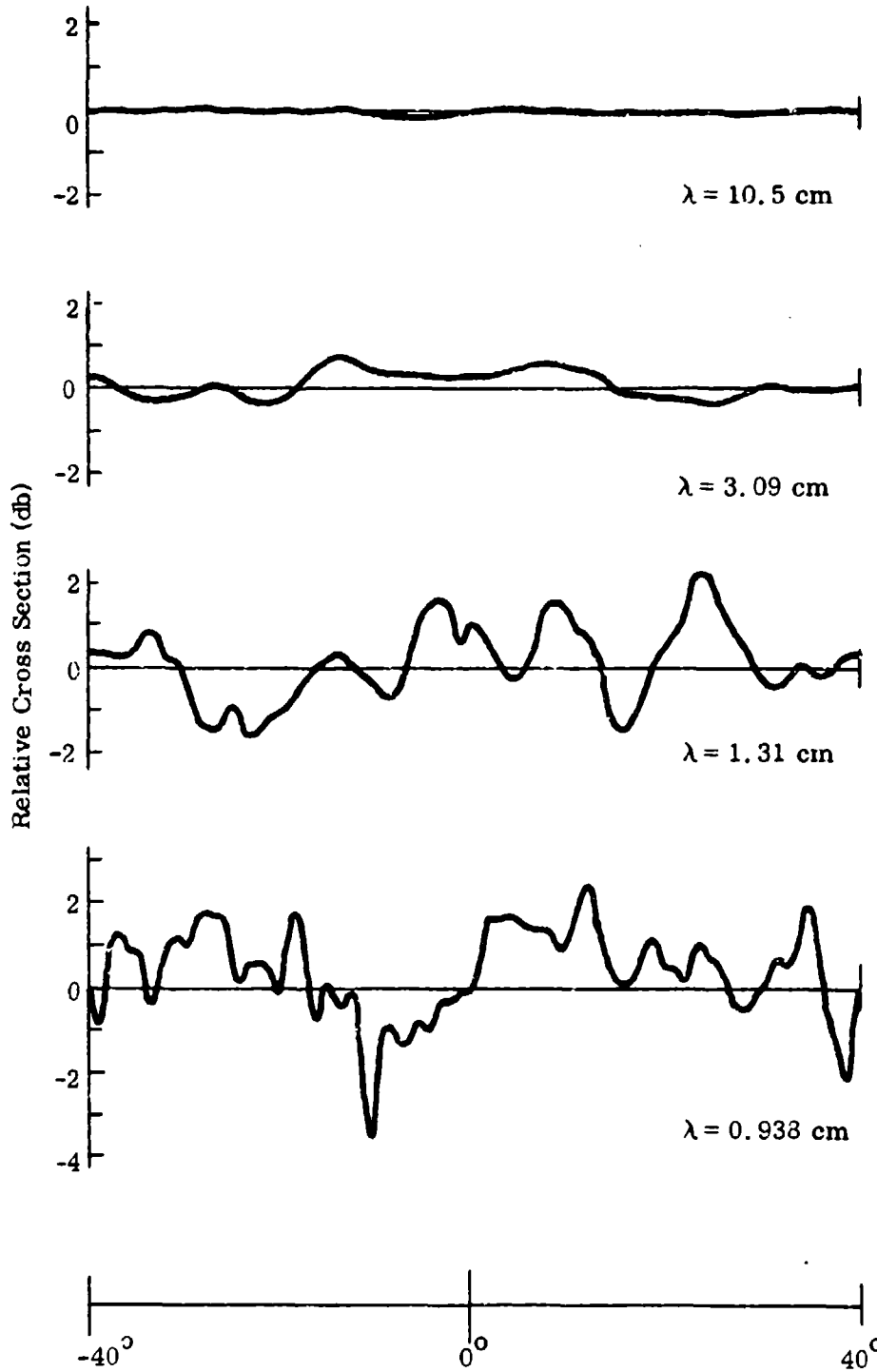


Figure 1: Relative Back Scattering Cross Section of 10-inch Diameter Sphere

summarized. Note that the standard deviations are pure numbers (not db) and that differences attributable to the slight discrepancy in size between the rough and smooth (calibrating) sphere have been removed.

K_R -band measurements have also been made with a sphere of larger radius ($a = 19.50$ cm), and since the results are quite similar to the above, it would appear that the size of the sphere is not a major factor at these frequencies.

Perhaps the most striking feature of all the data is the rapidity with which an increase of frequency brings out the roughness effect and this is particularly noticeable in the peak deviations. At S-band the roughness produces no really observable change in cross section and the aspect traces are sensibly uniform, but at X-band variations of 1 to 2 db are common, rising to as much as 6 db at K_R -band. The character of the patterns also changes, with the gentle oscillations found at X-band giving way to jagged and almost noisy traces at the highest frequency. In spite of this, the average cross section shows little frequency dependence over the above range, and at K and K_R bands at least the individual values of σ_T/σ_R are normally distributed. A typical distribution curve is that for the K_R -band data in Figure 2. Since the horizontal scale is linear, it is obvious that in any db plot the minima will tend to be deeper than the maxima are high, and this is true of all our measurements for the larger roughnesses. It is also evident from Table II.

If the frequency is increased still further, the average cross section will ultimately decrease. Although the initial effect of small roughness is to increase the apparent radius of the sphere and thereby increase the cross section, the change is relatively small and will sooner or later be swamped by the decrease in the apparent reflection coefficient of the surface. The decrease is actually due to the diffuse scattering but is indistinguishable from absorption as regards the direct polarized return in the monostatic case. Nevertheless, the true source of the reduction can be discovered by examining the cross-polarized signal, and this fact was pointed out by Senior and Siegel (1960) who presented some experimental data for a condition of extreme roughness. When the 10-inch diameter smooth (calibrating) sphere was partially covered with bumps whose dimensions were of order 1 inch and illuminated at X-band, the average back scattering cross section was found to be 7 db below that of the sphere without bumps. Minima as deep as -25 db were observed, and even the maximum return was 4 db below the smooth sphere value. In contrast, the average cross-polarized return was only 6 db below the direct one and for our present purposes this data is important in providing an effective continuation of Table II. Based on the size of the roughness alone, these changes in cross section should be comparable to what the original rough sphere would show at a frequency of around 200 Gc.

When the general roughness investigation was resumed in late 1961 it was decided to give most attention to a low cross section shape for which the back

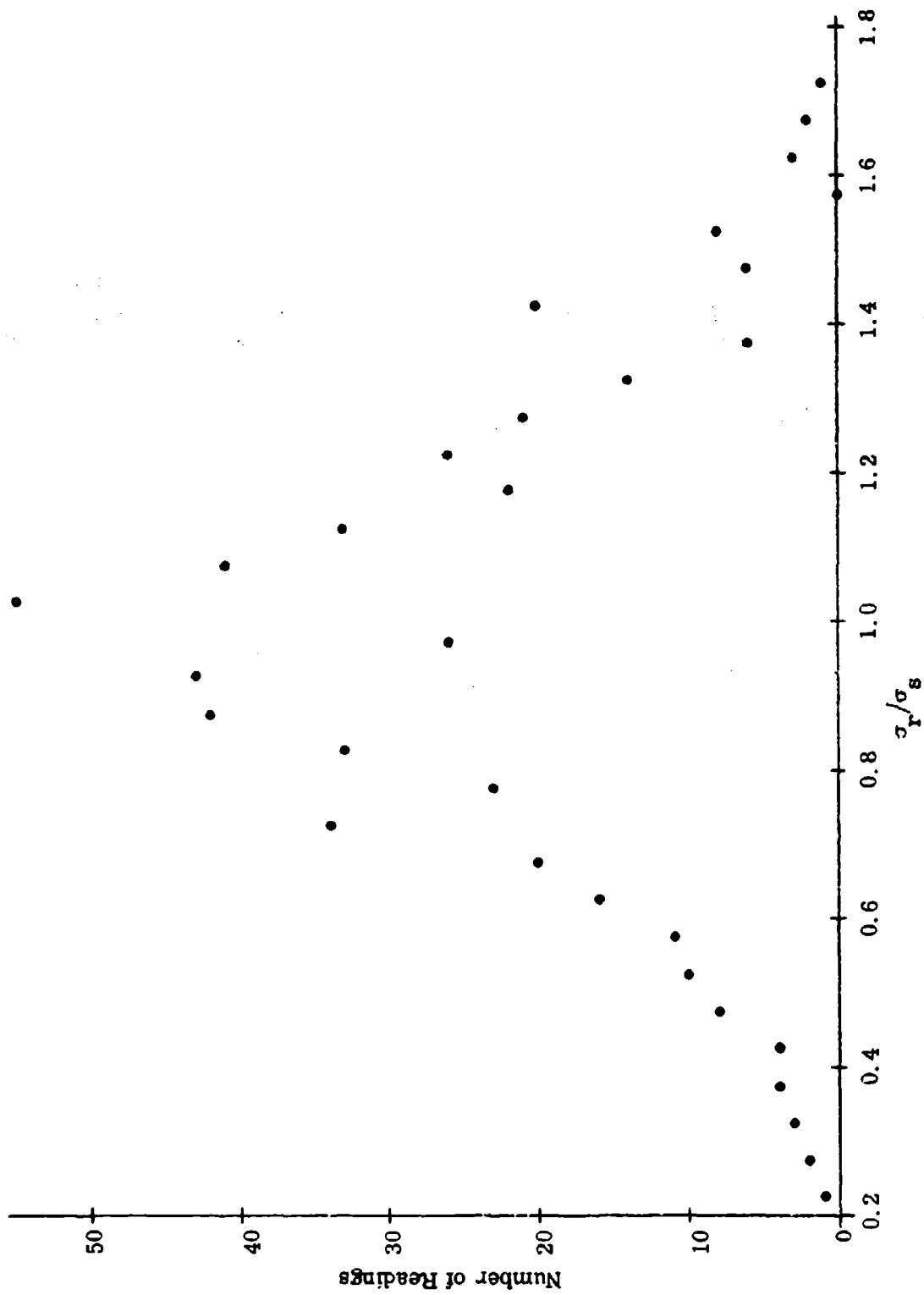


Figure 2: Distribution Curve for Relative Cross Section of 10-inch Diameter Sphere at K_a -band

scattered returns over a reasonable aspect range were not specular in character. The cone-sphere was selected. Three rough bodies were constructed with half-cone angles $\alpha = 7\text{-}1/2^\circ$, $12\text{-}1/2^\circ$ and 15° , and mean cap radii 5.613, 4.513 and 10.104 cm respectively. Each was composed of two identical portions cast in aluminum and after the slight ridge at the join had been removed, the seam was roughened with a hand tool. The resulting bodies seemed reasonably symmetrical, with a roughness which was sensibly uniform in character and of approximately the same dimensions as for the rough sphere previously described. For purposes of calibration, companion smooth bodies of similar size were milled from cold rolled stock.

The back scattering cross sections were measured at a variety of S, X and K_a band frequencies. Full 360° aspect patterns were obtained as well as -48° to 48° patterns and a host of individual nose-on values. For brevity, only the earliest data on the $12\text{-}1/2^\circ$ half-angle body will be discussed, and even this has not yet been analyzed with the thoroughness that it deserves.

At S-band the nose-on cross section of the smooth cone-sphere varied from $0.097\lambda^2$ at a frequency of 2.67 Gc to $0.25\lambda^2$ at 3.07 Gc, and though the simplest creeping wave approximations are not valid for ka as small as it was here, it seems reasonable to attribute the variation to an interference between a return from the join and a disturbance which has travelled around the rear of the cap. For horizontal polarization the cross section remained fairly constant at aspects out to (about) 24° , and then fell to a deep minimum at 40° to 48° , before rising through the side lobes of the specular flash. Beyond the flash the cross section was highly oscillatory and continued so out to 180° . Since there was no such oscillation with vertical polarization, it was probably due to a travelling wave contribution interfering with the specular sphere return.

The S-band rough cone-sphere measurements were carried out at 2.67(0.10)3.07 Gc using horizontal polarization and, in one case, vertical as well. The average variation in the cross section for the aspect range $-36^\circ \leq \theta \leq 36^\circ$ was 0.2 db, but this is somewhat misleading as the roughness appeared to enhance the return at frequencies for which the nose-on value was near to a minimum, and decrease it when the cross section was near a maximum, suggesting a differential action on the main contributors. The maximum cross sectional change in this aspect range was 1.1 db, but 0.5 db was more typical. There was some filling-in of minima (by as much as 2 db at 15 db minima and 5 db at 25 db ones), but part of this was undoubtedly due to background effects. For $|\theta| > 60^\circ$, no variations due to roughness could be detected.

In the expectation that roughness would play a major role at X-band, the investigation at these frequencies was more extensive. For the smooth body the aspect patterns were similar in character to the S-band ones and the interpretation follows the same general lines. The nose-on cross section had a pronounced variation as a function of frequency with a maximum of $0.19\lambda^2$ at

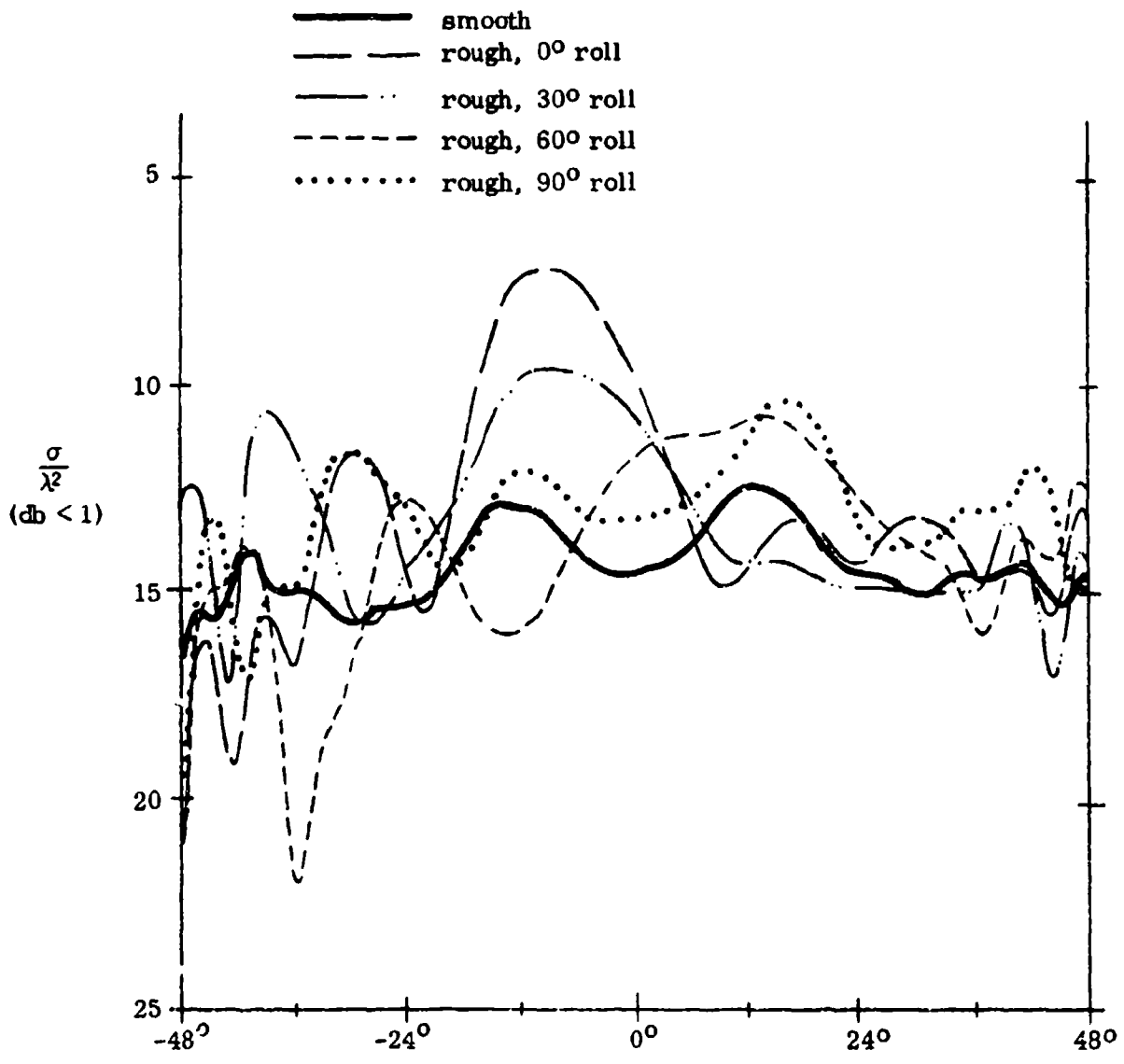


Figure 3: Cross Section versus Aspect Angle, 9.3 Gc, Vertical Polarization

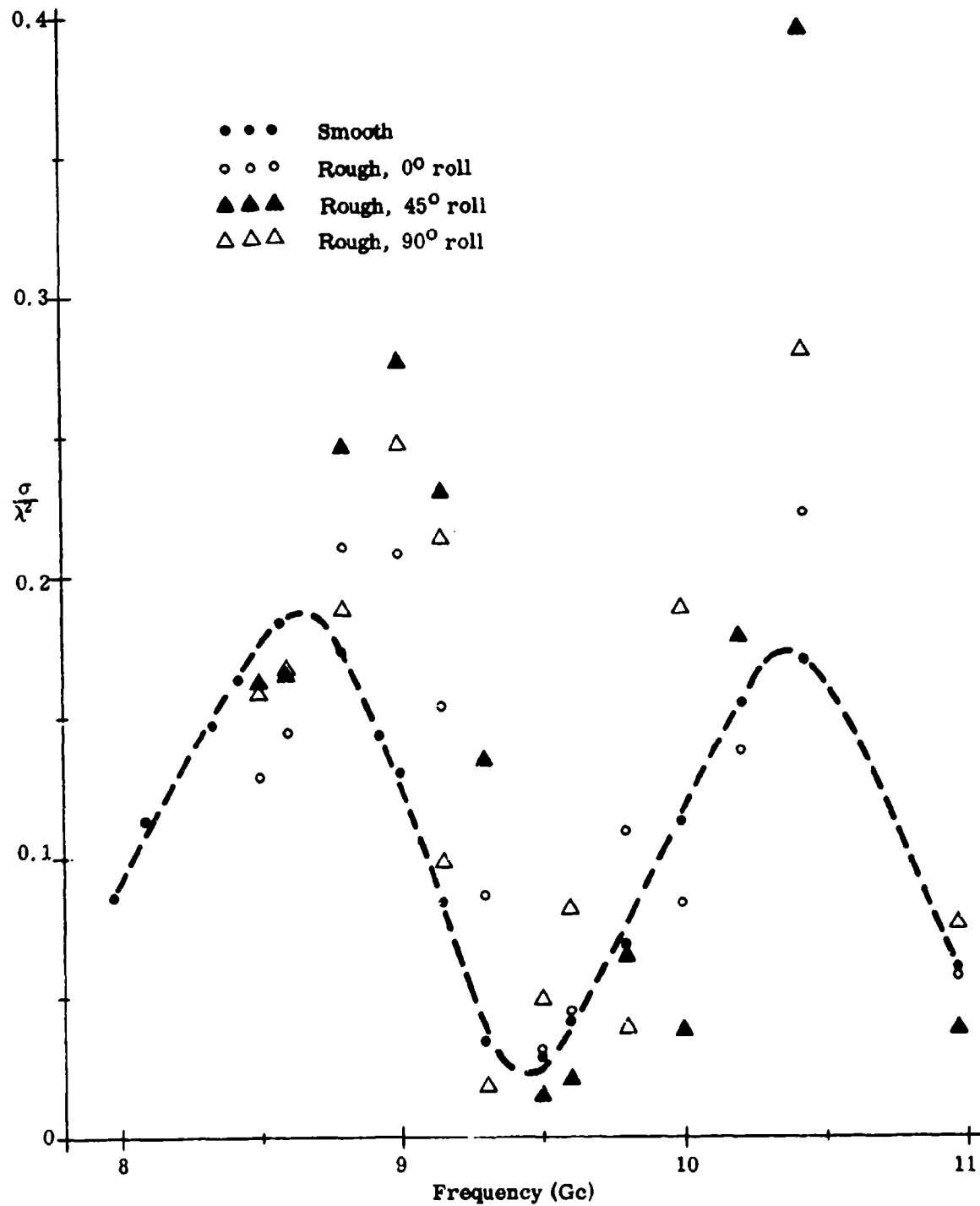


Figure 4: Nose-on Cross Sections of Rough and Smooth Cone-Spheres

8.6 Gc and a minimum of $0.025\lambda^2$ at 9.5 Gc. To pin down this oscillation with the highest possible accuracy a total of 17 separate frequencies in the range 7.98 to 10.97 Gc were employed, and at each of these 9 or more individual measurements of the cross section were made using vertical polarization (see Figure 4). As the aspect moved away from $\theta=0$ the cross section rose or fell according as the nose-on value was near a maximum or a minimum respectively, and at frequencies corresponding to these extreme cases the pattern was comparable to that of a ring with the same radius as the cone-sphere join. For θ greater than (about) 15° a behavior similar to that at S-band obtained.

As soon as the rough cone-sphere was measured, it was apparent that the body was not as uniform as had been supposed. The aspect patterns were no longer symmetrical about nose-on and in addition a marked roll sensitivity existed. When the radius of the cap was re-examined it was found to vary from 4.463 to 4.560 cm (equivalent to a tolerance of only $3 \times 10^{-2}\lambda$ at X-band), and though two new rough models were immediately ordered, the program had lapsed by the time they were delivered. There was no alternative, therefore, but to pursue the study with the imperfect model that was available and to think of the asymmetry as an added blessing. It should be added that when subsequent tests were made at S-band, the variations which had been attributed to roughness alone turned out to be sensitive to roll. Though the overall magnitude of the cross sectional changes were not affected, the details were, and some of these were almost certainly a consequence of the asymmetry of the mean surface.

The cross section of the rough cone-sphere was measured at 12 X-band frequencies for a variety of roll angles. Complete 360° patterns were obtained in each case as well as supplementary patterns for the -48° to 48° aspect range. As an example of the latter, the results for 9.3 Gc with vertical polarization are shown in Figure 4 with the smooth body trace for comparison. The roll sensitivity is clearly apparent and at some roll angles the main features of the pattern are entirely obscured. From a study of data such as this it was concluded that the average change in cross section in the forward aspect range was about 2 db, but changes of as much as 5 db were quite common and 10 db not unusual. At aspects corresponding to the specular flash and beyond, the changes were considerably less and rolling had little effect. The main structure of the smooth body pattern came through with only slight disturbance, and the cross sectional variations found with the rough sphere (see Table II) were fairly typical here.

For $\theta = 0^\circ$ the above data was reinforced with 'point by point' measurements, and some of the results are presented in Figure 4. Each point is the average of between 9 and 27 individual readings of the cross section for vertical polarization, and in spite of the roll sensitivity the regular oscillation characteristic of the smooth body is still evident. The minimum cross section at about 9.5 Gc is not substantially changed, but the maxima are increased (and perhaps displaced), suggesting an enhancement of both contributors. With the same

weighting for each point regardless of the number of readings which composed it, the average values of σ_r/σ_s for 0° , 45° and 90° roll angles were 1.2, 1.5 and 1.3 db respectively. The overall standard deviation of the ratios was 0.76, but nevertheless some of the cross sections differed from the corresponding smooth body values by as much as 6 db.

The K_2 -band measurements of the $12-1/2^\circ$ half-angle cone-sphere were confined to 360° aspect patterns for different roll angles with vertical polarization. In the aspect range out to the side lobes of the specular flash, the return corresponding to a smooth body was entirely swamped by contributions from the roughness and other perturbations. The average increase in cross section here was of order 10 db, with individual maxima rising 10 db above this, and the roll sensitivity merely jiggled an already jumbled mass of peaks. For aspects greater than 70° , however, the smooth body behavior was still discernible, with a superimposed structure which was comparable to the roughness effect observed in the sphere experiments at this frequency.

VI. CONCLUSION

The theoretical and experimental studies described above strongly suggest that a high degree of surface finish is not essential for model scattering work. Of necessity, the investigation has been limited to specific shapes and roughnesses, but it is believed that the cases chosen were of sufficient generality to allow a definitive conclusion to be reached. In none of these cases was a surface finish better than $10^{-3}\lambda$ required, and we have no direct knowledge of any evidence to indicate that this would not be satisfactory in all circumstances. Any imperfections of magnitude $10^{-3}\lambda$ should affect the dominant features of a back scattering pattern by only a small fraction of a db, and the 'deep' minima by no more than a db or so. A similar criterion for the overall tolerances should be more than adequate.

VII. ACKNOWLEDGMENTS

The author is indebted to several organizations in Industry and Government for sponsoring portions of this study, and to Messrs. E. F. Knott and T. E. Hon for the painstaking experimental work described in Section 5.

VIII. REFERENCES

- Clemmow, P. C. and V. H. Weston 1961 Proc. Roy. Soc. 264 A, p. 246.
Dawson, T. W. G. 1960 Royal Aircraft Establishment Report No. RAD 290.
SECRET.
Hiatt, R. E., T. B. A. Senior and V. H. Weston 1960 Proc. IRE 48, p. 2008.
Primich, R. I. 1959 Personal Communication to R. E. Hiatt (3 March).

Senior, T. B. A. 1959 Can. J. Phys. 37, pp. 787 and 1572.

Senior, T. B. A. 1960 Appl. Sci. Res. 8 B, p. 437.

Senior, T. B. A. 1963 "Analyses Associated with the Cross Sections of Nose
Cones", University of Michigan Radiation Laboratory Report
No. 5519-1-F. SECRET.

Senior, T. B. A. and K. M. Siegel 1960 J. Res. NBS 64D, p. 217.

Siegel, K. M. 1958 Appl. Sci. Res. 7 B, p. 293.

Siegel, K. M. 1963 Proc. IEEE 51, p. 232.

Weston, V. H. 1960 University of Michigan Radiation Laboratory Memorandum
No. 2987-515-M.

ESTIMATES OF THE 'VOLUME' RETURN FROM STYROFOAM⁺

T. B. A. Senior and E. F. Knott
Radiation Laboratory, The University of Michigan

I. INTRODUCTION

Styrofoam is a cellular material produced by the extrusion of polystyrene and is by its very nature inhomogeneous. Not only does the refractive index vary from unity (inside the cells) to 2.55 (the value for polystyrene), but in addition the cell size, shape and wall thickness differ from place to place in a manner which, for a well chosen sample of material, appears to be quite random. As a direct consequence of these fluctuations, the interior of a sample will provide a contribution to the backscattered field over and above the more regular and predictable return associated with the outer surfaces. Theoretically at least, it is expected that the 'volume' return will be incoherent, with a phase which is random from sample to sample (or aspect to aspect with a single sample) and an intensity which is Rayleigh distributed and proportional to the volume. It therefore represents the minimum to which the effective cross section of a column of this material could be reduced, and whereas the coherent surface scattering could conceivably be decreased to an arbitrarily small level by shaping and/or cancellation, it cannot be assumed that the volume return is susceptible to these techniques.

II. THEORY

Theoretical estimates of the magnitude of the incoherent scatter have been made by Plonus¹ using the concept of a medium whose index of refraction is a variable function of position defined only by a mean value and a correlation function, and also by assuming an aggregate of Rayleigh scatterers. When the physical constants of a typical cellular material are inserted into the equations, both methods yield cross sections per m³ in the range 10⁻⁴ to 10⁻⁶m² at X-band and as an example of the formulae obtained we have

$$\sigma_1 = 8 \pi^5 \frac{t^2 a}{\lambda^4} (\epsilon - 1)^2 V, \quad (1)$$

⁺ The work reported here was performed for the General Dynamics Corporation (PO 905616X) as part of the program being carried out under Contract AF30(602)2831 with the Rome Air Development Center.

based on the assumption of closely spaced spherical shells of mean radius a and thickness t . V is the volume, λ the wavelength and ϵ the relative permittivity of polystyrene. For the Dow Chemical Company styrofoam used in the later experiments, the cell wall thickness deduced from the density of the material was $t=0.009a$. Visual inspection indicated that the average cell radius was about 0.05 cm and since $\epsilon=2.55$, the cross section associated with the incoherent return is

$$\sigma_i = 7.4 \times 10^{-5} \text{ m}^2 \text{ per m}^3,$$

at 10 Gc. Observe that the right hand side of (1) is inversely proportional to λ^4 in accordance with the Rayleigh scattering of the individual cells, so that the cross section decreases rapidly with decreasing frequency.

III. EXPERIMENT

In an attempt to measure the electrical properties of styrofoam including the volume return, an experiment was undertaken in which the back scattering from a sequence of shaped blocks was determined at a series of closely spaced frequencies in the X-band range. The scheme was to take a large rectangular block and measure its end-on cross section at sufficient frequencies to locate the maxima and minima in the oscillatory curve produced by the interference of the front and rear returns as a function of frequency. From this data, having the dimensions of the block, the permittivity and loss factor of the material could be deduced. The rear end of the block was then sliced off at such an angle as to remove the return from it, leaving only the contribution from the front. Apart from any volume contribution, the resulting values for $\sigma\lambda^2$ should be frequency independent. Finally, the front of the block was also sliced off, and hopefully any residual return could be attributed to incoherent scatter alone.

The process was now reversed by first squaring off the front edge, then the rear edge, leading to a sequence of blocks of three basic shapes but of ever decreasing volume. If the scattering from the third type of block was due only to the volume effect, the average cross section should decrease at the same rate as the volume, leading to an estimate of this return.

The original parent block had dimensions 5 inches x 12 inches x 36 inches and was cut from a Dow Chemical Company buoyancy billet. Care was taken in the selection of the billet to ensure a piece whose cellular structure was as uniform as possible and devoid of large cavities. The measurements were all made for normal incidence on the smaller face, using vertical polarization with the 12 inch dimension lying in a horizontal plane. For the entire experiment over 100 different frequencies in the range 8.5 to 9.9 Gc were employed, but

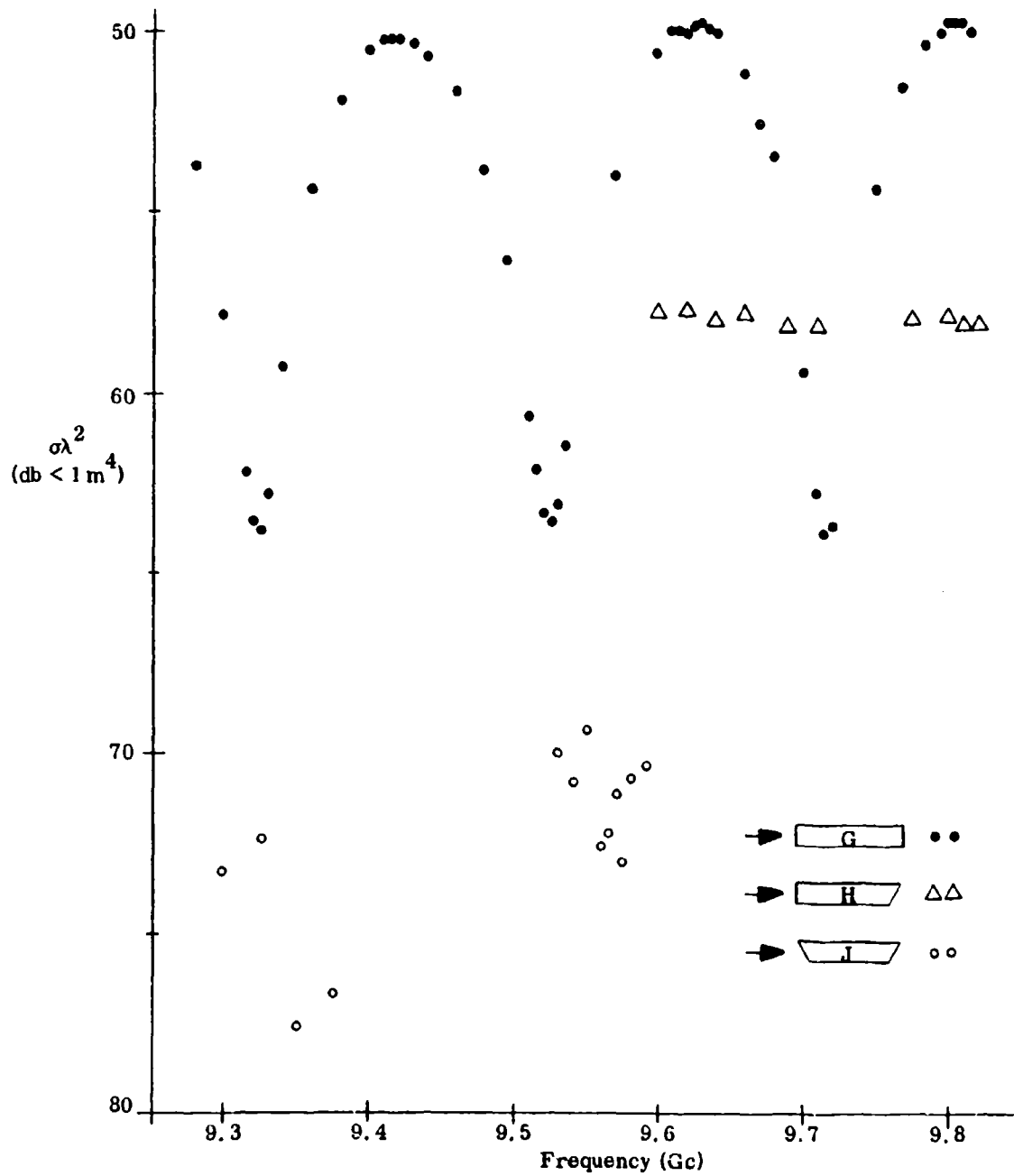


Figure 1: Scattering From a Styrofoam Block

with any given block the frequencies are limited to those necessary to pinpoint the cross section versus frequency curve. This generally required only 30 or so, and at each of them, several measurements were made to minimize experimental error.

Typical of the results obtained are those shown in Figure 1. The sinusoidal oscillations expected for the squared block (G) are regular and well developed, and from the maximum and minimum values estimates of the dielectric constant and loss factors can be deduced. When the rear was sliced off (block H) almost the entire oscillation was suppressed, and when both ends were sliced (block J) the cross section was still further reduced. The measured values were now more scattered as would be expected if only the volume return were present, with some indication of an increase in the mean level with frequency. The average cross section σ computed from this curve is $2.8 \times 10^{-3} \text{ m}^2 \text{ per m}^3$, which is an order of magnitude greater than the theoretical estimate of the volume return. Later blocks of the same type in the sequence gave 1.8 and $1.2 \times 10^{-3} \text{ m}^2 \text{ per m}^3$ which are somewhat closer to the predicted values, but more important is the fact that as more data was accumulated a regular variation was detected due apparently to an interference between the side lobes of the specular contributions from the faces. Although the ends had been cut at an angle to the vertical corresponding to the third minimum in the back scattering pattern from these surfaces at the center frequency, it was clear that their contribution was still significant in comparison with σ_v , and consequently the above estimates can only be regarded as upper bounds for the volume return.

An alternative approach was therefore tried based on the use of an ogive in place of the slanted blocks. The ogive (an arc of a circle rotated about its chord) was cut from a similar piece of styrofoam, with overall dimensions 17.2 inches by 5.8 inches and volume $4.1 \times 10^{-3} \text{ m}^3$. To minimize the return from the support, the ogive was suspended with fine cotton threads and its nose-on cross section measured at a series of X-band frequencies for both horizontal and vertical polarizations. Some of the data obtained is presented in Figure 2. The values vary quite widely from frequency to frequency and were often different for the two polarizations, but when averaged for each polarization, the mean values were quite similar: $6.1 \times 10^{-7} \text{ m}^2$ for horizontal and $6.9 \times 10^{-7} \text{ m}^2$ for vertical. The accuracy of the measurements was better than 3 db at the smaller values (-70 dbm^2) and of the order of 1 db at the larger values. It was verified that the return from the support threads was small in comparison with the means.

Although there is some evidence of a periodic variation, particularly at the lower frequencies, it is probable that the above cross sections are mainly due to incoherent scattering from the inhomogeneities within the styrofoam.

The estimated value for the volume return is therefore

$$\sigma_v = 1.6 \times 10^{-4} \text{ m}^2 \text{ per m}^3,$$

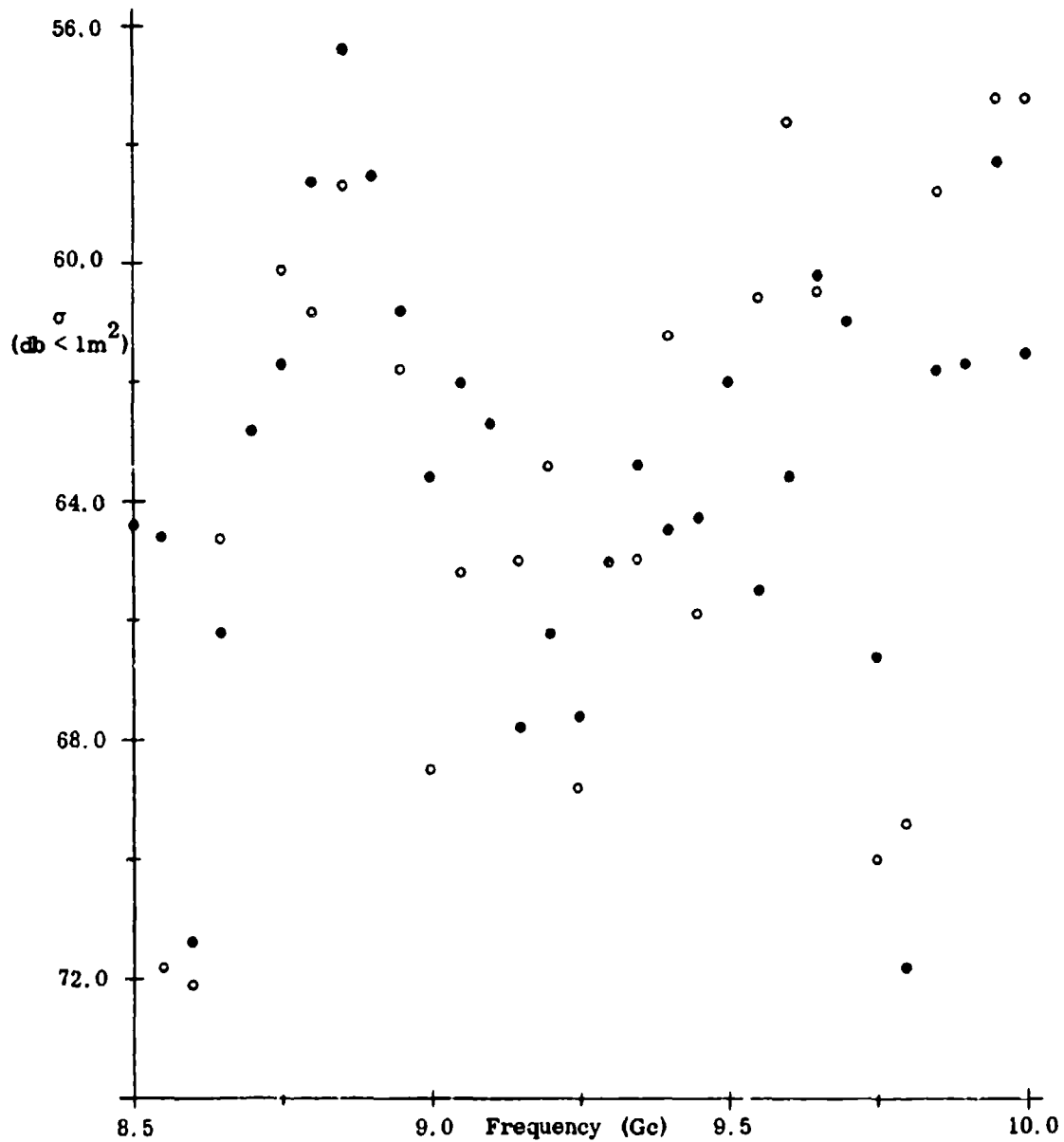


Figure 2: Nose-On Cross Section of a Styrofoam Ogive (●) Horizontal Polarization (○) Vertical Polarization

and some confirmation is provided by the fact that when the same ogive was examined at S-band (2.69 and 2.87 Gc) the return was below the system sensitivity. This implies a reduction of more than 8 db, compared with the theoretically expected reduction of 21 db.

It is hoped to measure other ogives, including ones of different cellular material, in the near future.

REFERENCES

- 1 Plonus, M. A., "Theoretical Investigations of Scattering From Plastic Foams," To be submitted to the Trans. IEEE-PTGAP for publication (1964).

THE NEAR FIELD OF A STYROFOAM CYLINDER⁺

T. B. A. Senior and E. F. Knott
Radiation Laboratory, The University of Michigan

I. INTRODUCTION

At the request of the General Dynamics Corporation a study was undertaken to explain an unusual scattering effect observed when a sphere was mounted on a long styrofoam cradle. The nature of this effect can be seen from Figure 1. The cradle was here a circular cylinder 6 inches in diameter and 43 1/2 inches in length, with ends at right angles to the axis, and was milled from a Dow Chemical Company buoyancy billet. To support a sphere in a stable manner, a saucer-shaped depression was cut into the surface to a maximum depth of 1 inch. The diameter (at the surface) was approximately 3 1/2 inches and the lip was some 3 inches from one end of the cylinder. A metal sphere of diameter 3.935 inches was now placed in the hollow and the back scattering cross section measured as a function of the rotation angle θ of the entire assembly in the horizontal plane, where $\theta = 180^\circ$ is the aspect at which the sphere was furthest from the transmitter. The results for horizontal polarization at 9.3 Gc are shown in Figure 1.

Apart from aspects within about 20° of 180° , the cross section is almost independent of aspect and differs by less than 1 db from that appropriate to the sphere alone. As θ increases beyond 160° , however, the net return begins to oscillate with a period of approximately 7° about a level which falls rapidly to a minimum some 16 db below the free space return from the sphere. This behavior appears to be independent of polarization and is similar to that previously found by the General Dynamics Corporation using a larger sphere and a cradle of somewhat more complicated shape. On the other hand, when the sphere was raised 7 inches above the cradle, no reduction in the cross section near to $\theta = 180^\circ$ was found.

It is obvious that these effects are of major importance in the design of target support pedestals, and an understanding of their origin is therefore essential. Several possible mechanisms were examined and in the light of this study it was concluded that only an amplitude and/or phase disturbance, confined to the immediate vicinity of the surface and increasing with the length of styrofoam

⁺ The work reported here was performed for the General Dynamics Corporation (PO 905616X) as part of the program being carried out under Contract AF30(602)2831 with the Rome Air Development Center.

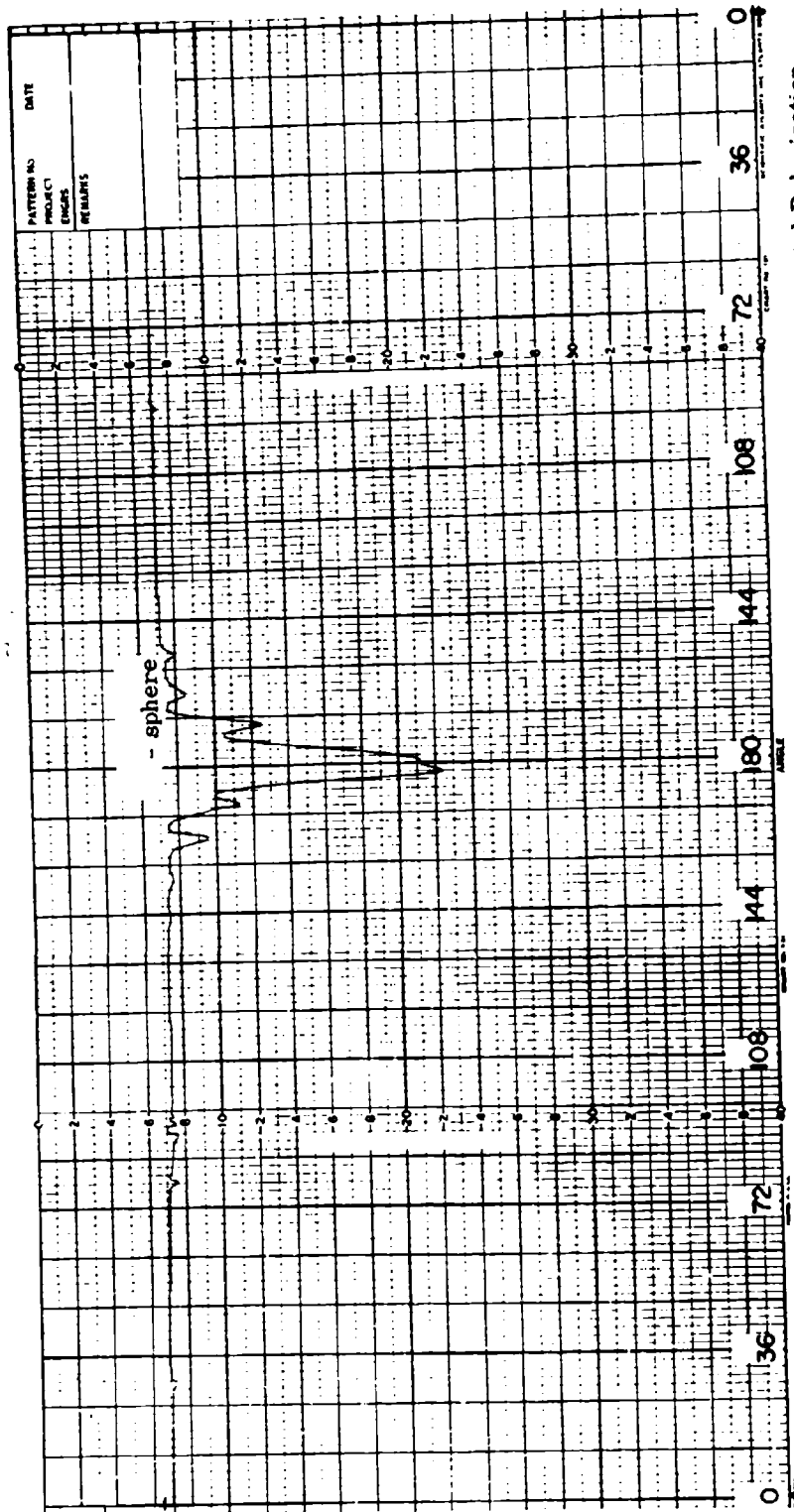


Figure 1: Cross Section of Styrofoam Cylinder and 3.935 in Diameter Sphere, 9.3 Gc, Horizontal Polarization

over which the field has travelled, could suffice to explain the observations. Direct measurement of the amplitude and phase of the field near to a styrofoam cylinder have since confirmed the existence of a disturbance, and it is the purpose of this paper to detail the results.

II. METHOD

The measurements discussed here were carried out with the styrofoam cylinder described in Section I. For the early ones the frequency was 9.2 Gc, and these were made before the saucer-shaped depression was cut into the surface. Subsequently, however, the frequency was increased to 9.3 Gc. This was used for all the work on the cut cylinder, and to minimize the effect of the depression on the near field measurements, the cylinder was placed on the support pedestal with the hollow on the side opposite to that being probed. The probe traverses were in a horizontal plane at several stations along the side of the cylinder. The illumination was at end-on incidence from a horn situated 15 feet (approx.) from the mid-point of the cylinder using vertical polarization.

A sketch showing a plan view of the experimental components is given in Fig. 2. A receiving dipole, 1.51 cm long, was attached to a rigid, horizontal coaxial line $1/8$ inch in diameter and 22 inches in length. The output was fed to one of the symmetrical arms of a hybrid tee through a section of flexible RG-9/U coaxial cable, and based on a few trial positions of the cable, it is estimated that flexing introduced no more than 5° of phase shift.

The illuminating antenna was fed by a suitably-padded cavity-stabilized oscillator. Some of the energy was sampled, and passed through attenuators and a phase shifter to the other symmetrical arm of the hybrid tee, after which the sum of this signal and the one from the dipole was detected and fed to a superheterodyne receiver. The amplitude of the received signal at its highest was 50 to 60 db below that delivered to the illuminating antenna. The amplitude and phase were obtained by adjusting the attenuators and phase shifter in the symmetrical arm of the tee for a null at the receiver, and could be read directly from these devices.

All the hardware was shielded by a 2 inch thick barrier of hairflex. The operator of the equipment was likewise shielded, as was the wooden framework which supported the coaxial line feed from the dipole.

III. PROCEDURE

In the initial experiment the probe was traversed in a radial direction at three selected stations along the length of the cylinder, corresponding roughly to the two ends and the mid-point. The actual distances d of these stations

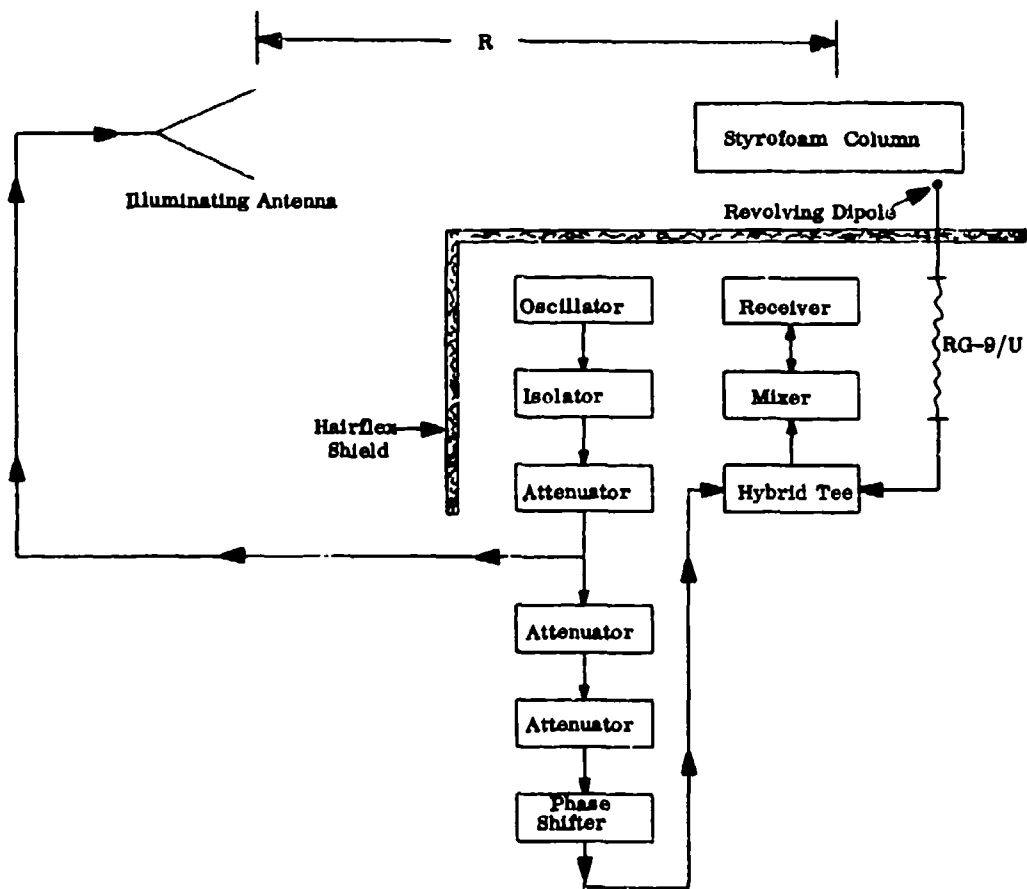


Figure 2: Experimental System

from the front end were 2, 22 and 42 inches, and at each location the field was measured at a variety of different radii starting at $1/8$ inch above the surface ($r = 3 \frac{1}{8}$ inch, where r is the distance from the axis) and continuing out to $r = 14 \frac{1}{8}$ or $15 \frac{1}{8}$ inch.

To provide some basis for comparison, most of the measurements were repeated without the cylinder in place, but since the main purpose of the work at this stage was to confirm the capability of the probe technique, no attempt was made to achieve common amplitude and phase calibration with and without the cylinder present. It was not possible, therefore, to deduce the amplitude and phase of the scattered field from a comparison of the total and incident field data without additional information, and in this connection we remark that a change of station of only 0.6 inches between the two cases would change the phase by 180° . Nevertheless, the marked differences in the shape of the curves after the cylinder was introduced were sufficient to show the existence of a relatively large perturbation, and as this appeared to increase with distance from the front end of the cylinder, additional measurements were made at two stations $13 \frac{1}{4}$ and 21 inches beyond the cylinder. These will be discussed later.

At the conclusion of the above work, a depression was cut into the cylinder to support a metal sphere for the back scattering experiment, but the interesting and challenging nature of the near-field results demanded a renewal of this study. The frequency was now increased to 9.3 Gc, and to ensure accurate and uniform calibration, the following procedure was adopted. At each station, measurements were carried out with the cylinder present starting $1/8$ inch above the surface and going out to the furthest desired distance. The cylinder was then removed with the probe left untouched, after which the incident field was sampled as the probe retraced its original path. To determine the extent to which such data was repeatable, the measurements at one station were reinforced with incident field values taken as the probe was moved out again to its maximum distance. The average amplitude discrepancy was a mere 0.04 db, and though the phase differences were somewhat larger, averaging 3° , this was mainly due to a single 15° change at one point.

IV. RESULTS

Incident and total field data at the middle station for which $d = 22$ inches is presented in Figures 3 and 4 respectively, and the analogous results for a far station ($d = 41\text{-}1/2$ inches) are given in Figures 5 and 6. Since the amplitude and phase scales are now the same for both fields, the graphs can be compared directly and, if required, the scattered field deduced.

Taking first the incident field measurements at the two stations, the general trends of the amplitude and phase curves are reasonably consistent

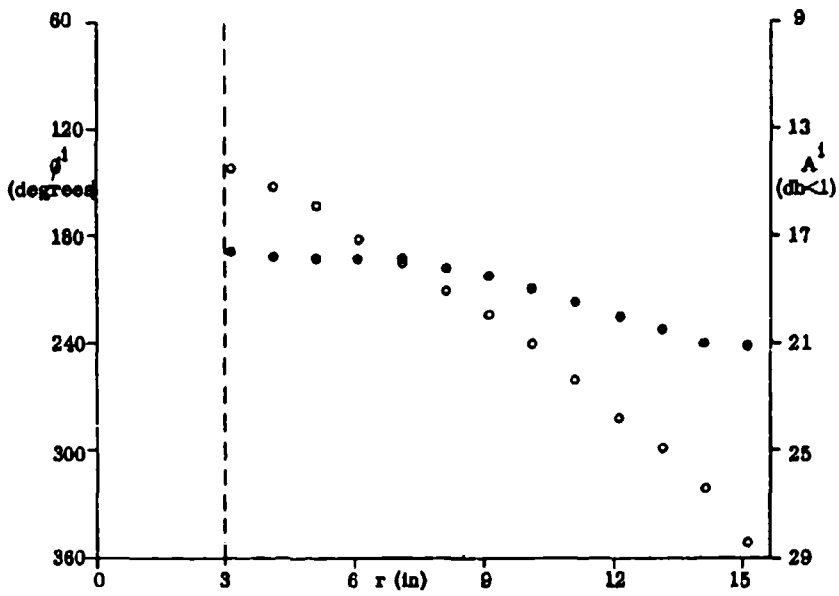


Figure 3: Amplitude (ϕ) and Phase (ψ) of Incident Field for $d = 22$ in.

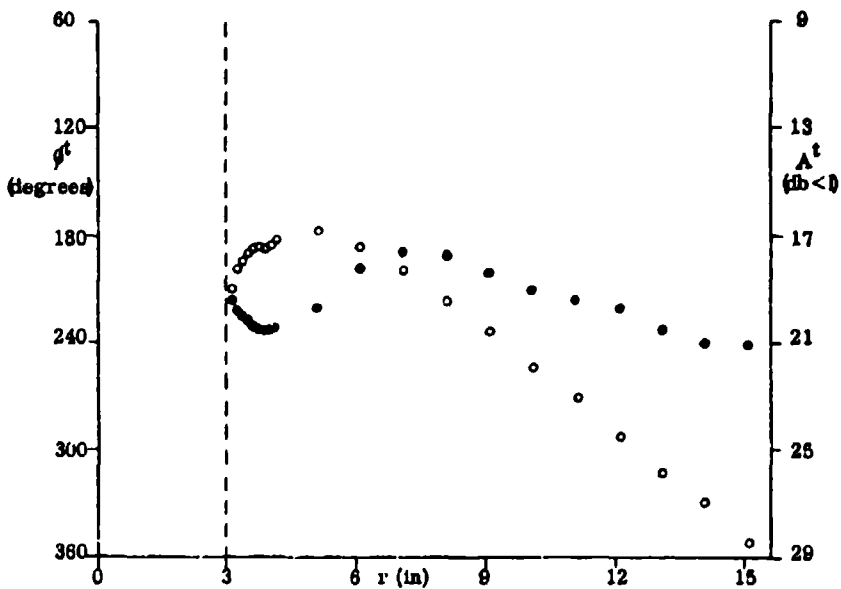


Figure 4: Amplitude (ψ) and Phase (ϕ) of Total Field for $d = 22$ in.

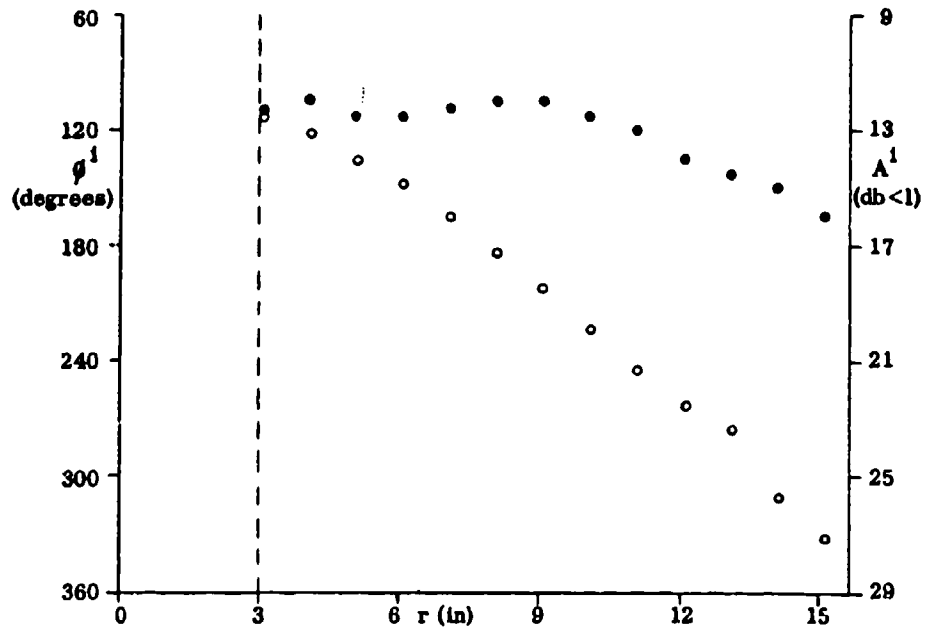


Figure 5: Amplitude (●) and Phase (○) of Incident Field for $d = 4\frac{1}{2}$ in.

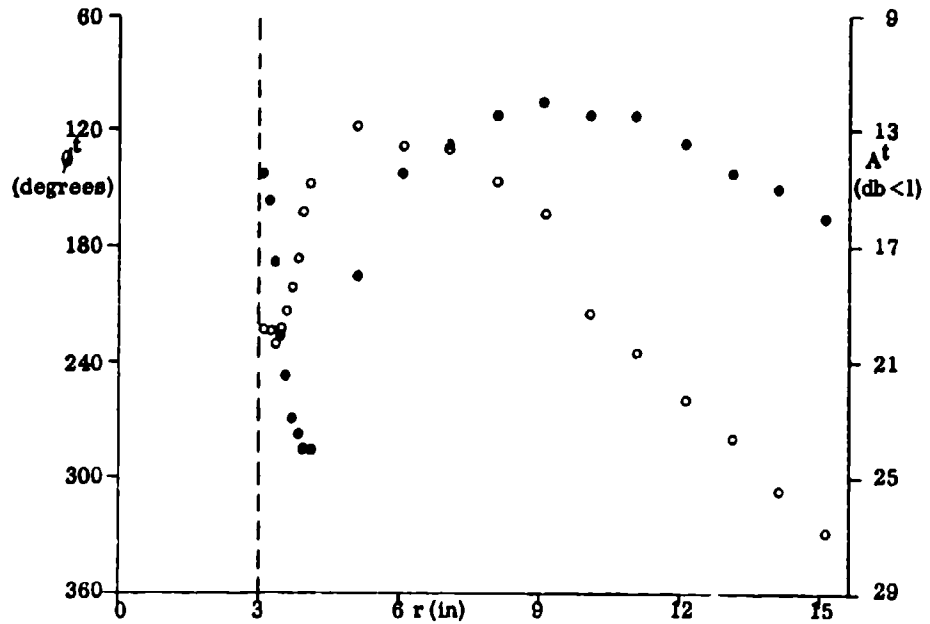


Figure 6: Amplitude (●) and Phase (○) of Total Field for $d = 4\frac{1}{2}$ in.

with a planar intersection of a spherical wave pattern originating some 15 to 17 feet away. What small variations there are, are almost certainly due to the support pedestal and/or to room reflections, and we observe that the amplitude seems to vary a little more at the far station (behind the pedestal) than it does at the middle station where the pedestal is located.

The effect of introducing the cylinder can be seen by comparing Figures 3 and 4, 5 and 6. For $d = 22$ inches the regular decrease in phase as the probe approaches the surface is arrested some 2 inches away and thereafter the phase increases rapidly. This turn-over is accompanied by a dip in the amplitude curve which is apparent even out to a distance of 3 inches from the surface, but is centered about 1 to 1 1/2 inches away. Such perturbations are even more apparent at the far station. The phase of the total field changes by over 100° within the first two inches from the surface and there is some evidence of a levelling of the curve as the probe makes its nearest approach. We remark in passing that later measurements of the field with a cylinder 57 1/4 inches long (probe station 50 inches from the front) have shown that the phase does indeed remain constant very close to the surface. The radial extent of this platform increases with d , confining the phase swing to a smaller and smaller radial span.

Perhaps more striking is the amplitude behavior when $d = 41$ 1/2 inches. The dip observed in Figure 4 is accentuated in Figure 6. Its depth has increased to about 12 db and since the width is less, the position of the minimum amplitude can be located at almost precisely 1 inch above the surface. At distances less than this the amplitude increases, and has almost achieved the incident field value by the time the probe gets to 1/8 inch from the surface.

A comparison of the incident and total field data also shows that as r increases beyond the position of the minimum the two fields approach one another. At all the stations examined the differences were negligible for r greater than (about) 10 inches and consequently, whatever the true origin of the scattered field, its influence is restricted to the first few wavelengths from the surface. This is in accordance with the conclusion reached from the experiment conducted by the General Dynamics Corporation in which the sphere was raised above the cradle, and suggests that the scattered field is some form of surface wave. It also enabled us to resurrect the earlier measurements of the near field by introducing a calibration based on the equality of the incident and total fields for $r > 10$ inches. Such calibration confirmed that the scattered field at the forward station ($d = 2$ inches) was insignificant, a fact which was otherwise obvious from the complete identity of the curves with and without the cylinder in place. It is therefore unnecessary to present the data.

At stations beyond the cylinder, however, the results are more interesting, and for $d = 56\text{-}3/4$ inches the incident and total field data is given in Figures 7 and 8, with the analogous results for $d = 64\text{-}1/2$ inches in Figures 9 and 10. Note that the frequency is here 9.2 Gc, and that the calibration has been based on the assumed equality of the fields for $r = 11$ and 12 inches. Bearing in mind that the measurements now go down to $r = 0$, the incident field values are similar to those found at stations along the cylinder. The total field, on the other hand, does show some differences. The phase decreases uniformly with r , changing rapidly for r between 6 and 4 inches, and tapering off as the probe enters into the shadow region. There is no longer the turn-over characteristic of the measurements at $d = 22$ and $41\ 1/2$ inches. The minima in the amplitude curves are deeper than before (about 15 db instead of 12) and occur at a somewhat greater radius, though the precise location is difficult to determine because of the radial separation of the probe positions. For r less than about 5 inches, the amplitude increases, rapidly at first but more slowly within the shadow, and achieves a value some 6 to 8 db greater than the incident field on the continuation of the axis. No important differences in behavior at $d = 56\ 3/4$ and $64\ 1/2$ inches are apparent, and the most that can be detected from the total field data is a slight tendency for the radial distance of the minimum to increase with d .

Knowing the amplitude and phase of the incident and total fields, it is a trivial matter to deduce the scattered field. For the two stations along the length of the cylinder, the results normalized relative to the incident field values, are shown in Figures 11 and 12. The rapid and possibly exponential attenuation of the field in the radial direction is now obvious, and both the surface value and the rate of attenuation increase with d . For $r > 8$ inches the ratio of the incident and total field amplitudes is so close to unity that small errors in the measured data (primarily of phase) produce quite sizable effects on the scattered field values, and at least some of the behavior at $r = 7$ and 8 inches may also be attributable to this. Nevertheless, the startlingly different character of the phase curves at $d = 22$ and $41\ 1/2$ inches is believed genuine. At the middle station, the phase remains constant for the first two inches, and then decreases slowly, whereas at the far station the phase increases almost uniformly out to the largest distance at which data is available. It may be pertinent that the difference in the phase velocities in styrofoam and free space would create a phase lag of 115° at the middle station and 218° at the far one, and on this basis the results for $d = 22$ inches might be expected to resemble those for $d = 52$ inches rather than $41\ 1/2$ inches. Measurements at $d = 50$ inches made with the longer cylinder have indeed shown that the scattered field phase is once again constant for the first inch or so, and then increases.

At the two stations beyond the cylinder the derived values for the scattered field are given in Figures 13 and 14. The results are quite similar. At the nearer station the amplitude decreases steadily from a (relative) value of 3.0 at $r = 0$ and is negligible for $r > 10$ inches. The phase, on the other hand, increases after

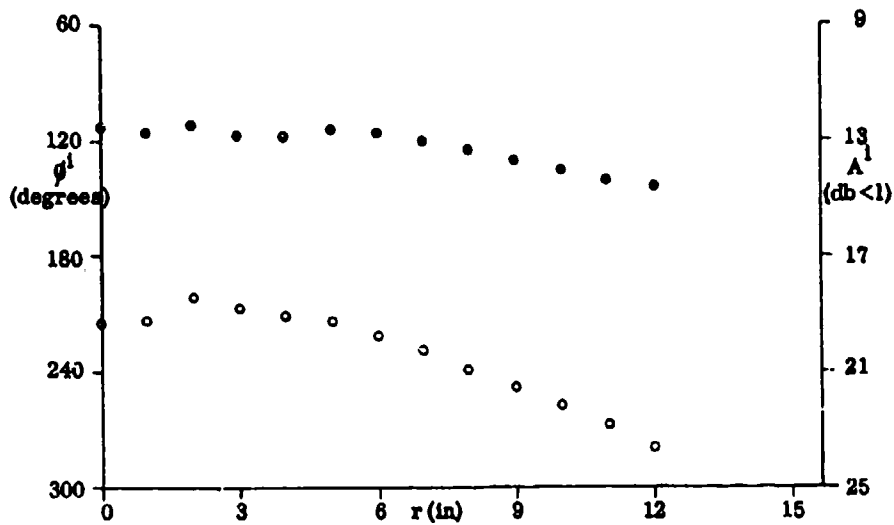


Figure 7: Amplitude (•) and Phase (o) of Incident Field for $d = 56 \frac{3}{4}$ in.

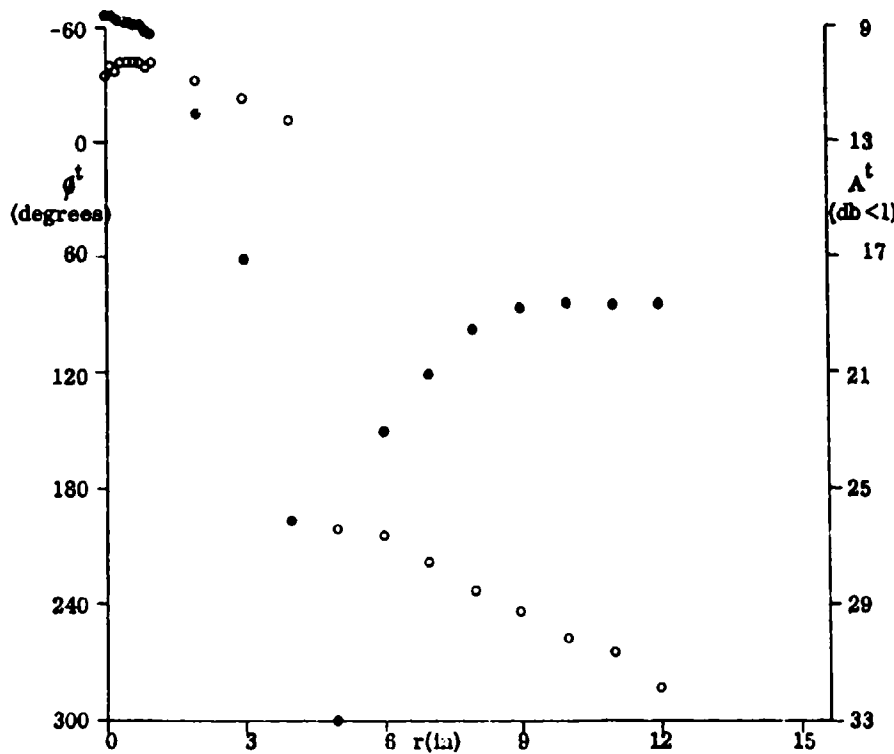


Figure 8: Amplitude (•) and Phase (o) of Total Field for $d = 56 \frac{3}{4}$ in.

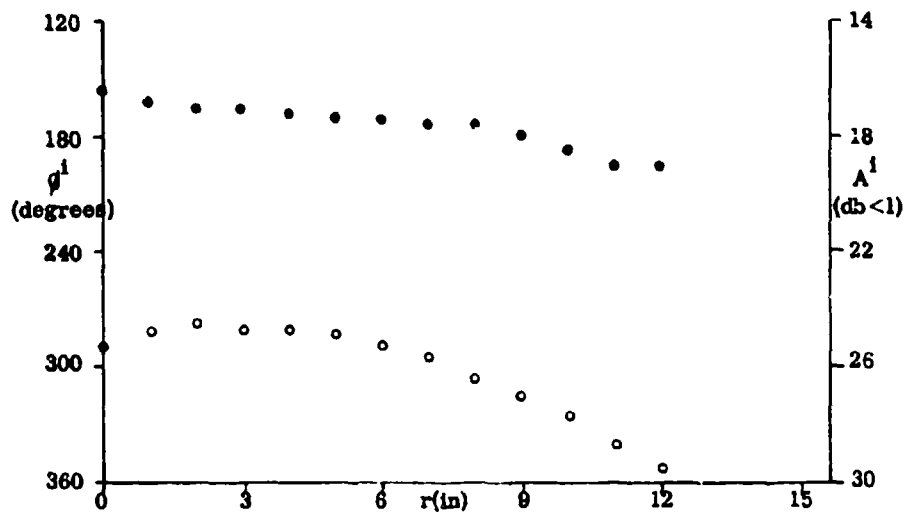


Figure 9: Amplitude (●) and Phase (○) of Incident Field for $d = 64 \frac{1}{2}$ in.

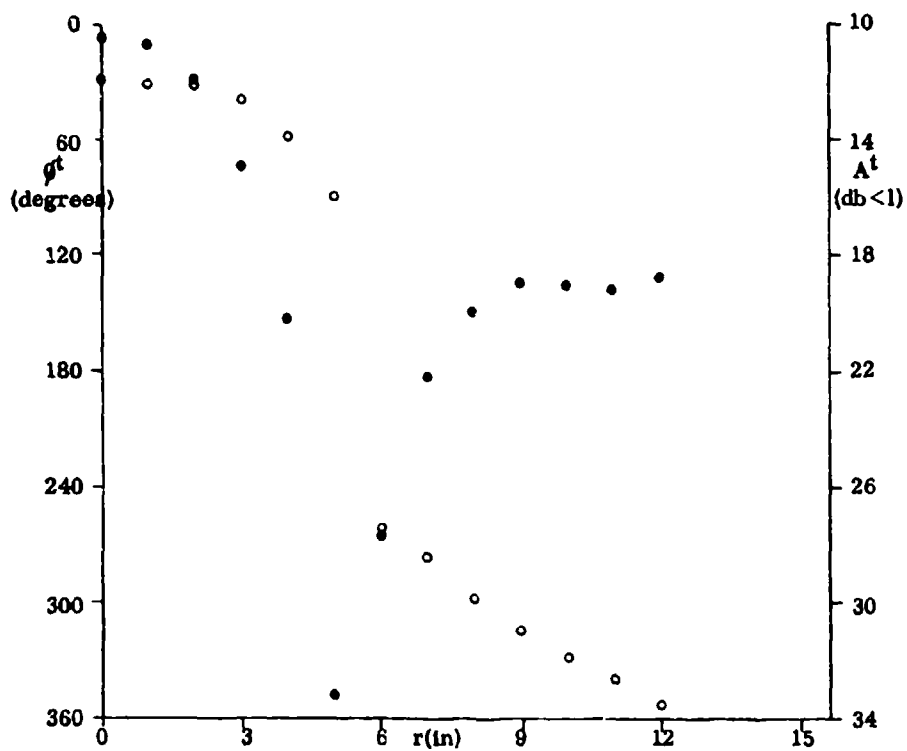


Figure 10: Amplitude (●) and Phase (○) of Total Field for $d = 64 \frac{1}{2}$ in.

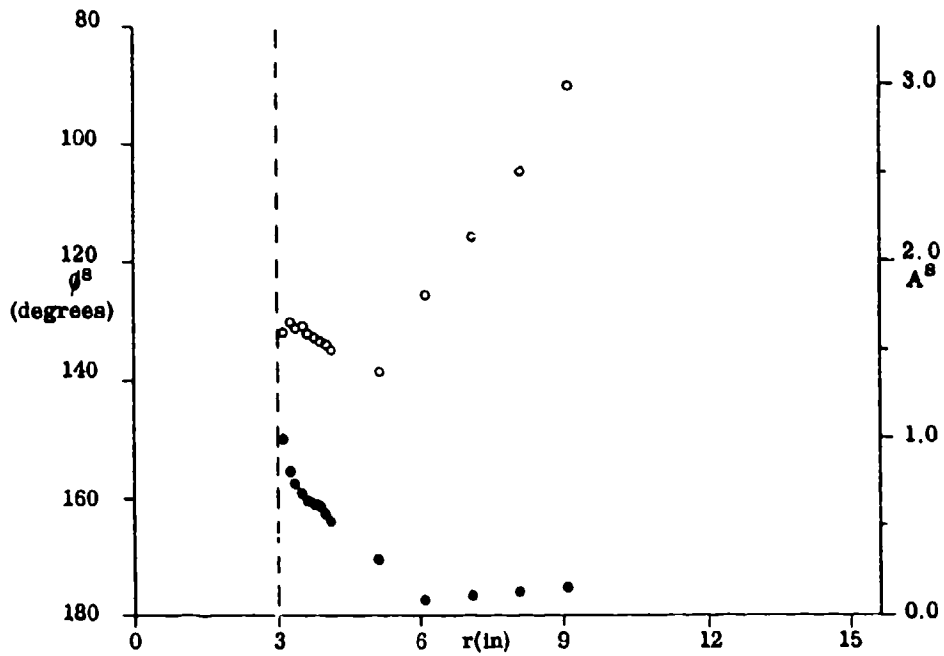


Figure 11: Relative Amplitude (●) and Phase (○) of Scattered Field for $d = 22$ in.

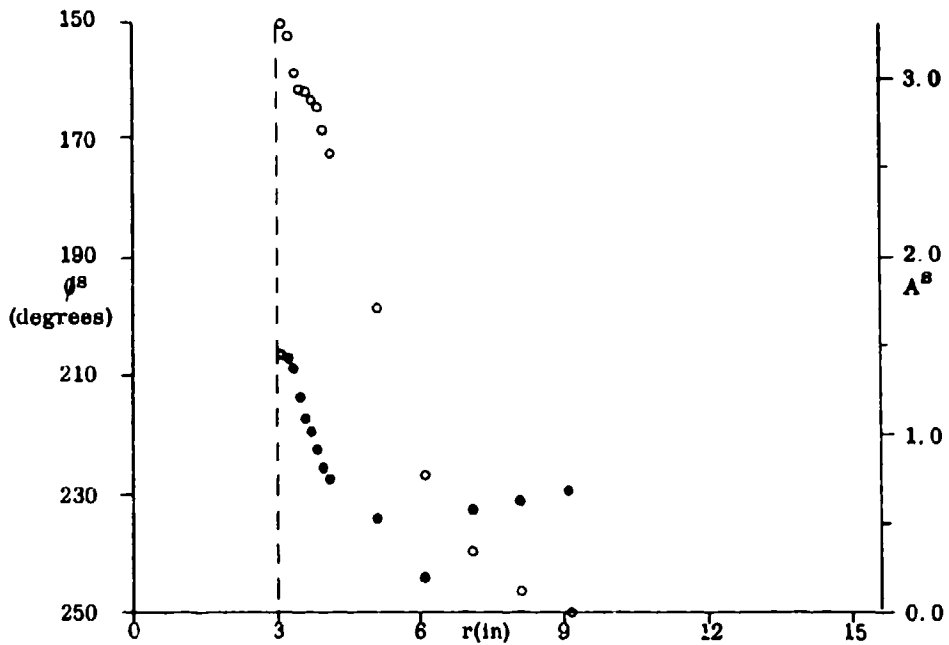


Figure 12: Relative Amplitude (●) and Phase (○) of Scattered Field for $d = 41\frac{1}{2}$ in.

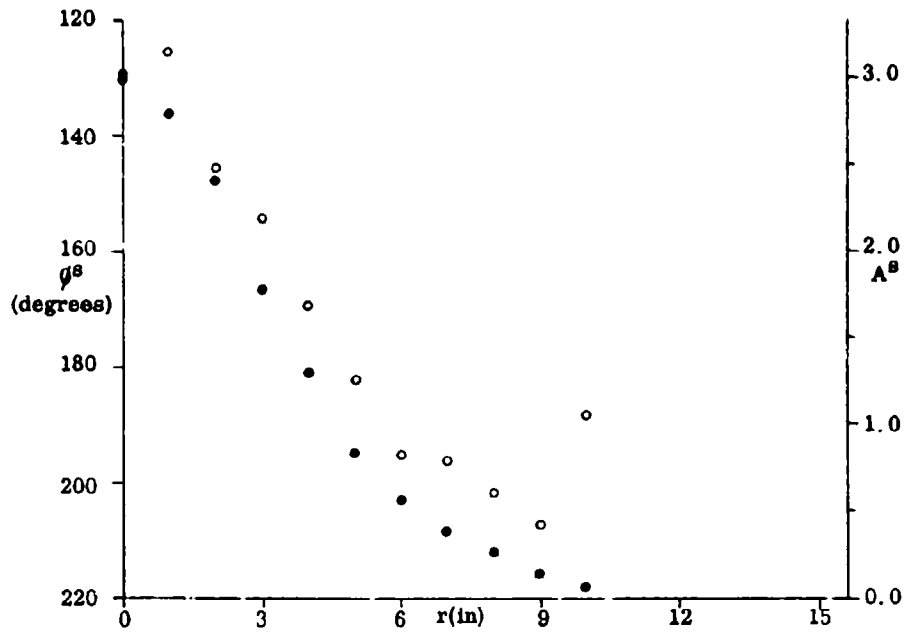


Figure 13: Relative Amplitude (\bullet) and Phase (\circ) of Scattered Field for $d=56 \frac{3}{4}$ in.

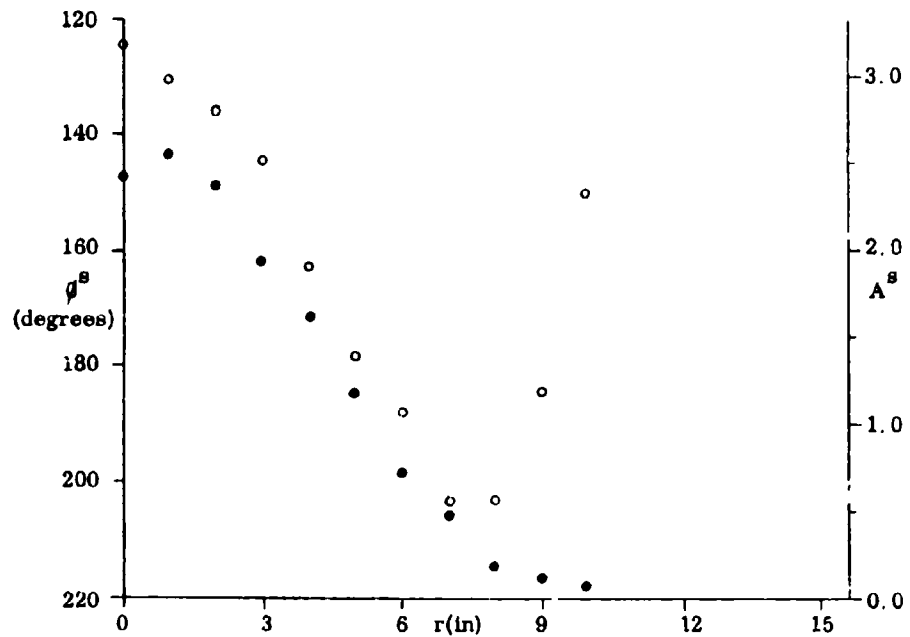


Figure 14: Relative Amplitude (\bullet) and Phase (\circ) of Scattered Field for $d=64 \frac{1}{2}$ in.

an initial fall, but appears to decrease sharply beyond $r = 9$ inches. It is not known if this effect is real, although it does occur at the further station as well. The amplitudes here are fractionally less than for $d = 56 \frac{3}{4}$ inches, and show a slight increase as the probe moves away from $r = 0$. Outside the optical shadow of the cylinder both sets of curves are not unlike those of Figure 12 in general character, which suggests that the perturbation simply launches itself into space when the cylinder terminates.

V. CONCLUDING REMARKS

In an attempt to explain the above results, two different theoretical studies have been undertaken. Since the scattered field at any point is almost certainly affected by the progressive phase lag between a wave attempting to propagate down the cylinder and the incident field streaming past the outside, the simple problem of a source placed above a flat styrofoam medium was considered. This is analogous to the problem of propagation over a flat earth, but instead of the pole which is responsible for many features of the solution when the refractive index n is large and complex (the usual case), the dominant singularity for n almost real and near to unity is a branch point. As a consequence of this, the region where the diffraction effects are important is stretched out in directions parallel to the surface, and there the total field has a sinusoidal behavior, with maxima and minima whose magnitude and position are determined by $(n - 1)d$, where d is the horizontal distance from the source.

Of more immediate application to the physical problem is an investigation of the surface or Goubau waves which could be supported by a cylinder of this size and material. This is currently in progress, and it is hoped to model the experimental set-up by considering a styrofoam cylinder of infinite length excited by a circumferential ring source. Until such time as more information is obtained about the scattered field either by analyses of this type or by more experimental work, it is premature to attempt a detailed interpretation of its influence of the far zone scattering pattern of an object placed on the cylinder, but it is clear that the magnitude of the perturbation is quite sufficient to explain results such as those shown in Figure 1.

It is equally obvious that the existence of a large surface wave has an important bearing on the design of support pedestals for cross section measurements, and the cross section of the pedestal itself is not necessarily an indication of the effect that it will have. Since the intensity of the wave apparently increases with the length of styrofoam over which it has travelled, it is essential to keep to a minimum the diameter of the upper portions of the pedestal. The shaping of the upper surface, leading to an effective immersion of part of the target within the styrofoam, should be as little as possible consistent with the required stability, and this is particularly vital for such bodies as the cone-sphere

where a dominant contributor to the cross section is a surface wave. It may well be that for the measurement of heavy low-observable shapes, the design of a styrofoam support with an acceptable surface field perturbation is more difficult than the construction of one with a small enough cross section.

MODELING OF RAM-COVERED COMPLEX BODIES

A. S. Thomas
A. S. Thomas, Incorporated
Westwood, Massachusetts

ABSTRACT

It can be shown that scaling of complex bodies covered with lossy materials may be possible with materials having parameters somewhat different from those used on the full-scale model, provided that the experimenter can immerse the model in a medium with permittivity greater than free space and adjust the permittivity of the materials on the model by the same factor over that of the full-scale model.

INTRODUCTION

Both, from the point of view of defense and offense at least an approximate value of the radar cross section versus aspect angle of complex bodies covered by RAM materials is essential. The most desirable approach would be to compute the radar cross section of such objects. Unfortunately, even the slightest deviation from the simple figures of revolution represent a formidable theoretical problem when covered with a lossless dielectric. The next best approach is to measure the radar cross section on a model scale, preferably at X- or K- band in an indoor anechoic chamber. The scaling principle here is quite straightforward; linearly scale all physical dimensions, but preserve ϵ and μ . Here the experimenter is faced with a materials problem. Since complex ϵ and complex μ are generally monotonically decreasing functions with increasing frequency, the materials developed for the full-scale model do not lend themselves for the use at the model frequency. This would imply a serious materials development, at least comparable to that of obtaining the original material used or to be used on the full-scale model. It is doubtful that the magnitudes of μ' , μ'' , ϵ' and ϵ'' over the range needed can be obtained. However, if a reasonable range of values of these materials can be obtained, it is conceivable, if the experimenter is not restricted to free space as the medium, that scaling with materials having parameters somewhat different from those on the full-scale model may be used.

It is clear, of course, that the reflection coefficient, or the scattering coefficient, at a given frequency is uniquely determined by the geometry and the materials. Conversely, there is an unlimited number of geometries and materials that could give the identical reflection or scattering coefficient. Lacking a theoretical capability of computing the radar cross section of complex bodies covered with RAM materials, the problem of obtaining a geometry and materials that will give a representative description of the full-scale model is formidable indeed; however, one may infer a great deal from the simple geometries.

A study of the exact expressions for reflectivity from a stratified planar medium and for scattering from a set of concentric cylindrical shells about a perfectly conducting cylindrical core will give insight as to the probability of successfully modeling with material parameters different from those on the full-scale model.

PLANAR MEDIUM

Let us consider first the planar medium at normal incidence consisting of N layers, each homogeneous in ϵ and/or μ , backed by a perfectly conducting plane sheet. The reflection coefficient R is given by:¹

$$R = e^{j2Q} \quad (1)$$

where

$$Q = \tan^{-1} \left[\frac{Z_1}{Z_0} \tan(-K_1 t_1 + \tan^{-1} \left[\frac{Z_2}{Z_1} \tan(-K_2 t_2 + \dots \dots + \tan^{-1} \left[\frac{Z_m}{Z_{m-1}} \tan(-K_m t_m + \dots \dots + \tan^{-1} \left[\frac{Z_N}{Z_{N-1}} \tan(-K_N t_N) \dots \dots \right] \right] \right] \right] \right], \quad (2)$$

$$Z_m = \sqrt{\frac{\mu_m}{\epsilon_m}}, \quad m=0, 1, 2, \dots, N$$

$$K_m = 2\pi f \sqrt{\mu_m \epsilon_m},$$

f operating frequency,

μ_m complex permeability of the m^{th} layer,
 ϵ_m complex permittivity of the m^{th} layer, and
 t_m thickness of the m^{th} layer.

Now let the superscript "s" relate to the model scale parameters. The standard scaling criteria for a scale model frequency f^s such that $f = pf^s$ requires:

$$\mu_m^s = \mu_m, \quad \epsilon_m^s = \epsilon_m, \quad \text{and} \quad t^s = pt.$$

Basically, to satisfy equation (2), it is merely required that

$$K_m^s t_m^s = K_m t_m, \quad \text{and} \quad (3)$$

$$\frac{Z_m^s}{Z_{m-1}^s} = \frac{Z_m}{Z_{m-1}} \quad (4)$$

throughout.

Now assume that it is possible to obtain materials such that

$$\frac{\mu_m^s}{\mu_m} = q_1 \quad \text{and} \quad \frac{\epsilon_m^s}{\epsilon_m} = q_2,$$

with q_1 and q_2 real positive numbers, it is readily seen that

1. If $q_1 = q_2 = q$ and $f = pf^s$, then

$$t_m^s = \frac{pt_m}{q}, \quad \mu_m^s = q\mu_m, \quad \text{and} \quad \epsilon_m^s = q\epsilon_m$$

will give an exact scale model at the frequency f^s .

2. If $q_1 \neq q_2$ and $f = pf^s$, then

$$t_m^s = \frac{pt_m}{\sqrt{q_1 q_2}}, \quad \mu_m^s = q_1 \mu_m, \quad \epsilon_m^s = q_2 \epsilon_m$$

and $Z_o^s = \sqrt{\frac{q_1 \mu_o}{q_2 \epsilon_o}}$ will satisfy equation (2).

This then requires that the model be immersed in a medium having a permeability $q_1 \mu_0$ and a permittivity $q_2 \epsilon_0$. If, however, ϵ_m^s can be chosen such that $q_2 > q_1$, immersing the model in a medium with permeability μ_0 and permittivity $q_2 \epsilon_0 / q_1$ will satisfy equation (2). This therefore requires for example that the antenna and the model be immersed in an anechoic chamber filled with a suitable substance having a relative permeability q_2 / q_1 .

CYLINDRICAL MEDIUM

It is of interest to examine the scaling conditions developed for the planar medium as they apply to the infinite cylindrical medium. For the sake of brevity, the discussion will be restricted to normal incidence and the electric vector parallel to the plane of incidence. The normalized radar cross section S is given by

$$S = \frac{2}{\pi^2 R_0^2 f \sqrt{\mu_0 \epsilon_0}} \left| \sum_{-\infty}^{\infty} (-1)^n C_n^0 \right|^2 \quad (5)$$

Now for M homogeneous concentric layers C_n^0 is obtained from the following recursive relationship:²

$$\left[\frac{C_n^{m-1} H_n^{(2)}(K_{m-1} R_{m-1}) + H_n^{(1)}(K_{m-1} R_{m-1})}{C_n^{m-1} H_n^{(2)'}(K_{m-1} R_{m-1}) + H_n^{(1)'}(K_{m-1} R_{m-1})} \right] = \quad (6)$$

$$\frac{Z_m}{Z_{m-1}} \left[\frac{C_n^m H_n^{(2)}(K_m R_{m-1}) + H_n^{(1)}(K_m R_{m-1})}{C_n^m H_n^{(2)'}(K_m R_{m-1}) + H_n^{(1)'}(K_m R_{m-1})} \right]$$

where

$$m = 0, 1, 2, \dots, M \text{ relates to the } m^{\text{th}} \text{ layer with } 0 \text{ relating to free space.}$$

$$K_m = 2\pi f \sqrt{\mu_m \epsilon_m}$$

$$Z_m = \sqrt{\frac{\mu_m}{\epsilon_m}}$$

R_m radius of the boundaries of the layers with R_o , the total radius, and R_M , the radius of the cylindrical perfectly conducting core, and μ_m , ϵ_m and f as previously defined.

Now for $m = M$

$$C_n^M = - \frac{H_n^{(1)}(K_M R_M)}{H_n^{(2)}(K_M R_M)}, \quad (7)$$

hence, starting at the metallic core and applying equation (7), C_n^{M-1} is obtained, then C_n^{M-2} , etc. to C_n^1 , with C_n^0 finally obtained from the following relationship:

$$\frac{J_n(K_o R_o) + C_n^0 H_n^{(2)}(K_o R_o)}{J_n'(K_o R_o) + C_n^0 H_n^{(2)'}(K_o R_o)} = \quad (8)$$

$$\frac{Z_1 \left[\frac{C_n^1 H_n^{(2)}(K_1 R_o) + H_n^{(1)}(K_1 R_o)}{C_n^1 H_n^{(2)'}(K_1 R_o) + H_n^{(1)'}(K_1 R_o)} \right]}{Z_o}$$

Here again the classical scaling criteria for $f = pf^s$ requires that:

$$\mu_m^s = \mu_m, \quad \epsilon_m^s = \epsilon_m, \quad \text{and} \quad R_m^s = pR_m$$

and hence equation (5) is satisfied.

Now let $\mu_m^s = q_1 \mu_m$ and $\epsilon_m^s = q_2 \epsilon_m$ and $f = pf^s$ for the case

1. $q_1 = q_2 = q$,
 C_n^M to C_n^1 are satisfied by:

$$\mu_m^s = q \mu_m, \quad \epsilon_m^s = q \epsilon_m, \quad \text{and} \quad R_m^s = pR_m / q.$$

However, equation (8), relating C_n^1 to C_n^0 is not satisfied unless $\mu_0 \epsilon_0$ is replaced by $\mu_0 \epsilon_0 q_1^2$ to satisfy the requirement that $R_0^s = pR_0/q$. This, unlike the planar medium for this case, requires immersion in a medium with permittivity or permeability p times that of free space.

2. $q_1 \neq q_2$
 C_n^M to C_n^1 are satisfied by:

$$\mu_m^s = q_1 \mu_m, \epsilon_m^s = q_2 \epsilon_m, \text{ and } R_m^s = pR_m / \sqrt{q_1 q_2}.$$

Here again, to satisfy equation (8), it is required that $\mu_0 \epsilon_0$ be replaced by $q_1 \mu_0 q_2 \epsilon_0$ and for $q_2 < q_1$ the immersing medium could consist of a relative permittivity $q_2/q_1 > 1.0$.

Although this discussion has been restricted to normal incidence, it is readily shown that these results also apply to oblique incidence by demonstrating that the scaled parameters satisfy the scattering coefficients and hence the scattered field.

CONCLUSIONS

In the event that the complex permeability and complex permittivity of materials on a full scale model cannot be satisfactorily reproduced at the higher model frequency, it may be possible to scale lossy materials provided one can obtain a magnetic material having approximately the same $\tan \delta$ of the scale model frequency as at the full scale and can properly adjust the dielectric loading to satisfy the scaling criteria given above.

BIBLIOGRAPHY

1. Thomas, A. S. Theory of Graded Dielectric Radar Absorber Materials (U), Quarterly Engineering Report No. 5, A. S. Thomas, Inc., Contract AF33(616)-7185 July 1961 (CONFIDENTIAL).

2. "Feasibility Studies in Connection with the Camouflage of the ICBM Re-Entry Vehicle" (U), A. S. Thomas, Inc. Final Report M58-2 under Subcontract AD157-S to AVCO Corp., under Prime Contract AF04(647)-305, 26 January 1960 (SECRET)
3. Wait, James, R., "Electromagnetic Radiation from Sources On and Near Cylindrical Surfaces" National Bureau of Standards, Report 5553, January 15, 1958.